



Les rôles de Te, As, Bi, Sb et Sn (TABS) lors de la formation des gisements d'éléments du groupe du platine

par Eduardo Mansur

**Thèse présentée à l'Université du Québec à Chicoutimi en vue de l'obtention du grade de
Docteur (Ph.D.) en Sciences de la Terre et de l'atmosphère**

Québec, Canada

© Eduardo Mansur, 2020

RÉSUMÉ

Les processus requis pour former un gisement magmatique à sulfures de Ni-Cu et éléments du groupe du platine (EGP) comprennent: la saturation d'un magma mafique ou ultramafique avec un liquide sulfure de métal de base; interaction du liquide sulfuré avec le magma mafique; cristallisation d'une solution solide de monosulfure (*MSS*), d'une solution solide intermédiaire (*ISS*) et éventuellement de minéraux du groupe du platine (*MGP*) à partir du liquide sulfuré; exsolution de *MSS* et *ISS* pour former des sulfures de métaux de base (*SMB*) et *MGP*; et modification des *SMB* par des fluides magmatiques tardifs ou métamorphiques. Indépendamment des processus impliqués au cours de la genèse, dans la plupart des dépôts de sulfures magmatiques, les EGP sont trouvés généralement dans la structure des *SMB*, ou sous la forme de *MGP*. Ces *MGP* consistent principalement en la combinaison de EGP avec au moins un des éléments Te, As, Bi, Sb et Sn (*TABS*). Par conséquent, l'association fréquente des EGP avec les *TABS* amène à la question principale de ce projet: quel est le rôle de *TABS* lors de la formation des gisements de EGP?

Les rôles suggérés pour *TABS* lors de la formation de dépôts de sulfures magmatiques sont:

- i) La présence des concentrations élevées de *TABS* provoque la cristallisation directe des *MGP* à partir d'un magma silicaté;
- ii) Le liquide sulfuré pourrait devenir saturé dans un liquide immiscible riche en *TABS*, qui collecte des EGP, et les *MGP* pourraient cristalliser à partir de ce liquide;
- iii) Des concentrations progressivement plus élevées de *TABS* dans le liquide sulfuré pourraient amener à la cristallisation directe des *MGP*.

iv) Pendant le refroidissement, les EGP peuvent se combiner avec les TABS et se dissolvé sous la forme des MGP à partir des SMB.

v) Les TABS peuvent soit être remobilisés avec le EGP pendant l'altération post-magmatique, ou soit agir comme des agents de fixation des EGP pendant la remobilisation tardive.

Une partie du problème dans l'étude des TABS est que ces éléments ne sont pas systématiquement déterminés dans les analyses de roche en totale ou dans les minéraux. La très faible concentration de TABS, combinée à leur volatilité, a conduit à les négliger au cours des dernières décennies. Par conséquent, la première étape du projet a été de mettre en place une routine analytique pour déterminer les TABS dans la roche totale à de faibles concentrations, en utilisant la spectroscopie de fluorescence atomique couplée à un générateur d'hydrure (*HG-AFS*).

À la suite du développement analytique, les concentrations de TABS dans la roche totale, les SMB et les minéraux silicatés ont été mesurées dans des échantillons provenant: i) du district minier de Noril'sk-Talnakh; ii) les gisements de type *PGE-reef* des complexes du Bushveld et Stillwater (*Merensky Reef, J-M Reef et Picket Pin*); iii) des horizons stériles en EGP localisés à l'extérieur des intervalles minéralisés des complexes du Bushveld et Stillwater et; iv) la *Marginal Zone* du complexe du Bushveld. Les échantillons du district minier de Noril'sk-Talnakh comprennent des sulfures massifs, ce qui a permis d'étudier le comportement des TABS lors de la cristallisation fractionnée du liquide sulfuré. Par contre, les échantillons des *Reefs* de EGP des complexes du Bushveld et Stillwater contiennent des sulfures disséminés, ce qui a permis d'étudier la distribution de TABS dans les minerais qui ont subi une cristallisation à l'équilibre. Les échantillons de la *Marginal Zone* du complexe du Bushveld ont permis de déterminer la concentration de TABS dans les liquides initiaux

qui ont cristallisé cette intrusion, ainsi que les processus qui ont affecté la distribution de TABS dans ces liquides.

Pendant la cristallisation fractionnée du liquide sulfuré, les TABS (avec Pt et Pd) sont incompatibles dans le *MSS* et *ISS*, et restent dans le dernier liquide sulfuré, plus fractionné. Bien que les concentrations de TABS n'atteignent pas des niveaux suffisamment élevés pour qu'un liquide immiscible riche en TABS se forme, elles se combinent avec Pd et Pt et cristallisent sous la forme des MGP, directement à partir du liquide sulfuré fractionné. D'un autre côté, les minerais formés par cristallisation à l'équilibre, tels que les *Reefs* à EGP des complexes du Bushveld et Stillwater, enregistrent l'effet de l'exsolution des MGP à partir des SMB. Dans ces cas, des concentrations élevées des EGP dans les SMB ont créé un potentiel chimique pour l'exsolution des MGP. Par conséquent, les EGP ont combiné avec les TABS et ont exsolvé sous la forme des MGP. Par conséquent, le SMB trouvé dans les *Reefs* sont épuisé dans TABS par rapport au SMB trouvé dans des échantillons provenant de l'extérieur des *Reefs*.

Les résultats obtenus pour les TABS dans les liquides initiaux qui ont cristallisé le complexe du Bushveld (*Marginal Zone*) ont montré que leur distribution dépend en grande partie de leur comportement chalcophile. Le Te et le Se sont des éléments fortement chalcophiles, et leur distribution est principalement contrôlée par les sulfures. Par contre, As et Sb ne sont que des éléments légèrement chalcophiles, et leur distribution est principalement contrôlée par le degré de cristallisation fractionnée et l'assimilation crustale des magmas. Le Bi est modérément chalcophile et sa distribution résulte d'une combinaison des processus susmentionnés.

ABSTRACT

Processes required to form magmatic sulfide Ni-Cu and platinum-group element (PGE) deposits include: saturation of a mafic or ultramafic magma with a base metal sulfide liquid; interaction of the sulfide liquid with the mafic magma; crystallization of monosulfide solid solution (MSS), intermediate solid solution (ISS) and possibly platinum-group minerals (PGM) from the sulfide liquid; exsolution of MSS and ISS to form base metal sulfides and PGM; and modification of the magmatic BMS by late magmatic or metamorphic fluids. However, regardless of the processes involved during the genesis, at most magmatic sulfide deposits the PGE generally occur within BMS structure, or as discrete PGM. These PGM mainly consist on the bounding of PGE with at least one of the elements Te, As, Bi, Sb and Sn (TABS). Therefore, the frequent association of PGE with TABS leads to the main question of this project: what is the role of TABS during the formation of PGE deposits?

Suggested roles for TABS during the formation of magmatic sulfide deposits are:

- i) The presence of high concentrations of TABS leads to direct crystallization of PGM from silicate magma;
- ii) The sulfide liquid could become saturated in an immiscible TABS-rich liquid, which collects PGE, and PGM could further crystallize from this liquid;
- iii) Progressively higher concentrations of TABS in the sulfide liquid could lead to the direct crystallization of PGM.
- iv) Upon cooling PGE may combine with TABS and exsolve as PGM from BMS.
- v) TABS may either be remobilized together with PGE during post-magmatic alteration, or alternatively, act as fixing agents for PGE during late remobilization.

Part of the problem in studying TABS is that these elements are not routinely determined in whole rock or mineral analyses. The very low concentration of TABS, combined with their volatility, has resulted in them being neglected over the past decades. Therefore, the first step of

the project was to implement an analytical routine to determine TABS in whole-rock at low concentrations, using hydride generation-atomic fluorescence spectrometry (HG-AFS).

Following the analytical development, concentrations of TABS in whole-rocks, BMS and silicate minerals were measured in samples from: i) the Noril'sk-Talnakh mining district; ii) the PGE-reef type deposits of the Bushveld and Stillwater Complexes (Merensky Reef, J-M Reef and Picket Pin deposit); iii) PGE-barren horizons from outside the reef intervals of the Bushveld and Stillwater Complexes and; iv) the Marginal Zone of the Bushveld Complex. The samples from the Noril'sk-Talnakh mining district comprise massive sulfide ores, which allowed investigating the behaviour of TABS during fractional crystallization of the sulfide liquid. In contrast, samples from the PGE-reefs of the Bushveld and Stillwater Complexes contain disseminated sulfide minerals, which allowed investigating the distribution of TABS in ores that underwent predominantly equilibrium crystallization. Finally, the samples from the Marginal Zone of the Bushveld Complex allowed constraining the concentration of TABS in the initial liquids that crystallized this intrusion, and also which processes affected the distribution of TABS in initial liquids.

During fractional crystallization of the sulfide liquid, TABS (together with Pt and Pd) are incompatible into the crystallizing MSS and ISS, and remain in the lattermost fractionated sulfide liquid. Although concentrations of TABS do not reach sufficiently high levels for an immiscible TABS-rich liquid to segregate, they combine with Pd and Pt and crystallize as composite PGM, directly from the fractionated sulfide liquid. On the other hand, ores formed by equilibrium crystallization, such as the PGE reefs of the Bushveld and Stillwater Complexes, record the effect of PGM exsolution from BMS. In these cases, high PGE concentrations in BMS created a chemical potential for the exsolution of PGM. Therefore, PGE combined with TABS and exsolved as PGM. Consequently, the BMS found within the PGE reefs are depleted in TABS relative to the BMS found in samples from outside the reef intervals.

The results for TABS in the initial liquids that crystallized the Bushveld Complex (Marginal Zone) revealed that their distribution largely relies on their chalcophile behaviour. Tellurium and Selenium are strongly to highly chalcophile elements, and their distribution is

mainly controlled by sulfide minerals. In contrast, As and Sb are only slightly chalcophile elements, and their distribution is mainly controlled by the degree of fractional crystallization, and crustal assimilation of the magmas. Bismuth is moderately chalcophile, and its distribution results from a combination of the aforementioned processes.

TABLE DES MATIÈRES

RÉSUMÉ	i
ABSTRACT	iv
Chapitre 1 - Introduction, problème et méthodologie	1
1.1 - Introduction.....	2
1.2 – Problème	5
1.2.1 – Cycle géochimique des TABS	5
1.2.2 – La formation des gisements de sulfures magmatiques	8
1.2.3 – Hypothèses	14
1.3 – Objectifs	22
1.4 – Zones d'étude.....	24
1.4.1 – Le district minier de Noril'sk-Talnakh.....	24
1.4.2 – Le complexe du Bushveld.....	26
1.4.3 – Le complexe de Stillwater.....	29
1.5 – Méthodologie	31
1.5.1 – Fluorescence atomique couplée à un générateur d'hydrure (<i>HG-AFS</i>).....	31
1.5.2 - Microscope électronique à balayage.....	32
1.5.3 – Ablation laser et spectroscopie de masse (<i>LA-ICP-MS</i>).....	32
1.6 – Format de la thèse	33
1.7 - Références.....	36
Chapter 2 - Determination of Te, As, Bi, Sb and Se (TABs) in Geological Reference Materials and GeoPT Proficiency Test Materials by Hydride Generation-Atomic Fluorescence Spectrometry (HG-AFS)	2
2.1 - Abstract.....	3
2.2 – Introduction	4
2.3 – Experimental	6
2.3.1 - Digestion of the rock samples.....	6
2.3.2 - Preparation of analytical solutions.....	6
2.3.3 - Instrumentation	7
2.3.4 - Calibration.....	8
2.3.5 - Detection limits of the method.....	8
2.4 – Results and Discussion.....	9
2.4.1 – Precision and accuracy based on geological reference materials.....	9
2.4.2 – IAG GeoPT Proficiency Test Samples.....	17

2.4.3 - Variability of TABS values in GeoPT Proficiency Test Results	27
2.5 – Conclusion.....	29
2.6 - Acknowledgements.....	30
2.7 - References.....	31
Chapter 3 - Distribution of chalcophile and platinum-group elements among pyrrhotite, pentlandite, chalcopyrite and cubanite from the Noril'sk-Talnakh ores: implications for the formation of platinum-group minerals	42
3.1 - Abstract.....	43
3.2 - Introduction.....	44
3.3 - Methodology.....	46
3.3.1 - Sample selection	46
3.3.2 - Scanning electron microscope and laser ablation-inductively coupled plasma-mass spectrometry	47
3.4 - Results.....	49
3.4.1 - Distribution of chalcophile elements among the base-metal sulfides	51
3.4.2 - Partition coefficients between base-metal sulfides	55
3.4.3 - Mass balance.....	58
3.5 - Discussion.....	60
3.5.1 - Variations in chalcophile element content of the minerals with fractional crystallization	60
3.5.2 - Timing of PGM formation	62
3.5.3 - Fractional crystallization of massive sulfides and constraints for the formation of platinum-group minerals	65
3.5.4 - Assessing the evolution of magmatic sulfide deposits via comparison of BMS compositions	68
3.6 - Conclusions.....	71
3.7 - Acknowledgments.....	72
3.8 - References.....	73
Chapter 4 - Textural and compositional evidence for the formation of pentlandite via peritectic reaction: Implications for the distribution of highly siderophile elements.....	83
4.1 - Abstract.....	84
4.2 – Introduction	85
4.3 - Textural occurrences of pentlandite.....	87
4.4 - Composition and distribution of trace elements in pentlandite.....	87
4.5 - Formation of pentlandite via peritectic reaction	90
4.6 - Implications for the incorporation of palladium into pentlandite	94
4.7 - Conclusions.....	94

4.7 - Acknowledgements.....	95
4.8 - References.....	96
Chapter 5 - Concentrations of Te, As, Bi, Sb and Se in the Marginal Zone of the Bushveld Complex: Evidence for crustal contamination and the nature of the magma that formed the Merensky Reef	99
5.1 - Abstract.....	100
5.2 – Introduction	101
5.3 – Geological Setting.....	103
5.4 – Sample description.....	105
5.5 – Analytical techniques	107
5.6 – Results	108
5.7 – Discussion	114
5.7.1 - Crustal contamination and the external addition of TABS	114
5.7.2 – Modelling the distribution of TABS in the Merensky Reef.....	117
5.7.3 – Constraints for the evolution of Bushveld magmas and formation of the Merensky Reef	121
5.7.4 – Implications for the formation of PGE deposits.....	124
5.8 – Conclusions.....	126
5.9 - Acknowledgements.....	127
5.10 - References.....	128
Chapter 6 - The role of Te, As, Bi, Sn and Sb during the formation of platinum-group-element reef deposits: Examples from the Bushveld and Stillwater Complexes	137
6.1 - Abstract.....	138
6.2 – Introduction.....	139
6.3 – Description of studied samples.....	142
6.3.1 – Bushveld Complex	142
6.3.2 – Stillwater Complex.....	145
6.4 – Analytical Methods	147
6.5 – Results	149
6.5.1 – Whole-rock concentrations of TABS in the PGE reefs.....	149
6.5.2 - Trace elements in BMS.....	156
6.5.3 – Mass balance	159
6.5.4 – Variations in PGE to TABS ratios in base metal sulfides	163
6.6 – Discussion	167
6.6.1 - Constrains for the formation of PGE pre-nucleation clusters	167
6.6.2 – The role of TABS during PGM exsolution	170

6.6.3 - External addition of TABS and the implications for the PGM formation	172
6.7 - Conclusions.....	174
6.8 - Acknowledgements.....	175
6.9 - References.....	176
Chapitre 7 – Synthèse et remarques finales	189
7.1 – Introduction.....	190
7.2 – Synthèse des résultats.....	190
7.2.1 – Améliorations analytiques pour déterminer TABS dans les matériaux géologiques	190
7.2.2 – L'histoire de cristallisation d'un liquide sulfuré immiscible	191
7.2.3 – Rôle de TABS lors de la cristallisation fractionnée du liquide sulfuré	192
7.2.4 – Rôle des TABS pendant l'exsolution des MGP.....	193
7.2.5 – La concentration de TABS dans les magmas initiaux qui forment des gisements de EGP	194
7.3 – Contribution au débat actuel	194
7.4 – Future investigations	195
7.5 – Références	197

LISTE DES FIGURES

CHAPITRE 1

- Figure 1.1** - Matières premières critiques indiquées par la Commission européenne en 2013... **3**
- Figure 1.2** - Concentrations TABS et Se normalisées au manteau primitif dans le noyau, les basaltes komatiitiques, le MORB moyen et la croûte continentale moyenne. **6**
- Figure 1.3** - Modèles schématiques illustrant l'histoire de la formation et de la cristallisation d'un gisement de sulfure magmatique et la distribution des éléments chalcophiles..... **10**
- Figure 1.4** - Coefficients de partage entre un magma mafique et une liquide sulfuré. Les lignes verticales indiquent la plage de valeurs des essais menées à fO_2 entre -2 FMQ +2; Les traces horizontales indiquent des coefficients de partage entre le MORB et les gouttelettes de sulfure. Les TABS et Se sont mis en évidence pour référence. Données de Barnes et Ripley (2016), ainsi que Li et Audétat (2015). Figure modifiée de Barnes (2016). **12**
- Figure 1.5** - Images d'électrons rétrodiffusées des MGP aux marges des cristaux de chromite: (a) un grain d'alliage à Pt – Fe à la marge d'un cristal de chromite; (b) une laurite euhédrique (RuS₂) à la marge d'un cristal de chromite.. **15**
- Figure 1.6** - Variation de la concentration de platine dans le magma silicaté en fonction de la fugacité en oxygène pour les expériences saturées en alliage à Pt-Fe (\pm As dans le magma silicaté), Pt-As fondu et sperrylite (PtAs₂).. **15**
- Figure 1.7** - Lumière réfléchie (a) et images d'électrons rétrodiffusées (b) de produits expérimentaux de Cafagna et Jugo (2016) illustrant la présence d'un liquide immiscible riche en métalloïdes (TABS).. **17**
- Figure 1.8** - Images électroniques rétrodiffusées de grains composites de MGP provenant des gisements McCreedy East, Sudbury et Talnakh, district de Noril'sk..... **19**
- Figure 1.9** - Images électroniques rétrodiffusées des grains de MGP allongés et inclus dans les SMB du (a) district de Noril'sk-Talnakh, (b) gisement Creighton, Sudbury, (c) Merensky Reef et (d) Platreef, Complex du Bushveld. **20**
- Figure 1.10** - Coefficients de partage fluide / roche calculés en divisant les concentrations d'éléments dans les inclusions fluides (FI) par leur concentration dans les résidus mafiques dans les expériences de Guo et Audétat (2017)..... **22**

Figure 1.11 - Carte géologique simplifiée de la région de Noril'sk montrant les projections de surface des intrusions minéralisées et la section stratigraphique idéalisée montrant les emplacements des intrusions minéralisées dans la séquence de la stratigraphie.	26
Figure 1.12 - Carte géologique simplifiée du complexe du Bushveld et carte stratigraphique de la Rustenburg Layered Suite.	27
Figure 1.13 - Échantillon macroscopique du Merensky Reef et diagramme stratigraphique schématique illustrant les variations lithologiques à travers le Reef. L'échantillon provient de Rustenburg Platinum Mine. Modifié à partir de Godel et al. (2007).	28
Figure 1.14 - Échantillon macroscopique du Merensky Reef et diagramme stratigraphique schématique illustrant les variations lithologiques à travers le Reef.....	30

CHAPTER 2

Figure 2.1 - Schematic flow diagram showing the main preparation steps for reagents and aliquots.....	11
Figure 2.2 - Comparison of new HG-AFS determinations and literature values for (a) Sb, (b) Se, (c) As, (d) Bi and (e) Te	18
Figure 2.3 - Comparison of new HG-AFS determinations with assigned and provisional values from GeoPT reports and median values of GeoPT proficiency test materials for (a) Sb, (b) Bi, (c) As, (d) Se and (e) Te.....	25
Figure 2.4 - Comparison of new determinations and all previously reported results by other laboratories for GeoPT	28

CHAPTER 3

Figure 3.1 - Reflected light photomicrographs of representative textures of main massive sulfides from Noril'sk-Talnakh mining district, and backscattered electron images of platinum-group minerals in Cu-poor and Cu-rich ores.....	50
Figure 3.2 - LA-ICP-MS elemental maps showing the distribution of chalcophile elements in chalcopyrite and pentlandite exsolution lamellae in pyrrhotite from Cu-poor massive sulfides..	52

Figure 3.3 - LA–ICP–MS elemental maps showing the distribution of chalcophile elements in cubanite exsolution lamellae in chalcopyrite from Cu-rich massive sulfides.	53
Figure 3.4 - LA–ICP–MS elemental maps showing the distribution of chalcophile elements among pyrrhotite, pentlandite, chalcopyrite and troilite, in Cu-poor massive sulfide.	54
Figure 3.5 - LA–ICP–MS elemental maps showing the distribution of Ag, Bi, Cd, Pb, Te and Tl among galena, pyrrhotite, pentlandite, chalcopyrite and magnetite, in Cu-rich massive sulfide.....	55
Figure 3.6 - Plots of median partition coefficients of each trace element between a) pentlandite and pyrrhotite, b) pentlandite and chalcopyrite, c) chalcopyrite and pyrrhotite, and d) chalcopyrite and cubanite.....	57
Figure 3.7 - Average proportion of each element hosted in pyrrhotite, pentlandite, chalcopyrite, cubanite and sum, from the a) Cu-poor and Transitional, b) Cu-rich and c) Cu-rich (with cubanite) ores of the Noril’sk-Talnakh mining district.....	59
Figure 3.8 - Binary plots of Rh (a), Os (b), Re (c), Ru (d), Zn (e and m), Bi (f), Sn (g), Pb (h), Pd (i), Se (j), Te (k), In (l), Cd (n) and Ag (o) median concentrations (ppm) in pyrrhotite, chalcopyrite and pentlandite versus (Pt+Pd)/(Rh+Ru+Ir+Os) in whole-rock, for massive sulfides from Noril’sk I, Kharaelakh and Talnakh intrusions, and disseminated sulfides from the Noril’sk I intrusion.....	61
Figure 3.9 - Mantle-normalized Te, As, Bi, Sb and Sn (TABS) whole-rock concentrations of Cu-rich massive sulfides from McCreeedy East and Creighton deposits, and Noril’sk I and Kharaelakh intrusions.....	64
Figure 3.10 - Schematic models illustrating the crystallization history of massive sulfides from the Noril’sk-Talnakh mining district, and the processes controlling the distribution of PGE and other chalcophile elements.....	67
Figure 3.11 - Primitive mantle normalized multi-element diagrams of median compositions of pyrrhotite (a-b), pentlandite (c-d), chalcopyrite (e-f) and cubanite (g) in Cu-poor and Cu-rich ores from different deposits.....	70

CHAPTER 4

- Figure 4.1** - Reflected light images of pentlandite textures from the disseminated sulfides of the Merensky Reef of the Bushveld Complex (A), and massive sulfides of the Noril'sk-Talnakh mining district (B, C and D)..... **88**
- Figure 4.2** - LA-ICP-MS elemental maps showing the distribution of chalcophile elements in pentlandite and associated pyrrhotite and chalcopyrite..... **90**
- Figure 4.3** - Time-resolved analysis for the LA-ICP-MS lines indicated in Fig. 2B (A) and 2C (B) **92**
- Figure 4.4** - Schematic model illustrating the crystallization history of a sulfide liquid, and the formation of pentlandite via peritectic reaction. **93**

CHAPTER 5

- Figure 5.1** - Simplified geology of the Bushveld Complex and surrounding rocks, and location of samples utilized in this study. **104**
- Figure 5.2** - Photomicrographs of the marginal rocks **106**
- Figure 5.3** - Binary plots of Se vs S (a), Sb (b), As (c), Bi (d), and Te (e) vs Se, and As vs Sb (f) in samples from the Marginal Zone of the Bushveld Complex..... **109**
- Figure 5.4** - Mantle-normalized TABS diagrams for (a) B-1 rocks, (b) B-2 rocks and (c) B-3 rocks..... **112**
- Figure 5.5** - Mantle-normalized TABS diagrams for (a) B-1 rocks compositional field relative to komatiite, upper continental crust, and a AFC model of a mixture of a komatiite with 30% upper crust and 27% fractional crystallization; (b) B-2 and B-3 rocks compositional fields compared to komatiitic basalt and lower continental crust. **114**
- Figure 5.6** - Binary plots of As (a), Sb (b), Bi (c), Se and Te vs Hf in samples from the Marginal Zone, and Merensky Reef at the Impala and Rustenburg mines. **116**
- Figure 5.7** - Variations of Pd, Se, Te, Bi, As and Sb measured concentrations, and modeled contributions from cumulate sulfide liquid, trapped silicate liquid, and a mixture of both, with height across the Impala section..... **119**

Figure 5.8 - Variations of Pd, Se, Te, Bi, As and Sb measured concentrations, and modeled contributions from cumulate sulfide liquid, trapped silicate liquid, and a mixture of both, with height across the Rustenburg section..120

Figure 5.9 - Schematic models illustrating the evolution of Bushveld magmas and crystallization of the Merensky Reef interval.123

CHAPTER 6

Figure 6.1 - a) Geology of the western lobe and generalized stratigraphy of the Bushveld Complex, Republic of South Africa. b) Geology and generalized stratigraphy of the Stillwater Complex.143

Figure 6.2 - Types (a) and textural association (b) of platinum-group minerals found in the Merensky Reef at the Impala and Rustenburg platinum mines, and the J-M Reef at the East Boulder Mine.146

Figure 6.3 - Variations in whole-rock concentrations of chalcophile elements with height across the (a) Impala section and (b) Rustenburg section.151

Figure 6.4 - Plots of (a) Se, (b) Te, (c) Bi, (d) As and (e) Sb vs S in whole rock.....153

Figure 6.5 - Plots of (a) As and (b) Sb vs Hf in whole rock.154

Figure 6.6 - Plots of (a) As vs Sb, (b) Hf vs As, (c) Hf vs Sb, and (d) Ba, (e) TiO₂ and (f)Cr₂O₃ vs As in K-phlogopite.....155

Figure 6.7 - LA-ICP-MS elemental maps showing the distribution of chalcophile elements among pyrrhotite, pentlandite and chalcopyrite, in disseminated sulfide from the Merensky Reef at the Impala section.....157

Figure 6.8 - LA-ICP-MS elemental maps showing the distribution of chalcophile elements among pyrrhotite, pentlandite and chalcopyrite, in disseminated sulfide from the Merensky Reef at the Rustenburg section..158

Figure 6.9 - LA-ICP-MS elemental maps showing the distribution of chalcophile elements among pyrrhotite, pentlandite and chalcopyrite, in disseminated sulfide from the J-M Reef at the Stillwater mine.159

Figure 6.10 - Average proportion of each element hosted in pyrrhotite, pentlandite, chalcopyrite and phlogopite from the Rustenburg (a and b), and Impala (c, d and e) sections of the Bushveld Complex.	161
Figure 6.11 - Average proportion of each element hosted in pyrrhotite, pentlandite and chalcopyrite from the J-M Reef at the East Boulder (a), and Stillwater (b) mines, and the Banded Series (c) of the Stillwater Complex.	162
Figure 6.12 - Plots of Te, As, Bi, Sb and Sn vs Pt+Pd and Rh+Ru+Ir+Os in pentlandite from samples of the Bushveld Complex.	164
Figure 6.13 - Plots of Te, As, Bi, Sb and Sn vs Pt+Pd and Rh+Ru+Ir+Os in pentlandite from samples of the Stillwater Complex.....	165
Figure 6.14 - Variations in median concentrations of Pt, Pd, Rh, Ru, Ir, Os, Te, As, Bi, Sb and Sn in pentlandite, pyrrhotite and chalcopyrite with height across the Impala section.	166
Figure 6.15 - Schematic models illustrating the crystallization history of sulfide liquid in the reef samples, and the potential importance of TABS for stabilizing PGE nanoclusters, and consequently form PGM.	169
Figure 6.16 - Schematic models illustrating the crystallization history of sulfide liquid in the reef samples, and the formation of PGM by exsolution from the BMS upon cooling.....	171

LISTE DES TABLEAUX

CHAPITRE 1

Tableau 1.1 - Concentration moyenne de TABS (ppm) dans le noyau, le manteau primitif, les basaltes komatiitiques, le MORB et la croûte continentale, leurs coefficients de partage entre les liquides sulfurés et les liquides silicatés, et les températures de condensation.....**6**

CHAPTER 2

Table 2.1 - Te, As, Bi, Sb and Se results for geological reference materials by HG-AFS.....**62**

Table 2.2 - Te, As, Bi, Sb and Se results for geological reference materials by HG-AFS using different samples weights.....**63**

Table 2.3 - Te, As, Bi, Sb and Se results for GeoPT proficiency test samples by HG-AFS....**69**

Table 2.4 - Assigned, provisional and median values for GeoPT proficiency test samples.....**74**

CHAPTER 3

Table 3.1 - Median concentrations (in ppm) of chalcophile elements in base-metal sulfides from different intrusions and ores from the Noril'sk-Talnakh mining district.....**106**

CHAPTER 5

Table 5.1 - Concentrations of As, Bi, S, Sb, Se and Te, and Se/Te and S/Se ratios in the Marginal Zone rocks of the Bushveld Complex.....**160**

Table 5.2 – Modelling of distribution of TABS, Se and Pd in the Merensky Reef at Impala and Rustenburg sections.....**163**

LISTE DES ANNEXES

ANNEXE 1 - Complete dataset for Te, As, Bi, Sb and Se results for international reference materials, and GeoPt proficiency test samples, obtained by HG-AFS.....	253
ANNEXE 2 - Whole-rock compositions of the samples from the Noril'sk-Talnakh mining district.	258
ANNEXE 3 – Analyses of reference materials used in the calibration of the LA-ICP-MS and in-house reference materials used to monitor the data quality for results from the Noril'sk-Talnakh mining district.....	261
ANNEXE 4 - Complete data set of SEM-EDS and LA-ICP-MS analyses of pyrrhotite obtained for the Noril'sk-Talnakh mining district and median values for each sample.....	264
ANNEXE 5 - Complete data set of SEM-EDS and LA-ICP-MS analyses of pentlandite obtained for the Noril'sk-Talnakh mining district and median values for each sample.....	273
ANNEXE 6 - Complete data set of SEM-EDS and LA-ICP-MS analyses of chalcopyrite obtained for the Noril'sk-Talnakh mining district and median values for each sample.....	282
ANNEXE 7 - Complete data set of SEM-EDS and LA-ICP-MS analyses of cubanite obtained for the Noril'sk-Talnakh mining district and median values for each sample.....	295
ANNEXE 8 - Partition coefficients of elements between pentlandite and pyrrhotite, Pn and chalcopyrite, Ccp and Po, and Ccp and cubanite calculated for each sample from the Noril'sk-Talnakh mining district.....	298
ANNEXE 9 - Average proportion (%) of each element hosted in pyrrhotite, pentlandite, chalcopyrite, cubanite and sum, from the Cu-poor and Transitional, Cu-rich and Cu-rich (with cubanite) ores of the Noril'sk-Talnakh mining district.....	313
ANNEXE 10 - Analyses of reference materials used to monitor the data quality for whole-rock TABS and Se results from the Marginal Zone of the Bushveld Complex.....	315
ANNEXE 11 - Complete dataset of whole-rock TABS and Se analyses of samples from the Marginal Zone of the Bushveld Complex obtained in this study, and results previously reported by Barnes and Maier (2002) and Barnes et al. (2009; 2010) used for comparison.....	317

ANNEXE 12 - Modelling of the distribution of TABS, Se and Pd in the Merensky Reef at the Impala and Rustenburg sections.....	321
ANNEXE 13 - Analyses of reference materials used to monitor the data quality for whole-rock TABS and Se results from the Merensky Reef and J-M Reef of the Bushveld and Stillwater Complexes.....	326
ANNEXE 14 - Analyses of reference materials used in the calibration of the LA-ICP-MS and in-house reference materials used to monitor the data quality for analyses of sulfide minerals and phlogopite from the Bushveld and Stillwater Complexes.....	328
ANNEXE 15 - Complete dataset of whole-rock TABS and Se analyses of samples from the Bushveld and Stillwater Complexes obtained in this study, and results previously reported by Barnes and Maier (2002), Godel et al. (2007), Godel and Barnes (2008) and Barnes et al. (2020) used for comparison.....	335
ANNEXE 16 - Complete data set of LA-ICP-MS analyses of K-Phlogopite obtained in this study for the Merensky Reef at the Impala mine.....	340
ANNEXE 17 - Complete data set of LA-ICP-MS analyses of pyrrhotite obtained in this study and median values for each sample from the Bushveld and Stillwater Complexes.....	344
ANNEXE 18 - Complete data set of LA-ICP-MS analyses of pentlandite obtained in this study and median values for each sample from the Bushveld and Stillwater Complexes.....	367
ANNEXE 19 - Complete data set of LA-ICP-MS analyses of chalcopyrite obtained in this study and median values for each sample from the Bushveld and Stillwater Complexes.....	390
ANNEXE 20 - Average proportion (%) of each element hosted in pyrrhotite, pentlandite, chalcopyrite, phlogopite and sum, from different localities of the Bushveld and Stillwater Complexes.....	413

1
2
3
4
5
6
7
8
9
10
11
12
13
14
15
16
17
18
19
20
21
22
23
24
25

Chapitre 1 - Introduction, problème et méthodologie

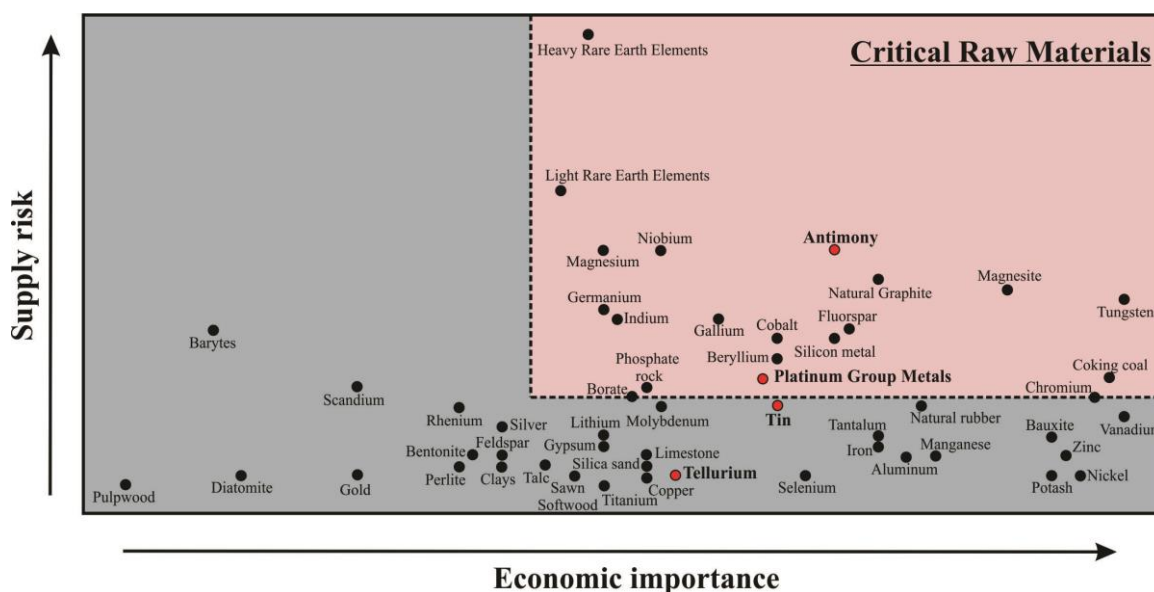
26 **1.1 - Introduction**

27

28 Les éléments critiques et les matières premières critiques sont définis comme des
29 ressources d'importance économique qui présentent un risque lié à leur approvisionnement
30 (European Commission, 2014). Ces ressources sont généralement utilisées dans le
31 développement de technologies durables. Des études récentes ont présenté une liste de
32 matières premières (Fig. 1.1) qui sont essentielles pour de nombreuses technologies
33 émergentes (European Commission, 2010 et 2014). Parmi ces matériaux critiques figurent
34 les éléments du groupe du platine (EGP) et les éléments appelés TABS (Te, As, Bi, Sb et
35 Sn; Barnes, 2016). Bien que certains ne soient pas indiqués comme étant une matière
36 première critique dans ces études, ils ont une importance économique significative (Fig.
37 1.1). D'autres études soulignent également que certains des TABS sont essentiels au
38 développement de technologies énergétiques à faible émission de carbone (Zweibel, 2010;
39 Moss et al., 2013). La production de ces éléments et matériaux est souvent limitée à la
40 production de sous-produits de l'extraction des métaux de base (USGS, 2020). Étant donné
41 que le développement récent de sources d'énergie durables accroît la demande pour ces
42 éléments essentiels, il est très intéressant de comprendre leur distribution dans les différents
43 réservoirs terrestres.

44 Les TABS sont aussi étudiés en raison du risque qu'ils présentent pour l'environnement
45 (notamment As et Sb). Diverses études ont mis en évidence plusieurs zones sensibles à la
46 contamination par l'antimoine et l'arsenic (par exemple, le sol, les eaux de surface et
47 souterraines; Singh et al., 2015; Jamieson, 2016). Par conséquent, l'intérêt pour la surveillance
48 de ces éléments pendant les opérations minières et la récupération des zones contaminées a
49 considérablement augmenté au cours des dernières années (Jamieson, 2016 et références y
50 contenues). Ce problème a également conduit les agences gouvernementales à développer des
51 routines analytiques pour contrôler la concentration de ces éléments dans les aliments (U.S
52 Food and Drug Administration, 2015).

53 Les EGP sont essentiels dans les industries de l'énergie durable, des catalyseurs
 54 automatiques et des bijoux (revue annuelle Johnson Matthey 2019). De nombreuses études
 55 ont révélé que les EGP sont généralement trouvés dans la structure des SMB (Barnes et
 56 Ripley, 2016 et références), ou sous forme de MGP. Ces MGP consistent principalement en
 57 la combinaison des EGP avec au moins un des TABS. Compte tenu de l'association
 58 fréquente de EGP avec TABS, une question majeure se pose: quel est le rôle des TABS
 59 lors de la formation des gisements de EGP?



60
 61 Figure 1.1 - Matières premières critiques indiquées par la Commission européenne en 2013. Les matières premières
 62 critiques sont indiquées comme celles ayant une importance économique élevée, associées à un risque
 63 d'approvisionnement élevé. Au total, 54 matériaux ont été étudiés et un groupe de 20 est indiqué comme critique.
 64 L'antimoine, l'étain, le tellure et des EGP sont mis en évidence. Données de la Commission européenne, 2014.

65
 66 Différents processus ont été proposés. Certaines études indiquent que les MGP
 67 cristallisent directement à partir du magma silicaté (Park et al., 2013; Maier et al., 2015; Barnes
 68 et al., 2016). D'autres que les MGP cristallisent à partir d'un liquide sulfuré immiscible (Barnes
 69 et al., 2006; Hutchinson et McDonald, 2008; Dare et al., 2010a et 2010b). Le liquide sulfuré
 70 pourrait devenir saturé dans une liquide immiscible riche en TABS, et les MGP pourraient
 71 cristalliser à partir de cette liquide (Hanley, 2007; Helmy et al. 2007, 2013; Holwell et
 72 McDonald 2007; Cafagna et Jugo, 2016; Sinyakova et al., 2017). Alternativement, les EGP

73 peuvent se combiner avec les TABS et exsolver comme MGP à partir des SMB (Prichard et al.,
74 2004; Godel et al., 2007; Barnes et al., 2008).

75 D'autres auteurs préfèrent une origine hydrothermale pour les gisements des EGP
76 (Boudreau et Meurer, 1999; Tuba et al., 2014). La mobilité des EGP et des TABS dans les
77 fluides magmatiques / hydrothermaux a été abordée dans des expériences récentes (Guo et
78 Audétat, 2017; Sullivan et al., 2018) et des études empiriques (Zelenski et al., 2013 et 2014;
79 Edmonds et al., 2018; Cox et al., 2019; Wiesener et al., 2020). Par contre, à des températures
80 plus basses, les TABS se sont révélés avoir une faible solubilité, et ils pourraient donc agir
81 comme agents de fixation pendant le transport hydrothermal des EGP (Wood, 2002). Le rôle
82 précis des TABS lors de la remobilisation des EGP est encore mal contraint.

83 Un problème majeur dans l'étude du rôle des TABS est leurs niveaux intrinsèquement
84 faibles dans les roches silicatées des gisements de EGP (Barnes et Ripley, 2016). Cependant, la
85 forte volatilité des TABS entrave les procédures analytiques courantes (Lodders, 2003). Par
86 conséquent, les concentrations de TABS dans les gisements de EGP sont limitées. Par
87 conséquent, le développement d'une routine analytique pour TABS dans les roches silicatées est
88 une partie essentielle de ce projet.

89 Afin d'explorer le rôle que jouent les TABS dans la minéralisation de EGP, des
90 échantillons des gisements des EGP dans des différents milieux géologiques ont été étudiés.
91 Les gisements sélectionnés sont: i) le district minier de Noril'sk-Talnakh ii) le Complexe du
92 Bushveld – *Merensky Reef*; iii) le Complexe du Stillwater - *John Manville Reef*. De plus, des
93 échantillons de la *Marginal Zone* du Complexe du Bushveld ont également été étudiés. Ces
94 derniers échantillons sont interprétés pour enregistrer la composition des magmas initiaux qui
95 ont cristallisé le Complexe du Bushveld. Par conséquent, ils permettent d'évaluer la distribution
96 de TABS dans les liquides qui ont cristallisé certains des gisements de EGP le plus bien étudiés
97 dans le monde. Dans l'ensemble, les caractéristiques générales des échantillons sélectionnés ont

98 fait l'objet d'études antérieures, qui fournissent une solide base géologique à la présente enquête.
99 Une brève revue de la littérature des concepts pertinents pour le projet est présentée comme suit.

100

101 **1.2 – Problème**

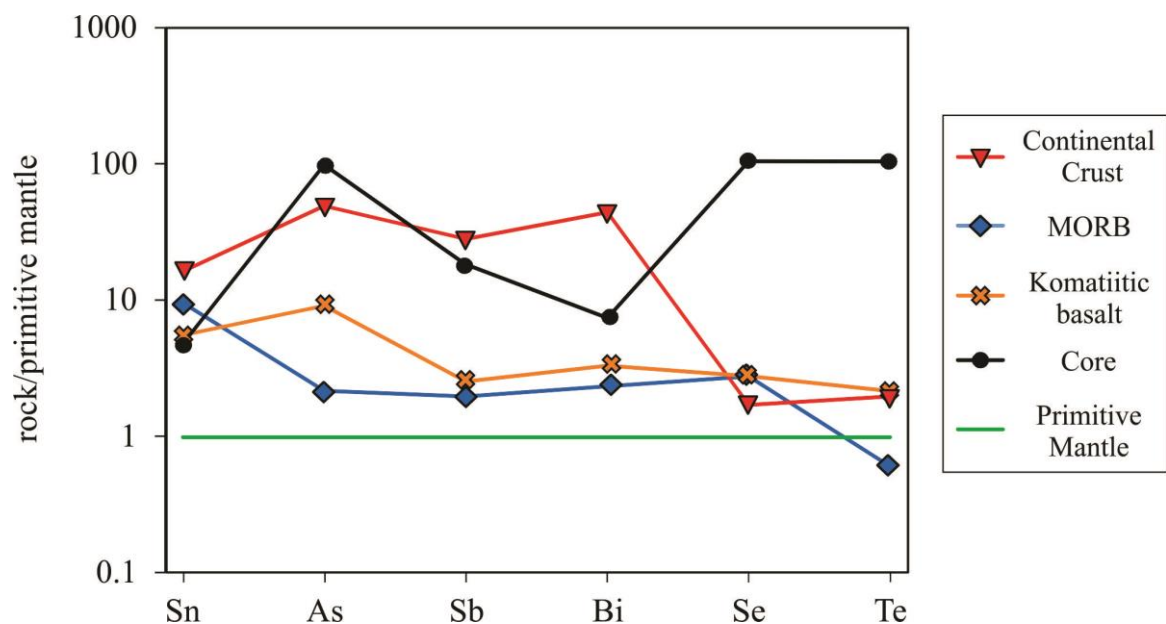
102 **1.2.1 – Cycle géochimique des TABS**

103 Étant donné le comportement similaire et également l'association avec des EGP, Se sera
104 considéré avec des TABS dans cette section.

105 Selon la classification séculaire de Goldschmidt, les TABS sont considérés comme des
106 éléments chalcophiles (aimant le soufre) (Goldschmidt, 1923). Cependant, des concentrations
107 plus élevées de TABS dans le noyau de la Terre par rapport au manteau primitif soutiennent que
108 les TABS se sont comportés comme des éléments sidérophiles pendant la ségrégation du noyau
109 (Tableau 1.1). Les concentrations de As, de Se et de Te dans le noyau sont 100 fois plus
110 élevées, tandis que les concentrations de Sn, Sb et Bi sont 5 à 20 fois plus élevées que celles du
111 manteau primitif (Fig. 1.2). Cela reflète probablement des conditions de faible fugacité en
112 oxygène au cours des premiers stades de différenciation de la terre (Lodders, 2003).

113 Une fois que la fugacité en oxygène dans le manteau primitif ne permet pas la formation
114 extensive d'alloys, les TABS se comportent comme des éléments chalcophiles lors de la fusion
115 du manteau (Harvey et Day, 2016 et références). Par conséquent, leur distribution dépend
116 fortement de la présence des sulfures résiduels dans le manteau. Cependant, les sulfures
117 n'exercent pas un contrôle uniforme sur tous les TABS. Sur la base des coefficients de partage
118 entre les liquides sulfurés et silicatés, Sn, As et Sb peuvent être classés comme éléments
119 légèrement chalcophiles, Bi et Se comme éléments modérément chalcophiles et Te comme
120 élément fortement chalcophile (Tableau 1.1; Li et Audétat, 2015; Liu et Brenan, 2015; Barnes,
121 2016). Le résultat du comportement chalcophile distinct de TABS pendant la fusion du manteau
122 devient évident lorsque l'on compare différents magmas.

123



124

125 Figure 1.2 - Concentrations TABS et Se normalisées au manteau primitif dans le noyau (McDonough, 2003), les
 126 basaltes komatiitiques (Barnes, 2016), les MORB moyen (Arevalo et McDonough, 2010) et la croûte continentale
 127 moyenne (Rudnick et Gao, 2003). Les éléments sont mis par ordre d'incompatibilité avec un basalte komatiitique,
 128 d'après Barnes (2016). Valeurs du manteau primitif de Lyubetskaya et Korenaga (2007).

129

130 Tableau 1.1 - Concentration moyenne de TABS (ppm) dans le noyau, le manteau primitif, les basaltes komatiitiques,
 131 le MORB et la croûte continentale, leurs coefficients de partage entre les liquides sulfurés et les liquides silicatés, et
 132 les températures de condensation. Sources: 1- McDonough (2003); 2- Lubetskaya and Korenaga (2007); 3- Arevalo
 133 and McDonough (2010); 4- Barnes (2016); 5- Rudnick and Gao (2003); 6- Barnes and Ripley (2016); 7- Lodders
 134 (2003).

	Noyau ¹	Manteau primitif ²	Basalte komatiitique ⁴	MORB ³	Croûte continentale ⁵	coefficients de partage entre les liquides sulfurés et les liquides silicatés ($K_D^{sulf/sil}$) ⁶	Températures de condensation (K) ⁷
Te	0.85	0.008	0.017	0.005	0.016	1005 - 8789	709
As	5	0.05	0.46	0.11	2.5	0.3 - 15	1065
Bi	0.03	0.004	0.013	0.01	0.18	130 - 1130	746
Sn	0.5	0.103	0.58	1	1.7	2.7-8.6	704
Sb	0.13	0.007	0.018	0.014	0.2	1.4 - 67	979
Se	8	0.075	0.211	0.21	0.13	226 - 2339	697

135

136 Les concentrations de Te dans les MORB sont légèrement inférieures à celles du
 137 manteau primitif, tandis que les concentrations de Se, Bi, Sb, As et Sn dans les MORB sont de 2

138 à 100 fois plus élevées que celles du manteau primitif. Par contre, les concentrations de tous les
139 TABS dans les basaltes komatiitiques sont de 2 à 10 plus élevées par rapport à celles trouvées
140 dans le manteau primitif (Fig. 1.2). En effet, les sulfures résiduels garderaient une fraction
141 d'éléments fortement chalcophiles (par exemple Se et Te) dans le manteau pendant la
142 ségrégation des MORB. Cependant, une fusion plus étendue du manteau, et donc une
143 consommation totale de sulfures, permettrait des concentrations plus élevées de TABS dans les
144 basaltes komatiitiques (Fig. 1.2).

145 Il est à noter que bien que de nombreuses contributions aient étudié le rôle des sulfures
146 contrôlant la distribution de Te et Se pendant la fusion du manteau (Rose-Weston et al., 2009;
147 Lorand et Alard, 2010; König, et al., 2012; Wang et Becker , 2013; Lissner et al., 2014; Luguët
148 et al., 2015; Yierpan et al., 2019), il n'en va pas de même pour Bi, Sb, Sn et As. Par exemple,
149 Hattori et al. (2002) ont étudié la distribution d'As et de Sb dans les sulfures du manteau.
150 Cependant, des études plus récentes montrent que des minéraux tels que l'apatite ou les micas
151 peuvent également héberger des quantités variables d'As et de Sb (Maciag et Brenan, 2020). De
152 plus, les résultats de Kamenetsky et Eggins (2012), Jenner et O'Neill (2012), Jenner (2017) et
153 Maciag et Brenan (2020) soutiennent le comportement incompatible d'As et de Sb même à des
154 petites degrés de fusion partielle du manteau, où les sulfures resteraient encore comme phase
155 réfractaire. Le besoin de plus d'études sur l'influence de phases autres que les minéraux sulfurés
156 sur la distribution de As, Sb, Sn et Bi pendant la fusion du manteau est soulignée.

157 La croûte continentale moyenne a des concentrations de Se et de Te proches des valeurs
158 du manteau primitif, tandis que les concentrations de As, Sb, Sn et Bi sont 10 à 50 fois
159 supérieures aux valeurs du manteau primitif (Fig. 1.2). Par conséquent, l'interaction des magmas
160 ultramafiques et mafiques avec les roches crustales est susceptible d'augmenter leurs
161 concentrations en As, Sb, Sn et Bi, mais peu susceptible de modifier les teneurs en Se et Te.
162 Cela devient encore plus critique lorsque on considère l'assimilation de roches sédimentaires
163 telles que les schistes noirs, qui sont considérablement enrichis en éléments chalcophiles (Ketris
164 et Yudovich, 2009). En effet, plusieurs études ont démontré l'augmentation des concentrations

165 en As, Sb, Sn et Bi dans les magmas ultramafiques et mafiques en raison de l'assimilation des
166 roches crustales (Godel et al., 2012; Piña et al., 2013, 2015; Duran et al. , 2017; Samalens et al.,
167 2017; LeVaillant et al., 2018).

168 À des pressions plus faibles, les magmas peuvent devenir saturés dans une phase de
169 vapeur, ce qui pourrait affecter la distribution des TABS. En effet, les TABS sont classés
170 comme éléments volatils en raison de leurs températures de condensation relativement élevées
171 lors de la formation du système solaire (Tableau 1.1; Lodders, 2003). Les études expérimentales
172 portant sur la concentration des éléments dans les inclusions fluides par rapport à leurs magmas
173 mafiques hôtes soutiennent également que le TABS se partage à une phase vapeur (Guo et
174 Audétat, 2017). De plus, les TABS sont enrichis en gaz volcaniques (Mather et al., 2012;
175 Zelensky et al., 2013, 2014; Edmonds et al., 2018; Cox et al., 2019; Wiesener et al., 2020) et en
176 fluides provenant de systèmes hydrothermaux (Aguilera et al., 2016; Patten et al., 2017, 2019;
177 Stucker et al., 2017; Shevko et al 2018; Genna et Gaboury, 2019). Récemment, Forrest et al.
178 (2017) ont montré que les basaltes progressivement moins profonds de la crête de Reykjanes
179 vers l'Islande ont des concentrations plus faibles de Se et Te par rapport à leurs équivalents de la
180 dorsale médio-atlantique, ce qui soutient leur perte par dégazage. Cox et al. (2019) ont
181 également trouvé des résultats similaires soutenant le dégazage du Se à basse pression lors de
182 l'enquête sur les laves d'Antuco, au Chili.

183

184 **1.2.2 – La formation des gisements de sulfures magmatiques**

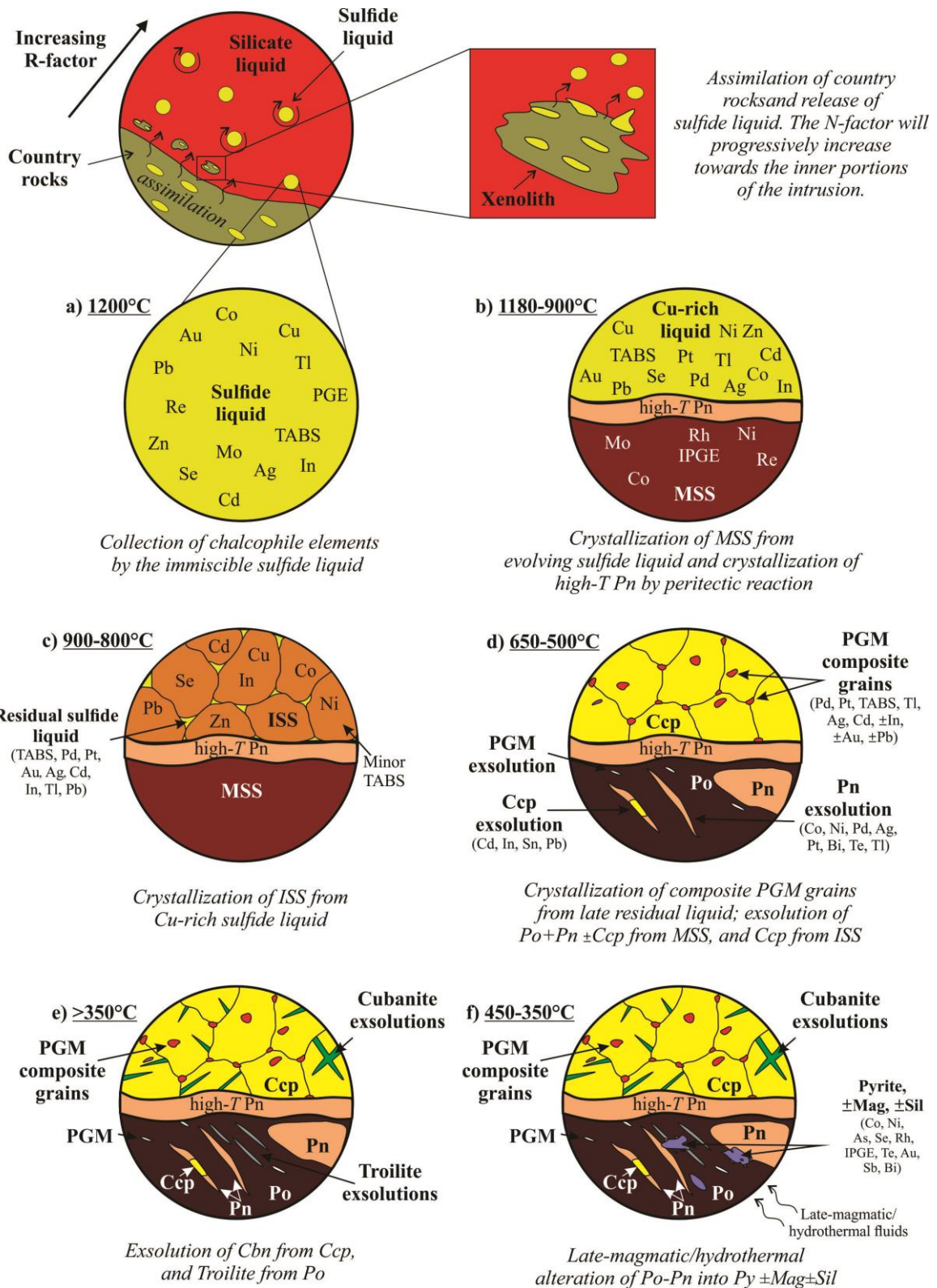
185

186 Afin de mieux comprendre la relation entre TABS et PGE dans les gisements de
187 sulfures magmatiques, les principaux processus impliqués dans la formation de ces gisements
188 seront brièvement décrits. Les processus affectant la formation des gisements de sulfure
189 magmatique sont: i) la saturation d'un magma mafique ou ultramafique avec un liquide sulfuré
190 des métaux de base; ii) Interaction du liquide sulfuré avec le magma mafique; iii) Cristallisation

191 d'une solution solide de monosulfure (MSS), d'une solution solide intermédiaire (ISS) et
192 éventuellement des MGP à partir du liquide sulfuré; iv) Exsolution du MSS et de l'ISS pour
193 former de la pyrrhotite (Po), de la pentlandite (Pn), de la chalcopyrite (Ccp) et des MGP; et v)
194 modification des SMB magmatique par des fluides magmatiques tardifs ou métamorphiques
195 (Fig.1.3; Campbell et Naldrett 1979; Brüggmann et al.1993; Li et al.1996; Naldrett 2004;
196 Prichard et al.2004; Barnes et Lightfoot 2005; Godel et al.2007; Barnes et al.2008; Godel et
197 Barnes 2008; Dare et al.2010b, 2011, 2014; Djon et Barnes 2012; Wirth et al.2013; Duran et
198 al.2015, 2017; Junge et al. 2015; Mota-e-Silva et al.2015; Holwell et al.2017).

199 Les magmas dérivés directement du manteau ne sont pas saturés dans un liquide sulfuré
200 (Mavrogenes et O'Neill 1999). Par conséquent, pour qu'un magma devienne saturé dans un
201 liquide sulfuré, il est généralement proposé que l'assimilation des sédiments riches en S soit la
202 première étape de la formation d'un gisement (Grinenko 1985; Lesher et Burnham 2001; Ripley
203 et Li 2003; Ripley et al.2003, 2010; Keays et Lightfoot 2010; Fiorentini et al.2012; Robertson et
204 al.2015). Lors de leur mise en place, les magmas mafiques incorporent des xénolithes avec des
205 sulfures des roches hôtes, qui sont progressivement fondus, séparant ainsi les gouttelettes de
206 sulfure dans le magma (Fig.1.3; Queffurus et Barnes 2014; Robertson et al.2015; Samalens et
207 al.2017; Barnes et Robertson 2019). Par conséquent, le liquide sulfuré qui se sépare initialement
208 est enrichi en éléments qui ont des concentrations élevées dans la croûte (Sn, Mo, As, Sb, Pb,
209 Tl, Bi) et pauvres en éléments concentrés dans le magma mafique (PGE, Se, Te, Nico). Les
210 détails concernant le transfert du liquide sulfuré des xénolithes crustaux vers au magmas
211 mafiques, et les effets sur les concentrations d'éléments chalcophiles dans le liquide sulfuré, ont
212 été expliqués en détail par Samalens et al. (2017).

213



214

215

Figure 1.3 - Modèles schématiques illustrant l'histoire de la formation et de la cristallisation d'un gisement de sulfure magmatique et la distribution des éléments chalcophiles. Voir le texte pour plus d'explications. MSS, solution solide de monosulfure; ISS, solution solide intermédiaire, MGP, minéraux du groupe du platine; Po, pyrrhotite; Pn, pentlandite; Ccp, chalcopyrite; Py, pyrite; Mag, magnétite; Sil, silicates.

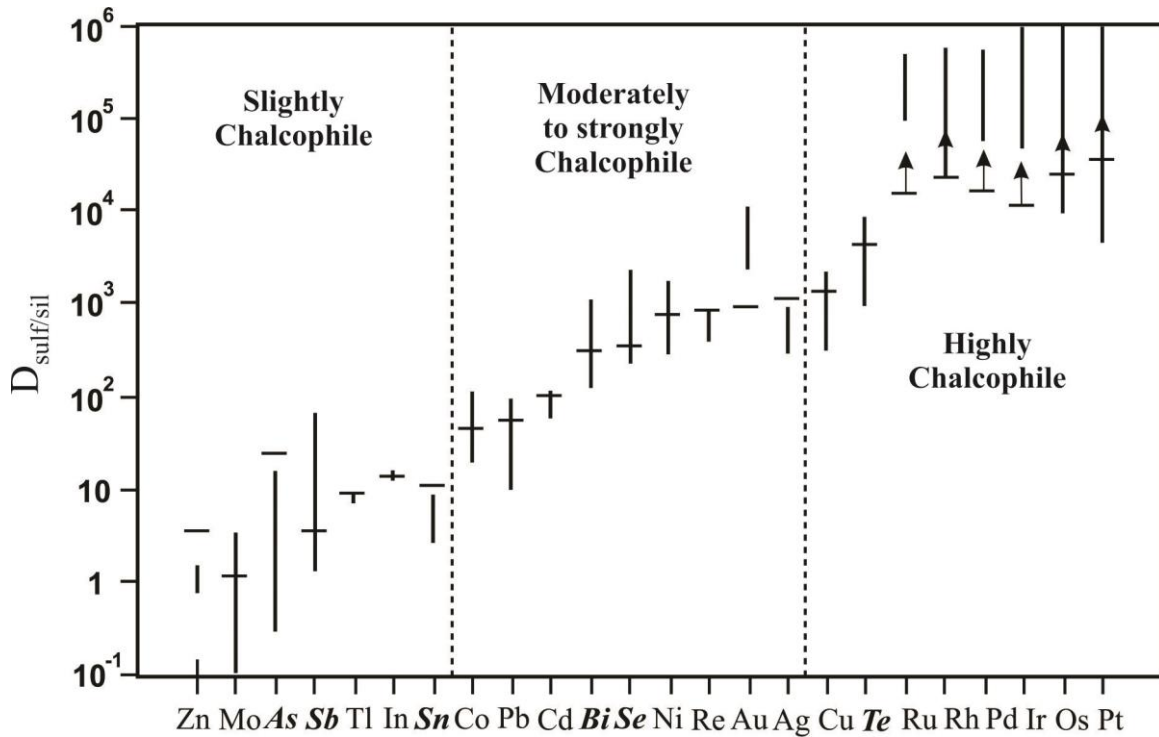
219

220 Une fois que le liquide sulfuré a été incorporé des roches assimilées, il commence à
221 s'équilibrer avec le magma silicaté (Fig. 1.3a). Les concentrations d'éléments chalcophiles dans
222 le liquide sulfuré équilibré dépendent de leur concentration dans le magma silicaté, du
223 coefficient de partage de l'élément entre le liquide silicaté et le liquide sulfuré et du rapport du
224 liquide sulfuré en relation au liquide silicaté présent (Campbell et Naldrett 1979; Brüggmann et
225 al. 1993). La plupart des éléments apportés par la croûte ne sont que légèrement à modérément
226 chalcophiles ($D^{\text{sulf liq} / \text{sil liq}} = 1-100$), tandis que la plupart des éléments chalcophiles dérivés du
227 magma mafique sont fortement ($D^{\text{sulf liq} / \text{sil liq}} = 100-1000$) à très chalcophile ($D^{\text{sulf liq} / \text{sil liq}} > 1000$)
228 (Fig.1.4; Barnes 2016). Plus le liquide sulfuré réagit avec le magma mafique (c.-à-d. Facteur R
229 ou N plus élevé; Campbell et Naldrett 1979; Brüggmann et al. 1993), plus le degré
230 d'enrichissement se rapprochera de son coefficient de partage (Campbell et Barnes 1984) .
231 Ainsi, les éléments fortement chalcophiles (par exemple Se et Te) s'enrichissent dans le liquide
232 sulfuré en réagissant avec plus de magma, tandis que les éléments légèrement à modérément
233 chalcophiles (par exemple Sn, As, Sb et Bi) ne sont pas aussi fortement enrichis (Leshner et
234 Burnham 2001; Queffurus et Barnes 2014; Samalens et al.2017).

235 Lors du refroidissement (en dessous de 1190 °C), le MSS commence à cristalliser. Le
236 Re, l'IPGE, le Rh et le Mo sont compatibles avec le MSS, et le Ni, le Co et le Se sont
237 compatibles à légèrement incompatibles (selon la température: Li et al.1996; Barnes et al.1997;
238 Mungall et al.2005). La plupart des autres éléments chalcophiles sont incompatibles: TABS, Cu,
239 Pt, Pd, Au, Zn, Ag, Pb, Cd, In, Tl (Fig.1.3b; Li et al.1996; Mungall et al.2005; Mungall 2007; Li
240 et Audétat 2015; Liu et Brenan 2015, Sinyakova et al.2016, 2019). En dessous de 950 ° C, le
241 liquide riche en Cu commence à cristalliser sous forme d'ISS (Cabri 1973; Dutrizac 1976;
242 Kosyakov et al. 2012), qui incorpore Cu, Cd, In, Se, Sn, Pb et Zn. Le Pd, le Pt, le TABS, l'Ag et
243 le Tl sont incompatibles avec l'ISS et le MSS, et leurs concentrations dans le liquide sulfure
244 riche en Cu augmentent (Fig.1.3c; Dare et al.2014; Li et Audétat 2015; Liu et Brenan 2015). À
245 environ 900 ° C, une réaction péritectique entre le liquide fractionné et le MSS est possible, ce
246 qui conduit à la formation de Pn (figure 1.3b; Kosyakov et Sinyakova 2012; Kitakaze et

247 al.2016). Aux stades avancés de la cristallisation, le liquide sulfuré piégé peut devenir
 248 suffisamment enrichi en éléments incompatibles (en particulier Pt, Pd et TABS) pour cristalliser
 249 sous forme de grains de MGP (Dare et al. 2014; Liu et Brenan 2015; Duran et al. 2017) .

250



251

252 Figure 1.4 - Coefficients de partage entre un magma mafique et une liquide sulfuré. Les lignes verticales indiquent la
 253 plage de valeurs des essais menées à fO_2 entre -2 FMQ +2; Les traces horizontales indiquent des coefficients de
 254 partage entre le MORB et les gouttelettes de sulfure. Les TABS et Se sont mis en évidence pour référence. Données
 255 de Barnes et Ripley (2016), ainsi que Li et Audétat (2015). Figure modifiée de Barnes (2016).

256

257 Vers 650°C, le MSS se dissout en Po + Pn ± Ccp (Kelly et Vaughan 1983), et les
 258 éléments présents dans le MSS (Mo, Re, Rh et IPGE) se partagent entre Pn et Po. En dessous de
 259 500 ° C, l'ISS s'exsolvé principalement en Ccp et Py. À fS_2 intermédiaire, l'ISS est présent à
 260 335 ° C, et en dessous il s'exsolvé en Ccp et Po (Fig. 1.3d et 1.3e). À faible fS_2 , l'ISS est stable
 261 à 210 ° C, et en dessous de cette température, il s'exsolvé en cubanite et Po (Lusk et Bray
 262 2002). Enfin, la troilite peut exsoudre à partir de Po en dessous de 145 ° C (Fig. 1.3e; Kissin et
 263 Scott 1982; Naldrett 2011). Au fur et à mesure que la température baisse, le MSS et l'ISS

264 peuvent devenir saturés en EGP et en TABS, et les MGP peut s'exsolver du MSS et de l'ISS
265 (Fig.1.3e; Makovicky et al.1990; Prichard et al.2004; Godel et al.2007; Godel et Barnes 2008;
266 Wirth et al.2013; Junge et al.2015; Duran et al.2017).

267 Bien que la formation de dépôts de sulfures magmatiques puisse être considérée comme
268 un continuum de processus ignés, le produit final peut avoir subi des modifications telles que
269 l'interaction avec des fluides magmatiques tardifs, la déformation et le métamorphisme. La
270 pyrite est couramment trouvée en remplacement des assemblages des SMB préexistants
271 (principalement Po) en raison de la rééquilibration post-cumulus avec des fluides magmatiques
272 tardifs qui entraînent la stabilisation de Py sur Po (Fig.1.3f; Dare et al.2011; Djon et al. 2012;
273 Kanitpanyacharoen et Boudreau 2013; Piña et al.2013, 2016; Boudreau et al.2014; Duran et
274 al.2015; Holwell et al.2017; Knight et al.2017). Dans ce cas, la pyrite forme des grains
275 anédriques et l'assemblage des SMB est généralement entouré de minéraux silicatés hydratés
276 secondaires tels que la chlorite et l'actinolite, et occasionnellement par la magnétite. Le
277 développement de la pyrite peut être le résultat d'une perte de Fe, d'un gain de S ou d'une
278 oxydation, comme indiqué par les réactions:

279 1) Perte de Fe: $\text{FeS} + \text{silicate} + \text{H}_2\text{O} \rightleftharpoons \text{FeS}_2 + \text{silicate riche en Fe}$

280 $\text{Po} + \text{silicate magmatique} = \text{pyrite} + \text{silicate hydraté riche en Fe}$

281 2) Gain de S (sulfuration): $\text{FeS} + \text{H}_2\text{S} \rightleftharpoons \text{FeS}_2 + \text{H}_2$

282 $\text{Po} + \text{fluide} = \text{pyrite} + \text{gaz}$

283 3) Oxydation: $\text{FeS} + \text{O}_2 \rightleftharpoons \text{FeS}_2 + \text{Fe}_3\text{O}_4 + \text{S}_2$

284 $\text{Po} + \text{fluide} = \text{pyrite} + \text{magnétite} + \text{soufre}$

285 Dans certains cas, une forte altération peut entraîner le remplacement total de Po et le
286 remplacement de Pn et Ccp par la millérite et la cubanite (Djon et Barnes 2012),
287 respectivement. L'évaluation quantitative par Holwell et al. (2017) a montré que l'altération

288 continue des SMB est associée à une perte de masse se produisant couramment avec des pertes
289 combinées de Fe et de S, conduisant finalement à une remobilisation des métaux communs et
290 précieux lors d'une altération complète de l'assemblage primaire.

291

292 **1.2.3 – Hypothèses**

293 L'association fréquente des EGP avec des TABS soit dans la structure des SMB, soit
294 sous forme des MGP conduit à la question principale de cette étude: Quel est le rôle des TABS
295 lors de la formation des gisements de EGP? Cinq hypothèses principales peuvent être mises en
296 évidence pour tenter de répondre à cette question.

297 **1.2.3.1 – Cristallisation directe des MGP à partir du liquide silicaté**

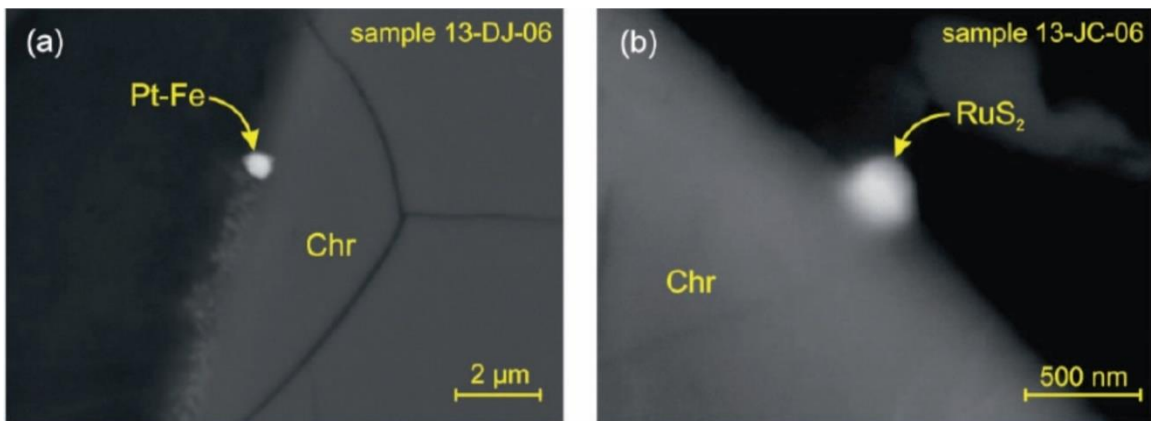
298

299 La première possibilité est la cristallisation directe des MGP à partir du magma silicaté,
300 en réponse à l'augmentation des concentrations de TABS et des EGP avec l'assimilation des
301 roches crustales. Ici, la présence des TABS dans un magma déclencherait la cristallisation des
302 MGP. Arguin et al. (2016) montrent des preuves texturales de la cristallisation des MGP aux
303 marges des cristaux de chromite (Fig. 1.5). Des descriptions détaillées des horizons minéralisés
304 de PGE dans le complexe des Monts de Cristal suggèrent également une cristallisation directe
305 des arséniures de Pt à partir d'un magma basaltique (Maier et al., 2015; Barnes et al., 2016).

306 La cristallisation directe des arséniures de Pt, comme il est suggéré qu'elle se
307 produise dans le complexe des Monts de Cristal (Maier et al., 2015; Barnes et al., 2016),
308 n'est pas appuyée par les données expérimentales actuelles. Canali et al. (2017) ont
309 effectué une série d'expériences pour limiter la solubilité du Pt et des arséniures de Pt
310 dans les magmas silicatés. Les résultats de cette étude indiquent que la saturation de Pt
311 peut être atteinte, dans des conditions réductrices, avec seulement quelques ppb en
312 concentration (Fig. 1.6). Ces concentrations sont similaires aux concentrations dans un
313 magma basaltique typique, et soutiennent la cristallisation directe des phases de Pt,

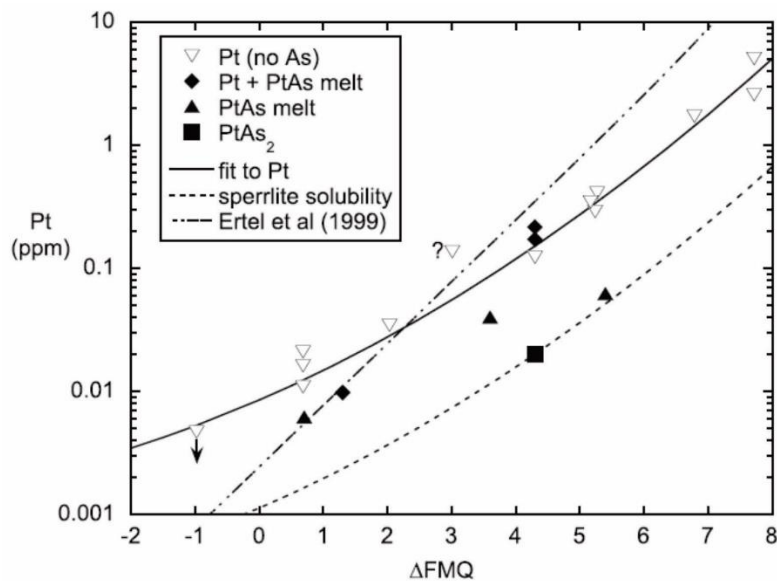
314 induite par la formation de chromite (Finnigan et al., 2008; Arguin et al., 2016).
 315 Cependant, les niveaux d'As requis pour la saturation en Pt-arséniure sont d'environ 50 à
 316 500 ppm, beaucoup plus élevés que ceux observés dans le magma mafique et
 317 nécessitant un énorme enrichissement en arsenic pour que la saturation en Pt-arséniure
 318 se produise (Canali et al., 2017), peu probable dans les cas naturels.

319



320

321 Figure 1.5 - Images d'électrons rétrodiffusées des MGP aux marges des cristaux de chromite: (a) un grain d'alliage à Pt
 322 - Fe à la marge d'un cristal de chromite; (b) une laurite euhédrique (RuS₂) à la marge d'un cristal de chromite.
 323 Figures d'Arguin et al. (2016).



324

325 Figure 1.6 - Variation de la concentration de platine dans le magma silicaté en fonction de la fugacité en oxygène
 326 pour les expériences saturées en alliage à Pt-Fe (\pm As dans le magma silicaté), Pt-As fondu et sperrilite (PtAs₂). La
 327 figure de Canali et al. (2017).

328

329 Pour les autres TABS, il n'y a pas de données expérimentales pour évaluer leur effet sur
330 la saturation en MGP dans les magmas silicatés.

331

332 **1.2.3.2 – Ségrégation d'un liquide immiscible riche en TABS**

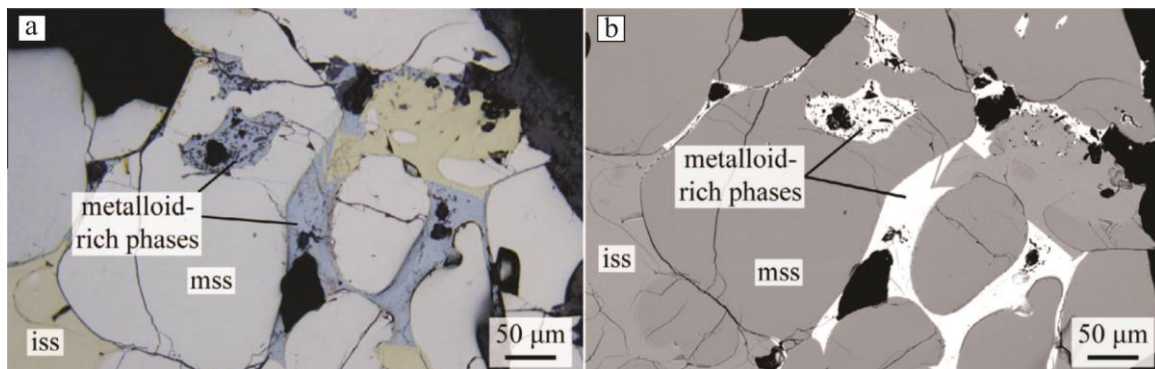
333

334 La deuxième hypothèse est que le liquide sulfuré pourrait devenir saturé dans un
335 liquide immiscible riche en TABS (Fig. 1.7), qui recueille des EGP, et des MGP
336 pourrait cristalliser à partir de ce liquide. En effet, des études expérimentales montrent
337 que des liquides immiscible riche en TABS peuvent se former à partir d'un liquide
338 sulfuré (Hanley 2007; Helmy et al.2007, 2013; Holwell et McDonald 2007; Cafagna et
339 Jugo, 2016; Sinyakova et al., 2017) et des exemples naturels de ce processus ont été
340 proposés. Par exemple, Piña et al. (2015) ont fait valoir que l'assimilation de roches
341 riches en As lors de la mise en place d'un magma pourrait conduire à la ségrégation
342 d'une liquide riche en As, pour laquelle les EGP ont un coefficient de partage élevé. Les
343 auteurs ont documenté la présence de ces liquides immiscibles riches en As dans les
344 dépôts magmatiques de la Serranía de Ronda, en Espagne.

345 Cependant, le modèle de ségrégation d'un liquide immiscible riche en TABS
346 présente une limitation majeure. Les concentrations de TABS nécessaires pour atteindre
347 la saturation sont très élevées (200 à 1000 ppm), et la plupart des liquides sulfurés
348 naturels ne semblent pas atteindre ces niveaux. Par conséquent, bien que des
349 expériences aient démontré qu'un liquide immiscible riche en TABS peut se former
350 (Fig. 1.7), les matériaux de départ ne sont pas compatibles avec la plupart des
351 concentrations naturelles dans les matériaux géologiques. Cela signifie que bien
352 qu'applicable, le modèle nécessiterait des processus conduisant à un enrichissement

353 extrême des concentrations de TABS dans le liquide sulfuré (Piña et al., 2015), qui ne
354 semblent pas s'être produits dans la plupart des gisements magmatiques. Par exemple,
355 Liu et Brenan (2015) ont appliqué leurs résultats expérimentaux aux minerais de
356 McCreey East (Sudbury) et ont conclu que le liquide sulfuré ne contenait pas
357 suffisamment de TABS pour avoir séparé un liquide immiscible riche en TABS. Des
358 conclusions similaires ont également été tirées par Duran et al. (2017) pour les minerais
359 sulfurés massifs du district de Noril'sk-Talnakh.

360



362 Figure 1.7 - Lumière réfléchie (a) et images d'électrons rétrodiffusées (b) de produits expérimentaux de Cafagna et
363 Jugo (2016) illustrant la présence d'un liquide immiscible riche en métalloïdes (TABS). Notez que le liquide
364 immiscible riche en TABS est interstitiel à le MSS et l'ISS de forme ronde. Figure de Cafagna et Jugo (2016).

365

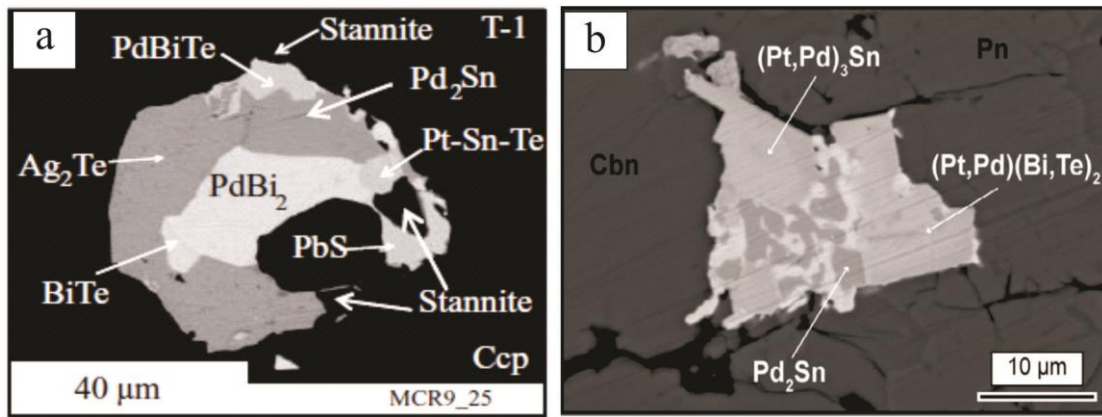
366 1.2.3.3 – Cristallisation des MGP à partir du liquide sulfuré

367

368 La troisième hypothèse est une variation du modèle d'un liquide immiscible
369 riche en TABS, et soutient que des concentrations progressivement plus élevées de
370 TABS dans le liquide sulfuré pourraient conduire à la cristallisation directe de PGM,
371 avant la formation d'un liquide immiscible. Les concentrations plus élevées pourraient
372 être obtenues soit par addition externe de TABS pendant la contamination crustale, soit
373 par cristallisation fractionnée du liquide sulfuré. Plusieurs études au complexe de

374 Sudbury montrent les effets de l'ajout de TABS sur l'évolution de différents gisements
375 de Ni-Cu-PGE (Ames et Farrow, 2007; Dare et al., 2010a et 2011). Les dépôts hébergés
376 sur la chaîne sud contiennent des concentrations d'As plus élevées que celles de la
377 chaîne nord. Cette anomalie régionale dans As sur la chaîne sud est attribuée à
378 l'assimilation des roches volcano-sédimentaires (Ames et Farrow, 2007). Dare et al
379 (2010a) soutiennent que l'activité plus élevée d'As dans le gisement Creighton (c.-à-d. la
380 chaîne sud) a mené à la cristallisation précoce des MGP contenant de l'As à haute
381 température (c.-à-d. jusqu'à 1200 ° C).

382 Alternativement, les MGP peut ne pas cristalliser à des températures élevées en
383 raison d'une augmentation de TABS dans le liquide sulfuré par assimilation crustale,
384 mais aux derniers stades de la cristallisation fractionnée du liquide sulfuré. Comme
385 indiqué ci-dessus, le Pd, le Pt et le TABS sont incompatibles avec le MSS et l'ISS, et
386 leurs concentrations dans le liquide sulfuré riche en Cu progressivement plus fractionné
387 augmentent. Par conséquent, au cours des derniers stades de la cristallisation, le liquide
388 sulfuré piégé peut devenir saturé en Pd, Pt et TABS, et les grains composites des MGP
389 peuvent cristalliser (Dare et al.2014; Liu et Brenan 2015; Duran et al.2017). Des
390 exemples de grains de PGM composites interstitiels au SMB dans des minerais riches
391 en Cu ont été décrits par Dare et al. (2014) et Duran et al. (2017) dans les districts de
392 Noril'sk-Talnakh et de Sudbury, respectivement (figure 1.8). Les auteurs ont interprété
393 les grains composites des MGP comme le résultat d'une cristallisation directe à partir du
394 liquide sulfuré fractionné, sans formation d'un liquide immiscible riche en TABS.



395

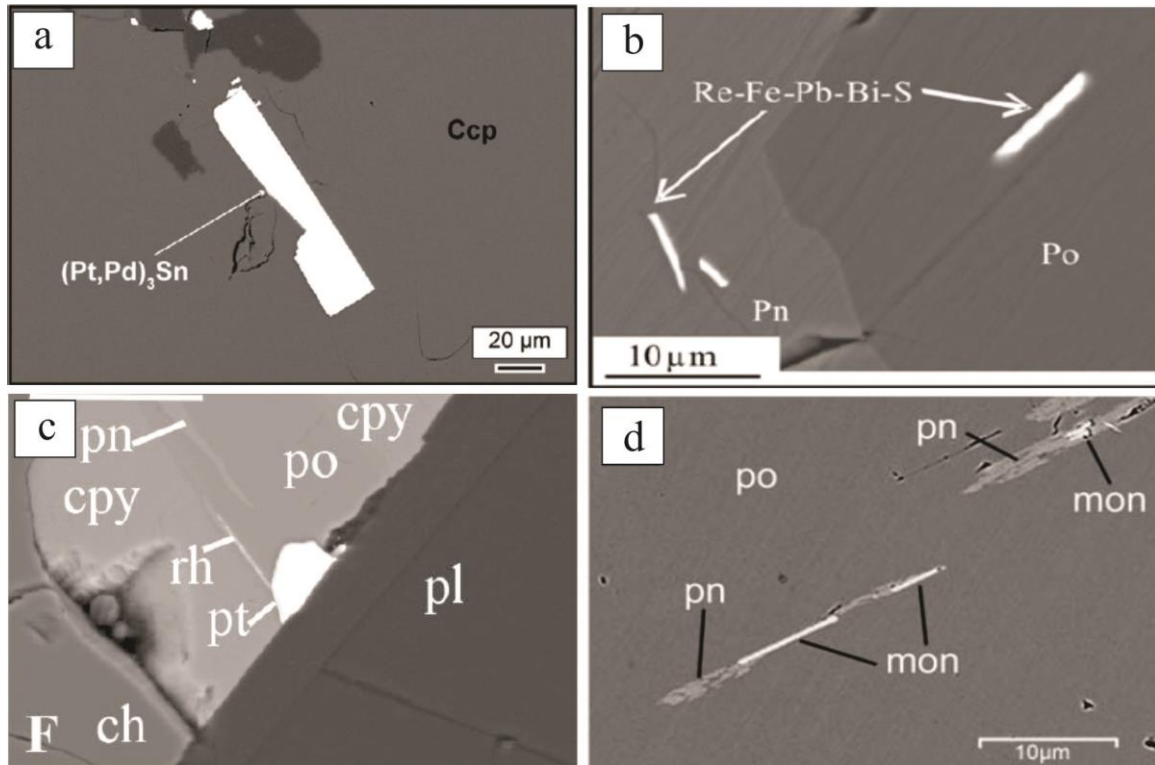
396 Figure 1.8 - Images électroniques rétrodiffusées de grains composites de MGP provenant des gisements McCreedy
 397 East, Sudbury (Dare et al., 2014) et Talnakh, district de Noril'sk (Duran et al., 2017). Les deux échantillons
 398 comprennent des sulfures massifs fractionnés riches en Cu. Notez que les grains de MGP se produisent interstitiels
 399 dans des SMB. Abréviations: Cbn - cubanite; Ccp - chalcopyrite; Pn - pentlandite.

400

401 1.2.3.4 – Combinaison des EGP et TABS et exsolution des MGP

402

403 La quatrième hypothèse est que lors du refroidissement, les EGP peuvent se
 404 combiner avec les TABS et s'exsolver sous forme de MGP à partir des SMB. Bien que
 405 Pt, Pd et TABS soient incompatibles avec le MSS et l'ISS, leurs coefficients de partage
 406 ne sont pas 0 (Mungall et al., 2005; Mungall et Brenan, 2014; Liu et Brenan, 2015), et
 407 donc une petite fraction de ces éléments sont inclus dans l'ISS et le MSS. Lors du
 408 refroidissement, ou pendant la perte de S, Pd, Pt et TABS pourraient s'exsolver de l'ISS
 409 et du MSS. En effet, des travaux expérimentaux ont montré que les SMB contient moins
 410 d'EGP lors du refroidissement (Makovicky et al., 1990; Makovicky, 2002), ainsi que la
 411 forme allongée des MGP inclus dans les SMB (Prichard et al., 2004; Godel et al., 2007 ;
 412 Holwell et McDonald, 2007; Godel et Barnes, 2008; Duran et al., 2017) soutiennent le
 413 modèle d'exsolution (Fig. 1.9).



414

415 Figure 1.9 - Images électroniques rétrodiffusées des grains de MGP allongés et inclus dans les SMB du (a) district de
 416 Noril'sk-Talnakh (Duran et al., 2017), (b) gisement Creighton, Sudbury (Dare et al., 2010), (c) Merensky Reef et (d)
 417 Platreef, Complex du Bushveld (Prichard et al., 2004; Holwell et McDonald, 2007). Il a été interprété que les MGP
 418 de ces diverses localités se sont formées par exsolution des SMB en raison de leur forme allongée. Abréviations: Ccp
 419 / Cpy - chalcopryrite; Po - pyrrhotite; Pn - pentlandite; Pl - plagioclase; Mon - moncheite.

420

421 Récemment, Wirth et al. (2013) et Junge et al. (2015) ont étudié la distribution
 422 minéralogique des EGP dans des échantillons de chromitite du *UG-2* et du *Merensky*
 423 *Reef*, en utilisant la microscopie électronique à transmission. Les auteurs ont découvert
 424 que les EGP se produisent en solution solide dans les SMB (en particulier Pn), et
 425 également sous forme de lamelles de MGP alignées dans la structure des SMB, qu'ils
 426 ont interprétées comme des lamelles d'exsolution. De plus, Junge et al. (2015) ont
 427 suggéré que la concentration initiale des TABS dans les SMB pourrait contrôler
 428 l'étendue de l'exsolution de MGP. En effet, les EGP nécessiteraient des partenaires de
 429 réaction nécessaires pour former les MGP, qui seraient les TABS. Bien que les preuves
 430 actuelles soutiennent la formation des MGP par exsolution, il n'est pas clair si le

431 contenu de TABS peut limiter le processus d'exsolution, d'autant plus que les EGP
432 peuvent s'exsolver non seulement sous la forme des MGP porteur des TABS, mais
433 également sous la forme des sulfures et des alliages (Prichard et al., 2004; Godel et al.,
434 2007; Godel et Barnes, 2008). Ceci est important car si les TABS limitent le processus
435 d'exsolution, la concentration de TABS dans les SMB affectera probablement la
436 distribution minéralogique des EGP.

437

438 **1.2.3.5 – Redistribution post-magmatique des EGP**

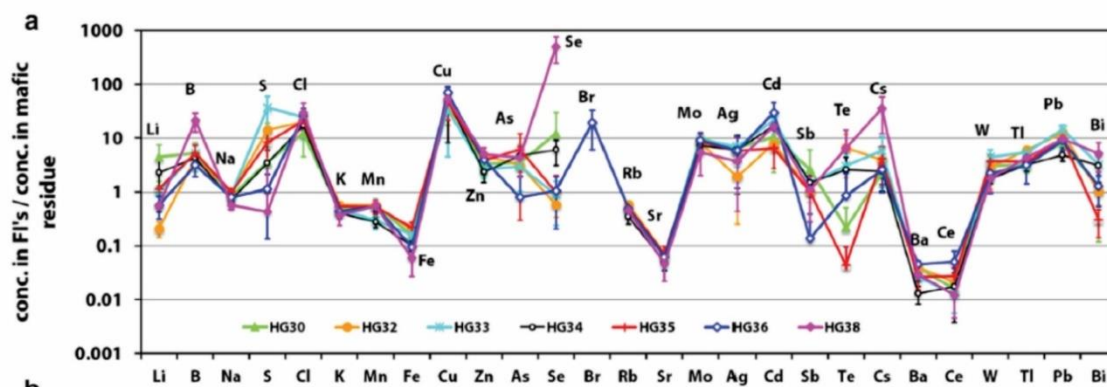
439

440 La cinquième hypothèse est que les TABS peuvent soit être remobilisés avec les EGP
441 pendant l'altération post-magmatique, ou soit agir comme agents de fixation des EGP pendant
442 les processus de remobilisation tardive. En effet, la formation de gisements de sulfures
443 magmatiques par des processus hydrothermaux a également été argumentée par plusieurs
444 auteurs (Boudreau et Meurer, 1999; Péntek et al., 2008; Tuba et al., 2014). Dans ces modèles,
445 un fluide magmatique tardif (généralement très salin et acide) dissout les SMB magmatique et le
446 redépose lorsque les conditions physico-chimiques changent. La migration de ces fluides
447 contenant des métaux pourrait conduire à la formation de zones à faible S-haut-Pd-Pt entourant
448 les intrusions. Par exemple, Péntek et al. (2008) et Tuba et al. (2014) soutiennent que les fluides
449 riches en Cl ont lessivé les métaux des gisements de Ni-Cu-PGE de type contact de Sudbury
450 pour former des dépôts à faible S-haut-Pd-Pt. Cependant, bien que des études expérimentales
451 récentes soutiennent le transport des TABS par les fluides hydrothermaux (Fig.1.10; Guo et
452 Audétat, 2017), il n'en va pas de même pour les EGP, qui sont immobiles (Sullivan et al., 2018).

453 Bien que les EGP ne semblent pas être remobilisés par les fluides hydrothermaux, les
454 TABS peuvent toujours être importants lors de l'altération des gisements de sulfures
455 magmatiques et peuvent agir comme agents de fixation des EGP. Wood (2002) soutient que les
456 TABS forment des composés insolubles avec les EGP. Par exemple, certains gisements de EGP
457 sont considérés comme ayant subi une perte de soufre en raison de processus post-magmatiques

458 (Godel et Barnes, 2008; Polovina et al., 2004; Kawohl et Frimmel, 2016). Par conséquent, le
 459 TABS peut agir comme des éléments de fixation et éviter, dans une certaine mesure, la perte des
 460 EGP avec le S et d'autres métaux de base. Si cette hypothèse est valide, la caractérisation des
 461 TABS dans les roches métamorphisées et altérées est fondamentale pour mieux contraindre la
 462 mobilité des EGP lors de la recristallisation.

463



464

465 Figure 1.10 - Coefficients de partage fluide / roche calculés en divisant les concentrations d'éléments dans les
 466 inclusions fluides (FI) par leur concentration dans les résidus mafiques dans les expériences de Guo et Audétat
 467 (2017). Notez que As, Sb, Te et Bi affichent un coefficient de partage dans la phase fluide supérieur à 1 pour la
 468 plupart des produits de test expérimental. Les éléments sont classés par masse ascendante.

469

470 1.3 – Objectifs

471 Cette thèse se concentrera sur le test des hypothèses de i) la ségrégation d'un liquide
 472 immiscible riche en TABS, ii) la cristallisation des MGP à partir du liquide sulfuré et iii)
 473 l'exsolution des EGP et TABS à partir des SMB sous la forme des MGP. Les principaux
 474 objectifs sont les suivants:

475 ➤ **Développer une routine analytique pour déterminer les TABS dans des**
 476 **échantillons de roche totale à des concentrations faibles à ultra faibles, au**
 477 **LabMaTer (UQAC)**

- 478 • Mettre en œuvre l'utilisation de la spectroscopie de fluorescence atomique couplée à
 479 un générateur d'hydrure (HG-AFS) dans les échantillons géologiques.

- 480 • Analyser différents matériaux de référence, avec des concentrations variables en
481 TABS, afin de vérifier l'exactitude et la précision de la méthode.
- 482
483 ➤ **Comprendre si la concentration des TABS peut permettre la ségrégation d'un**
484 **liquide immiscible riche en TABS, ou la cristallisation directe de PGM à partir**
485 **du liquide sulfuré**
- 486 • Mesurer la concentration des TABS dans des échantillons de roche totale à degré de
487 fractionnement variable du district minier de Noril'sk-Talnakh.
- 488 • Examiner la distribution des TABS dans le SMB des sulfures massifs du district minier
489 de Noril'sk-Talnakh.
- 490 • Combiner les compositions de roche totale et des SMB pour calculer un bilan de masse
491 pour des TABS dans différents types de minerai et comprendre les variations possibles.
- 492
- 493 ➤ **Etudier la formation des MGP par exsolution des EGP et TABS à partir des SMB**
- 494 • Déterminer les concentrations de TABS en roches totale dans les échantillons des
495 gisements *Merensky Reef*, *J-M Reef* et *Picket Pin* et comparer les résultats avec ceux
496 des échantillons stériles en EGP.
- 497 • Étudier la distribution des TABS dans les SMB provenant des intervalles des *PGE Reef*
498 et d'échantillons en dehors des *PGE Reef*.
- 499 • Comparer le bilan de masse des TABS dans des échantillons de minéralisés en EGP et
500 stériles.
- 501
- 502 ➤ **Vérifier si la distribution des TABS peut être utilisée pour comprendre les**
503 **processus conduisant à la formation des gisements de sulfures magmatiques**
- 504 • Étudier la distribution des TABS dans les échantillons de la *Marginal Zone* du
505 complexe du Bushveld, qui enregistrent la composition des magmas initiaux qui ont
506 cristallisé l'intrusion.

- 507 • Comprendre quels sont les principaux processus affectant la distribution des TABS dans
508 les magmas initiaux qui ont cristallisé les gisements de EGP du complexe du Bushveld.
- 509 • Utiliser la concentration de TABS dans les roches de la *Marginal Zone* pour essayer de
510 modéliser les concentrations observées dans le *Merensky Reef*.
- 511 • Comprendre comment les SMB affectent la distribution des TABS dans le *Merensky*
512 *Reef*.
- 513

514 **1.4 – Zones d'étude**

515 Afin d'étudier les hypothèses proposées, trois zones d'étude ont été sélectionnés. Les
516 zones comprennent le district minier de Noril'sk-Talnakh, le complexe du Bushveld et le
517 complexe de Stillwater. Seulement un bref contexte est fourni ici, tandis qu'une description plus
518 détaillée des zones d'étude et des échantillons peut être trouvée dans les chapitres suivants.

519 **1.4.1 – Le district minier de Noril'sk-Talnakh**

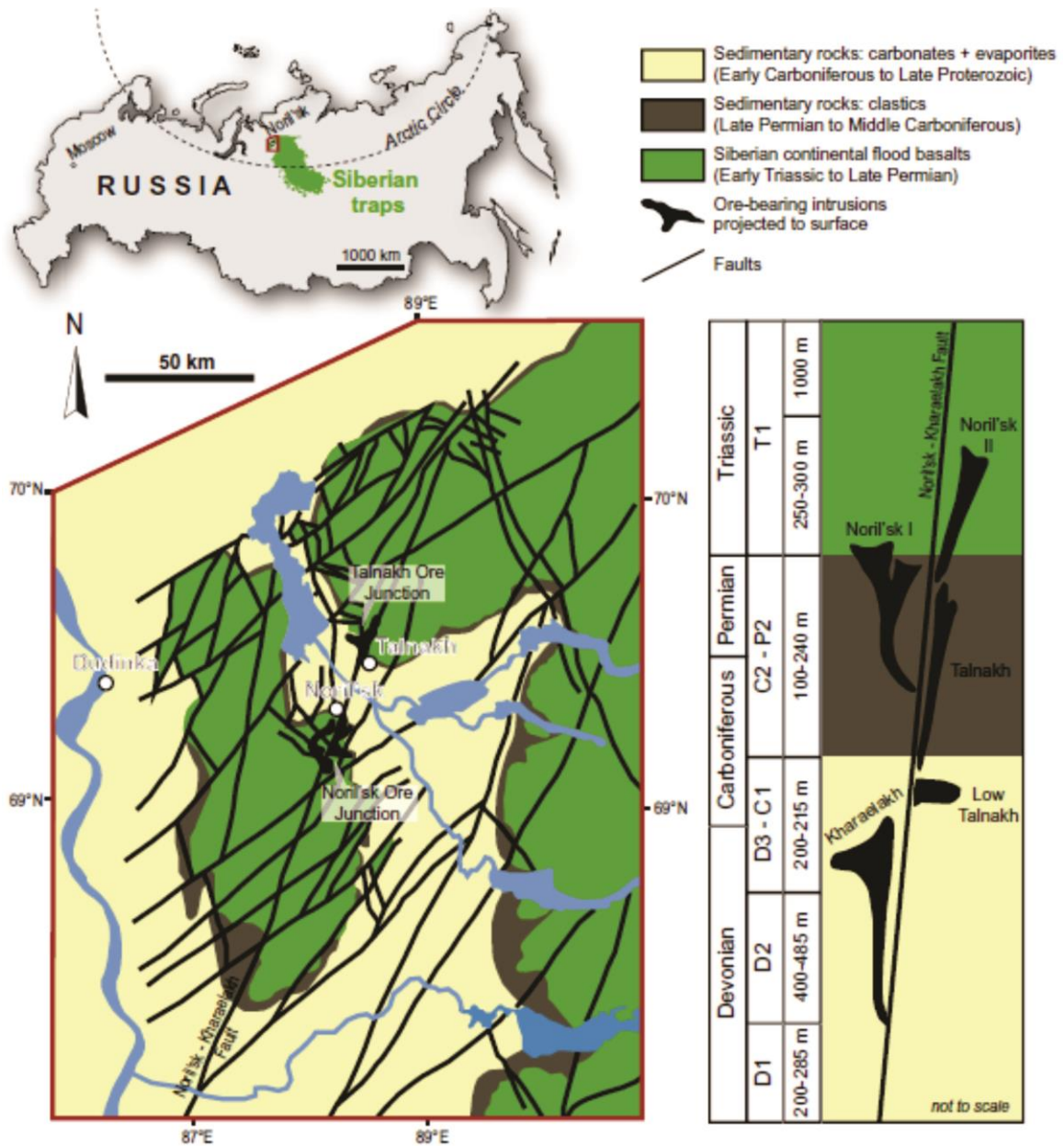
520

521 La plate-forme sibérienne, située à travers la Sibérie occidentale et orientale (Fig. 1.11),
522 comprend un très grand magmatisme alcalin ultramafique, mafique et felsique qui a été mis en
523 place à la limite permo-triasique. Les études géochronologiques soutiennent que la mise en
524 place du *Large Igneous Province (LIP)* sibérien a duré moins de 1 Ma (entre 252,3 et 251,3 Ma;
525 Milanovskiy, 1976; Reichow et al., 2009; Burgess et al., 2014). Les magmas ont interagi avec
526 les roches sédimentaires riches en volatiles et les gaz associés libérés pendant l'événement LIP
527 sibérien seraient responsables de l'extinction de masse du Permien final (Polozov et al., 2016, et
528 les références qui s'y trouvent).

529 Le district minier de Noril'sk-Talnakh est situé à la limite nord-ouest de la plate-forme
530 sibérienne (Fig. 1.11). Dans la région, la séquence volcanique complète a été forée et 11
531 formations ont été identifiées sur la base des caractéristiques pétrographiques et géochimiques
532 (Fedorenko, 1994). Les formations les plus basses sont dérivées de magmas modérément riches

533 en Ti, tandis que les formations les plus hautes sont dérivées de magmas pauvres en Ti. Le
534 degré de contamination a progressivement diminué la séquence ascendante et la formation la
535 plus contaminée (la formation Nadezhdinsky) est épuisée en Ni, Cu et EGP (Naldrett et al.,
536 1992; Brüggmann et al., 1993). Cet épuisement des métaux a été interprété comme le résultat
537 d'un piégeage des métaux par des sulfures magmatiques avant l'extrusion des magmas
538 basaltiques.

539 Des intrusions hypabyssales traversent les roches sédimentaires sous-jacentes à la
540 séquence volcanique et certaines sont considérées comme synchrones avec les différentes
541 roches basaltiques (Fedorenko et Czamanske, 1997). Les sulfures magmatiques se trouvent
542 exclusivement dans des intrusions différenciées mafiques-ultramafiques au sein desquelles les
543 roches varient de l'olivinegabbroïte à la gabbroïte. Les trois principales intrusions
544 minéralisées, Noril'sk I, Kharaelakh et Talnakh, se trouvent dans les jonctions de Noril'sk et de
545 Talnakh (Fig. 1.11). L'assimilation des roches sédimentaires riches en S a conduit à la saturation
546 en S et à la ségrégation des liquides sulfurés (Gorbachev et Grinenko, 1973; Grinenko, 1985;
547 Ripley et al., 2003, 2010). Les liquides sulfurés s'équilibraient avec un grand volume de
548 magmas, collectant ainsi de grandes quantités de métaux de base et précieux avant de
549 s'accumuler dans les parties inférieures des intrusions hypabyssales (Naldrett et al., 1992).



550

551 Figure 1.11 - Carte géologique simplifiée (modifiée après Zientek et al., 1994) de la région de Noril'sk montrant les
 552 projections de surface des intrusions minéralisées et la section stratigraphique idéalisée (modifiée après Likhachev,
 553 1994) montrant les emplacements des intrusions minéralisées dans la séquence de la stratigraphie. La figure de Duran
 554 et al. (2017).

555

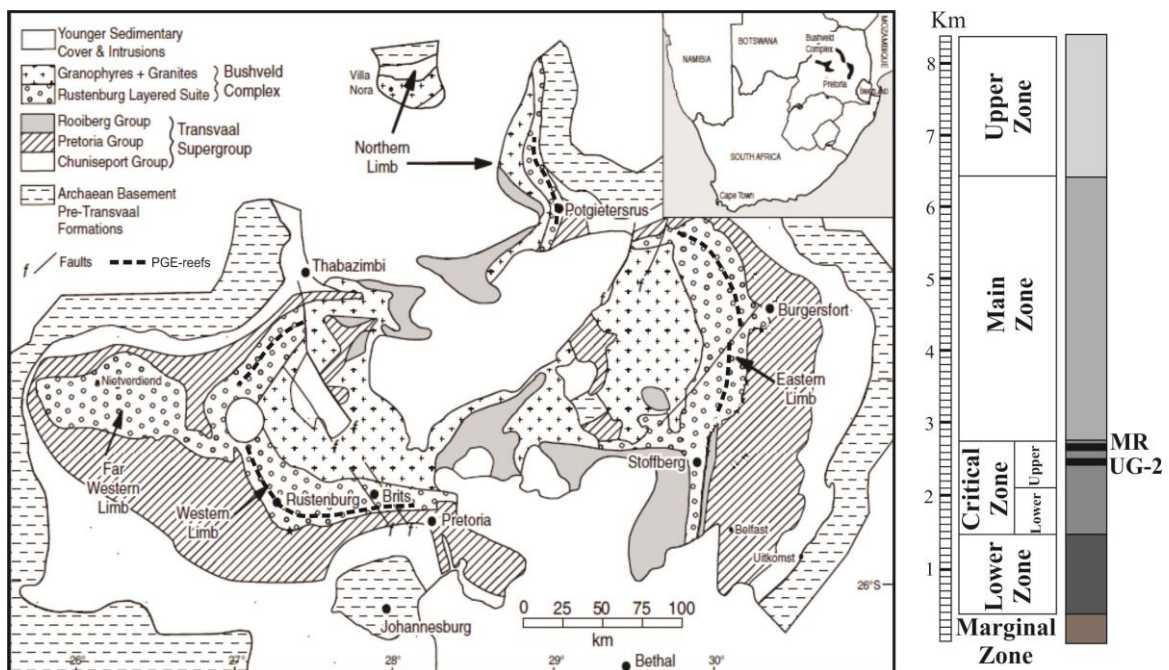
556 1.4.2 – Le complexe du Bushveld

557

558 Le complexe du Bushveld (Fig. 1.12), situé près du milieu du craton de Kaapvaal, en
 559 Afrique du Sud, est le plus grand complexe intrusif au monde (240 km sur 350 km). Le
 560 complexe a été mis en place dans des roches sédimentaires du Supergroupe Transvaal à 2054

561 +/- 1,3 Ma (Scoates et Friedman, 2008), et se compose de trois unités stratigraphiques (*South*
 562 *African Committee for Stratigraphy, 1980*): i) les roches stratifiées ultramafiques à mafiques de
 563 la *Rustenburg Layered Suite*, ii) les granophyres et granites recouvrant la *Rustenburg Layered*
 564 *Suite*, et iii) une suite de filons-couches ultramafiques à mafiques injectés dans les sédiments
 565 rocheux sous-jacents à la *Rustenburg Layered Suite*. La *Rustenburg Layered Suite* (Fig. 1.12)
 566 est divisée, de la base au sommet, en cinq zones (Hall, 1932): la *Marginal Zone*(gabbro-norites),
 567 la *Lower Zone* (péridotites et pyroxénites), la *Critical Zone* (pyroxénites et chromitites) , *Main*
 568 *Zone* (gabbro-norites) et *Upper Zone* (anorthosites, diorites et magnétites). La *Critical Zone*
 569 abrite plusieurs *Reefs* riches en EGP, dont le *Merensky Reef*, étudié dans le cadre du projet.

570



571

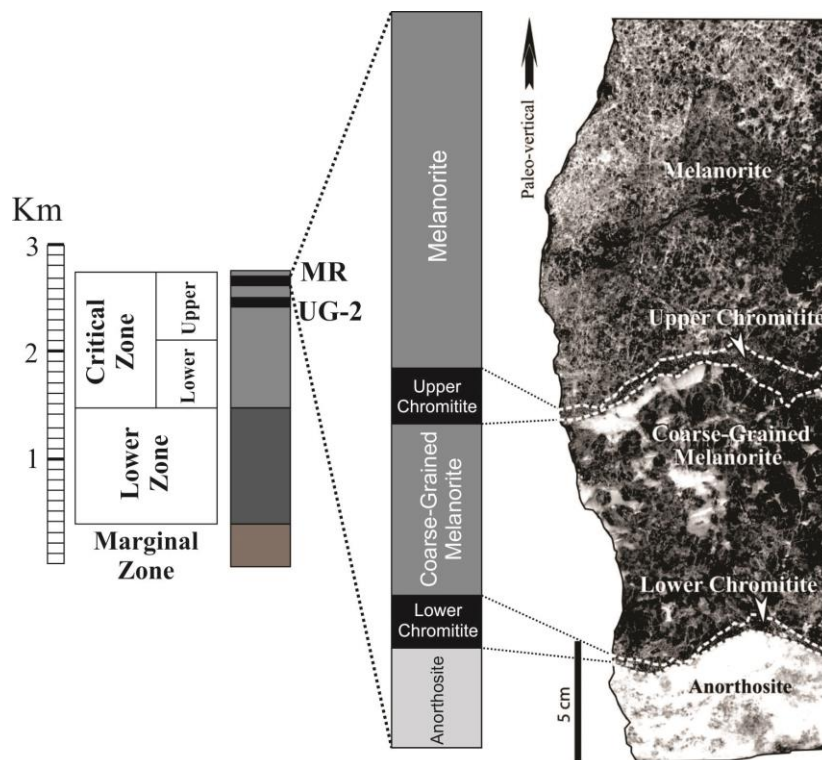
572 Figure 1.12 - Carte géologique simplifiée du complexe du Bushveld (à gauche) et carte stratigraphique de la
 573 Rustenburg Layered Suite (à droite). MR – Merensky Reef; UG2- Upper Group 2 Chromitite. Carte modifiée de
 574 Barnes et al. (2010) et carte stratigraphique de Godel et al. (2007).

575

576 Le *Merensky Reef* est situé dans la partie supérieure de la *Upper Critical Zone* (fig.
 577 1.13) et s'étend latéralement sur plus de 280 km (Cawthorn, 2002). En moyenne, le *Reef* a une
 578 épaisseur de 1 m, avec 1 à 3% de SMB disséminé et environ 6-8 ppm de Pt et Pd (Barnes et

579 Maier, 2002; Godel et al., 2007). Le Reef présente des variations lithologiques régionales et
 580 locales considérables (Leeb-du Toit, 1986). En dehors des variations lithologiques, la
 581 stratigraphie du Reef normal peut être largement divisée, de la base au sommet, sous forme
 582 d'anorthosite basale, de chromitite inférieure, de mélanorite à gros grains, de chromitite
 583 supérieure et de mélanorite (Fig.1.13; Barnes et Maier, 2002; Godel et al., 2007). Différents
 584 processus ont été proposés pour expliquer l'origine du *Merensky Reef*, tels que: i) la collecte de
 585 l'EGP du magma silicaté par un liquide sulfuré (Campbell et al., 1983; Naldrett et al., 1986;
 586 Barnes et Maier, 2002; Godel et al., 2007), ii) la cristallisation des EGP directement à partir du
 587 magma silicaté sous la forme des MGP (Hiemstra, 1979; Cawthorn, 1999), et iii) la collecte des
 588 EGP par le dessous du Reef par un fluide riche en Cl ascendant (Boudreau et Meurer, 1999).

589



590

591 Figure 1.13 - Échantillon macroscopique du Merensky Reef et diagramme stratigraphique schématisé illustrant les
 592 variations lithologiques à travers le Reef. L'échantillon provient de Rustenburg Platinum Mine. Modifié à partir de
 593 Godel et al. (2007).

594

595

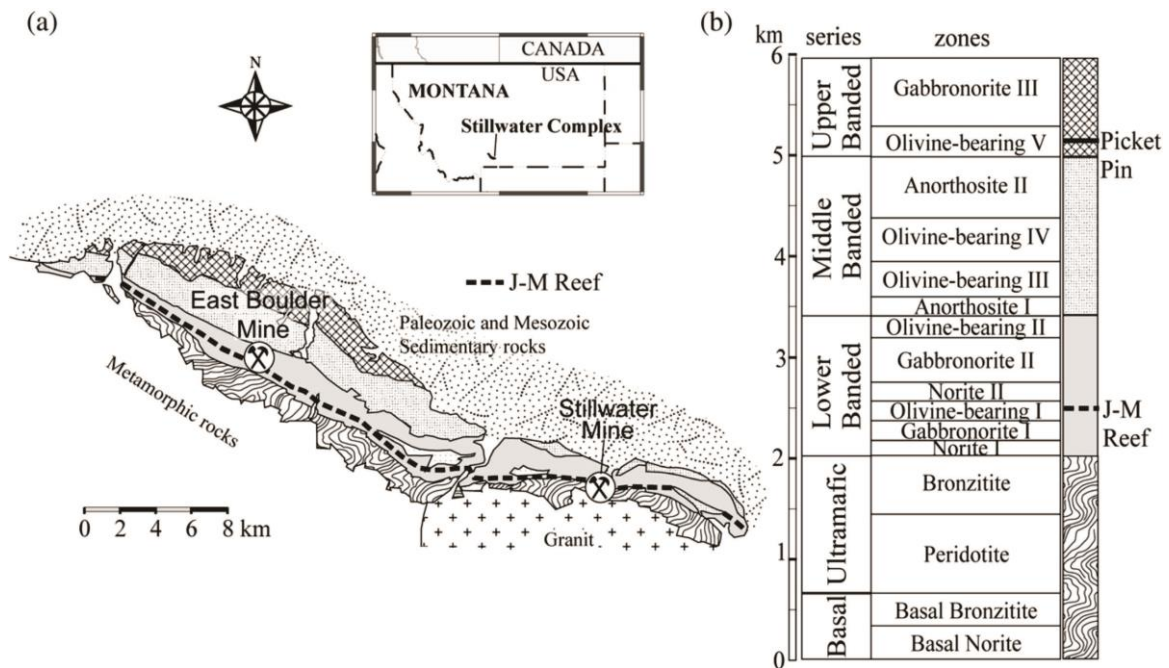
596 1.4.3 – Le complexe de Stillwater

597

598 Le complexe de Stillwater (Fig. 1.14) est une intrusion litée ultramafique à mafique
599 située dans le centre-sud du Montana. Le complexe est daté de 2709 +/- 1 Ma et a été mis en
600 place dans les roches métasédimentaires Archéennes (Wall et al., 2010). Le complexe a subi un
601 métamorphisme au faciès schiste vert inférieur à environ 1700 Ma (Page, 1977). La taille
602 d'origine de l'intrusion n'est pas connue car ses parties supérieures ont été érodées et une faille
603 limitée aux deux extrémités. À partir de la section exposée, le complexe a une structure alignée
604 NW-SE et mesure environ 42 km de long et 5-6 km d'épaisseur (Zientek et al., 2002).

605 Les roches du complexe sont divisées en cinq séries (Fig. 1.14), de bas en haut: la *Basal*
606 *Series* se compose de norites et de bronzitites avec des SMB mineurs; la *Ultramafic Series* est
607 formée essentiellement de harzburgite et de bronzitite, avec des lits mineurs de chromitites; les
608 *Lower, Middle* et *Upper Banded Series* contiennent principalement de la norite, de la
609 gabbronorite, de la gabbronorite olivine et de l'anorthosite (Zientek et al., 2002; Boudreau,
610 2016). Le complexe Stillwater abrite plusieurs *Reefs* enrichies en EGP, dont le *John Manville*
611 *Reef (JM Reef)* et le gisement *Picket Pin* dans les *Lower Banded* et *Upper Banded Series*,
612 respectivement (figure 1.14; McCallum et al., 1980; Zientek et al., 2002; Godel et Barnes,
613 2008). Ce projet se concentre principalement sur le *J-M Reef*.

614 Le *JM Reef* est un lit situé à la base de la *Olivine-bearing I zone* avec des sulfures
615 disséminés riches en EGP (c.-à-d. 0,5-3% vol.) (Bow et al., 1982; Zientek et al., 2002) . Le *Reef*
616 a généralement une épaisseur de 1 à 3 m et présente la teneur moyenne la plus élevée en Pt + Pd
617 (c'est-à-dire environ 18 ppm) de tous les gisements de EGP connus (Zientek et al., 2002). Trois
618 modèles principaux ont été proposés pour expliquer l'enrichissement en EGP de cette *Reef*: i) la
619 collecte des EGP par un liquide sulfuré (Campbell et al., 1983), ii) la collecte des EGP par des
620 fluides magmatiques (Boudreau et McCallum, 1992; Boudreau, 2016), ou iii) une combinaison
621 des deux processus (Godel et Barnes, 2008).



622

623 Figure 1.14 - Échantillon macroscopique du Merensky Reef et diagramme stratigraphique schématique illustrant les
 624 variations lithologiques à travers le Reef. L'échantillon provient de Rustenburg Platinum Mine. Modifié à partir de
 625 Godel et al. (2007).

626

627 Dans le modèle magmatique, la ségrégation d'un liquide sulfuré et son interaction avec
 628 un volume élevé de magma silicaté conduisent à la collecte des EGP. Par contre, le modèle
 629 hydrothermal suppose que les fluides magmatiques interstitiels tardifs sous-saturés en S
 630 lessivent les EGP et d'autres métaux des roches des parties inférieures de l'intrusion et les
 631 redéposent à l'horizon du Reef. Godel et Barnes (2008) soutiennent qu'aucun des deux processus
 632 ne peut expliquer uniquement les caractéristiques observées du J-M Reef. Les auteurs
 633 soutiennent que la formation du J-M Reef a nécessité une ségrégation initiale du liquide sulfuré
 634 pour collecter les EGP et une addition postérieure de Pd et de Pt par les fluides hydrothermaux
 635 tardifs (Godel et Barnes, 2008).

636

637

638

639 **1.5 – Méthodologie**

640

641 Cette section présente une synthèse des méthodes utilisées pour enquêter sur les
642 hypothèses susmentionnées et ainsi atteindre les objectifs fixés. Plus de détails sur les méthodes
643 analytiques sont fournis dans les chapitres individuels.

644

645 **1.5.1 – Fluorescence atomique couplée à un générateur d'hydrure (*HG-AFS*)**

646

647 In order to determine Te, As, Bi, Sb and Se concentrations at low levels, the Hydride
648 Generation-Atomic Fluorescence Spectrometry (*HG-AFS*) technique was implemented at
649 LabMaTer (UQAC). The detailed description of the method is provided in Chapter 2 and only a
650 summary is presented here.

651 Afin de déterminer les concentrations de Te, As, Bi, Sb et Se à de faibles niveaux, la
652 technique de fluorescence atomique couplée à un générateur d'hydrure (*HG-AFS*) a été mise en
653 place au LabMaTer (UQAC). La description détaillée de la méthode est fournie au chapitre 2 et
654 seul un résumé est présenté ici.

655 Environ 0.4 g d'échantillon ont été digérés avec 5 ml d'aqua regia (1: 3 HNO₃: HCl)
656 dans un bécher à capuchon fermé à 70 °C pendant 24 heures. L'aliquote a été laissée à refroidir
657 et diluée à 25 ml avant d'être mélangée avec une solution réductrice (0.7% NaBH₄ et 0.4%
658 NaOH). La solution mélangée a été analysée par *HG-AFS*, en utilisant un PSA Millennium
659 Excalibur 10.055 à flux continu de PS Analytical. Six solutions d'étalonnage avec des
660 concentrations de 0.1, 0.25, 0.5, 1, 2.5 et 5 ppb ont été préparées en utilisant des solutions
661 standard de chaque élément (PlasmaCAL, SCP Science, Québec, Canada). Les solutions
662 d'étalonnage ont été mélangées avec le blanc réactif avant la mesure, dans la même proportion
663 que les aliquotes d'échantillon. Des matériaux de référence internationaux et un blanc ont été

664 déterminés en même temps que les échantillons pour contrôler la qualité des résultats. Dans
665 l'ensemble, les limites de détection 3σ sont de 0.005, 0.003, 0.005, 0.005 et 0.002 ppm pour Te,
666 As, Bi, Sb et Se, respectivement.

667

668 **1.5.2 - Microscope électronique à balayage**

669

670 Un microscope électronique à balayage a été utilisé pour mesurer les concentrations des
671 principaux éléments dans les sulfures, et également pour rechercher la présence des MGP.
672 Ceux-ci ont été acquis à l'aide d'un microscope électronique à balayage Zeiss Sigma 300 VP,
673 équipé d'un système EDS d'Oxford Instruments Ultim Max chez IOS Services Géocientifiques,
674 Chicoutimi, Québec. L'instrument a été étalonné en utilisant des étalons de puremetal et la
675 dérive instrumentale a été surveillée en utilisant les matériaux de référence des étalons Astimex.
676 Le détail des résultats se trouve au chapitre 3.

677

678 **1.5.3 – Ablation laser et spectroscopie de masse (LA-ICP-MS)**

679

680 La concentration et la distribution des éléments mineurs et traces dans les sulfures et silicates
681 ont été déterminées par Ablation laser et spectroscopie de masse (LA-ICP-MS) chez LabMaTer
682 (UQAC), à l'aide d'un laser Excimer 193 nm RESOlution M-50 laser ablation system
683 (*Australian Scientific Instrument*) équipé d'une cellule double volume S-155 (*Laurin Technic*) et
684 couplé à un spectromètre de masse Agilent 7900. Les paramètres de réglage de LA-ICP-MS
685 pour chaque section analytique, les mesures des isotopes, les corrections d'interférence et les
686 résultats pour les matériaux de référence sont rapportés dans les chapitres 3, 4 et 6. La réduction
687 des données a été effectuée en utilisant le package Iolite pour le logiciel Igor Pro (Paton et al.,
688 2011).

689 Des cartes de distribution des éléments ont été faites sur différents assemblages de
690 sulfure en utilisant une fréquence laser de 15 Hz et une puissance de 5 mJ / pulse. La taille du
691 faisceau (15 à 58 µm) et la vitesse de déplacement (10 à 15 µm / s) ont été adaptées pour
692 optimiser la résolution spatiale et le temps d'analyse pour des grains de tailles différentes. Les
693 cartes ont été générées à l'aide du logiciel Iolite sur la base de la composition résolue en temps
694 de chaque élément. Les cartes indiquent la concentration relative des éléments et sont semi-
695 quantitatives.

696

697 **1.6 – Format de la thèse**

698

699 Cette thèse est organisée sous forme d'articles de recherche qui sont publiés au
700 moment de la soumission finale. Chaque article est inséré sous la forme d'un chapitre distinct,
701 qui n'est pas organisé dans l'ordre chronologique de publication.

702 Le premier article a été publié dans la revue « Geostandards and Geoanalytical
703 Research » en juillet 2019 et s'intitule « Determination of Te, As, Bi, Sb and Se (TABS) in
704 Geological Reference Materials and GeoPT Proficiency Test Materials by Hydride Generation-
705 Atomic Spectrométrie de fluorescence (HG-AFS) ». Cet article constitue le chapitre 2 de la
706 thèse. Le manuscrit présente une description détaillée de la méthode *HG-AFS* qui a été
707 développée pour mesurer la concentration de TABS dans les matériaux géologiques. Afin de
708 valider la méthode, plusieurs matériaux de référence internationaux d'échantillons géologiques
709 ont été analysés. L'étude fournit le support analytique pour les autres études présentées dans la
710 thèse.

711 Le deuxième article a été publié dans la revue « Mineralium Deposita » en novembre
712 2019 et s'intitule « Distribution of chalcophile and platinum-group elements among pyrrhotite,
713 pentlandite, chalcopyrite and cubanite from the Noril'sk-Talnakh ores: implications for the
714 formation of platinum-group minerals ». Cet article constitue le chapitre 3 de la thèse. Le

715 manuscrit étudie la variation cryptique des SMB lors de la cristallisation fractionnée d'un liquide
716 sulfuré, en utilisant des minerais sulfurés massifs du district minier de Noril'sk Talnakh. Les
717 résultats permettent d'évaluer si un liquide immiscible riche en TABS peut se former dans des
718 cas naturels, et également si les MGP peuvent cristalliser directement à partir du liquide sulfuré.

719 Le troisième article est intitulé «Textural and compositional evidence for the formation
720 of pentlandite via peritectic reaction: Implications for the distribution of highly siderophile
721 elements» et a été publié en février 2019 dans la revue «Geology». Cet article constitue le
722 chapitre 4 de la thèse. L'article traite de la formation de pentlandite par réaction péritectique
723 entre le MSS et le liquide sulfuré à des températures élevées (~ 900 ° C), qui est une alternative
724 à la formation de pentlandite exclusivement à partir de l'exsolution du MSS à des températures
725 plus basses (~ 650 ° C). Bien que l'étude ne soit pas directement liée au sujet principal de la
726 thèse, les résultats fournissent des informations importantes sur les étapes conduisant à la
727 formation de gisements de sulfure magmatique, ainsi que l'incorporation d'éléments
728 chalcophiles dans le réseau des SMB. Par conséquent, étant donné que l'hypothèse à étudier est
729 l'exsolution des EGP et TABS à partir du réseau des SMB, il faut d'abord bien comprendre
730 comment différents éléments sont incorporés dans des SMB.

731 Le quatrième article est intitulé «Concentrations of Te, As, Bi, Sb and Se in the
732 Marginal Zone of the Bushveld Complex: Evidence for crustal contamination and the nature of
733 the magma that formed the Merensky Reef», et a été publié en avril 2020, dans la revue
734 "Lithos". Cet article constitue le chapitre 5 de la thèse. Le manuscrit explore la distribution de
735 TABS dans des échantillons de la *Marginal Zone* du complexe du Bushveld. Cette étude permet
736 de comprendre les principaux processus affectant la distribution des TABS dans les magmas
737 initiaux qui ont cristallisé certains des gisements de EGP les plus importants au monde
738 (*Merensky Reef* et *UG-2 chromitite*). De plus, les résultats permettent de modéliser la
739 distribution attendue des TABS dans le *Merensky Reef*, et ainsi de comprendre comment
740 l'accumulation de sulfure dans le *Reef* affecte la distribution des TABS.

741 Le cinquième article a été publié dans la revue "Geochimica et Cosmochimica Acta" en
742 mars 2020 et s'intitule " The role of Te, As, Bi, Sn and Sb during the formation of platinum-
743 group-element reef deposits: Examples from the Bushveld and Stillwater Complexes». Cet
744 article constitue le chapitre 6 de la thèse. Le manuscrit présente la distribution des TABS dans
745 des échantillons de roches totale et des SMB du *Merensky Reef*, du *J-M Reef*, du gisement
746 *Picket Pin* et également des échantillons stériles en EGO provenant de l'extérieur des *Reefs*.
747 L'étude permet de comprendre le rôle de TABS lors de l'exsolution des MGP à partir du réseau
748 des SMB. De plus, les résultats obtenus fournissent également des moyens de tester si les
749 compositions d'échantillons de la *Marginal Zone* (chapitre 5) conviennent comme liquides
750 initiaux pour cristalliser le *Merensky Reef*.

751 Le chapitre 7 donne un aperçu des principales conclusions de la thèse. Cela permet de
752 comprendre quelles hypothèses sont plus appropriées pour le rôle des TABS lors de la
753 formation des gisements de EGP.

754

755

756

757

758

759

760

761

762

763 1.7 - Références

- 764 Aguilera, F., Layana, S., Rodríguez-Díaz, A., González, C., Cortés, J., Inostroza, M. (2016)
765 Hydrothermal alteration, fumarolic deposits and fluids from Lastarria Volcanic
766 Complex: A multidisciplinary study. *Andean Geology*, 43(2): 166-196.
- 767 Ames, D.E., Farrow, C.E.G. (2007) Metallogeny of the Sudbury mining camp, Ontario. In:
768 Goodfellow WD (ed) *Mineral deposits of Canada: a synthesis of major deposit-types,*
769 *district metallogeny, the evolution of geological provinces, and exploration methods.*
770 *Geological Association of Canada, Special Publication No. 5, Mineral Deposits*
771 *Division*, 329–350.
- 772 Arevalo, R., McDonough, W. F. (2010) Chemical variations and regional diversity observed in
773 MORB. *Chemical Geology*, 271(1-2): 70-85.
- 774 Arguin, J.P., Pagé, P., Barnes, S.-J., Yu, Y., Song, X.Y., (2016) The Effect of Chromite
775 Crystallization on the Distribution of Osmium, Iridium, Ruthenium and Rhodium in
776 Picritic Magmas: an Example from the Emeishan Large Igneous Province,
777 Southwestern China. *Journal of Petrology*, 57(5): 1019-1048.
- 778 Barnes, S.J., Fisher, L.A., Godel, B., Maier, W.D., Paterson, D., Howard, D.L., Ran, C.G.,
779 Laird, J.S., Pearce, M.A. (2016) Primary cumulus platinum minerals in the Monts de
780 Cristal Complex, Gabon: magmatic microenvironments inferred from high-resolution
781 X-ray fluorescence microscopy. *Contributions to Mineralogy and Petrology*, 171: 23.
- 782 Barnes, S.J., Robertson, J.C. (2019) Time scales and length scales in magma flow pathways and
783 the origin of magmatic Ni–Cu–PGE ore deposits. *Geoscience Frontiers*, 10(1): 77-87.
- 784 Barnes, S.-J. (2016) Chalcophile Elements. In *Encyclopedia of Geochemistry: A Comprehensive*
785 *Reference Source on the Chemistry of the Earth* (ed. W.M. White), pp. 1-5.
- 786 Barnes, S.-J., Makovicky, E., Makovicky, M., Rose-Hansen, J., Karup-Moller, S. (1997)
787 Partition coefficients for Ni, Cu, Pd, Pt, Rh, and Ir between monosulfide solid solution
788 and sulfide liquid and the formation of compositionally zoned Ni–Cu sulfide bodies by
789 fractional crystallization of sulfide liquid. *Canadian Journal of Earth Sciences*, 34: 366-
790 374.
- 791 Barnes, S.-J., Cox, R.A., Zientek, M.L. (2006) Platinum-group element, Gold, Silver and Base
792 Metal distribution in compositionally zoned sulfide droplets from the Medvezky

793 CreekMine, Noril'sk, Russia. *Contributions to Mineralogy and Petrology*, 152: 187–
794 200.

795 Barnes, S-J., Prichard, H.M., Cox, R.A., Fisher, P.C., Godel, B. (2008) The location of the
796 chalcophile and siderophile elements in platinum-group element ore deposits (a textural,
797 microbeam and whole rock geochemical study): Implications for the formation of the
798 deposits. *Chemical Geology*, 248: 295–317.

799 Barnes, S-J., Maier, W.D., Curl, E. (2010) Composition of the marginal rocks and sills of the
800 Rustenburg layered suite, Bushveld Complex, South Africa: implications for the
801 formation of the PGE deposits. *Economic Geology*, 105: 1491–1511.

802 Barnes S-J., Maier W.D. (2002) Platinum-group elements and microstructures of Normal
803 Merensky Reef from Impala Platinum Mines, Bushveld Complex. *Journal of Petrology*,
804 43(1): 103-128.

805 Barnes, S.-J., Ripley, E.M. (2016) Highly siderophile and strongly chalcophile elements in
806 magmatic ore deposits. *Reviews in Mineralogy and Geochemistry*, 81: 725–774.

807 Boudreau, A.E. (2016) The Stillwater Complex, Montana – Overview and the significance of
808 volatiles. *Mineralogical Magazine*, 80(4): 585-637.

809 Boudreau, A.E., Mc Callum, I.S. (1992) Infiltration metasomatism in layered intrusions - an
810 example from the Stillwater Complex, Montana. *Journal of Volcanology and
811 Geothermal Research*, 52 (1–3): 171–183.

812 Boudreau, A.E., Meurer, W.P. (1999) Concentration of platinum-group elements by magmatic
813 fluids in layered intrusions. *Economic Geology*, 87: 1830–1848.

814 Boudreau, A., Djon, L., Tchalikian, A., Corkery, J. (2014) The Lac Des Iles Palladium deposit,
815 Ontario, Canada part I. The effect of variable alteration on the offset zone. *Mineralim
816 Deposita*, 49(5): 625-654.

817 Bow, C., Wolfgram, D., Turner, A., Barnes, S., Evans, J., Zdepski, M., Boudreau, A.E. (1982)
818 Investigations of the Howland reef of the Stillwater Complex, Minneapolis Adit area:
819 Stratigraphy, structure and mineralization. *Economic Geology*, 77: 1481-1492.

820 Brüggemann, G.E., Naldrett, A.J., Asif, M., Lightfoot, P.C., Gorbachev, N.S., Fedorenko, V.A.
821 (1993) Siderophile and chalcophile metals as tracers of the evolution of the Siberian

822 Trap in the Noril'sk region, Russia. *Geochimica et Cosmochimica Acta*, 57(9): 2001-
823 2018.

824 Burgess, S.D., Bowring, S., Shen, S.Z. (2014) High-precision timeline for Earth's most severe
825 extinction. *Proceedings of the National Academy of Sciences*, 111: 3316–3321.

826 Cabri, L.J. (1973) New data on phase relations in the Cu-Fe-S system. *Economic Geology*, 68:
827 443–454.

828 Cafagna, F., Jugo, P.J. (2016) An experimental study on the geochemical behavior of highly
829 siderophile elements (HSE) and metalloids (As, Se, Sb, Te, Bi) in a mss-iss-pyrite
830 system at 650° c: A possible magmatic origin for Co-HSE-bearing pyrite and the role of
831 metalloid-rich phases in the fractionation of HSE. *Geochimica et Cosmochimica Acta*,
832 178: 233-258.

833 Campbell, I.H., Naldrett, A.J. (1979) The influence of silicate: sulfide ratios on the
834 geochemistry of magmatic sulfides. *Economic Geology*, 74(6): 1503-1506.

835 Campbell, I.H., Barnes, S.J. (1984) A model for the geochemistry of the platinum-group
836 elements in magmatic sulfide deposits. *The Canadian Mineralogist*, 22(1): 151-160.

837 Campbell, I.H., Naldrett, A.J., Barnes, S.J. (1983) A model for the origin of the platinum-rich
838 sulfide horizons in the Bushveld and Stillwater Complexes. *Journal of Petrology*, 24(2):
839 133-165.

840 Canali, A.C., Brenan, J.M., Sullivan, N.A. (2017) Solubility of platinum-arsenide melt and
841 sperrylite in synthetic basalt at 0.1 MPa and 1200°C with implications for arsenic
842 speciation and platinum sequestration in mafic igneous systems. *Geochimica et*
843 *Cosmochimica Acta*, 216: 153-168.

844 Cawthorn, R.G. (1999) The platinum and palladium resources of the Bushveld Complex. *South*
845 *African Journal of Science*, 95(11-12): 481.

846 Cawthorn, R.G. (2002) Platinum-Group Element deposits of the Bushveld Complex in South
847 Africa. In *Geology, Geochemistry, Mineralogy and Mineral Benefication of Platinum*
848 *Group Element* (ed. L.J. Cabri). Canadian Institute of Mining, Metallurgy and
849 Petroleum, Special volume 54: 389-429.

850 Cox, D., Watt, S.F.L., Jenner, F.E., Hastie, A.R., Hammond, S.J. (2019) Chalcophile element
851 processing beneath a continental arc stratovolcano. *Earth and Planetary Science Letters*,
852 522: 1-11.

853 Dare, S.A.S., Barnes, S.-J., Prichard, H.M., Fisher, P.C. (2010a) The timing and formation of
854 platinum-group minerals from the Creighton Ni-Cu-platinum-group element sulfide
855 deposit, Sudbury, Canada: Early crystallization of PGE-rich sulfarsenides. *Economic
856 Geology*, 105: 1071-1096.

857 Dare, S.A.S., Barnes, S.-J., Prichard, H.M. (2010b) The distribution of platinum group elements
858 (PGE) and other chalcophile elements among sulfides from the Creighton Ni–Cu–PGE
859 sulfide deposit, Sudbury, Canada, and the origin of palladium in pentlandite.
860 *Mineralium Deposita* 45: 765-793.

861 Dare, S., Barnes, S.-J., Prichard, H., Fisher, P. (2011) Chalcophile and platinum-group element
862 (PGE) concentrations in the sulfide minerals from the McCreedy East deposit, Sudbury,
863 Canada, and the origin of PGE in pyrite. *Mineralium Deposita*, 46: 381-407.

864 Dare, S.A.S., Barnes, S.-J., Prichard, H.M., Fisher, P.C. (2014) Mineralogy and geochemistry of
865 Cu-rich ores from the McCreedy East Ni-Cu-PGE deposit (Sudbury, Canada):
866 Implications for the behavior of platinum group and chalcophile elements at the end of
867 crystallization of a sulfide liquid. *Economic Geology*, 109: 343-366.

868 Djon, M.L.N., Barnes, S.-J. (2012) Changes in sulfides and platinum-group minerals with the
869 degree of alteration in the Roby, Twilight, and High Grade Zones of the Lac des Iles
870 Complex, Ontario, Canada. *Mineralium Deposita*, 47: 875-896.

871 Duran, C.J., Barnes, S.-J., Corkery, J.T. (2015) Chalcophile and platinum-group element
872 distribution in pyrites from the sulfide-rich pods of the Lac des Iles Pd deposits,
873 Western Ontario, Canada: implications for post-cumulus reequilibration of the ore and
874 the use of pyrite compositions in exploration. *Journal of Geochemical Exploration*, 158:
875 223-242.

876 Duran, C.J., Barnes, S-J., Pleše, P., Prašek, M.K., Zientek, M.L., Pagé, P. (2017) Fractional
877 crystallization-induced variations in sulfides from the Noril'sk-Talnakh mining district
878 (polar Siberia, Russia). *Ore Geology Reviews*, 90: 326-351.

879 Dutrizac, J.E. (1976) Reactions in cubanite and chalcopyrite. *The Canadian Mineralogist*, 14(2):
880 172-181.

881 Edmonds, M., Mather, T.A., Liu, E.J. (2018) A distinct metal fingerprint in arc volcanic
882 emissions. *Nature Geoscience*, 11(10): 790-794.

883 European Commission, (2010) Critical Raw Materials for the EU. Report of the Ad-hoc
884 Working Group on Defining Critical Raw Materials. European Commission, Enterprise
885 and Industry.

886 European Commission, (2014) Report on critical raw materials for the EU. Report of the Ad-
887 hoc Working Group on Defining Critical Raw Materials. European Commission,
888 Enterprise and Industry.

889 Fedorenko, V.A. (1994) Evolution of magmatism as reflected in the volcanic sequence of the
890 Noril'sk region. In: Lightfoot, P.C., Naldrett, A.J. (Eds), *Proceedings of the Sudbury-
891 Noril'sk Symposium*, Ontario Geological Survey, special publication issue 5. Ontario
892 Geological Survey, Greater Sudbury: 171–184.

893 Fedorenko, V.A., Czamanske, G.K. (1997) Results of new field and geochemical studies of the
894 volcanic and intrusive rocks of the Maymecha-Kotuy area, Siberian Flood-Basalt
895 Province, Russia. *International Geology Review*, 39: 479-531.

896 Fiorentini, M.L., Bekker, A., Rouxel, O., Wing, B.A., Maier, W., Rumble, D. (2012) Multiple
897 sulfur and iron isotope composition of magmatic Ni-Cu-(PGE) sulfide mineralization
898 from eastern Botswana. *Economic Geology*, 107(1): 105-116.

899 Finnigan, C.S., Brenan, J.M., Mungall, J.E., McDonough, W.F. (2008) Experiments and model
900 bearing on the role of chromite as a collector of platinum group minerals by local
901 reduction. *Journal of Petrology*, 49: 1647–1665.

902 Forrest, A., Keller, K.A., Schilling, J.G. (2017) Selenium, tellurium and sulfur variations in
903 basalts along the Reykjanes Ridge and extension over Iceland, from 50°N to
904 65°N. Interdisciplinary Earth Data Alliance (IEDA), Palisades, NY.

905 Genna, D., Gaboury, D. (2019) Use of semi-volatile metals as a new vectoring tool for VMS
906 exploration: Example from the Zn-rich McLeod deposit, Abitibi, Canada. *Journal of*
907 *Geochemical Exploration*, 207: 106358.

908 Godel, B., Barnes, S-J., Maier, W.D. (2007) Platinum-group elements in sulphide minerals,
909 platinum-group minerals, and whole-rocks of the Merensky Reef (Bushveld Complex,
910 South Africa): Implications for the formation of the reef. *Journal of Petrology*, 48:
911 1569-1604.

912 Godel, B., González-Álvarez, I., Barnes, S.J., Barnes, S-J., Parker, P., Day, J. (2012) Sulfides
913 and sulfarsenides from the Rosie nickel prospect, Duketon greenstone belt, Western
914 Australia. *Economic Geology*, 107: 275-294.

915 Goldschmidt, V. M. (1923) *Geochemische Verteilungsgesetze der Elemente*. Skrifter utg. av det
916 Norske Visenskaps-Akademii i Oslo I. Mat.-Naturv. Klasse, 2, p. 1–17.

917 Gorbachev, N.S., Grinenko, L.N. (1973) The sulfur-isotope ratios of the sulfides and sulfates of
918 the Oktyabr'sky sulfide deposit, Noril'sk region, and the problem of its origin.
919 *Geokhimiya*, 8: 1127–1136.

920 Grinenko, L.I. (1985) Sources of sulfur of the nickeliferous and barren gabbro-dolerite
921 intrusions of the northwest Siberian platform. *International Geology Review*, 27(6):
922 695-708.

923 Guo, H., Audetat, A. (2017) Transfer of volatiles and metals from mafic to felsic magmas in
924 composite magma chambers: An experimental study. *Geochimica et Cosmochimica*
925 *Acta*, 198: 360-378.

926 Hall, A.L. (1932) *The Bushveld Igneous Complex in the central Transvaal*. Geological Society,
927 South Africa, Memoir 28, 544 p.

928 Hanley, J.J. (2007) The role of arsenic-rich melts and mineral phases in the development of
929 high-grade Pt-Pd mineralization within komatiite-associated magmatic Ni-Cu sulfide
930 horizons at Dundonald Beach South, Abitibi subprovince, Ontario, Canada. *Economic*
931 *Geology*, 102: 305-317.

- 932 Harvey, J., Day, J.M. (2016) Highly Siderophile and Strongly Chalcophile Elements in High-
933 Temperature Geochemistry and Cosmochemistry. *Reviews in Mineralogy and*
934 *Geochemistry*, 81: 774 p.
- 935 Hattori, K.H., Arai, S., Clarke, D.B. (2002) Selenium, tellurium, arsenic and antimony contents
936 of primary mantle sulfides. *The Canadian Mineralogist*, 40(2): 637-650.
- 937 Helmy, H.M., Ballhaus, C., Berndt, J., Bockrath, C. (2007) Wohlgemuth-Ueberwasser, C.
938 Formation of Pt, Pd and Ni tellurides: Experiments in sulfide–telluride systems.
939 *Contributions to Mineralogy and Petrology*, 153: 577-591.
- 940 Helmy, H.M., Ballhaus, C., Fonseca, R., Nagel, T. (2013) Fractionation of platinum, palladium,
941 nickel, and copper in sulfide–arsenide systems at magmatic temperature. *Contributions*
942 *to Mineralogy and Petrology*, 166: 1725-1737.
- 943 Hiemstra, S. A. (1979) The role of collectors in the formation of the platinum deposits in the
944 Bushveld Complex. *The Canadian Mineralogist*, 17: 469-482.
- 945 Holwell, D., McDonald, I. (2007) Distribution of platinum-group elements in the Platreef at
946 Overysel, northern Bushveld Complex: A combined PGM and LA-ICP-MS study.
947 *Contributions to Mineralogy and Petrology*, 154: 171-190.
- 948 Holwell, D., Adeyemi, Z., Ward, L.A., Smith, D.J., Graham, S.D., McDonald, I., Smith, J.W.
949 (2017) Low temperature alteration of magmatic Ni-Cu-PGE sulfides as a source for
950 hydrothermal Ni and PGE ores: A quantitative approach using automated
951 mineralogy. *Ore Geology Reviews*, 91: 718-740.
- 952 Hutchinson, D., McDonald, I. (2008) Laser ablation ICP-MS study of platinum-group elements
953 in sulphides from the Platreef at Turfspruit, northern limb of the Bushveld Complex,
954 South Africa. *Mineralium Deposita*, 43: 695–711.
- 955 Jamieson, H.E. (2016) The Legacy of Arsenic Contamination from Mining and Processing
956 Refractory Gold Ore at Giant Mine, Yellowknife, Northwest Territories, Canada.
957 *Reviews in Mineralogy and Geochemistry*, 79: 533-551.
- 958 Jenner, F.E. (2017) Cumulate causes for the low contents of sulfide-loving elements in the
959 continental crust. *Nature Geoscience*, 10(7): 524-529.

- 960 Jenner, F.E., O'Neill, H.S.C. (2012) Analysis of 60 elements in 616 ocean floor basaltic
961 glasses. *Geochemistry, Geophysics, Geosystems*, 13(2).
- 962 Junge, M., Wirth, R., Oberthür, T., Melcher, F., Schreiber, A. (2015) Mineralogical siting of
963 platinum-group elements in pentlandite from the Bushveld Complex, South Africa.
964 *Mineralium Deposita*, 50: 41-54.
- 965 Kamenetsky, V.S., Eggins, S.M. (2012) Systematics of metals, metalloids, and volatiles in
966 MORB melts: effects of partial melting, crystal fractionation and degassing (a case
967 study of Macquarie Island glasses). *Chemical Geology*, 302: 76-86.
- 968 Kanitpanyacharoen, W., Boudreau, A.E. (2013) Sulfide-associated mineral assemblages in the
969 Bushveld Complex, South Africa: platinum-group element enrichment by vapor
970 refining by chloride-carbonate fluids. *Mineralium Deposita*, 48(2): 193-210.
- 971 Kawohl, A., Frimmel, H.E. (2016) Isoferroplatinum-pyrrhotite-troilite intergrowth as evidence
972 of desulfurization in the Merensky Reef at Rustenburg (western Bushveld Complex,
973 South Africa). *Mineralogical Magazine*, 80: 1041-1053.
- 974 Keays, R.R., Lightfoot, P.C. (2010) Crustal sulfur is required to form magmatic Ni-Cu sulfide
975 deposits: Evidence from chalcophile element signatures of Siberian and Deccan Trap
976 basalts. *Mineralium Deposita*, 45: 241-257.
- 977 Kelly, D.P., Vaughan, D.J. (1983) Pyrrhotine-pentlandite ore textures: a mechanistic approach.
978 *Mineralogical Magazine*, 47: 453-463.
- 979 Ketris, M.P., Yudovich, Y.E. (2009) Estimations of Clarkes for Carbonaceous biolithes: World
980 averages for trace element contents in black shales and coals. *International Journal of*
981 *Coal Geology*, 78(2): 135-148.
- 982 Kissin, S.A., Scott, S.D. (1982) Phase relations involving pyrrhotite below 350 degrees
983 C. *Economic Geology*, 77(7): 1739-1754.
- 984 Kitakaze, A., Machida, T., Komatsu, R. (2016) Phase relations in the Fe-Ni-S system from 875
985 to 650°C. *The Canadian Mineralogist*, 54: 1175-1186.
- 986 Knight, R.D., Prichard, H.M., Ferreira Filho, C.F. (2017) Evidence for As Contamination and
987 the Partitioning of Pd into Pentlandite and Co+ Platinum Group Elements into Pyrite in
988 the Fazenda Mirabela Intrusion, Brazil. *Economic Geology*, 112(8): 1889-1912.
- 989 König, S., Luguet, A., Lorand, J-P., Wombacher, F., Lissner, M. (2012) Selenium and tellurium
990 systematics of the Earth's mantle from high precision analyses of ultra-depleted
991 orogenic peridotites. *Geochimica et Cosmochimica Acta*, 86: 354-366.

- 992 Kosyakov, V.I., Sinyakova, E.F. (2012) Physicochemical prerequisites for the formation of
993 primary orebody zoning at copper-nickel sulfide deposits (by the example of the
994 systems Fe–Ni–S and Cu–Fe–S). *Russian Geology and Geophysics*, 53(9): 861-882.
- 995 Le Vaillant, M., Barnes, S.J., Fiorentini, M.L., Barnes, S.-J., Bath, A., Miller, J. (2018)
996 Platinum-group element and gold contents of arsenide and sulfarsenide minerals
997 associated with Ni and Au deposits in Archean greenstone belts. *Mineralogical*
998 *Magazine*, 82(3): 625-647.
- 999 Leeb-du Toit, A. (1986) The Impala Platinum Mines. In: Anhaeusser CR, Maske S (ed) *Mineral*
1000 *deposits of Southern Africa*. Geol Soc S Afr Johannesburg, 1091–1106.
- 1001 Leshner, C.M., Burnham, O.M. (2001) Multicomponent elemental and isotopic mixing in Ni–
1002 Cu–(PGE) ores at Kambalda, Western Australia. *The Canadian Mineralogist*, 39(2):
1003 421-446.
- 1004 Li, C., Barnes, S.J., Makovicky, E., Karup-Moller, S., Makovicky, M., Rose-Hansen, J. (1996)
1005 Partitioning of Ni, Cu, Ir, Rh, Pt and Pd between monosulfide solid solution and sulfide
1006 liquid: effects of composition and temperature. *Geochimica et Cosmochimica Acta*, 60:
1007 1231–1238.
- 1008 Li Y., Audétat, A. (2015) Effects of temperature, silicate melt composition, and oxygen fugacity
1009 on the partitioning of V, Mn, Co, Ni, Cu, Zn, As, Mo, Ag, Sn, Sb, W, Au, Pb, and Bi
1010 between sulfide phases and silicate melt. *Geochimica et Cosmochimica Acta* 162, 25-
1011 45.
- 1012 Likhachev, A.P. (1994) Ore-bearing intrusions of the Noril'sk region. In: Lightfoot, P. C.,
1013 Naldrett, A.J. (Eds.), *Proceedings of the Sudbury-Noril'sk Symposium*, Ontario
1014 Geological Survey, special publication issue 5. Ontario Geological Survey, Greater
1015 Sudbury: 185–201.
- 1016 Liu, Y., Brenan, J. (2015) Partitioning of platinum-group elements (PGE) and chalcogens (Se,
1017 Te, As, Sb, Bi) between monosulfide-solid solution (MSS), intermediate solid solution
1018 (ISS) and sulfide liquid at controlled f_{O_2} – f_{S_2} conditions. *Geochimica et Cosmochimica*
1019 *Acta*, 159: 139-161.
- 1020 Lissner, M., König, S., Luguët, A., Le Roux, P., Schuth, S., Heuser, A., le Roex, A.P. (2014)
1021 Selenium and tellurium systematics in MORBs from the southern Mid-Atlantic Ridge
1022 (47–50 S). *Geochimica et Cosmochimica Acta*, 144: 379-402.
- 1023 Lodders, K. (2003) Solar system abundances and condensation temperatures of the elements.
1024 *The Astrophysical Journal*, 591: 1220-1247.

- 1025 Lorand, J-P., Alard, O. (2010) Determination of selenium and tellurium concentrations in
1026 Pyrenean peridotites (Ariege, France): new insight into S/Se/Te systematics of the upper
1027 in mantle samples. *Chemical Geology*, 278(1-2): 120-130.
- 1028 Luguet, A., Behrens, M., Pearson, D.G., König S., Herwartz, D. (2015) Significance of the
1029 whole rock Re–Os ages in cryptically and modally metasomatised cratonic peridotites:
1030 constraints from HSE–Se–Te systematics. *Geochimica et Cosmochimica Acta*, 164:
1031 441–463.
- 1032 Lusk, J., Bray, D.M. (2002) Phase relations and the electrochemical determination of sulfur
1033 fugacity for selected reactions in the Cu–Fe–S and Fe–S systems at 1 bar and
1034 temperatures between 185 and 460°C. *Chemical Geology*, 192(3-4): 227-248.
- 1035 Lyubetskaya, T., Korenaga, J. (2007) Chemical composition of Earth's primitive mantle and its
1036 variance: 1. Method and results. *Journal of Geophysical Research*, 112: B03211.
- 1037 Maciag, B.J., Brenan, J.M. (2020) Speciation of Arsenic and Antimony in Basaltic
1038 Magmas. *Geochimica et Cosmochimica Acta*, 276: 198-218.
- 1039 Maier, W.D., Rasmussen, B., Fletcher, I., Godel, B., Barnes, S.J., Fisher, L., Yang, S.H.,
1040 Huhma, H., Lahaye, Y. (2015) Petrogenesis of the ~2.77 Ga Monts de Cristal Complex,
1041 Gabon: evidence for direct precipitation of Pt-arsenides from basaltic magma. *Journal*
1042 *of Petrology*, 56: 1285-1308.
- 1043 Makovicky, E., Karup-Møller, S., Makovicky, M., Rose-Hansen, J. (1990) Experimental studies
1044 on the phase systems Fe-Ni-Pd-S and Fe-Pt-Pd-As-S applied to PGE
1045 deposits. *Mineralog and Petrology*, 42(1-4): 307-319.
- 1046 Makovicky, E. (2002) Ternary and quaternary phase systems in PGE: Canadian Institute of
1047 Mining, Metallurgy and Petroleum, Special Volume 54: 131–175.
- 1048 Mather, T.A., Witt, M.L.I., Pyle, D.M., Quayle, B.M., Aiuppa, A., Bagnato, E., Ilyinskaya, E.
1049 (2012) Halogens and trace metal emissions from the ongoing 2008 summit eruption of
1050 Kīlauea volcano, Hawaii. *Geochimica et Cosmochimica Acta*, 83: 292-323.
- 1051 Mavrogenes, J.A., O'Neill, H.S.C. (1999) The relative effects of pressure, temperature and
1052 oxygen fugacity on the solubility of sulfide in mafic magmas. *Geochimica et*
1053 *Cosmochimica Acta*, 63(7-8): 1173-1180.

- 1054 McCallum, I.S., Raedeke, L.D., Mathez, E.D. (1980) Investigations of the Stillwater Complex:
1055 Part I. Stratigraphy and structure of the Banded zone. *American Journal of Science*,
1056 280: 59–87.
- 1057 McDonough, W.F. (2003) 2.15 - Compositional model for the earth's core. *Treatise on*
1058 *geochemistry*, 547-568.
- 1059 Milanovskiy, Y.Y. (1976) Rift zones of the geological past and their associated formations,
1060 report 2. *International Geology Review*, 18, 619–639.
- 1061 Moss, R.L., Tzimas, E., Kara, H., Willis, P., Kooroshy, J. (2013) The potential risks from
1062 metals bottlenecks to the deployment of strategic energy technologies. *Energy Policy*,
1063 55: 556-564.
- 1064 Mota-e-Silva, J., Prichard, H.M., Ferreira Filho, C.F., Fisher, P.C., McDonald, I. (2015)
1065 Platinum-group minerals in the Limoeiro Ni–Cu–(PGE) sulfide deposit, Brazil: the
1066 effect of magmatic and upper amphibolite to granulite metamorphic processes on PGM
1067 formation. *Mineralium Deposita*, 50(8): 1007–1029.
- 1068 Mungall, J.E. (2007) Crystallization of magmatic sulfides: An empirical model and application
1069 to Sudbury ores. *Geochimica et Cosmochimica Acta*, 71(11): 2809-2819.
- 1070 Mungall, J.E., Andrews, D.R., Cabri, L.J., Sylvester, P.J., Tubrett, M. (2005) Partitioning of Cu,
1071 Ni, Au, and platinum-group elements between monosulfide solid solution and sulfide
1072 melt under controlled oxygen and sulfur fugacities. *Geochimica et Cosmochimica Acta*,
1073 69: 4349-4360.
- 1074 Naldrett, A.J. (2004) *Magmatic sulfide deposits: Geology, geochemistry and exploration:*
1075 *Berlin, Germany, Springer Verlag: 727 p.*
- 1076 Naldrett, A.J. (2011) Fundamentals of magmatic sulfide deposits. *Reviews in Economic*
1077 *Geology*, 17: 1-50.
- 1078 Naldrett, A.J., Gasparini, E.C., Barnes, S-J., Von Gruenewaldt, G., Sharpe, M.R. (1986) The
1079 upper critical zone of the Bushveld Complex and the origin of Merensky-type ores.
1080 *Economic Geology*, 81: 1105–1117.
- 1081 Naldrett, A.J., Lightfoot, P.C., Fedorenko, V.A., Gorbachev, N.S., Doherty, W. (1992) *Geology*
1082 *and geochemistry of intrusions and flood basalts of the Noril'sk region, USSR, with*
1083 *implications for the origin of the Ni-Cu Ores. Economic Geology*, 87, 975– 1004.
- 1084 Page, N.J. (1977) *Stillwater Complex, Montana: rock succession, metamorphism and structure*
1085 *of the Complex and adjacent rocks. U.S. Geological Survey Professional Paper*, 999.
1086 *Reston, Virginia, USA.*
- 1087 Park, J-W., Campbell, I.H., Arculus, R.J. (2013) Platinum alloy and sulfur saturation in an arc-
1088 related basalt to rhyolite suite; evidence from the Pual Ridge lavas, the eastern Manus
1089 Basin. *Geochimica et Cosmochimica Acta*, 101: 76-95.

- 1090 Paton, C., Hellstrom, J., Paul, B., Woodhead, J., Hergt, J. (2011) Iolite: Freeware for the
1091 visualisation and processing of mass spectrometric data. *The Journal of*
1092 *Analytical Atomic Spectrometry*, 26: 2508-2518.
- 1093 Patten, C.G., Pitcairn, I.K., Teagle, D.A.H. (2017) Hydrothermal mobilisation of Au and other
1094 metals in supra-subduction oceanic crust: Insights from the Troodos ophiolite. *Ore*
1095 *Geology Reviews*, 86: 487-508.
- 1096 Patten, C.G.C., Pitcairn, I.K., Alt, J.C., Zack, T., Lahaye, Y., Teagle, D.A.H., Markdahl, K.
1097 (2019) Metal fluxes during magmatic degassing in the oceanic crust: sulfide
1098 mineralisation at ODP site 786B, Izu-Bonin forearc. *Mineralium Deposita*: 1-21.
- 1099 Péntek, A., Molnár, F., Watkinson, D.H., Jones, P.C. (2008) Footwall-type Cu-Ni-PGE
1100 Mineralization in the Broken Hammer Area, Wisner Township, North Range, Sudbury
1101 Structure. *Economic Geology*, 103: 1005-1028.
- 1102 Piña, R., Gervilla, F., Barnes, S-J., Ortega, L., Lunar, R. (2013) Partition coefficients of
1103 platinum group and chalcophile elements between arsenide and sulfide phases as
1104 determined in the Beni Bousera Cr-Ni mineralization (North Morocco). *Economic*
1105 *Geology*, 108(5): 935-951.
- 1106 Piña, R., Gervilla, F., Barnes, S-J., Ortega, L., Lunar, R. (2015) Liquid immiscibility between
1107 arsenide and sulfide melts: evidence from a LA-ICP-MS study in magmatic deposits at
1108 Serranía de Ronda (Spain). *Mineralium Deposita*, 50(3): 265-279.
- 1109 Piña, R., Gervilla, F., Barnes, S-J., Oberthür, T., Lunar, R. (2016) Platinum-group element
1110 concentrations in pyrite from the Main Sulfide Zone of the Great Dyke of
1111 Zimbabwe. *Mineralium Deposita*, 51(7): 853-872.
- 1112 Polovina, J.S., Hudson, D.M., Jones, R.E. (2004) Petrographic and geochemical characteristics
1113 of postmagmatic hydrothermal alteration and mineralization in the J-M Reef, Stillwater
1114 Complex, Montana. *The Canadian Mineralogist*, 42: 261-278.
- 1115 Polozov, A.G., Svensen, H.H., Planke, S., Grishina, S.N., Fristad, K.E., Jerram, D.A. (2016)
1116 The basalt pipes of the Tunguska Basin (Siberia, Russia): High temperature processes
1117 and volatile degassing into the end-Permian atmosphere. *Palaeogeography,*
1118 *Palaeoclimatology, Palaeoecology*, 441: 51-64.
- 1119 Prichard, H., Hutchinson, D., Fisher, P. (2004) Petrology and crystallization history of
1120 multiphase sulfide droplets in a mafic dike from Uruguay: Implications for the origin of
1121 Cu-Ni-PGE sulfide deposits. *Economic Geology*, 99: 365-376.

- 1122 Queffurus, M., Barnes, S-J. (2014) Selenium and sulfur concentrations in country rocks from
1123 the Duluth Complex, Minnesota, USA: Implications for formation of the Cu-Ni-PGE
1124 sulfides. *Economic Geology*, 109(3): 785-794.
- 1125 Reichow, M.K., Pringle, M.S., Al'Mukhamedov, A.I., Allen, M.B., Andreichev, V.L., Buslov,
1126 M.M., Davies, C.E., Fedoseev, G.S., Fitton, J.G., Inger, S., Medvedev, A.Y., Mitchell,
1127 C., Puchkov, V.N., Safonova, I.Y., Scott, R.A., Saunders, A.D. (2009) The timing and
1128 extent of the eruption of the Siberian traps large igneous province: implications for the
1129 end-Permian environmental crisis. *Earth and Planetary Science Letters*, 277: 9–20.
- 1130 Ripley, E.M., Li, C. (2003) Sulfur isotope exchange and metal enrichment in the formation of
1131 magmatic Cu-Ni-(PGE) deposits. *Economic Geology*, 98: 635-641.
- 1132 Ripley, E.M., Lightfoot, P.C., Li, C., Elswick, E.R. (2003) Sulfur isotopic studies of continental
1133 flood basalts in the Noril'sk region: Implications for the association between lavas and
1134 ore-bearing intrusions. *Geochimica et Cosmochimica Acta*, 67(15): 2805-2817.
- 1135 Ripley, E.M., Li, C., Moore, C.H., Schmitt, A.K. (2010) Micro-scale S isotope studies of the
1136 Kharaelakh intrusion, Noril'sk region, Siberia: constraints on the genesis of coexisting
1137 anhydrite and sulfide minerals. *Geochimica et Cosmochimica Acta*, 74(2): 634-644.
- 1138 Robertson, J., Ripley, E.M., Barnes, S.J., Li, C. (2015) Sulfur liberation from country rocks and
1139 incorporation in mafic magmas. *Economic Geology*, 110(4): 1111-1123.
- 1140 Rose-Weston, L., Brenan, J.M., Fei, Y.W., Secco, R.A., Frost, D.J. (2009) Effect of pressure,
1141 temperature, and oxygen fugacity on the metal-silicate partitioning of Te, Se, and S:
1142 Implications for earth differentiation. *Geochimica et Cosmochimica Acta*, 73(15): 4598-
1143 4615.
- 1144 Rudnick, R. L., Gao, S. (2003) Composition of the continental crust. *The crust*, 3: 1-64.
- 1145 Samalens, N., Barnes, S-J., Sawyer, E.W. (2017) The role of black shales as a source of sulfur
1146 and semimetals in magmatic nickel-copper deposits: Example from the Partridge River
1147 Intrusion, Duluth Complex, Minnesota, USA. *Ore Geology Reviews*, 81(1): 173-187.
- 1148 Scoats, J.S., Friedman, R.M. (2008) Precise age of the platiniferous Merensky reef, Bushveld
1149 Complex, South Africa, by U-Pb zircon chemical abrasion ID-TIMS technique.
1150 *Economic Geology*, 103: 465–471.
- 1151 Shevko, E.P., Bortnikova, S.B., Abrosimova, N.A., Kamenetsky, V.S., Bortnikova, S.P., Panin,
1152 G.L., Zelenski, M. (2018) Trace elements and minerals in fumarolic sulfur: the case of
1153 Ebeko volcano, Kuriles. *Geofluids*: 16.

- 1154 Singh, R., Singh, S., Parihar, P., Singh, V.P., Prasad, S.M. (2015) Arsenic contamination,
1155 consequences and remediation techniques: a review. *Ecotoxicology and Environmental*
1156 *Safety*, 112: 247–270.
- 1157 Sinyakova, E., Kosyakov, V., Distler, V., Karmanov, N. (2016) Behavior of Pt, Pd, and Au
1158 during crystallization of Cu-rich magmatic sulfide minerals. *The Canadian*
1159 *Mineralogist*, 54(2): 491-509.
- 1160 Sinyakova, E. F., Kosyakov, V. I., Borisenko, A. S. (2017). Effect of the presence of As, Bi, and
1161 Te on the behavior of Pt metals during fractionation crystallization of sulfide magma.
1162 *Doklady Earth Sciences*, 477: 1422-1425.
- 1163 Sinyakova, E., Kosyakov, V., Palyanova, G., Karmanov, N. (2019) Experimental Modeling of
1164 Noble and Chalcophile Elements Fractionation during Solidification of Cu-Fe-Ni-S
1165 Melt. *Minerals*, 9(9): 531.
- 1166 South African Committee for Stratigraphy (1980) Stratigraphy of Southern Africa. Part I.
1167 Lithostratigraphy of South Africa, South West Africa/Namibia, and the Republics of
1168 Boputhatswana, Transkei and Venda. Geological Survey of South Africa Handbook 8:
1169 690pp.
- 1170 Stucker, V.K., Walker, S.L., de Ronde, C.E., Caratori Tontini, F., Tsuchida, S. (2017)
1171 Hydrothermal Venting at Hinepuia Submarine Volcano, Kermadec Arc: Understanding
1172 Magmatic-Hydrothermal Fluid Chemistry. *Geochemistry, Geophysics,*
1173 *Geosystems*, 18(10): 3646-3661.
- 1174 Sullivan, N.A., Zajacz, Z., Brenan, J.M. (2018) The solubility of Pd and Au in hydrous
1175 intermediate silicate melts: The effect of oxygen fugacity and the addition of Cl and
1176 S. *Geochimica et Cosmochimica Acta*, 231: 15-29.
- 1177 Tuba, G., Molnár, F., Ames, D.E., Péntek, A., Watkinson, D.H., Jones, P.C. (2014) Multi-stage
1178 hydrothermal processes involved in —low-sulfide Cu (-Ni)-PGE mineralization in the
1179 footwall of the Sudbury Igneous Complex (Canada): Amy Lake PGE zone, East Range.
1180 *Mineralium Deposita*, 49: 7-47.
- 1181 U.S Food and Drug Administration, (2015) Inductively Coupled Plasma-Mass Spectrometric
1182 Determination of Arsenic, Cadmium, Chromium, Lead, Mercury, and Other Elements in
1183 Food Using Microwave Assisted Digestion. Accessed at <<
1184 [https://www.fda.gov/food/laboratory-methods-food/elemental-analysis-manual-eam-](https://www.fda.gov/food/laboratory-methods-food/elemental-analysis-manual-eam-food-and-related-products)
1185 [food-and-related-products](https://www.fda.gov/food/laboratory-methods-food/elemental-analysis-manual-eam-food-and-related-products) >>

- 1186 U.S. Geological Survey, (2020) MineralCommodity Summaries. Accessed at
1187 <<<https://www.usgs.gov/media/images/mineral-commodities-february-2020>>>
- 1188 Wall, C.J., Scoates, J.S., Friedman, R.M., Meurer, W.P. (2010) Refining the precise age and
1189 duration of magmatism related to the Stillwater Complex. In: 11th International
1190 Platinum Symposium, Sudbury, Ontario, June 20–24, 2010.
- 1191 Wang, Z., Becker, H. (2013) Ratios of S, Se and Te in the silicate Earth require a volatile-rich
1192 late veneer. *Nature*, 499: 328-331.
- 1193 Wieser, P., Jenner, F., Edmonds, M., MacLennan, J., Kunz, B. (2020) Chalcophile elements
1194 track the fate of sulfur at Kīlauea Volcano, Hawai‘i. *Geochimica et Cosmochimica*
1195 *Acta*.
- 1196 Wirth, R., Reid, D., Schreiber, A. (2013) Nanometer-sized platinum-group minerals (PGM) in
1197 base metal sulfides: new evidence for an orthomagmatic origin of the Merensky Reef
1198 PGE ore deposit, Bushveld Complex, South Africa. *The Canadian Mineralogist*, 51:
1199 143-155.
- 1200 Wood, S.A. (2002) The aqueous geochemistry of the platinum-group elements with applications
1201 to the ore deposits. In *Geology, Geochemistry, Mineralogy and Mineral Beneficiation of*
1202 *Platinum Group Element* (ed. L.J. Cabri). Canadian Institute of Mining, Metallurgy and
1203 Petroleum, Special volume 54: 211–249.
- 1204 Yierpan, A., König, S., Labidi, J., Schoenberg, R. (2019) Selenium isotope and S-Se-Te
1205 elemental systematics along the Pacific-Antarctic ridge: Role of mantle
1206 processes. *Geochimica et Cosmochimica Acta*, 249: 199-224.
- 1207 Zelenski, M.E., Fischer, T.P., de Moor, J.M., Marty, B., Zimmermann, L., Ayalew, D.,
1208 Nekrasov, AN., Karandashev, V.K. (2013) Trace elements in the gas emissions from the
1209 Erta Ale volcano, Afar, Ethiopia. *Chemical Geology*, 357: 95-116.
- 1210 Zelenski, M., Malik, N., Taran, Y. (2014) Emissions of trace elements during the 2012–2013
1211 effusive eruption of Tolbachik volcano, Kamchatka-enrichment factors, partition
1212 coefficients and aerosol contribution. *Journal of Volcanology and Geothermal Research*,
1213 285: 136–149.
- 1214 Zientek, M.L., Likhachev, A.P., Kunilov, V.E., Barnes, S-J., Meier, A.L., Carlson, R.R., Briggs,
1215 P.H., Fries, T.L., Adrian, B.M. (1994) Cumulus processes and the composition of
1216 magmatic ore deposits: examples from the Talnakh District, Russia. In: Lightfoot, P.C.,
1217 Naldrett, A.J. (Eds.), *Proceedings of the Sudbury-Noril’sk Symposium*, Ontario
1218 Geological Survey, special publication issue 5. Ontario Geological Survey, Greater
1219 Sudbury: 373–392.

1220 Zientek, M.L., Cooper, R.W., Corson, S.R., Geraghty, E.P. (2002) Platinum-group element
1221 mineralization in the Stillwater Complex, Montana. In *Geology, Geochemistry,
1222 Mineralogy and Mineral Benefication of Platinum Group Element* (ed. L.J. Cabri).
1223 Canadian Institute of Mining, Metallurgy and Petroleum, Special volume 54: 459–481.
1224 Zweibel, K. (2010) The Impact of Tellurium Supply on Cadmium Telluride Photovoltaics.
1225 *Science*, 328: 699-701.

1226

1227

1228

1229

1230

1231

1232

1233

1234

1235

1236

1237

1238

1239

1240

1241

1242

1243

1244

1245

1

2
3
4
5
6
7
8
9
10
11
12
13
14
15
16
17
18
19
20
21
22
23
24
25
26
27
28
29
30
31

Chapter 2 - Determination of Te, As, Bi, Sb and Se (TABS) in Geological Reference Materials and GeoPT Proficiency Test Materials by Hydride Generation-Atomic Fluorescence Spectrometry (HG-AFS)

Eduardo Teixeira **Mansur** (1), Sarah-Jane **Barnes** (1), Dany **Savard** (1) and Peter **Webb** (2)

(1) Sciences de la Terre, Université du Québec à Chicoutimi, Québec, G7H 2B1, Canada

(2) Formerly of the Department of Environment, Earth and Ecosystems, The Open University, Walton Hall, Milton Keynes, MK7 6AA, United Kingdom

Author contributions:

Mansur wrote the manuscript, collected and analyzed the data and created the figures. **Barnes** edited the manuscript and analyzed the data. **Savard** and **Webb** helped implementing the analytical protocol presented in the manuscript as well as contributed to the interpretation of the analyzed and literature data.

32 **2.1 - Abstract**

33 The study of Te, As, Bi, Sb and Se (TABS) has increased over the past years due to
34 their use in the development of low-carbon energy technologies. However, there is a
35 scarcity of concentrations of TABS in geological reference materials. This underlines
36 the difficulty in undertaking routine analysis of these elements. The concentrations of
37 TABS were determined in geological reference materials using hydride generation-
38 atomic fluorescence spectrometry (HG-AFS), calibrated with standard solutions.
39 Comparisons with literature values were used to validate the method. Samples from the
40 *GeoPT* proficiency test were also analyzed. For most elements there are no assigned or
41 even provisional values for many of the *GeoPT* and reference materials because of the
42 wide range of results reported. For concentrations above the quantification limit of the
43 method our results are in good agreement with the median of *GeoPT* results. Thus, we
44 propose *GeoPT* median values as informational values for these elements. In contrast, at
45 concentrations $< 0.5 \mu\text{g/g}$ median values of Se from *GeoPT* are systematically higher
46 than our results. Our Se results are in agreement with the reference materials down to
47 $0.02 \mu\text{g/g}$, which suggest that many of the results for Se reported in *GeoPT* testing are
48 too high.

49

50 Keywords: Te, As, Bi, Sb, Se; HG-AFS; geological reference materials; *GeoPT*.

51

52

53

54

55

56 **2.2 – Introduction**

57

58 The determination of Te, As, Bi, Sb and Se (TABS; Barnes 2016) is critical for
59 both environmental and economic reasons. These elements pose risks to the
60 environment (especially As and Sb), such as through the contamination of soils, surface
61 drainage and groundwater (*e.g.* Jamieson 2014; Singh *et al.* 2015). Consequently, most
62 TABS are routinely monitored in various materials as elevated concentrations can be
63 highly toxic (Wu 2004; Duker *et al.* 2005; Sundar and Chakravarty 2010). On the other
64 hand, TABS are also classified as critical raw materials for the development of low-
65 carbon energy technologies (Zweibel 2010; Moss *et al.* 2013). Thus, the demand for
66 analytical methods capable of quantifying these elements down to low levels is
67 continually increasing.

68 Although most studies have focused on the importance of TABS in
69 environmental and health issues over the past decades, there is a growing demand to
70 understand their geochemical cycles (Hattori *et al.* 2002; Wang and Becker 2013;
71 Brenan 2015). For example, TABS may be particularly important during the formation
72 of platinum-group elements and gold deposits (Pitcairn *et al.* 2015; Barnes and Ripley
73 2016). However, there are very few values for TABS concentrations in geological
74 reference materials (especially of Bi, Se and Te), and consequently analytical protocols
75 are difficult to validate. Therefore, the geological interpretations of the data are
76 weakened by the uncertainty in the analytical results.

77 Atomic fluorescence spectrometry (AFS), coupled to hydride generation (HG),
78 is an effective method for determining elements such as TABS that form covalent
79 hydrides (Corns *et al.* 1993). Consequently, HG-AFS has been applied for monitoring

80 trace amounts of TABS in materials such as food (Reyes *et al.* 2008; Zhang *et al.* 2011;
81 Cava-Montesinos *et al.* 2013; Lai *et al.* 2016) and water (He *et al.* 1998; Yan *et al.*
82 2002). This technique has also been used by geologists to assess the behaviour of TABS
83 during various geological processes (Pitcairn 2004; Pitcairn *et al.* 2015; Patten *et al.*
84 2016). The concentrations of TABS in geological materials are variable (Hattori *et al.*
85 2002; Ketriss and Yudovich 2009; Samalens *et al.* 2017; Henrique-Pinto *et al.* 2015),
86 and in some cases (especially for Se and Te), very low (Wang and Becker 2014; König
87 *et al.* 2012, 2014; Lissner *et al.* 2014). The method appears suitable for studying the
88 distribution of TABS in geological materials. However, to date HG-AFS has not been
89 comprehensively tested using geological reference materials.

90 In this work we first establish the effectiveness of HG-AFS by determining the
91 concentrations of TABS in a series of geological reference materials and comparing the
92 results with literature values. In addition, we report results for TABS in GeoPT
93 proficiency test materials, and compare the results with GeoPT assigned and provisional
94 values where available, and where not, with ranges of values reported by participating
95 laboratories. We will show that our results mostly agree with the median values of
96 results reported by GeoPT participating laboratories for Te, As, Bi and Sb and propose
97 that these values could be used as informational values. However, the median values for
98 the generally rather small Se datasets reported in GeoPT proficiency tests are elevated
99 in comparison to our results. Because the values that we determined for Se in the
100 reference materials are in agreement with certified or provisional values we suggest that
101 many of the results contributed to the GeoPT tests are probably overestimations.

102

103

104

105 **2.3 – Experimental**

106 The analytical protocol is a slightly modified version of the method implemented
107 by Pitcairn (2004).

108 **2.3.1 - Digestion of the rock samples**

109 Around 0.2 g of rock powder was mixed with 5 ml of aqua regia (1:3
110 HNO₃:HCl; PlasmaPURE – SPC Science) in a 50 ml-disposable beaker (Digi TUBES –
111 SCP Science). The closed-cap beaker was swirled and then placed in a digestion block
112 for 2 hours at room temperature, and further heated up to 80°C for 22 hours. The
113 solution was then allowed to cool and diluted to 25 ml with distilled water (Fig. 2.1). A
114 different sample digest was prepared for each individual measurement.

115 The digestion of rock samples has to take into account the volatile behaviour of
116 TABS (Corns *et al.* 1993; König *et al.* 2012; Wang and Becker 2014), and thus avoid a
117 loss by volatilization. The use of closed-cap beakers and low temperature are
118 fundamental (Wang and Becker 2014). Previous studies indicate that heating the sample
119 up to 80°C in a closed system results in digestion without any analyte loss. In fact,
120 heating the analytes to temperatures below 100°C is a common step adopted in several
121 analytical routines to ensure the reduction of TABS prior to analysis without any loss
122 (Pitcairn 2004; He *et al.* 1998; Savard *et al.* 2006, 2009; König *et al.* 2012; Wang and
123 Becker 2014).

124

125 **2.3.2 - Preparation of analytical solutions**

126

127 The hydride generation method makes use of the ability of TABS to form
128 covalent gaseous hydrides (*e.g.*, AsH₃, SbH₃). However, the formation of hydrides by

129 these elements depends on them being in the reduced oxidation state (Corns *et al.*
130 1993). Consequently, the preparation of solutions for analysis requires a pre-reduction
131 step, which varies for each element. Hence, As and Sb were measured in a different
132 aliquot from Te, Se and Bi.

133 The aliquots were prepared by adding 10 ml of the digested rock solution to 30
134 ml of a reagent blank (Fig. 2.1) in a 50 ml disposable beaker. For the As and Sb aliquot,
135 the reagent blank was a solution of 6 mol l⁻¹ HCl, 13 g l⁻¹ potassium iodide (KI; VWR
136 Chemicals), and 3.5 g l⁻¹ ascorbic acid (VWR Chemicals; Fig. 2.1). The KI and the
137 ascorbic acid are used to reduce the oxidation state of Sb^V and As^V to Sb^{III} and As^{III},
138 respectively (Nielsen and Hansen 1997; Potin-Gautier *et al.* 2005). For the Te, Se and
139 Bi aliquot the reagent blank does not need any KI or ascorbic acid, and consists only of
140 a 6 mol l⁻¹ HCl solution (Fig. 2.1). The pre-reduction of Se and Te was achieved by
141 heating the aliquot to 80°C for 40 minutes in a water bath, in a closed-cap beaker (Cava-
142 Montesinos *et al.* 2003; Savard *et al.* 2006). During this step, the Se^{VI} and the Te^{VI} are
143 converted to Se^{IV} and Te^{IV}, respectively, which is necessary to ensure the formation of
144 hydrides (Corns *et al.* 1993).

145

146 **2.3.3 - Instrumentation**

147 Analyses were performed at LabMaTer, Université du Québec à Chicoutimi
148 (UQAC), using a continuous flow hydride generation-atomic fluorescence spectrometer,
149 the PSA Millenium Excalibur 10.055 from PS Analytical. The instrument was equipped
150 with boosted hollow cathode discharge (BHCD) lamps for As, Sb, Se, Te and Bi, and
151 the primary currents were 27.5, 17.5, 20, 15 and 20 mA, respectively. The analytical
152 solution was mixed with a reductant solution (Fig. 2.1), at flow rates of 9 ml min⁻¹ and

153 4.5 ml min⁻¹, respectively. The reductant solution was prepared by mixing 14 g of
154 NaBH₄ and 8 g of NaOH with 2 l of distilled water. Hence, the gaseous hydrides were
155 formed after the reaction between HCl and NaBH₄, and further atomised using a
156 hydrogen flame fed by excess H₂ gas created during the reaction. The BHCD lamp
157 focussed on the flame provided the excitation source for the fluorescence of the element
158 analysed, which was then measured by an AFS detector. Atomic fluorescence signals
159 were recorded and measured on the basis of the peak height of the signal.

160

161 **2.3.4 - Calibration**

162 Six calibration solutions with concentrations of 0.1, 0.25, 0.5, 1, 2.5 and 5 ng ml⁻¹
163 were prepared for each element of interest. These solutions were prepared from 1000
164 µg ml⁻¹ standard solutions of each element (PlasmaCAL, SPC Science). All the
165 calibration solutions were mixed with the reagent blank prior to measurement, in the
166 same proportion as sample aliquots (i.e. 10 ml of calibration solution and 30 ml of
167 reagent blank). Calibration solutions were measured at the beginning and the end of
168 each sequence of analysis to monitor fluctuations of the fluorescence signal. The
169 calibration curves obtained were all linear.

170

171 **2.3.5 - Detection limits of the method**

172 As the detection limit (LoD) for each element we used three times the standard
173 deviation (3σ) of corresponding measurements on the blank solutions (Long and
174 Winefordner 1983; Potts 1987). These values were calculated using the results for thirty
175 blank solutions prepared in the same manner as the samples (total procedure). The
176 detection limits obtained were 0.01, 0.019, 0.016, 0.026 and 0.002 µg g⁻¹ for Te, As, Bi,

177 Sb and Se, respectively (Table 2.1). We chose to use ten times the standard deviation
178 (10σ) of the blank solutions to estimate limits of quantification for each element (LoQ;
179 Potts 1987).

180

181 **2.4 – Results and Discussion**

182 **2.4.1 – Precision and accuracy based on geological reference materials**

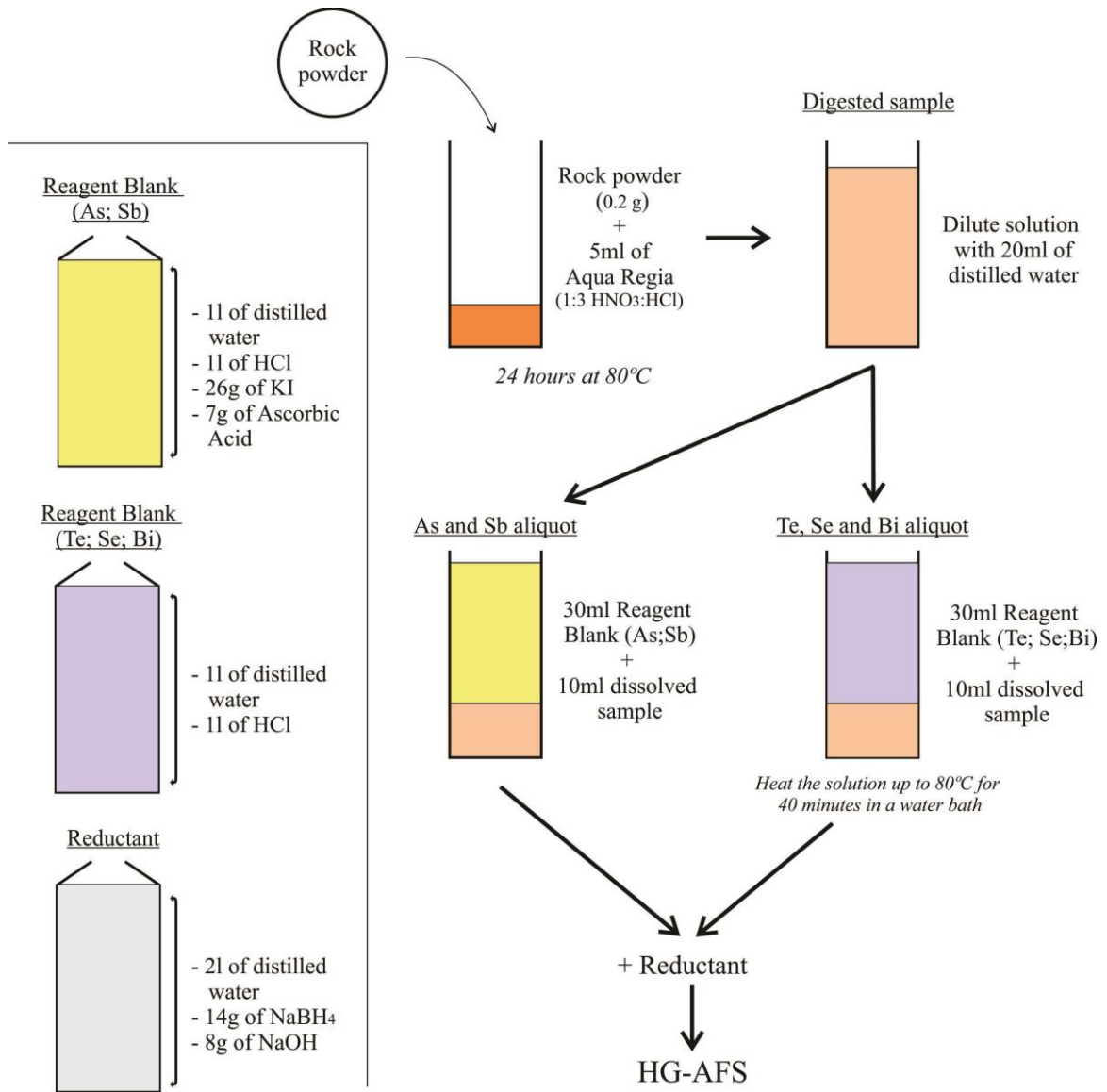
183 The average HG-AFS measurements, the standard deviations (1σ) and the
184 relative standard deviations (% RSD) obtained for ten geological reference materials
185 (CH-4, TDB-1, OKUM, WPR-1, WMG-1, AN-G, BE-N, BIR-1, W-2 and WGB-1) and
186 one in-house reference material (KPT-1) are presented in Table 2.1. The full dataset is
187 available in the *ANNEXES (ANNEXE 1)*. Three reference materials (CH-4, TDB-1 and
188 KPT-1) were measured in every round to monitor the reproducibility of the method.
189 Only reference materials CH-4 and TDB-1 have been previously analyzed using HG-
190 AFS (Pitcairn *et al.* 2015; Patten *et al.* 2016), and the reported values for Te, Se, As and
191 Sb are in the same range of our results (*ANNEXE 1*).

192 The Horwitz function (Horwitz *et al.* 1980) was used to evaluate the acceptable
193 variability of the measurements, which will vary following the concentration in the
194 material. For example, according to the Horwitz function a relative uncertainty of 32%
195 is acceptable at a concentration of $0.01 \mu\text{g g}^{-1}$, whereas the uncertainty should fall to
196 11.3% at a concentration of $10 \mu\text{g g}^{-1}$. The HG-AFS measurement results have % RSD
197 values below the acceptable limits as derived from the Horwitz function (%RSD (Hz);
198 Table 2.1) for most samples. A characteristic of the Horwitz function is for greater
199 variations in the %RSD to be obtained for lower concentrations of an element.
200 Moreover, individual measurements of the same sample digest for reference materials

201 CH-4, TDB-1 and KPT-1 were carried out (Table 2.1), and were characterised by lower
202 %RSD than those from different sample digests (Table 2.1). This suggests that the
203 general variations in %RSD mostly reflect different concentrations of TABS in the
204 reference materials.

205 The only two HG-AFS measurements with %RSD greater than the acceptable
206 variability were the Bi and Sb determinations for reference material TDB-1 (Table 2.1).
207 High uncertainties reported for Bi and Sb in the certificate of analysis for TDB-1
208 suggest that high % RSD may reflect sample heterogeneity. In order to evaluate the
209 problem, different sample masses were used in digestion of materials CH-4, TDB-1 and
210 KPT-1 (i.e. 0.1, 0.2 and 0.4g). The HG-AFS results are recorded in Table 2.2. The
211 %RSD are similar to slightly lower for sample digests of 0.4 g. However, for Bi and Sb
212 determinations in TDB-1 the %RSD are significantly lower for sample digests of 0.4 g
213 (Table 2.2). This supports the belief that %RSD values greater than the acceptable
214 variability are likely reflect minor heterogeneities of some elements. Therefore, for most
215 reference materials 0.2 g is suitable, whereas measurements with high %RSD may be
216 improved by preparing a sample of a greater sample mass.

217



218

219 Figure 2.1 - Schematic flow diagram showing the main preparation steps for reagents and aliquots. See text for
 220 further explanation. HG-AFS – hydride generation-atomic fluorescence spectrometry.

221

222

223

224

225

226

227

228

229 Table 2.1 - Te, As, Bi, Sb and Se results for geological reference materials by HG-AFS.

Sample ID	n*	Rock type		Te	As	Bi	Sb	Se
LoD		Blank	3σ (μg g ⁻¹)	0.010	0.019	0.016	0.026	0.002
LoQ		Blank	10σ (μg g ⁻¹)	0.032	0.064	0.055	0.088	0.0081
CH-4	7	Anorthosite	Ave (μg g ⁻¹)	0.414	8.534	0.676	0.844	1.942
			SD (1σ)	0.073	0.355	0.094	0.062	0.044
			% RSD	17.712	4.163	13.900	7.334	2.272
			% RSD (Hz)	18.266	11.585	16.968	16.409	14.476
TDB-1	7	Diabase	Ave (μg g ⁻¹)	0.043	2.127	0.064	1.034	0.344
			SD (1σ)	0.006	0.207	0.024	0.176	0.029
			% RSD	12.961	9.717	37.609	16.984	8.494
			% RSD (Hz)	25.656	14.279	24.186	15.916	18.785
KPT-1	7	Quartz diorite	Ave (μg g ⁻¹)	0.498	2.151	0.907	11.077	2.959
			SD (1σ)	0.060	0.280	0.085	0.247	0.113
			% RSD	11.959	13.041	9.361	2.232	3.832
			% RSD (Hz)	17.768	14.255	16.234	11.139	13.587
OKUM	3	Komatiite	Ave (μg g ⁻¹)	0.053	0.241	0.072	0.111	0.101
			SD (1σ)	0.006	0.039	0.011	0.014	0.011
			% RSD	10.340	16.128	15.799	12.234	10.950
			% RSD (Hz)	24.862	19.819	23.785	22.271	22.588
WPR-1	3	Peridotite	Ave (μg g ⁻¹)	0.474	1.070	0.194	0.876	3.859
			SD (1σ)	0.027	0.130	0.015	0.108	0.083
			% RSD	5.606	12.111	7.568	12.326	2.143
			% RSD (Hz)	17.900	15.834	20.471	16.319	13.055
WMG-1	3	Gabbro	Ave (μg g ⁻¹)	1.419	7.087	0.489	1.920	13.635
			SD (1σ)	0.081	0.207	0.050	0.081	0.536
			% RSD	5.716	2.915	10.277	4.216	3.930
			% RSD (Hz)	15.176	11.913	17.817	14.501	10.796
AN-G	3	Anorthosite	Ave (μg g ⁻¹)	<0.01	0.024	0.070	0.117	0.028
			SD (1σ)	n.a.	0.003	0.014	0.007	0.005
			% RSD	n.a.	12.633	20.204	6.278	17.726
			% RSD (Hz)	n.a.	28.069	23.893	22.096	27.430
BEN	3	Basalt	Ave (μg g ⁻¹)	<0.01	1.808	<0.016	0.294	0.070
			SD (1σ)	n.a.	0.045	n.a.	0.006	0.006
			% RSD	n.a.	2.473	n.a.	1.894	8.975
			% RSD (Hz)	n.a.	14.633	n.a.	19.238	23.895
BIR-1	3	Basalt	Ave (μg g ⁻¹)	<0.01	0.054	0.017	0.543	0.016
			SD (1σ)	n.a.	0.005	0.002	0.024	0.002
			% RSD	n.a.	8.968	14.280	4.428	14.863
			% RSD (Hz)	n.a.	24.801	29.449	17.539	29.689
W-2	3	Diabase	Ave (μg g ⁻¹)	0.011	0.767	0.073	0.786	0.087
			SD (1σ)	0.001	0.048	0.016	0.037	0.004
			% RSD	4.660	6.259	21.623	4.659	4.981
			% RSD (Hz)	31.379	16.650	23.731	16.588	23.121
WGB-1	3	Gabbro	Ave (μg g ⁻¹)	0.013	1.595	0.052	1.810	0.092
			SD (1σ)	0.002	0.047	0.009	0.040	0.008
			% RSD	18.085	2.946	17.925	2.184	8.549
			% RSD (Hz)	30.674	14.911	24.934	14.630	22.903

230 LoD = limit of detection; LoQ = limit of quantification; Ave= Average value; % RSD (Hz)= Target % RSD calculated
 231 using the Horwitz function; n.a= non applicable; * Number of individual determinations

1 Table 2.2 - Te, As, Bi, Sb and Se results for geological reference materials by HG-AFS using different samples weights.

		CH-4					TDB-1				KPT-1			
		Anorthosite					Diabase				Quartz diorite			
	Sample weight (grams)	N	Ave ($\mu\text{g g}^{-1}$)	SD (1σ)	% RSD	% RSD (Hz)	Ave ($\mu\text{g g}^{-1}$)	SD (1σ)	% RSD	% RSD (Hz)	Ave ($\mu\text{g g}^{-1}$)	SD (1σ)	% RSD	% RSD (Hz)
Te	0.1 (n=4)	4	0.369	0.094	25.4	18.6	0.047	0.006	13.6	25.3	0.533	0.070	13.2	17.6
	0.2 (n=7)	7	0.414	0.073	17.7	18.3	0.043	0.006	13.0	25.7	0.498	0.060	12.0	17.8
	0.4 (n=4)	4	0.43	0.04	8.1	18.2	0.030	0.004	14.6	27.1	0.49	0.04	8.2	17.8
	0.2 (n=3)	1	0.469	0.035	7.4	17.9	0.047	0.004	8.5	25.4	0.533	0.048	9.1	17.6
As	0.1 (n=4)	4	8.773	0.245	2.8	11.5	2.210	0.270	12.2	14.2	1.878	0.131	7.0	14.5
	0.2 (n=7)	7	8.534	0.355	4.2	11.6	2.127	0.207	9.7	14.3	2.151	0.280	13.0	14.3
	0.4 (n=4)	4	8.400	0.219	2.6	11.6	2.041	0.213	10.4	14.4	2.246	0.111	4.9	14.2
	0.2 (n=3)	1	8.455	0.320	3.8	11.6	2.210	0.196	8.9	14.2	1.878	0.100	5.3	14.5
Bi	0.1 (n=4)	4	0.610	0.092	15.1	17.2	0.062	0.030	48.9	24.3	0.847	0.068	8.1	16.4
	0.2 (n=7)	7	0.676	0.094	13.9	17.0	0.064	0.024	37.6	24.2	0.907	0.085	9.4	16.2
	0.4 (n=4)	4	0.800	0.074	9.2	16.5	0.084	0.005	6.0	23.2	0.943	0.075	7.9	16.1
	0.2 (n=3)	1	0.748	0.063	8.4	16.7	0.046	0.002	5.1	25.4	0.847	0.048	5.6	16.4

Table 2.2 – Continuation

Sb	0.1 (n=4)	4	0.876	0.068	7.8	16.3	0.857	0.136	15.8	16.4	11.113	0.240	2.2	11.1
	0.2 (n=7)	7	0.844	0.062	7.3	16.4	1.034	0.176	17.0	15.9	11.077	0.247	2.2	11.1
	0.4 (n=4)	4	0.877	0.082	9.4	16.3	0.931	0.064	6.9	16.2	11.031	0.153	1.4	11.1
	0.2 (n=3)	1	0.790	0.019	2.4	16.6	0.857	0.018	2.1	16.4	11.113	0.173	1.6	11.1
Se	0.1 (n=4)	4	1.944	0.057	3.0	14.5	0.343	0.026	7.5	18.8	3.029	0.134	4.4	13.5
	0.2 (n=7)	7	1.942	0.044	2.3	14.5	0.344	0.029	8.5	18.8	2.959	0.113	3.8	13.6
	0.4 (n=4)	4	1.928	0.039	2.0	14.5	0.394	0.071	13.1	18.4	2.934	0.054	1.8	13.6
	0.2 (n=3)	1	1.936	0.044	2.3	14.5	0.343	0.020	5.8	18.8	3.029	0.102	3.4	13.5

2 Abbreviations: Ave= Average value; % RSD (Hz)= Target % RSD calculated using the Horwitz function; n = number of individual determinations; N= number of sample digests.

1 The accuracy of the method was evaluated by comparing measured quantities for
2 reference materials with literature values. The literature values of TABS for all the
3 reference materials were compiled from the GeoReM database (Jochum et al. 2005).
4 Comparisons are shown in Fig. 2.2., where measures values mostly fall within the range
5 of literature values.

6 All determinations of Sb and Se are above their respective limits of quantification,
7 i.e. $0.088 \mu\text{g g}^{-1}$ and $0.008 \mu\text{g g}^{-1}$ (Table 2.1), and are within uncertainties with literature
8 values for all the reference materials (Fig. 2.2a and 2.2b). For five reference materials
9 (TDB-1, OKUM, AN-G, BIR and BEN), Se measurements by the isotopic dilution
10 method are available (König *et al.* 2012, 2014; Wang and Becker 2013). Our results are
11 within uncertainties of the results for TDB-1, BIR and BEN, but are slightly lower
12 compared to OKUM and AN-G. However, results obtained by other methods for these
13 materials are within uncertainties of our results. Thus, the method is validated for Sb and
14 Se down to $0.09 \mu\text{g g}^{-1}$ and $0.008 \mu\text{g g}^{-1}$, respectively (the limits of quantification).

15 Arsenic and Bi concentrations in most of the reference materials are above the
16 limits of quantification (0.064 and $0.055 \mu\text{g g}^{-1}$ respectively). Measured quantities of As
17 are within the range of literature values except for the two samples (AN-G and BIR-1),
18 which are below the limit of quantification, but above the limit of detection (Fig. 2.2c).
19 For these samples, the results are lower than literature values but still within range of
20 literature results when the uncertainties of the literature values are considered. Therefore,
21 we consider the method validated for As down to the limit of quantification. For Bi there
22 is a more limited range of reference materials available and the results are variable. The
23 results are in the same range as the literature values down to $0.2 \mu\text{g g}^{-1}$ (Fig. 2.2d), and we
24 consider the method validated down to this level. There are a number of reference
25 materials with concentrations close to the limit of quantification, for three of these the

26 obtained values are higher than the literature values and for two they are lower than
27 literature values. The source of the differences is not clear, but a weakness of the
28 literature values is that all were determined by the same method (ICP-MS).

29 For Te, literature values are very sparse and variable making comparison
30 problematic. For the six reference materials above the limits of quantification of $0.032 \mu\text{g}$
31 g^{-1} the values fall within the range of literature values except for OKUM, where the value
32 is slightly higher (Fig. 2.2e). For the reference materials TDB-1, OKUM, AN-G, BIR and
33 BEN, Te measurements by the isotopic dilution method are also available (König *et al.*
34 2012, 2014; Wang and Becker 2013). Obtained results are below the quantification limits
35 for materials AN-G, BIR and BEN, which is in accord with isotopic dilution results lower
36 than $0.004 \mu\text{g g}^{-1}$ for these materials. For TDB-1 and OKUM our Te measurements (0.043
37 $\mu\text{g g}^{-1}$ and $0.053 \mu\text{g g}^{-1}$, respectively) are higher than those obtained by isotopic dilution
38 ($0.006 \mu\text{g g}^{-1}$ and $0.025 \mu\text{g g}^{-1}$, respectively). However, our results are within
39 uncertainties of literature values of TDB-1, including results by HG-AFS by Patten *et al.*
40 (2016), obtained at a different laboratory. For the reference material OKUM, only a Te
41 measurement by isotopic dilution data is available, not allowing a comparison with
42 results from various studies, ideally using different analytical methods. The discrepancies
43 of Te results for these two reference materials suggest that either the HG-AFS
44 measurements (Patten *et al.* 2016 and this study) are slightly overestimated, or isotopic
45 dilution results are slightly underestimated (Wang and Becker 2013; König *et al.* 2012,
46 2014).

47 In summary, the HG-AFS method is considered sufficiently accurate for
48 measuring concentrations of Te, As, Bi, Sb and Se above their respective limits of
49 quantification (Table 2.1). The % RSD values are below the acceptable limits calculated

50 from the Horwitz function in almost all of the reference materials, which demonstrates
51 that the method is sufficiently precise to satisfy the analytical requirements.

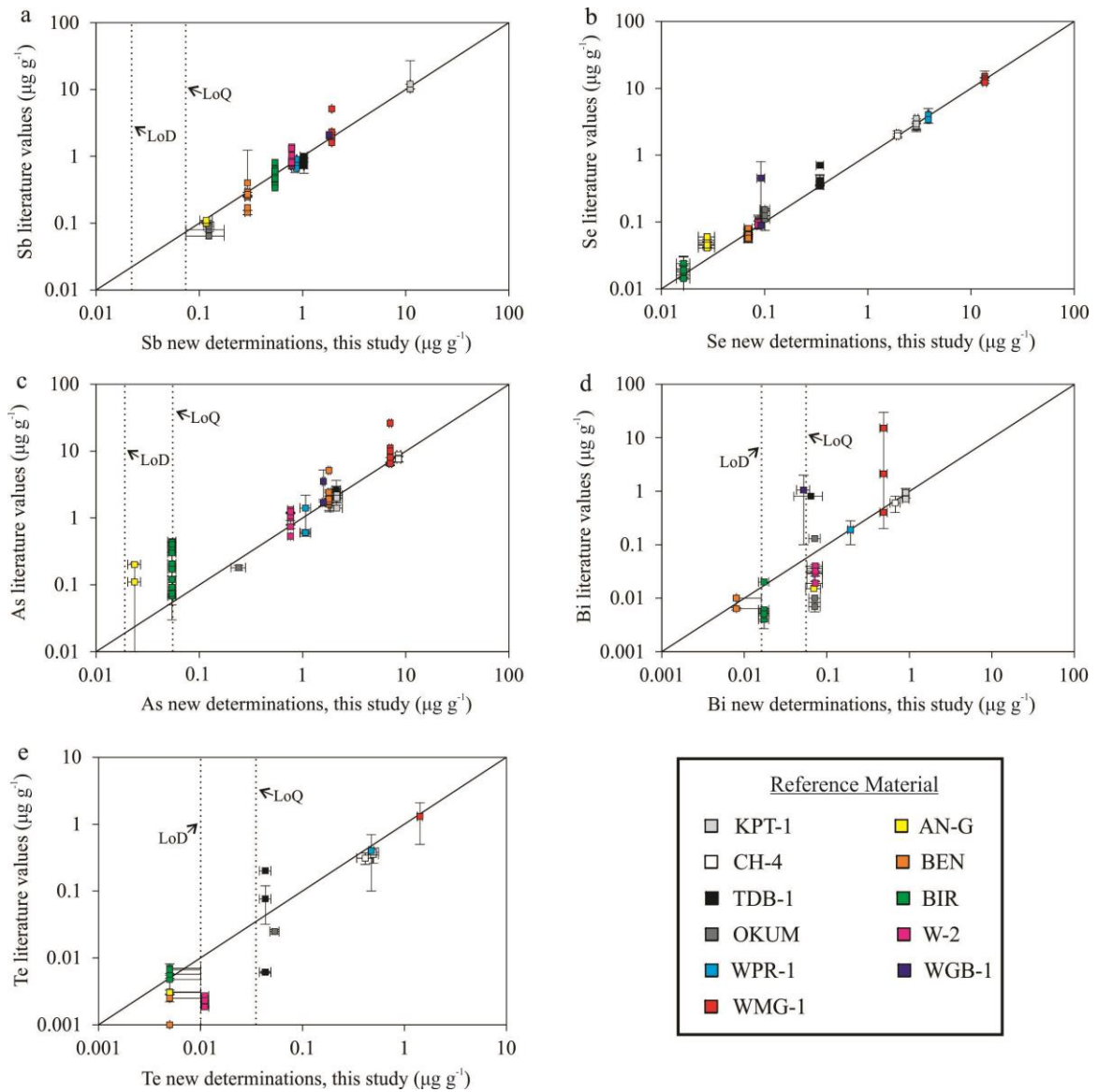
52

53 **2.4.2 – IAG GeoPT Proficiency Test Samples**

54 The International Association of Geoanalysts (IAG) conducts a proficiency testing
55 program, named *GeoPT*, designed to enable geoanalytical laboratories to routinely assess
56 their analytical performance. In each round of *GeoPT*, participating laboratories analyze
57 powders of the same test material (*GeoPT* samples), and report quantity values of major
58 and trace element constituents to the *GeoPT* organisers. A detailed account of the
59 proficiency testing programme and how proficiency testing values are obtained may be
60 found in the *GeoPT* protocol (IAG 2018). To increase the dataset of measurement results
61 for TABS in geological materials, 34 test samples from previous *GeoPT* rounds were
62 analyzed by HG-AFS (Table 2.3), and the results compared with values derived from the
63 proficiency tests (Table 2.4).

64 The Horwitz function was calculated for the HG-AFS measurement results on
65 each sample, and 85% of the results had %RSD values lower than those acceptable limits
66 (Table 2.3), validating the precision of the method. For most results with % RSD values
67 higher than the tolerance provided by the Horwitz function, the measurements are close
68 to the LoD of the method, which may explain the discrepancy.

69



70

71 Figure 2.2 - Comparison of new HG-AFS determinations and literature values for (a) Sb, (b) Se, (c) As, (d) Bi and (e)
 72 Te. Uncertainties are shown by error bars at the 1 σ level. For materials with a compositional range, instead of a result,
 73 the range is plotted using an error bar. Dashed lines indicate the limit of detection (LoD) and limit of quantification
 74 (LoQ) for HG-AFS.

75

76

77

78

79

80

81

82

83

84 Table 2.3 - Te, As, Bi, Sb and Se results for GeoPT proficiency test samples by HG-AFS.

Sample ID	n*	Rock type		Te	As	Bi	Sb	Se
LoD		blank	3σ (μg g ⁻¹)	0.010	0.019	0.016	0.026	0.002
LoQ		blank	10σ (μg g ⁻¹)	0.032	0.064	0.055	0.088	0.0081
GeoPT-06 (OU-3)	4	Nanhoron microgranite	Ave (μg g ⁻¹)	0.020	0.917	0.227	0.221	0.028
			SD (1σ)	0.007	0.052	0.085	0.018	0.011
			% RSD	31.9	5.6	37.7	8.1	39.6
			% RSD (Hz)	28.7	16.2	20.0	20.1	27.4
GeoPT-08 (OU-4)	4	Penmaenmawr microdiorite	Ave (μg g ⁻¹)	0.019	1.317	0.090	0.289	0.019
			SD (1σ)	0.010	0.071	0.017	0.038	0.004
			% RSD	53.7	5.4	18.7	13.2	20.3
			% RSD (Hz)	29.1	15.3	23.0	19.3	29.1
GeoPT-10 (CH-1)	4	Marine sediment	Ave (μg g ⁻¹)	0.080	3.648	0.309	0.960	0.543
			SD (1σ)	0.009	0.184	0.033	0.022	0.019
			% RSD	11.3	5.1	10.6	2.3	3.6
			% RSD (Hz)	23.4	13.2	19.1	16.1	17.5
GeoPT-11 (OU-5)	4	Leiton dolerite	Ave (μg g ⁻¹)	0.028	2.413	0.073	0.470	0.021
			SD (1σ)	0.017	0.046	0.023	0.031	0.001
			% RSD	58.8	1.9	31.1	6.6	6.3
			% RSD (Hz)	27.4	14.0	23.7	17.9	28.7
GeoPT-12 (GAS)	4	Serpentine	Ave (μg g ⁻¹)	0.027	115.628	0.141	12.304	0.029
			SD (1σ)	0.008	3.514	0.046	0.340	0.003
			% RSD	30.9	3.0	32.8	2.8	11.4
			% RSD (Hz)	27.6	7.8	21.5	11.0	27.2
GeoPT-13 (UoK Loess)	4	Köln loess	Ave (μg g ⁻¹)	0.016	6.470	0.159	0.350	0.029
			SD (1σ)	0.008	0.230	0.020	0.056	0.001
			% RSD	51.9	3.6	12.7	16.0	3.7
			% RSD (Hz)	29.7	12.1	21.1	18.7	27.3
GeoPT-15 (MSAN)	4	Ocean Floor sediment	Ave (μg g ⁻¹)	0.078	7.161	0.112	0.457	0.533
			SD (1σ)	0.006	0.301	0.041	0.066	0.049
			% RSD	7.3	4.2	36.6	14.5	9.1
			% RSD (Hz)	23.5	11.9	22.2	18.0	17.6
GeoPT-16 (BNV-1)	4	Nevada basalt	Ave (μg g ⁻¹)	0.023	2.358	0.063	0.164	0.025
			SD (1σ)	0.013	0.112	0.002	0.019	0.004
			% RSD	58.9	4.7	3.0	11.5	15.5
			% RSD (Hz)	28.3	14.1	24.3	21.0	27.9
GeoPT-17 (OU-8)	4	Calcareous sandstone	Ave (μg g ⁻¹)	<0.01	0.963	0.058	0.165	0.007
			SD (1σ)	n.a.	0.076	0.016	0.022	0.002
			% RSD	n.a.	7.9	27.7	13.2	28.4
			% RSD (Hz)	n.a.	16.1	24.5	21.0	34.0
GeoPT-18 (KPT-1)	4	Quartz diorite	Ave (μg g ⁻¹)	0.500	2.199	0.854	10.720	2.988
			SD (1σ)	0.021	0.158	0.078	0.353	0.085
			% RSD	4.1	7.2	9.1	3.3	2.9
			% RSD (Hz)	17.8	14.2	16.4	11.2	13.6
GeoPT-19 (MGR-N)	4	Gabbro	Ave (μg g ⁻¹)	0.082	1.764	0.162	0.151	0.500
			SD (1σ)	0.009	0.070	0.013	0.008	0.055
			% RSD	11.4	4.0	7.9	5.1	11.0
			% RSD (Hz)	23.3	14.7	21.0	21.3	17.8
GeoPT-20 (OPY-1)	4	Ultramafic rock	Ave (μg g ⁻¹)	0.037	0.324	<0.016	0.188	0.105
			SD (1σ)	0.005	0.047	n.a.	0.028	0.009
			% RSD	13.1	14.4	n.a.	14.8	8.3
			% RSD (Hz)	26.3	19.0	n.a.	20.6	22.4

Table 2.3 - Continuation

GeoPT-21 (MGT-1)	4	Granite	Ave ($\mu\text{g g}^{-1}$) SD (1σ) % RSD % RSD (Hz)	0.043 0.020 46.0 25.7	2.080 0.115 5.5 14.3	1.102 0.041 3.7 15.8	0.244 0.033 13.6 19.8	0.009 0.005 54.5 32.6
GeoPT-22 (MBL-1)	4	Basalt	Ave ($\mu\text{g g}^{-1}$) SD (1σ) % RSD % RSD (Hz)	0.208 0.036 17.3 20.3	1.624 0.089 5.5 14.9	0.092 0.010 10.3 22.9	0.224 0.022 9.9 20.0	0.028 0.008 30.3 27.4
GeoPT-23 (OU-9)	4	Separation Lake pegmatite	Ave ($\mu\text{g g}^{-1}$) SD (1σ) % RSD % RSD (Hz)	0.211 0.017 8.1 20.2	2.670 0.073 2.7 13.8	0.064 0.028 43.8 24.2	6.443 0.437 6.8 12.1	0.006 0.000 6.7 34.5
GeoPT-24 (OU-10)	4	Longmyndian greywacke	Ave ($\mu\text{g g}^{-1}$) SD (1σ) % RSD % RSD (Hz)	0.186 0.036 19.1 20.6	1.769 0.015 0.9 14.7	0.143 0.016 11.0 21.4	0.242 0.027 11.2 19.8	0.010 0.002 20.3 32.0
GeoPT-25 (HTB-1)	4	Basalt	Ave ($\mu\text{g g}^{-1}$) SD (1σ) % RSD % RSD (Hz)	0.226 0.040 17.9 20.0	0.203 0.014 6.8 20.3	0.054 0.027 50.2 24.8	0.233 0.021 9.2 19.9	0.173 0.031 18.1 20.8
GeoPT-27 (MGL- AND)	4	Andesite	Ave ($\mu\text{g g}^{-1}$) SD (1σ) % RSD % RSD (Hz)	0.198 0.025 12.8 20.4	2.004 0.084 4.2 14.4	0.074 0.018 24.2 23.7	0.230 0.012 5.0 20.0	0.003 0.001 17.1 38.0
GeoPT-29 (NKT-1)	4	Nephelinite	Ave ($\mu\text{g g}^{-1}$) SD (1σ) % RSD % RSD (Hz)	<0.01 n.a. n.a. n.a.	1.836 0.064 3.5 14.6	0.052 0.016 31.1 24.9	0.358 0.019 5.4 18.7	0.035 0.002 5.0 26.6
GeoPT-30 (CG-2)	4	Syenite	Ave ($\mu\text{g g}^{-1}$) SD (1σ) % RSD % RSD (Hz)	<0.01 n.a. n.a. n.a.	4.244 0.138 3.2 12.9	0.169 0.021 12.5 20.9	0.819 0.046 5.7 16.5	0.011 0.001 9.9 31.4
GeoPT-31 (SdAR-1)	4	Modified River Sediment	Ave ($\mu\text{g g}^{-1}$) SD (1σ) % RSD % RSD (Hz)	0.399 0.031 7.9 18.4	35.139 0.538 1.5 9.4	1.775 0.066 3.7 14.7	5.923 0.384 6.5 12.2	0.300 0.020 6.6 19.2
GeoPT-32 (WG-1)	4	Woodstock basalt	Ave ($\mu\text{g g}^{-1}$) SD (1σ) % RSD % RSD (Hz)	0.016 0.009 60.2 29.9	0.575 0.065 11.3 17.4	0.052 0.018 35.2 24.9	0.071 0.014 19.6 23.8	0.021 0.001 4.4 28.6
GeoPT-33 (DBC-1)	4	Ball Clay	Ave ($\mu\text{g g}^{-1}$) SD (1σ) % RSD % RSD (Hz)	0.259 0.037 14.3 19.6	3.285 0.093 2.8 13.4	1.683 0.150 8.9 14.8	1.587 0.054 3.4 14.9	2.442 0.091 3.7 14.0
GeoPT-34 (GRI-1)	4	Granite	Ave ($\mu\text{g g}^{-1}$) SD (1σ) % RSD % RSD (Hz)	<0.01 n.a. n.a. n.a.	1.044 0.088 8.5 15.9	0.057 0.010 17.1 24.6	0.204 0.015 7.4 20.3	0.049 0.003 6.7 25.2

Table 2.3 - Continuation

GeoPT-35 (TLM-1)	4	Tonalite	Ave ($\mu\text{g g}^{-1}$)	<0.01	2.295	0.092	1.556	0.010
			SD (1σ)	n.a.	0.100	0.025	0.062	0.001
			% RSD	n.a.	4.4	27.4	4.0	5.7
			% RSD (Hz)	n.a.	14.1	22.9	15.0	31.9
GeoPT-36 (GSM-1)	4	Gabbro	Ave ($\mu\text{g g}^{-1}$)	0.032	2.470	0.116	1.934	0.213
			SD (1σ)	0.007	0.214	0.015	0.038	0.015
			% RSD	23.3	8.6	12.9	2.0	6.9
			% RSD (Hz)	26.8	14.0	22.1	14.5	20.2
GeoPT-36A (SdAR-M2)	4	Metal-rich sediment	Ave ($\mu\text{g g}^{-1}$)	1.096	72.972	1.051	111.793	3.321
			SD (1σ)	0.084	2.455	0.108	2.520	0.268
			% RSD	7.7	3.4	10.3	2.3	8.1
			% RSD (Hz)	15.8	8.4	15.9	7.9	13.4
GeoPT-37 (ORPT-1)	4	Rhyolite	Ave ($\mu\text{g g}^{-1}$)	<0.01	0.423	0.063	0.253	0.005
			SD (1σ)	n.a.	0.025	0.021	0.042	0.003
			% RSD	n.a.	5.9	33.1	16.7	53.8
			% RSD (Hz)	n.a.	18.2	24.2	19.7	35.3
GeoPT-38 (OU-7)	4	Ardnamurchan gabbro	Ave ($\mu\text{g g}^{-1}$)	<0.01	0.152	0.032	0.059	0.082
			SD (1σ)	n.a.	0.008	0.008	0.014	0.003
			% RSD	n.a.	5.3	24.8	24.5	3.2
			% RSD (Hz)	n.a.	21.2	26.8	24.5	23.3
GeoPT-38A (HARZ01)	4	Modified harzburgite	Ave ($\mu\text{g g}^{-1}$)	0.014	0.282	0.077	1.175	0.031
			SD (1σ)	0.004	0.029	0.018	0.050	0.005
			% RSD	26.4	10.4	23.1	4.3	14.9
			% RSD (Hz)	30.5	19.4	23.5	15.6	26.9
GeoPT-39 (SyMP-1)	4	Syenite	Ave ($\mu\text{g g}^{-1}$)	0.138	3.666	0.800	0.231	0.182
			SD (1σ)	0.011	0.117	0.028	0.012	0.004
			% RSD	7.6	3.2	3.5	5.2	2.1
			% RSD (Hz)	21.6	13.2	16.5	19.9	20.7
GeoPT-39A (MNS-1)	4	Nepheline syenite	Ave ($\mu\text{g g}^{-1}$)	0.020	22.144	1.062	3.176	0.035
			SD (1σ)	0.004	0.971	0.081	0.196	0.003
			% RSD	18.6	4.4	7.6	6.2	9.9
			% RSD (Hz)	28.8	10.0	15.9	13.4	26.5
GeoPT-40 (ShWYO-1)	4	Silty marine shale	Ave ($\mu\text{g g}^{-1}$)	0.071	10.275	0.334	0.907	0.565
			SD (1σ)	0.010	0.722	0.008	0.056	0.022
			% RSD	14.3	7.0	2.3	6.2	3.9
			% RSD (Hz)	23.8	11.3	18.9	16.2	17.4
GeoPT-41 (ORA-1)	4	Andesite	Ave ($\mu\text{g g}^{-1}$)	<0.01	0.258	0.050	0.975	0.004
			SD (1σ)	n.a.	0.020	0.011	0.050	0.001
			% RSD	n.a.	7.8	21.8	5.1	34.9
			% RSD (Hz)	n.a.	19.6	25.1	16.1	37.3

87

88 LoD = limit of detection; LoQ = limit of quantification; Ave= Average value; % RSD (Hz)= Target % RSD calculated

89 using the Horwitz function; n.a= non applicable; * Number of individual determinations

90

91 Whenever possible, assigned and provisional values from *GeoPT* reports were
92 taken for comparison with measured values of each element (Table 2.4). For the materials
93 for which neither assigned nor provisional values were available from *GeoPT* reports,
94 median values of all concentration values reported by participants were used as a
95 reference (Table 2.4). Figure 2.3 shows the comparison of our measurement results with
96 *GeoPT* assigned, provisional and median values. Our results are also compared with all
97 individual concentrations reported by the participating laboratories, for each element in
98 Fig. 2.4.

99

100 **2.4.2.1 - Antimony and Bismuth**

101

102 Our Sb and Bi measurement results are in close agreement with assigned and
103 provisional values for most of the test materials (Fig. 2.3a and 2.3b; Tables 2.3 and 2.4).
104 Exceptions are *GeoPT* samples 13, 29 and 33 for Sb, and *GeoPT* sample 36 for Bi.
105 Although these four results do not agree with the assigned or provisional values, they fall
106 well within the range of reported values (Fig. 2.4a and 2.4b). For those samples which
107 have neither assigned nor provisional values, and which are above the respective limits of
108 quantification, the Sb and Bi HG-AFS results are similar to the median values of the
109 *GeoPT* contributed data (Fig. 2.3a and 2.3b; Tables 2.3 and 2.4). Therefore, for most
110 samples without assigned or provisional values, and for which HG-AFS results are above
111 our quantification limits, we suggest that the median values for Bi and Sb could be used
112 as informational values. Exceptions to this are for Bi in *GeoPT* samples 12, 16, 19, 23
113 and 29, and Sb for *GeoPT* sample 25, where our results fall within the range of reported
114 results (Fig. 2.4a and 2.4b), but differ from the median value. All of these samples
115 contain less than $0.2 \mu\text{g g}^{-1}$ Bi according to the HG-AFS determination. Below $0.3 \mu\text{g g}^{-1}$

116 Bi, the range of values reported in some cases by *GeoPT* participants increases from one
117 order of magnitude to over three, and in some cases too few data were reported, thus the
118 median *GeoPT* values may not always be adequate, especially at low levels. Therefore,
119 there appears to be considerable room for improvement in determination of Bi at low
120 levels by the geoanalytical community.

121

122 **2.4.2.2 – Arsenic**

123

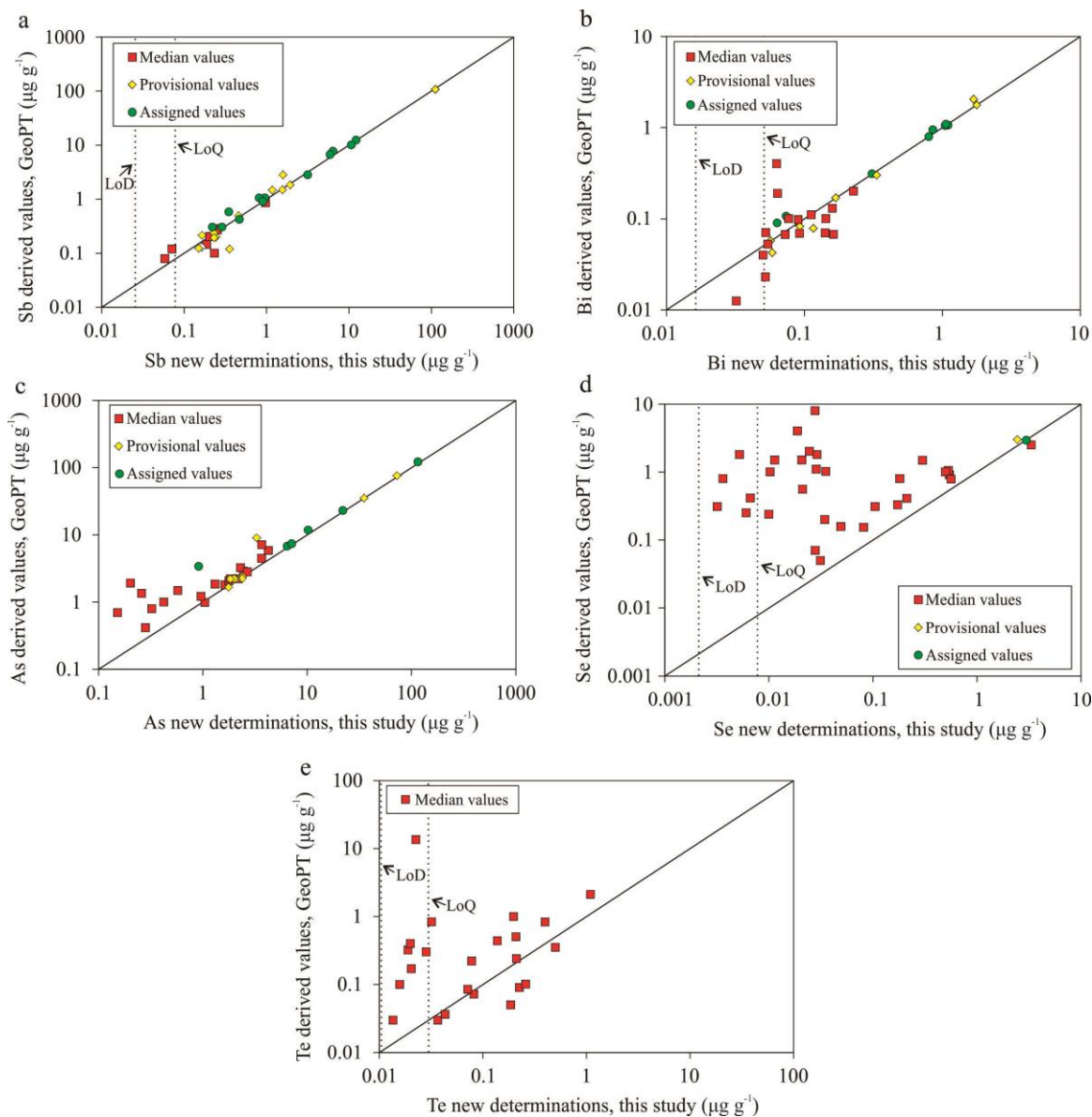
124 Arsenic results are in good agreement with most of the assigned and provisional
125 values (Fig. 2.3c; Tables 2.3 and 2.4). The exceptions are results on *GeoPT* test samples
126 06 and 33. Our results are lower than assigned and provisional values for these two
127 samples, and at the lower end of reported values (Fig. 2.4c). The reasons for these
128 discrepancies are not clear.

129 For samples with no assigned or provisional values, the medians of the *GeoPT*
130 rounds are in agreement with our results for concentrations above $1 \mu\text{g g}^{-1}$ (Fig. 2.3c, and
131 Table 2.4). However, for samples with As concentrations below $1 \mu\text{g g}^{-1}$, our results are
132 lower than *GeoPT* median values (Fig. 2.3c), although still within the range of reported
133 values (Fig. 2.4c). However, as discussed above we consider our method valid down to
134 the limit of quantification ($0.064 \mu\text{g g}^{-1}$), and all of these samples appear to contain more
135 than $0.1 \mu\text{g g}^{-1}$ As. Therefore, we suggest that the *GeoPT* median values for samples with
136 As concentrations below $1 \mu\text{g g}^{-1}$ overestimate the As concentrations. As in the case of Bi,
137 the ranges of the results reported from the *GeoPT* tests are much wider for samples with
138 less than $1 \mu\text{g g}^{-1}$ As (2 to 3 orders of magnitude), than for samples above $1 \mu\text{g g}^{-1}$
139 (generally 1 order of magnitude, Fig. 2.4c). We suggest that median values for samples
140 with As concentrations greater than $1 \mu\text{g g}^{-1}$ could be used as informational values.

141 Table 2.4 - Assigned, provisional and median values for GeoPT proficiency test samples.

Sample ID	Assigned, <i>provisional</i> and median values ($\mu\text{g g}^{-1}$)					Reference
	Te	As	Bi	Sb	Se	
GeoPT-06	0.17	3.379	0.2	0.305	8	Potts <i>et al.</i> 2000
GeoPT-08	0.32	1.85	0.098	0.302	4	Potts <i>et al.</i> 2000b
GeoPT-10	n.r.	4.465	0.31	1.05	0.9	Potts <i>et al.</i> 2001
GeoPT-11	0.30	<u>2.45</u>	0.067	0.42	1.5	Potts <i>et al.</i> 2002
GeoPT-12	n.r.	121.1	0.07	12.29	1.8	Potts <i>et al.</i> 2003
GeoPT-13	n.r.	6.746	0.13	0.58	1.1	Potts <i>et al.</i> 2003b
GeoPT-15	0.22	7.32	0.11	<u>0.49</u>	1.05	Potts <i>et al.</i> 2004
GeoPT-16	13.5	<u>2.328</u>	0.4	<u>0.13</u>	2	Potts <i>et al.</i> 2005
GeoPT-17	0.04	1.214	<u>0.043</u>	<u>0.215</u>	0.414	Potts <i>et al.</i> 2005b
GeoPT-18	0.35	2.21	0.945	10.005	2.93	Webb <i>et al.</i> 2006
GeoPT-19	0.072	<u>1.75</u>	0.068	<u>0.124</u>	1	Webb <i>et al.</i> 2006b
GeoPT-20	0.03	0.8	0.1	0.145	0.31	Webb <i>et al.</i> 2007
GeoPT-21	0.036	<u>2.315</u>	1.06	<u>0.2</u>	n.r.	Webb <i>et al.</i> 2007b
GeoPT-22	0.502	1.8	0.069	<u>0.29</u>	0.07	Webb <i>et al.</i> 2008
GeoPT-23	0.24	2.82	0.19	7.669	0.25	Webb <i>et al.</i> 2008b
GeoPT-24	0.05	2.02	0.1	0.287	0.238	Webb <i>et al.</i> 2009
GeoPT-25	0.09	1.915	0.053	0.1	0.329	Webb <i>et al.</i> 2009b
GeoPT-27	1	<u>2.346</u>	0.106	<u>0.237</u>	0.31	Webb <i>et al.</i> 2010
GeoPT-29	0.03	2.2	0.023	<u>0.12</u>	0.2	Webb <i>et al.</i> 2011
GeoPT-30	0.041	5.85	<u>0.17</u>	1.054	1.5	Webb <i>et al.</i> 2012
GeoPT-31	0.825	<u>36.43</u>	<u>1.77</u>	6.667	1.48	Webb <i>et al.</i> 2012b
GeoPT-32	0.1	1.486	0.07	0.12	0.556	Webb <i>et al.</i> 2013
GeoPT-33	0.101	<u>9</u>	<u>2.04</u>	<u>2.809</u>	<u>3.006</u>	Webb <i>et al.</i> 2013b
GeoPT-34	0.07	0.99	<u>0.057</u>	0.205	0.158	Webb <i>et al.</i> 2014
GeoPT-35	0.023	3.255	<u>0.083</u>	<u>1.49</u>	1	Webb <i>et al.</i> 2014b
GeoPT-36	0.836	2.86	<u>0.079</u>	<u>1.83</u>	0.41	Webb <i>et al.</i> 2015
GeoPT-36A	2.12	<u>75.82</u>	1.05	<u>106.6</u>	2.5	Webb <i>et al.</i> 2015b
GeoPT-37	0.19	1	0.09	0.27	1.8	Webb <i>et al.</i> 2015c
GeoPT-38	0.424	0.7	0.013	0.079	0.153	Webb <i>et al.</i> 2016
GeoPT-38A	0.03	0.39	0.1	<u>1.473</u>	0.05	Webb <i>et al.</i> 2016b
GeoPT-39	0.439	7.1	0.79	<u>0.194</u>	0.8	Webb <i>et al.</i> 2016c
GeoPT-39A	0.4	22.94	1.086	2.8	1.02	Webb <i>et al.</i> 2016d
GeoPT-40	0.085	11.75	<u>0.3</u>	0.9	0.784	Webb <i>et al.</i> 2017
GeoPT-41	0.048	1.35	0.04	0.858	0.801	Webb <i>et al.</i> 2017b

142



143

144 Figure 2.3 - Comparison of new HG-AFS determinations with assigned and provisional values from GeoPT reports and
 145 median values (this work, from Table 2.4) of GeoPT proficiency test materials for (a) Sb, (b) Bi, (c) As, (d) Se and (e)
 146 Te. Values with mass fractions below the detection limits (Table 2.3) are not plotted. Dashed lines indicate the limit of
 147 detection (LoD) and limit of quantification (LoQ) for HG-AFS.

148

149 2.4.2.3 - Selenium

150

151 Among the *GeoPT* samples only KPT-1 (*GeoPT*-18) and DBC-1 (*GeoPT*-33)
 152 have assigned and provisional values for Se, respectively (Table 2.4). The HG-AFS
 153 results for these samples are in excellent agreement with these assigned and provisional

154 values (Fig. 2.3d). In addition, the median values for samples 36A and 40 are close to our
155 determinations (Tables 2.3 and 2.4). For the other samples, the values determined for Se
156 by HG-AFS are lower than the *GeoPT* median values (Fig. 2.4d; Tables 2.3 and 2.4), and
157 below $0.1 \mu\text{g g}^{-1}$ most of our results are less than *GeoPT* results by one to two orders of
158 magnitude. All of the samples contain Se concentrations above the HG-AFS detection
159 limit, and all but four are above the quantification limit (i.e. $0.008 \mu\text{g g}^{-1}$). As discussed
160 above, the method was demonstrated to be sufficiently accurate at these concentrations as
161 evidenced by measurement of geological reference materials (Fig. 2.2b). Therefore, we
162 must conclude that the majority of Se values reported in the *GeoPT* test (especially those
163 below $0.1 \mu\text{g g}^{-1}$) are significant overestimates (see especially Fig. 2.4d).

164

165 **2.4.2.4 – Tellurium**

166

167 The number of laboratories that have reported Te concentrations for *GeoPT* test materials
168 is low, and thus no assigned or provisional values are available (Table 2.4). Moreover,
169 the median values are unlikely to be reliable unless a sufficient number of measurements
170 have been reported. For samples above the limit of quantification ($0.032 \mu\text{g g}^{-1}$) there is
171 broadly a positive correlation (0.86) between the HG-AFS Te results and the median
172 values of the *GeoPT* contributed values (Fig. 2.3e). This observation suggests that the
173 median results for the samples with Te concentrations greater than $0.032 \mu\text{g g}^{-1}$
174 approximate to the correct order of magnitude. However, the range of *GeoPT* test values
175 reported by participants is very large (0.01 to $10 \mu\text{g g}^{-1}$; Fig. 2.4e). Unlike the
176 observations for As and Bi the variability did not change regardless of the median
177 concentration. Based on the validation of the HG-AFS with reference materials (Fig.
178 2.2e), we propose that our HG-AFS Te results, above the limit of quantification ($0.032 \mu\text{g}$

179 g^{-1}), could be used as informational values. Once again, this illustrates the lack of well-
180 characterised reference materials for Te at sub $\mu\text{g g}^{-1}$ levels, and reinforces the need of
181 further studies.

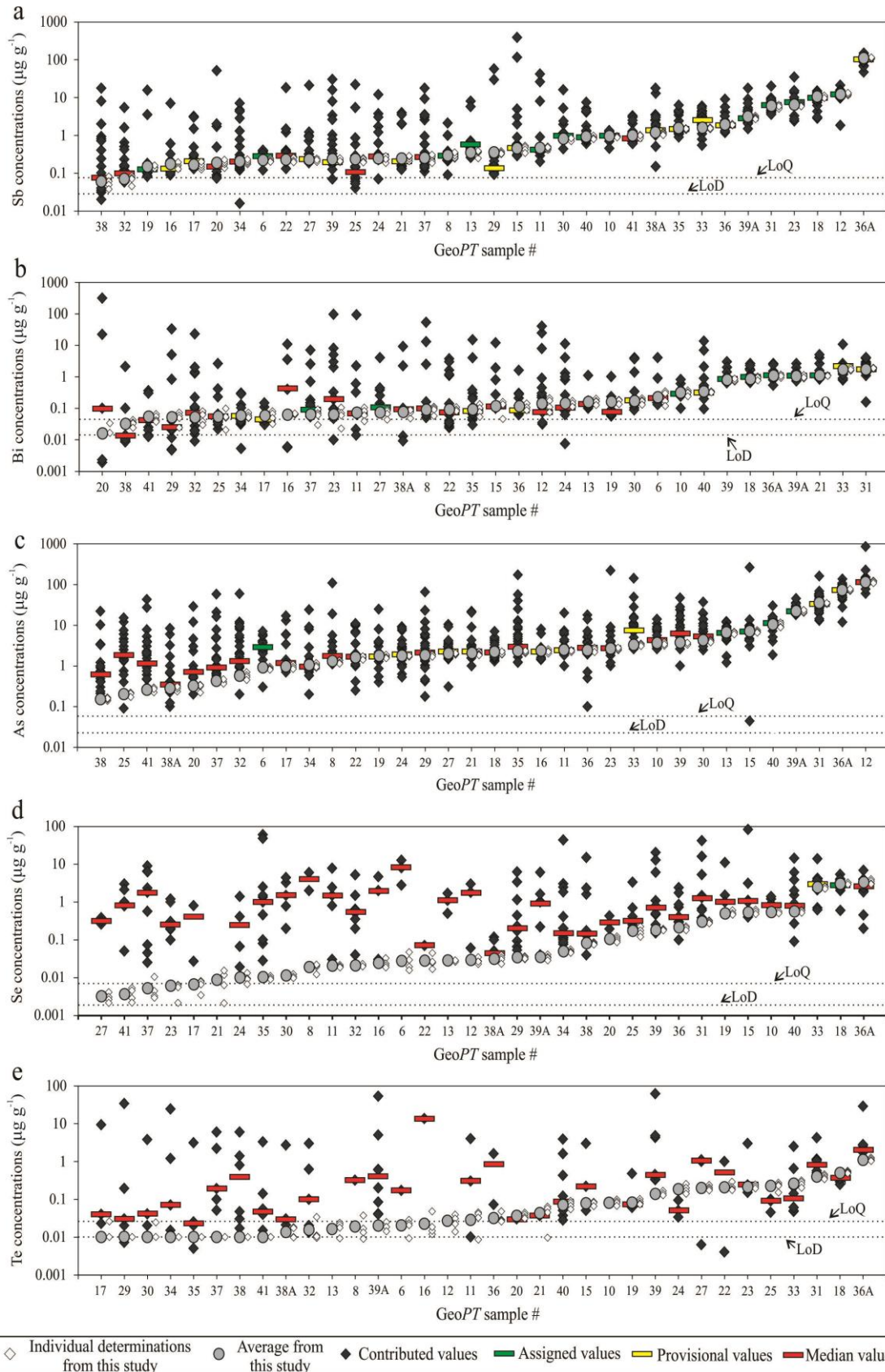
182

183 **2.4.3 - Variability of TABS values in GeoPT Proficiency Test Results**

184

185 The datasets of measurement results for TABS in GeoPT samples are, in some
186 cases, extremely variable. The variability of results is greater for samples with low
187 concentrations of a given element. Such variability may be due to some participating
188 laboratories reporting measurements close to their detection limits. These measurements
189 may have consequently been overestimated, resulting in a wide range of measurements
190 and in some cases overestimated median values. For less commonly analyzed elements
191 such as Se and Te, precise and accurate measurements normally require a highly
192 specialized analytical procedure (Savard *et al.* 2006, 2009; Wang and Becker 2014;
193 König *et al.* 2012, 2014; Lissner *et al.* 2014). Therefore, the wide range of measurements
194 may reflect analyses performed in routine analytical procedures, which may not properly
195 account for properties such as the oxidation state, and volatile behaviour of these
196 elements.

197 A final consideration is the “nugget” effect. All of these elements are chalcophile
198 and could be present in the samples only as minute sulfide grains, thus at low
199 concentrations nugget effects maybe in part the source of the variation (Bédard *et al.*
200 2016). Tellurium, Bi and Se are strongly to highly chalcophile elements with partition
201 coefficients into sulfides greater than 400 (Barnes and Ripley 2016), and their
202 concentrations are very low, thus they are particularly vulnerable to the nugget effect.



203

204

205

206

Figure 2.4 - Comparison of new determinations and all previously reported results by other laboratories for GeoPT proficiency test materials for (a) Sb, (b) Bi, (c) As, (d) Se and (e) Te. Dashed lines indicate the limit of detection (LoD) and limit of quantification (LoQ) for HG-AFS.

207 **2.5 – Conclusion**

208 The characterisation of TABS in geological reference materials is a subject that
209 needs more attention, as illustrated by the paucity of information and wide variation of
210 literature values. This work demonstrates that aqua regia digestion followed by HG-AFS
211 is an appropriate method for determination of TABS in geological materials to sub $\mu\text{g g}^{-1}$
212 level. The study provides results for TABS in 10 international geological reference
213 materials (CH-4, TDB-1, OKUM, WPR-1, WMG-1, AN-G, BE-N, BIR-1, W-2 and
214 WGB-1) and 34 test materials from the *GeoPT* programme. The comparison between
215 HG-AFS results and geological reference materials results validates the method for
216 measuring Te, As, Bi, Sb and Se above their respective limits of quantification. Our
217 results agree with *GeoPT* results for Sb, and we suggest that for those samples with no
218 assigned or provisional values the *GeoPT* median values could be used as informational
219 values. Above $0.3 \mu\text{g g}^{-1}$ Bi, and $1 \mu\text{g g}^{-1}$ As, our results agree with the *GeoPT* results,
220 and for those samples with no assigned or provisional values the *GeoPT* median values
221 could potentially be used as informational values. Below $1 \mu\text{g g}^{-1}$ As the median *GeoPT*
222 values are systematically higher than ours. For Se the median *GeoPT* values are
223 systematically higher than our values. Considering that for these two elements the HG-
224 AFS method was successful in determining the concentrations in a range of geological
225 reference materials, we consider that the median results from the *GeoPT* test overestimate
226 As concentrations below $1 \mu\text{g g}^{-1}$ and Se in most samples. This overestimation is
227 probably related with the fact that fewer and less reliable results are reported for materials
228 with low concentrations, and the medians may not be an appropriate estimate. The *GeoPT*
229 dataset for Te is limited, but above the limit of quantification the median *GeoPT* test
230 results correlate with the HG-AFS results. We suggest that the HG-AFS results could be
231 used as informational values for As in *GeoPT* test samples with less than $1 \mu\text{g g}^{-1}$. The

232 HG-AFS results could also be used as informational values for Se and Te in GeoPT
233 materials with concentrations above the quantification limits.

234

235 **2.6 - Acknowledgements**

236 *This work was supported by a Canada Research Chair program grant to Sarah-Jane*
237 *Barnes (215503). This manuscript benefited from insightful comments from two*
238 *anonymous reviewers, and careful editorial handling by the editor Mary Horan.*

239

240

241

242

243

244

245

246

247

248

249

250

251

252 **2.7 - References**

- 253 Amereih S., Meisel T., Scholger R. and Wegscheider W. (2005) Antimony speciation in soil
254 samples along two Austrian motorways by HPLC-ID-ICP-MS. *Journal of Environmental*
255 *Monitoring*, 7, 1200-1206.
- 256 Babechuk M.G., Kamber B.S., Greig A., Canil D. and Kodolányi J. (2010) The behaviour of
257 tungsten during mantle melting revisited with implications for planetary differentiation time
258 scales. *Geochimica et Cosmochimica Acta*, 74, 1448-1470.
- 259 Baranov B.V., Werner R., Hoernle K.A., Tsoy I.B., van den Bogaard P. and Tararin I.A. (2002)
260 Evidence for compressionally induced high subsidence rates in the Kurile Basin (Okhotsk Sea).
261 *Tectonophysics*, 350, 63-97.
- 262 Barnes S.-J. (2016) Chalcophile elements. *Encyclopedia of Geochemistry*. Springer, pp. 1-5.
- 263 Barnes S.-J., Prichard H.M., Cox R.A., Fisher P.C. and Godel B. (2008) The location of the
264 chalcophile and siderophile elements in platinum-group element ore deposits (a textural,
265 microbeam and whole rock geochemical study): Implications for the formation of the deposits.
266 *Chemical Geology*, 248, 295-317.
- 267 Barnes S.-J. and Gomwe T.S. (2011) The Pd deposits of the Lac des Iles complex, northwestern
268 Ontario. *Reviews in Economic Geology*, 17, 351–370.
- 269
- 270 Barnes S.-J. and Ripley E.M. (2016) Highly siderophile and strongly chalcophile elements in
271 magmatic ore deposits. *Reviews in Mineralogy and Geochemistry*, 81, 725-774.
- 272 Bédard L.P. and Barnes S.-J. (2002) A comparison of N-type semi-planar and coaxial INAA
273 detectors for 33 geochemical reference samples. *Journal of radioanalytical and nuclear chemistry*,
274 254, 485-497.
- 275 Bédard L.P., Esbensen, K.H. and Barnes, S.-J. (2016) Empirical Approach for Estimating
276 Reference Material Heterogeneity and Sample Minimum Test Portion Mass for “Nuggety”
277 Precious Metals (Au, Pd, Ir, Pt, Ru). *Analytical chemistry*, 88(7), 3504-3511.
- 278 Bossy A., Grosbois C., Beauchemin S., Courtin-Nomade A., Hendershot W. and Bril H. (2010)
279 Alteration of As-bearing phases in a small watershed located on a high grade arsenic-geochemical
280 anomaly (French Massif Central). *Applied Geochemistry* 25, 1889-1901.
- 281 Branch S., Ebdon L., Ford M., Foulkes M. and O'Neill P. (1991) Determination of arsenic in
282 samples with high chloride content by inductively coupled plasma mass spectrometry. *Journal of*
283 *Analytical Atomic Spectrometry*, 6(2), 151-154.
- 284 Brenan J.M. (2015) Se–Te fractionation by sulfide–silicate melt partitioning: Implications for the
285 composition of mantle-derived magmas and their melting residues. *Earth and Planetary Science*
286 *Letters*, 422, 45-57.
- 287 Carignan J., Hild P., Mevelle G., Morel J. and Yeghicheyan D. (2001) Routine analyses of trace
288 elements in geological samples using flow injection and low pressure on-line liquid

- 289 chromatography coupled to ICP-MS: A study of geochemical reference materials BR, DR-N, UB-
290 N, AN-G and GH. *Geostandards Newsletter*, 25, 187-198.
- 291 Cava-Montesinos P., Cervera M.L., Pastor A. and de la Guardia M. (2003) Hydride generation
292 atomic fluorescence spectrometric determination of ultratrace of selenium and tellurium in cow
293 milk. *Analytica Chimica Acta*, 481, 291-300.
- 294 Chauvel C., Maury R.C., Blais S., Lewin E., Guillou H., Guille G., Rossi P. and Gutscher M.A.
295 (2012) The size of plume heterogeneities constrained by Marquesas isotopic stripes.
296 *Geochemistry, Geophysics, Geosystems*, 13, 1-23.
- 297 Constantin M. (2006) Determination of Au, Ir and thirty-two other elements in twelve
298 geochemical reference materials by instrumental neutron activation analysis. *Journal of*
299 *Radioanalytical and Nuclear Chemistry*, 267, 407-414.
- 300 Corns W.T., Stockwell P.B., Ebdon L.C. and Hill S.J. (1993) Development of an atomic
301 fluorescence spectrometer for the hydride forming elements. *Journal of Analytical Spectrometry*,
302 8, 71-76.
- 303 Cotta A.J. and Enzweiler J. (2012) Classical and new procedures of whole rock dissolution for
304 trace element determination by ICP-MS. *Geostandards and Geoanalytical Research*, 36, 27-50.
- 305 Dampare S., Shibata T., Asiedu D., Osa S. and Banoeng-Yakubo B. (2008) Geochemistry of
306 Paleoproterozoic metavolcanic rocks from the southern Ashanti volcanic belt, Ghana:
307 Petrogenetic and tectonic setting implications. *Precambrian Research*, 162, 403-423.
- 308 Dare S.A., Barnes S.-J., Prichard H.M. and Fisher P.C. (2011) Chalcophile and platinum-group
309 element (PGE) concentrations in the sulfide minerals from the McCreedy East deposit, Sudbury,
310 Canada, and the origin of PGE in pyrite. *Mineralium Deposita*, 46, 381-407.
- 311 Debret B., Andreani M., Godard M., Nicollet C., Schwartz S. and Lafay R. (2013) Trace element
312 behavior during serpentinization/de-serpentinization of an eclogitized oceanic lithosphere: A LA-
313 ICPMS study of the Lanzo ultramafic massif (Western Alps). *Chemical Geology*, 357, 117-133.
- 314 Duker A.A., Carranza E.J.M. and Hale M. (2005) Arsenic geochemistry and health. *Environment*
315 *International*, 31, 631-641.
- 316 Eggins S., Woodhead J., Kinsley L., Mortimer G., Sylvester P., McCulloch M., Hergt J. and
317 Handler M. (1997) A simple method for the precise determination of ≥ 40 trace elements in
318 geological samples by ICPMS using enriched isotope internal standardisation. *Chemical Geology*,
319 134, 311-326.
- 320 Elmaleh A., Galy A., Allard T., Dairon R., Day J., Michel F., Marriner N., Morhange C. and
321 Couffignal F. (2012) Anthropogenic accumulation of metals and metalloids in carbonate-rich
322 sediments: Insights from the ancient harbor setting of Tyre (Lebanon). *Geochimica et*
323 *Cosmochimica Acta*, 82, 23-38.
- 324 Falloon T.J., Danyushevsky L.V., Crawford T.J., Maas R., Woodhead J.D., Eggins S.M.,
325 Bloomer S.H., Wright D.J., Zlobin S.K. and Stacey A.R. (2007) Multiple mantle plume
326 components involved in the petrogenesis of subduction-related lavas from the northern
327 termination of the Tonga Arc and northern Lau Basin: Evidence from the geochemistry of arc and
328 backarc submarine volcanics. *Geochemistry, Geophysics, Geosystems*, 8, 1-45.

329 Fávvaro D., Damatto S., Moreira E., Mazzilli B., Campagnoli F. (2007) Chemical characterization
330 and recent sedimentation rates in sediment cores from Rio Grande reservoir, SP, Brazil. *Journal*
331 *of Radioanalytical and Nuclear Chemistry*, 273, 451-463.

332 Fourny A., Weis D. and Scoates J.S. (2016) Comprehensive Pb-Sr-Nd-Hf isotopic, trace element,
333 and mineralogical characterization of mafic to ultramafic rock reference materials. *Geochemistry,*
334 *Geophysics, Geosystems*, 17, 739-773.

335 Freymuth H., Ivko B., Gill J.B., Tamura Y. and Elliott T. (2016) Thorium isotope evidence for
336 melting of the mafic oceanic crust beneath the Izu arc. *Geochimica et Cosmochimica Acta*, 186,
337 49-70.

338 Gaeta M., Giuliani A., Perilla S. and Misiti V. (2013) Reddish metagranites from the
339 Gennargentu Igneous Complex (Sardinia, Italy): insight into metasomatism induced by magma
340 mingling. *Journal of petrology*, 54, 839-859.

341 Garbe-Schönberg C.D. (1993) Simultaneous determination of thirty-seven trace elements in
342 twenty-eight international rock standards by ICP-MS. *Geostandards Newsletter*, 17, 81-97.

343 Garçon M., Chauvel C., France-Lanord C., Huyghe P. and Lavé J. (2013) Continental
344 sedimentary processes decouple Nd and Hf isotopes. *Geochimica et Cosmochimica Acta*, 121,
345 177-195.

346 Gaschnig R.M., Rudnick R.L. and McDonough W.F. (2015) Determination of Ga, Ge, Mo, Ag,
347 Cd, In, Sn, Sb, W, Tl and Bi in USGS Whole-Rock Reference Materials by Standard Addition
348 ICP-MS. *Geostandards and Geoanalytical Research*, 39, 371-379.

349 Gladney E. and Knab D. (1981) Determination of selenium in twenty geological reference
350 materials by neutron activation and inorganic ion exchange. *Geostandards Newsletter*, 5, 67-69.

351 Godel B. and Barnes S.-J. (2008) Platinum-group elements in sulfide minerals and the whole
352 rocks of the JM Reef (Stillwater Complex): Implication for the formation of the reef. *Chemical*
353 *Geology*, 248, 272-294.

354 Govindaraju K. (1994) 1994 compilation of working values and sample description for 383
355 geostandards. *Geostandards Newsletter*, 18, 1-158.

356 Gurenko A., Hoernle K., Hauff F., Schmincke H.-U., Han D., Miura Y. and Kaneoka I. (2006)
357 Major, trace element and Nd–Sr–Pb–O–He–Ar isotope signatures of shield stage lavas from the
358 central and western Canary Islands: insights into mantle and crustal processes. *Chemical*
359 *Geology*, 233, 75-112.

360 Haase K.M., Lima S., Krumm S. and Garbe-Schönberg D. (2014) The magmatic evolution of
361 young island arc crust observed in gabbroic to tonalitic xenoliths from Raoul Island, Kermadec
362 Island Arc. *Lithos*, 210, 199-208.

363 Hattori K.H., Arai S. and Clarke D.B. (2002) Selenium, tellurium, arsenic and antimony contents
364 of primary mantle sulfides. *The Canadian Mineralogist*, 40, 637-650.

365 He Y., Moreda-Pineiro J., Cervera M.L. and de la Guardia M. (1998) Direct determination of
366 dissolved selenium (vi) and selenium (vi) in sea-water by continuous flow hydride generation
367 atomic fluorescence spectrometry. *Journal of Analytical Atomic Spectrometry*, 13, 289-293.

- 368 Henrique-Pinto R., Barnes S.J., Savard D. and Mehdi S. (2017) Quantification of Metals and
369 Semimetals in Carbon-Rich Rocks: A New Sequential Protocol Including Extraction from Humic
370 Substances. *Geostandards and Geoanalytical Research*, 41(1), 41-62.
- 371 Horwitz W., Kamps L.R. and Boyer, K.W. (1980) Quality assurance in the analysis of foods and
372 trace constituents. *Journal-Association of Official Analytical Chemists*, 63(6), 1344-1354.
- 373 Hu Z., Gao S., Hu S., Yuan H., Liu X. and Liu Y. (2005) Suppression of interferences for direct
374 determination of arsenic in geological samples by inductively coupled plasma mass spectrometry.
375 *Journal of Analytical Atomic Spectrometry*, 20, 1263-1269.
- 376 Hu Z. and Gao S. (2008) Upper crustal abundances of trace elements: a revision and update.
377 *Chemical Geology*, 253, 205-221.
- 378 IAG (2018) Protocol for the Operation of the GeoPT Proficiency Testing Scheme. International
379 Association of Geoanalysts, Keyworth, England ([http://www.geoanalyst.org/wp-](http://www.geoanalyst.org/wp-content/uploads/2018/06/GeoPT-revised-protocol-2018.pdf)
380 [content/uploads/2018/06/GeoPT-revised-protocol-2018.pdf](http://www.geoanalyst.org/wp-content/uploads/2018/06/GeoPT-revised-protocol-2018.pdf)).
- 381 Jamieson H.E. (2014) The legacy of arsenic contamination from mining and processing refractory
382 gold ore at Giant Mine, Yellowknife, Northwest Territories, Canada. *Reviews in Mineralogy &*
383 *Geochemistry*, 79, 533-551.
- 384 Jochum K. and Hofmann A.W. (1997) Constraints on earth evolution from antimony in mantle-
385 derived rocks. *Chemical Geology*, 139, 39-49.
- 386 Jochum K.P., Nohl U., Herwig K., Lammel E., Stoll B. and Hofmann A.W. (2005) GeoReM: a
387 new geochemical database for reference materials and isotopic standards. *Geostandards and*
388 *Geoanalytical Research*, 29, 333-338
- 389 Jochum K., Seufert H., Midinet-Best S., Rettmann E., Schönberger K. and Zimmer M. (1988)
390 Multi-element analysis by isotope dilution-spark source mass spectrometry (ID-SSMS)
391 Multielement-Analyse mit Isotopenverdünnung-Funkenmassenspektrometrie (ID-SSMS).
392 *Fresenius' Zeitschrift für Analytische Chemie*, 331, 104-110.
- 393 Jochum K.P., Weis U., Schwager B., Stoll B., Wilson S.A., Haug G.H., Andreae M.O. and
394 Enzweiler J. (2016) Reference values following ISO guidelines for frequently requested rock
395 reference materials. *Geostandards and Geoanalytical Research*, 40, 333-350.
- 396 Ketris M.P. and Yudovich Y. E. (2009) Estimations of Clarkes for Carbonaceous biolithes: World
397 averages for trace element contents in black shales and coals. *International Journal of Coal*
398 *Geology*, 78(2), 135-148.
- 399 Kodolányi J., Pettke T., Spandler C., Kamber B.S. and Gméling K. (2011) Geochemistry of ocean
400 floor and fore-arc serpentinites: constraints on the ultramafic input to subduction zones. *Journal*
401 *of Petrology*, 53, 235-270.
- 402 Kokfelt T.F., Hoernle K., Lundstrom C., Hauff F. and van den Bogaard C. (2009) Time-scales for
403 magmatic differentiation at the Snaefellsjökull central volcano, western Iceland: constraints from
404 U–Th–Pa–Ra disequilibria in post-glacial lavas. *Geochimica et Cosmochimica Acta*, 73, 1120-
405 1144.

- 406 Komorowicz I. and Baralkiewicz D. (2011) Arsenic and its speciation in water samples by high
407 performance liquid chromatography inductively coupled plasma mass spectrometry—last decade
408 review. *Talanta*, 84(2), 247-261.
- 409 König S., Luguet A., Lorand J.-P., Wombacher F. and Lissner M. (2012) Selenium and tellurium
410 systematics of the Earth's mantle from high precision analyses of ultra-depleted orogenic
411 peridotites. *Geochimica et Cosmochimica Acta*, 86, 354-366.
- 412 König S., Lorand J.-P., Luguet A., Pearson D.G. (2014) A non-primitive origin of near-chondritic
413 S–Se–Te ratios in mantle peridotites; implications for the Earth's late accretionary history. *Earth
414 and Planetary Science Letters*, 385, 110-121.
- 415 Konter J.G., Staudigel H., Blichert-Toft J., Hanan B., Polvé M., Davies G., Shimizu N. and
416 Schiffman P. (2009) Geochemical stages at Jasper Seamount and the origin of intraplate
417 volcanoes. *Geochemistry, Geophysics, Geosystems*, 10, 1-24.
- 418 Korotev R.L. (1996) A self-consistent compilation of elemental concentration data for 93
419 geochemical reference samples. *Geostandards Newsletter*, 20, 217-245.
- 420 Lai G., Chen G. and Chen T. (2016) Speciation of AsIII and AsV in fruit juices by dispersive
421 liquid–liquid microextraction and hydride generation-atomic fluorescence spectrometry. *Food
422 Chemistry*, 190, 158-163.
- 423 Lissner M., König S., Luguet A., Le Roux P., Schuth S., Heuser A. and le Roex A.P. (2014)
424 Selenium and tellurium systematics in MORBs from the southern Mid-Atlantic Ridge (47–50 S).
425 *Geochimica et Cosmochimica Acta*, 144, 379-402.
- 426 Locmelis M., Fiorentini M.L., Rushmer T., Arevalo Jr R., Adam J. and Denyszyn S.W. (2016)
427 Sulfur and metal fertilization of the lower continental crust. *Lithos* 244, 74-93.
- 428 Long G.L. and Winefordner J.D. (1983) Limit of detection: a closer look at the IUPAC definition.
429 *Analytical Chemistry*, 55, 712A–724A.
- 430 Maghraoui M.E., Joron J.L., Etoubleau J., Cambon P. and Treuil M. (1999) Determination of
431 forty four major and trace elements in GPMA magmatic rock reference materials using X-ray
432 Fluorescence Spectrometry (XRF) and Instrumental Neutron Activation Analysis (INAA).
433 *Geostandards Newsletter* 23, 59-68.
- 434 Mariano D.B., Figueiredo A.M. and Semmler R. (2014) Implementation of the k0-standardization
435 method for analysis of geological samples at the Neutron Activation Analysis Laboratory, São
436 Paulo, Brazil. *Journal of Radioanalytical and Nuclear Chemistry*, 299, 725-731.
- 437 Marin L., Lhomme J. and Carignan J. (2001) Determination of selenium concentration in sixty
438 five reference materials for geochemical analysis by GFAAS after separation with thiol cotton.
439 *Geostandards Newsletter*, 25, 317-324.
- 440 Martin A.P., Price R.C., Cooper A.F. and McCammon C.A. (2015) Petrogenesis of the rifted
441 southern Victoria Land lithospheric mantle, Antarctica, inferred from petrography, geochemistry,
442 thermobarometry and oxybarometry of peridotite and pyroxenite xenoliths from the Mount
443 Morning eruptive centre. *Journal of Petrology*, 56, 193-226.

- 444 Melluso L., Morra V., Riziky H., Veloson J., Lustrino M., Del Gatto L. and Modeste V. (2007)
 445 Petrogenesis of a basanite–tephrite–phonolite volcanic suite in the Bobaomby (Cap d’Ambre)
 446 peninsula, northern Madagascar. *Journal of African Earth Sciences*, 49, 29-42.
- 447 Mizera J. and Řanda Z. (2010) Instrumental neutron and photon activation analyses of selected
 448 geochemical reference materials. *Journal of radioanalytical and nuclear chemistry*, 284, 157-163.
- 449 Mohan M.R., Kamber B.S., Piercey S.J. (2008) Boron and arsenic in highly evolved Archean
 450 felsic rocks: implications for Archean subduction processes. *Earth and Planetary Science Letters*,
 451 274, 479-488.
- 452 Moss R.L., Tzimas E., Kara H., Willis P. and Kooroshy J. (2013) The potential risks from metals
 453 bottlenecks to the deployment of Strategic Energy Technologies. *Energy Policy*, 55, 556-564.
- 454 Nielsen S. and Hansen E.H. (1997) Determination of As (III) and As (V) by flow injection-
 455 hydride generation-atomic absorption spectrometry via on-line reduction of As (V) by KI.
 456 *Analytica Chimica Acta* 343, 5-17.
- 457 Norman M., Duncan R.A. and Huard J.J. (2010) Imbrium provenance for the Apollo 16 Descartes
 458 terrain: Argon ages and geochemistry of lunar breccias 67016 and 67455. *Geochimica et*
 459 *Cosmochimica Acta*, 74, 763-783.
- 460 Norman M., Taylor L.A., Shih C.-Y. and Nyquist L. (2016) Crystal accumulation in a 4.2 Ga
 461 lunar impact melt. *Geochimica et Cosmochimica Acta*, 172, 410-429.
- 462 Parks J., Lin S., Davis D.W., Yang X.-M., Creaser R.A. and Corkery M.T. (2014) Meso-and
 463 Neoproterozoic evolution of the Island Lake greenstone belt and the northwestern Superior Province:
 464 Evidence from litho-geochemistry, Nd isotope data, and U–Pb zircon geochronology. *Precambrian*
 465 *Research*, 246, 160-179.
- 466 Patten C.G., Pitcairn I.K., Teagle D.A. and Harris M. (2016) Mobility of Au and related elements
 467 during the hydrothermal alteration of the oceanic crust: implications for the sources of metals in
 468 VMS deposits. *Mineralium Deposita*, 51, 179-200.
- 469 Paul D.K. (2005) Petrology and geochemistry of the Salma dike, Raniganj coalfield (Lower
 470 Gondwana), eastern India: linkage with Rajmahal or Deccan volcanic activity?. *Journal of Asian*
 471 *Earth Sciences*, 25, 903-913.
- 472 Peters D. and Pettke T. (2017) Evaluation of Major to Ultra Trace Element Bulk Rock Chemical
 473 Analysis of Nanoparticulate Pressed Powder Pellets by LA-ICP-MS. *Geostandards and*
 474 *Geoanalytical Research* 41, 5-28.
- 475 Pitcairn I.K. (2004) Sources of fluids and metals in orogenic gold deposits: the Otago Schists,
 476 New Zealand. University of Southampton.
- 477
- 478 Pitcairn I.K., Craw D. and Teagle D.A.H. (2015) Metabasalts as sources of metals in orogenic
 479 gold deposits. *Mineralium Deposita*, 50, 373-390.
- 480 Potin-Gautier M., Pannier F., Quiroz W., Pinochet H. and De Gregori I. (2005) Antimony
 481 speciation analysis in sediment reference materials using high-performance liquid

482 chromatography coupled to hydride generation atomic fluorescence spectrometry. *Analytica*
483 *Chimica Acta*, 553, 214-222.

484 Potra A., Dodd J.W. and Ruhl L.S. (2017) Distribution of trace elements and Pb isotopes in
485 stream sediments of the Tri-State mining district (Oklahoma, Kansas, and Missouri), USA.
486 *Applied Geochemistry*, 82, 25-3.

487 Potts P.J. (1987) *A handbook of silicate rock analysis*. Blackie (London), 622pp.

488 Potts P.J., Thompson M., Kane J.S., Webb P.C. and Carignan J. (2000) GeoPT6 - an international
489 proficiency test for analytical geochemistry laboratories - report on round 6 (OU-3: Nanhoron
490 microgranite) and 6A (CAL-S: CRPG limestone). International Association of Geoanalysts
491 report.

492 Potts P.J., Thompson M., Kane J.S., Webb, P.C. and Watson J.S. (2000) GeoPT8 - an
493 international proficiency test for analytical geochemistry laboratories - report on round 8 /
494 February 2001 (OU-4 Penmaenmawr microdiorite). International Association of Geoanalysts
495 report.

496 Potts P.J., Thompson M., Webb, P.C., Watson J.S. and Wang Yimin (2001) GeoPT10 - an
497 international proficiency test for analytical geochemistry laboratories - report on round 10 /
498 December 2001 (CH1 Marine sediment). International Association of Geoanalysts report.

499 Potts P.J., Thompson M., Chenery S.R., Webb, P.C. and Watson J.S. (2002) GeoPT11 - an
500 international proficiency test for analytical geochemistry laboratories - report on round 11 / July
501 2002 (OU-5 Leaton dolerite). International Association of Geoanalysts report.

502 Potts P.J., Thompson M., Chenery S.R., Webb, P.C. and Batjargal B. (2003) GeoPT12 - an
503 international proficiency test for analytical geochemistry laboratories - report on round 12 /
504 January 2003 (GAS Serpentinite). International Association of Geoanalysts report.

505 Potts P.J., Thompson M., Chenery S.R., Webb, P.C. and Kaspar H.U. (2003) GeoPT13 - an
506 international proficiency test for analytical geochemistry laboratories - report on round 13 / July
507 2003 (Köln Loess). International Association of Geoanalysts report.

508 Potts P.J., Thompson M., Chenery S.R., Webb, P.C. and Wang Yimin (2004) GeoPT15 - an
509 international proficiency test for analytical geochemistry laboratories - report on round 15 / June
510 2004 (Ocean floor sediment MSAN). International Association of Geoanalysts report.

511 Potts P.J., Thompson M., Webb, P.C. and S.Wilson (2005) GeoPT16 - an international
512 proficiency test for analytical geochemistry laboratories - report on round 16 / February 2005
513 (Nevada basalt, BNV-1). International Association of Geoanalysts report.

514 Potts P.J., Thompson M., Webb, P.C. and J. Nicholas Walsh (2005) GeoPT17 - an international
515 proficiency test for analytical geochemistry laboratories - report on round 17 / July 2005
516 (Calcareous sandstone, OU-8). International Association of Geoanalysts report.

517 Reyes M.N.M., Cervera M.L., Campos R.C. and de la Guardia M. (2008) Non-chromatographic
518 speciation of toxic arsenic in vegetables by hydride generation-atomic fluorescence spectrometry
519 after ultrasound-assisted extraction. *Talanta*, 75, 811-816.

- 520 Riley T., Curtis M., Flowerdew M. and Whitehouse M.J. (2016) Evolution of the Antarctic
521 Peninsula lithosphere: Evidence from Mesozoic mafic rocks. *Lithos*, 244, 59-73.
- 522 Robin-Popieul C.C., Arndt N.T., Chauvel C., Byerly G.R., Sobolev A.V. and Wilson A. (2012) A
523 new model for Barberton komatiites: deep critical melting with high melt retention. *Journal of*
524 *Petrology*, 53, 2191-2229.
- 525 Rukhlov A.S., Blinova A.I. and Pawlowicz J.G. (2013) Geochemistry, mineralogy and petrology
526 of the Eocene potassic magmatism from the Milk River area, southern Alberta, and Sweet Grass
527 Hills, northern Montana. *Chemical Geology*, 353, 280-302.
- 528 Samalens N., Barnes S.J. and Sawyer E.W. (2017) The role of black shales as a source of sulfur
529 and semimetals in magmatic nickel-copper deposits: Example from the Partridge River Intrusion,
530 Duluth Complex, Minnesota, USA. *Ore Geology Reviews*, 81, 173-187.
- 531 Savard D., Bédard L.P. and Barnes S.-J. (2006) TCF selenium preconcentration in geological
532 materials for determination at sub- $\mu\text{g g}^{-1}$ with INAA (Se/TCF-INAA). *Talanta*, 70, 566-571.
- 533 Savard D., Bédard L.P., Barnes S.-J. (2009) Selenium concentrations in twenty-six geological
534 reference materials: New determinations and proposed values. *Geostandards and Geoanalytical*
535 *Research*, 33, 249-259.
- 536 Sheppard B.S., Shen W.L., Caruso J.A., Heitkemper D.T. and Fricke F.L. (1990) Elimination of
537 the argon chloride interference on arsenic speciation in inductively coupled plasma mass
538 spectrometry using ion chromatography. *Journal of Analytical Atomic Spectrometry*, 5(6), 431-
539 435.
- 540 Singer B.S., Smith K.E., Jicha B.R., Beard B.L., Johnson C.M. and Rogers N.W. (2011) Tracking
541 open-system differentiation during growth of Santa María volcano, Guatemala. *Journal of*
542 *Petrology*, 52, 2335-2363.
- 543 Singh R., Singh S., Parihar P., Singh V.P. and Prasad S.M.J.E. (2015) Arsenic contamination,
544 consequences and remediation techniques: a review. *Ecotoxicology and Environmental Safety*,
545 112, 247-270.
- 546 Søgner N., Portnyagin M., Hoernle K., Holm P.M., Hauff F. and Garbe-Schönberg D. (2015)
547 Olivine major and trace element compositions in southern Payenia basalts, Argentina: evidence
548 for pyroxenite-peridotite melt mixing in a back-arc setting. *Journal of Petrology*, 56, 1495-1518.
- 549 Sundar S. and Chakravarty J. (2010) Antimony toxicity. *International Journal of Environmental*
550 *Research and Public Health*, 7, 4267-4277.
- 551 Terashima S. and Imai N. (2000) Determination of selenium in fifty two geochemical reference
552 materials by hydride generation atomic absorption spectrometry. *Geostandards Newsletter*, 24,
553 83-86.
- 554 Terashima S. (2001) Determination of indium and tellurium in fifty nine geological reference
555 materials by solvent extraction and graphite furnace atomic absorption spectrometry.
556 *Geostandards Newsletter*, 25, 127-132.

- 557 Van der Sloot H., Hoede D., Klinkers T.J. and Das H. (1982) The determination of arsenic,
558 selenium and antimony in rocks, sediments, fly ash and slag. *Journal of Radioanalytical*
559 *Chemistry*, 71, 463-478.
- 560 Volkert R.A., Feigenson M.D., Mana S. and Bolge L. (2015) Geochemical and Sr–Nd isotopic
561 constraints on the mantle source of Neoproterozoic mafic dikes of the rifted eastern Laurentian
562 margin, north-central Appalachians, USA. *Lithos*, 212, 202-213.
- 563 Wang Z. and Becker H. (2013) Ratios of S, Se and Te in the silicate Earth require a volatile-rich
564 late veneer. *Nature*, 499, 328-331.
- 565 Wang Z. and Becker H. (2014) Abundances of sulfur, selenium, tellurium, rhenium and platinum-
566 group elements in eighteen reference materials by isotope dilution sector-field ICP-MS and
567 negative TIMS. *Geostandards and Geoanalytical Research*, 38, 189-209.
- 568 Webb, P.C., Thompson M., Potts P.J. and L. Paul Bedard (2006) GeoPT18 - an international
569 proficiency test for analytical geochemistry laboratories - report on round 18 / Jan 2006 (Quartz
570 Diorite, KPT-1). International Association of Geoanalysts report.
- 571 Webb, P.C., Thompson M., Potts P.J. and B. Batjargal (2006) GeoPT19 - an international
572 proficiency test for analytical geochemistry laboratories - report on round 19 / July 2006 (Gabbro,
573 MGR-N). International Association of Geoanalysts report.
- 574 Webb, P.C., Thompson M., Potts P.J. and M. Burnham (2007) GeoPT20 - an international
575 proficiency test for analytical geochemistry laboratories - report on round 20 / Jan 2007
576 (Ultramafic rock, OPY-1). International Association of Geoanalysts report.
- 577 Webb, P.C., Thompson M., Potts P.J. and B. Batjargal (2007) GeoPT21 - an international
578 proficiency test for analytical geochemistry laboratories - report on round 21 / July 2007 (Granite,
579 MGT-1). International Association of Geoanalysts report.
- 580 Webb, P.C., Thompson, M., Potts, P.J. and Batjargal, B. (2008) GeoPT22 - an international
581 proficiency test for analytical geochemistry laboratories - report on round 22 / January 2008
582 (Basalt, MBL-1). International Association of Geoanalysts report.
- 583 Webb, P.C., Thompson, M., Potts, P.J., Watson, J.S. and Kriete, C. (2008) GeoPT23 - an
584 international proficiency test for analytical geochemistry laboratories - report on round 23 /
585 September 2008 (Separation Lake pegmatite, OU-9) and 23A (Manganese nodule, FeMn-1).
586 International Association of Geoanalysts report.
- 587 Webb, P.C., Thompson, M., Potts, P.J. and Watson, J.S. (2009) GeoPT24 - an international
588 proficiency test for analytical geochemistry laboratories - report on round 24 / January 2009
589 (Longmyndian greywacke, OU-10). International Association of Geoanalysts report.
- 590 Webb, P.C., Thompson, M., Potts, P.J. and Enzweiler, J. (2009) GeoPT25 - an international
591 proficiency test for analytical geochemistry laboratories - report on round 25 / July 2009 (Basalt,
592 HTP-1). International Association of Geoanalysts report.
- 593 Webb, P.C., Thompson, M., Potts, P.J. and Batjargal, B. (2010) GeoPT27 - an international
594 proficiency test for analytical geochemistry laboratories - report on round 27 / July 2010
595 (Andesite, MGL-AND). International Association of Geoanalysts report.

596 Webb, P.C., Thompson, M., Potts, P.J. and Wilson, S. (2011) GeoPT29 - an international
597 proficiency test for analytical geochemistry laboratories - report on round 29 / July 2011
598 (Nephelinite, NKT-1). International Association of Geoanalysts report.

599 Webb, P.C., Thompson, M., Potts, P.J., Long, D. and Batjargal, B. (2012) GeoPT30 - an
600 international proficiency test for analytical geochemistry laboratories - report on round 30 /
601 January 2012 (Silty marine shale, CG-2) and 30A (Limestone, ML-2). International Association
602 of Geoanalysts report.

603 Webb, P.C., Thompson, M., Potts, P.J. and Wilson, S. (2012) GeoPT31 - an international
604 proficiency test for analytical geochemistry laboratories - report on round 31 / July 2012
605 (Modified river sediment, SdAR-1). International Association of Geoanalysts report.

606 Webb, P.C., Thompson, M., Potts, P.J. and Webber, E. (2013) GeoPT32 - an international
607 proficiency test for analytical geochemistry laboratories - report on round 32 / January 2013
608 (Woodstock Basalt, WG-1). International Association of Geoanalysts report.

609 Webb, P.C., Thompson, M., Potts, P.J., Prusisz, B., and Young, K. (2013) GeoPT33 - an
610 international proficiency test for analytical geochemistry laboratories - report on round 33 / July-
611 August 2013 (Ball Clay, DBC1). International Association of Geoanalysts report.

612 Webb, P.C., Thompson, M., Potts, P.J. and Wilson, S. (2014) GeoPT34 - an international
613 proficiency test for analytical geochemistry laboratories - report on round 34 (Granite, GRI-1) /
614 January 2014. International Association of Geoanalysts report.

615 Webb, P.C., Thompson, M., Potts, P.J. and Wilson, S. (2014) GeoPT35 - an international
616 proficiency test for analytical geochemistry laboratories - report on round 35 (Tonalite, TLM-1) /
617 August 2014. International Association of Geoanalysts report.

618 Webb, P.C., Thompson, M., Potts, P.J. and Wilson, S. (2015) GeoPT36 - an international
619 proficiency test for analytical geochemistry laboratories - report on round 36 (Gabbro, GSM-1) /
620 January 2015. International Association of Geoanalysts report.

621 Webb, P.C., Thompson, M., Potts, P.J. and Wilson, S. (2015) GeoPT36A - an international
622 proficiency test for analytical geochemistry laboratories - report on round 36A (Metal-rich
623 sediment, SdAR-M2) / January 2015. International Association of Geoanalysts report.

624 Webb, P.C., Thompson, M., Potts, P.J., Gowing, C.J.B. and Burnham, M. (2015) GeoPT37 - an
625 international proficiency test for analytical geochemistry laboratories - report on round 37
626 (Rhyolite, ORPT-1) / July 2015. International Association of Geoanalysts report

627 Webb, P.C., Thompson, M., Potts, P.J., Gowing, C.J.B. and Wilson, S.A. (2016) GeoPT38 - an
628 international proficiency test for analytical geochemistry laboratories - report on round 38
629 (Gabbro, OU-7) / January 2016. International Association of Geoanalysts report.

630 Webb, P.C., Thompson, M., Potts, P.J., Gowing, C.J.B. and Meisel, T. (2016) GeoPT38A - an
631 international proficiency test for analytical geochemistry laboratories – special report on round
632 38A (Modified harzburgite, HARZ01) / June 2016. International Association of Geoanalysts
633 report.

634 Webb, P.C., Thompson, M., Potts, P.J, Gowing, C.J.B. and Wilson, S.A. (2016) GeoPT39 - an
635 international proficiency test for analytical geochemistry laboratories - report on round 39
636 (Syenite, SyMP-1) / July 2016. International Association of Geoanalysts report.

637 Webb, P.C., Thompson, M., Potts, P.J, and Gowing, C.J.B. (2016) GeoPT39A - an international
638 proficiency test for analytical geochemistry laboratories - report on round 39A (Nepheline
639 syenite, MNS-1) / July 2016. International Association of Geoanalysts report.

640 Webb, P.C., Thompson, M., Potts, P.J, Gowing, C.J.B. and Wilson, S.A. (2017) GeoPT40 - an
641 international proficiency test for analytical geochemistry laboratories - report on round 40 (Silty
642 marine shale, ShWYO-1) / January 2017. International Association of Geoanalysts report.

643 Webb, P.C., Thompson, M., Potts, P.J, Gowing, C.J.B. and Wilson, S.A. (2017) GeoPT41 — an
644 international proficiency test for analytical geochemistry laboratories - report on round 41
645 (Andesite, ORA-1) / July 2017. International Association of Geoanalysts report.

646 Wu L.J.E. (2004) Review of 15 years of research on ecotoxicology and remediation of land
647 contaminated by agricultural drainage sediment rich in selenium. *Ecotoxicology and
648 Environmental Safety*, 57(3), 257-269.

649 Yan X.-P., Yin X.-B., He X.-W. and Jiang Y. (2002) Flow injection on-line sorption
650 preconcentration coupled with hydride generation atomic fluorescence spectrometry for
651 determination of (ultra) trace amounts of arsenic (III) and arsenic (V) in natural water samples.
652 *Analytical Chemistry*, 74, 2162-2166.

653 Yi W., Halliday A.N., Lee D.C. and Rehkämper M. (1998) Precise determination of cadmium,
654 indium and tellurium using multiple collector ICP-MS. *Geostandards Newsletter*, 22, 173-179.

655 Yu Z., Robinson P., Townsend A.T., Mnker C. and Crawford A.J. (2000) Determination of high
656 field strength elements, Rb, Sr, Mo, Sb, Cs, Tl and Bi at ng g⁻¹ levels in geological reference
657 materials by magnetic sector ICP-MS after HF/HClO₄ high pressure digestion. *Geostandards
658 Newsletter*, 24, 39-50.

659 Zhang N., Fu N., Fang Z., Feng Y. and Ke L. (2011) Simultaneous multi-channel hydride
660 generation atomic fluorescence spectrometry determination of arsenic, bismuth, tellurium and
661 selenium in tea leaves. *Food Chemistry*, 124, 1185-1188.

662 Zweibel K.J.S. (2010) The impact of tellurium supply on cadmium telluride photovoltaics.
663 *Science*, 328, 699-701.

664

665

666

667

668

1
2
3
4
5
6
7

8 **Chapter 3 - Distribution of chalcophile and platinum-group elements**
9 **among pyrrhotite, pentlandite, chalcopyrite and cubanite from the**
10 **Noril'sk-Talnakh ores: implications for the formation of platinum-**
11 **group minerals**

12
13
14
15
16
17
18 *Eduardo T. Mansur¹, Sarah-Jane Barnes¹, Charley J. Duran¹ Sergey F. Sluzhenikin²

19 ¹Sciences de la Terre, Université du Québec à Chicoutimi, Québec, G7H 2B1, Canada

20 ²Institute of Geology of Ore Deposits, Mineralogy, Petrography, and Geochemistry (IGEM RAS),
21 Staromonetny 35, Moscow 119017 Russia

22
23
24
25 **Author contributions:**

26 **Mansur** wrote the manuscript, collected and analyzed the data and created the figures.
27 **Barnes** edited the manuscript and analyzed the data. **Duran** collected part of the data and
28 also analyzed the results. **Sluzhenikin** helped collecting the samples used in the
29 preparation of the manuscript.

30
31
32
33
34 Mineralium Deposita

35 DOI: 10.1007/s00126-019-00926-z

36 **3.1 - Abstract**

37 In most magmatic sulfide deposits, platinum-group elements (PGE) are found both within the
38 structure of the base metal sulfides (BMS), pyrrhotite (Po), pentlandite (Pn), chalcopyrite (Ccp)
39 and cubanite (Cbn) and as platinum-group minerals (PGM). Tellurium, As, Bi, Sb, Sn (TABS) are
40 essential elements in many of these PGM. The potential role of TABS in collecting PGE, and thus
41 forming a PGE deposit has not been closely investigated. We have determined the concentrations
42 of a full suite of chalcophile elements in Po, Pn, Ccp and Cbn using laser ablation-inductively
43 coupled plasma-mass spectrometry on samples from the Noril'sk-Talnakh Ni-deposits. In these
44 deposits the Po-rich ore is thought to represent monosulfide solid solution (MSS) cumulate of the
45 initial sulfide liquid, and the Ccp-rich ore a mixture of the fractionated sulfide liquid and
46 intermediate solid solution (ISS). The BMS from the Po-rich ore contain lower concentrations of
47 TABS, Pd, Pt and Au, and higher concentrations of Mo, Ru, Rh, Re, Os and Ir than BMS from
48 the Ccp-rich ores. This observation is consistent with the results from experimental results which
49 show that TABS, Pd, Pt and Au are incompatible with MSS, whereas the other elements are
50 compatible in MSS. Counter intuitively, in the Po-rich ore the bulk of the Pd and TABS are
51 hosted by BMS. This is because during crystallization although only a small amount of the
52 incompatible elements partitioned into the BMS, the fractionated liquid has migrated away, thus
53 the Po-rich ores represent MSS adcumulates. Therefore, as the Po-rich ores contain very little
54 trapped liquid fraction the BMS host the bulk of Pd and TABS. In contrast, in the Ccp-rich ore
55 the bulk of Au, Pd, Pt and TABS are present as PGM or electrum grains. This is because more
56 trapped liquid is present, and as TABS Au, Pd and Pt are not compatible with ISS, they
57 concentrated into the very last sulfide liquid, and crystallized as intergrowths of Pd-Pt-TABS
58 PGM. The TABS then do not appear to collect Pd, Pt and Au but rather all elements are
59 concentrated in the most fractionated sulfide liquid by crystal fractionation.

60

61 Keywords: LA-ICP-MS, pyrrhotite, pentlandite, chalcopyrite, cubanite, PGE, Te, As, Bi, Sb,
62 chalcophile elements, Noril'sk-Talnakh.

63 **3.2 - Introduction**

64 Chalophile elements are collected by magmatic sulfide liquid during the formation of
65 Ni-Cu-platinum-group element (PGE) deposits. The concentration of these elements in the sulfide
66 liquid is affected by: i) Partition coefficients between silicate and sulfide liquid; ii) The ratio of
67 silicate to sulfide liquid present (R-factor); and iii) The composition of the silicate liquid, which
68 may be contaminated by a variety of crustal sources (Naldrett 2004; Barnes and Ripley 2016).
69 The distribution of these elements within the deposits is controlled by: i) the degree of fractional
70 crystallization of the sulfide liquid; ii) subsolidus cooling history of the sulfides; and iii)
71 metamorphic and hydrothermal history of the deposit (Li et al. 1996; Naldrett et al. 1996; Barnes
72 et al. 1997; Frost et al. 2002; Mungall et al. 2005; Dare et al. 2010b, 2011, 2014; Cafagna 2015;
73 Liu and Brenan 2015; Mota-e-Silva et al. 2015). Whereas the distributions of Ni, Cu, Co and PGE
74 have been studied, both in whole rock and base-metal-sulfide minerals (BMS), the behaviour of
75 most of the other chalcophile elements has not been closely examined.

76 Constraining the distribution of trace chalcophile elements in Ni-Cu-PGE deposits is
77 important for a number of reasons. Firstly, many platinum-group minerals (PGM) contain the
78 chalcophile elements Te, As, Bi, Sb and Sn (TABS) as essential elements (Barnes and Ripley
79 2016). However, the exact role these elements may play in forming PGE deposits has not been
80 established. Secondly, some (e.g. Co, Te and Bi) are considered important for the development of
81 the Green economy (Zweibel 2010; Moss et al. 2013), but are only produced as by-products.
82 Therefore, establishing whether magmatic sulfides could be a source of these elements is of
83 economic importance. Thirdly, some (As, Cd and Pb) are pollutants (Jamieson 2014; Singh et al.
84 2015), and tracking their distribution is important in controlling pollution when exploiting the
85 deposits.

86 It has been shown that in most deposits investigated to date, Pt is present mainly as PGM
87 associated with BMS, whereas the other PGE exhibit variable behaviour. In some deposits, the
88 IPGE (Os, Ir, Ru, Rh) and Pd are largely accommodated in pyrrhotite (Po) and/or pentlandite
89 (Pn), whereas in other deposits TABS-rich PGM are the main carriers (Barnes et al. 2006, 2008;

90 Godel et al. 2007, 2012; Holwell and McDonald 2007; Godel and Barnes 2008; Dare et al. 2010b,
91 2011, 2014; Piña et al. 2012; Osbahr et al. 2014; Smith et al. 2014; Chen et al. 2015; Duran et al.
92 2016). The distribution of the TABS is thus important as they may influence the timing of the
93 formation of the PGM. Several processes have been proposed for the formation of PGM: i)
94 During crystallization of a sulfide liquid, monosulfide solid solution (MSS) and intermediate solid
95 solution (ISS) are the two main phases to crystallize. Palladium, Pt and TABS are incompatible
96 with both MSS and ISS, and thus the concentration of these elements in the fractionated liquid
97 could reach levels sufficiently elevated to permit PGM to crystallize (Barnes et al. 2006;
98 Hutchinson and McDonald 2008; Dare et al. 2010a, 2010b, 2014); ii) In some cases the TABS
99 concentrations in the sulfide liquid could reach the levels that are sufficiently elevated for an
100 immiscible TABS-rich liquid to segregate and collect the PGE, from which the PGM could
101 crystallize (Cafagna 2015; Hanley 2007; Helmy et al. 2007, 2013; Holwell and McDonald 2007;
102 Liu and Brenan 2015); iii) The PGM could form by exsolution, when TABS and PGE are
103 expelled from the BMS lattice during subsolidus cooling (Makovicky 2002; Prichard et al. 2004;
104 Godel et al. 2007; Barnes et al. 2008; Godel and Barnes 2008; Hutchinson and McDonald 2008;
105 Junge et al. 2015); iv) Hydrothermal fluids could concentrate TABS and PGE, and the PGM
106 could further precipitate from these fluids (Pentek et al. 2008; Tuba et al. 2014); and v) Late
107 magmatic or metamorphic fluids could dissolve most of the BMS, but the PGE are not mobilized
108 and combine with TABS to form PGM (Wood 2002; Djon and Barnes 2012; Sullivan et al. 2018).

109 In this contribution we examine the distribution of chalcophile elements in BMS from
110 samples of the Noril'sk-Talnalk Ni-deposits (Fig. 1.11; Distler et al. 1977; Fedorenko 1994;
111 Lightfoot et al. 1994; Kosyakov et al. 2012; Ryabov et al. 2014; Sluzhenikin et al. 2014;
112 Krivolutskaya 2016; Krivolutskaya et al. 2018). The wide range of textures and compositions of
113 the ores have been attributed to fractional crystallization of a sulfide liquid. The absence of
114 metamorphism, and limited deformation of the ores permitted us to examine the behaviour of
115 chalcophile elements during fractional crystallization of a sulfide liquid, as well as during sub-
116 solidus cooling.

117 This work will show that the chalcophile elements collected by the immiscible sulfide
118 liquid (with the exception of As, Au and Pt) are predominantly present in Po, Pn and Ccp in Po-
119 rich ores, whereas in the Ccp-rich ores most of the Au, Pd, Pt and TABS are found in
120 intergrowths of PGM among the BMS. It will also show that there is a systematic variation in the
121 concentration of elements in BMS with the degree of fractionation of the sulfide liquid. Pyrrhotite
122 and Pn contain higher concentrations of compatible elements, and lower concentrations of
123 incompatible elements in the Po-rich ores compared to the Ccp-rich ores. Partition coefficients
124 among Po, Pn, Ccp and Cbn will also be presented.

125

126 **3.3 - Methodology**

127 **3.3.1 - Sample selection**

128 Our samples were selected from 113 specimens described by Duran et al. (2017), who
129 presented BMS textures, platinum-group mineralogy and whole-rock geochemistry for the full
130 collection. Both massive and disseminated sulfides are present. The massive sulfides show a wide
131 mineralogical variation from Po-rich samples to Ccp-rich samples. The Po-rich samples contain
132 only Pt-PGM, interpreted to be exsolutions from the enclosing BMS, whereas the Ccp-rich
133 samples contain a variety of Pd-Pt-TABS PGM that occur as intergrowths among the BMS
134 (Duran et al. 2017). In terms of whole rock composition, the Po-rich samples are richer in IPGE,
135 Rh and Mo, but have similar Ni, Co and Se concentrations to the Ccp-rich ores. On the other
136 hand, the Ccp-rich ores are richer in Ag, As, Au, Bi, Cd, Cu, In, Pb, Pd, Pt, Sb, Sn, Te, Tl and Zn
137 than the Po-rich ores (Duran et al. 2107). The disseminated sulfides occur as 1 to 5 cm globules
138 (Czmanske et al., 1992; Barnes et al., 2006; Le Vaillant et al. 2017). These globules show a
139 similar zonation to the massive ores with a Po-rich and a Ccp-Cbn-rich zone. The variations in
140 texture and composition are thought to reflect fractional crystallization of sulfide liquid (Distler
141 1994; Zientek et al. 1994; Ryabov et al. 2014; Duran et al. 2017).

142 Eighteen samples (16 massive sulfides and 2 disseminated globular sulfide ores) were
143 chosen to reflect the range in texture, mineralogy and composition present in the ores, aiming to
144 investigate the behaviour of the chalcophile elements during differentiation. The whole rock
145 (Pd+Pt)/(Os+Ir+Ru+Rh) ratio, previously determined in Duran et al. (2017), was used to reflect
146 the degree of fractionation of the liquid (*ANNEXE 2*). The samples were also selected to cover
147 all 3 ore bearing intrusions, Noril'sk-I, Talnakh and Kharaelakh (Fig. 1.11).

148

149 **3.3.2 - Scanning electron microscope and laser ablation-inductively coupled plasma-** 150 **mass spectrometry**

151 The concentrations of major elements in BMS were determined using a Zeiss Sigma 300
152 VP scanning electron microscope, equipped with an Oxford Instruments Ultim Max EDS system
153 at IOS Services Géocientifiques, Chicoutimi - Québec. The instrument was calibrated using pure
154 metal standards, and instrumental drift was monitored using the Astimex Standards reference
155 materials.

156 The concentration and distribution of the minor and trace elements were determined by
157 laser ablation-inductively coupled plasma-mass spectrometry (LA-ICP-MS) at LabMaTer,
158 Université du Québec à Chicoutimi (UQAC), using an Excimer 193 nm RESOLUTION M-50 laser
159 ablation system (Australian Scientific Instrument) equipped with a double volume cell S-155
160 (Laurin Technic) and coupled with an Agilent 7900 mass spectrometer. The LA-ICP-MS tuning
161 parameters were a laser frequency of 10 Hz, a power of 3 to 5 mJ/pulse, a dwell time of 7.5 ms, a
162 rastering speed of 5 to 10 $\mu\text{m/s}$, and a fluence of 3 J/cm^2 . Line scans across the surface of sulfides
163 grains were made with beam sizes of 44, 33, and 25 μm , depending on grain size. The gas blank
164 was measured for 30s before switching on the laser for at least 60s. The ablated material was
165 carried into the ICP-MS by an Ar-He gas mix at a rate of 0.8–1 L/min for Ar and 350 mL/min for
166 He, and 2mL/min of nitrogen was also added to the mixture. Data reduction was carried out using
167 the Iolite package for Igor Pro software (Paton et al. 2011).

168 Maps of element distribution were made on different sulfide assemblages using a laser
169 frequency of 15 Hz and a power of 5 mJ/pulse. The beam size (15 to 58 μm) and the stage
170 movement speed (10 to 15 $\mu\text{m/s}$) were adapted to optimize spatial resolution and analysis time for
171 grains of different sizes. The maps were generated using the Iolite software package on the basis
172 of the time-resolved composition of each element. The maps indicate the relative concentration of
173 the elements and are semi-quantitative.

174 The following isotopes were measured: ^{57}Fe , ^{59}Co , ^{61}Ni , ^{65}Cu , ^{66}Zn , ^{75}As , ^{82}Se , ^{95}Mo ,
175 ^{101}Ru , ^{103}Rh , ^{108}Pd , ^{109}Ag , ^{111}Cd , ^{115}In , ^{118}Sn , ^{121}Sb , ^{130}Te , ^{185}Re , ^{189}Os , ^{193}Ir , ^{195}Pt , ^{197}Au , ^{205}Tl ,
176 ^{208}Pb and ^{209}Bi . In addition, ^{28}Si , ^{34}S and ^{44}Ca were monitored to ensure no silicate or sulphate
177 inclusions were present. Polyatomic interference of $^{63}\text{Cu}^{40}\text{Ar}$ on ^{103}Rh was corrected using ^{103}Rh
178 measured in MASS-1, which contains 13.4% ^{63}Cu but no ^{103}Rh . One percent Cu produced ~ 1
179 ppm Rh interference. Thus, the ^{103}Rh values in Ccp and Cbn are not reported as the interference is
180 too large to be corrected. Direct interferences of ^{108}Cd on ^{108}Pd and ^{115}Sn on ^{115}In were corrected
181 manually by monitoring ^{111}Cd and ^{118}Sn , respectively. Interference of $^{68}\text{Zn}^{40}\text{Ar}$ on ^{108}Pd is
182 negligible as Zn occurs as at trace element. Polyatomic interference of $^{61}\text{Ni}^{40}\text{Ar}$ on ^{101}Ru was
183 corrected using ^{101}Ru measured in a NiS blank, which does not contain Ru. The Ni interference is
184 only significant for Pn.

185 ^{57}Fe was used for internal standardization. Three certified reference materials were used
186 for external calibration: Laflamme Po727, which is a synthetic FeS doped with ~ 40 ppm PGE and
187 Au supplied by Memorial University of Newfoundland, was used to calibrate for PGE and Au;
188 MASS-1, which is a ZnCuFeS pressed powder pellet doped with 50–70 ppm of most chalcophile
189 elements, supplied by the United States Geological Survey (USGS), was used to calibrate for Cu,
190 Se, Te, Tl and Zn; GSE-1g, which is a natural basaltic glass fused and doped with most elements
191 at 300–500 ppm, supplied by the USGS, was used to calibrate for Ag, As, Bi, Cd, Co, In, Mo, Ni,
192 Pb, Re, Sb and Sn using preferred values from the GeoReM database (Jochum et al. 2005).
193 MASS-1, GSE-1g and JB-MSS5 (an FeS sulfide containing 50–70 ppm of most chalcophile
194 elements, supplied by James Brennan) were used to monitor the results. The reference materials
195 were analyzed at the beginning and the end of each analytical session to monitor a potential

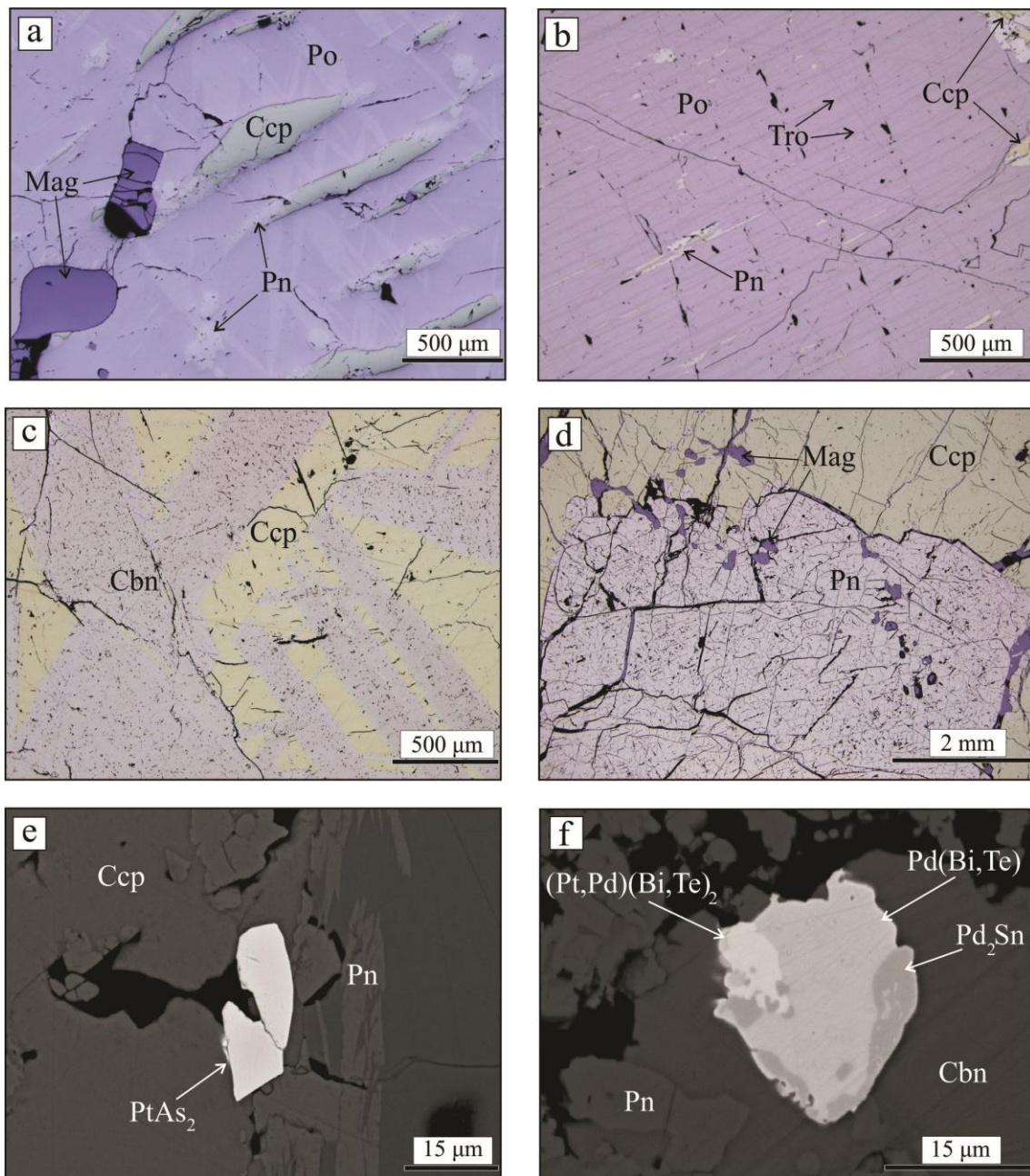
196 instrumental drift. The results obtained for the monitors were generally in good agreement with
197 the working values (*ANNEXE 3*).

198 **3.4 - Results**

199 The samples are described in detail in Czamanske et al. (1992), Zientek et al. (1994) and
200 Duran et al. (2017), and only a brief summary is provided here. In the disseminated ore, sulfides
201 occur as millimetric to centimetric droplets within olivine-gabbro-norite. Typical droplets are
202 characterized by Po at the base and Ccp and Cbn at the top, with a thin Pn layer in between (Fig.
203 10 of Barnes and Ripley 2016; Duran et al. 2017; Le Vaillant et al. 2017).

204 The Po-poor massive sulfides are characterized by abundant Po (50 to 80 modal %), Pn
205 (10 to 20 modal %), and minor Ccp (5 to 20 modal %; Fig. 1a). Pyrrhotite occurs as centimetric
206 anhedral grains. Pentlandite is mostly observed as coarse grains (generally >1mm in apparent
207 diameter), thin exsolution flames (<100 μm) within Po (Fig. 1a and 1b), and loops at the contact
208 between Po and Ccp grains. The loop-textured Pn is described in detail in Mansur et al. (2019).
209 Chalcopyrite occurs either as small anhedral grains dispersed among Po and Pn grains, or
210 associated with Pn in exsolution lamellae within Po grains (Figs. 1a and b). Magnetite (Mag) is
211 present in minor proportions and occurs as euhedral to anhedral grains (Fig. 1a). In some samples,
212 Po hosts sub parallel exsolution lamellae of troilite (Tro; Fig. 1b).

213 The Ccp-rich massive sulfides are dominated by the presence of Ccp (60 to 90% vol.),
214 together with Pn (5 to 20% vol.), and magnetite (Figs. 1c and d). Minor Po (<5% vol.) is present
215 in a few samples. Chalcopyrite occurs as centimetric anhedral patches and in some cases contains
216 Cbn exsolutions (<25% vol.; Fig. 1c). Pentlandite mainly occurs as large grains (i.e. up to several
217 cm in apparent diameter), associated with Ccp (Fig. 1d). Pyrrhotite occurs mostly as anhedral
218 patches, and in a few cases as exsolution lamellae in Ccp (Figs. 5b and 5d of Duran et al. 2017).
219 Galena is present in minor amounts (<<0.01% vol.) as grains <0.05 mm. Magnetite occurs as
220 euhedral to anhedral grains, and in some cases as late veins crosscutting Ccp and/or Pn grains
221 (Fig. 1d).



222

223 Figure 3.1 - Reflected light photomicrographs of representative textures of main massive sulfides from Noril'sk-
 224 Talnakh mining district, and backscattered electron images of platinum-group minerals in Cu-poor and Cu-rich ores. a)
 225 Exsolution of pentlandite and chalcopyrite in pyrrhotite. b) Thin exsolution lamellae (<20 μ m) of troilite in pyrrhotite.
 226 c) Large (>100 μ m wide) exsolution lamellae of cubanite in chalcopyrite. d) Coarse-granular pentlandite in contact with
 227 chalcopyrite. Note inclusions of magnetite in pentlandite and chalcopyrite, and magnetite veinlets crosscutting both
 228 sulfides. e) Sperrylite (PtAs₂) grain enclosed in pentlandite and chalcopyrite in Cu-poor massive sulfide. f) Composite
 229 grain of maslovite ((Pt,Pd)(Bi,Te)₂) sobolevskite (Pd(Bi,Te)), and paolovite (Pd₂Sn) included in cubanite in a Cu-rich
 230 massive sulfide. Cbn- cubanite; Ccp- chalcopyrite; Mag- magnetite; Pn- pentlandite; Po- pyrrhotite; Tro- troilite.

231

232 The PGM and accessory phases of the samples are described in detail in Duran et al.
233 (2017), and only a brief summary is provided here for the purpose of our study. In the
234 disseminated sulfides and Cu-poor massive sulfides, Pt-bearing PGM (mainly sperrylite; Fig. 1e)
235 and minor electrum are the main precious metal minerals. No Pd-, Rh- or IPGE-bearing PGM
236 were observed in these ore types. In contrast, in the Cu-rich massive sulfides, Pt-only-PGM are
237 rare, and most PGM consist of Pd-Pt-bismuthtellurides, arsenides and stanides. These minerals
238 commonly form sub-spherical composite grains, showing intergrowth textures (Fig. 1f). The
239 PGM of all ore types occur mainly enclosed by and/or in contact with BMS. No discrete phases
240 that could potentially host significant levels of PGE other than PGM (e.g. Le Vaillant et al. 2018)
241 were identified in previous studies (Duran et al. 2017).

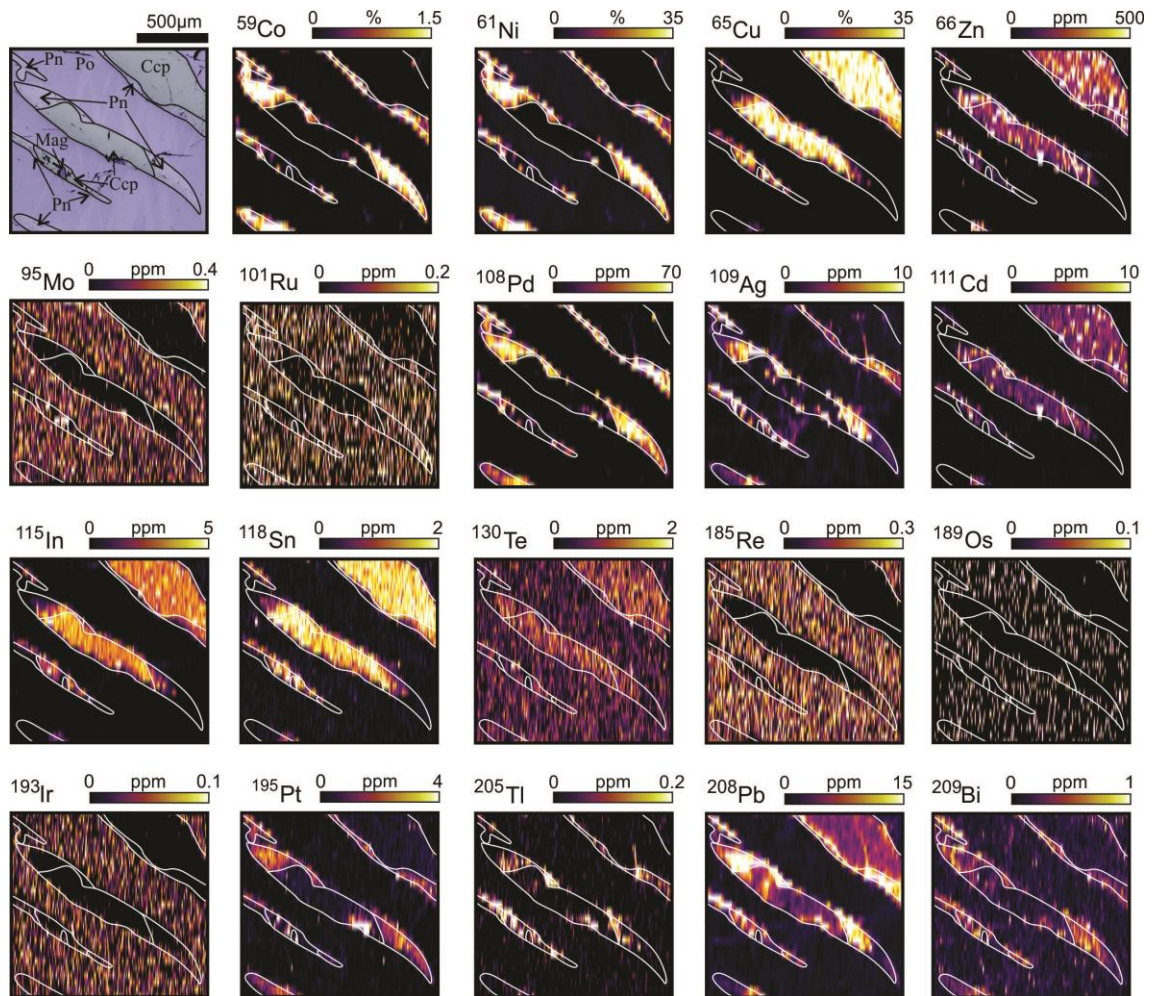
242

243 **3.4.1 - Distribution of chalcophile elements among the base-metal sulfides**

244 The LA-ICP-MS compositional maps of samples containing Po, Pn and Ccp (Fig. 2)
245 show that Mo, Re, Os and Ir are concentrated in Po. Cobalt, Ni, Pd, Ag, Pt, Tl, Pb and Bi are
246 preferentially concentrated in Pn, and Cu, Zn, Cd, In, Sn and Te are concentrated in Ccp (Fig. 2).
247 Ruthenium is evenly distributed between Po and Pn. In samples containing both Ccp and Cbn,
248 Cu, In, Se, Te and Tl are more concentrated in Ccp, whereas Zn, Ag, Cd and Pb are more
249 concentrated in Cbn (Fig. 3). The distribution of the trace elements in Cbn lamellae is not
250 homogeneous. Higher concentrations of Zn, Ag and Cd are observed in the center of the Cbn
251 lamellae relative to the edges (Fig. 3). Troilite lamellae are present in a few samples and
252 compositional maps indicate similar trace-element concentrations between Po and Tro (Fig. 4).
253 Compositional LA-ICP-MS maps of the rare galena grains (Fig. 5) indicate that they are enriched
254 in Ag Cd, Te, Tl, Pb and Bi relative to the other base metal sulfides, but they do not contain PGE.

255

256



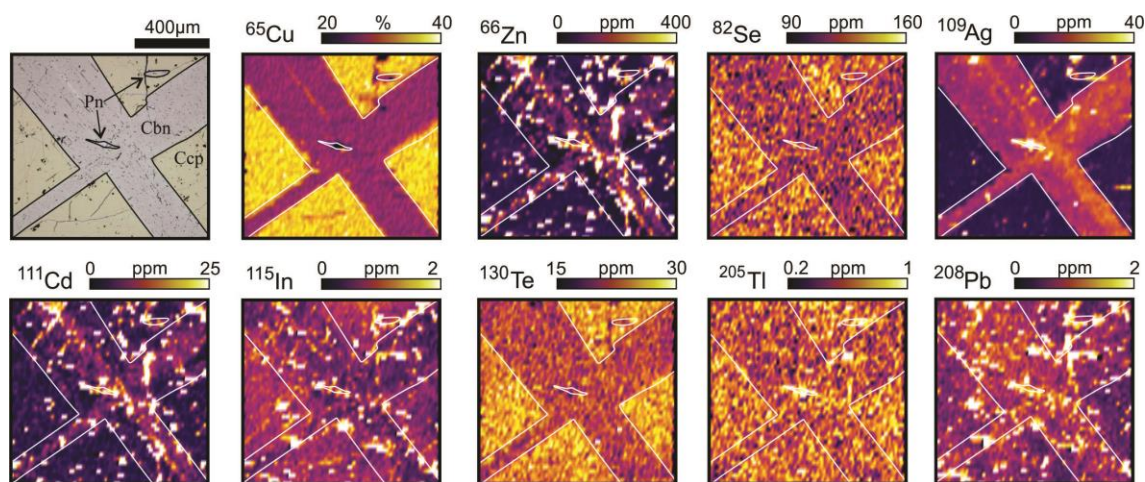
257

258 Figure 3.2 - LA-ICP-MS elemental maps showing the distribution of chalcophile elements in chalcopyrite and
 259 pentlandite exsolution lamellae in pyrrhotite from Cu-poor massive sulfides. White lines show the grain outlines. The
 260 concentrations of the elements are semi-quantitative. Ccp- chalcopyrite; Mag- magnetite; Pn- pentlandite; Po-
 261 pyrrhotite.

262

263 Median concentrations of Pn, Po, Ccp and Cbn from each sample, and the full LA-ICP-
 264 MS data set are reported in *ANNEXE 4 to 7*. Medians for each ore type and each locality are
 265 reported in Table 1.1. Typical time-signal diagrams show flat patterns for all of the elements,
 266 illustrating their homogeneous distribution within BMS. In some cases, the time-signal diagrams
 267 show peaks for some elements, indicating inclusions of PGM within BMS, these were not
 268 included in the integration that calculated the compositions.

269



270

271 Figure 3.3 - LA-ICP-MS elemental maps showing the distribution of chalcophile elements in cubanite exsolution
 272 lamellae in chalcopyrite from Cu-rich massive sulfides. White lines show the grain outlines. The concentrations of the
 273 elements are semi-quantitative. Cbn- cubanite; Ccp- chalcopyrite; Pn- pentlandite.

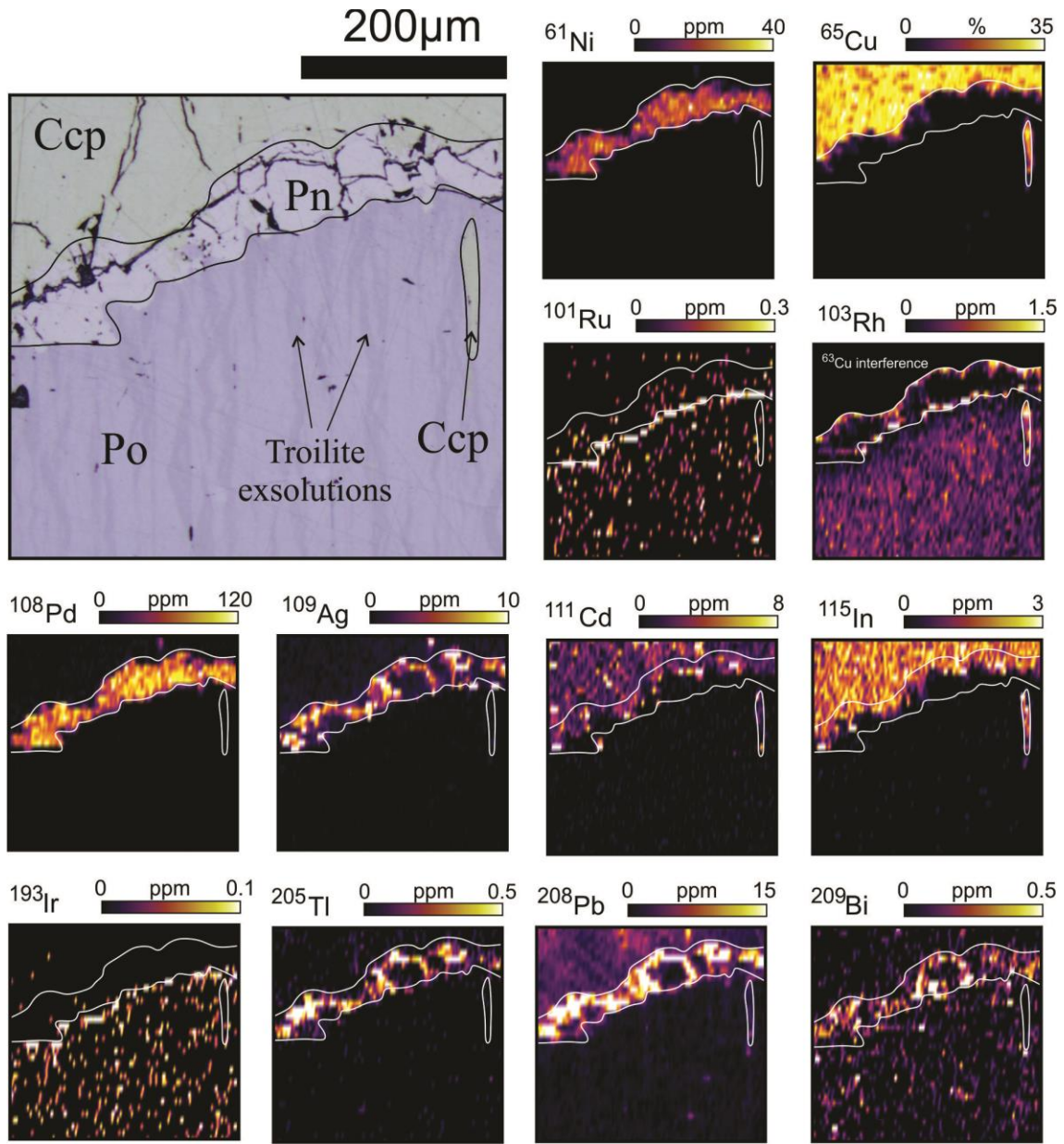
274

275 As indicated by the maps of element distributions Co, Ni, As, Pd, Pt and Tl
 276 concentrations are highest in Pn (Table 1). Cobalt median concentrations in Pn are in the 0.4 to
 277 1.5 weight percent range. Cobalt and Ni median concentrations in Po are in the 20 to 400 ppm,
 278 and 2000 to 25000 ppm range respectively, and are much higher than in Ccp or Cbn, which
 279 contain 0.1 to 10 ppm Co and 50 to 100 ppm Ni. Palladium is in the 50 to 1000 ppm range for Pn,
 280 whereas Po and Ccp contain only 0.01 to 7 ppm. Arsenic, Pt and Tl concentrations are in the 0.1
 281 to 15 ppm range. In Po and Ccp the concentrations of As and Tl are close to detection limits and
 282 mostly <0.1 ppm.

283 Molybdenum, Ru, Rh, Re, Os and Ir are preferentially concentrated in Po, with Mo, Ru,
 284 Rh and Re in the 0.1 to 10 ppm range and Os and Ir in the 0.02 to 2 ppm range. Concentrations of
 285 these elements in Ccp and Cbn are close to detection limit. Pentlandite contains intermediate
 286 levels of the elements.

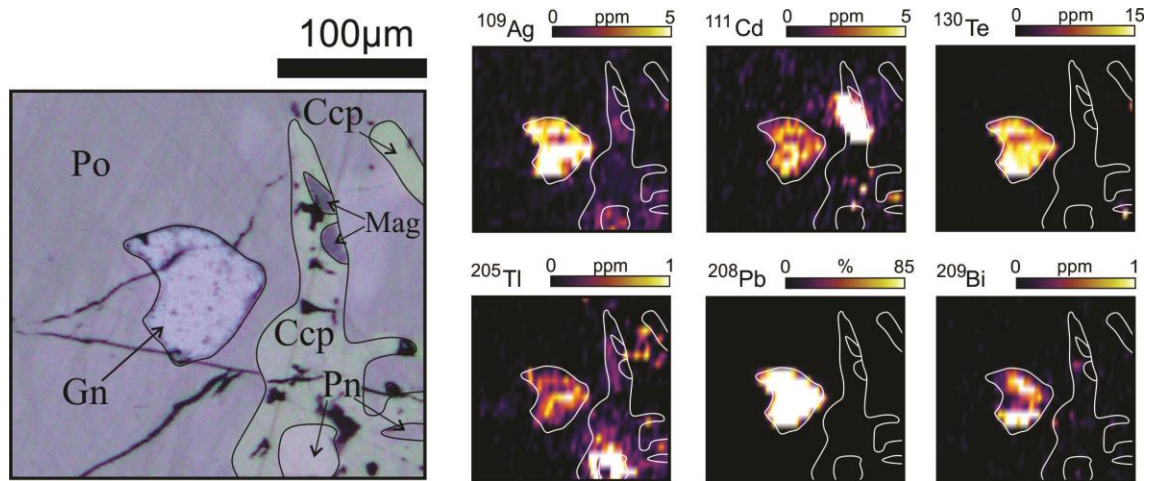
287 Zinc, Ag, Cd, In, Sn, Te and Pb are enriched in Ccp and Cbn (generally 100 to 1000 ppm
 288 for Zn, 1-50 ppm for Ag, Cd, Te and Pb and 0.1 to 10 ppm for In and Sn) relative to Pn and Po
 289 (Table 1). Overall, concentrations of these elements are higher in Pn than Po and concentrations
 290 covering the range of 0.05 to 10 ppm (Table 1). Copper concentrations in Pn and Po are similar in
 291 both minerals mostly in the 1 to 500 ppm range.

292 Selenium and Bi have similar concentrations in all sulfides in the 30 to 130 ppm and 0.1
 293 to 1 ppm ranges, respectively. Gold concentrations are low in all sulfides at 0.01 to 0.1 ppm.
 294 Antimony concentrations are less than detection level for most of the sulfides (<0.05 ppm).
 295



296
 297 Figure 3.4 - LA-ICP-MS elemental maps showing the distribution of chalcophile elements among pyrrhotite (Po),
 298 pentlandite (Pn), chalcopyrite (Ccp) and troilite, in Cu-poor massive sulfide. White lines show the grain outlines. The
 299 concentrations of the elements are semi-quantitative.

300
 301
 302



303

304 Figure 3.5 - LA-ICP-MS elemental maps showing the distribution of Ag, Bi, Cd, Pb, Te and Tl among galena (Gn),
 305 pyrrhotite (Po), pentlandite (Pn), chalcopyrite (Ccp) and magnetite (Mag), in Cu-rich massive sulfide. White lines show
 306 the grain outlines. The concentrations of the elements are semi-quantitative.

307

308 3.4.2 - Partition coefficients between base-metal sulfides

309 Partition coefficients were calculated for each sample using the median values of the
 310 minerals from the sample (*ANNEXE 8*). Figure 6 shows the median, minimum and maximum
 311 partition coefficients calculated between Pn and Po ($D_{Pn/Po}$), Pn and Ccp ($D_{Pn/Ccp}$), Ccp and Po
 312 ($D_{Ccp/Po}$), and Ccp and Cbn ($D_{Ccp/Cbn}$). The 25th and 75th percentile of the results are also shown for
 313 each element.

314 Estimates of the partitioning between Pn and Po (Fig. 6a) show that Pd and Co have the
 315 highest partition coefficients ($D_{Pn/Po} > 10^2$), and Au, Tl, Pb, Pt and Ag have moderately high
 316 partition coefficients into Pn ($D_{Pn/Po} = 1$ to 10^2). Bismuth, Te, Sn, Se, As, Ru, Os, Ir, Rh, Re, Mo
 317 and Cd have partition coefficients around 1. Indium has a slightly preference for Po in
 318 comparison to Pn ($D_{Pn/Po}$ around 0.5). Copper and Zn have a median $D_{Pn/Po}$ of 1, but show wide
 319 variation according to the sample (Fig. 6a; *ANNEXE 8*).

320 The partition coefficients between Pn and Ccp (Fig.6b) for Co, Ir, Pd, Pt Au and Tl are all
 321 high and vary from 10 to 10^3 . Selenium, Pb, Ag, Bi, As, Te and Ru are evenly distributed
 322 between Pn and Ccp ($D_{Pn/Ccp}$ around 1), whereas Sn, Zn, Cd and In ($D_{Pn/Ccp} = 10^{-2}$ to 10^{-1}) partition
 323 into Ccp. The partitioning between Ccp and Po (Fig. 6c) for Pt, Bi and Se is around 1. However,

324 Co, Ni, Mo ($D_{Ccp/Po} = 10^{-2}$ to 10^{-1}), Pd, Ru and Re ($D_{Ccp/Po} = 10^{-1}$ to 1) partition into Po and, Te, Tl,
 325 Au, Ag, Sn, Pb ($D_{Ccp/Po} = 1$ to 10), Cd, In and Zn ($D_{Ccp/Po} = 10$ to 10^3) partition into Ccp (Fig. 6c).
 326 Estimates of the partitioning between Ccp and Cbn (Fig. 6d) reveal a more evenly
 327 distribution of elements in comparison to Pn and Po. The median partition coefficients between
 328 Ccp and Cbn ($D_{Ccp/Po}$) for Mo, Pd, Ru, Pt, Bi, Se, Te, Sn, Pb, As, In and Zn are around 1. Cobalt,
 329 Ni ($D_{Ccp/Cbn} = 10^{-2}$ to 10^{-1}), Tl, Ag and Cd ($D_{Ccp/Cbn} = 10^{-1}$ to 1) partition into Cbn, whereas Au
 330 ($D_{Ccp/Cbn} = 1$ to 10) shows a preference for Ccp (Fig. 6d).

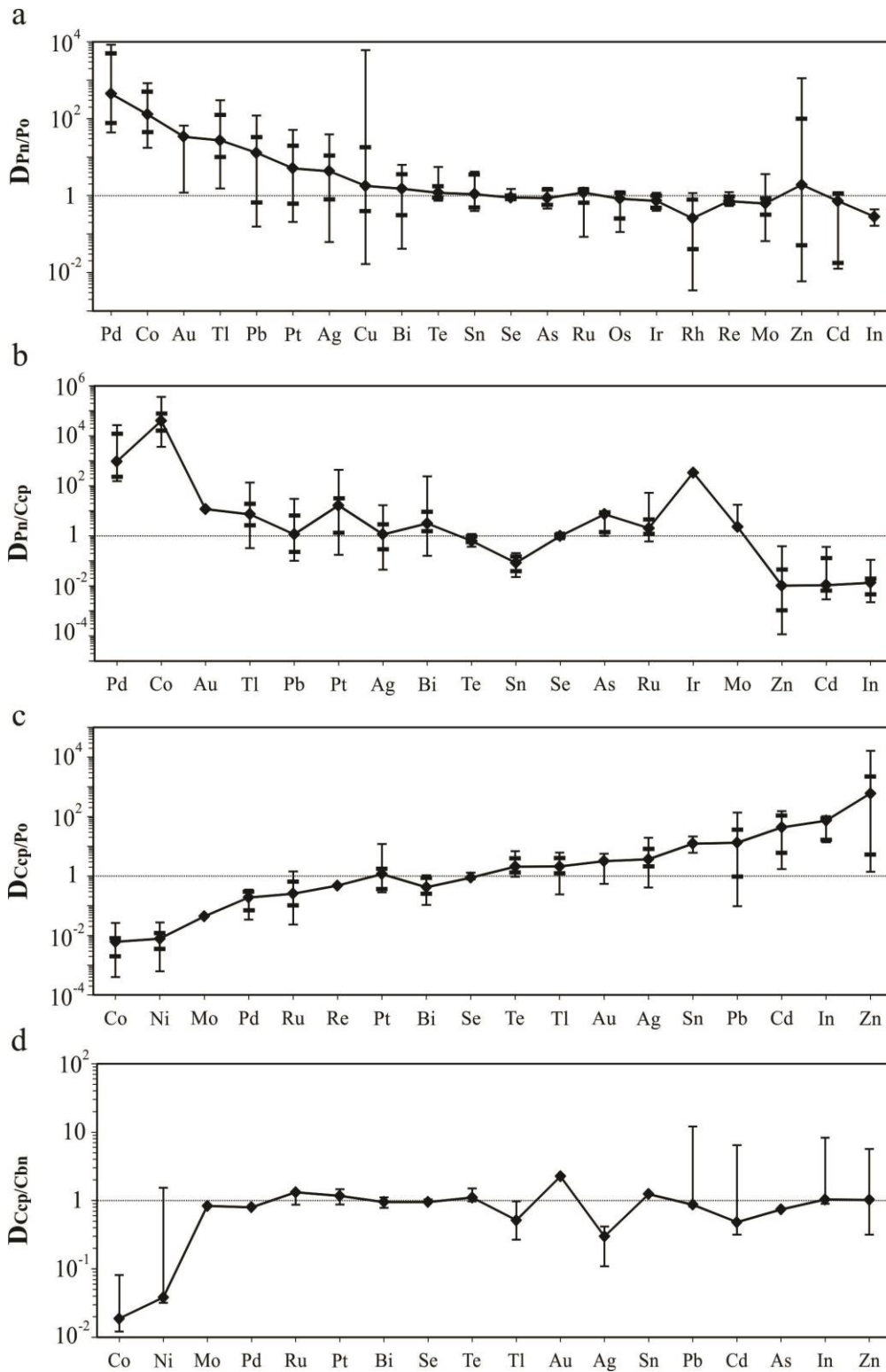
331

332 Table 3.1 - Median concentrations (in ppm) of chalcophile elements in base-metal sulfides from different intrusions and
 333 ores from the Noril'sk-Talnakh mining district.

Intrusion	Pyrrhotite					Pentlandite				
	Kharaelakh		Noril'sk I			Talnakh	Kharaelakh		Noril'sk I	
	Ore type	Cu-poor	Cu-rich	Cu-poor	Cu-rich	Dissem.	Cu-poor	Cu-poor	Cu-rich	Cu-poor
N (n)	4 (26)	4 (19)	2 (10)	1 (3)	1 (6)	1 (6)	4 (20)	5 (24)	2 (9)	3 (15)
Ag	0.35	3.22	1.63	0.90	2.85	1.34	4.55	4.20	2.98	33.5
As	bdl	bdl	0.45	0.60	0.18	bdl	0.22	0.17	0.23	0.57
Au	bdl	0.01	0.02	bdl	0.01	bdl	0.01	bdl	0.03	bdl
Bi	0.09	0.76	0.82	0.34	0.09	0.16	0.25	0.65	0.59	0.89
Cd	bdl	2.96	bdl	0.09	bdl	bdl	0.14	0.07	bdl	0.45
Co	50.9	48.6	368	99.7	534	399	13521	10256	10633	4370
Cu	3.14	269	1.39	22.44	0.97	1.10	195	71	13.4	11103
In	bdl	0.05	bdl	bdl	bdl	bdl	0.02	0.01	0.01	bdl
Ir	0.08	bdl	0.35	bdl	1.89	0.43	0.02	bdl	0.27	bdl
Mo	0.38	0.02	1.91	0.12	0.55	1.38	0.25	bdl	1.38	0.12
Ni	4151	2368	22367	8913	24433	17172	296052	354090	377696	308018
Os	0.06	bdl	0.17	bdl	0.89	0.21	bdl	bdl	0.12	bdl
Pb	1.12	36.2	9.70	2.72	0.06	0.17	15.7	25.6	45.9	8.35
Pd	bdl	1.50	1.37	0.37	0.61	1.83	54.9	180	390	1007
Pt	0.07	0.05	0.29	bdl	0.59	0.27	1.00	0.11	0.92	3.99
Re	0.16	0.14	0.15	bdl	0.16	0.34	0.09	bdl	0.11	0.16
Rh	0.91	bdl	3.55	bdl	16.7	3.78	0.11	bdl	3.90	1.80
Ru	0.20	bdl	0.69	bdl	4.73	0.53	0.21	0.13	0.68	0.21
Sb	bdl	bdl	bdl	bdl	bdl	bdl	bdl	bdl	bdl	bdl
Se	49.0	73.7	64.5	38.0	106	69.6	42.5	72.1	55.5	123
Sn	bdl	0.16	0.05	bdl	bdl	bdl	0.14	0.23	0.06	0.07
Te	0.89	3.66	2.11	0.39	11.70	1.60	1.00	5.18	1.88	35.88
Tl	bdl	0.04	0.01	bdl	bdl	bdl	0.15	0.89	1.00	0.37
Zn	0.28	111	0.19	1.43	0.21	bdl	17.3	1.27	63.7	1.81

334 Abbreviations: Dissem.= disseminated; N= number of samples; n= number of individual analysis; bdl= below detection

335 limit; n.r.= not reported.



336

337 Figure 3.6 - Plots of median partition coefficients of each trace element between a) pentlandite and pyrrhotite
 338 ($D_{Pn/Po}$), b) pentlandite and chalcopyrite ($D_{Pn/Ccp}$), c) chalcopyrite and pyrrhotite ($D_{Ccp/Po}$), and d)
 339 chalcopyrite and cubanite ($D_{Ccp/Cub}$). The range indicates the minimum and maximum values obtained for each element in
 340 individual samples. The black dashes in the central part of the variation ranges indicate the 25th and 75th percentile of
 341 results. The results are reported in ANNEXE 8.

342

343 3.4.3 - Mass balance

344 The weight fraction of each element in each BMS was calculated to examine which
345 mineral(s) host the bulk of each element for each ore type. The proportion of each element hosted
346 in each BMS was calculated following the method used by Barnes et al. (2006). This calculation
347 requires: i) the concentration of each element in the whole rock; ii) the median concentration of
348 each element in each BMS (Table 1); and iii) the weight fraction of each BMS. The weight
349 fraction of Ccp, Cbn, Po, and Pn were calculated using whole-rock Cu, Ni, and S and the
350 concentrations of Cu and Ni in each mineral. The contribution of Ni present in Po was determined
351 by LA-ICP-MS (*ANNEXE 4*) and subtracted from the Ni in the whole rock before the amount of
352 Pn was calculated. In Cbn-free samples, all of the Cu was assigned to Ccp. In samples containing
353 Cbn, Cu was assigned to Ccp and Cbn, using the Cbn/Ccp ratio obtained by petrographic
354 observations (approximately 1:5). The remaining S was attributed to Po. The accumulated error of
355 the different results used for the mass balance calculation is approximately 20% at one standard
356 deviation (1σ). The mass balance of Re was not calculated as the whole-rock concentrations are
357 too low (Duran et al. 2017). The mass balance for Rh, Ru, Ir and Os was also not calculated for
358 the Cu-rich ores because of the low levels of these elements in the whole rock (*ANNEXE 9*).

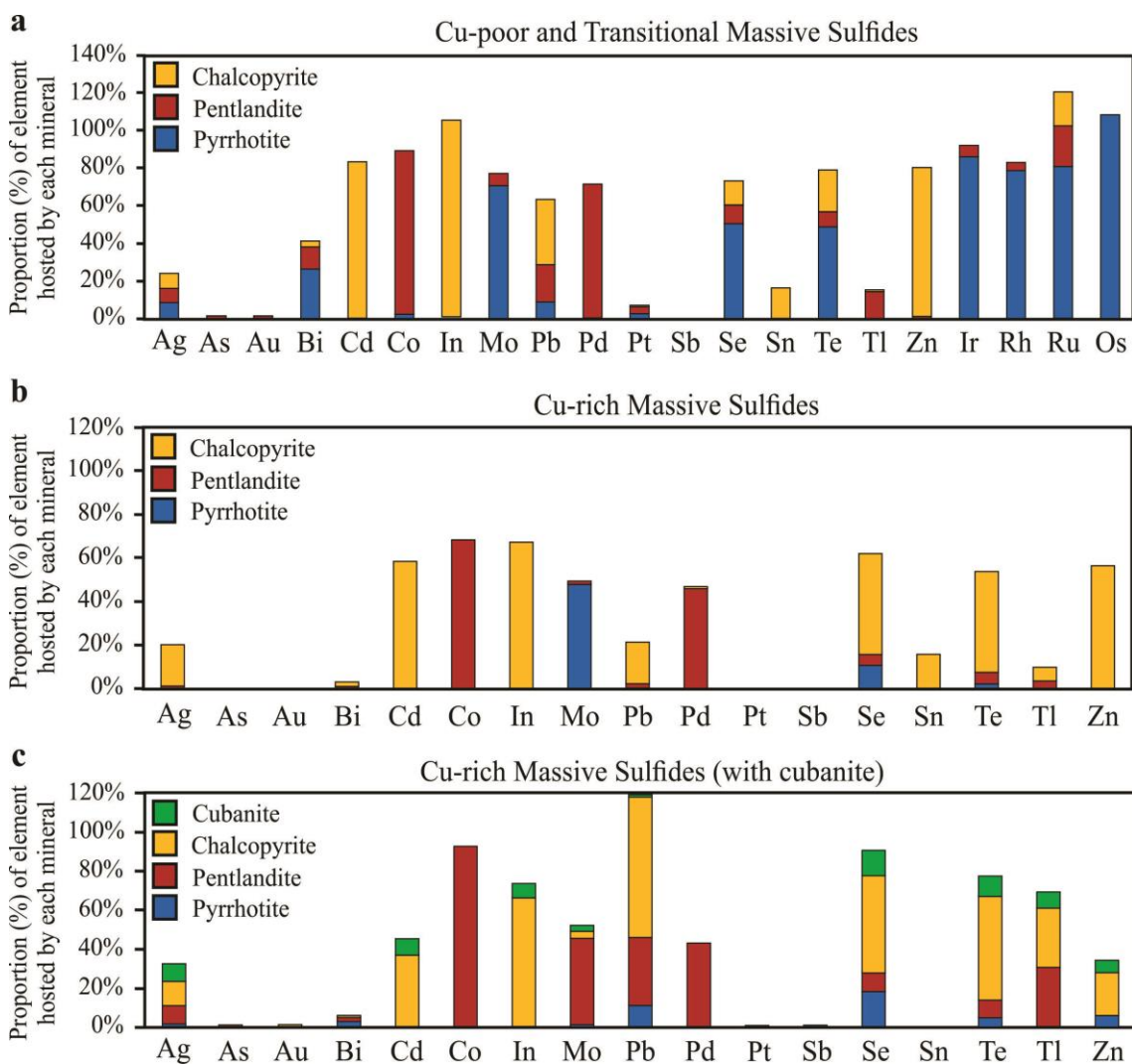
359 The BMS from the Cu-poor ores host the bulk (>70%) of the Cd, Co, In, Mo, Pd, Te, Se,
360 Zn, Rh, Ru, Ir and Os (Fig. 7a; *ANNEXE 9*). Given the various uncertainties in the calculation
361 (e.g. sampling, precision of whole-rock and LA-ICP-MS analyses), we consider that all of these
362 elements are essentially present in the BMS. The BMS assemblage also hosts significant amounts
363 of the Bi, Pb, Ag, Sn and Tl (15-70%), but only minor amounts (<10%) of the As, Au and Pt.

364 In Cu-rich ores (Fig. 7b), the BMS host a significantly lower proportion of chalcophile
365 elements in comparison to Cu-poor ores. The BMS host the bulk (>50%) of the Co, Cd, In, Se, Te
366 and Zn, and significant amounts (20 to 50 %) of the Ag, Pb and Pd. Less than 10 % of the As, Au,
367 Bi, Mo, Pt and Tl is present in BMS. Samples with Cbn were treated separately in order to
368 consider the contribution of this mineral, which hosts less than 10% of bulk Ag, Cd, In, Mo, Pb,
369 Te, Tl and Zn (Fig. 7c). The mass balance for samples with Cbn is similar to other Cu-rich

370 samples but with some minor differences for Ag, Cd, Co, Mo, Pb, Sn, Te, Tl and Zn (Fig. 7b and
 371 7c).

372 Pyrrhotite hosts most of Os, Ir, Ru, Rh, and Mo. Chalcopyrite and cubanite host most of the Cd,
 373 In, Sn, Pb and Zn. Pentlandite hosts most of the Co and Pd. Selenium and Te are present in all
 374 BMS, and the main host is the most common mineral in each ore type. Thus, Po is the main host
 375 of Se and Te in the Cu-poor ore, whereas Ccp is the main host in the Cu-rich ore.

376



377

378 Figure 3.7 - Average proportion (%) of each element hosted in pyrrhotite (Po), pentlandite (Pn), chalcopyrite (Ccp),
 379 cubanite (Cbn) and sum, from the a) Cu-poor and Transitional, b) Cu-rich and c) Cu-rich (with cubanite) ores of the
 380 Noril'sk-Talnakh mining district. The whole-rock data used for the calculation is reported by Duran et al. (2017).
 381 Values above 100% are related to low whole-rock concentrations.

382

383 **3.5 - Discussion**

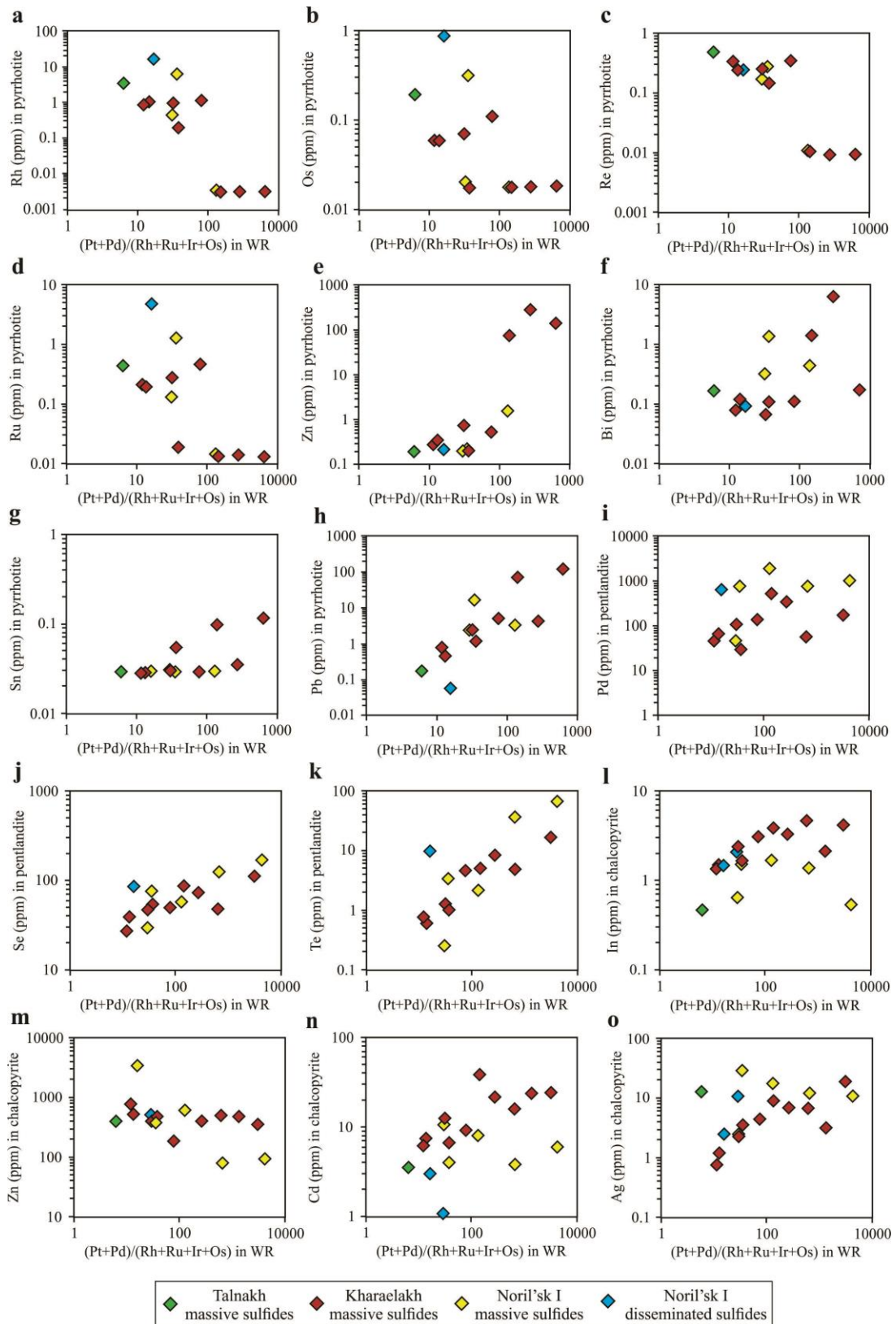
384 **3.5.1 - Variations in chalcophile element content of the minerals with fractional** 385 **crystallization**

386 There is a systematic variation in the median trace elements concentration in the BMS
387 with $(\text{Pt}+\text{Pd})/(\text{Ru}+\text{Rh}+\text{Ir}+\text{Os})$ of the whole rocks. The median concentrations of elements
388 predominantly hosted by Po: Ru, Rh, Re, Os, Ir and Mo, decrease as the whole-rock
389 $(\text{Pt}+\text{Pd})/(\text{Ru}+\text{Rh}+\text{Ir}+\text{Os})$ increases (Fig. 8a-d). The median concentration of elements hosted by
390 Ccp: Cd, In, Sn and Pb increases as the whole-rock $(\text{Pt}+\text{Pd})/(\text{Ru}+\text{Rh}+\text{Ir}+\text{Os})$ increases (Fig. 8l-o).
391 Zinc is the only element showing a different behaviour with respect to different BMS, with
392 increasing concentrations in Po, and decreasing concentrations in Ccp as the whole-rock
393 $(\text{Pt}+\text{Pd})/(\text{Ru}+\text{Rh}+\text{Ir}+\text{Os})$ increases (Fig. 8e and m). Decreasing Zn concentrations in Ccp likely
394 reflect a dilution caused by the larger amount of ISS (and consequently Ccp) crystallizing, with
395 progressive fractionation of the sulfide liquid.

396 Our results support the model that progressive crystallization of the sulfide liquid
397 fractionates PGE, and other chalcophile elements, at least partially in response to their different
398 compatibility with MSS and ISS. As the sulfide liquid evolves, concentration of the elements
399 compatible with MSS (Co, Mo, Re, Rh and IPGE; Barnes et al., 1997; Mungall, 2005; Liu and
400 Brenan, 2015) decreases in the liquid. This is reflected in a decrease in their concentrations in
401 BMS antithetical to whole-rock $(\text{Pt}+\text{Pd})/(\text{Rh}+\text{Ru}+\text{Os}+\text{Ir})$ (Fig. 8a-d). In contrast, a striking
402 outcome is that BMS crystallizing from the evolving liquid become richer in most incompatible
403 elements (Pd, Ag, Bi, Cd, In, Pb, Sn, Te, Tl and Zn; Patten et al. 2013; Liu and Brenan, 2015; Fig.
404 9e-o), but at the same time account for lesser amounts of their whole-rock budget (Fig. 7).

405

406



407

408 Figure 3.8 - Binary plots of Rh (a), Os (b), Re (c), Ru (d), Zn (e and m), Bi (f), Sn (g), Pb (h), Pd (i), Se (j), Te (k), In
 409 (l), Cd (n) and Ag (o) median concentrations (ppm) in pyrrhotite, chalcopyrite and pentlandite versus
 410 (Pt+Pd)/(Rh+Ru+Ir+Os) in whole-rock (WR), for massive sulfides from Noril'sk I, Kharaelakh and Talnakh intrusions,
 411 and disseminated sulfides from the Noril'sk I intrusion.

412 In the ore formed from the least fractionated liquid (Cu-poor), the BMS host the majority
413 of trace chalcophile elements, but in the ore formed from the most fractionated liquid (Cu-rich),
414 BMS host significantly less of these elements (Fig. 7). To further assess how fractional
415 crystallization affects the distribution of chalcophile elements within a crystallizing sulfide liquid,
416 especially in the latest stages, we discuss below the possible scenarios for the origin of PGM.
417 Thereafter, we will summarize the fractional crystallization history of BMS in the Noril'sk-
418 Talnakh mining district, and reconstruct the partition of chalcophile elements during the evolution
419 of the sulfide liquid.

420 It is noteworthy that although the concentration of trace elements in BMS is controlled by
421 the fractional crystallization of the sulfide liquid, other processes may also affect their
422 distribution. This may be particularly important considering that not all BMS crystallized at the
423 same time. Mansur et al. (2019) showed that loop-textured Pn, located at the contact between Po
424 and Ccp formed via peritectic reaction at higher temperatures (i.e. around 950°C) relative to
425 granular and flame Pn, which exsolved from the MSS at low temperatures (i.e. below 650°C). The
426 authors also indicate that some incompatible elements such as Pd could be incorporated from the
427 fractionated sulfide liquid into this high-form of Pn. Thus, higher concentrations of Pd in Pn
428 could be also found in Pn from Cu-poor massive sulfides, even though these crystallized from a
429 less fractionated sulfide liquid. A possible illustration of this process is the distribution of Pd in
430 Pn from massive sulfides of the Noril'sk I intrusion, which is not entirely controlled by the
431 whole-rock fractionation (Fig. 8i). In this case, the Pn grains most likely formed during two
432 different stages, and their composition is not exclusively controlled by the degree of fractionation
433 of the sulfide liquid.

434

435 **3.5.2 - Timing of PGM formation**

436 In both the Cu-poor and Cu-rich ores, the bulk of trace elements that are not entirely
437 hosted by BMS minerals must be accounted for by the presence of PGM and other discrete
438 minerals. In Cu-poor ore, Pt, As, Au, Ag and Sb are hosted by Pt-arsenides (mostly sperrylite),

439 isoferroplatinum, and minor electrum (Duran et al. 2017). In contrast, a greater variety of PGM
440 was observed by Duran et al. (2017) in the Cu-rich ores. The PGM assemblage consists of Pd-Pt-
441 bismuthtellurides, arsenides and stanides, which occur either as single-phased grains, or sub-
442 spherical composite grains (Fig. 1e and f). Laser profiles reveal the presence of Ag, Pb, Sb, and
443 Tl within these composite PGM grains. In addition to their presence in the PGM some of the Ag,
444 Cd, Te, Tl and Pb and Bi could be also hosted by the galena as indicated by the LA-ICP-MS map
445 (Fig. 5). Duran et al. (2017) interpreted these composite grains as the crystallization product of
446 the lattermost fractionated sulfide liquid.

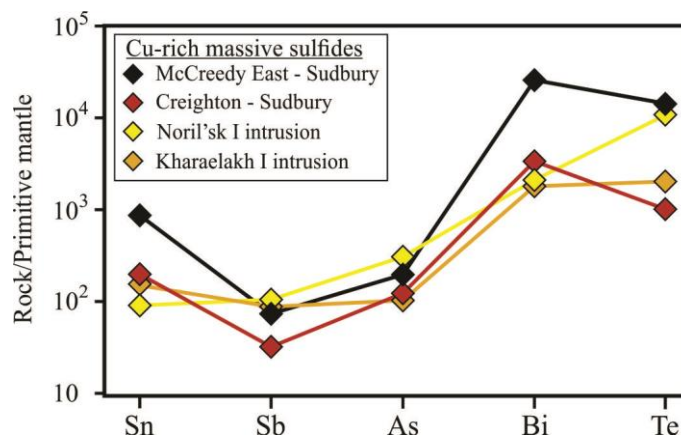
447 In contrast to this model of late crystallization of the PGM, it has been shown that the
448 PGM may directly crystallize from the sulfide liquid prior to MSS crystallization at some
449 localities e.g. the Creighton deposit, Sudbury (Dare et al. 2010a), the Platreef (Bushveld. Power et
450 al. 2004; Hutchinson and McDonald 2008). Assimilation of TABS the from surrounding country
451 rocks is thought to have favoured this direct crystallization (Hutchinson and McDonald 2008;
452 Dare et al. 2010a). However, although the contamination of TABS from country rocks appears to
453 be an important process in the Noril'sk-Talnakh mining district, there is no evidence for early
454 crystallization of PGM from the sulfide liquid. On the contrary, high-resolution X-Ray computed
455 tomography in Cu-poor ores indicated that the few PGM present in this ore type have an
456 elongated shape, and likely formed by exsolution from the BMS (Duran et al. 2017).

457 The progressive concentration of TABS during fractionation could lead to the
458 crystallization of PGM from a much fractionated sulfide liquid, or as suggested by a number of
459 authors, to the segregation of an immiscible TABS-rich liquid (Hanley 2007; Helmy et al. 2007,
460 2013; Holwell and McDonald 2007; Mavrogenes et al. 2013). The form of PGM in the Cu-rich
461 ores as intergrowths of Pd-Pt-Au-TABS minerals in small sub spherical patches (Fig. 1f and
462 Duran et al. 2017) could be interpreted to support either model.

463 Experimental studies show that immiscible TABS-rich liquids can form from a BMS
464 liquid (Helmy et al. 2007, 2010, 2013; Mavrogenes et al. 2013; Liu and Brennan 2015; Cafagna
465 and Jugo 2016; Distler et al. 2016; Sinyakova et al. 2017; Bai et al. 2017) and natural examples of

466 this process have been proposed (Piña et al. 2015). However, the concentrations of TABS
 467 required to achieve saturation are very high (200 to 1000 ppm), and most natural sulfide liquids
 468 do not appear to reach these levels. Liu and Brenan (2015) applied their experimental results to
 469 the Cu-rich ores of McCreedy East (Sudbury) and concluded that the liquid did not contain
 470 sufficient TABS to have segregated an immiscible TABS liquid. The Noril'sk and Kharaelakh
 471 Cu-rich samples are similar to McCreedy East, both in terms of textures of PGM and
 472 concentrations of TABS (Fig. 9). The Cu-rich samples with highest TABS concentrations only
 473 contain ~50 ppm (Duran et al. 2017), insufficient to form an immiscible TABS liquid. Duran et
 474 al. (2017) calculated that the sulfide liquid would have to have undergone more than 99.9%
 475 fractional crystallization for the liquid to be sufficiently rich in TABS to form an immiscible
 476 liquid. Therefore we propose that the PGM intergrowths in the Cu-rich ores crystallized from the
 477 sulfide liquid after extensive fractional crystallization of MSS and ISS.

478



479

480 Figure 3.9 - Mantle-normalized Te, As, Bi, Sb and Sn (TABS) whole-rock concentrations of Cu-rich massive sulfides
 481 from McCreedy East (Dare et al. 2014) and Creighton (Dare et al. 2010a) deposits, and Noril'sk I and Kharaelakh
 482 intrusions (Duran et al. 2017). Concentrations have been recalculated to 100% sulfides following Barnes and Lightfoot
 483 (2005). Primitive mantle values from Lyubetskaya and Korenaga (2007).

484

485

486 **3.5.3 - Fractional crystallization of massive sulfides and constraints for the**
487 **formation of platinum-group minerals**

488

489 We used the systematic variation of trace elements in BMS, and mass balance to assess
490 the behaviour of PGE and other chalcophile elements during fractional crystallization of sulfide
491 liquid (Fig. 10a). Upon cooling (below 1190 °C), MSS started to crystallize from the initial
492 sulfide liquid and incorporated IPGE, Rh, Re, Mo and some Ni, Co, Se, whereas Cu, Pt, Pd, Au,
493 TABS, Zn, Ag, Pb, Cd, In, Tl largely partitioned into the fractionated liquid (Fig. 10b; Li et al.
494 1996; Barnes et al. 1997; Mungall et al. 2005; Liu and Brenan 2015). We interpret the Cu-poor
495 ores as being representative of MSS adcumulates.

496 Below 950°C, the Cu-rich liquid started to crystallize as ISS, which incorporated Cu, Cd,
497 Co, In, Se, Sn and Zn. Palladium, TABS, Ag, Pb, and Tl are moderately to strongly incompatible
498 with ISS, and their concentrations in the remaining sulfide liquid increased (Fig. 10c). In the late
499 stages of crystallization, the trapped sulfide liquid became sufficiently enriched in incompatible
500 elements (i.e. especially TABS) to crystallize as composite PGM grains, electrum and galena
501 (Duran et al., 2017; Fig. 10d). We interpret the Cu-rich ores as ISS cumulates with variable
502 amounts of fractionated sulfide liquid trapped among the grains.

503 Not all Pn formed in the same way. Pentlandite found at the contact between Ccp and Po
504 formed by peritectic reaction between MSS and Cu-rich liquid, below 900°C (Mansur et al.
505 2019). The distribution of trace elements in Pn formed during this peritectic reaction is detailed
506 by Mansur et al. (2019). Some Pn formed during exsolutions of MSS. Below 650°C, MSS
507 exsolved into Po+Pn±Ccp (Fig. 10d). During this exsolution the elements compatible with MSS
508 (Mo, Re, Rh and IPGE) distributed evenly between Pn and Po ($D_{Pn/Po}$ around 1; Fig. 7). The
509 elements slightly to moderately incompatible with MSS partitioned either into Pn (Ni, Co, Pd and
510 Tl), Ccp (Zn, Cd, In, Sn) and PGM (Pt,As) (Fig. 10d). Some incompatible elements (Ag, Te, Pb,
511 Bi) partitioned into both Pn and Ccp, whereas Se shows no preference among the BMS (Fig. 6).
512 Thus, although concentrations of incompatible elements are expected to be low in BMS exsolved
513 from the MSS, slightly higher concentrations can be locally found, such as Pd in exsolved Pn

514 (Fig. 2). This is because the small fraction of incompatible elements incorporated by the MSS
515 have partitioned into reduced volumes of exsolved Pn, leading to locally higher concentrations.

516 Intermediate solid solution exsolved into Ccp+Pn±Cbn (Fig. 10d and 10e). During the
517 exsolution of the ISS, the elements distributed themselves between Ccp and Pn in a similar
518 manner to that observed during the exsolutions of the MSS. However, some PGM that exsolved
519 from BMS are more varied with some containing Pd-Te-Bi and many containing Pt-Pd-Sn (Fig.
520 10a to c of Duran et al. 2017). Cubanite only exsolves below 200°C and the partition coefficients
521 between Ccp and Cbn ($D_{Ccp/Cbn}$) are normally around 1 for most elements. Exceptions to this are
522 Ni, Co, Tl and Ag which partition into Cbn (Fig. 6).

523 The partition coefficients between Pn and Po (Fig. 6a) for Pd and Co are much higher
524 (with $D_{Pn/Po}$ up to 10^3) than the partition coefficients between Ccp and Cbn (with $D_{Ccp/Cbn}$ normally
525 below 10; Fig. 6d). This may be due to relative similarity of the Ccp and Cbn structures as
526 compared with to Pn and Po structures. Alternatively, this may be related to the temperatures at
527 which these minerals formed. Pentlandite starts to form via peritectic reaction between the MSS
528 and the sulfide liquid around 950°C (Mungall 2007; Mansur et al. 2019). Furthermore, MSS
529 begins to exsolve into Pn around 650 °C, whereas Cbn only forms around 200 °C (Cabri 1973;
530 Dutrizac 1976; Kelly and Vaughan 1983;). In fact, Tro exsolutions in Po, which form at even
531 lower temperatures (i.e. <145°C; Kissin and Scott 1982; Naldrett 2011; Fig. 10e), do not affect
532 the distribution of chalcophile elements (Fig. 4).

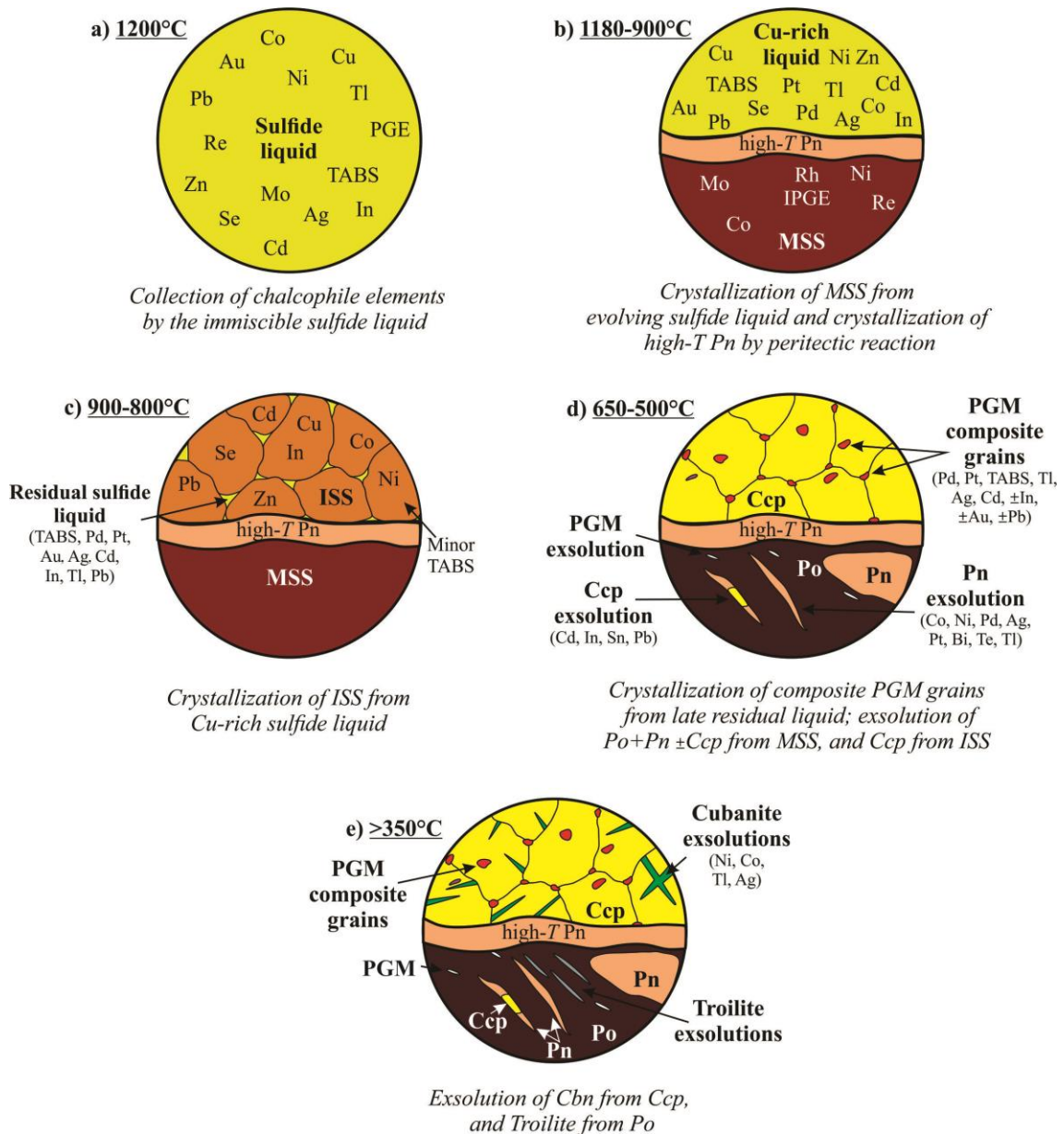
533

534

535

536

537



538

539 Figure 3.10 - Schematic models illustrating the crystallization history of massive sulfides from the Noril'sk-Talnakh
 540 mining district, and the processes controlling the distribution of PGE and other chalcophile elements. See text for
 541 further explanation. Abbreviations: MSS- monosulfide solid solution ; ISS- intermediate solid solution; Po- pyrrhotite;
 542 Pn- pentlandite; Ccp- chalcopyrite; Cbn- cubanite.

543

544

545

546

547 **3.5.4 - Assessing the evolution of magmatic sulfide deposits via comparison of BMS**
548 **compositions**

549 Over the past few years, many authors have investigated the distribution of PGE among
550 BMS in Ni-Cu-PGE deposits (Barnes et al. 2006, 2008; Godel et al. 2007, 2012; Holwell and
551 McDonald 2007; Godel and Barnes 2008; Smith et al. 2014; Chen et al. 2015; Junge et al. 2015;
552 Sessa et al. 2017; Yudovskaya et al. 2017). Recent studies have determined the concentrations of
553 a wider range of chalcophile elements (e.g. Sudbury – Dare et al. 2010b, 2011, 2014; Aguablanca
554 – Piña et al. 2012; Lac des Iles – Duran et al. 2016, 2019; Voisey's Bay – Amaral 2017).
555 Comparisons of the deposits using a wide suite of trace element in BMS may now begin to be
556 used as an attempt to access processes that took place during ore formation.

557 Compositions of the minerals are compared on mantle normalized diagrams with the
558 elements in increasing order of incompatibility with picritic basalt mantle sources (Barnes 2016).
559 We have plotted the compositions of Po, Pn, Ccp and Cbn from Cu-poor and Cu-rich ores from
560 Sudbury (Creighton and McCreedy East deposits), Voisey's Bay (Ovoid body) and Noril'sk I,
561 Talnakh and Kharaelakh intrusions (Fig. 11). Given that in the Aguablanca and Lac des Iles
562 deposits massive sulfide bodies are relatively minor and poorly zoned in terms of Cu, we only
563 compare the massive sulfide from the Noril'sk-Talnakh mining district, with those of Sudbury
564 and Voisey's Bay.

565 In most magmatic sulfide deposits Pt, As, Sb and Au concentrations in BMS are very
566 low, but Pt concentrations in BMS (especially in Pn and Po) from Noril'sk I, Talnakh and
567 Kharaelakh intrusions are slightly higher (Fig. 11a to 11d). This observation supports the
568 interpretation of Barnes et al. (2008), which related the higher concentrations of PGE in BMS to
569 faster cooling rate at Noril'sk I. In addition, Pd concentrations are also higher in Pn from Noril'sk
570 I and Kharaelakh intrusions in comparison to Voisey's Bay and Sudbury (Fig. 11c and d). The
571 higher concentrations of Pd in BMS are thought to be the result of the higher concentration of Pd
572 in the Noril'sk-Talnakh sulfide liquid.

573 The degree of fractional crystallization experienced by the sulfide liquid is also recorded
574 by BMS. The concentrations of elements incompatible with MSS (Cd, Se, Ag and Te) are higher
575 in Ccp and Cbn from Cu-rich ores from the Noril'sk I and McCreedy East deposits (Fig. 11f and
576 g) relative to those from Kharaelakh and Voisey's Bay. This probably indicates that sulfides from
577 Noril'sk I and McCreedy East have experienced more extensive fractionation. In fact, Cu-rich
578 ores at Noril'sk I and McCreedy East show a physical separation (as veins) from the MSS
579 (Mungall 2007; Dare et al. 2014; Duran et al. 2017). Mungall (2007) supports that these
580 physically separated sulfides record an extensive degree of fractional crystallization, and may be
581 regarded as ISS cumulates segregated from a fractionated sulfide liquid. This is not the case for
582 the samples from the other localities that were analysed.

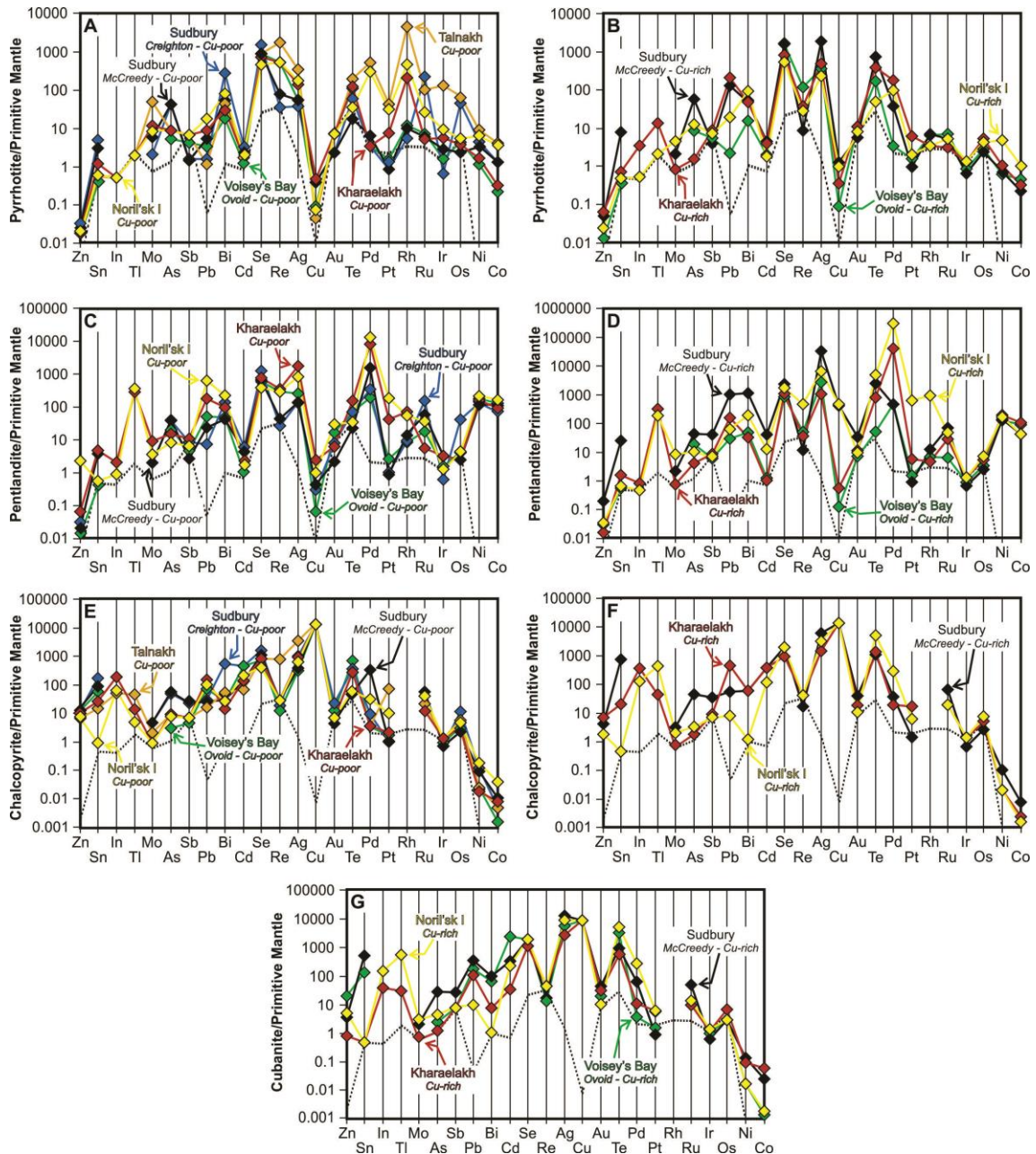
583 Another variable that affects the distribution of chalcophile elements in magmatic sulfide
584 deposits is the nature of the co-crystallizing phases. Chalcopyrite and Cbn from McCreedy East
585 and the Ovoid, respectively, host significant amounts of Sn, whereas Ccp and Cbn from Noril'sk I
586 and Kharaelakh, are not main hosts of Sn (Fig 11f and g). Magnetite can be important for the Sn
587 budget (Dare et al. 2012). At Noril'sk and Kharaelakh Sn is present in composite PGM grains and
588 magnetite. It seems likely that the crystallization of these other phases affected the composition of
589 co-crystallizing BMS, but this still need to be investigated.

590 The compositions of BMS from Voisey's Bay (Amaral 2017) also give some clues about
591 the influence of BMS assemblage on the distribution of trace elements. Cubanite from Cu-rich
592 ores at Voisey's Bay has high concentrations of incompatible elements (Ag, Bi, Cd, Pb, Sn, Te
593 and Zn; Fig. 11g). These high contents are probably related to a greater proportion of Cbn in
594 comparison to Ccp in the Cu-rich ores. Therefore, in the absence of Ccp, incompatible elements
595 that were once incorporated by ISS partitioned into Cbn exsolutions.

596

597

598



599

600 Figure 3.11 - Primitive mantle normalized multi-element diagrams of median compositions of pyrrhotite (a-b),
 601 pentlandite (c-d), chalcopyrite (e-f) and cubanite (g) in Cu-poor and Cu-rich ores from different deposits. Comparison
 602 of BMS from Noril'sk I, Kharaelakh and Talnakh intrusion (this study), with Creighton (Dare et al. 2010b), McCreedy
 603 East (Dare et al. 2014), and Voisey's Bay (Amaral 2017). Primitive mantle values from Lyubetskaya and Korenaga
 604 (2007). Elements are plotted from left to right in increasing order of incompatibility with picritic basalt mantle sources
 605 (Barnes 2016). Detection limits are plotted for reference (dashed line).

606

607

608

609 **3.6 - Conclusions**

610 This study provides insights into the behaviour of chalcophile elements during fractional
611 crystallization of sulfide liquid, and whether Te, As, Bi, Sb and Sn (TABS) are important for
612 controlling the timing for the formation of PGM. Our main findings are summarized as follows:

613 1 – Massive sulfides formed via fractional crystallization of a sulfide liquid. Cu-poor ores consist
614 of early formed MSS adcumulates, and Cu-rich ores consist of ISS cumulates with various
615 amounts of trapped fractionated sulfide liquid.

616 2- Mass balance reveals that in Cu-poor ores, BMS minerals contain the bulk of the PGE and
617 other chalcophile elements. Platinum, Au, As and Sb are exceptions to this. Platinum, Au and As
618 are present as PGM. In contrast, in the Cu-rich ores, the BMS minerals host a significantly lower
619 proportion of the PGE and chalcophile elements. In the Cu-rich ores the balance of chalcophile
620 elements are accounted by subspherical intergrowths of PGM and Au, and grains of galena.

621 3 – In the Cu-poor ores, TABS do not play a role in controlling the PGE, with most IPGE and Pd
622 in Po and Pn. Platinum is an exception. Platinum and As appear to be pushed to out of the MSS
623 structure and to have formed discrete minerals, but these are still enclosed in Po or Pn. In the Cu-
624 rich ore the Pd is partly present in Pn, and some Pt and Pd are present as exsolutions of Pd-Te-Bi
625 and sperrylite and rustenburgite. However most of the Pd and Pt are present as intergrowths of
626 Pd-Pt-TABS-rich minerals, representing the lattermost sulfide liquid.

627 4 – Cryptic variations in trace element contents of the BMS show variable co-variance with the
628 degree of crystallization as indicated by whole rock $(Pd+Pt)/(Rh+Ru+Ir+Os)$. Elements
629 compatible with MSS (Co, Mo, Re, Rh and IPGE) are enriched in Po and Pn in rocks with low
630 $(Pd+Pt)/(Rh+Ru+Ir+Os)$, relative to rocks with high $(Pd+Pt)/(Rh+Ru+Ir+Os)$. Similarly, Po, Pn
631 and Ccp from early formed MSS are depleted in elements incompatible with MSS (Ag, Bi, Cd,
632 Cu, In, Se, Sn, Te, Tl, Pb, Pd and Zn) relative to BMS that formed from the more fractionated
633 sulfide liquid. These variations support that the composition of BMS is partially controlled by the
634 degree of fractional crystallization underwent by the sulfide liquid.

635 5 – Comparison of a wide suite of trace element in BMS from different Ni-Cu-PGE deposits may
636 allow for the assessment of different steps of the evolution of magmatic sulfide deposits
637 including: i) the degree of fractionation of the sulfide liquid, and ii) the possible influences of co-
638 crystallizing phases in the composition of BMS.

639

640 **3.7 - Acknowledgments**

641 *This work was supported by a Canada Research Chair program grant to Sarah-Jane Barnes*
642 *(215503). We would like to thank Dany Savard (LabMaTer, UQAC) for his assistance with LA-*
643 *ICP-MS analyses, and Michael Zientek (USGS) for sharing his valuable samples. Organizers of*
644 *the 12th International Platinum Symposium, field trip leaders (Nadezhda Krivolustskaya, Viktor*
645 *Rad'ko, Kreshimir Malitch, Vadim Distler, and Valery Fedorenko), and Noril'sk Nickel geologists*
646 *are gratefully acknowledged for providing rare access to the Noril'sk area. This manuscript*
647 *benefited from insightful comments from Marco Fiorentini and Steve Barnes, and careful*
648 *editorial handling by the editors Wolfgang Maier and Georges Beaudoin.*

649

650

651

652

653

654

655

656

657

658 **3.8 - References**

- 659 Amaral LFS (2017) The distribution of platinum-group elements and other chalcophile elements
660 among sulfide minerals from the ovoid ore body of the voisey's bay Ni-Cu sulfide
661 deposit, Canada. Unpubl MSc thesis, Université du Québec à Chicoutimi, 166 pp
- 662 Bai L, Barnes S-J, Baker DR (2017) Sperrylite saturation in magmatic sulfide melts: Implications
663 for formation of PGE-bearing arsenides and sulfarsenides. *Am Mineral* 102(5): 966-974
- 664 Barnes S-J (2016) Chalcophile Elements. In: White, W.M. (Ed.) *Encyclopedia of Geochemistry:*
665 *A Comprehensive Reference Source on the Chemistry of the Earth*, Part of the series
666 *Encyclopedia of Earth Sciences Series* pp 1–5
- 667 Barnes S-J, Lightfoot PC (2005) Formation of magmatic nickel sulfide ore deposits and processes
668 affecting their copper and platinum group element contents. *Economic Geology* 100th
669 Anniversary. pp 179–213
- 670 Barnes S-J, Makovicky E, Makovicky M, Rose-Hansen J, Karup-Moller S (1997) Partition
671 coefficients for Ni, Cu, Pd, Pt, Rh, and Ir between monosulfide solid solution and sulfide
672 liquid and the formation of compositionally zoned Ni–Cu sulfide bodies by fractional
673 crystallization of sulfide liquid. *Can J Earth Sci* 34:366-374
- 674 Barnes S-J, Cox R, Zientek M (2006) Platinum-group element, gold, silver and base metal
675 distribution in compositionally zoned sulfide droplets from the Medvezky Creek Mine,
676 Noril'sk, Russia. *Contrib Mineral Petrol* 152:187-200
- 677 Barnes S-J, Prichard HM, Cox RA, Fisher PC, Godel B (2008) The location of the chalcophile
678 and siderophile elements in platinum-group element ore deposits (a textural, microbeam
679 and whole rock geochemical study): Implications for the formation of the deposits. *Chem*
680 *Geol* 248:295-317
- 681 Barnes S-J, Ripley EM (2016) Highly siderophile and strongly chalcophile elements in magmatic
682 ore deposits. *Rev Mineral Geochem* 81:725-774
- 683 Cabri LJ (1973) New data on phase relations in the Cu-Fe-S system. *Econ Geol* 68:443-454

684 Cafagna F (2015) The geochemical behavior of metalloids and their effect on the highly
685 siderophile elements during the crystallization of a magmatic sulfide liquid in relation to
686 the formation of Ni-Cu-PGE magmatic sulfide deposits. Unpubl PhD thesis, Laurentian
687 University, 206 pp

688 Cafagna F, Jugo PJ (2016) An experimental study on the geochemical behavior of highly
689 siderophile elements (HSE) and metalloids (As, Se, Sb, Te, Bi) in a mss-iss-pyrite system
690 at 650° c: A possible magmatic origin for Co-HSE-bearing pyrite and the role of
691 metalloid-rich phases in the fractionation of HSE. *Geochim Cosmochim Acta* 178:233-
692 258

693 Chen L-M, Song XY, Danyushevsky LV, Wang Y-S, Tian Y-L, Xiao J-F (2015) A laser ablation
694 ICP-MS study of platinum-group and chalcophile elements in base metal sulfide minerals
695 of the jinchuan Ni–Cu sulfide deposit, NW China. *Ore Geol Rev* 65:955-967

696 Czamanske GK, Kunilov VE, Zientek ML, Cabri LJ, Likhachev AP, Calk LC, Oscarson RL
697 (1992) A proton microprobe study of magmatic sulfide ores from the Noril'sk-Talnakh
698 District, Siberia. *Can Mineral* 30:249-287

699 Dare SAS, Barnes S-J, Prichard HM, Fisher PC (2010a) The timing and formation of platinum-
700 group minerals from the Creighton Ni-Cu-platinum-group element sulfide deposit,
701 Sudbury, Canada: Early crystallization of PGE-rich sulfarsenides. *Econ Geol* 105:1071-
702 1096

703 Dare SAS, Barnes S-J, Prichard HM (2010b) The distribution of platinum group elements (PGE)
704 and other chalcophile elements among sulfides from the Creighton Ni–Cu–PGE sulfide
705 deposit, Sudbury, Canada, and the origin of palladium in pentlandite. *Miner Deposita*
706 45:765-793

707 Dare SAS, Barnes S-J, Prichard HM, Fisher PC (2011) Chalcophile and platinum-group element
708 (PGE) concentrations in the sulfide minerals from the McCreedy East deposit, Sudbury,
709 Canada, and the origin of PGE in pyrite. *Miner Deposita* 46:381-407

710 Dare SAS, Barnes S-J, Beaudoin G (2012) Variation in trace element content of magnetite
711 crystallized from a fractionating sulfide liquid, Sudbury, Canada: Implications for
712 provenance discrimination. *Geochim Cosmochim Acta* 88:27-50

713 Dare SAS, Barnes S-J, Prichard HM, Fisher PC (2014) Mineralogy and geochemistry of Cu-rich
714 ores from the McCreeley East Ni-Cu-PGE deposit (Sudbury, Canada): Implications for
715 the behavior of platinum group and chalcophile elements at the end of crystallization of a
716 sulfide liquid. *Econ Geol* 109:343-366

717 Distler VV (1994) Platinum mineralization of the Noril'sk deposits. In: Lightfoot PC, Naldrett AJ
718 (eds) *Proceedings of Sudbury- Noril'sk Symposium*, Ontario Geological Survey Special
719 Volume 5, pp 243–260

720 Distler VV, Malevsky AY, Laputina IP (1977) Distribution of platinoids between pyrrhotite and
721 pentlandite in crystallization of a sulphide melt. *Geochim Int* 14:30-40

722 Distler V.V., Sinyakova E. F. and Kosyakov V. I. (2016) Behavior of noble metals upon
723 fractional crystallization of copper-rich sulfide melts. *Dokl Earth Sci* 469:811-814.

724 Djon MLN, Barnes S-J (2012) Changes in sulfides and platinum-group minerals with the degree
725 of alteration in the Roby, Twilight, and High Grade Zones of the Lac des Iles Complex,
726 Ontario, Canada. *Miner Deposita* 47:875-896

727 Duran CJ, Barnes S-J, Corkery JT (2016) Trace element distribution in primary sulfides and Fe–
728 Ti oxides from the sulfide-rich pods of the Lac des Iles Pd deposits, Western Ontario,
729 Canada: Constraints on processes controlling the composition of the ore and the use of
730 pentlandite compositions in exploration. *J Geochem Explor* 166:45-63

731 Duran CJ, Barnes S-J, Pleše P, Prašek MK, Zientek ML, Pagé P (2017) Fractional crystallization-
732 induced variations in sulfides from the Noril'sk-Talnakh mining district (polar Siberia,
733 Russia). *Ore Geol Rev* 90:326-351

734 Duran CJ, Dubé-Loubert H, Pagé P, Barnes S-J, Roy M, Savard D, Cave B, Arguin, JP, Mansur E
735 (2019) Applications of trace element chemistry of pyrite and chalcopyrite in glacial
736 sediments to mineral exploration targeting: Example from the Churchill Province,
737 northern Quebec, Canada. *J Geochem Explor* 196: 105-130

738 Dutrizac J (1976) Reactions in cubanite and chalcopyrite. *Can Mineral* 14:172-181

739 Fedorenko V (1994) Evolution of magmatism as reflected in the volcanic sequence of the
740 Noril'sk region. In: Lightfoot PC, Naldrett AJ (eds) *Proceedings of Sudbury- Noril'sk*
741 *Symposium, Ontario Geological Survey Special Volume 5*, pp 171-184

742 Frost BR, Mavrogenes JA, Tomkins AG (2002) Partial melting of sulfide ore deposits during
743 medium-and high-grade metamorphism. *Can Mineral* 40(1):1-18

744 Godel B, Barnes S-J (2008) Platinum-group elements in sulfide minerals and the whole rocks of
745 the JM Reef (Stillwater Complex): Implication for the formation of the reef. *Chem Geol*
746 248:272-294

747 Godel B, Barnes S-J, Maier WD (2007) Platinum-group elements in sulphide minerals, platinum-
748 group minerals, and whole-rocks of the Merensky Reef (Bushveld Complex, South
749 Africa): Implications for the formation of the reef. *J Petrol* 48:1569-1604

750 Godel B, González-Álvarez I, Barnes SJ, Barnes S-J, Parker P, Day J (2012) Sulfides and
751 sulfarsenides from the Rosie nickel prospect, Duketon greenstone belt, Western Australia.
752 *Econ Geol* 107:275-294

753 Hanley JJ (2007) The role of arsenic-rich melts and mineral phases in the development of high-
754 grade Pt-Pd mineralization within komatiite-associated magmatic Ni-Cu sulfide horizons
755 at Dundonald Beach South, Abitibi subprovince, Ontario, Canada. *Econ Geol* 102:305-
756 317

757 Helmy HM, Ballhaus C, Berndt J, Bockrath C (2007) Wohlgemuth-Ueberwasser, C. Formation of
758 Pt, Pd and Ni tellurides: Experiments in sulfide–telluride systems. *Contrib Mineral Petrol*
759 153:577-591

760 Helmy HM, Ballhaus C, Wohlgemuth-Ueberwasser C, Fonseca RO, Laurenz V (2010)
761 Partitioning of Se, As, Sb, Te and Bi between monosulfide solid solution and sulfide
762 melt–application to magmatic sulfide deposits. *Geochim Cosmochim Acta* 74:6174-6179

763 Helmy HM, Ballhaus C, Fonseca R, Nagel T (2013) Fractionation of platinum, palladium, nickel,
764 and copper in sulfide–arsenide systems at magmatic temperature. *Contrib Mineral Petrol*
765 166:1725-1737

766 Holwell D, McDonald I (2007) Distribution of platinum-group elements in the Platreef at
767 Overysel, northern Bushveld Complex: A combined PGM and LA-ICP-MS study.
768 Contrib Mineral Petrol 154:171-190

769 Hutchinson D McDonald I (2008) Laser ablation ICP-MS study of platinum-group elements in
770 sulphides from the Platreef at Turfspruit, northern limb of the Bushveld Complex, South
771 Africa. Miner Deposita 43:695-711

772 Jamieson HE (2014) The Legacy of Arsenic Contamination from Mining and Processing
773 Refractory Gold Ore at Giant Mine, Yellowknife, Northwest Territories, Canada. Rev
774 Mineral Geochem 79:533-551

775 Jochum KP, Nohl U, Herwig K, Lammel E, Stoll B, Hofmann AW (2005) GeoReM: a new
776 geochemical database for reference materials and isotopic standards. Geostand Geoanal
777 Res 29:333-338

778 Junge M, Wirth R, Oberthür T, Melcher F, Schreiber A (2015) Mineralogical siting of platinum-
779 group elements in pentlandite from the Bushveld Complex, South Africa. Miner Deposita
780 50(1):41-54

781 Kelly D, Vaughan D (1983) Pyrrhotine-pentlandite ore textures: A mechanistic approach. Mineral
782 Mag 47:453-463.

783 Kissin S, Scott S (1982) Phase relations involving pyrrhotite below 350 degrees C. Econ Geol
784 77:1739-1754

785 Kosyakov F, Sinyakova E, Distler V (2012) Experimental simulation of phase relationships and
786 zoning of magmatic nickel-copper sulfide Ores, Russia. Geol Ore Deposits 54:179-208

787 Krivolutskaya NA (2016) Siberian traps and Pt-Cu-Ni deposits in the Noril'sk area. Springer,
788 Amsterdam, 377 pp

789 Krivolutskaya NA, Gongalsky BI, Kedrovskaya TB, Kubrakova IV, Tyutyunnik OA, Chikatueva
790 VY, Bychkova YV, Magazina L, Kovalchuk EN, Yakushev AI, Kononkova NN (2018)
791 Geology of the western flanks of the Oktyabr'skoe deposit, Noril'sk district, Russia:
792 evidence of a closed magmatic system. Miner Deposita 1-20

793 Le Vaillant M, Barnes SJ, Mungall JE, Mungall EL (2017) Role of degassing of the Noril'sk
794 nickel deposits in the Permian-Triassic mass extinction event. PNAS 114:2485-2490

795 Le Vaillant M, Barnes SJ, Fiorentini ML, Barnes SJ, Bath AB, Miller JM (2018)
796 Platinum group element and gold contents of arsenide and sulfarsenide minerals
797 associated with Ni and Au deposits in Archean greenstone belts. Mineral Mag 82:
798 625-47

799 Li C, Barnes S-J, Makovicky E, Rose-Hansen J, Makovicky M (1996) Partitioning of Ni, Cu, Ir,
800 Rh, Pt and Pd between monosulfide solid solution and sulfide liquid: Effects of
801 composition and temperature. Geochim Cosmochim Acta 60:1231-1238

802 Lightfoot PC, Naldrett AJ, Gorbachev NS, Fedorenko VA, Howkesworth CJ, Hergt J, Doherty W
803 (1994) Chemistratigraphy of Siberian trap lavas, Noril'sk district: implication for the
804 source of flood basalts magmas and their associated Ni-Cu mineralization. In: Lightfoot
805 PC, Naldrett AJ (eds) Proceedings of Sudbury- Noril'sk Symposium, Ontario Geological
806 Survey Special Volume 5, pp 185–201

807 Likhachev AP (1994) Ore-bearing intrusions of the Noril'sk region. In: Proceeding of the
808 Noril'sk-Sudbury symposium, vol 5. Geol Surv Spec, Ontario, pp 185–201

809 Liu Y, Brenan J (2015) Partitioning of platinum-group elements (PGE) and chalcogens (Se, Te,
810 As, Sb, Bi) between monosulfide-solid solution (MSS), intermediate solid solution (ISS)
811 and sulfide liquid at controlled fO_2 – fS_2 conditions. Geochim Cosmochim Acta 159:139-
812 161

813 Lyubetskaya T. Korenaga J (2007) Chemical composition of Earth's primitive mantle and its
814 variance: 1. Method and results. J Geophys Res 112:B03211

815 Makovicky E (2002) Ternary and quaternary phase systems in PGE. In: Cabri LJ (ed) The
816 geology, geochemistry, mineralogy and mineral beneficiation of the platinum-group
817 elements. Canadian Institute of Mining, Metallurgy and Petroleum, vol 54, pp 131-175

818 Mansur ET, Barnes S-J, Duran CJ (2019) Textural and compositional evidence for the formation
819 of pentlandite via peritectic reaction: Implications for the distribution of highly
820 siderophile elements. *Geology* 47 (4): 351-354.

821 Mavrogenes JA, Frost R, Sparks HA (2013) Experimental evidence of sulfide melt evolution via
822 immiscibility and fractional crystallization. *Can Mineral* 51:841–850

823 Moss RL, Tzimas E, Kara H, Willis P, Kooroshy J (2013) The potential risks from metals
824 bottlenecks to the deployment of strategic energy technologies. *Energy Policy* 55:556-
825 564

826 Mota-e-Silva J, Prichard H, Ferreira Filho C, Fisher PC, McDonald I (2015) Platinum-group
827 minerals in the Limoeiro Ni–Cu–(PGE) sulfide deposit, Brazil: The effect of magmatic
828 and upper amphibolite to granulite metamorphic processes on PGM formation. *Miner
829 Deposita* 50:1007-1029

830 Mungall JE (2007) Crystallization of magmatic sulfides: an empirical model and application to
831 Sudbury ores. *Geochim Cosmochim Acta* 71: 2809-2819

832 Mungall JE, Andrews DR, Cabri LJ, Sylvester PJ, Tubrett M (2005) Partitioning of Cu, Ni, Au,
833 and platinum-group elements between monosulfide solid solution and sulfide melt under
834 controlled oxygen and sulfur fugacities. *Geochim Cosmochim Acta* 69:4349-4360

835 Naldrett AJ (2004) *Magmatic sulfide deposits: geology, geochemistry and exploration*. Springer,
836 Berlin, 727 pp

837 Naldrett AJ (2011) Fundamentals of magmatic sulfide deposits. *Rev Econ Geol* 17:1-50

838 Naldrett AJ, Fedorenko V, Asif M, Lin S, Kunilov V, Stekhin A, Lightfoot PC, Gorbachev N
839 (1996) Controls on the composition of Ni-Cu sulfide deposits as illustrated by those at
840 Noril'sk, Siberia. *Econ Geol* 91:751-773

841 O'Driscoll B, González-Jiménez JM (2016) Petrogenesis of the platinum-group minerals. *Rev
842 Mineral Geochem* 81:489-578

843 Osbahr I, Oberthür T, Klemd R, Josties A (2014) Platinum-group element distribution in base-
844 metal sulfides of the UG2 chromitite, Bushveld Complex, South Africa - a
845 reconnaissance study. *Miner Deposita* 49(6):655-665

846 Paton C, Hellstrom J, Paul B, Woodhead J, Hergt J (2011) Iolite: Freeware for the visualisation
847 and processing of mass spectrometric data. *J Anal Atom Spec* 26:2508-2518

848 Patten C, Barnes S-J, Mathez EA, Jenner FE (2013) Partition coefficients of chalcophile elements
849 between sulfide and silicate melts and the early crystallization history of sulfide liquid:
850 LA-ICP-MS analysis of MORB sulfide droplets. *Chem Geol* 358:170-188

851 Péntek A, Molnár F, Watkinson DH, Jones PC (2008) Footwall-type Cu-Ni-PGE Mineralization
852 in the Broken Hammer Area, Wisner Township, North Range, Sudbury Structure. *Econ*
853 *Geol* 103:1005-1028

854 Piña R, Gervilla F, Barnes S-J, Ortega L, Lunar R (2012) Distribution of platinum-group and
855 chalcophile elements in the aguablanca Ni-Cu sulfide deposit (SW Spain): Evidence from
856 a LA-ICP-MS study. *Chem Geol* 302:61-75

857 Piña R, Gervilla F, Barnes S-J, Ortega L, Lunar R (2015) Liquid immiscibility between arsenide
858 and sulfide melts: Evidence from a LA-ICP-MS study in magmatic deposits at Serranía
859 de Ronda (Spain). *Mineral Depos* 50:265–279

860 Power M, Pirrie D, Jedwab J, Stanley C (2004) Platinum-group element mineralization in an As-
861 rich magmatic sulphide system, Talnoy, southwest Scotland. *Mineral Mag* 68:395-411

862 Prichard H, Hutchinson D, Fisher P (2004) Petrology and crystallization history of multiphase
863 sulfide droplets in a mafic dike from Uruguay: Implications for the origin of Cu-Ni-PGE
864 sulfide deposits. *Econ Geol* 99:365-376

865

866 Ryabov VV, Shevko AY, Gora MP (2014) Trap magmatism and ore formation in the Siberian
867 Noril'sk region. v. 1, 2. Springer

868 Samalens N, Barnes S-J, Sawyer EW (2017) The role of black shales as a source of sulfur and
869 semimetals in magmatic nickel-copper deposits: Example from the Partridge River
870 Intrusion, Duluth Complex, Minnesota, USA. *Ore Geol Rev* 81(1):173-187

871 Sessa G, Moroni M, Tumiati S, Caruso S, Fiorentini ML (2017) Ni-Fe-Cu-PGE ore deposition
872 driven by metasomatic fluids and melt-rock reactions in the deep crust: The ultramafic
873 pipe of Valmaggia, Ivrea-Verbanò, Italy. *Ore Geol Rev* 90: 485-509

874 Singh R, Singh S, Parihar P, Singh VP, Prasad SM (2015) Arsenic contamination, consequences
875 and remediation techniques: a review. *Ecotoxicol Environ Saf* 112:247-270

876 Sinyakova E, Kosyakov V, Borisenko A (2017) Effect of the presence of As, Bi, and Te on the
877 behavior of Pt metals during fractionation crystallization of sulfide magma. *Dokl Earth*
878 *Sci* 477:1422-1425

879 Sluzhenikin SF, Krivolutskaya NA, Rad'ko VA, Malitch KN, Distler VV, Fedorenko VA (2014)
880 Ultramafic-mafic intrusions, volcanic rocks and PGE-cu-Ni sulfide ores of the Noril'sk
881 province. IGM, Yekaterinburg

882 Smith J, Holwell DA, McDonald I (2014) Precious and base metal geochemistry and mineralogy
883 of the Grasvally Norite–Pyroxenite–Anorthosite (GNPA) member, northern Bushveld
884 Complex, SouthAfrica: Implications for a multistage emplacement. *Miner Deposita*
885 49:667-692

886 Sullivan NA, Zajacz Z, Brenan JM (2018) The solubility of Pd and Au in hydrous intermediate
887 silicate melts: the effect of oxygen fugacity and the addition of Cl and S. *Geochim*
888 *Cosmochim Acta* 231:15-29

889 Tuba G, Molnár F, Ames DE, Péntek A, Watkinson DH, Jones PC (2014) Multi-stage
890 hydrothermal processes involved in “low-sulfide” Cu (–Ni)–PGE mineralization in the
891 footwall of the Sudbury Igneous Complex (Canada): Amy Lake PGE zone, East Range.
892 *Miner Deposita* 49:7-47

893 Wilson SA, Ridley WI, Koenig AE (2002) Development of sulfide calibration standards for the
894 laser ablation inductively-coupled plasma mass spectrometry technique. *J Anal At*
895 *Spectrom* 17:406-409

896 Wood SA (2002) The aqueous geochemistry of the platinum group elements with applications to
897 ore deposits. *Can Inst Min Metall* 54:211-249

898 Yudovskaya MA, Kinnaird JA, Grobler DF, Costin G, Abramova VD, Dunnett T, Barnes S-J
899 (2017) Zonation of Merensky-Style Platinum-Group Element Mineralization in
900 Turfspruit Thick Reef Facies (Northern Limb of the Bushveld Complex). *Econ Geol*
901 112:1333-1365

902 Zientek M, Likhachev A, Kunilov V, Barnes S-J, Meier AL, Carlson R, Briggs PH, Fries T,
903 Adrian B, Lightfoot PC (1994) Cumulus processes and the composition of magmatic ore
904 deposits: Examples from the Talnakh district, Russia. In: Lightfoot PC, Naldrett AJ (eds)
905 Proceedings of Sudbury- Noril'sk Symposium, Ontario Geological Survey Special
906 Volume 5, pp 373-392

907 Zweibel K (2010) The Impact of Tellurium Supply on Cadmium Telluride Photovoltaics. Science
908 328:699-701

909

910

911

912

913

914

915

916

917

918

919

920

921

922

923

924

925

926

927

928

929

930

931

932

933

934

935

936

937

938

939

940

1
2
3
4
5
6
7
8
9
10
11
12

13 **Chapter 4 - Textural and compositional evidence for the formation of**
14 **pentlandite via peritectic reaction: Implications for the distribution of**
15 **highly siderophile elements**

16
17
18

19 **Eduardo T. Mansur¹, Sarah-Jane Barnes¹, Charley J. Duran¹**

20 *¹Sciences de la Terre, Université du Québec à Chicoutimi, Québec, G7H 2B1,*
21 *Canada*

22

23
24 **Author contributions:**

25 **Mansur** wrote the manuscript, collected and analyzed the data and created the figures.
26 **Barnes** edited the manuscript and analyzed the data. **Duran** collected part of the data and
27 also analyzed the results.

28
29
30
31
32
33
34
35
36
37
38
39
40
41
42

Geology, 2019, 47 (4): 351–354
DOI : 10.1130/G45779.1

43 **4.1 - Abstract**

44 The distribution of the highly siderophile elements is used in a wide variety of
45 geological studies, from planet formation and evolution to the formation of ore deposits.
46 Under mantle and crustal conditions, these elements behave as highly chalcophile
47 elements and pentlandite (Pn) is an important host for most of these elements. Therefore,
48 understanding how Pn forms is important to understanding the processes that control
49 these elements. The classic model for the formation of Pn is that below 650° C the high
50 temperature sulfides: monosulfide solid solution (MSS) and intermediate solid solution
51 (ISS), are no longer stable and exsolve into pyrrhotite (Po), Pn and chalcopyrite (Ccp).
52 However, Pn has been shown to be the main host of Pd in many ore deposits and given
53 that Pd is incompatible with both MSS and ISS this observation is inconsistent with the
54 exsolution model. Furthermore, experimental work has shown that Pn can form by
55 peritectic reaction between MSS and fractionated sulfide liquid. To date this type of Pn
56 has not been reported in natural samples. In our study of chalcophile element
57 concentrations in Pn from iconic magmatic Ni-Cu-PGE deposits we observed three
58 textures of Pn: contact-Pn in between Po and Ccp, granular Pn included within Ccp or Po,
59 and flame-Pn included within Po. The contact-Pn shows zonation in Mo, Rh, Ru, Re, Os
60 and Ir with these elements being enriched towards the Po contact, and depleted towards
61 the Ccp contact. In some cases, Pd displays a zonation antithetical to these elements. In
62 this contribution we propose that the contact-Pn formed via this peritectic reaction and
63 inherited Mo, Ru, Rh, Re, Os and Ir from the MSS, whereas Pd was contributed from the
64 fractionated sulfide liquid. We predict that this type of Pn should be present wherever
65 MSS and fractionated sulfide liquid remained in contact.

66

67 Keywords: Pentlandite; Peritectic reaction; Highly siderophile elements; Magmatic
68 sulfide deposits; Merensky reef; Noril'sk; LA-ICP-MS.

69 **4.2 – Introduction**

70

71 The distribution of highly siderophile elements (Ru, Rh, Pd, Re, Os, Ir, Pt and Au)
72 is studied in numerous branches of geology such as the planetary evolution, timing of
73 segregation of the Earth's core, the late planetary bombardment, evolution of the Earth's
74 mantle and basalts (Harvey and Day, 2016 and references therein). Furthermore, many of
75 these elements are of economic importance and hence their behaviour during ore
76 formation is of interest. In the Earth's crust and mantle, most of these elements behave as
77 highly chalcophile elements and are found either in base metal sulfides or as platinum-
78 group minerals associated with base metal sulfides (Barnes and Ripley, 2016; O'Driscoll
79 and González-Jiménez, 2016). Pentlandite is a major host of many of the HSE. Therefore,
80 understanding when and how Pn forms is important to many branches of geology.

81 Magmatic Ni-Cu-Platinum-group elements (PGE) sulfide deposits offer an
82 opportunity to study the formation of Pn. These deposits are formed when a sulfide liquid
83 segregates from mafic/ultramafic magmas and collects Ni, Cu, PGE and other chalcophile
84 elements (Naldrett, 2004). Upon cooling of this sulfide liquid, chalcophile elements
85 partition between the fractionating liquid and the crystallizing phases: initially
86 monosulfide solid solution (MSS), followed by intermediate solid solution (ISS), and
87 finally discrete precious metal minerals that accommodate the elements incompatible
88 with MSS and ISS (e.g. bismuthtellurides, arsenides, stanides). Experimental work has
89 shown that MSS and ISS subsequently exsolve essentially into pyrrhotite (Po),
90 pentlandite (Pn), chalcopyrite (Ccp) and cubantite (Kelly and Vaughan, 1983;
91 Etschmann et al., 2004; Peregoedova and Ohnenstetter, 2002). Furthermore, the texture
92 of Pn depends on the temperature at which it started to exsolve (Kelly and Vaughan,
93 1983). Exsolutions that start at relatively high temperature (650°C) have more time to
94 form and result in coarse granular Pn. Exsolution that commence at intermediate

95 temperature (400°C) form veins, and exsolutions that form at lower temperature (200°C)
96 form flames. Most studies of magmatic sulfides attribute different textures observed for
97 Pn to this exsolution history (Dare et al., 2010; Piña et al., 2012). However, experimental
98 studies also reveal that a Ni-rich phase (referred to as high-temperature Pn) can form via
99 peritectic reaction between MSS and the fractionated sulfide liquid at temperatures
100 around 870°C (Waldner and Pelton, 2004; Kosyakov and Sinyakova, 2012; Kitakaze et
101 al., 2016). Pentlandite formed by peritectic reaction has the potential to explain some
102 observations in natural samples that exsolution cannot. Although this problem has been
103 addressed experimentally, studies of natural samples have not considered this alternative
104 Pn origin.

105 The exsolutions model does not explain some aspects of texture and composition
106 of some Pn. Pentlandite is the main host for Pd in many magmatic Ni-Cu-PGE sulfide
107 deposits (Barnes et al. 2006; Dare et al., 2010; Osbar et al., 2014), but Pd is incompatible
108 with both MSS and ISS (Li et al., 1996; Liu and Brennan, 2015; Cafagna and Jugo, 2016).
109 Therefore, Pn formed by exsolutions from these phases would not be expected to contain
110 significant amounts of Pd. Furthermore, rims of a Ni-rich phase are found between Po
111 and Ccp in sulfide droplets from Mid-Ocean-Ridge Basalt (MORB; Patten et al., 2012).
112 These droplets have cooled too quickly for the rims to have formed by exsolution.

113 To address this problem, we have combined petrographic examination and trace-
114 element chemistry of Pn from the disseminated and massive sulfides of the Noril'sk-
115 Talnakh mining district, and the disseminated sulfides from the Impala Mine of the
116 Merensky Reef of the Bushveld Complex. The effects of metamorphism, deformation,
117 and alteration on sulfide minerals in these deposits are limited, and their textures and
118 chemical compositions record the original ore-forming processes (Barnes and Maier,
119 2002; Duran et al., 2017). On the basis of our textural and geochemical investigation, this

120 contribution supports the formation of Pn via peritectic reaction between MSS and the
121 fractionated sulfide liquid in natural cases, thus supporting previous experimental work.

122

123 **4.3 - Textural occurrences of pentlandite**

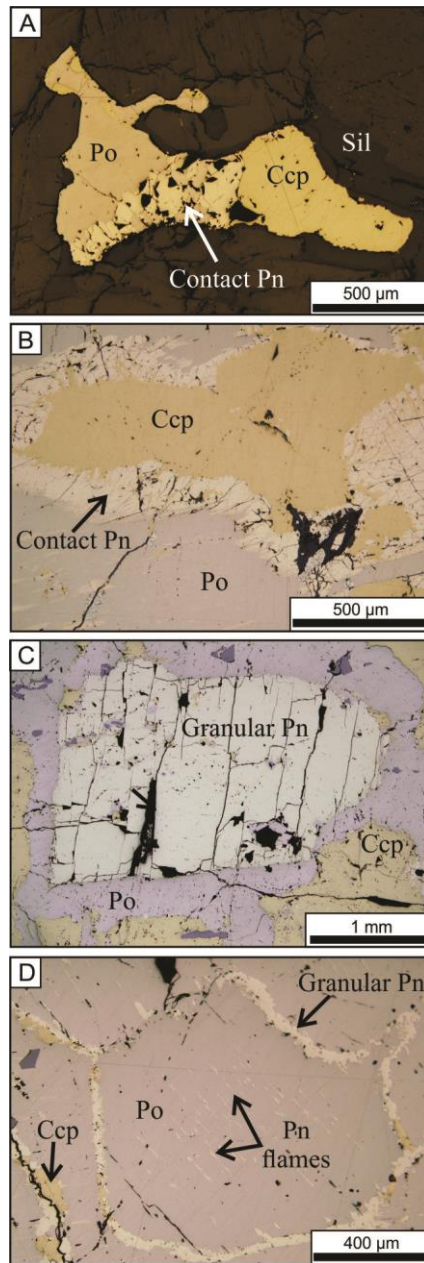
124 The investigated samples are described in detail in Duran et al. (2017) for the
125 Noril'sk-Talnakh mining district and in Barnes and Maier (2002) for the Merensky Reef.
126 All samples contain the typical Po-Pn-Ccp assemblage, and Pn displays three distinct
127 textures, referred as contact-, granular and flame-Pn. Contact-Pn occurs as μm - to mm-
128 thick layers at the contact between Ccp and Po grains (Fig. 4.1a and 4.1b). Granular Pn
129 occurs as coarse grains (mm to cm in apparent diameter) associated with either Po or
130 Ccp, but not both (Fig. 4.1c), whereas Pn flames occur as thin (μm thick) lamellas within
131 Po (Fig. 4.1d). In disseminated sulfide samples from the Noril'sk I intrusion and the
132 Merensky Reef (Fig. 4.1a) the main Pn texture is contact-Pn, whereas in massive sulfide
133 samples from the Kharaelakh intrusion of the Noril'sk-Talnakh mining district (Fig. 4.1b,
134 4.1c and 4.1d) all three Pn textures occur.

135 **4.4 - Composition and distribution of trace elements in pentlandite**

136 Pentlandite was analyzed using laser ablation-inductively coupled plasma-mass
137 spectrometry (LA-ICP-MS). Details of the methodology are presented in Appendix 1.
138 The full data set is available in the Appendix 2.

139

140



141

142 Figure 4.1 - Reflected light images of pentlandite textures from the disseminated sulfides of the Merensky Reef of the
 143 Bushveld Complex (A), and massive sulfides of the Noril'sk-Talnakh mining district (B, C and D). A) Typical
 144 disseminated sulfide bleb with contact-pentlandite between pyrrhotite and chalcopyrite. B) Contact-pentlandite
 145 surrounding a chalcopyrite grain, at the contact with pyrrhotite. C) Typical coarse granular pentlandite enclosed within
 146 pyrrhotite. D) Exsolution flames of pentlandite in pyrrhotite, and veinlets of granular pentlandite grains in between or
 147 included within pyrrhotite grains. Ccp- chalcopyrite; Pn- pentlandite; Po- pyrrhotite; Sil- silicates.

148

149

150

151 Granular Pn from massive sulfides of the Kharaelakh intrusion displays
152 homogenous distribution of trace elements. In contrast, contact-Pn from disseminated
153 sulfides of the Noril'sk I intrusion (Fig. 4.2a), massive sulfides of the Kharaelakh
154 intrusion (Fig. 4.2b and 4.2c), and disseminated sulfides of the Merensky Reef (Fig. 4.2d
155 and 4.2e) show a trace element zonation. The trace elements compatible with MSS (Os,
156 Ir, Ru, Rh, Re and Mo) have higher concentrations where Pn is in contact with Po,
157 whereas Pd (Fig. 4.2b) and to a lesser extent Te, Bi and Pb (Fig. 4.2c and Fig. 1 of
158 Appendix 1) (which are incompatible with MSS) have higher concentrations where Pn is
159 in contact with Ccp. These zonation patterns are not an analytical artefact. As shown in
160 Figure 4.3, the time-resolved analysis for two LA-ICP-MS lines (red lines indicated in
161 Fig. 4.2b and 4.2c) indicate no mixing between the different sulfide phases. The Pd is
162 clearly concentrated in Pn, with higher concentration at the contact close to the Ccp (Fig.
163 4.3a). In contrast, Mo, Ru, Rh, Re, Os and Ir are present in Po and constrained to the Pn
164 contact close to the Po (Fig. 4.3b).

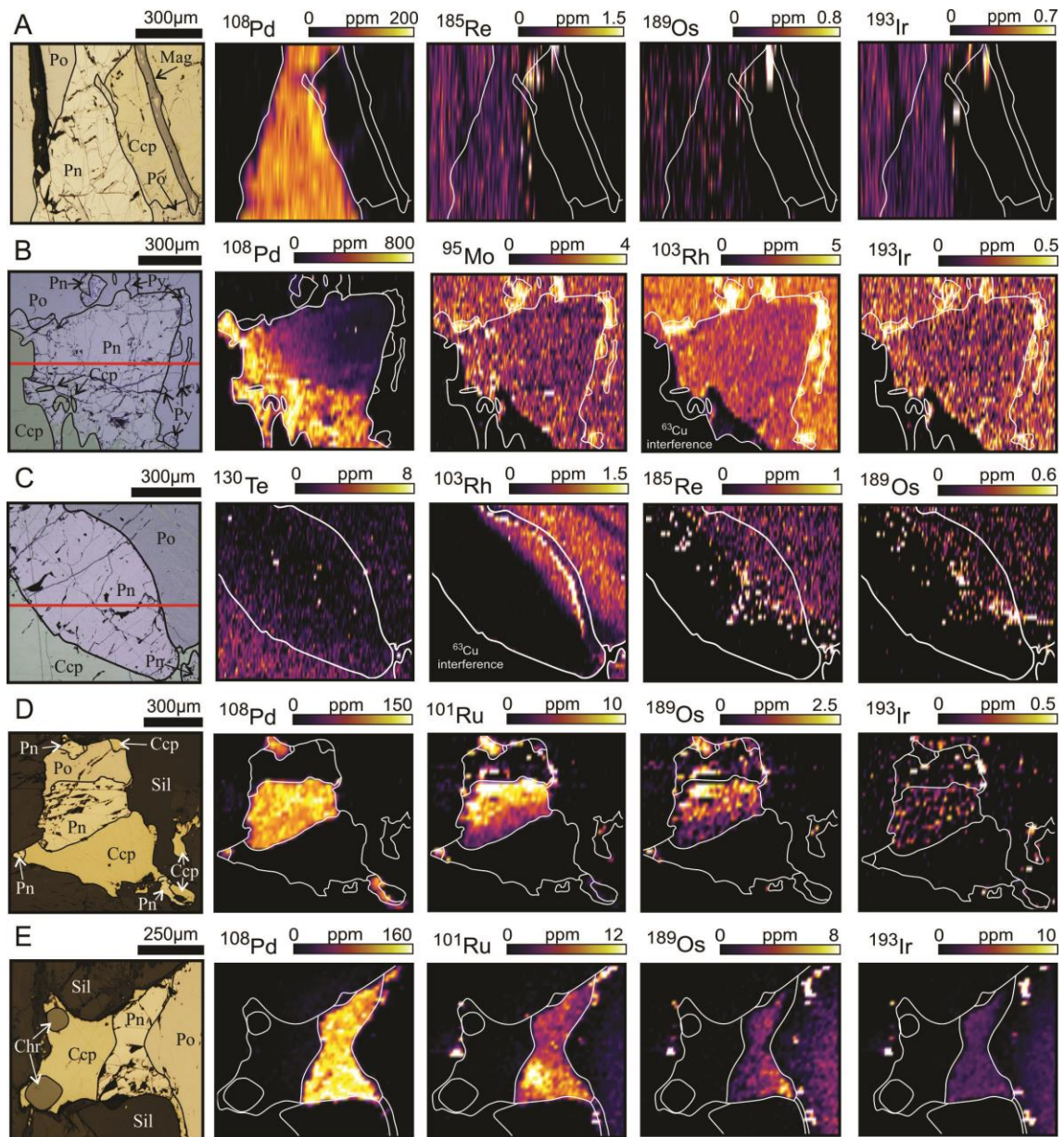
165 The LA-ICP-MS compositional maps also reveal that in some grains the
166 distribution of trace elements is homogeneous in contact-Pn from Merensky Reef, but is
167 heterogeneous in associated Po (Fig. 4.2e). Elements compatible with MSS have lower
168 concentrations where Po is in contact with Pn, and this distribution seems to form a
169 depletion halo in Po close to the contact with Pn (Fig. 4.2e). This texture suggests that
170 Ru, Os and Ir were inherited from Po.

171

172

173

174



175

176 Figure 4.2 - LA-ICP-MS elemental maps showing the distribution of chalcophile elements in pentlandite and
 177 associated pyrrhotite and chalcopyrite. A) Contact-pentlandite from disseminated sulfide droplets of the Noril'sk I
 178 intrusion. B) and C) Contact-pentlandite from massive sulfides of the Kharaelakh intrusion. D) and E) Contact-
 179 pentlandite from disseminated sulfides of the Merensky Reef. Ccp- chalcopyrite; Pn- pentlandite; Po- pyrrhotite; Py -
 180 Pyrite; Sil- silicates.

181

182 4.5 - Formation of pentlandite via peritectic reaction

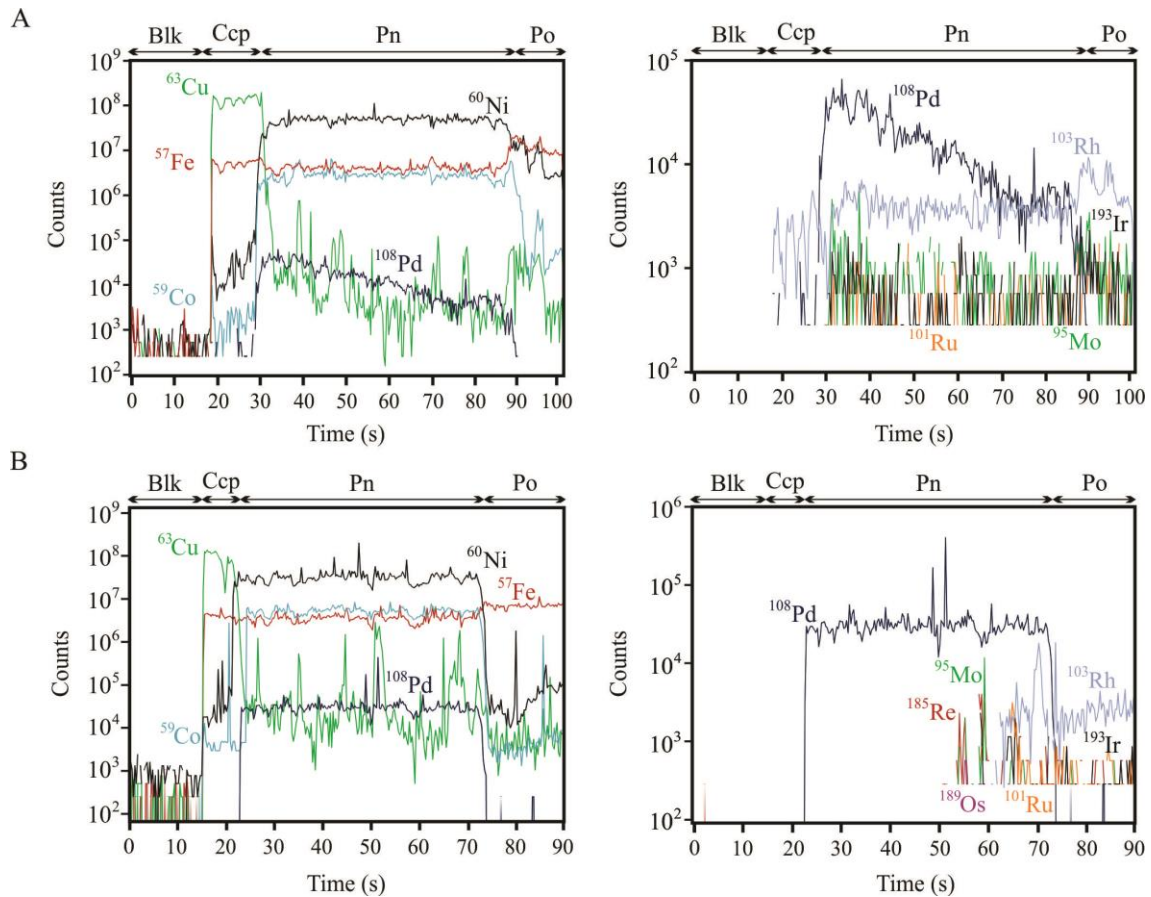
183 In their studies of Pn from the Creighton ores of the Sudbury Complex and
 184 Aquablanca ores, Dare et al. (2010) and Piña et al. (2012) noted that coarse grained Pn is
 185 richer in Pd than flame-Pn. These authors attributed this to the diffusion of Pd into the

186 granular Pn from the MSS at high temperature, leaving the remaining MSS depleted in Pd
187 at the time of flame-Pn formation. In addition, they noted that coarse grained Pn
188 associated with Ccp is richer in Pd relative to coarse grained Pn associated with Po. They
189 interpreted this difference as the result of ISS being richer in Pd than MSS, and that Pd
190 diffused from ISS into Pn. Given that the partition coefficient for Pd into ISS is higher
191 (~0.5) than for Pd into MSS (~0.1) (Liu and Brenan, 2015), and considering that Ccp
192 exsolved from ISS, Pn grains associated with Ccp would be enriched in Pd relative to Pn
193 grains associated with Po. Whereas these processes could explain some of the variations
194 in the Pn composition, they do not explain why Pn contains most of the Pd in the
195 Noril'sk-Talnakh and Merensky Reef sulfides (Barnes and Ripley 2016) despite Pd
196 incompatibility with MSS and ISS. Additionally, they do not explain the zonation in the
197 concentrations of Mo, Ru, Rh, Re, Os and Ir observed in contact-Pn (Fig. 4.2). Therefore,
198 we suggest that contact-Pn formed by peritectic reaction.

199 Experimental work shows that Pn can form by reaction between MSS and the
200 fractionated sulfide liquid (Waldner and Pelton, 2004; Kosyakov and Sinyakova, 2012;
201 Kitakaze et al., 2016) between 870 and 800 °C. Therefore, when cumulus MSS is not
202 separated from the fractionating sulfide liquid, Pn could form by reaction prior to Pn
203 exsolution from MSS or ISS below 650 °C. We interpret the different textures and
204 distribution of trace elements in Pn as reflecting these two stages of Pn formation during
205 the crystallization of sulfide liquid (Fig. 4.4a). Homogeneous distribution of trace
206 elements in granular Pn is consistent with MSS and ISS exsolving into Po+Pn, and
207 Ccp+Pn, respectively. In contrast, heterogeneous distribution of trace elements in contact-
208 Pn is consistent with reaction between MSS and fractionated sulfide liquid.

209

210



211

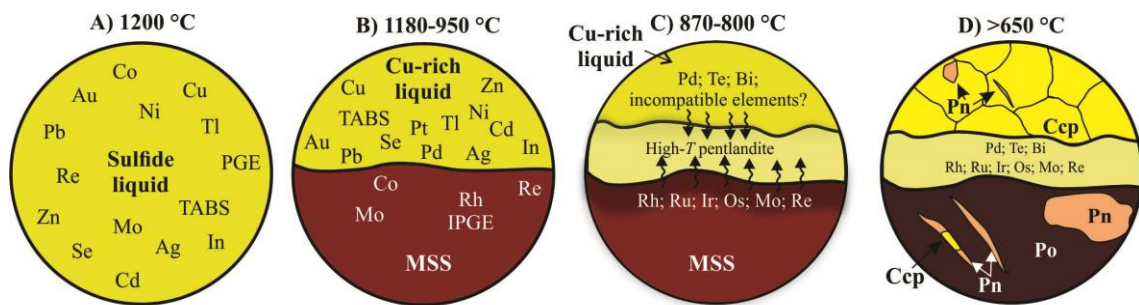
212 Figure 4.3 - Time-resolved analysis for the LA-ICP-MS lines indicated in Fig. 2B (A) and 2C (B). Note that the
 213 zonation patterns are not caused by mixing between different sulfides. A) The Pd signal is uniform across Pn, whereas
 214 Mo, Ru, Rh, Re, Os and Ir are present in Po and constrained to the Pn contact close to the Po. B) The Mo, Ru, Rh and Ir
 215 signals are uniform across Pn, whereas Pd is higher at the contact close to Ccp, decreasing towards Po. Blk- blank;
 216 Ccp- chalcopyrite; Pn- pentlandite; Po- pyrrhotite.

217

218 In contact-Pn, concentrations of elements compatible with MSS (Ru, Rh, Ir, Os,
 219 Re, Mo; Fig. 4.4b) are higher at the Po-Pn boundary and decrease towards Ccp. These
 220 elements were inherited from the MSS as it reacted with the fractionated sulfide liquid to
 221 form Pn (Fig. 4.4c). The abrupt decrease in the concentration of elements compatible
 222 with MSS (Fig. 4.2a, 4.2b and 4.2c) could represent the original grain boundary between
 223 the MSS and the fractionated liquid. Experimental work (Kitakaze et al., 2016) indicates
 224 that the high-T Pn keeps growing from the sulfide liquid below the peritectic temperature
 225 (i.e. 850°C). Therefore, the further growth beyond the initial contact between MSS and

226 sulfide liquid could result in Pn being depleted in these compatible elements. On the other
 227 hand, Pd, Te, Pb and Bi concentrations (incompatible with MSS; Liu and Brenan, 2015;
 228 Cafagna and Jugo, 2016) decrease from the Ccp-Pn boundary towards the Po-Pn
 229 boundary, and record the incorporation of these elements from the fractionated sulfide
 230 liquid towards Pn (Fig. 4.4c and Fig. 1 of Appendix 1).

231



232

233 Figure 4.4 - Schematic model illustrating the crystallization history of a sulfide liquid, and the formation of pentlandite
 234 via peritectic reaction. See text for further explanation. MSS- monosulfide solid solution; ISS- intermediate solid
 235 solution; Ccp- chalcopyrite; Po- pyrrhotite; Pn- pentlandite.

236

237 The formation of Pn via peritectic reaction may be expected to occur wherever
 238 MSS remains in contact with the fractionated liquid. In sulfide blebs or droplets that
 239 formed via equilibrium crystallization, such as those from the Merensky Reef (Barnes
 240 and Maier, 2002) and the Noril'sk I intrusion (Barnes et al., 2006; Barnes et al., 2017),
 241 the MSS and the fractionated liquid were not separated and reacted at high temperature to
 242 form Pn. A similar interpretation can be inferred for Pn at the MSS-ISS interface in
 243 sulfide droplets of MORB glasses described in Patten et al. (2012).

244 In MSS cumulates, where the fractionated liquid has largely been expelled,
 245 contact-Pn is less common. However, if the separation is not complete, some liquid
 246 remains trapped among the MSS grains. This liquid has the potential to react with the
 247 MSS and form peritectic Pn. In the case of the massive sulfide samples of the Kharaelakh

248 intrusion, some samples have compositions similar to the initial sulfide liquid (Duran et
249 al., 2017), implying that the MSS component remained associated with the fractionated
250 liquid.

251

252 **4.6 - Implications for the incorporation of palladium into pentlandite**

253 In many magmatic sulfide deposits, Pn hosts significant amounts of Pd (Holwell
254 and McDonald, 2007; Dare et al., 2010; Piña et al., 2012; Barnes and Ripley, 2016). If
255 Pn only formed by exsolutions from MSS and ISS, and given that Pd is incompatible with
256 both MSS and ISS, the majority of Pd should not be present in pentlandite. However, if
257 Pn formed via peritectic reaction between MSS and the fractionated sulfide liquid, then
258 the Pd concentrated in the fractionated liquid could have partitioned into Pn during the
259 peritectic reaction (Fig. 4.2b and 4.4c). We suggest that not all Pn described in previous
260 studies are formed by MSS and ISS exsolution, but also via peritectic reaction at higher
261 temperature. For example, some Pn in the Creighton ores from Sudbury are located at the
262 contact between Po and Ccp (Fig. 3a of Dare et al., 2010), and could have formed via
263 peritectic reaction. The partitioning of Pd from the fractionated sulfide liquid into
264 peritectic Pn provides an elegant explanation for the mass balance of Pd.

265

266 **4.7 - Conclusions**

267 Our study provides textural and compositional evidence for the formation of Pn
268 by two distinct processes at two distinct stages of sulfide liquid evolution: i) at a higher
269 temperature (870 to 800°C) via peritectic reaction between MSS and fractionated sulfide
270 liquid, and ii) at a lower temperature (<650°C) via exsolution of MSS and ISS.
271 Pentlandite formed via peritectic reaction is enriched in Ru, Rh, Ir, Os, Re and Mo close

272 to the contact with Po, and in Pd, Te, Bi and Pb close to the contact with Ccp. The
273 formation of Pn via peritectic reaction also explains the presence of almost 100% of the
274 whole-rock Pd in the Pn of some deposits, even though Pd is neither compatible with
275 MSS nor ISS. Our study confirms previous experiments in that Pn can form via peritectic
276 reaction in natural cases, and suggest that this process occurred in the main Ni-Cu-PGE
277 deposits worldwide and magmatic sulfides in general.

278 **4.7 - Acknowledgements**

279 *This work was supported by a Canada Research Chair program grant to Sarah-Jane*
280 *Barnes (215503). We would like to thank Dany Savard (LabMaTer, UQAC) for his*
281 *assistance with LA-ICP-MS analyses. This manuscript benefited from insightful*
282 *comments from David Holwell, Rubén Piña and one anonymous reviewer and careful*
283 *editorial handling by the editor Chris Clark.*

284

285

286

287

288

289

290

291

292

293 4.8 – References

294

295 Barnes, S.-J., and Maier, W.D., 2002, Platinum-group elements and microstructures of
296 normal Merensky Reef from Impala Platinum Mine, Bushveld Complex: *Journal*
297 *of Petrology*, v. 43, p. 103–128.

298 Barnes, S.-J., Cox, R., and Zientek, M., 2006, Platinum-group element, gold, silver and
299 base metal distribution in compositionally zoned sulfide droplets from the
300 Medvezky Creek Mine, Noril'sk, Russia: *Contributions to Mineralogy and*
301 *Petrology*, v. 152, no. 2, p. 187-200.

302

303 Barnes, S.-J., and Ripley, E. M., 2016, Highly siderophile and strongly chalcophile
304 elements in magmatic ore deposits: *Reviews in Mineralogy and Geochemistry*, v.
305 81, no. 1, p. 725-774.

306 Barnes, S. J., Holwell, D. A., and Le Vaillant, M., 2017, Magmatic sulfide ore
307 deposits: *Elements*, v. 13, no. 2, p. 89-95.

308 Cafagna, F., and Jugo, P. J., 2016, An experimental study on the geochemical behavior of
309 highly siderophile elements (HSE) and metalloids (As, Se, Sb, Te, Bi) in a mss-
310 iss-pyrite system at 650° C: a possible magmatic origin for Co-HSE-bearing
311 pyrite and the role of metalloid-rich phases in the fractionation of HSE:
312 *Geochimica et Cosmochimica Acta*, v. 178, p. 233-258.

313 Dare, S. A., Barnes, S.-J., and Prichard, H. M., 2010, The distribution of platinum group
314 elements (PGE) and other chalcophile elements among sulfides from the
315 Creighton Ni–Cu–PGE sulfide deposit, Sudbury, Canada, and the origin of
316 palladium in pentlandite: *Mineralium Deposita*, v. 45, no. 8, p. 765-793.

317 Duran, C.J., Barnes, S.-J., Pleše, P., Prašek, M. K., Zientek, M. L., and Pagé, P., 2017,
318 Fractional crystallization-induced variations in sulfides from the Noril'sk-Talnakh
319 mining district (polar Siberia, Russia): *Ore Geology Reviews*, v. 90, p. 326-351.

320 Etschmann, B., Pring, A., Putnis, A., Grguric, B. A., and Studer, A., 2004, A kinetic
321 study of the exsolution of pentlandite (Ni, Fe)₉S₈ from the monosulfide solid
322 solution (Fe,Ni)S: *American Mineralogist*, v. 89, p. 39-50.

323 Harvey, J., and Day, J. M., 2016, Highly siderophile and strongly chalcophile elements in
324 high temperature geochemistry and cosmochemistry: *Reviews in Mineralogy and*
325 *Geochemistry*, v. 81, no. 1, p. 1-774.

- 326 Holwell, D., and McDonald, I., 2007, Distribution of platinum-group elements in the
327 Platreef at Overysel, northern Bushveld Complex: a combined PGM and LA-ICP-
328 MS study: *Contributions to Mineralogy and Petrology*, v. 154, no. 2, p. 171-190.
- 329 Jochum, K. P., Nohl, U., Herwig, K., Lammel, E., Stoll, B., and Hofmann, A.W., 2005,
330 GeoReM: a new geochemical database for reference materials and isotopic
331 standards: *Geostandards and Geoanalytical Research*, v. 29, p. 333-338.
- 332 Kelly, D., and Vaughan, D., 1983, Pyrrhotine-pentlandite ore textures: a mechanistic
333 approach: *Mineralogical Magazine*, v. 47, no. 4, p. 453-463.
- 334 Kitakaze, A., Machida, T., and Komatsu, R., 2016, Phase Relations in the Fe–Ni–S
335 System from 875 To 650° C: *The Canadian Mineralogist*, v. 54, no. 5, p. 1175-
336 1186.
- 337 Kosyakov, V. I., and Sinyakova, E. F., 2012, Physicochemical prerequisites for the
338 formation of primary orebody zoning at copper-nickel sulfide deposits (by the
339 example of the systems Fe–Ni–S and Cu–Fe–S): *Russian Geology and*
340 *Geophysics*, v. 53, no. 9, p. 861-882.
- 341 Li, C., Barnes, S.-J., Makovicky, E., Rose-Hansen, J., and Makovicky, M., 1996,
342 Partitioning of Ni, Cu, Ir, Rh, Pt and Pd between monosulfide solid solution and
343 sulfide liquid: effects of composition and temperature: *Geochim Cosmochim*
344 *Acta*, v. 60, p. 1231-1238.
- 345 Liu, Y., and Brenan, J., 2015, Partitioning of platinum-group elements (PGE) and
346 chalcogens (Se, Te, As, Sb, Bi) between monosulfide-solid solution (MSS),
347 intermediate solid solution (ISS) and sulfide liquid at controlled fO₂–fS₂
348 conditions: *Geochimica et Cosmochimica Acta*, v. 159, p. 139-161.
- 349 Naldrett, A. J., 2004, *Magmatic sulfide deposits: geology, geochemistry and exploration:*
350 *Berlin, Springer, 727 p.*
- 351 O'Driscoll, B. and González-Jiménez J. M., 2016, Petrogenesis of the platinum-group
352 minerals: *Reviews in Mineralogy and Geochemistry*, v. 81, p. 489-578.
- 353 Osbahr, I., Oberthür, T., Klemd, R., and Josties, A., 2014, Platinum-group element
354 distribution in base-metal sulfides of the UG2 chromitite, Bushveld Complex,
355 South Africa - a reconnaissance study: *Mineralium Deposita*, v. 49, p. 655–665.
- 356 Paton, C., Hellstrom, J., Paul, B., Woodhead, J., and Hergt, J., 2011, Iolite: Freeware for
357 the visualisation and processing of mass spectrometric data: *Journal of Analytical*
358 *Atomic Spectrometry*, v. 26, no. 12, p. 2508-2518.

359 Patten C., Barnes S.-J., and Mathez E. A., 2012, Textural variations in MORB sulfide
360 droplets due to differences in crystallization history: *The Canadian Mineralogist*,
361 v. 50, p. 675–692.

362 Peregoedova, A., and Ohnenstetter, M., 2002, Collectors of Pt, Pd and Rh in a S-poor Fe–
363 Ni–Cu sulfide system at 760 C: experimental data and application to ore deposits:
364 *The Canadian Mineralogist*, v. 40, no. 2, p. 527-561.

365 Piña, R., Gervilla, F., Barnes, S.-J., Ortega, L., and Lunar, R., 2012, Distribution of
366 platinum-group and chalcophile elements in the Aguablanca Ni–Cu sulfide
367 deposit (SW Spain): evidence from a LA-ICP-MS study: *Chemical Geology*, v.
368 302, p. 61-75.

369 Waldner, P., and Pelton, A. D., 2004, Critical thermodynamic assessment and modeling
370 of the Fe-Ni-S system: *Metallurgical and Materials Transactions B*, v. 35, no. 5, p.
371 897-907.

372 Wilson, S. A., Ridley, W. I., and Koenig, A. E., 2002, Development of sulfide calibration
373 standards for the laser ablation inductively-coupled plasma mass spectrometry
374 technique: *Journal of Analytical Atomic Spectrometry*, v. 17, p. 406-409.

375
376
377
378
379
380
381
382
383
384
385
386
387
388
389
390
391
392
393
394
395
396
397
398
399

1
2
3
4
5
6
7
8
9
10
11
12

13 **Chapter 5 - Concentrations of Te, As, Bi, Sb and Se in the Marginal**
14 **Zone of the Bushveld Complex: Evidence for crustal contamination and**
15 **the nature of the magma that formed the Merensky Reef**
16

17

18 Eduardo T. Mansur¹, Sarah-Jane Barnes¹

19 ¹Sciences de la Terre, Université du Québec à Chicoutimi, Québec, G7H 2B1, Canada
20

21

22

Author contributions:

23 **Mansur** wrote the manuscript, collected and analyzed the data and created the figures.

24 **Barnes** edited the manuscript and analyzed the data.
25

26

27

28

29

30

31

32

Lithos, 2020, 358-359: 105407

33

DOI : 10.1016/j.lithos.2020.105407

34

35 **5.1 - Abstract**

36

37 The association of platinum-group elements (PGE) and the chalcophile elements Te, As, Bi, Sb
38 and Sn (TABS) has been extensively documented in several magmatic sulfide deposits over the
39 past years. However, understanding the roles of TABS during the formation of magmatic sulfide
40 deposits partially depends on constraining the concentration of TABS on the liquids from which
41 they crystallized. This study presents the distribution of TABS (apart from Sn) in rocks of the
42 Marginal Zone of the Bushveld Complex. These rocks record the composition of the parental
43 magmas from which the Bushveld Complex have crystallized. The major and trace elements of
44 the marginal rocks have been modelled as mixtures of komatiite, continental crust and a
45 plagioclase-rich residuum. Similar mixtures are required to model the TABS in the marginal
46 rocks, with the continental crust component contributing a large part of the As, Sb and Bi budgets
47 in these melts. The concentrations of the TABS in the Merensky Reef can be modelled as a
48 mixture of two of the magma types present in the Marginal Zone (the B-1 and B-2). The
49 modelling also reveals that the distributions of Se, Te and Bi in the reef are essentially controlled
50 by the presence of sulfide minerals, whereas As and Sb distributions are controlled by both
51 sulfide minerals and melt component. This is because Se, Te and Bi are moderately to strongly
52 chalcophile elements, but As and Sb are only slightly chalcophile elements. Thus, whole-rock As
53 and Sb concentrations are not upgraded by the formation of the sulfide minerals, and may still be
54 used to trace crustal contamination.

55 Keywords: Te, As, Bi, Sb, Se; platinum-group elements; magmatic sulfide deposits; Bushveld
56 Complex; Marginal Zone.

57

58

59

60

61 **5.2 – Introduction**

62 The number of studies investigating the roles of the chalcophile elements Te, As, Bi, Sb
63 and Sn (TABS) and Se during the formation of magmatic sulfide deposits has significantly
64 increased over the past years (Hattori et al., 2002; Queffurus and Barnes, 2015; Duran et al.,
65 2017; Samalens et al., 2017; Keith et al., 2018; LeVaillant et al., 2018; Liang et al., 2019; Mansur
66 et al., 2019a; Mansur and Barnes, 2020). The main motivation for studying the TABS is to
67 understand the frequent association of platinum-group elements (PGE) and TABS in the form of
68 platinum-group minerals (PGM; O’Driscoll and González-Jiménez, 2016 and references therein).
69 It has been suggested: i) that TABS stabilize PGE nanoclusters in silicate liquids leading to the
70 inclusion of clusters in magmatic sulfide liquids (Tredoux et al., 1995; Helmy et al., 2013;
71 González-Jiménez et al., 2018, 2019; Liang et al., 2019); ii) that high TABS concentrations lead
72 to the saturation of PGM in magmatic sulfide liquid (Dare et al., 2010a; Hutchinson et al., 2015;
73 Duran et al., 2017); iii) that TABS control the formation of PGM during exsolutions of sulfide
74 minerals (Hutchinson and McDonald, 2008; Wirth et al., 2013; Junge et al., 2015; Mansur and
75 Barnes, 2020); and iv) that TABS affect the post-magmatic remobilization of PGE (Péntek et al.,
76 2008; Djon and Barnes, 2012; Tuba et al., 2014; Scholten et al., 2018; Sullivan et al., 2018).
77 However, these studies are hampered by the lack of data on the concentrations of TABS in the
78 parental magmas from which magmatic sulfide liquid segregated.

79 There are several reasons for the limited information on the concentration of TABS in
80 parental liquids. First, the concentration of TABS in mafic magmas is low (generally <1 ppm,
81 Hattori et al., 2002; Wang and Becker, 2013; Lissner et al., 2014; Mansur et al., 2019b; Yierpan
82 et al., 2019) and the elements suffer from a number of interferences using the common method of
83 analysis (ICP-MS). Secondly, due to their volatility (Lodders, 2003) TABS are not reliably
84 determined during routine analysis and specific protocols must be used to obtain accurate results
85 (Pitcairn, 2004; König et al., 2012, 2014; Patten et al., 2016; Mansur et al., 2019b). Consequently,
86 most studies have concentrated on the distribution of TABS in sulfide ore deposits, where
87 concentrations are high and simple aqua regia digest will dissolve the sample (e.g., Dare et al.,

88 2010b, 2014; Piña et al., 2012, 2013; Godel et al., 2012; Duran et al., 2016, 2017; Yudovskaya et
89 al., 2017; LeVaillant et al., 2018; Liang et al., 2019; Mansur et al., 2019a).

90 In this contribution, we report the concentrations of TABS (apart from Sn) and Se in
91 samples from the Marginal Zone of the Bushveld Complex, measured by hydride generation-
92 atomic fluorescence spectrometry, which allows precise and accurate measurements at low levels.
93 These rocks have been proposed as representative of the liquids from which the Bushveld
94 Complex crystallized (Sharpe and Hulbert, 1985; Barnes et al., 2009, 2010; Godel et al., 2011;
95 Wilson, 2012; Maier et al., 2016; Yang et al., 2018), thus allowing us to assess the concentration
96 of Se and TABS in the liquids from which some of the largest PGE deposits in the world have
97 formed.

98 This work will show that the concentrations of As and Sb in the initial Bushveld liquid
99 (B-1) are significantly higher than in primary magmas, whereas the Se and TABS of later
100 magmas (B-2 and B-3) are similar to primary magmas. We attribute the difference due upper
101 crustal contamination of the B-1 magma, whereas the B-2 and B-3 magmas were most likely
102 contaminated with a plagioclase-rich residuum from the partial melting of the upper crust. We
103 show that the distributions of the Se, Te and Bi across the Merensky Reef are controlled by the
104 sulfide liquid component. In contrast, As and Sb distributions are influenced by the amount of
105 silicate melt component in the cumulates. As suggested by Lesher and Burnham (2001) the effect
106 of crustal contamination for elements with high partition coefficients between sulfide and silicate
107 liquid (Te, Bi and Se) is obscured by the interaction of sulfides with a large volume of silicate
108 magma. In contrast, for elements with lower partition coefficients (As and Sb) the effect of
109 contamination is more evident. The implications for the formation of PGE deposits are also
110 discussed.

111

112

113

114 **5.3 – Geological Setting**

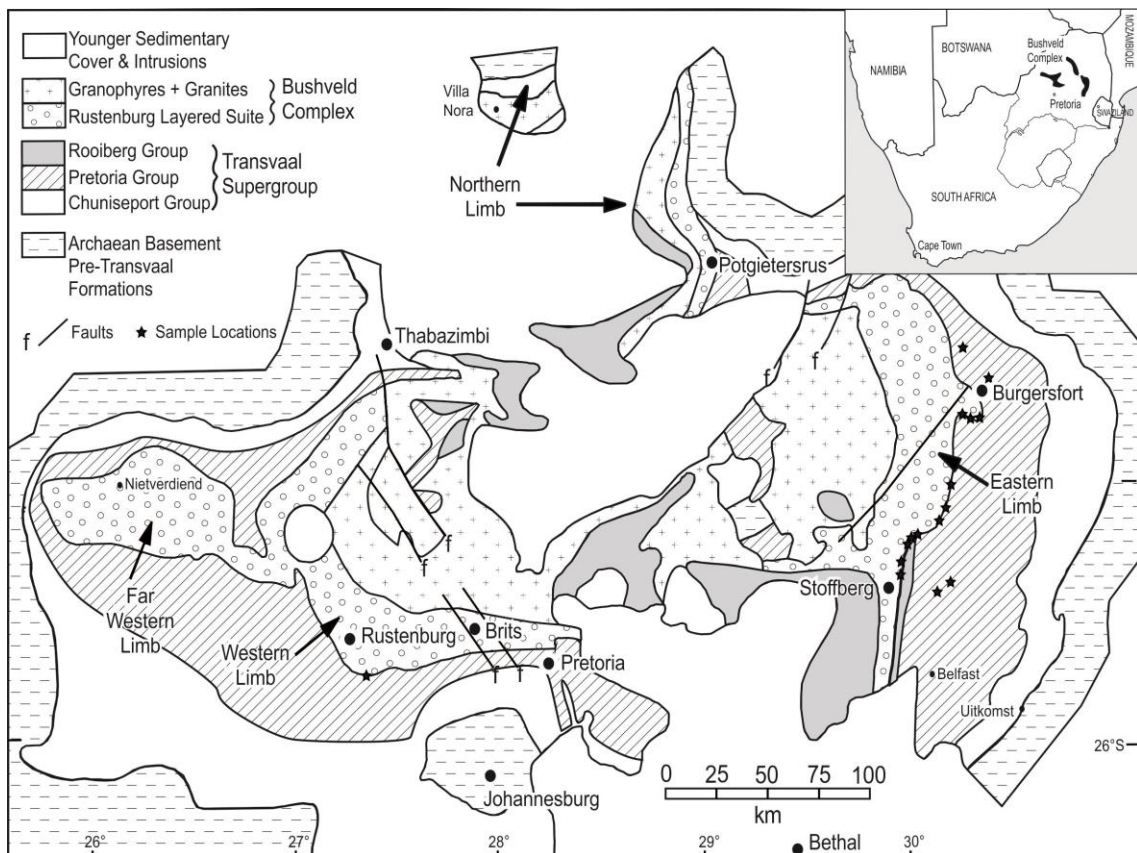
115 The Bushveld Complex (Fig. 5.1) occurs in the northeastern portion of South Africa,
116 covering an area of approximately 450 km x 350 km, with a total areal extent greater than 65,000
117 km² (Cawthorn, 2015 and references therein). The mafic-ultramafic rocks of the Bushveld
118 Complex were emplaced discordantly into Neoproterozoic to Paleoproterozoic sedimentary rocks of
119 the Transvaal Supergroup and Archean basement granites and gneisses at approximately 2,055
120 Ma (Scoates and Wall, 2015; Zeh et al., 2015; Mungall et al., 2016). The stratigraphic succession
121 of the Bushveld Complex, which attains a maximum thickness of 8 km, is divided into five main
122 zones (Hall, 1932). From the base to the top these are the noritic Marginal Zone at the bottom,
123 followed by the ultramafic Lower Zone, the ultramafic to mafic Critical Zone, the gabbronoritic
124 Main Zone, and the ferrogabbroic Upper Zone at the top. The major PGE-rich layers of the
125 intrusion, Merensky Reef and UG-2 chromitite, are found in the upper part of the Critical Zone. A
126 detailed description of these zones is provided by Maier et al. (2013) and references therein, and a
127 summary of the features given here for the purpose of the study.

128 The Marginal Zone consists of fine-grained rocks at the margins of the intrusion and sills
129 in the adjacent country rocks. Harmer and Sharpe (1985) and Sharpe and Hulbert (1985) divided
130 the rocks into three groups based on their stratigraphic position and geochemistry. The *Bushveld 1*
131 (B-1) rocks have textures ranging from quench (consisting of a skeletal orthopyroxene with a
132 matrix of plagioclase laths) to fine-grained equigranular norite. These rocks occur mainly in
133 contact or adjacent to the Lower Zone and lower Critical Zone. The *Bushveld 2* and *3* (B-2 and B-
134 3) are in contact with or adjacent to the upper Critical Zone, and the Main Zone, respectively.
135 Both consist mainly of gabbronorite with grain size varying from very fine (i.e. below 0.1 mm) at
136 contact zones, and fine to medium (i.e. up to 2mm) within sills.

137 In terms of major element compositions, B-1 magmas are Mg-rich basaltic andesites, and
138 the B-2 and B-3 are tholeiitic basalts (Barnes et al., 2010). The trace elements and Sr, Nd and O
139 isotopes show evidence that all of the magmas have been contaminated with 30-50% continental
140 crust (Harmer and Sharpe, 1985; Harris et al., 2005; Barnes et al., 2010). Barnes et al. (2010)

141 argued that the B-1 requires upper continental crust as a contaminant. However, Maier et al.
 142 (2000) argued against the model of simple crustal contamination for B-2 and B-3 rocks based on
 143 high Sr_i in these rocks. Instead, the authors propose that B-2 and B-3 magmas were contaminated
 144 with the residuum of the partial melt which was added to the B-1 magma. This residuum would
 145 have been rich in radiogenic plagioclase. The modelling of lithophile elements also supports the
 146 assimilation of a plagioclase-rich residuum by B-2 and B-3 magmas (Barnes et al. 2010).
 147 Furthermore, Barnes et al. (2010) and Godel et al. (2011) modeled the Lower Zone and lower
 148 Critical Zone as having crystallized from the B-1 magma. Barnes et al. (2010) found that to
 149 model the upper Critical Zone a 60:40 mixture of the B-1:B-2 magmas is required. Barnes et al.
 150 (2010) and Yang et al. (2018) also model the crystallization of the Main Zone using the B-3
 151 magma composition.

152



153

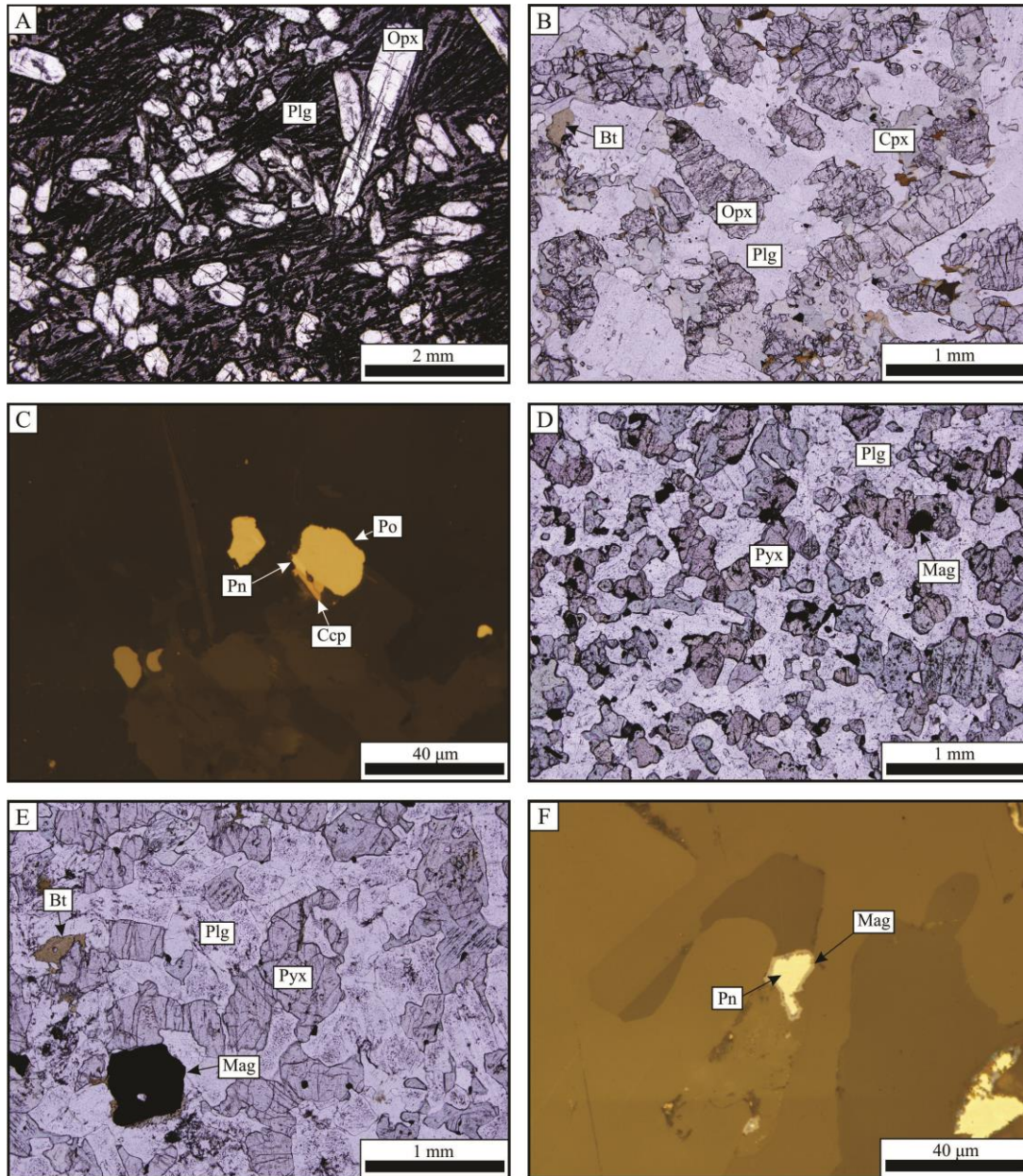
154 Figure 5.1 - Simplified geology of the Bushveld Complex and surrounding rocks, and location of samples utilized in
 155 this study. Modified from Reczko et al. (1995), Eales and Cawthorn (1996), and Barnes et al. (2010).

156 **5.4 – Sample description**

157

158 A suite of 23 samples, including 11 samples from B-1, 8 samples from B-2, and 4
159 samples from B-3 rocks, have been used in this study. Our samples were previously studied by
160 Barnes et al. (2009), which investigated the distributions of S and Se, and also by Barnes et al.
161 (2010), who documented their petrography and microstructures, as well as investigated their
162 major and trace-element concentrations. All but one (ECBV111) of the selected samples are from
163 the Eastern Limb of the Bushveld Complex, where the contact rocks are better exposed (Fig. 5.1).
164 A detailed description on the petrography of the rocks from the Marginal Zone can be found in
165 Harmer and Sharpe (1985) and Sharpe and Hulbert (1985), and a description of our samples is
166 provided here.

167 The B-1 rocks show textures varying from quenched to granular. The quench-textured B-
168 1 rocks show elongated skeletal crystals of orthopyroxene (up to 1cm) in a fine-grained matrix of
169 devitrified glass. Plagioclase laths are also present in the matrix, and in some cases present a flow
170 texture with plan parallel aligned crystals (Fig. 5.2a). Biotite, chromite and sulfide minerals are
171 observed in trace abundances (< 1%) in almost all samples. The granular B-1 rocks consist of
172 fine-grained (1–4 mm) orthopyroxene and plagioclase, with minor clinopyroxene (Fig. 5.2b).
173 Biotite, chromite and sulfide minerals are also present as accessory phases. In both quench and
174 granular B-1 rocks the sulfide assemblage is composed of fine intergrowths of pyrrhotite,
175 pentlandite and chalcopyrite. The sulfides form mostly rounded droplets, which do not show any
176 reaction features with the enclosing silicates (Fig. 5.2c). The quench-textured samples occur
177 mainly as 10 to 100 meter thick sills, whereas the granular rocks occur both as contact rocks and
178 sills (Barnes et al., 2010).



179

180 Figure 5.2 - Photomicrographs of the marginal rocks: (a) B-1 quenched textured sample with medium-grained
 181 orthopyroxene crystals in a fine matrix of plan parallel aligned plagioclase laths, and devitrified glass; (b) Fine-grained
 182 gabbronorite with orthopyroxene, clinopyroxene and plagioclase crystals. Biotite occurs as an accessory phase; (c)
 183 Sulfide intergrowth in a B-1 sample comprising pyrrhotite (Po), pentlandite (Pn), and chalcopyrite (Ccp). The sulfides
 184 have curved, regular boundaries and appear to be in equilibrium with surrounding silicates; (d) Fine-grained B-2
 185 gabbronorite with plagioclase, orthopyroxene and clinopyroxene, and accessory magnetite crystals; (e) Medium-
 186 grained B-3 gabbronorite with plagioclase, orthopyroxene and clinopyroxene, and accessory magnetite, and biotite
 187 crystals; (f) Very fine-grained pentlandite (Pn) crystal with thin magnetite rim at the contact with surrounding silicates.
 188 The texture suggests that the sulfide minerals have reacted with the surrounding silicates. Abbreviations: Bt – biotite ;
 189 Cpx – clinopyroxene; Mag – magnetite; Opx – orthopyroxene; Plg – plagioclase; Pyx – pyroxene.

190

191 Both the B-2 (Fig. 5.2d) and B-3 (Fig. 5.2e) rocks show very similar mineralogy and
192 texture. The samples consist of equigranular, fine-grained plagioclase, orthopyroxene and
193 clinopyroxene. Biotite, magnetite, ilmenite and sulfide minerals also occur as accessory minerals.
194 In some of the B-2 samples the sulfide minerals have thin magnetite rims (Fig. 5.2f). The texture
195 suggests that in these samples the sulfide minerals have reacted with the surrounding silicates,
196 and thus developed the magnetite rims. The B-2 and B-3 rocks are found at both the contact of the
197 Marginal Zone and within sills. The samples found at the contact of the Marginal Zone tend to be
198 slightly more finely grained relative to those found at the interior of sills (Barnes et al., 2010).

199

200 **5.5 – Analytical techniques**

201

202 Tellurium, As, Bi, Sb and Se analyses have been carried out following the technique
203 described by Mansur et al. (2019b) at LabMaTer, Université du Québec à Chicoutimi (UQAC).
204 Approximately 0.4 g of sample were digested with 5 ml of aqua regia (1:3 HNO₃:HCl) in close-
205 capped beaker at 70°C for 24 hours. The aliquot was allowed to cool and diluted to 25 ml prior to
206 mixing with a reductant solution (0.7% NaBH₄ and 0.4% NaOH). The mixed solution was
207 analysed by Hydride Generation-Atomic Fluorescence Spectrometry (HG-AFS), using a
208 continuous flow PSA Millenium Excalibur 10.055 from PS Analytical. Six calibration solutions
209 with concentrations of 0.1, 0.25, 0.5, 1, 2.5 and 5 ppb were prepared using standard solutions of
210 each element (PlasmaCAL, SCP Science, Quebec, Canada). The calibration solutions were mixed
211 with the reagent blank prior to measurement, in the same proportion as sample aliquots.
212 Calibration solutions were measured at the beginning and the end of each sequence of analysis to
213 monitor fluctuations of the fluorescence signal, which were not observed. International reference
214 materials (CH-4 and TDB-1; Natural Resources Canada), GeoPt18 (KPT-1), and a blank were
215 determined at the same time as the samples, and the results agree with working values (*ANNEXE*

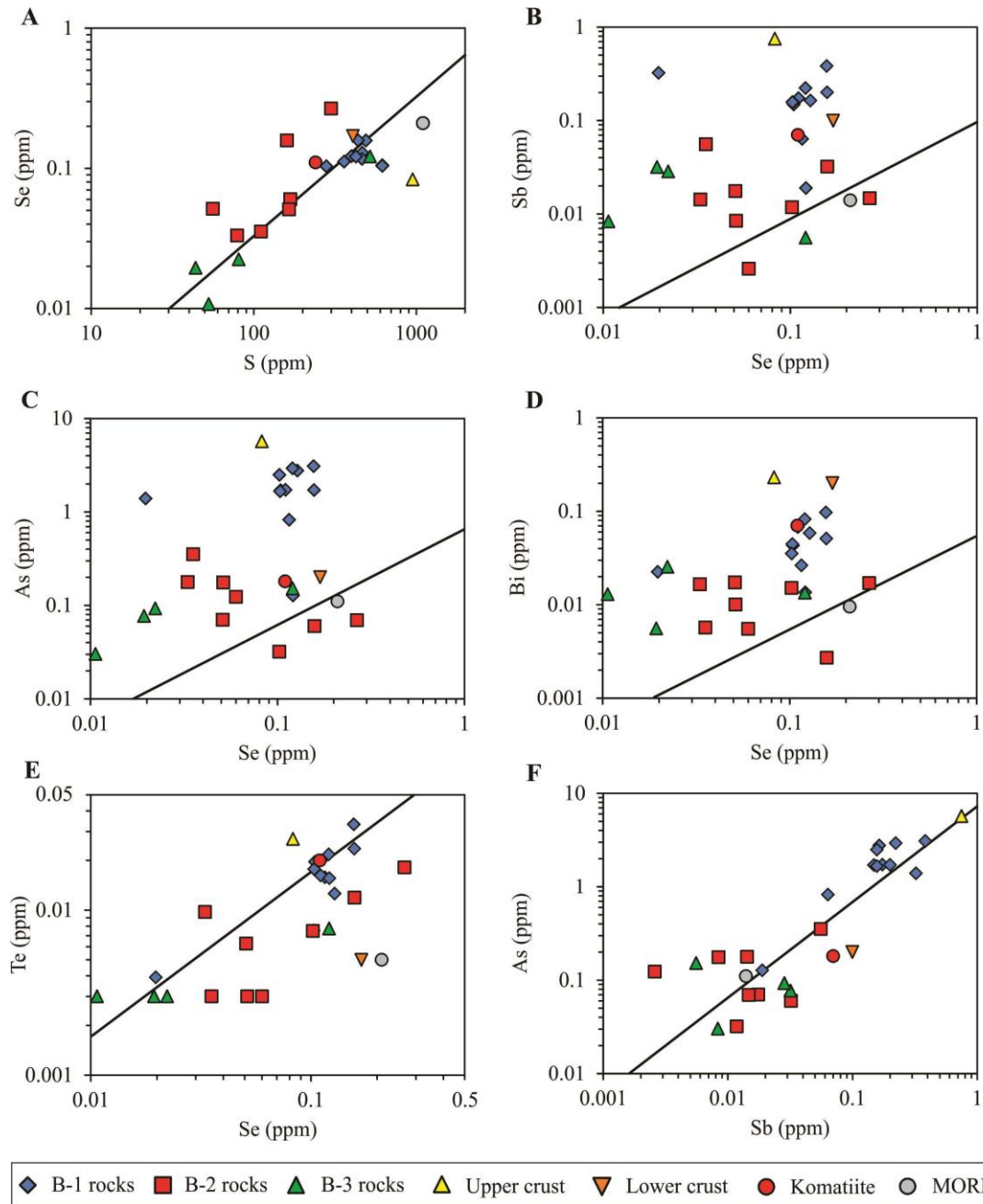
216 10). The 3σ detection limits are 0.006, 0.003, 0.005, 0.005 and 0.002 ppm for Te, As, Bi, Sb and
217 Se, respectively.

218 **5.6 – Results**

219

220 The concentrations of the TABS, Se and S for each sample and average concentrations of
221 B-1, B-2 and B-3 rocks are listed in Table 5.1. Also, previously published PGE, Hf, La, Sm and
222 Th whole-rock analyses can be found in the EMS, Table 2. The B-1 and B-3 rocks have S/Se
223 ratios close to mantle (~3000 McDonough and Sun, 1995; Hattori et al., 2002; Lorand et al.,
224 2003), with B-1 rocks having higher S and Se than then B-3 rocks (Fig. 5.3a). The S/Se ratios
225 close to mantle most likely reflect no S-loss in these samples (Queffurus and Barnes, 2015). Most
226 B-2 rocks have lower S/Se ratios of ~ 1000, although 2 are similar to mantle (Fig. 5.3a). Given
227 the presence of magnetite rims on the sulfides in some B-2 samples (Fig. 5.2f) the low ratios are
228 interpreted as the product of S-loss from some samples (Peck and Keays, 1990; Ripley, 1990;
229 Queffurus and Barnes, 2015). Barnes et al. (2009), have determined the S and Se contents through
230 a complete stratigraphic section of the Bushveld Complex, and also found S/Se ratios lower than
231 mantle values for some B-2 samples. Nevertheless, although some S may have been loss, the
232 relation observed between S and TABS is the same as that between Se and TABS (*ANNEXE*
233 *11*). Because of the possibility of S loss, and because the precision of the Se analyses is higher
234 than of S analyses, Se is used as a proxy for S in the following section.

235



236

237 Figure 5.3 - Binary plots of Se vs S (a), Sb (b), As (c), Bi (d), and Te (e) vs Se, and As vs Sb (f) in samples from the
 238 Marginal Zone of the Bushveld Complex. Average concentrations in upper continental crust (Hu and Gao, 2008), lower
 239 continental crust (Rudnick and Gao, 2003), MORB (Arevalo and McDonough, 2010) and komatiite (OKUM reference
 240 material - IAG) are shown for reference. The black lines indicate the mantle ratios (Lyubetskaya and Korenaga, 2007).

241

242

243

244

245 Table 5.1 - Concentrations of As, Bi, S, Sb, Se and Te, and Se/Te and S/Se ratios in the Marginal Zone rocks of the
 246 Bushveld Complex.

Sample	Unit	Texture	As ppm	Bi ppm	S ppm	Sb ppm	Se ppm	Te ppm	Se/Te	S/Se
<i>DL</i>			<i>0.003</i>	<i>0.005</i>		<i>0.005</i>	<i>0.002</i>	<i>0.006</i>		
DI-225	B-1	Quenched	1.702	0.043	619	0.148	0.104	0.020	5.3	5926
CD-001		Quenched	2.765	0.058	466	0.164	0.128	0.013	10.2	3634
CD-017		Quenched	3.079	0.097	491	0.383	0.157	0.033	4.7	3130
DI-204		Quenched	0.824	0.026	465	0.064	0.116	0.016	7.4	4008
ECBV-018		Granular	1.720	0.068	360	0.174	0.111	0.016	6.8	3247
ECBV-019		Quenched	1.716	0.051	439	0.200	0.157	0.024	6.7	2788
ECBV-021		Quenched	1.663	0.044	619	0.157	0.104	0.018	5.9	5970
ECBV-049A		Granular	0.127	0.014	400	0.019	0.122	0.016	7.8	3292
ECBV-105		Granular	2.927	0.082	426	0.222	0.121	0.022	5.5	3527
ECBV-106		Quenched	2.490	0.035	280	0.157	0.103	0.008	13.7	2722
ECBV-111		Granular	1.395	0.022	n.r.	0.322	0.020	0.004	5.1	n.r.
Average B-1			1.855	0.049	457	0.183	0.113	0.017	6.6	4042
Bc-6	B-2	Fine-grained	0.124	0.006	168	0.003	0.060	0.003	19.0	2798
Bc-25		Fine-grained	0.176	0.010	56	0.008	0.051	0.003	16.2	1089
CO-066		Granular	0.070	0.017	165	0.018	0.051	0.006	8.1	3240
CO-253		Granular	0.069	0.017	299	0.015	0.267	0.018	14.7	1122
ECBV-025		Granular	0.032	0.015	n.r.	0.012	0.102	0.007	13.7	n.r.
ECBV-026		Granular	0.060	0.003	160	0.032	0.158	0.012	13.3	1013
ECBV-058		Granular	0.178	0.017	79	0.014	0.033	0.010	3.4	2387
ECBV-064		Granular	0.354	0.006	111	0.056	0.035	0.003	11.2	3135
Average B-2			0.133	0.011	148	0.020	0.095	0.008	12.0	1566
CO-048	B-3	Fine-grained	0.077	0.006	44	0.032	0.019	0.003	6.1	2264
CO-252		Fine-grained	0.030	0.013	53	0.008	0.011	0.003	3.4	4959
ECBV-013		Fine-grained	0.093	0.003	81	0.028	0.022	0.003	7.0	3635
ECBV-063		Fine-grained	0.152	0.013	520	0.006	0.121	0.008	15.7	4291
Average B-3			0.088	0.009	175	0.019	0.043	0.004	10.1	4021

247

248 Abbreviations: n.r. - not reported; DL - Detection limit. Sulfur values are reported by Barnes et al. (2009, 2010). Values
 249 in bold are below the detection limit and were replaced by half of the detection limit values.

250

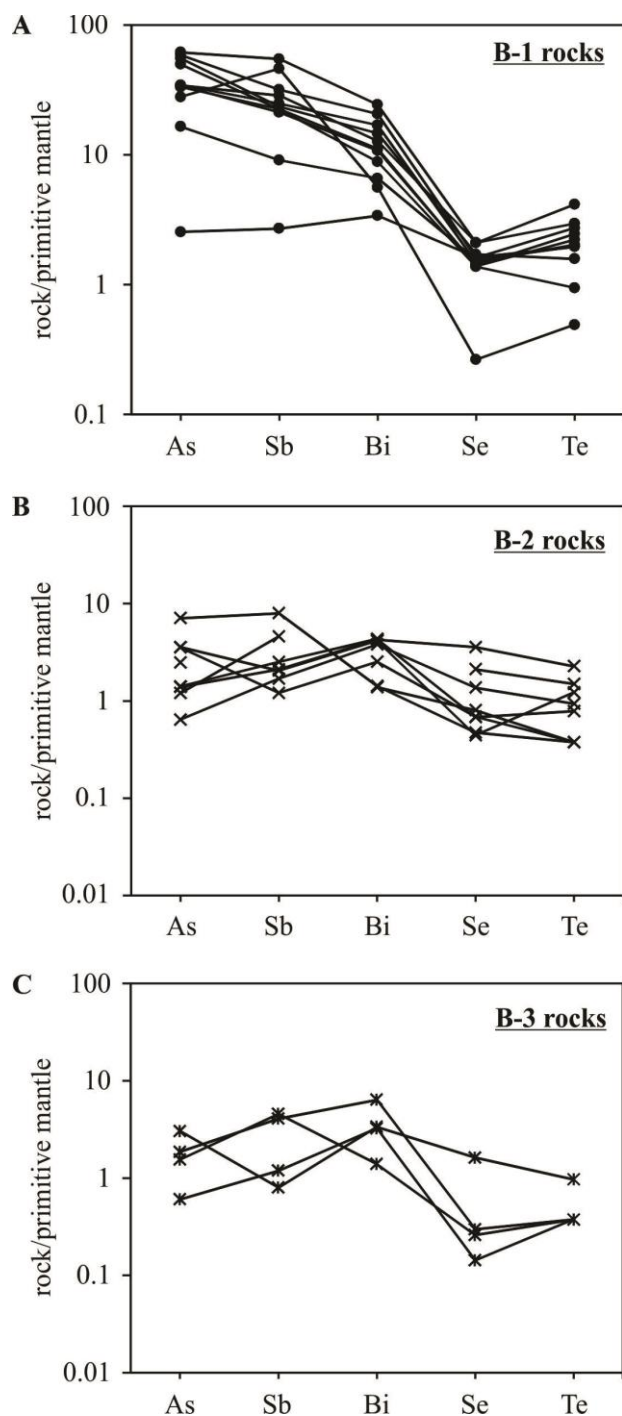
251 The B-1 samples are enriched in all of the TABS relative to the B-2 and B-3 samples
 252 (Table 5.1), with the B-1 samples having values between upper crust and komatiite, whereas the
 253 B-2 and B-3 samples have very low concentrations, close to MORB or lower crust (Figs. 5.3b to

254 5.3f; Rudnick and Gao, 2003; Arevalo and McDonough, 2010). There are no significant
255 correlations between Se and As, Bi or Sb (Figs. 5.3b to 5.3d). The lack of correlation with Se
256 implies that sulfide liquid was not the controlling phase for these elements during the formation
257 of these rocks. Most samples have higher Sb/Se, As/Se and Bi/Se ratios than mantle (solid lines
258 on Fig. 5.3b to 5.3d). In all of the samples, As shows a strong positive correlation with Sb (Fig.
259 5.3f), and both show a slightly positive correlation with Bi (not shown). In contrast to the other
260 TABS, Te shows a positive correlation with Se for the B-1 samples (Fig. 5.3e) with Se/Te ratios
261 close to mantle values (~7; Lyubetskaya and Korenaga, 2007; Wang and Becker, 2013). Where
262 detectable, the B-2 samples have Se/Te ratios higher than mantle (Fig. 5.3e). The concentrations
263 of Te in the B-3 rocks are mainly less than detection limit of 0.006 ppm.

264

265

266 Mantle-normalized TABS plots for B-1, B-2 and B-3 rocks are shown in Fig. 5.4. The
267 elements are plotted in order of incompatibility with a picritic/komatiitic basalt mantle source
268 (Barnes, 2016). The TABS mantle-normalized patterns for the B-1 rocks are enriched in As, Sb
269 and Bi, and decrease from approximately 10 to 80 times mantle at As, Sb and Bi to 1 to 5 times
270 mantle at Se and Te (Fig. 5.4a). In contrast, the TABS mantle-normalized patterns for the B-2
271 (Fig. 5.4b) and B-3 (Fig. 5.4c) rocks are much flatter at 0.1 to 10 times mantle. Most B-2 and
272 some B-3 rocks show a slightly positive Bi anomaly.



273

274 Figure 5.4 - Mantle-normalized TABS diagrams for (a) B-1 rocks, (b) B-2 rocks and (c) B-3 rocks. The elements are
 275 plotted in order of incompatibility with a picritic/komatiitic basalt mantle source (Barnes, 2016). Primitive mantle
 276 values from Lyubetskaya and Korenaga (2007).

277

278

279

280

281 Table 5.2 – Modelling of distribution of TABS, Se and Pd in the Merensky Reef at Impala and Rustenburg sections.

	N	As	Bi	Sb	Te	Se	Pd				
Comp. cumulate sulfide inside reef (Csul)	20000	2.3	17.3	0.6	43.5	126.8	164.9				
Comp. cumulate sulfide outside reef (Csul)	350	2.3	8.7	0.6	4.8	32.2	3.7				
Ci = 60:40 mixture B1+B2		1.16	0.03	0.12	0.01	0.11	0.01				
D sul/sil		2*	500*	5*	3000**	1200**	40000***				
Locality	Impala mine						Rustenburg mine				
Sample	IM-3	IM-13	IM-21	IM-24	IM-25	IM-26	M4	M1	UC	CGM-2	AN
Rock	M	M	M	LC	AN	L	M	M	UC	CGM	AN
wt frac melt	0.19	0.51	0.24	0.10	0.10	0.07	0.12	0.13	0.13	0.11	0.11
wt frac cum sul	0.00	0.00	0.06	0.01	0.01	0.05	0.03	0.09	0.01	0.04	0.01
wt frac sil and oxide	0.80	0.49	0.71	0.89	0.89	0.88	0.85	0.78	0.85	0.85	0.88
As melt	0.22	0.59	0.27	0.12	0.12	0.08	0.14	0.15	0.15	0.13	0.13
As sul	0.01	0.00	0.13	0.03	0.03	0.12	0.06	0.21	0.03	0.09	0.02
As total	0.24	0.59	0.41	0.15	0.14	0.20	0.21	0.37	0.19	0.22	0.16
As observed	0.09	0.44	0.12	0.07	0.08	0.10	0.12	0.14	0.07	0.20	0.07
Bi melt	0.01	0.02	0.01	0.00	0.00	0.00	0.00	0.00	0.00	0.00	0.00
Bi sul	0.04	0.00	1.00	0.20	0.20	0.90	0.48	1.58	0.25	0.68	0.18
Bi total	0.05	0.02	1.01	0.20	0.20	0.90	0.48	1.58	0.26	0.68	0.18
Bi observed	0.02	0.01	0.94	0.17	0.16	0.73	0.38	1.40	0.33	0.61	0.22
Sb melt	0.02	0.06	0.03	0.01	0.01	0.01	0.01	0.02	0.02	0.01	0.01
Sb sul	0.00	0.00	0.03	0.01	0.01	0.03	0.02	0.05	0.01	0.02	0.01
Sb total	0.03	0.06	0.06	0.02	0.02	0.04	0.03	0.07	0.02	0.04	0.02
Sb observed	0.02	0.03	0.04	0.02	0.06	0.05	0.03	0.06	0.04	0.03	0.01
Te melt	0.00	0.01	0.00	0.00	0.00	0.00	0.00	0.00	0.00	0.00	0.00
Te sul	0.02	0.00	2.51	0.49	0.49	2.27	1.20	3.97	0.64	1.71	0.45
Te total	0.03	0.01	2.52	0.50	0.50	2.27	1.20	3.97	0.64	1.71	0.45
Te observed	0.12	0.02	2.39	0.40	0.51	2.60	0.86	4.45	0.75	1.76	0.67
Se melt	0.02	0.05	0.02	0.01	0.01	0.01	0.01	0.01	0.01	0.01	0.01
Se sul	0.15	0.02	7.33	1.44	1.44	6.61	3.51	11.58	1.87	4.99	1.30
Se total	0.18	0.07	7.36	1.45	1.45	6.62	3.52	11.59	1.89	5.01	1.31
Se observed	0.56	0.23	7.10	1.36	1.63	5.92	4.14	14.65	1.99	5.66	1.57
Pd melt	0.00	0.01	0.00	0.00	0.00	0.00	0.00	0.00	0.00	0.00	0.00
Pd sul	0.02	0.00	9.54	1.87	1.88	8.60	4.56	15.06	2.43	6.50	1.69
Pd total	0.02	0.01	9.54	1.87	1.88	8.60	4.56	15.06	2.44	6.50	1.69
Pd observed	0.02	0.01	6.33	4.17	3.03	9.87	2.16	11.90	4.27	5.94	4.03

282 All values in ppm. * Li and Audétat (2015) ** Liu and Brenan (2015) *** Mungall and Brenan (2014). AN -

283 anorthosite; L - leuconorite; LC - lower chromitite; CGM - coarse-grained melanorite; UC - upper chromitite; M -

284 melanorite. Observed values are from Mansur and Barnes (2020) for Se and TABS, and from Barnes and Maier (2002)

285 and Godel et al. (2007) for Pd.

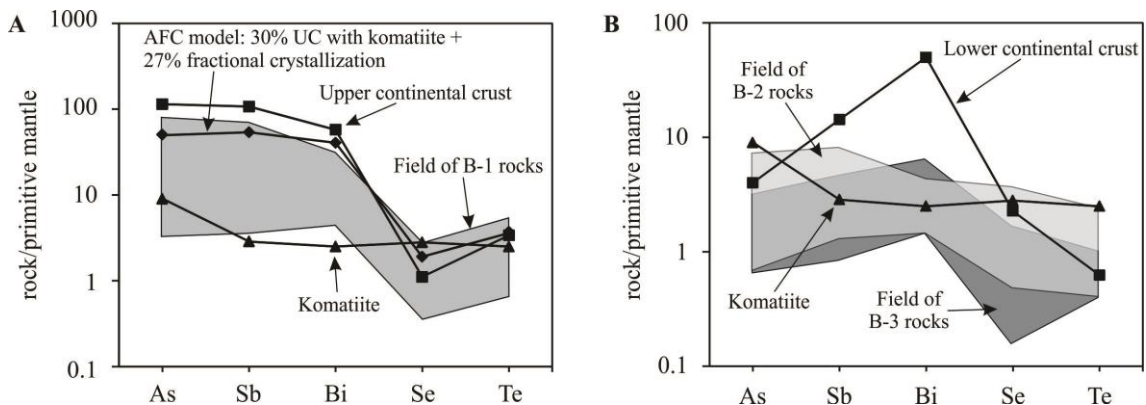
286 **5.7 – Discussion**

287 **5.7.1 - Crustal contamination and the external addition of TABS**

288

289 It has been shown that the Bushveld magmas were contaminated with continental crust,
290 which affected the major and trace elements concentrations in these liquids (Maier et al., 2000;
291 Harris et al., 2005; Barnes et al., 2010; Eales and Costin, 2012; Roelofse and Ashwal, 2012;
292 Wilson, 2012; Roelofse et al., 2015; Maier et al., 2016). Many of these authors argue that B-1
293 magma represents a komatiitic magma contaminated with upper continental crust. Indeed, B-1
294 TABS patterns most closely resemble the average upper continental crust, with higher
295 concentrations of As, Sb and Bi relative to komatiite pattern (Fig. 5.5a). Maier et al. (2016)
296 modelled the B-1 magma and associated cumulates as the product of approximately 35%
297 assimilation of upper crust accompanied by 27 % crystal fraction (AFC) of komatiite liquid. The
298 product of AFC modelling of a komatiite with continental crust (*ANNEXE 11*) has a TABS-
299 pattern that closely resembles that of B-1 rocks, supporting the addition of upper continental
300 crustal material (Fig. 5.5a).

301



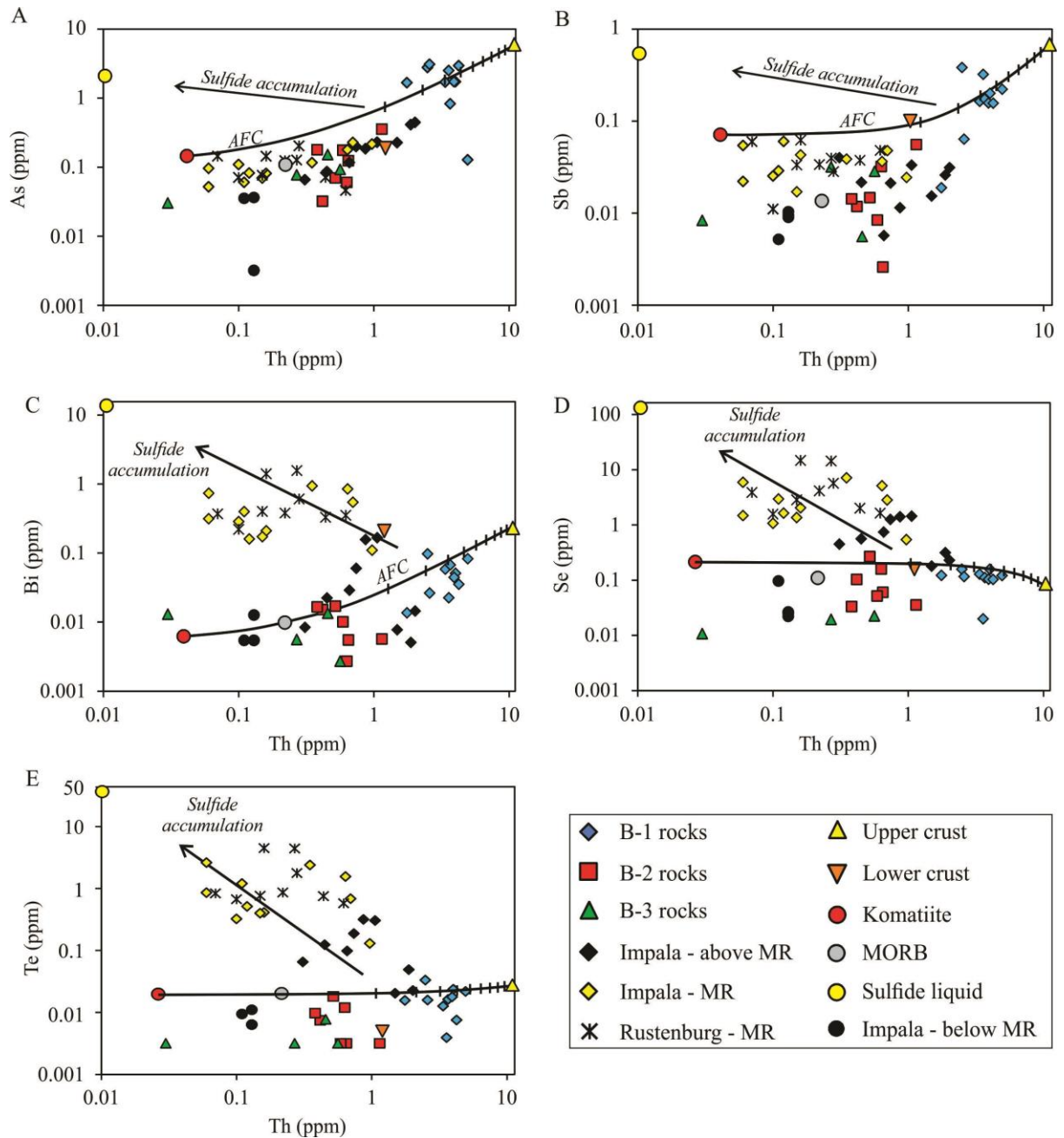
302

303 Figure 5.5 - Mantle-normalized TABS diagrams for (a) B-1 rocks compositional field relative to komatiite (Barnes,
304 2016), upper continental crust (Hu and Gao, 2008), and a AFC model of a mixture of a komatiite with 30% upper crust
305 (UC) and 27% fractional crystallization; (b) B-2 and B-3 rocks compositional fields compared to komatiitic basalt
306 (Barnes, 2016) and lower continental crust (Rudnick and Gao, 2003). Primitive mantle values from Lyubetskaya and
307 Korenaga (2007).

308 Thorium is also strongly concentrated in the upper crust (10.5 ppm; Hu and Gao, 2008)
309 relative to primitive mantle (0.06ppm; Lyubetskaya and Korenaga, 2007), and can also be used as
310 a proxy for crustal contamination. Plots of As, Sb and Bi versus Th show that the B-1 magmas
311 can be indeed modelled as the product of AFC of komatiite contaminated with average upper
312 crust (Fig. 5.6a to 5.6c). However, the Se and Te concentrations of upper crust (0.083 and
313 0.027ppm, respectively) and komatiite (0.21 and 0.02ppm, respectively) are similar, thus
314 contamination is not readily apparent for these two elements (Fig. 5.6d and 5.6e).

315 The origin of the B-2 and B-3 magmas is less well established. Possibly they are also
316 product of AFC of komatiite, but in this case the contaminant is argued to have been plagioclase-
317 rich residuum formed during partial melting of the upper crust during the formation of the B-1
318 magma (Maier et al., 2000; Barnes et al., 2010). Isotopic work support that the rocks have a large
319 crustal component (Maier et al., 2000; Harris et al., 2005; Karykowski et al., 2017), but the low
320 incompatible lithophile element content indicates that the contaminant is not average upper
321 continental crust (Barnes et al., 2010). The low TABS content is in agreement with this. Neither
322 is average lower continental crust suitable as it contains too much Sb (0.1ppm) and Bi (0.2ppm)
323 to be a contaminant (Fig. 5.3d and 5.3f; Rudnick and Gao, 2003), and also the whole-rock Sr
324 isotopic signature does not match lower crust (Maier et al., 2000).

325 Overall the B-2 and B-3 patterns are similar to komatiite and presumably the crustal
326 contaminant contained very little TABS and thus did not affect the patterns (Fig. 5.5b). Therefore,
327 our results support that a plagioclase-rich residuum is a suitable contaminant for these melts
328 (Maier et al., 2010; Barnes et al., 2010). The partial melting of upper crust by B-1 magmas, and
329 incorporation of As, Sb and Bi (Fig. 5.5a) possibly led to the formation of a residuum depleted in
330 these elements. Consequently, during further assimilation by B-2 and B-3 magmas, the As, Sb,
331 and Bi content of the melts remained mostly unaffected, and most likely resemble that of the
332 parental komatiitic magmas. This suggestion is also in agreement with the previous modelling of
333 lithophile elements (Barnes et al., 2010), and isotopic studies (Maier et al., 2000; Harris et al.,
334 2005; Karykowski et al., 2017).



335

336 Figure 5.6 - Binary plots of As (a), Sb (b), Bi (c), Se and Te vs Hf in samples from the Marginal Zone, and Merensky
 337 Reef (MR) at the Impala and Rustenburg mines (Barnes and Maier 2002; Godel et al. 2007; Mansur and Barnes, 2020).
 338 Average concentrations in upper continental crust (Hu and Gao, 2008), lower continental crust (Rudnick and Gao,
 339 2003), MORB (Arevalo and McDonough, 2010) and komatiite (OKUM reference material; IAG) are shown for
 340 reference. The black lines represent the AFC model of a mixture of a komatiite with 30% upper crust and 27%
 341 fractional crystallization, and the dash lines represent 10% increments. Individual analyses for the Merensky Reef
 342 samples are reported in the ANNEXE 15, whereas modelled composition of sulfide liquid is given in Table 5.2.

343

344

345 **5.7.2 – Modelling the distribution of TABS in the Merensky Reef**

346 The Merensky Reef is thought to have formed from a mixture of the B-1 and B-2 magmas
347 (Naldrett and von Gruenewaldt, 1989; Li et al., 2001; Godel et al., 2007; Naldrett et al., 2009;
348 Barnes et al., 2002, 2010; Maier et al., 2016). A 60:40 mixture of these magmas was shown as
349 suitable for modelling the concentrations of a wide range of major, minor and trace elements in
350 the reef (Barnes et al., 2009, 2010; Maier et al., 2016). The concentrations of TABS and Se across
351 two sections of Merensky Reef (one from Impala Mine and one from Rustenburg Mine) have
352 been determined (Mansur and Barnes, 2020; Fig. 5.7 and 5.8; *ANNEXE 15*). Below we model
353 the TABS concentrations across the two reef locations assuming that the magma that formed the
354 reefs was a 60:40 mixture of the B-1 and B-2 magmas (following Barnes et al., 2010).

355 The components of the reef have been modelled as cumulate sulfide liquid, silicate liquid
356 and cumulate (silicate minerals and oxides). A summary of the modelling parameters and the
357 results for selected samples are given in Table 5.2, and the complete modelling results are
358 reported in the *ANNEXE 12*. The composition of the sulfide liquid was modelled using the zone
359 refining equation of Brugmann et al. (1993)

360

361 (1)
$$C_{Sul} = C_{Sil} \{ D^{Sul/Sil} - (D^{Sul/Sil} - 1) \exp^{[-(1/D^{Sul/Sil}) * N]} \}$$

362 where C_{Sul} is the concentration of an element in the sulfide liquid, C_{Sil} is the concentration of an
363 element in the silicate liquid, $D^{Sul/Sil}$ is the partition coefficient for the element between sulfide
364 and silicate liquid, and N is the ratio of silicate to sulfide liquid. The silicate liquid fraction in
365 each sample was estimated based on the concentration of the incompatible elements (Hf, La and
366 Sm) in the rocks divided by the composition of the magma (Table 5.2). The cumulate sulfide
367 liquid fraction in each rock was estimated by

368 (2)
$$\text{Wt \% sulf} = (S_{\text{rock}} - 1000 * \text{wt. fraction silicate liquid}) / 350000$$

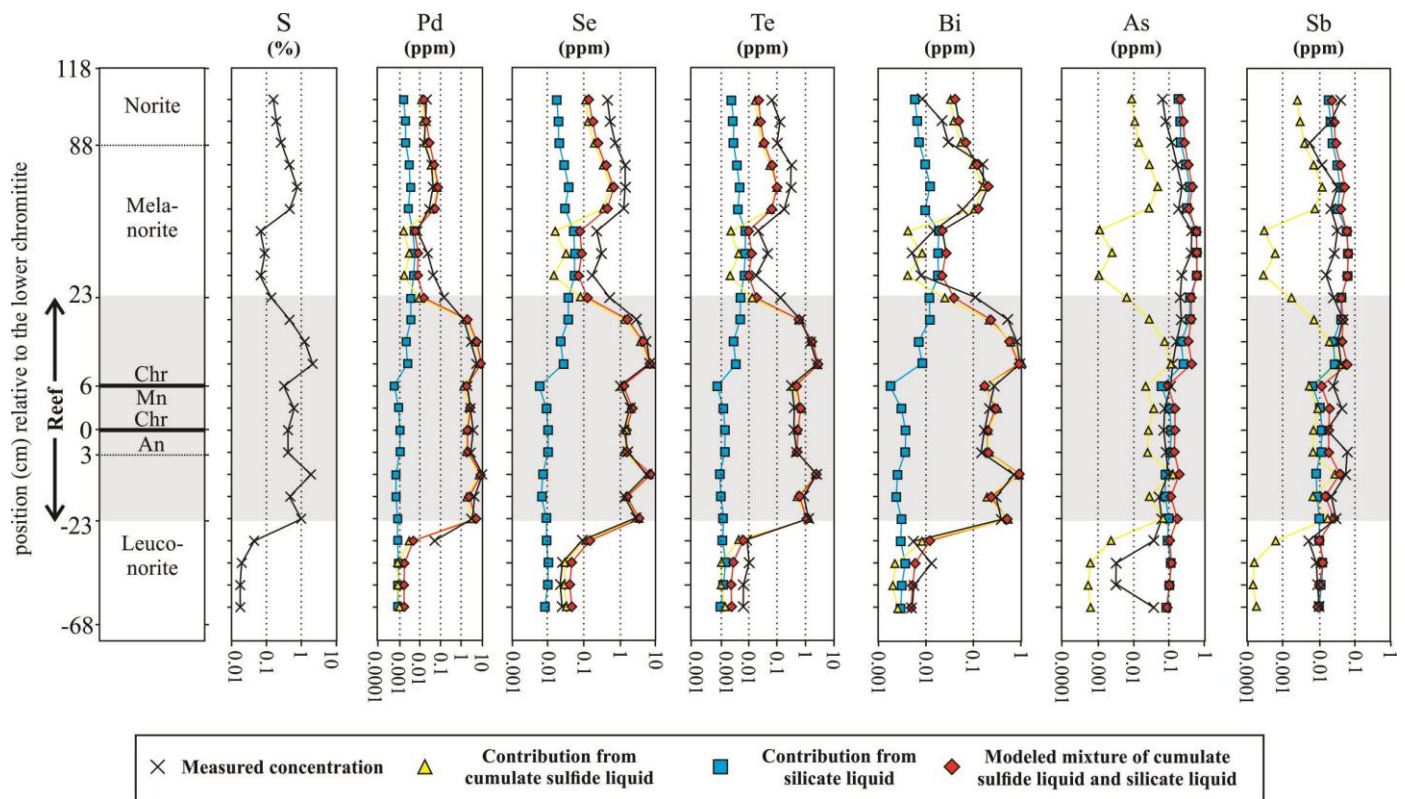
369 assuming that sulfide saturation occurred at ~1000 ppm (Li and Ripley, 2005) and that the sulfide
370 liquid contained 35 weight percent S. The cumulate silicate and oxide minerals were assumed to

371 not contribute to mass balance of TABS, although experiments on this subject are still lacking.
372 More details of the modelling can be found in *ANNEXE 12*.

373 Plots of modelling results versus depth across the Impala (Fig. 5.7) and Rustenburg (Fig.
374 5.8) sections show that the distributions of Se, Te and Bi closely follow each other and the PGE
375 (here represented by Pd). These distributions can be modelled by variations in the fraction of
376 cumulate sulfide liquid of the rocks, and thus their contribution to the whole rock budget (Fig. 5.7
377 and 5.8). In contrast, the As and Sb in large part follow the incompatible elements (Fig. 5.6), and
378 are better modelled by the silicate liquid fraction, which represents the trapped melt component in
379 the rocks (Fig. 5.7 and 5.8). The difference in behaviour between the two groups of elements
380 reflects the differences in partition coefficients. Arsenic and Sb are only slightly chalcophile with
381 partition coefficients between sulfide and silicate liquid of 1-10 (Table 5.2; Li and Audétat,
382 2015). In contrast, Bi and Se are strongly chalcophile with partition coefficients in the 100 to
383 1000 range, and Te and Pd are highly chalcophile with partition coefficients greater than 1000
384 (Table 5.2; Mungall and Brenan, 2014; Liu and Brenan, 2015; Barnes, 2016 and references
385 therein).

386 If we regard the results for individual samples, we can see that the melt component in
387 samples below and in the lower parts (below 6 cm height) of the Merensky Reef is low (i.e. 5 to
388 15%; *ANNEXE 15*). However, greater amounts of melt component are observed in the upper
389 parts (above 8 cm height) and above the Merensky Reef (i.e. 15 to 55%; *ANNEXE 15*). This
390 variation suggests that the reef interval has experienced compaction during crystallization (Godel
391 et al., 2006), and the interstitial melt component was squeezed out from the reef interval into the
392 upper portions. The compaction is also supported by petrographic studies (Barnes and Maier,
393 2002; Godel et al., 2007; Vukmanovic et al., 2013; Holness et al., 2017).

394
395
396



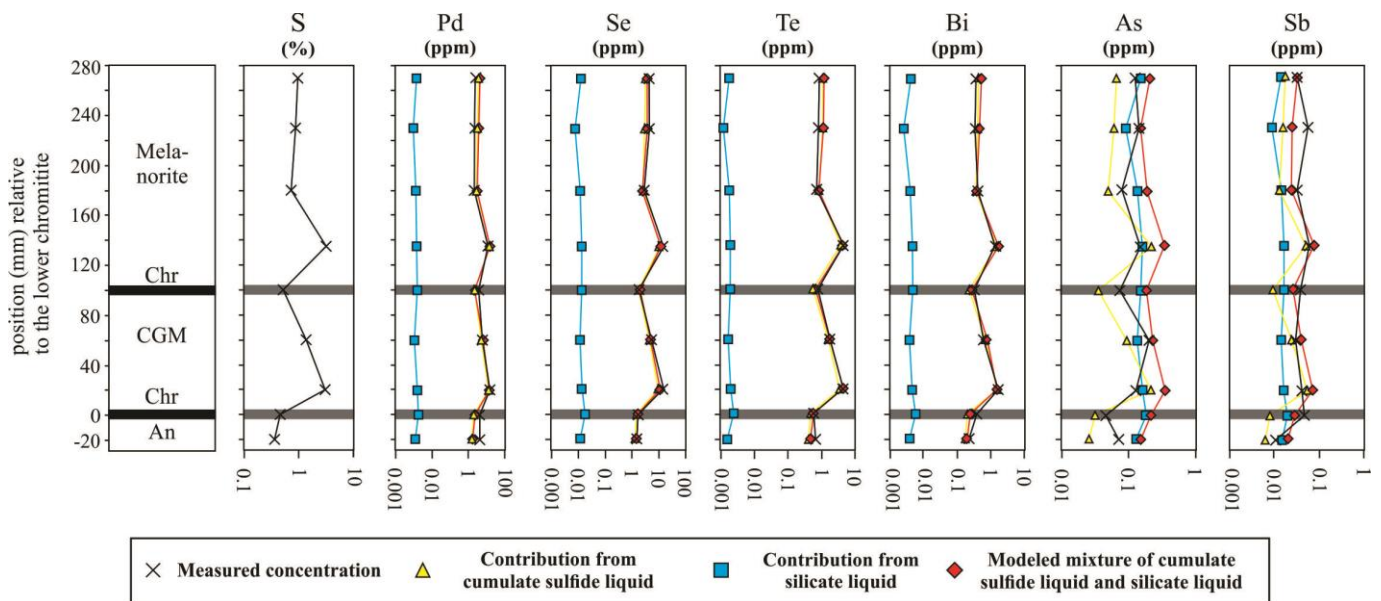
398 Figure 5.7 - Variations of Pd, Se, Te, Bi, As and Sb measured concentrations, and modeled contributions from
 399 cumulate sulfide liquid, trapped silicate liquid, and a mixture of both, with height across the Impala section. Note that
 400 the vertical scale is not linear and the samples are spaced out evenly. The reef interval (shade gray) is defined by rocks
 401 containing more than 1.5 ppm Pt+Pd in whole-rock analysis, and starts 23cm below the lower chromitite and ends
 402 23cm above it (Barnes and Maier, 2002). Individual analyses and complete modelling results are reported in the
 403 ANNEXE 12. Abbreviations: An: anorthosite; Chr: chromitite; Mn: melanorite.

404

405 Although the modeled and measured distributions of PGE, Se and TABS across the
 406 Merensky Reef are correlated spatially, some divergences are observed. Modelled concentrations
 407 of As are higher (1 to 2 times) relative to measured concentrations across the entire section (Fig.
 408 5.7 and 5.8; Table 5.2). Given its volatile behaviour (Lodders, 2003), this could suggest that some
 409 of the As was lost during the formation of the reef. However, all the other TABS and Se also
 410 show a volatile behaviour (Lodders, 2003), but their measured concentrations are not lower than
 411 modelled values.

412 The differences between modelled and measured As concentrations may also reflect
 413 regional heterogeneities in the compositions of rocks that contaminated the magmas. Most of the
 414 samples of the marginal rocks were collected at the eastern limb of the Bushveld Complex,

415 whereas the Impala and Rustenburg sections are located at the western limb of the intrusion (Fig.
 416 5.1). Possibly the contaminant on the eastern limb was slightly richer in As than the contaminant
 417 on the western limb. Moreover, Willie et al. (2007) also reported variable As concentrations in
 418 sediments from the Transvaal Supergroup that support their regional heterogeneity.
 419



421 Figure 5.8 - Variations of Pd, Se, Te, Bi, As and Sb measured concentrations, and modeled contributions from
 422 cumulate sulfide liquid, trapped silicate liquid, and a mixture of both, with height across the Rustenburg section.
 423 Individual analyses and complete modelling results are reported in the ANNEXE 12. Abbreviations: An: anorthosite;
 424 Chr: chromitite; CGM: coarse-grained melanorite.

425

426 Another minor divergence between modelled and measured values is observed for Se and
 427 Te results (Table 5.2). Although the measured and modelled results are similar within the reef, the
 428 Se and Te modelled concentrations are lower (1 to 2 times) relative to measured values in
 429 samples above the reef interval (Fig. 5.7; ANNEXE 12). These differences most likely reflect the
 430 depletion of Te and Se in the silicate liquid as sulfides liquid segregated upon the formation of the
 431 Merensky Reef. This is because Te and Se behave as strongly chalcophile elements (Liu and
 432 Brenan, 2015; Barnes, 2016) and would partitioned into the sulfide liquid upon the formation of
 433 the reef. Moreover, the differences may also originate from various uncertainties during the
 434 calculations. These are important to be considered given the strong control of Te and Se by the

435 cumulate sulfide fraction (Fig. 5.7 and 5.8), combined with very low values of S found in rocks
436 above the reef interval (Fig. 5.7). Therefore, it is possible that the calculation of the sulfide liquid
437 fraction (Wt % Sulf in equation 2) is not completely accurate for samples above the reef.

438 Overall, the modelled and measured concentrations of PGE, Se and TABS in samples
439 from the Merensky Reef are similar. This supports that a B-1:B-2 mixture (60:40) is appropriate
440 as initial liquid for the formation of the upper Critical Zone, and crystallization of the Merensky
441 Reef (Barnes et al., 2010; Maier et al., 2016). Moreover, the modelling results support that the
442 distributions of PGE, Se, Te and Bi in the reef are essentially controlled by the fraction of
443 cumulate sulfides. In contrast, As and Sb are strongly influenced by the amount of silicate liquid
444 trapped in the cumulates, as well as the presence of sulfides.

445

446 **5.7.3 – Constraints for the evolution of Bushveld magmas and formation of the** 447 **Merensky Reef**

448

449 Precisely determining the composition of the parental magma of the upper Critical Zone
450 is crucial for understanding the formation of the PGE deposits of the Bushveld Complex. Our
451 results show that the concentrations of TABS in the Bushveld parental magmas have been
452 upgraded in response to the assimilation of crustal material (Fig. 5.9a). Furthermore, the upper
453 Critical Zone of the Bushveld Complex, and thus its main PGE deposits, formed upon the mixing
454 of B-1 and B-2 magmas. The new magma pulses would explain the higher N-factors (20000;
455 Table 5.2) of sulfides from the reef interval (Barnes and Maier, 2002; Robertson et al., 2015; Fig.
456 5.8b).

457 The Se and Te concentrations in mantle rocks and derived magmas are used to assess the
458 control of sulfide minerals on the distribution of chalcophile elements (Hattori et al., 2002; Rose-
459 Weston et al., 2009; Lorand and Alard, 2010; Wang and Becker, 2013; Konig et al., 2012; Lissner
460 et al., 2014; Lugué et al., 2015). The partition coefficient of Te between silicate and sulfide
461 liquid is much higher than that of Se (Patten et al., 2013; Wang and Becker, 2013; Brenan, 2015;

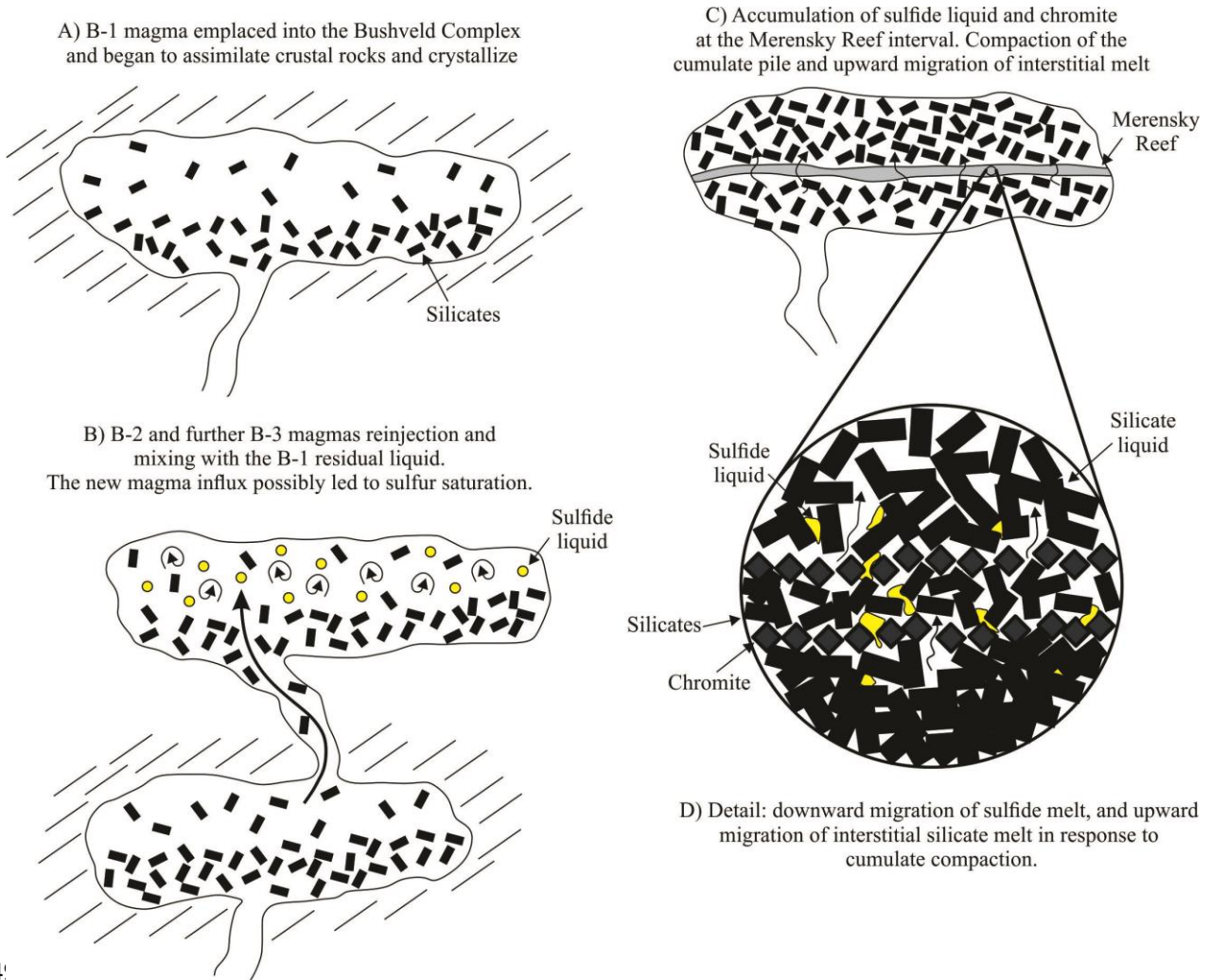
462 Konig et al., 2015). Therefore, upon the segregation of an immiscible sulfide liquid, Te is
463 preferentially collected relative to Se. Consequently, liquids that have experienced sulfide
464 segregation may have higher Se/Te ratios relative to sulfide-undersaturated liquids. The high
465 Se/Te ratio in B-2 rocks (average of 12) relative to other marginal rocks (averages of 6.6 and 10.1
466 for B-1 and B-3 rocks, respectively) suggests that B-2 rocks crystallized from a liquid that have
467 segregated a sulfide liquid. This is in agreement with results reported by Barnes et al. (2010)
468 which showed that B-2 liquids are also depleted in PGE, and have higher Cu/Pd ratios (above
469 8000) relative to other marginal rocks (below 4500). The authors have also interpreted the
470 differences as the results of the segregation of an immiscible sulfide liquid, and subsequent
471 collection of PGE from the silicate liquid.

472 Although the importance of crustal contamination for the addition of TABS is recorded in
473 the B-1 rocks from the Marginal Zone, it is not equally recorded by all the TABS in samples from
474 the reef interval. The interaction of sulfides with large volumes of silicate magma (i.e. high N
475 factor; Fig. 5.9b) obscures the effect of crustal contamination for elements with high partition
476 coefficients between sulfide and silicate liquids (Leshner and Burnham, 2001). Therefore,
477 concentrations of Bi, Se and Te are higher in the reef samples relative to marginal rocks (Fig. 5.6c
478 to 5.6e), whereas concentrations of As and Sb are similar in reef samples and marginal rocks (Fig.
479 5.6a and 5.6b). Thus, the presence of sulfide minerals do not markedly increase the whole-rock
480 concentrations of As and Sb (Fig. 5.6a and 5.6b). Consequently, their concentrations in the reef
481 samples still reflect those from the parental magmas, and can be used to assess the effects of
482 crustal contamination.

483 The upward melt migration through the Merensky Reef cumulate pile in response to
484 compaction is also recorded by the distribution of TABS. Slightly chalcophile elements such as
485 As and Sb behave incompatibly during the formation of the reef, and remained in the more
486 fractionated silicate liquid. Thus, upon compaction of the cumulate pile, the lattermost
487 fractionated silicate liquid was squeezed up in the stratigraphy into cumulates directly above the
488 reef interval (Fig. 5.9c and 5.9d). Consequently, these rocks became richer in As and Sb relative

489 to rocks from within and below the reef interval (Fig. 5.7). This difference in compatibility with a
 490 sulfide liquid led to a decoupling of TABS. Selenium, Te and Bi are richer in sulfide-bearing
 491 samples from the reef interval, whereas As and Sb are richer in cumulates with greater amounts of
 492 trapped silicate liquid (Fig. 5.7; Table 5.2).

493



494

495 Figure 5.9 - Schematic models illustrating the evolution of Bushveld magmas and crystallization of the Merensky Reef
 496 interval. See text for further explanation.

497

498

499

500 **5.7.4 – Implications for the formation of PGE deposits**

501

502 There is an increasing interest in studying the distribution of TABS in magmatic sulfide
503 deposits (Godel et al., 2012; Piña et al., 2013, 2015; Canali et al., 2017; Duran et al., 2017;
504 Samalens et al., 2017; LeVaillant et al., 2018; Wang et al. 2018; Liang et al., 2019; Mansur et al.
505 2019a; Mansur and Barnes, 2020). This is mainly because the presence of TABS has been
506 suggested to affect the distribution of PGE. However, assessing the concentration of TABS in
507 parental magmas from which the PGE deposits formed is still a missing step for understanding
508 the ore forming processes. Therefore, our study contributes by determining TABS concentrations
509 in rocks interpreted to represent the parental liquids of some of the largest PGE deposits in the
510 world (Harmer and Sharpe, 1985; Sharpe and Hulbert, 1985; Barnes et al., 2009, 2010; Wilson,
511 2012; Maier et al., 2016). Below, we use these results to evaluate some of the recently proposed
512 models for the collection of PGE, and formation of the deposits, as follows.

513 It has been long argued that PGE have very high partition coefficients between sulfide
514 and silicate liquids (Mungall and Brenan, 2014; Liu and Brenan, 2015 and references therein),
515 and are collected by an immiscible sulfide liquid (Barnes and Ripley, 2016, and references
516 therein). Moreover, experimental studies have also demonstrated that TABS also behave as
517 chalcophile elements, and would also be collected by an immiscible sulfide liquid (Li and
518 Audétat, 2015; Liu and Brenan, 2015 and references therein). Alternatively, some authors
519 propose that PGE atoms self-organize as nanometer size clusters in the silicate liquid, which
520 would be stabilized the by the surface adsorption of S, Fe and TABS atoms (Tredoux et al., 1995;
521 Ballhaus et al., 2006; Helmy et al., 2013; Gonzalez-Jimenez et al., 2018, 2019).

522 In the cluster model, the distribution of PGE would be physically controlled by the
523 surface properties of nanometer-sized particles (Tredoux et al., 1995; Ballhaus et al., 2006).
524 Therefore, the main implication of this model is that the partition coefficients of PGE, and other
525 cluster-forming elements, would not control their distribution. Once the clusters are physically
526 captured by the sulfide liquid, they are incorporated into the crystallizing base metal sulfides

527 (Wirth et al., 2013; Junge et al., 2015; González-Jiménez et al., 2018, 2019; Liang et al., 2019).
528 Indeed, recent studies in material science support that pre-nucleation clusters can be the
529 precursors for nano-particles prior to their nucleation (Chakraborty and Pradeep, 2017, and
530 references therein).

531 Some authors have also found nanometer-sized PGM in natural cases (Wirth et al., 2013;
532 Junge et al., 2015; González-Jiménez et al., 2018, 2019; Liang et al., 2019). However, these
533 particles are mainly Pt-arsenides (Kamenetsky et al., 2015; Maier et al., 2015; Arguin et al., 2016;
534 Barnes et al., 2016; González-Jiménez and Reich, 2017; González-Jiménez et al., 2018, 2019).
535 Experimental studies show that Pt and As are able to self-organize into nanometer-sized particles
536 (Helmy et al., 2013; Helmy and Bragagni, 2017). Helmy et al. (2013) argue for the nanocluster
537 model for the collection of PGE based on Pt-As clusters found in their high-temperature
538 experiments, supporting the formation of PGE nanoclusters.

539 Although experimental and empirical studies provide substantial evidence for the
540 existence of Pt-As nanometer-sized particles, our results do not support that PGE distribution can
541 be exclusively physically controlled by cluster properties. Our modelling results were calculated
542 taking into account the different partition coefficients of PGE (Mungall and Brenan, 2014), and
543 TABS (Li and Audétat, 2015; Liu and Brenan, 2015) between silicate and sulfide liquids, and
544 closely reproduce natural concentrations measured in PGE deposits (Fig. 5.7 and 5.8). Moreover,
545 the results also support that sulfide minerals have a different control on the distribution of PGE
546 and TABS, based on their different chalcophile behaviours. For instance, the distribution of As,
547 which is the most frequently related element to the formation of PGE clusters (Helmy et al., 2013;
548 Helmy and Bragagni, 2017), does not follow that of PGE (Fig. 5.7). This is because As is only
549 slightly chalcophile, whereas PGE are strongly chalcophile elements.

550 Overall, although we do acknowledge for the presence of nanometer-sized PGE particles
551 in natural cases (Wirth et al., 2013; Junge et al., 2015; Kamenetsky et al., 2015; Maier et al.,
552 2015; Barnes et al., 2016; González-Jiménez et al., 2018, 2019; Liang et al., 2019), our findings
553 do not support the thesis that PGE distribution is mainly controlled by the physical properties of
554 nanoclusters. Also, the whole-rock PGE/TABS ratios do not support the PGE collection by

555 nanoclusters (Mansur and Barnes, 2020). Another restriction of the nanocluster model is the
556 limitation of experimental work demonstrating the formation of PGE nanoclusters other than Pt-
557 arsenides, and using realistic starting materials. Given that future studies will surely expand and
558 support this discussion, our results on the concentrations of TABS in parental liquids may likely
559 be used as an additional tool for evaluating the processes controlling the formation of PGE
560 deposits.

561

562 **5.8 – Conclusions**

563

564 We have measured the concentrations of TABS in rocks from the Marginal Zone of the
565 Bushveld Complex. Our main findings are summarized as follows:

566 1 – The B-1 samples are enriched in As, Sb and Bi relative to primary magmas and can be
567 modelled by contamination of komatiite with upper crust. In contrast, the B-2 and B-3 magmas
568 are not enriched and can be modelled by contamination of komatiitic magmas with a plagioclase-
569 rich residuum.

570 2 - The distribution of TABS, Se and PGE below, above, and within the Merensky Reef can be
571 modelled by a mixture of magmatic sulfide formed in equilibrium with a mixture of B-1 and B-2
572 melts, and trapped silicate liquid.

573 3 – In the Merensky Reef section the distributions of Te, Se, Bi and PGE are controlled by the
574 presence of sulfide minerals, whereas the distributions of As and Sb are controlled by both sulfide
575 minerals and trapped silicate liquid.

576 4 – The effect of crustal contamination in samples from the Merensky Reef is not equally
577 recorded by all TABS. This is because the interaction of sulfides with large volumes of silicate
578 magma obscures the effect of crustal contamination for more chalcophile elements. Therefore, As
579 and Sb concentrations are more likely to record crustal contamination.

580 5 – The distribution of PGE, TABS and Se within the Merensky Reef does not require the
581 presence of nanoclusters and can be modelled using the partition coefficients of each element.

582

583 **5.9 - Acknowledgements**

584 *This work was supported by a Canada Research Chair program grant to Sarah-Jane Barnes*
585 *(215503) and Discovery Grant 1884-2013. We would like to thank Dany Savard and Audrey*
586 *Lavoie (LabMaTer, UQAC) for their assistance with HG-AFS analyses. This manuscript*
587 *benefited from insightful comments from Dr. Hannah Hughes and one anonymous reviewer, and*
588 *careful editorial handling by Dr. Greg Shellnutt.*

589

590

591

592

593

594

595

596

597

598

599

600

601 **5.10 - References**

- 602 Arevalo, R., McDonough, W.F., 2010. Chemical variations and regional diversity observed in
603 MORB. *Chemical Geology* 271(1-2), 70-85.
- 604 Arguin, J.P., Pagé, P., Barnes, S-J., Yu, S.Y., Song, X.Y., 2016. The effect of chromite
605 crystallization on the distribution of osmium, iridium, ruthenium and rhodium in picritic
606 magmas: an example from the Emeishan Large Igneous Province, Southwestern
607 China. *Journal of Petrology* 57(5), 1019-1048.
- 608 Ballhaus, C., Bockrath, C., Wohlgemuth-Ueberwasser, C., Laurenz, V., Berndt, J., 2006.
609 Fractionation of the noble metals by physical processes. *Contributions to Mineralogy and
610 Petrology* 152(6), 667-684.
- 611 Barnes, S.J., Fisher, L.A., Godel, B., Pearce, M.A., Maier, W.D., Paterson, D., Howard D.L.,
612 Ryan C.G., Laird, J.S. (2016) Primary cumulus platinum minerals in the Monts de Cristal
613 Complex, Gabon: magmatic microenvironments inferred from high-definition X-ray
614 fluorescence microscopy. *Contributions to Mineralogy and Petrology* 171(3), 23.
- 615 Barnes, S-J., Ripley, E.M., 2016. Highly siderophile and strongly chalcophile elements in
616 magmatic ore deposits. *Reviews in Mineralogy and Geochemistry* 81(1), 725-774.
- 617 Barnes, S-J., 2016. Chalcophile Elements. In: White WM (Ed.) *Encyclopedia of Geochemistry: A
618 Comprehensive Reference Source on the Chemistry of the Earth*, Part of the series
619 *Encyclopedia of Earth Sciences Series*, pp 1-5.
- 620 Barnes, S-J., Savard, D., Bédard, L.P., Maier, W.D., 2009. Selenium and sulfur concentrations in
621 the Bushveld Complex of South Africa and implications for formation of the platinum-
622 group element deposits. *Mineralium Deposita* 44(6), 647.
- 623 Barnes, S-J., Maier, W.D., Curl, E.A., 2010. Composition of the marginal rocks and sills of the
624 Rustenburg Layered Suite, Bushveld Complex, South Africa: implications for the
625 formation of the platinum-group element deposits. *Economic Geology* 105(8), 1491-
626 1511.
- 627 Barnes, S-J., Maier, W.D., 2002. Platinum-group elements and microstructures of Normal
628 Merensky Reef from Impala Platinum Mines, Bushveld Complex. *Journal of Petrology*
629 43(1), 103-128.
- 630 Brenan, J.M., 2015. Se–Te fractionation by sulfide–silicate melt partitioning: Implications for the
631 composition of mantle-derived magmas and their melting residues. *Earth and Planetary
632 Science Letters* 422, 45-57.
- 633 Brüggemann, G.E., Naldrett, A.J., Asif, M., Lightfoot, P.C., Gorbachev, N.S., Fedorenko, V.A.,
634 1993. Siderophile and chalcophile metals as tracers of the evolution of the Siberian Trap
635 in the Noril'sk region, Russia. *Geochimica et Cosmochimica Acta* 57(9), 2001-2018.

636 Canali, A.C., Brenan, J.M., Sullivan, N.A., 2017. Solubility of platinum-arsenide melt and
637 sperrylite in synthetic basalt at 0.1 MPa and 1200° C with implications for arsenic
638 speciation and platinum sequestration in mafic igneous systems. *Geochimica et*
639 *Cosmochimica Acta* 216, 153-168.

640 Cawthorn, R.G., 2015. The Bushveld Complex, South Africa. In: *Layered Intrusions*, Springer,
641 Dordrecht, pp. 517-587.

642 Chakraborty, I., Pradeep, T., 2017. Atomically precise clusters of noble metals: emerging link
643 between atoms and nanoparticles. *Chemical Reviews* 117(12), 8208-8271.

644 Dare, S.A.S., Barnes, S-J., Prichard, H.M., Fisher, P.C., 2010a. The timing and formation of
645 platinum-group minerals from the Creighton Ni-Cu-platinum-group element sulfide
646 deposit, Sudbury, Canada: Early crystallization of PGE-rich sulfarsenides. *Economic*
647 *Geology* 105, 1071-1096.

648 Dare, S.A.S., Barnes, S-J., Prichard, H.M., 2010b. The distribution of platinum group elements
649 (PGE) and other chalcophile elements among sulfides from the Creighton Ni-Cu-PGE
650 sulfide deposit, Sudbury, Canada, and the origin of palladium in pentlandite. *Mineralium*
651 *Deposita* 45, 765-793.

652 Dare, S.A.S., Barnes, S-J., Prichard, H.M., Fisher, P.C., 2014. Mineralogy and geochemistry of
653 Cu-rich ores from the McCreedy East Ni-Cu-PGE deposit (Sudbury, Canada):
654 Implications for the behavior of platinum group and chalcophile elements at the end of
655 crystallization of a sulfide liquid. *Economic Geology* 109, 343-366.

656 Djon, M.L.N., Barnes, S-J., 2012. Changes in sulfides and platinum-group minerals with the
657 degree of alteration in the Roby, Twilight, and High Grade Zones of the Lac des Iles
658 Complex, Ontario, Canada. *Mineralium Deposita* 47, 875-896.

659 Duran, C.J., Barnes, S-J., Corkery, J.T., 2016. Trace element distribution in primary sulfides and
660 Fe-Ti oxides from the sulfide-rich pods of the Lac des Iles Pd deposits, Western Ontario,
661 Canada: Constraints on processes controlling the composition of the ore and the use of
662 pentlandite compositions in exploration. *Journal of Geochemical Exploration* 166, 45-63.

663 Duran, C.J., Barnes, S-J., Pleše, P., Prašek, M.K., Zientek, M.L., Pagé, P., 2017. Fractional
664 crystallization-induced variations in sulfides from the Noril'sk-Talnakh mining district
665 (polar Siberia, Russia). *Ore Geology Reviews* 90, 326-351.

666 Eales, H.V., Cawthorn, R.G., 1996. The Bushveld Complex. In: Cawthorn RG (Ed.) *Layered*
667 *intrusions*. Amsterdam, Elsevier, pp. 181-229.

668 Eales, H.V., Costin, G., 2012. Crustally contaminated komatiite: primary source of the
669 chromitites and Marginal, Lower, and Critical Zone magmas in a staging chamber
670 beneath the Bushveld Complex. *Economic Geology* 107(4), 645-665.

671 Godel, B., Barnes, S-J., Maier, W.D., 2006. 3-D distribution of sulphide minerals in the Merensky
672 Reef (Bushveld Complex, South Africa) and the JM Reef (Stillwater Complex, USA) and
673 their relationship to microstructures using X-ray computed tomography. *Journal of*
674 *Petrology* 47(9), 1853-1872.

675 Godel, B., Barnes, S-J., Maier, W.D., 2007. Platinum-group elements in sulphide minerals,
676 platinum-group minerals, and whole-rocks of the Merensky Reef (Bushveld Complex,
677 South Africa): Implications for the formation of the reef. *Journal of Petrology* 48, 1569-
678 1604.

679 Godel, B., Barnes, S-J., Maier, W.D., 2011. Parental magma composition inferred from in situ
680 trace elements in cumulus and intercumulus silicate minerals: example from the lower
681 and lower critical zones of the Bushveld Complex (South-Africa). *Lithos* 125, 537-552.

682 Godel, B., González-Álvarez, I., Barnes, S.J., Barnes, S-J., Parker, P., Day, J., 2012. Sulfides and
683 sulfarsenides from the Rosie nickel prospect, Duketon greenstone belt, Western Australia.
684 *Economic Geology* 107, 275-294.

685 González-Jiménez, J.M., Reich, M., 2017. An overview of the platinum-group element
686 nanoparticles in mantle-hosted chromite deposits. *Ore Geology Reviews* 81, 1236-1248.

687 González-Jiménez, J.M., Deditius, A., Gervilla, F., Reich, M., Suvorova, A., Roberts, M.P.,
688 Proenza, J.A., 2018. Nanoscale partitioning of Ru, Ir, and Pt in base-metal sulfides from
689 the Caridad chromite deposit, Cuba. *American Mineralogist* 103(8), 1208-1220.

690 González-Jiménez, J.M., Roqué-Rosell, J., Jiménez-Franco, A., Tassara, S., Nieto, F., Gervilla,
691 F., Schilling, M., 2019. Magmatic platinum nanoparticles in metasomatic silicate glasses
692 and sulfides from Patagonian mantle xenoliths. *Contributions to Mineralogy and*
693 *Petrology* 174(5), 47.

694 Hall, A.L., 1932. The Bushveld Igneous Complex in the central Transvaal. Geological Society,
695 South Africa, *Memoir* 28: pp. 544.

696 Harmer, R.E., Sharpe, M.R., 1985. Field relations and strontium isotope systematics of the
697 Eastern Bushveld Complex. *Economic Geology* 80, 813-837.

698 Harris, E.R., Kinnaird, J.A., Harris, C., Horstmann, U.E., 2005. A new look at sulphide
699 mineralisation of the northern limb, Bushveld Complex: a stable isotope study. *Applied*
700 *Earth Science* 114(4), 252-263.

701 Hattori, K.H., Arai, S., Clarke, D.B., 2002. Selenium, tellurium, arsenic and antimony contents of
702 primary mantle sulfides. *Canadian Mineralogy* 40(2), 637-650.

703 Helmy, H.M., Ballhaus, C., Fonseca, R., Nagel, T., 2013. Fractionation of platinum, palladium,
704 nickel, and copper in sulfide-arsenide systems at magmatic temperature. *Contributions to*
705 *Mineralogy and Petrology* 166, 1725-1737.

706 Helmy, H.M., Bragagni, A., 2017. Platinum-group elements fractionation by selective
707 complexing, the Os, Ir, Ru, Rh-arsenide-sulfide systems above 1020°C. *Geochimica et*
708 *Cosmochimica Acta* 216, 169-183.

- 709 Holness, M.B., Vukmanovic, Z., Mariani, E., 2017. Assessing the role of compaction in the
710 formation of adcumulates: a microstructural perspective. *Journal of Petrology* 58(4), 643-
711 673.
- 712 Hu, Z., Gao, S., 2008. Upper crustal abundances of trace elements: a revision and
713 update. *Chemical Geology* 253(3-4), 205-221.
- 714 Hutchinson, D., McDonald, I., 2008. Laser ablation ICP-MS study of platinum-group elements in
715 sulphides from the Platreef at Turfspruit, northern limb of the Bushveld Complex, South
716 Africa. *Mineralium Deposita* 43, 695-711.
- 717 Hutchinson, D., Foster, J., Pritchard, H., Gilbert, S., 2015. Concentration of particulate platinum-
718 group minerals during magma emplacement; a case study from the Merensky Reef,
719 Bushveld Complex. *Journal of Petrology* 56, 113-159.
- 720 Junge, M., Wirth, R., Oberthür, T., Melcher, F., Schreiber, A., 2015. Mineralogical siting of
721 platinum-group elements in pentlandite from the Bushveld Complex, South Africa.
722 *Mineralium Deposita* 50, 41-54.
- 723 Kamenetsky, V.S., Park, J.W., Mungall, J.E., Pushkarev, E.V., Ivanov, A.V., Kamenetsky, M.B.,
724 Yaxley, G.M., 2015. Crystallization of platinum-group minerals from silicate melts:
725 Evidence from Cr-spinel-hosted inclusions in volcanic rocks. *Geology* 43(10), 903-906.
- 726 Karykowski, B.T., Yang, S.H., Maier, W.D., Lahaye, Y., Lissenberg, C.J., O'Brien, H., 2017. In
727 situ Sr isotope compositions of plagioclase from a complete stratigraphic profile of the
728 Bushveld Complex, South Africa: Evidence for extensive magma mixing and
729 percolation. *Journal of Petrology* 58(11), 2285-2308.
- 730 Keith, M., Smith, D.J., Jenkin, G.R.T., Holwell, D.A., Dye, M.D., 2018. A review of Te and Se
731 systematics in hydrothermal pyrite from precious metal deposits: Insights into ore-
732 forming processes. *Ore Geology Reviews* 96, 269-282.
- 733 König, S., Luguet, A., Lorand, J-P., Wombacher, F., Lissner, M., 2012. Selenium and tellurium
734 systematics of the Earth's mantle from high precision analyses of ultra-depleted orogenic
735 peridotites. *Geochimica et Cosmochimica Acta* 86, 354-366.
- 736 König, S., Lorand, J-P., Luguet, A., Pearson, D.G., 2014. A non-primitive origin of near-
737 chondritic S–Se–Te ratios in mantle peridotites: implications for the Earth's late
738 accretionary history. *Earth Planetary Science Letters* 385, 110-121.
- 739 König, S., Lissner, M., Lorand, J-P., Bragagni, A., Luguet, A., 2015. Mineralogical control of
740 selenium, tellurium and highly siderophile elements in the Earth's mantle: Evidence from
741 mineral separates of ultra-depleted mantle residues. *Chemical Geology* 396, 16-24.

- 742 Le Vaillant, M., Barnes, S.J., Fiorentini, M.L., Barnes, S.-J., Bath, A., Miller, J., 2018. Platinum-
743 group element and gold contents of arsenide and sulfarsenide minerals associated with Ni
744 and Au deposits in Archean greenstone belts. *Mineralogical Magazine* 82(3), 625-647.
- 745 Leshner, C.M., Burnham, O.M., 2001. Multicomponent elemental and isotopic mixing in Ni–Cu–
746 (PGE) ores at Kambalda, Western Australia. *Canadian Mineralogist* 39(2), 421-446.
- 747 Li, Y., Audétat, A., 2015. Effects of temperature, silicate melt composition, and oxygen fugacity
748 on the partitioning of V, Mn, Co, Ni, Cu, Zn, As, Mo, Ag, Sn, Sb, W, Au, Pb, and Bi
749 between sulfide phases and silicate melt. *Geochimica et Cosmochimica Acta* 162, 25-45.
- 750 Li, C., Ripley, E.M., 2005. Empirical equations to predict the sulfur content of mafic magmas at
751 sulfide saturation and applications to magmatic sulfide deposits. *Mineralium
752 Deposita* 40(2), 218-230.
- 753 Li, C., Maier, W.D., de Waal, S.A., 2001. The role of magma mixing in the genesis of PGE
754 mineralization in the Bushveld Complex: Thermodynamic calculations and new
755 interpretations. *Economic Geology* 96(3), 653-662.
- 756 Liang, Q.L., Song, X.Y., Wirth, R., Chen, L.M., Dai, Z.H., 2019. Implications of nano-and
757 micrometer-size platinum-group element minerals in base metal sulfides of the
758 Yangliuping Ni-Cu-PGE sulfide deposit, SW China. *Chemical Geology* 517, 7-21.
- 759 Lissner, M., König, S., Luguët, A., Le Roux, P., Schuth, S., Heuser, A., le Roex, A.P., 2014.
760 Selenium and tellurium systematics in MORBs from the southern Mid-Atlantic Ridge
761 (47–50 S). *Geochimica et Cosmochimica Acta* 144, 379-402.
- 762 Liu, Y., Brenan, J., 2015. Partitioning of platinum-group elements (PGE) and chalcogens (Se, Te,
763 As, Sb, Bi) between monosulfide-solid solution (MSS), intermediate solid solution (ISS)
764 and sulfide liquid at controlled f_{O_2} – f_{S_2} conditions. *Geochimica et Cosmochimica Acta*
765 159, 139-161.
- 766 Lyubetskaya, T., Korenaga, J., 2007. Chemical composition of Earth's primitive mantle and its
767 variance: 1. Method and results. *Journal of Geophysical Research* 112, B03211.
- 768 Lodders, K., 2003. Solar system abundances and condensation temperatures of the elements. *The
769 Astrophysical Journal* 591, 1220-1247.
- 770 Lorand, J-P., Alard, O., Luguët, A., Keays, R.R., 2003. Sulfur and selenium systematics of the
771 subcontinental lithospheric mantle: inferences from the Massif Central xenolith suite
772 (France). *Geochimica et Cosmochimica Acta* 67(21), 4137-4151.
- 773 Lorand, J-P., Alard, O., 2010. Determination of selenium and tellurium concentrations in
774 Pyrenean peridotites (Ariege, France): new insight into S/Se/Te systematics of the upper
775 in mantle samples. *Chemical Geology* 278(1-2), 120-130.

776 Luguet, A., Behrens, M., Pearson, D.G., König, S., Herwartz, D., 2015. Significance of the whole
777 rock Re–Os ages in cryptically and modally metasomatised cratonic peridotites:
778 Constraints from HSE–Se–Te systematics. *Geochimica et Cosmochimica Acta* 164, 441-
779 463.

780 Maier, W.D., Arndt, N.T., Curl, E.A., 2000. Progressive crustal contamination of the Bushveld
781 Complex: evidence from Nd isotopic analyses of the cumulate rocks. *Contributions to
782 Mineralogy and Petrology* 140(3), 316-327.

783 Maier, W.D., Barnes, S-J., Groves, D.I., 2013. The Bushveld Complex, South Africa: formation
784 of platinum–palladium, chrome-and vanadium-rich layers via hydrodynamic sorting of a
785 mobilized cumulate slurry in a large, relatively slowly cooling, subsiding magma
786 chamber. *Mineralium Deposita* 48(1), 1-56.

787 Maier, W.D., Rasmussen, B., Fletcher, I., Godel, B., Barnes, S.J., Fisher, L., Yang, S., Huhma,
788 H., Lahaye, Y., 2015. Petrogenesis of the ~2.77 Ga Monts de Cristal Complex, Gabon:
789 evidence for direct precipitation of Pt- arsenides from basaltic magma. *Journal of
790 Petrology* 56, 1285-308.

791 Maier, W.D., Barnes, S-J., Karykowski, B.T., 2016. A chilled margin of komatiite and Mg-rich
792 basaltic andesite in the western Bushveld Complex, South Africa. *Contributions to
793 Mineralogy and Petrology* 171(6), 57.

794 Mansur, E.T., Barnes, S-J., Duran, C.J., Sluzhenikin, S.F., 2019a,.Distribution of chalcophile and
795 platinum-group elements among pyrrhotite, pentlandite, chalcopyrite and cubanite from
796 the Noril'sk-Talnakh ores: implications for the formation of platinum-group
797 minerals. *Mineralium Deposita*, 1-18.

798 Mansur, E.T., Barnes, S-J., Savard, D., Webb, P.C., 2019b. Determination of Te, As, Bi, Sb and
799 Se (TABS) in Geological Reference Materials and GeoPT Proficiency Test Materials by
800 Hydride Generation-Atomic Fluorescence Spectrometry (HG-AFS). *Geostandards and
801 Geoanalytical Research*.

802 Mansur, E.T., Barnes, S-J., 2020. The roles of Te, As, Bi, Sn and Sb during the formation of
803 platinum-group-element reef deposits: examples from the Bushveld and Stillwater
804 Complexes. *Geochimica et Cosmochimica Acta*. doi.org/10.1016/j.gca.2020.01.008

805 McDonough, W.F., Sun, S.S., 1995. The composition of the Earth. *Chemical Geology* 120(3-4),
806 223-253.

807 Mungall, J.E., Brenan, J.M., 2014. Partitioning of platinum-group elements and Au between
808 sulfide liquid and basalt and the origins of mantle-crust fractionation of the chalcophile
809 elements. *Geochimica et Cosmochimica Acta* 125: 265-289.

810 Mungall, J.E., Kamo, S.L., McQuade, S., 2016. U–Pb geochronology documents out-of-sequence
811 emplacement of ultramafic layers in the Bushveld Igneous Complex of South
812 Africa. *Nature Communications* 7, 13385.

813 Naldrett, A.J., Von Gruenewaldt, G., 1989. Association of platinum-group elements with
814 chromitite in layered intrusions and ophiolite complexes. *Economic Geology* 84(1), 180-
815 187.

816 Naldrett, A.J., Wilson, A., Kinnaird, J., Chunnett, G., 2009. PGE tenor and metal ratios within
817 and below the Merensky Reef, Bushveld Complex: implications for its genesis. *Journal of*
818 *Petrology* 50(4), 625-659.

819 O'Driscoll, B., González-Jiménez, J.M., 2016. Petrogenesis of the platinum-group minerals.
820 *Reviews in Mineralogy and Geochemistry* 81, 489-578.

821 Patten, C., Barnes, S-J., Mathez, E.A., Jenner, F.E., 2013. Partition coefficients of chalcophile
822 elements between sulfide and silicate melts and the early crystallization history of sulfide
823 liquid: LA-ICP-MS analysis of MORB sulfide droplets. *Chemical Geology* 358, 170-188.

824 Patten, C.G., Pitcairn, I.K., Teagle, D.A., Harris, M., 2016. Mobility of Au and related elements
825 during the hydrothermal alteration of the oceanic crust: implications for the sources of
826 metals in VMS deposits. *Mineralium Deposita* 51, 179-200.

827 Peck, D.C., Keays, R.R., 1990. Insights into the behavior of precious metals in primitive, S-
828 undersaturated magmas; evidence from the Heazlewood River Complex, Tasmania.
829 *Canadian Mineralogist* 28, 553-577.

830 Péntek, A., Molnár, F., Watkinson, D.H., Jones, P.C., 2008. Footwall-type Cu-Ni-PGE
831 Mineralization in the Broken Hammer Area, Wisner Township, North Range, Sudbury
832 Structure. *Economic Geology* 103, 1005-1028.

833 Piña, R., Gervilla, F., Barnes, S-J., Ortega, L., Lunar, R., 2012. Distribution of platinum-group
834 and chalcophile elements in the aguablanca Ni-Cu sulfide deposit (SW Spain): Evidence
835 from a LA-ICP-MS study. *Chemical Geology* 302, 61-75.

836 Piña, R., Gervilla, F., Barnes, S-J., Ortega, L., Lunar, R., 2013. Partition coefficients of platinum
837 group and chalcophile elements between arsenide and sulfide phases as determined in the
838 Beni Bousera Cr-Ni mineralization (North Morocco). *Economic Geology* 108(5), 935-
839 951.

840 Piña, R., Gervilla, F., Barnes, S-J., Ortega, L., Lunar, R., 2015. Liquid immiscibility between
841 arsenide and sulfide melts: Evidence from a LA-ICP-MS study in magmatic deposits at
842 Serranía de Ronda (Spain). *Mineralium Deposita* 50, 265-279.

843 Pitcairn, I.K., 2004. Sources of fluids and metals in orogenic gold deposits: the Otago Schists,
844 New Zealand. Dissertation, University of Southampton

- 845 Queffurus, M., Barnes, S-J., 2015. A review of sulfur to selenium ratios in magmatic nickel–
846 copper and platinum-group element deposits. *Ore Geology Reviews* 69, 301-324.
- 847 Reczko, B.F.F., Oberholzer, J.D., Res, M., Erikson, P.G., Schriber, U.M., 1995. A re-evaluation
848 of the volcanism of the Palaeoproterozoic Pretoria Group (Kaalvaal craton) and a
849 hypothesis on basin development. *Journal of African Earth Sciences* 21, 505–519.
- 850 Ripley, E.M., 1990. Se/S ratios of the Virginia Formation and Cu–Ni mineralization in the
851 Babbitt area, Duluth Complex, Minnesota. *Economic Geology* 85, 1935-1940.
- 852 Robertson, J.C., Barnes, S.J., Le Vaillant, M., 2015. Dynamics of magmatic sulphide droplets
853 during transport in silicate melts and implications for magmatic sulphide ore
854 formation. *Journal of Petrology* 56(12), 2445-2472.
- 855 Roelofse, F., Ashwal, L.D., 2012. The Lower Main Zone in the Northern Limb of the Bushveld
856 Complex – a >1.3 km thick sequence of intruded and variably contaminated crystal
857 mushes. *Journal of Petrology* 53(7), 1449-1476.
- 858 Roelofse, F., Ashwal, L.D., Romer, R.L., 2015. Multiple, isotopically heterogeneous plagioclase
859 populations in the Bushveld Complex suggest mush intrusion. *Geochemistry* 75(3), 357-
860 364.
- 861 Rose-Weston L, Brenan JM, Fei Y, Secco RA, Frost DJ (2009) Effect of pressure, temperature,
862 and oxygen fugacity on the metal-silicate partitioning of Te, Se, and S: Implications for
863 earth differentiation. *Geochim Cosmochim Acta* 73(15): 4598-4615.
- 864 Rudnick, R.L., Gao, S., 2003. Composition of the continental crust. In: Rudnick, R. L. (Ed.) *The*
865 *Crust*. Amsterdam: Elsevier, pp. 1-70.
- 866 Samalens, N., Barnes, S-J., Sawyer, E.W., 2017. The role of black shales as a source of sulfur and
867 semimetals in magmatic nickel-copper deposits: Example from the Partridge River
868 Intrusion, Duluth Complex, Minnesota, USA. *Ore Geology Reviews* 81(1), 173-187.
- 869 Scholten, L., Watenphul, A., Beermann, O., Testemale, D., Ames, D., Schmidt, C., 2018. Nickel
870 and platinum in high-temperature H₂O+ HCl fluids: Implications for hydrothermal
871 mobilization. *Geochimica et Cosmochimica Acta* 224, 187-199.
- 872 Scoates, J.S., Wall, C.J., 2015. Geochronology of layered intrusions. In: *Layered*
873 *intrusions*, Springer, Dordrecht, pp. 3-74.
- 874 Sharpe, M.R., Hulbert, L.J., 1985. Ultramafic sills beneath the eastern Bushveld Complex:
875 Mobilized suspensions of early lower zone cumulates in a parental magma with boninitic
876 affinities. *Economic Geology* 80, 849-871.
- 877 Sullivan, N.A., Zajacz, Z., Brenan, J.M., 2018. The solubility of Pd and Au in hydrous
878 intermediate silicate melts: the effect of oxygen fugacity and the addition of Cl and S.
879 *Geochimica et Cosmochimica Acta* 231, 15-29.
- 880 Tredoux, M., Lindsay, N.M., Davies, G., McDonald, I., 1995. The fractionation of platinum-
881 group elements in magmatic systems, with the suggestion of a novel causal mechanism.
882 *South African Journal of Geology* 98, 157-167.

- 883 Tuba, G., Molnár, F., Ames, D.E., Péntek, A., Watkinson, D.H., Jones, P.C., 2014. Multi-stage
884 hydrothermal processes involved in “low-sulfide” Cu (–Ni)–PGE mineralization in the
885 footwall of the Sudbury Igneous Complex (Canada): Amy Lake PGE zone, East Range.
886 *Mineralium Deposita* 49, 7-47.
- 887 Vukmanovic, Z., Barnes, S.J., Reddy, S.M., Godel, B., Fiorentini, M.L., 2013. Morphology and
888 microstructure of chromite crystals in chromitites from the Merensky Reef (Bushveld
889 Complex, South Africa). *Contributions to Mineralogy and Petrology* 165(6), 1031-1050.
- 890 Wang, C.Y., Wei, B., Zhou, M.F., Minh, D.H., Qi, L., 2018. A synthesis of magmatic Ni-Cu-
891 (PGE) sulfide deposits in the ~260 Ma Emeishan large igneous province, SW China and
892 northern Vietnam. *Journal of Asian Earth Sciences* 154, 162-186.
- 893 Wang, Z., Becker, H., 2013. Ratios of S, Se and Te in the silicate Earth require a volatile-rich late
894 veneer. *Nature* 499, 328-331.
- 895 Wille, M., Kramers, J.D., Nägler, T.F., Beukes, N.J., Schröder, S., Meisel, T., Voegelin, A.R.,
896 2007. Evidence for a gradual rise of oxygen between 2.6 and 2.5 Ga from Mo isotopes
897 and Re-PGE signatures in shales. *Geochimica et Cosmochimica Acta* 71(10), 2417-2435.
- 898 Wilson, A.H., 2012. A chill sequence to the Bushveld Complex: insight into the first stage of
899 emplacement and implications for the parental magmas. *Journal of Petrology* 53(6), 1123-
900 1168.
- 901 Wirth, R., Reid, D., Schreiber, A., 2013. Nanometer-sized platinum-group minerals (PGM) in
902 base metal sulfides: new evidence for an orthomagmatic origin of the Merensky Reef
903 PGE ore deposit, Bushveld Complex, South Africa. *Canadian Mineralogist* 51, 143-155.
- 904 Yang, S.H., Maier, W.D., Godel, B., Barnes, S.-J., Hanski, E., O’Brien, H., 2018. Parental magma
905 composition of the Main Zone of the Bushveld Complex: Evidence from in situ LA-ICP-
906 MS trace element analysis of silicate minerals in the cumulate rocks. *Journal of*
907 *Petrology* 60(2), 359-392.
- 908 Yierpan, A., König, S., Labidi, J., Schoenberg, R., 2019. Selenium isotope and S-Se-Te elemental
909 systematics along the Pacific-Antarctic ridge: Role of mantle processes. *Geochimica et*
910 *Cosmochimica Acta*, 249, 199-224.
- 911 Yudovskaya, M.A., Kinnaird, J.A., Grobler, D.F., Costin, G., Abramova, V.D., Dunnett, T.,
912 Barnes, S.-J., 2017. Zonation of Merensky-Style Platinum-Group Element Mineralization
913 in Turfspruit Thick Reef Facies (Northern Limb of the Bushveld Complex). *Economic*
914 *Geology* 112, 1333-1365.
- 915 Zeh, A., Ovtcharova, M., Wilson, A.H., Schaltegger, U., 2015. The Bushveld Complex was
916 emplaced and cooled in less than one million years—results of zirconology, and
917 geotectonic implications. *Earth Planetary Science Letters* 418, 103-114.

1
2
3
4
5
6
7
8

9 **Chapter 6 - The role of Te, As, Bi, Sn and Sb during the formation of**
10 **platinum-group-element reef deposits: Examples from the Bushveld and**
11 **Stillwater Complexes**

12
13
14
15

16 Eduardo T. Mansur¹, Sarah-Jane Barnes¹

17 ¹Sciences de la Terre, Université du Québec à Chicoutimi, Québec, G7H 2B1, Canada

18
19

20 **Author contributions:**

21 **Mansur** wrote the manuscript, collected and analyzed the data and created the figures.
22 **Barnes** edited the manuscript and analyzed the data.

23
24
25
26
27
28
29

30 Geochimica et Cosmochimica Acta, 2020, 272 : 235-258

31 DOI : 10.1016/j.gca.2020.01.008

32 **6.1 - Abstract**

33 The distribution of platinum-group element (PGE) and Te, As, Bi, Sb and Sn (TABS) in whole-
34 rock samples, and in disseminated base metal sulfides (BMS) pentlandite, pyrrhotite and
35 chalcopyrite from the Bushveld and Stillwater Complexes are reported. The samples are from: the
36 Merensky Reef (Bushveld), the J-M Reef (Stillwater), Picket Pin deposit (Stillwater), and also
37 barren sulfide-bearing samples, from outside the reef intervals from both intrusions. The objective
38 of the study was to document the distribution of PGE and TABS in PGE-reef deposits, and to
39 investigate whether TABS play a significant role during the formation of PGE-reef deposits.

40 The whole-rock concentrations of PGE and TABS (except for As) correlate with S and PGE, and
41 thus their distribution appear to be controlled by BMS. The distribution of As, and to a lesser
42 extent Sb, correlate with incompatible elements and with changes in K-phlogopite compositions,
43 suggesting that these elements are controlled both by the amount of trapped liquid in cumulate
44 rocks, and the amount of sulfides. The possible role of TABS in forming pre-nucleation clusters
45 (nanonuggets) to enrich the reefs in PGE is considered and discarded, because the ratio of
46 TABS/PGE < 0.3 is too low for TABS to form pre-nucleation clusters with PGE. A model where
47 both the PGE and TABS are initially collected by a base metal sulfide liquid is favoured. During
48 equilibrium crystallization of the sulfide liquid, Pd, Pt and the TABS were incompatible with the
49 crystallizing BMS, and concentrated in the fractionated liquid eventually crystallizing as TABS-
50 rich PGM. However, a portion of Pd, Pt and TABS also partitioned into the crystallizing BMS.
51 During cooling and S-loss they exsolved from the BMS as PGM included in the BMS. In the
52 reefs, the ratio of PGE/TABS is very high, and thus during exsolution all of the TABS could be
53 accommodated in PGM, and consequently the BMS of the reefs have very low TABS
54 concentrations. In contrast, outside the reefs the PGE/TABS ratios are low, and thus some TABS
55 remained in the BMS, resulting in the BMS outside the reefs having higher TABS concentrations
56 than those from within the reefs.

57 Keywords: Te, As, Bi, Sb, Sn; platinum-group elements; magmatic sulfide deposits; Bushveld Complex;
58 Stillwater Complex; platinum-group minerals.

59 **6.2 – Introduction**

60

61 It has been demonstrated that in magmatic Ni-Cu-PGE sulfide deposits the platinum-
62 group elements are bimodally distributed (Godel et al., 2007; Holwell and McDonald, 2007; Dare
63 et al., 2010b; 2014; Piña et al., 2012; Osbahr et al., 2013, 2014; Junge et al., 2015; Duran et al.,
64 2016). The PGE are present at the ppm level in the base metal sulfides (BMS) pyrrhotite,
65 pentlandite, and to a lesser extent chalcopyrite, and these host much of the PGE budget (Barnes
66 and Ripley, 2016, and references therein). The balance of the PGE is hosted by platinum-group
67 minerals (PGM). These PGM commonly consist of PGE plus one or more of the elements Te, As,
68 Bi, Sb and Sn (TABS; Barnes, 2016), or S (O’Driscoll and González-Jiménez, 2016 and
69 references therein). Understanding the influence of TABS on the distribution of PGE in magmatic
70 systems is critical given the importance of PGE in the study of various fields of geology (Harvey
71 and Day, 2016 and references therein). Moreover, there is an increasing interest in understanding
72 the geochemical cycle of volatile elements such as TABS, and in these studies BMS are
73 frequently proposed as controlling the TABS (Hattori et al., 2002; Lodders, 2003; Lorand and
74 Alard, 2010; Wang and Becker, 2013; Konig et al., 2012, 2014; Lissner et al., 2014; Patten et al.,
75 2016, 2017; Canali et al., 2017; D’Souza and Canil, 2018).

76 To date, the concentrations of TABS in Ni-Cu-PGE deposits has mainly been addressed
77 in relatively sulfide-rich deposits, for example those from Sudbury (Canada), Noril’sk-Talnakh
78 (Russia), the Platreef (South Africa) and Aguablanca (Spain) (Holwell and McDonald, 2007;
79 Dare et al., 2010a, 2010b, 2014; Piña et al., 2012; Yudovskaya et al., 2017; Mansur et al., 2019c).
80 In these deposits, the whole-rock concentrations of TABS, Pd and Pt are found to increase from
81 the Cu-poor parts of the deposits, thought to represent monosulfide solid solution (MSS)
82 cumulates, to the Cu-rich parts of the deposits, thought to represent the products of the
83 fractionated sulfide liquid (Dare et al., 2010b, 2014; Chen et al., 2013, 2015; Duran et al., 2017).
84 The TABS, Pd and Pt concentrations of the BMS show positive covariance with the whole-rock
85 values (Mansur et al., 2019c). However, the bulk of the TABS and Pt are not hosted by the BMS.

86 In the MSS cumulates, the PGM occur within BMS grains and appear to have formed
87 predominantly by exsolutions (Dare et al., 2010b; Piña et al., 2012; Duran et al., 2017; Mansur et
88 al., 2019c). In the Cu-rich portions of the deposits, some of the PGM occur as exsolutions, but
89 predominately they occur among the sulfide grains, and are thought to have crystallized from the
90 fractionated sulfide liquid (Dare et al., 2014; Duran et al., 2017; Mansur et al., 2019c).
91 Alternatively, they could have crystallized from an immiscible TABS-rich liquid which
92 segregated from the fractionated Cu-rich sulfide liquid (Helmy et al., 2007; 2010; Holwell and
93 McDonald, 2010; Piña et al., 2015; Cafagna and Jugo, 2016).

94 In the case of PGE-reef deposits, which contain disseminated sulfides, the distribution of
95 TABS has not been well documented, although a number of roles listed below have been
96 proposed for TABS. i) In order to explain the very high PGE content of the PGE-dominated
97 deposits, it has been proposed that TABS and PGE form pre-nucleation clusters (referred to as
98 nanoparticles or nanoclusters). The clusters are incorporated in a magmatic sulfide liquid, and
99 subsequently in the MSS and intermediate sulfide solid solutions (ISS) that crystallize from the
100 sulfide liquid. These clusters could remain in the BMS, or coalesce to form PGM (Tredoux et al.,
101 1995; Helmy et al., 2013; Wirth et al., 2013; Junge et al., 2015; Ling et al., 2019). ii)
102 Alternatively, the TABS and PGE could behave as in sulfide-rich deposits, but with the difference
103 that the disseminated sulfides in reefs are generally assumed to represent sulfide liquid
104 compositions, as the sulfides represent the product of equilibrium crystallization. In this case, a
105 small portion of these elements would have partitioned into MSS and ISS as they crystallized, and
106 PGM exsolved from the sulfides during cooling (Prichard et al., 2004; Godel et al., 2007; Godel
107 and Barnes, 2008a). However, given the incompatible nature of Pd, Pt and TABS (Helmy et al.,
108 2010; Patten et al., 2013; Liu and Brenan, 2015) the bulk of these elements would have
109 partitioned into the fractionated sulfide liquid, and crystallized as PGM among the sulfide grains.
110 iii) A variation of this model is that the trapped fractionated sulfide liquid became saturated in a
111 TABS-PGE rich liquid (Helmy et al., 2007, 2010; Piña et al., 2015; Cafagna and Jugo, 2016).
112 This liquid could migrate away from the sulfides, or crystallize among the sulfide grains (Holwell

113 and McDonald, 2010). iv) The TABS could have a role in fixing the PGE during dissolution of
114 the sulfides by late magmatic or metamorphic fluids. Loss of S from sulfides leads to the
115 exsolutions of PGM (Ballhaus et al., 1994; Peregoedova et al., 2004; Li and Ripley, 2006; Godel
116 and Barnes, 2008a; Djon and Barnes, 2012). If most of the BMS are dissolved leaving TABS and
117 PGE, the TABS serve to fix the PGE, as TABS-rich PGM (Wood, 2002; Scholten et al., 2018;
118 Sullivan et al., 2018).

119 In the current work we examine the distribution of PGE and TABS in whole-rock
120 samples, and in disseminated BMS from the Bushveld and Stillwater Complexes. The samples
121 comprise the main sulfide-related PGE reefs of the intrusions, the Merensky Reef (Bushveld), and
122 the J-M Reef and Picket Pin deposit (Stillwater), and also barren sulfide-bearing samples, from
123 outside the reef intervals from both intrusions. This allows assessment of the distribution of PGE
124 and TABS in PGE reef type deposits, and investigation whether TABS play a significant role
125 during the formation of PGE-dominated deposits.

126 This contribution will show that the whole-rock concentrations of Se and TABS (except
127 for As) correlate with S and PGE, and thus their distribution is controlled by BMS. The
128 distribution of As, and to a lesser extent Sb, are controlled by both the amount of liquid fraction
129 in cumulate rocks, and the amount of sulfides. The study will also show that the concentrations of
130 PGE are the highest in BMS from the reef samples, in contrast the concentrations of TABS are
131 the lowest in BMS from the same samples. The highest concentrations of TABS in BMS were
132 found in samples with the lowest whole-rock PGE contents. The formation of the PGM by pre-
133 nucleation clusters is considered, and discarded. The hypotheses that PGM are formed by
134 exsolutions, and by crystallization from the fractionated sulfide liquid is favoured. To explain the
135 contrast in the behaviour of TABS and PGE in BMS of the reefs, it is proposed that the high
136 concentration of PGE in BMS from the reef leads to the diffusion of the TABS from the BMS
137 into the PGM. Therefore, the BMS from the reefs are depleted in TABS, although the whole-rock
138 concentrations of TABS in the reefs are high.

139

140 **6.3 – Description of studied samples**

141

142 The samples of the Merensky Reef (Bushveld Complex, South Africa) are from the
143 Rustenburg and Impala mines (Fig. 6.1a). The samples from the JM-Reef (Stillwater Complex,
144 USA) are from the East Boulder and Stillwater mines (Fig. 6.1b). These rocks have been
145 previously studied documenting petrography, microstructures, PGM distribution, whole-rock
146 major and trace element, PGE and S contents of the reefs and surrounding rocks (Barnes and
147 Maier, 2002 and Prichard et al., 2004 - Impala section; Godel et al., 2007, 2010 - Rustenburg
148 section; Godel et al., 2008a, 2008b and Barnes et al., 2020 - J-M Reef package). Only a brief
149 description of the samples is provided here. The reader is directed to Barnes and Maier (2002),
150 Godel et al. (2006, 2007 and 2010), Godel and Barnes (2008a and 2008b) and Barnes et al. (2020)
151 for a more detailed description.

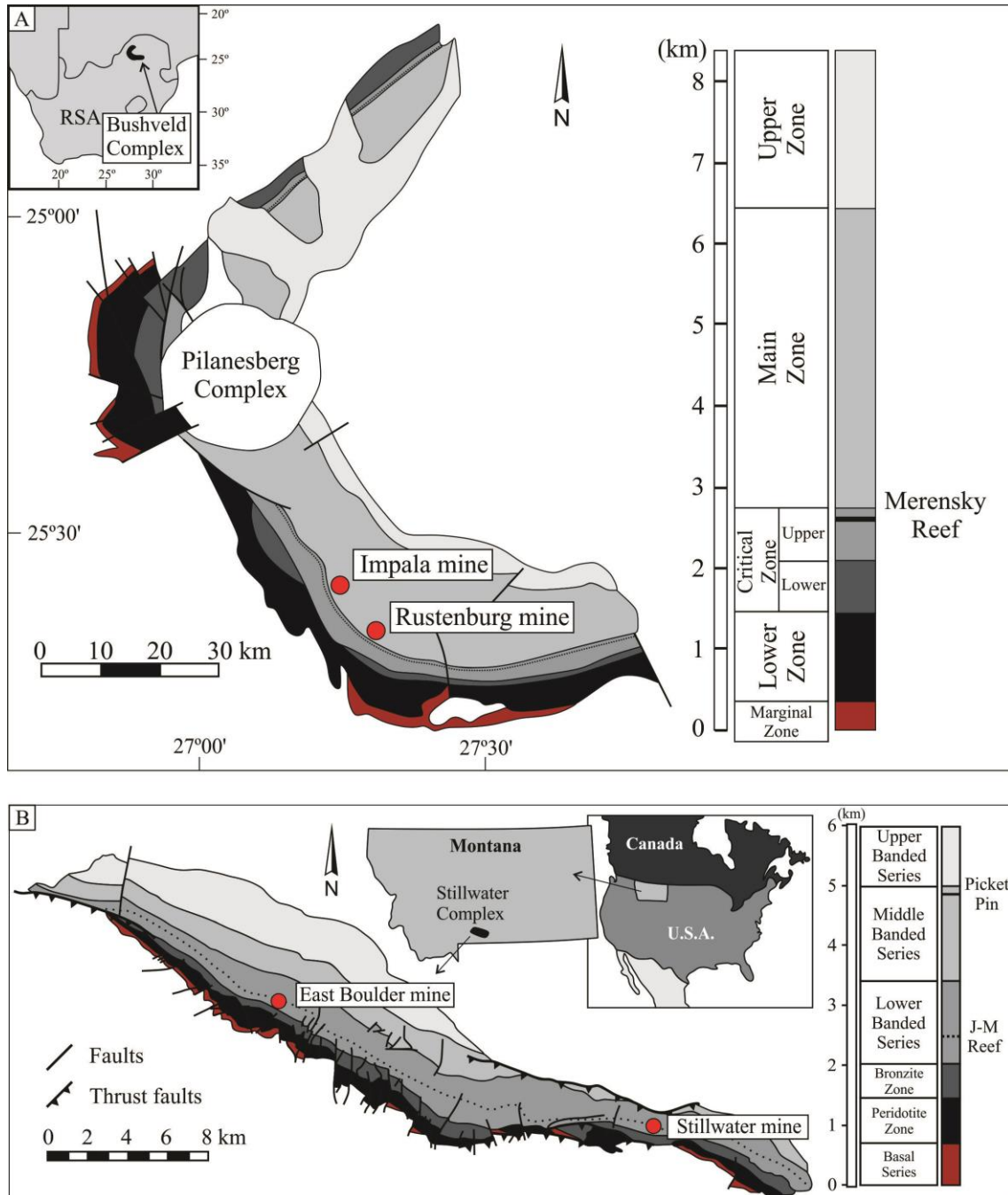
152

153 **6.3.1 – Bushveld Complex**

154

155 The Merensky Reef sections from both mines consist of a basal anorthosite followed by a
156 lower chromitite, a coarse-grained melanorite, an upper chromitite, and an overlying melanorite.
157 All lithologies contain disseminated BMS (from 0.5 to 8 vol.%), composed of pyrrhotite (Po),
158 pentlandite (Pn) and chalcopyrite (Ccp). These sulfides occur interstitial to silicate minerals. The
159 samples from the Rustenburg mine only cover the reef interval (Godel et al., 2006; 2007).
160 Sampling from the Impala section extends for around one meter below and above the Merensky
161 Reef interval into an anorthosite and a melanorite, respectively. The samples from above the reef
162 contain higher incompatible element concentrations, which were interpreted to indicate that the
163 samples have a higher amount of trapped liquid (Barnes and Maier, 2002). This section of the reef
164 also contains ~3% K-phlogoptite. Based on the concentrations of major and minor elements in K-

165 phlogopite from other localities Li et al. (2005) interpreted the K-phlogopite to have crystallized
 166 from the late silicate liquid, thus recording the presence of the fractionated liquid.
 167



168
 169 Figure 6.1 - a) Geology of the western lobe and generalized stratigraphy of the Bushveld Complex, Republic of South
 170 Africa (RSA; modified after Eales and Cawthorn, 1996; Von Gruenewaldt, 1986, 1989; Godel et al., 2006). Dashed line
 171 indicates the surficial projection of the Merensky Reef. The study localities are the Rustenburg and Impala mines. b)
 172 Geology and generalized stratigraphy of the Stillwater Complex (modified after McCallum et al., 1980; Zientek et al.,
 173 2002; Godel et al., 2006). Dashed line indicates the surficial projection of the J-M Reef. The study localities are the
 174 Stillwater and East Boulder mines.

175 Considering the Bushveld as a whole, the Merensky Reef displays significant regional
176 and local lithological variations, which are beyond the scope of this study. Details on the reef
177 variations are given by Naldrett et al. (2009) and Maier et al. (2013) and references therein.
178 Barnes and Maier (2002) and Godel et al. (2007) attributed the formation of the reef to the
179 collection of PGE by an immiscible sulfide liquid. Moreover, X-ray computed tomography results
180 show that the sulfide minerals form a vertical network on a scale of 30 centimeters. This was
181 interpreted to be the result of a sulfide liquid percolating downwards into the cumulate pile
182 (Godel et al., 2006). The higher concentrations of Os, Ir, Ru, Rh and Pt, and lower Pd/Ir ratios in
183 the chromite seams require an additional concentration step. Either laurite, (Ru,Os,Ir)S₂, and Pt-
184 Fe alloy crystallized together with chromite before BMS saturation (Prichard et al., 2004; Godel
185 et al., 2007), or the chromite layers originally contained more sulfide than currently observed. As
186 consequence of Fe loss to chromite during cooling, S and Pd were mobilized from BMS partially
187 dissolving the BMS, and enriching the remaining BMS in Os, Ir, Ru, Rh and Pt (Barnes and
188 Maier, 2002; Prichard et al., 2004).

189 Godel et al. (2007) showed that 30 to 70 % of the Os, Ir, Ru, Rh and Pd are present in the
190 BMS at the Rustenburg mine. Our current study for Rustenburg and Impala (to be presented
191 below) yields similar results. The balance of the PGE is found as PGM. The PGM assemblages
192 found in Impala and Rustenburg samples consist mainly of Pt-Pd sulfides, and Pd-Pt bismuth-
193 tellurides (Prichard et al., 2004; Godel et al., 2008b), with sulfides being more common at Impala
194 and bismuth-tellurides at Rustenburg (Fig. 6.2a). Arsenide, stanides, and antinomite PGM are
195 rare. The other PGM present in minor amounts are laurite (RuS₂), and Pt-alloys. These
196 observations are in broad agreement with PGM studies carried out on larger sample sets at both
197 mines (Kinloch, 1982; McLaren and de Villiers, 1982).

198 At both the Impala and Rustenburg mines the PGM are mainly found associated with
199 BMS, although some PGM are found included within silicate minerals (Fig. 6.2b). In both cases,
200 the majority were found in association with Ccp. Prichard et al. (2004) found that most of the
201 PGM were found at grain boundaries, or at the contact between BMS grains (Fig 6.2b). Godel et

202 al. (2010) found at Rustenburg that most of the PGM occur at the edges of the BMS grains. Based
203 on experimental work showing that BMS accommodate less PGE on cooling (Makovicky et al.,
204 1986; Makovicky, 2002), and the shape of the PGM, Prichard et al. (2004) and Godel et al.
205 (2007) interpreted the PGM included within sulfides to have formed by exsolution during
206 cooling. In addition, the reason that the PGM are more common at the edges of the sulfide grains
207 was attributed to S loss from the BMS, which results in the sulfide minerals being less able to
208 accommodate the PGE (Ballhaus et al., 1994; Peregoedova et al., 2004; Li and Ripley, 2006).
209 Based on our observations of PGM at Sudbury and Noril'sk-Talnakh (Dare et al., 2010b, 2014;
210 Duran et al., 2017; Mansur et al., 2019c), and the incompatible nature of Pd, Pt and TABS
211 (Mungall et al., 2005; Patten et al., 2013; Liu and Brennan, 2015), we would now suggest that Pd-
212 Pt PGM in contact with Ccp crystallized from the fractionated Cu-rich sulfide liquid.

213

214 **6.3.2 – Stillwater Complex**

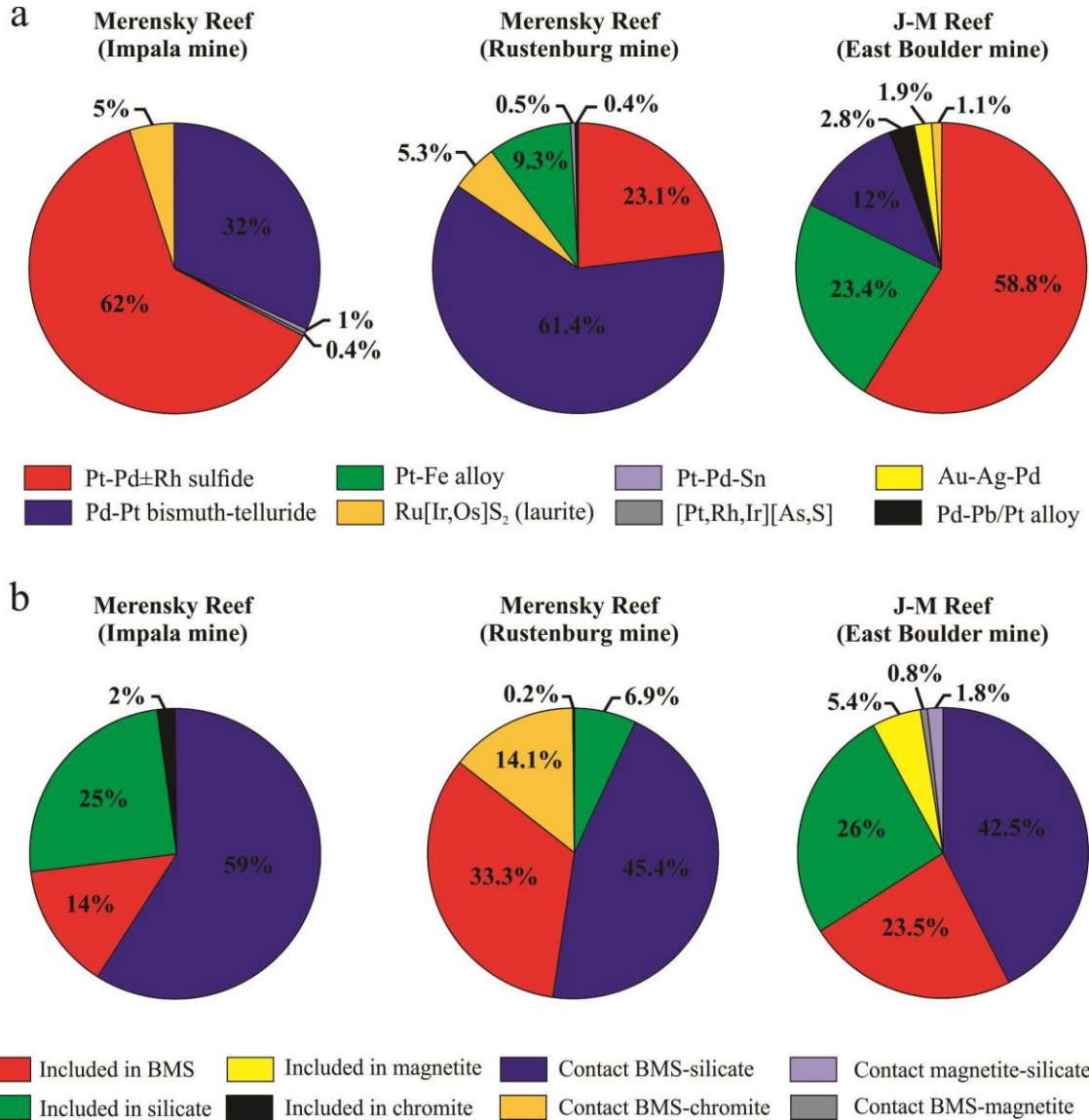
215

216 The Stillwater Complex (Fig. 6.1b) hosts the John Manville Reef (J-M Reef) and the
217 Picket Pin deposit (Boudreau, 2016 and references there in). Most of our samples come from the
218 J-M Reef, with one samples from the Picket Pin (Godel and Barnes, 2008a; Barnes et al., 2020).
219 In addition, a PGE-poor sample from the Banded series was also investigated. Samples from the
220 J-M Reef were collected from the East Boulder and Stillwater mines, and consist of anorthosite,
221 gabbronorite and troctolite. The sample from the Picket Pin deposit consists of an anorthosite,
222 whereas the sample from the lower Banded series is a leucogabbronorite of Gabbronorite II
223 (Barnes et al., 2020). All the samples contain disseminated BMS (from 2 to 7 vol.%), composed
224 of Po, Pn and Ccp.

225 Several processes are proposed to explain the enrichment of PGE in the J-M Reef. Some authors
226 propose that the BMS from the lower parts of the cumulate pile were dissolved by Cl-rich fluids
227 and PGE were collected by the fluid. When this fluid encountered a fluid-undersaturated layer,
228 the BMS and PGE precipitated (Boudreau, 2016 and references therein). In contrast, many

229 authors argue for an orthomagmatic model, where sulfide liquid collected the PGE from magma,
 230 and the sulfides collect on the cumulate pile (Campbell et al., 1983; Barnes and Naldrett, 1985;
 231 Irvine et al., 1983; Keays et al., 2012).

232



233

234 Figure 6.2 - Types (a) and textural association (b) of platinum-group minerals found in the Merensky Reef at the
 235 Impala and Rustenburg platinum mines, and the J-M Reef at the East Boulder Mine. The proportion of each mineral is
 236 given in area. Values from the Merensky Reef are from Prichard et al. (2004) for the Impala Mine, and Godel et al.
 237 (2007) for the Rustenburg Mine, and values for the J-M Reef are from Godel and Barnes (2008b).

238

239

240 In their study of the distribution of trace elements in BMS from the J-M Reef, Godel and
241 Barnes (2008a) found that Rh, Ru, Ir and Os are predominantly hosted by Pn and Po.
242 Approximately sixty percent of the Pd is hosted by Pn, with the remainder being present in PGM.
243 As in the case of the Merensky Reef samples, the PGM from the J-M Reef are predominantly Pt-
244 Pd sulfides, Pd-Pt tellurides and Pt-Fe alloy (Fig. 6.2a). In contrast to the Merensky Reef samples,
245 the Pt-Fe alloy grains are more common than the bismuth-tellurides. Minor amounts of alloys
246 (Au-Ag-Pd, Pd-Pb and Pt) and laurite are also present (Fig. 6.2a). Arsenides and antimonides
247 were not observed. Interpretation of the textures of the PGM and BMS are complicated by
248 greenschist metamorphic overprint. Most of the PGM occur included BMS, or at the contact
249 between BMS and surrounding silicates or magnetite (Fig. 6.2b). Godel et al. (2008b) interpreted
250 the PGM to have formed by two mechanisms. The PGM included in the BMS exsolved from the
251 BMS during cooling, and S-loss. In addition, a late magmatic fluid migrated into the reef and
252 partially dissolved the BMS and precipitated Pd and Pt in the form of alloys (Godel and Barnes
253 2008a).

254

255 **6.4 – Analytical Methods**

256

257 Tellurium, As, Bi, Sb and Se analyses were carried out at LabMaTer, Université du
258 Québec à Chicoutimi (UQAC). A slightly modified version of the Hydride Generation-Atomic
259 Fluorescence Spectrometry (HG-AFS) technique described by Mansur et al. (2019b) was used to
260 determine these elements. The modification was that sample size was increased from 0.2 g to 0.4
261 g. This modification was introduced to lower the dilution factor, and consequently lower the limit
262 of detection of the method. International reference materials (CH-4 and TDB-1; Natural
263 Resources Canada), GeoPt18 (KPT-1), and a blank were determined at the same time as the
264 samples. The obtained results agree with working values (*ANNEXE 13*).

265 The concentration and distribution of the minor and trace elements were determined by
266 laser ablation-inductively coupled plasma-mass spectrometry (LA-ICP-MS) at LabMaTer,
267 UQAC, using an Excimer 193 nm RESolution M-50 laser ablation system (Australian Scientific
268 Instrument) equipped with a double volume cell S-155 (Laurin Technic), and coupled with an
269 Agilent 7900 mass spectrometer. The LA-ICP-MS tuning parameters were a laser frequency of 10
270 Hz, a power of 3 to 5 mJ/pulse, a dwell time of 7.5 ms, a rastering speed of 5 to 10 $\mu\text{m/s}$, and a
271 fluence of 3 J/cm^2 . Line scans across the surface of grains were made with beam sizes of 44, 33,
272 and 25 μm , depending on grain size. The gas blank was measured for 30s before switching on the
273 laser for at least 60s. The ablated material was carried into the ICP-MS by an Ar-He gas mix at a
274 rate of 0.8–1 L/min for Ar and 350 mL/min for He, and 2mL/min of nitrogen was also added to
275 the mixture. Data reduction was carried out using the Iolite package for Igor Pro software (Paton
276 et al., 2011).

277 ^{57}Fe was used for internal standardization of BMS. Three certified reference materials
278 were used for external calibration of BMS: Laflamme Po727, which is a synthetic FeS doped with
279 ~40 ppm PGE and Au supplied by Memorial University of Newfoundland, was used to calibrate
280 for PGE, Au and S; MASS-1, which is a ZnCuFeS pressed powder pellet doped with 50–70 ppm
281 of most chalcophile elements, supplied by the United States Geological Survey (USGS), was used
282 to calibrate for Co, Cu, Zn, As, Se, Mo, Ag, Cd, Sn, Sb, Te, Tl, Pb and Bi; GSE-1g, which is a
283 natural basaltic glass fused and doped with most elements at 300-500 ppm, supplied by the
284 USGS, was used to calibrate for Ni, In, and Re using preferred values from the GeoReM database
285 (Jochum et al., 2005). MASS-1, GSE-1g, JB-MSS5 (an FeS sulfide containing 50-70 ppm of most
286 chalcophile elements, supplied by James Brennan) and UQAC-FeS1 (a synthetic sulfide developed
287 at UQAC) were used to monitor the results.

288 Polyatomic interference of $^{63}\text{Cu}^{40}\text{Ar}$ on ^{103}Rh was corrected using ^{103}Rh measured in
289 MASS-1, which contains 13.4% ^{63}Cu but no ^{103}Rh . One percent Cu produced ~0.1 ppm
290 interference. Thus, the ^{103}Rh values in Ccp are not reported as the interference is too large to be
291 corrected. Direct interferences of ^{108}Cd on ^{108}Pd and ^{115}Sn on ^{115}In were corrected by monitoring

292 ^{111}Cd and ^{118}Sn , respectively. Interference of $^{68}\text{Zn}^{40}\text{Ar}$ on ^{108}Pd is negligible as Zn is present at
293 <1000 ppm. Polyatomic interference of $^{61}\text{Ni}^{40}\text{Ar}$ on ^{101}Ru was corrected using ^{101}Ru measured in
294 a NiS blank, which does not contain Ru. One percent Ni produced ~ 0.007 ppm interference and
295 was not significant a significant part of the Ru signal.

296 For K-phlogopite analyses, ^{29}Si was used for internal standardization. GSE-1g was used
297 for external calibration, and NIST-610 and NIST-612 (silicate glasses reference materials
298 produced by National Institute of Standards and Technology), GSD-1g and Gprob-6 (USGS-
299 certified artificial basalt glasses) were used to monitor the results. The reference materials were
300 analyzed at the beginning and the end of each session to monitor a potential instrumental drift.
301 The results obtained for the monitors were generally allowing for standard deviations on the
302 working values (*ANNEXE 14*).

303 Maps of element distribution were made on different sulfide assemblages using a laser
304 frequency of 15 Hz and a power of 5 mJ/pulse. The beam size (25 to 44 μm) and the stage
305 movement speed (10 to 15 $\mu\text{m/s}$) were adapted to optimize spatial resolution and analysis time for
306 grains of different sizes. The maps were generated using the Iolite software package on the basis
307 of the time-resolved composition of each element. The maps indicate the relative concentration of
308 the elements and are semi-quantitative.

309 **6.5 – Results**

310 **6.5.1 – Whole-rock concentrations of TABS in the PGE reefs**

311

312 The whole-rock concentrations of TABS plus the previously published S, Ni, Cu and
313 PGE concentrations can be found in the *ANNEXE 15*.

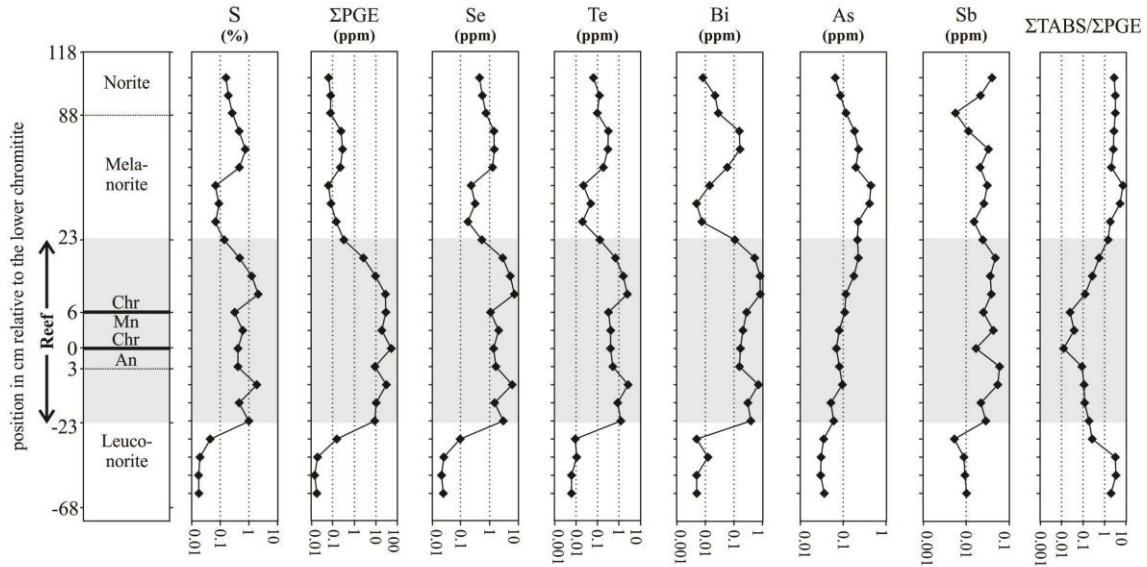
314 The concentrations of S, PGE, Se, Te, Bi, As and Sb in the Impala (Fig. 6.3a) and
315 Rustenburg (Fig. 6.3b) sections were plotted against the sample height to assess their distribution
316 through the Merensky Reef. The distributions of TABS in the Merensky Reef at both the Impala
317 and Rustenburg sections are similar. Selenium, Te and Bi correlate well with S and PGE. In the

318 reef interval, Se concentrations vary from 1 to 10 ppm, whereas Te and Bi concentrations vary
319 from 0.1 to 1 ppm. In the chromitite layers the Se, Te and Bi values are slightly lower. Above the
320 reef interval, Se ranges from 0.1 to 1 ppm, and below the reef interval the Se values are at their
321 lowest, ranging from 0.01 to 0.1 ppm. Tellurium and Bi also have a similar distribution outside
322 the reef interval, with values ranging from approximately 0.01 to 0.5 ppm above the reef, and
323 lower than 0.01 ppm below the reef. The correlation between S and Se, Te and Bi supports the
324 hypothesis that BMS are the main minerals controlling these elements. Moreover, the lowest
325 values found in samples below the reef are in agreement with the absence of BMS in the samples
326 (Fig. 6.3a).

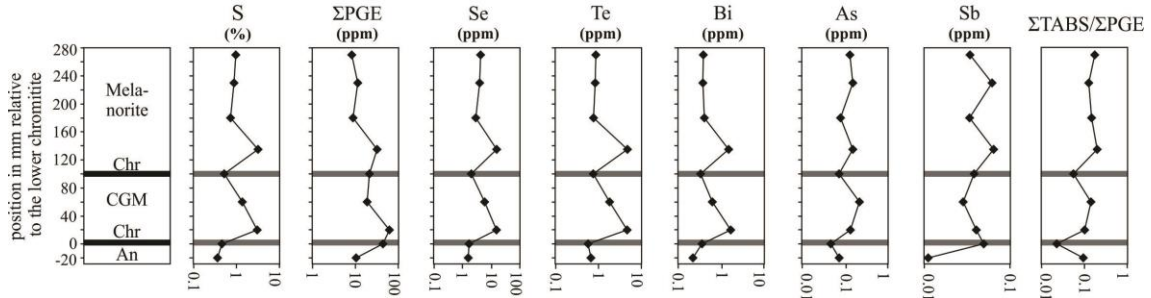
327 The Se/Te ratio ranges from 2 to 5 within the reef interval, and increases up to 10 in
328 samples above the reef (Fig. 6.3a and *ANNEXE 15*). This variation agrees with the distribution
329 of these elements being controlled by BMS. Tellurium has a higher partition coefficient into a
330 base metal sulfide liquid relative to Se (Liu and Brenan, 2015). Therefore, in samples with greater
331 amounts of sulfide minerals (higher S concentrations), Te is expected to be more concentrated
332 compared to Se (Brenan, 2015). Consequently, the Se/Te ratios are lower in samples from the reef
333 interval, compared to samples above the reef (*ANNEXE 15*).

334 Arsenic and Sb do not show a clear correlation with S, Se, Te and Bi. Arsenic
335 concentrations increase from 0.03ppm below the reef to 0.45ppm in samples slightly above the
336 reef (Fig. 6.3a). In the upper part of the Impala section they decrease. The concentrations of Sb
337 within and above the reef interval are similar, and range from 0.01 to 0.06 ppm, whereas Sb
338 concentrations below the reef interval are lower than 0.01 ppm. Arsenic concentrations are
339 slightly lower in the chromitite layers, and in contrast, the Sb values vary very little (Fig. 6.3a and
340 6.3b).

A - Impala section



B - Rustenburg section



341

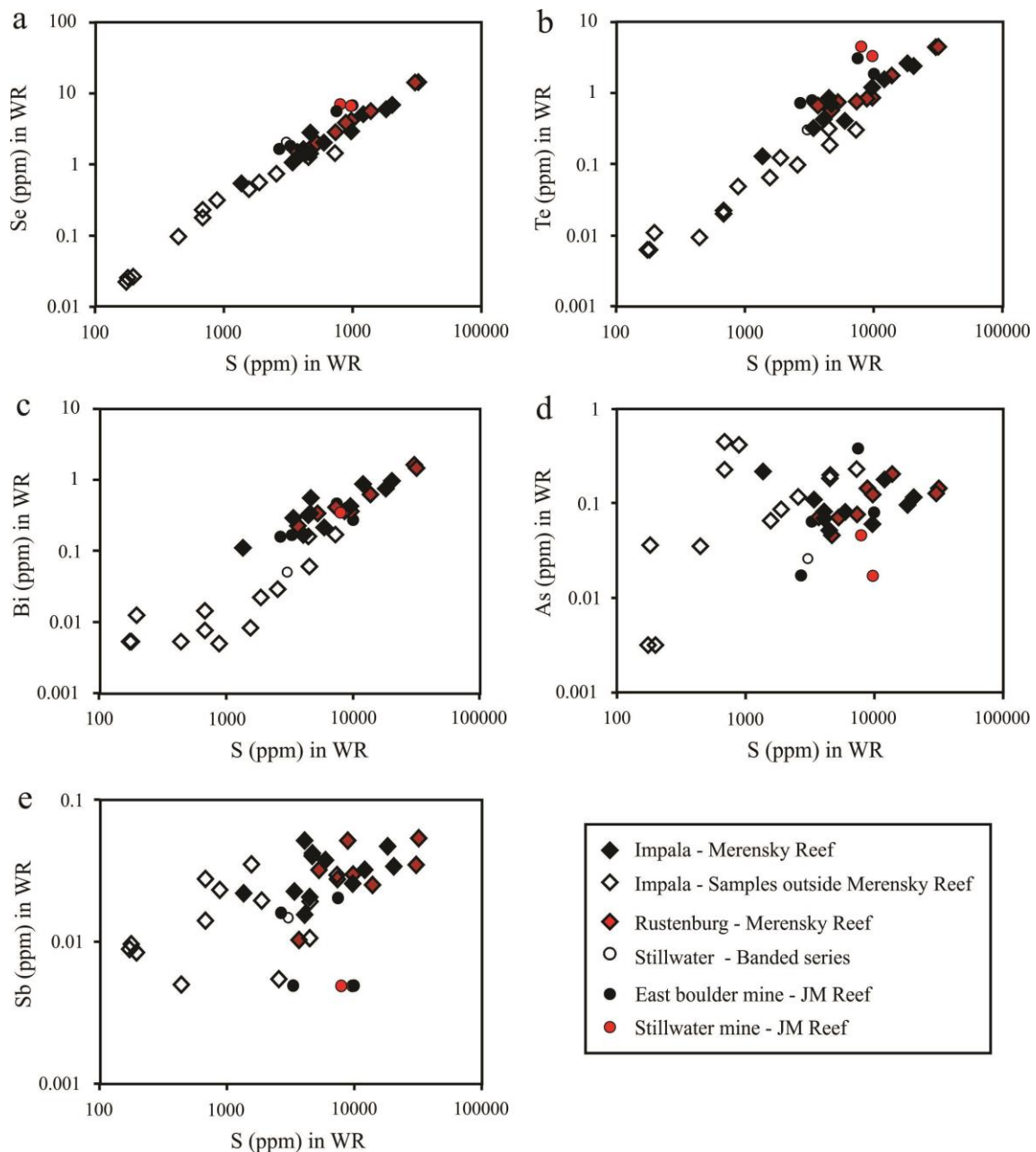
342 Figure 6.3 - Variations in whole-rock concentrations of chalcophile elements with height across the (a) Impala section
 343 and (b) Rustenburg section. Note that the vertical scales are not linear, the samples are spaced out evenly for clarity. At
 344 the Impala section the reef interval is defined by rocks containing more than 1.5 ppm Pt+Pd in whole-rock analyses,
 345 and starts 23cm below the lower chromitite and ends 23cm above it. Individual whole-rock are reported in the *ANNEXE*
 346 *15*. Abbreviations: ΣPGE: Pt+Pd+Rh+Ru+Ir+Os; ΣTABS: Te+As+Bi+Se+Sb; An: anorthosite; Chr: chromitite; CGM:
 347 coarse-grained melanorite; Mn: melanorite.

348

349 The absolute concentration of TABS relative to PGE is lower in samples from the reef
 350 interval (Fig. 6.3a). Within the reef interval, the ratio of the sum of TABS over the sum PGE
 351 ranges from 0.01 to 1, whereas above and below the reef this ratio is mostly higher than 1 (Fig.
 352 6.3a). Thus, although all these elements are concentrated in the reef samples, the PGE were more
 353 efficiently concentrated relative to TABS. This is in agreement with the observation that PGE
 354 have higher partition coefficients into a sulfide liquid than TABS (Mungall and Brenan, 2014;
 355 Barnes and Ripley, 2016 and references therein).

356 The concentrations of TABS are shown plotted against the concentrations of S in samples
357 from the Stillwater and Bushveld complexes (Fig. 6.4). For both the Stillwater and Bushveld
358 complexes, Se, Te and Bi concentrations correlate with S values (Fig. 6.4a, 6.4b and 6.4c). The
359 concentrations of these elements in samples from the J-M Reef, Banded Series and Merensky
360 Reef are in the same range (Fig. 6.4a, 6.4b and 6.4c). In the case of the Merensky Reef, Sb shows
361 a weak correlation with S, with samples from inside the Merensky Reef having slightly higher
362 values (0.1 to 0.6 ppm) than samples outside the reef (Fig. 6.3 and 6.4e). Some samples from the
363 Stillwater follow the same trend, but most contain less than detection level of Sb. Arsenic does
364 not show a clear correlation with S (Fig. 6.4d). In fact, As concentrations in samples from outside
365 the Merensky Reef are slightly higher compared to those found in samples from within the reef
366 (Fig. 6.3). The lack of clear correlation between As, and to a lesser extent Sb, with S shows that
367 BMS are not the only minerals controlling these elements. This is in agreement with the low
368 partition coefficients of As and Sb into the sulfide liquid (Li and Audétat, 2015), and thus their
369 status as slightly chalcophile elements, in contrast with PGE, defined as highly chalcophile
370 (Barnes, 2016).

371 Based on the incompatible element content of the rocks for the Impala section, Barnes
372 and Maier (2002) concluded that samples directly above the Merensky Reef interval have a
373 higher trapped liquid fraction. Given that both As and Sb are incompatible with the cumulate
374 minerals present (orthopyroxene and plagioclase), these elements could also be present in the
375 trapped liquid fraction. The positive correlation between the concentrations of As and Hf, with
376 samples lying along a tie-line between the B1-B-2 melt mixture and cumulate silicate minerals
377 (Barnes et al., 2002) support this hypothesis (Fig. 6.5a). Samples slightly displaced to the As-
378 enriched side of the line reflect the presence of sulfides (Fig. 6.5a). For Sb, in samples containing
379 less than 4000 ppm S the samples also lie along a tie-line between the melt and cumulate silicates.
380 Samples with more than 4000 ppm S are displaced on the Sb-rich side of the tie-line, reflecting
381 the presence of sulfides (Fig. 6.5b).



382

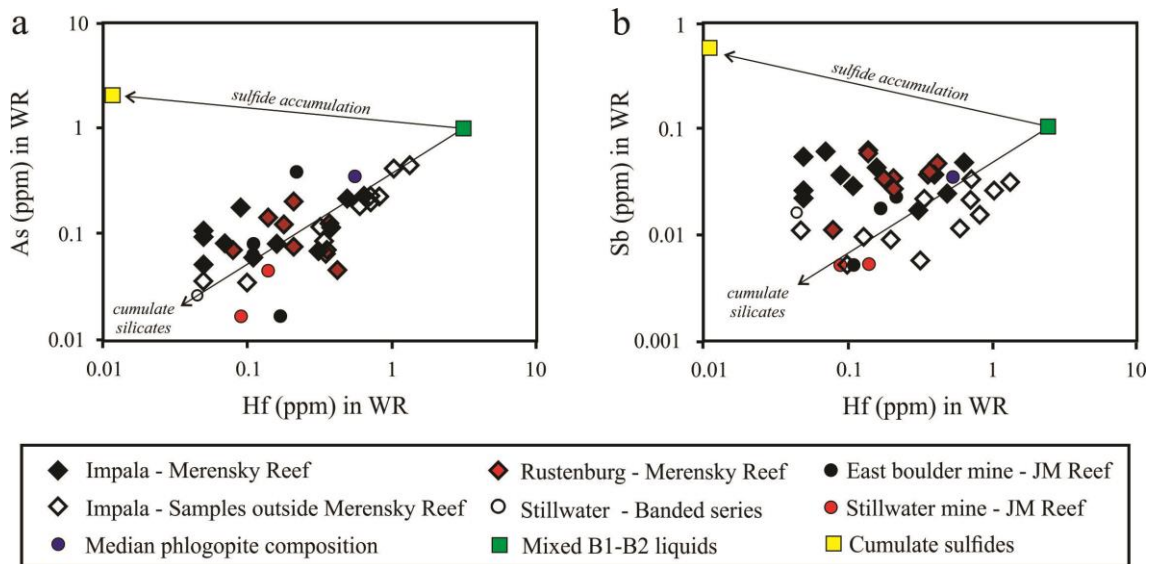
383 Figure 6.4 - Plots of (a) Se, (b) Te, (c) Bi, (d) As and (e) Sb vs S in whole rock (WR). Note that Se, Te and Bi correlate
 384 with S indicating sulfide control, whereas As and Sb do not. Individual whole-rock results are reported in the *ANNEXE*
 385 *15*.

386

387 Li et al. (2005) proposed that the K-phlogopite present in the Merensky Reef crystallized
 388 from the trapped liquid. Therefore, we analyzed K-phlogopite by LA-ICP-MS to investigate
 389 whether it is host for As and Sb (*ANNEXE 16*). The concentrations of As and Sb in the K-
 390 phlogopite range from 0.1 to 4.2 ppm and 0.02 to 0.25 ppm, respectively, and show a positive
 391 correlation (Fig. 6.6a). Moreover, the concentration of As and Sb in K-phlogopite show positive

392 correlation with Hf concentrations (Fig. 6.6b and 6.6c), and negative correlations with Ba, Ti and
 393 Cr in K-phlogopite (Figs. 6.6d to 6.6f). The positive correlations among As, Sb and Hf can be
 394 attributed to all three elements being incompatible during the formation of the reef, and
 395 concentrating in the silicate liquid until the crystallization of K- phlogopite. In contrast, Ba, Cr
 396 and Ti behave as compatible elements with Ba partitioning into plagioclase and Cr and Ti
 397 partitioning into pyroxene and chromite (Dunn and Sen, 1994; Pagé et al., 2009). The distribution
 398 of As and Sb is partially controlled by the amount of trapped liquid fraction present, and not only
 399 by BMS.

400



402 Figure 6.5 - Plots of (a) As and (b) Sb vs Hf in whole rock (WR). Note that samples plot along a tie-line between B1-B-
 403 2 melt mixture (Barnes and Maier, 2002) and silicate cumulates, indicating a melt control of As and Sb. However, some
 404 samples plot toward the cumulate sulfide composition (Barnes and Maier, 2002), suggesting a slight control by sulfide
 405 minerals. Individual whole-rock are reported in the ANNEXE 15.

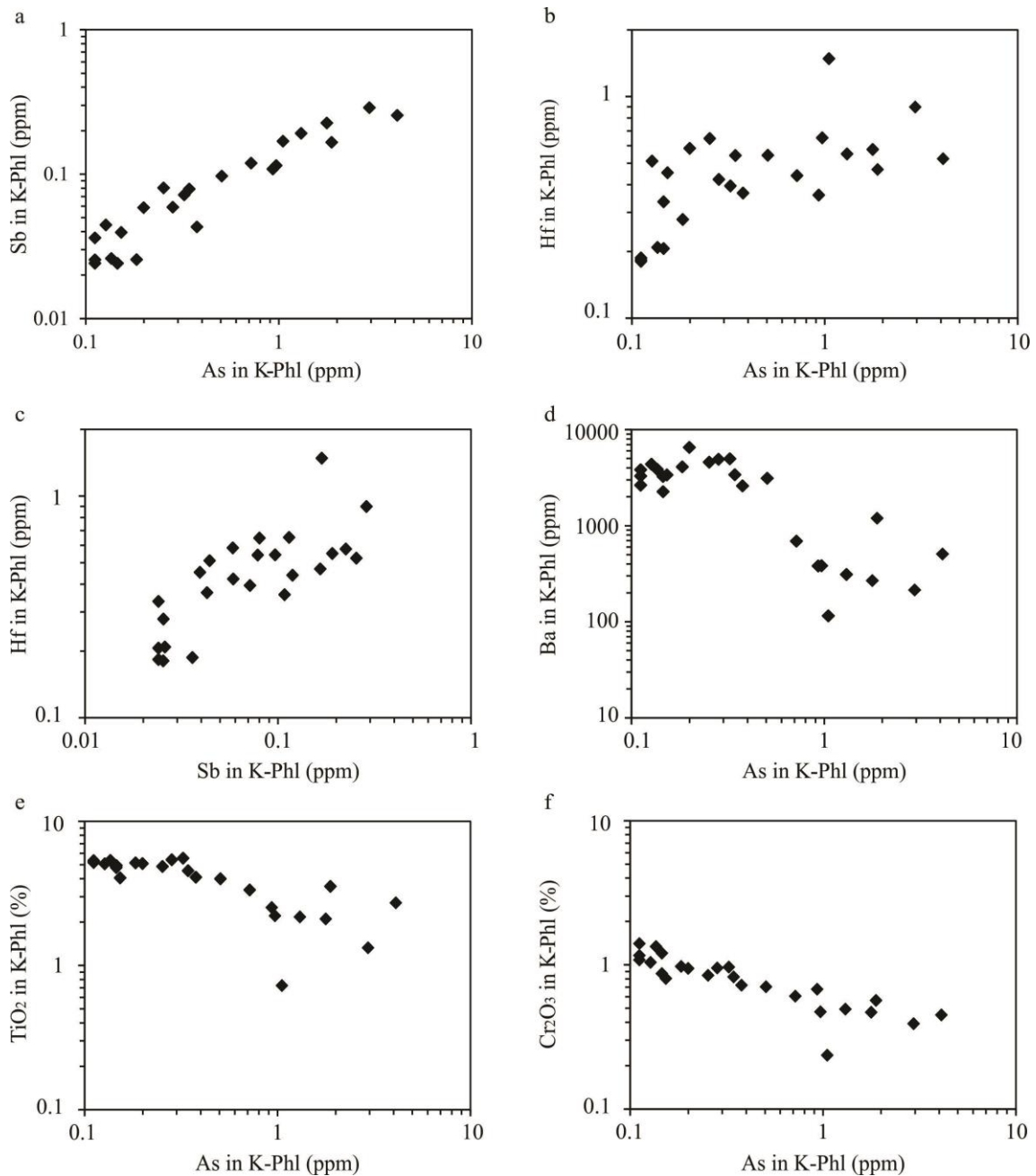
406

407

408

409

410



411

412 Figure 6.6 - Plots of (a) As vs Sb, (b) Hf vs As, (c) Hf vs Sb, and (d) Ba, (e) TiO₂ and (f)Cr₂O₃ vs As in K-phlogopite
 413 (K-Phl). There is a positive correlation between As and Sb concentrations and Hf concentrations, supporting that As
 414 and Sb become progressively more concentrated in the fractionated silicate liquid. However, the negative correlation
 415 between Ba, Ti and Cr, and Hf support the compatible behaviour of these elements. Individual analyses of K-
 416 phlogopite are reported in the ANNEXE 16.

417

418

419

420

421

422 **6.5.2 - Trace elements in BMS**

423

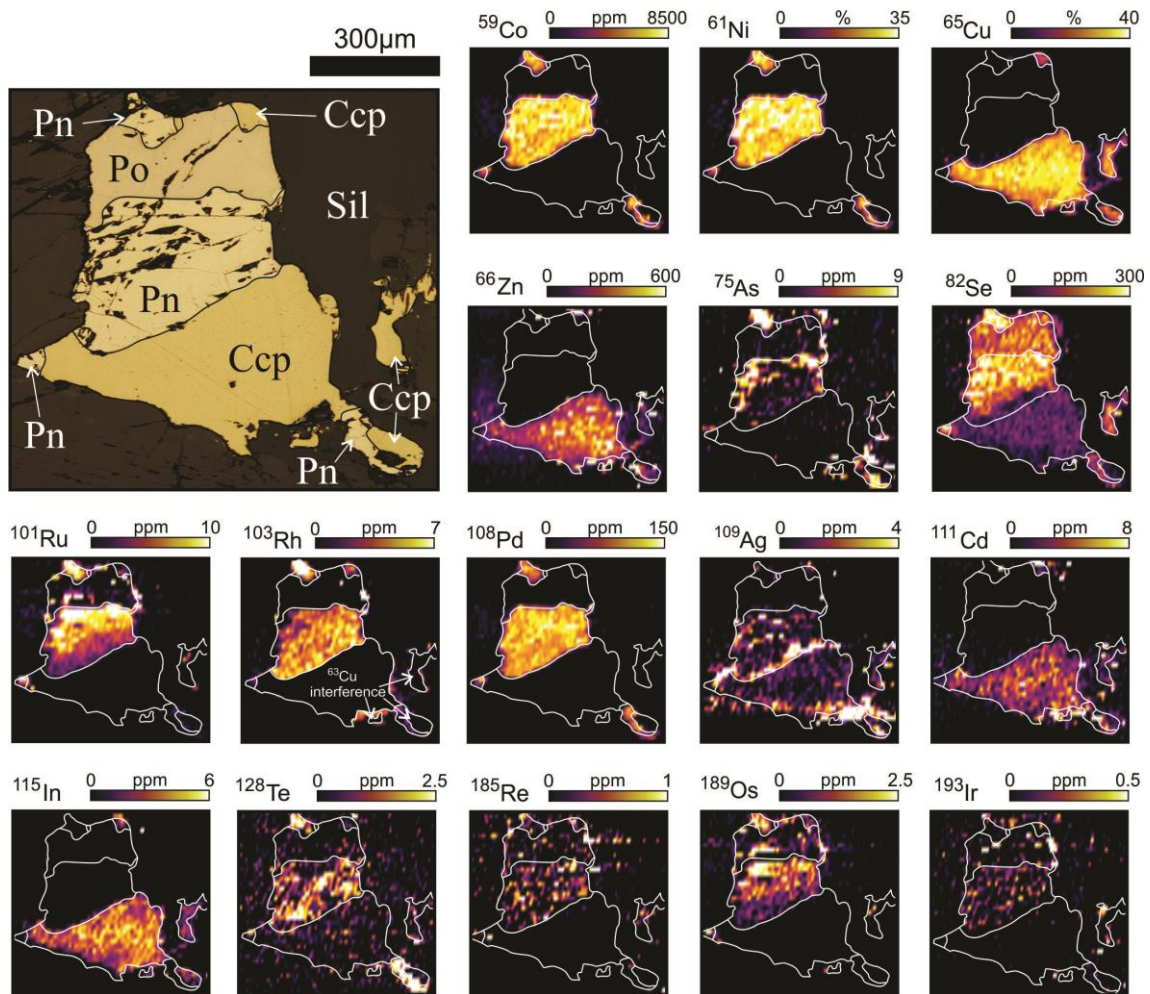
424 Median concentrations of trace elements in Po, Pn and Ccp from each sample, and the
425 full LA-ICP-MS data set are reported in *ANNEXE 17 to 19*. Time-resolved spectra were
426 monitored to ensure that PGM inclusions were not included in the integrations when calculating
427 the BMS compositions. Compositional LA-ICP-MS maps in typical BMS assemblages,
428 composed of Po, Pn and Ccp are shown in Fig. 6.7 to 6.9. The distribution of trace elements
429 among Po, Pn and Ccp is similar in all the different localities.

430 The LA-ICP-MS compositional maps show that the elements compatible with MSS (Ni,
431 Co, Se, Mo, Ru, Rh, Re, Os) are more concentrated in Po and Pn (Fig. 6.7 to 6.9). Molybdenum is
432 slightly more concentrated in Po than Pn, whereas Ru, Os, Ir and Re are distributed between Po
433 and Pn, with a slight preference for Pn. The distribution of these elements in Pn is not always
434 homogeneous, and in some cases they are more concentrated in the Pn next to the contact with Po
435 (e.g. Ru and Os in Fig. 6.7 and 6.8). Selenium displays the same zonation pattern, and although
436 present in all BMS, it is also more concentrated in the Pn next to the contact with Po (Fig. 6.7 to
437 6.9). Nickel and Co are preferentially concentrated in Pn.

438 Elements compatible, or only moderately incompatible with ISS (Cu, Zn, Cd, In and Sn),
439 are concentrated in Ccp (Fig. 6.7 to 6.9). Silver is present in both Pn and Ccp, with a slight
440 preference for Ccp (Fig. 6.7 and 6.9). Some elements incompatible with both MSS and ISS (As,
441 Pd, Te and Pt) are enriched in Pn. The presence of these elements in Pn, and the zonation patterns
442 in Pn for Se, Ru and Os are thought to be the product of peritectic reaction of MSS with
443 fractionated sulfide liquid and are described in detail by Mansur et al. (2019a). Lead and Tl are
444 found concentrated in the fractures of Pn grains (Fig. 6.8 and 6.9), which suggest that these
445 elements have either been expelled from the BMS lattice, or precipitated from late fluids at grain
446 boundaries. Antimony and Bi (not shown) do not show a clear preference for any of the BMS.

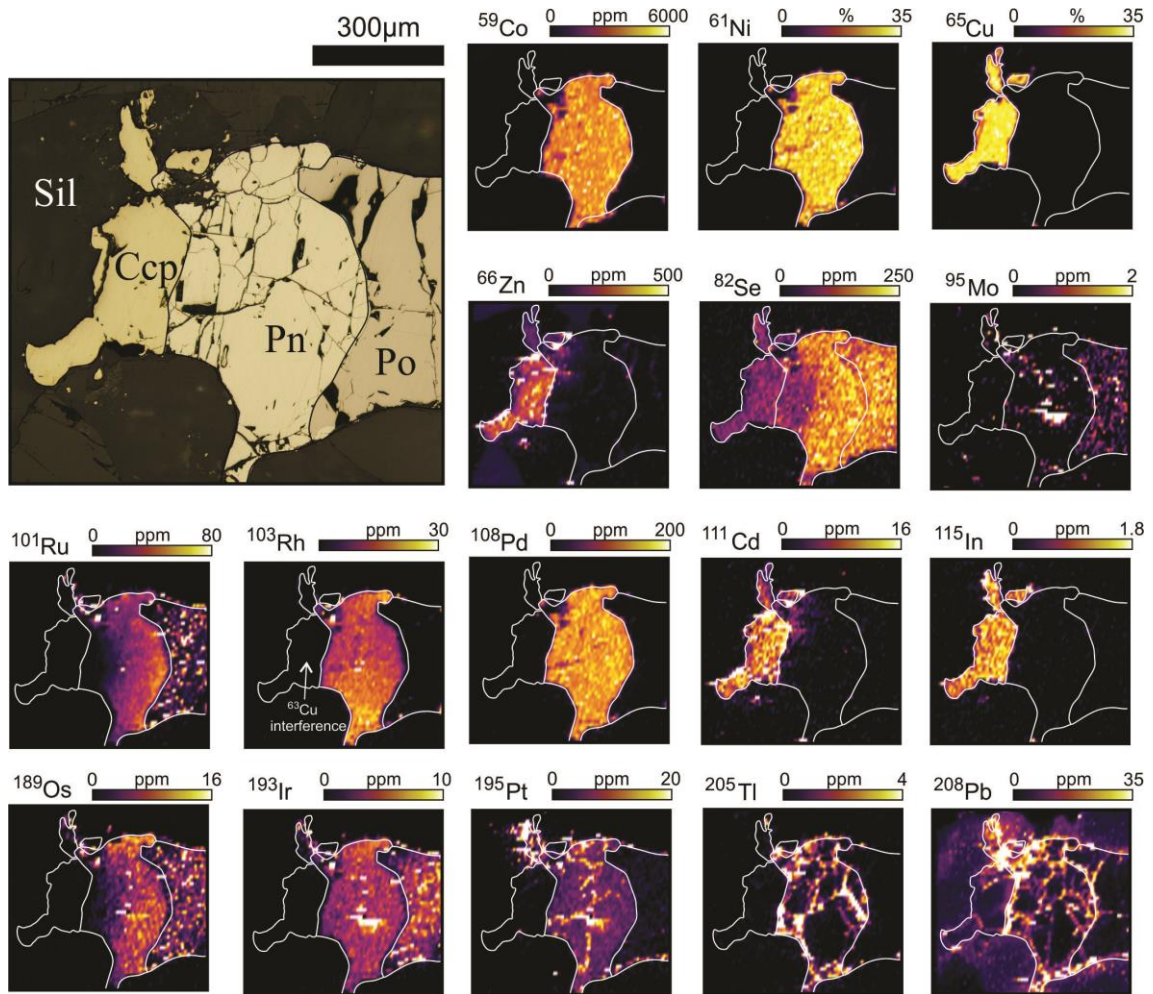
447

448



449

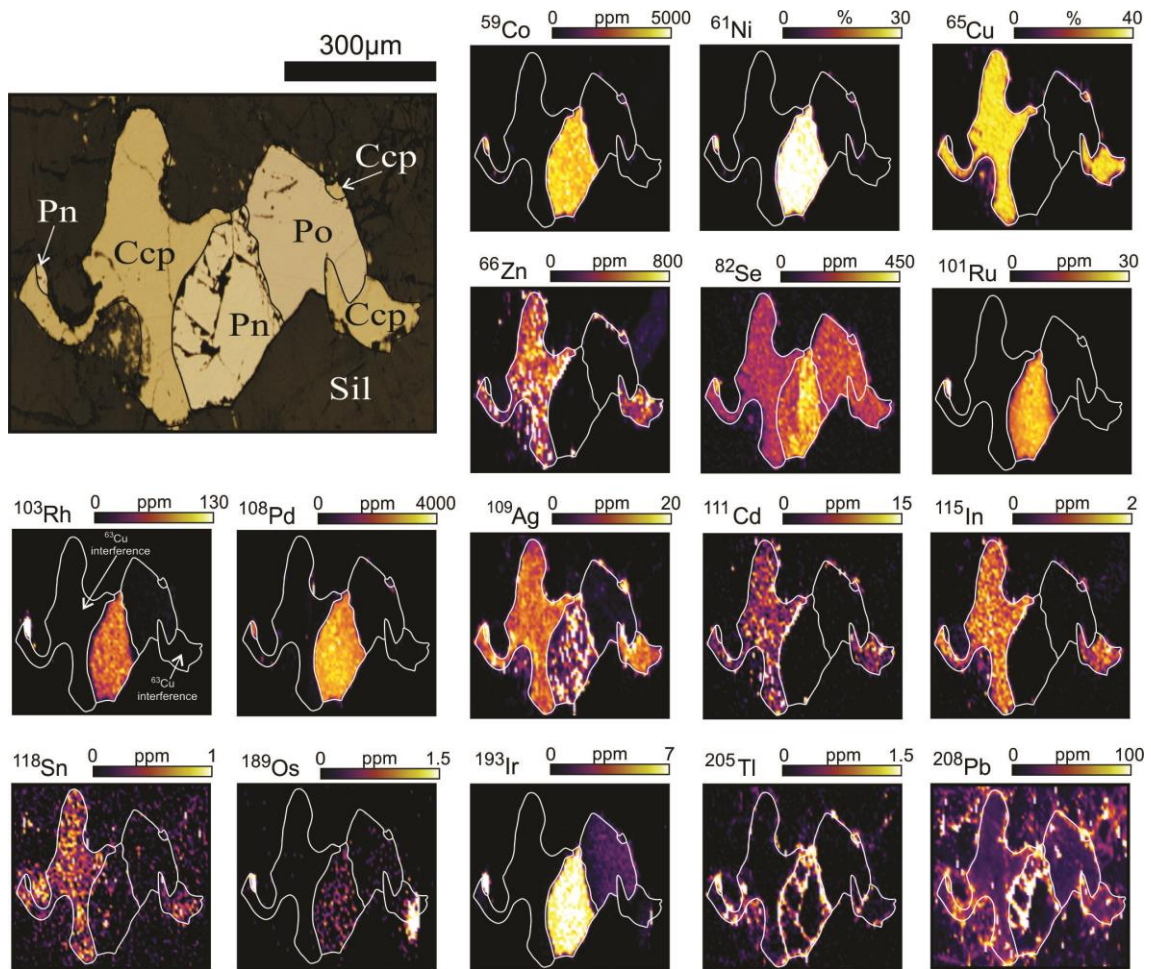
450 Figure 6.7 - LA-ICP-MS elemental maps showing the distribution of chalcophile elements among pyrrhotite (Po),
 451 pentlandite (Pn) and chalcopyrite (Ccp), in disseminated sulfide from the Merensky Reef at the Impala section. The
 452 zonation patterns for Ru and Os are thought to be the product of peritectic reaction of monosulfide solid solution (MSS)
 453 with fractionated sulfide liquid and are described in detail by Mansur et al. (2019a). White lines show the grain outlines.
 454 The relative concentrations of the elements are semi-quantitative.



455

456 Figure 6.8 - LA-ICP-MS elemental maps showing the distribution of chalcophile elements among pyrrhotite (Po),
 457 pentlandite (Pn) and chalcopyrite (Ccp), in disseminated sulfide from the Merensky Reef at the Rustenburg section.
 458 White lines show the grain outlines. The relative concentrations of the elements are semi-quantitative.

459



460

461 Figure 6.9 - LA-ICP-MS elemental maps showing the distribution of chalcophile elements among pyrrhotite (Po),
 462 pentlandite (Pn) and chalcopyrite (Ccp), in disseminated sulfide from the J-M Reef at the Stillwater mine. White lines
 463 show the grain outlines. The relative concentrations of the elements are semi-quantitative.

464

465 6.5.3 – Mass balance

466

467 The weight fraction of each element in each BMS was calculated to establish which
 468 mineral(s) host the bulk of each element at various localities. The proportion of each element
 469 hosted in each BMS was calculated following the method used by Barnes et al. (2006). This
 470 calculation requires: i) the concentration of each element in the whole rock (*ANNEXE 15*); ii) the
 471 median concentration of each element in each BMS (*ANNEXE 17 to 19*); and iii) the weight
 472 fraction of each BMS. The weight fraction of Ccp, Po, and Pn were calculated using whole-rock
 473 Cu, Ni, and S and the concentrations of Cu and Ni in each mineral. The Cu was assigned to Ccp,

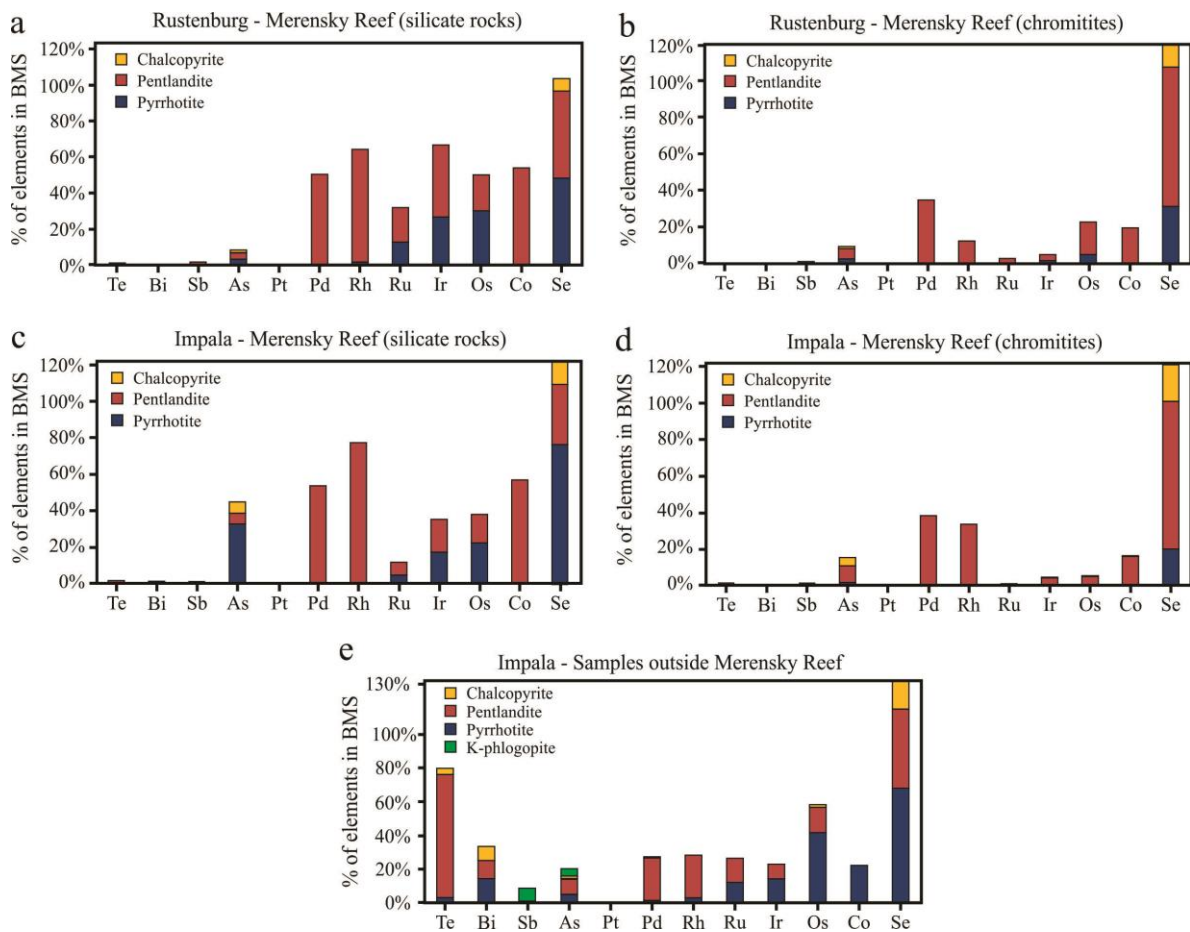
474 whereas the Ni was assigned to Pn. The contributions of Ni from olivine and orthopyroxene were
475 deducted prior to calculation the weight fraction of Pn. The concentrations of Ni in olivine and
476 orthopyroxene used in the calculation were 3000 ppm and 800ppm, respectively. These
477 concentrations correspond to average values found by Barnes and Naldrett (1985) in olivines
478 from the J-M Reef, and by Cawthorn and Boerst (2006), and Godel et al. (2011) in
479 orthopyroxenes from the Merensky Reef. The proportions of orthopyroxene and olivine in each
480 sample are given in detail by Barnes and Maier (2002) for the Impala section, Godel et al. (2007)
481 for the Rustenburg section, and Godel et al. (2008a) for the J-M Reef. The remaining S was
482 attributed to Po. The fraction of K-phlogopite was obtained from petrographic observations and is
483 around 3%. The K-phlogopite is restricted to samples above the Merensky Reef at the Impala
484 section. The accumulated error of the different results used for the mass balance calculation is
485 approximately 20% at one standard deviation (1σ). The results for mass balance calculations are
486 summarized in *ANNEXE 20*.

487 The results for mass balance calculations are similar for samples from both the
488 Rustenburg and Impala sections. The BMS from the silicate rocks account for a greater
489 proportion of whole-rock PGE relative to the BMS from the chromitites (Fig. 6.10). In the silicate
490 rocks, the BMS host most of Pd, Rh, Ir, Os (40 to 80 %), but only minor amounts of Ru (10 to
491 30%). However, in the chromitites the BMS host only 15 to 40% Pd, Rh and Os, and virtually no
492 Ru and Ir (<10%). In all the samples, almost no Pt is present in the BMS minerals. The BMS
493 from both silicate rocks and chromitites host all Se and variable amounts of Co and As (10 to
494 60%), but only account for minor Sb, Bi and Te (<5%). In contrast, BMS in samples above the
495 Merensky Reef interval host significant amounts of the Te, Bi, Pd and Os (30-80%), but only
496 minor Ir, Rh, Ru, Co and As (15 to 30%). The contribution of K-phlogopite to whole-rock budget
497 of TABS was calculated and it only hosts minor amounts of As, Sb and Bi (<10%).

498 In samples from the J-M Reef the BMS host between 60 to 90% of whole-rock PGE
499 (apart from Pt and Os) at the East Boulder mine, whereas only 10 to 50% at the Stillwater mine
500 (Fig. 6.11). At both localities, the BMS host all the Se and significant amounts of Co (40-50%).
501 In samples from the East Boulder mine the BMS do not host significant amounts of other

502 chalcophile elements (Fig. 6.11). However, BMS from the Stillwater mine also host virtually all
 503 of the Cd, and minor amounts of As, Sb and Zn (<30%). In the samples from the Banded Series
 504 the BMS host minor amounts of all PGE (<20%), whereas significant amounts of Te (>60%), and
 505 minor As and Bi (15-20%). As is observed in the J-M Reef samples, the BMS from the Banded
 506 Series (Fig. 6.11) also host virtually all Se, and variable amounts of Co, Cd and Zn (5-50%).

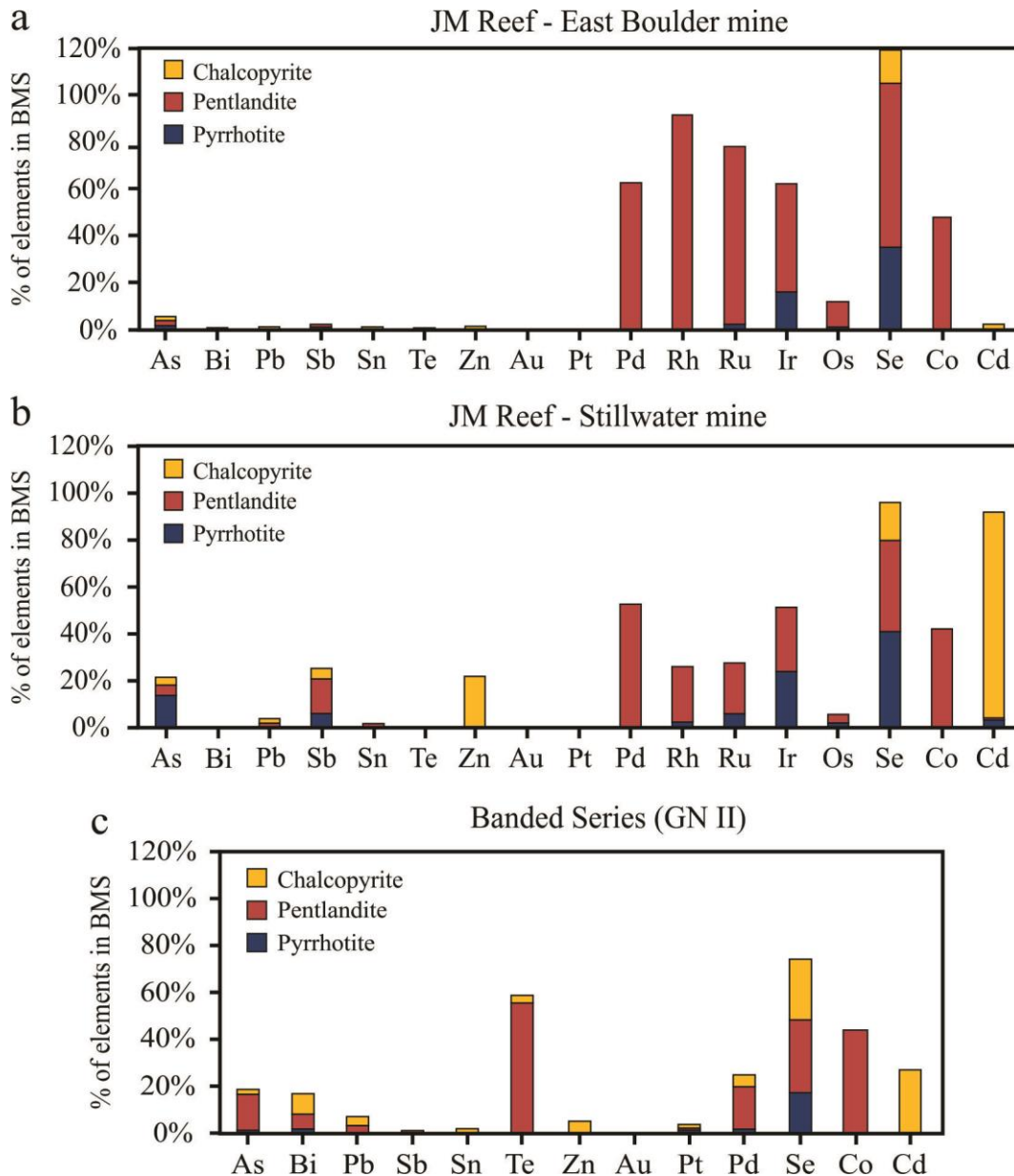
507



508

509 Figure 6.10 - Average proportion (%) of each element hosted in pyrrhotite, pentlandite, chalcopyrite and phlogopite
 510 from the Rustenburg (a and b), and Impala (c, d and e) sections of the Bushveld Complex. Samples from the reef
 511 interval were divide into silicate rocks (a and c) and chromitites (b and d), and separated from samples from outside the
 512 reef interval (e).

513



514

515 Figure 6.11 - Average proportion (%) of each element hosted in pyrrhotite, pentlandite and chalcopyrite from the J-M
 516 Reef at the East Boulder (a), and Stillwater (b) mines, and the Banded Series (c) of the Stillwater Complex.

517

518 In samples from both Bushveld (Fig. 6.10) and Stillwater (Fig. 6.11) complexes Pn hosts
 519 most of Co, Pd, Rh and Te, whereas Os, Ir and Ru are partitioned between Pn and Po.
 520 Chalcopyrite hosts most of the Cd and Zn. Selenium is evenly present in all BMS, and the main
 521 host is the most common mineral in each sample, normally Po and Pn. Arsenic, Bi, Pb, Sb are
 522 distributed among all the BMS, and no particular BMS seems to be the preferable host for these
 523 elements.

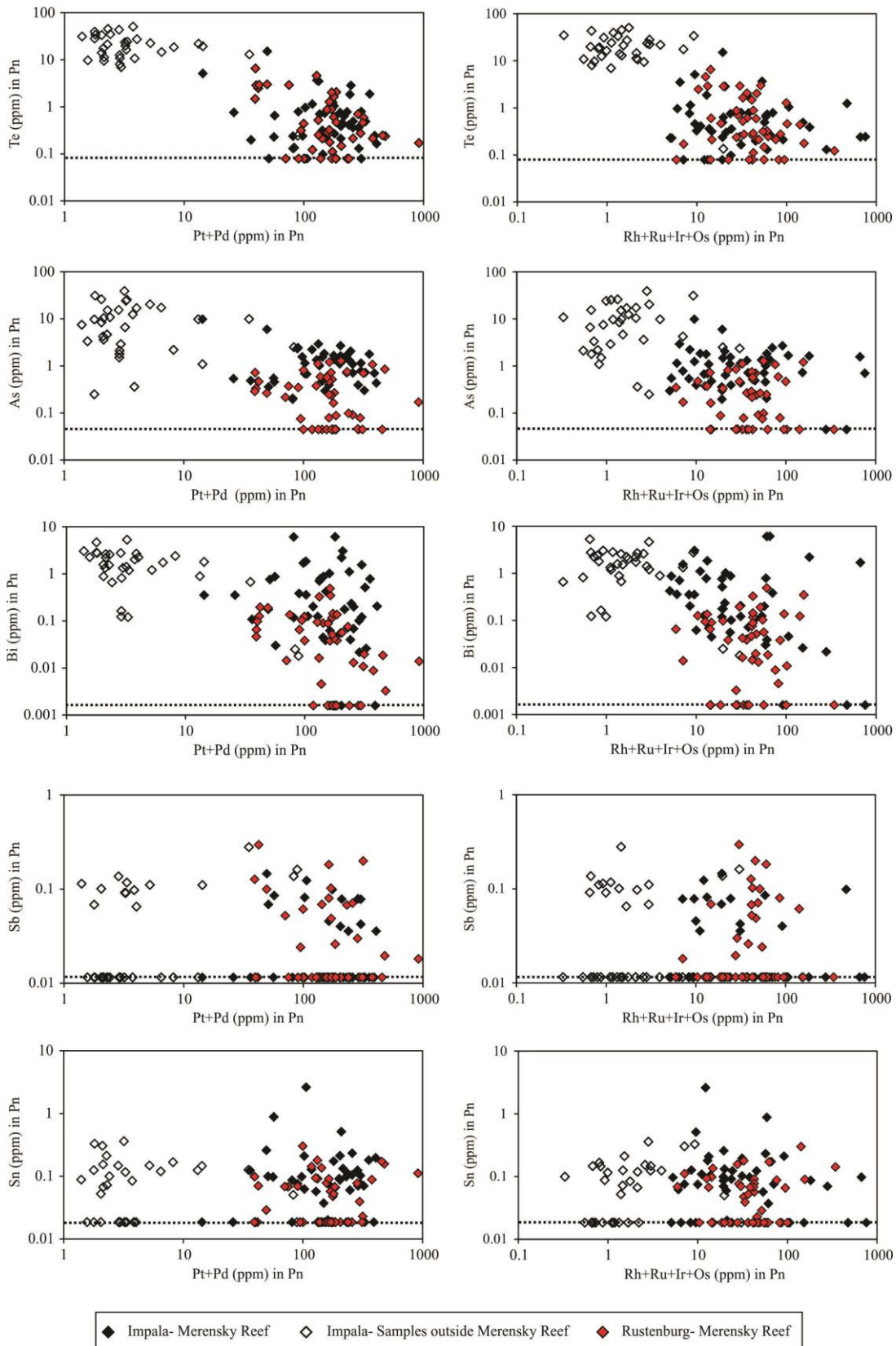
524 **6.5.4 – Variations in PGE to TABS ratios in base metal sulfides**

525

526 There appears to be a negative correlation between TABS contents of the BMS and PGE.
527 At both the Bushveld (Fig. 6.12) and Stillwater (Fig. 6.13) complexes there is a negative
528 correlation between the concentrations of Te, As and Bi, and the concentrations of PGE in Pn.
529 Pentlandite from samples outside the reefs (i.e. Banded Series and above the Merensky Reef) has
530 low concentrations of PGE, but high concentrations of Te, As and Bi. In contrast, Pn from the
531 Merensky Reef, Picket Pin deposit and J-M Reef have the highest PGE contents, but the lowest
532 concentrations of Te, As and Bi (Fig. 6.12 and 6.13).

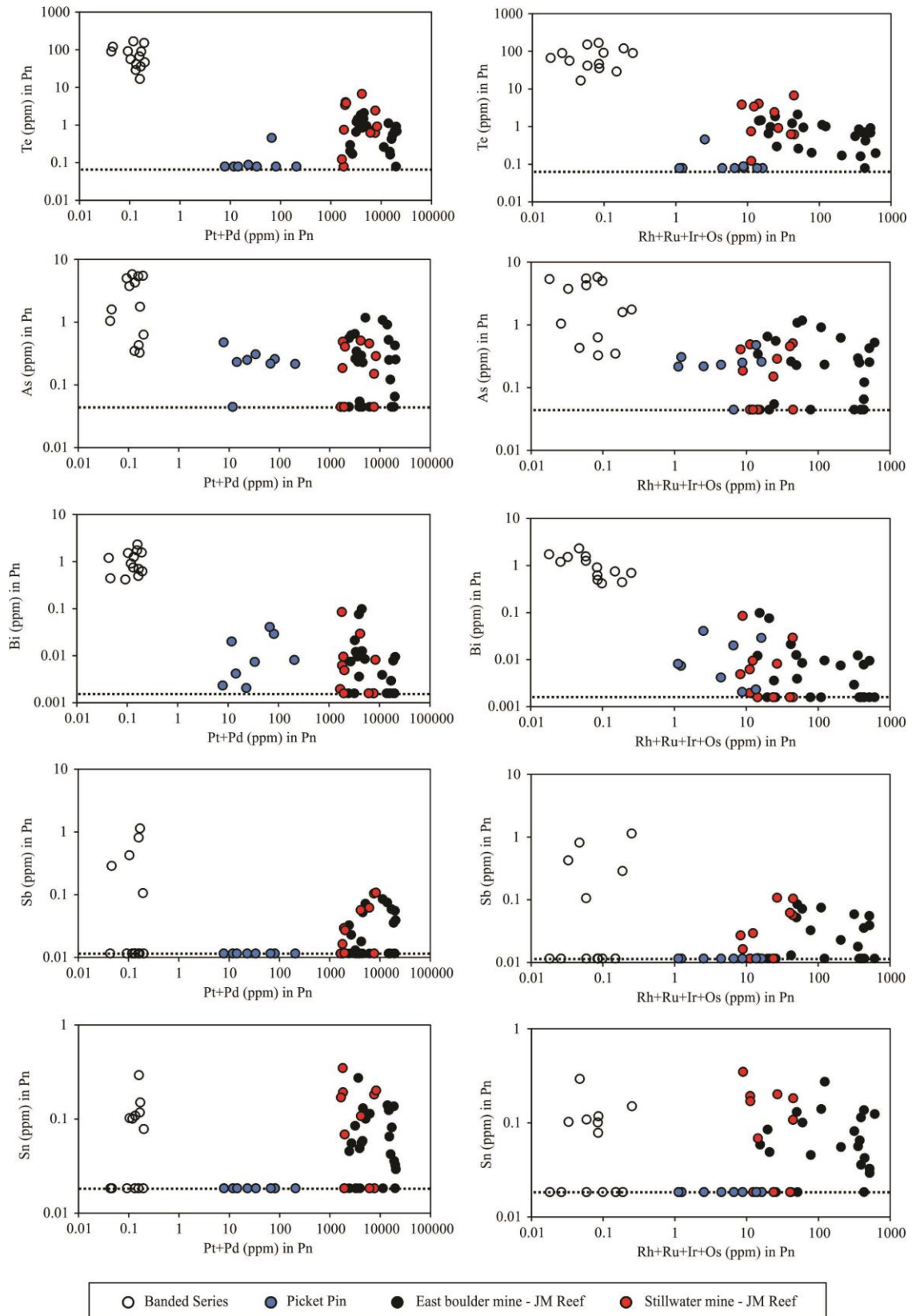
533 The relationship between TABS and PGE content can be investigated more closely in the
534 Impala mine section, where there is stratigraphic control. The median concentrations of PGE and
535 TABS in BMS are plotted against the sample height (Fig. 6.14). Pentlandite was used to monitor
536 median concentrations of Pt, Pd, Rh, Ir, Os, Te, As and Sb, whereas Po was used for Ru, and Ccp
537 was used for Bi and Sn (Fig. 6.14). Median compositions of other BMS in each sample are also
538 reported in *ANNEXE 17 to 19*. Median concentrations of PGE are higher in BMS from the reef
539 than in BMS from above the reef (Fig. 6.14). One exception is a sample above the reef interval
540 with higher PGE concentrations in BMS, which also correlates with slightly higher whole-rock
541 PGE contents (i.e. sample IM-7; *ANNEXE 15*).

542



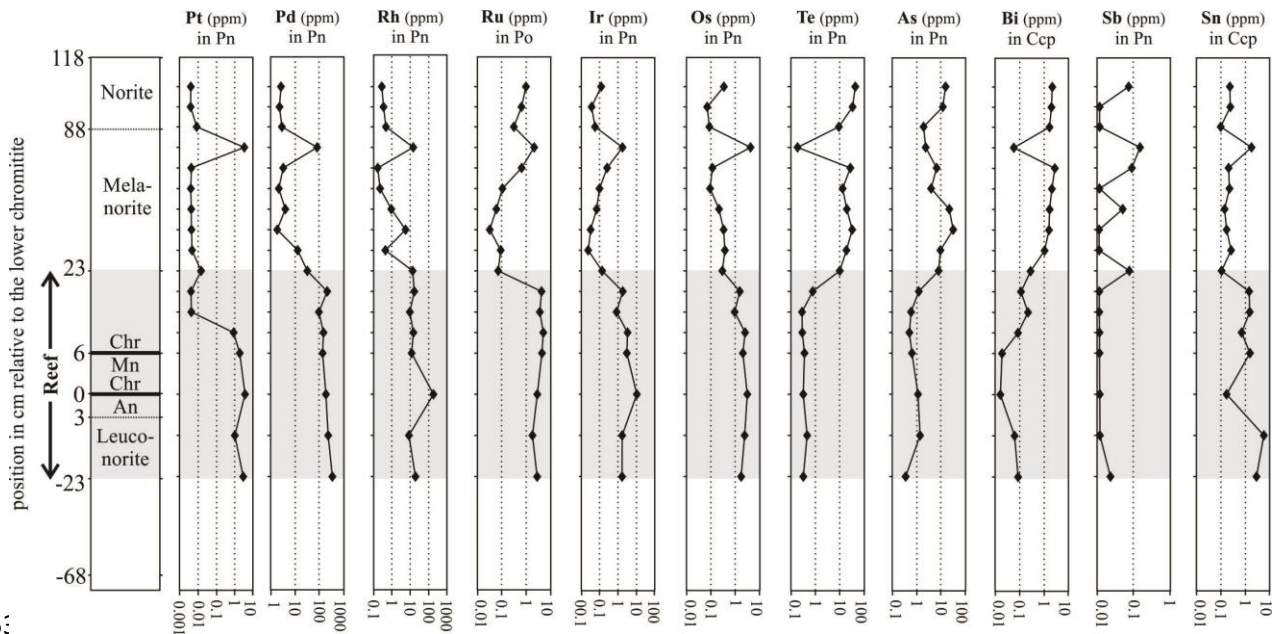
543

544 Figure 6.12 - Plots of Te, As, Bi, Sb and Sn vs Pt+Pd and Rh+Ru+Ir+Os in pentlandite (Pn) from samples of the
 545 Bushveld Complex. Note the negative correlation between Te, As and Bi concentrations and PGE concentrations in Pn.
 546 In contrast, there is no clear correlation between Sb and Sn concentrations and PGE contents in Pn. Dashed lines
 547 indicate the detection limits of LA-ICP-MS.



548

549 Figure 6.13 - Plots of Te, As, Bi, Sb and Sn vs Pt+Pd and Rh+Ru+Ir+Os in pentlandite (Pn) from samples of the
 550 Stillwater Complex. Note the negative correlation between Te, As and Bi concentrations and PGE concentrations in Pn.
 551 In contrast, there is no clear correlation between Sb and Sn concentrations and PGE contents in Pn. Dashed lines
 552 indicate the detection limits of LA-ICP-MS.



55:

554 Figure 6.14 - Variations in median concentrations of Pt, Pd, Rh, Ru, Ir, Os, Te, As, Bi, Sb and Sn in pentlandite (Pn),
 555 pyrrhotite (Po) and chalcopyrite (Ccp) with height across the Impala section. Note that the vertical scale is not linear,
 556 the samples are spaced out evenly for clarity. Note that PGE concentrations are highest in BMS from the reef interval,
 557 whereas TABS concentrations in BMS from outside the reef, contrary to whole-rock results. Median concentrations and
 558 individual analyses of each BMS are reported in *ANNEXE 17 to 19*. Abbreviations: An: anorthosite; Chr: chromitite;
 559 Mn: melanorite.

560

561 Tellurium, As, Bi and Sb concentrations in BMS show a negative correlation with PGE.
 562 The BMS from above the reef are richer in Te, As, Bi and Sb in comparison to BMS from the reef
 563 interval (Fig. 6.14). Median concentrations of Te and As range from 10 to 50 ppm and 2 to 30
 564 ppm above the reef interval, respectively, but fall below 1 ppm within the reef. Bismuth median
 565 concentrations range from 1 to 3 ppm above the reef, and from 0.01 to 0.3 ppm inside the reef
 566 interval. Median concentrations of Sb in BMS are below the detection limit of 0.01 ppm within
 567 the reef interval, whereas are scattered above the reef, ranging from 0.01 to 0.1 ppm (Fig. 6.14).
 568 The Sn median concentrations in BMS do not follow Te, As and Bi median concentrations.
 569 Median concentrations of Sn are in the 0.2 to 6 ppm range inside the reef interval, which is higher
 570 than the 0.1 to 0.3 ppm range above the reef (Fig. 6.14).

571

572

573 **6.6 – Discussion**

574

575 Our results show that BMS from PGE-rich samples (i.e. from the reef intervals) have
576 high concentrations of PGE, however, they have low concentrations of TABS. In contrast, BMS
577 from PGE-poor samples (i.e. from outside the reef intervals) have low concentrations of PGE, but
578 the highest concentrations of TABS. Consequently, in samples from outside the reefs the BMS
579 account for greater proportion of whole-rock budget of TABS compared to BMS from the reef
580 intervals. These variations suggest that the presence of high concentrations of PGE in BMS leads
581 to a depletion of TABS in the BMS.

582 To further assess how the presence of TABS may influence the distribution of PGE, we
583 discuss below the possible scenarios for the collection of PGE. For this purpose, we will first
584 discuss the possible role of TABS for the formation of PGE nanoparticles, and further explore the
585 importance of TABS during the exsolution of PGM. Given the notable association between PGE
586 and TABS, we discuss the importance of the external addition of TABS for the mineralogical
587 setting of PGE.

588

589 **6.6.1 - Constrains for the formation of PGE pre-nucleation clusters**

590

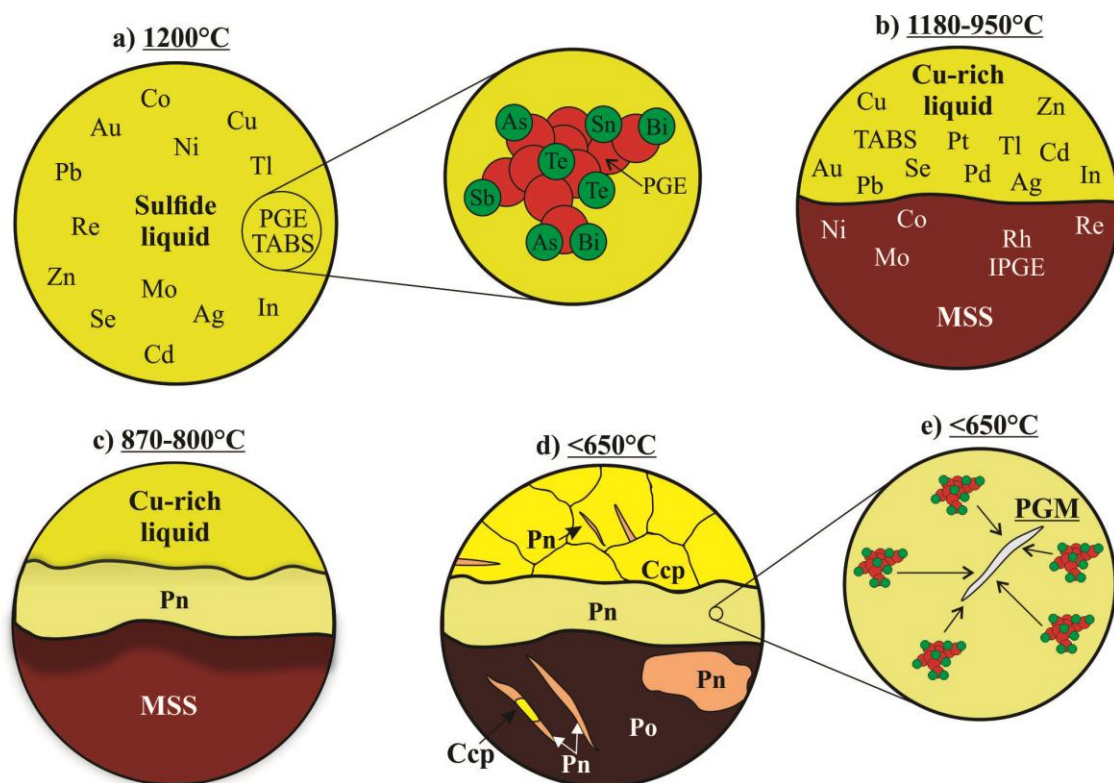
591 Platinum-group elements have very high partition coefficients between sulfide and
592 silicate liquids (Fonseca et al., 2009; Mungall and Brenan, 2014; Liu and Brenan, 2015 and
593 references therein), and are thus thought to be collected by a sulfide liquid to form PGE reefs
594 (Barnes and Ripley, 2016 and references therein). However, some authors have also proposed that
595 the distribution of PGE is more likely to be physically controlled by the surface properties of
596 nanometer-sized particles (Tredoux et al., 1995; Ballhaus et al., 2006; Helmy et al., 2013;
597 Gonzalez-Jimenez et al., 2018, 2019). In this model, PGE form clusters of 50-100 atoms. These
598 clusters are stabilized by the surface adsorption of S, Fe and TABS atoms. The clusters are
599 captured by the sulfide liquid (Fig. 6.15a), and incorporated into the crystallizing MSS, Pn and

600 ISS, which further exsolve into BMS (Fig. 6.15b and 6.15c) (Wirth et al., 2013; Junge et al.,
601 2015; González-Jiménez et al., 2018, 2019; Liang et al., 2019). Recent studies in material science
602 have shown nano-particles can exist prior to nucleation as pre-nucleation clusters (Chakraborty
603 and Pradeep, 2017 and references therein). Junge et al. (2015) suggest that they could form the
604 nucleation sites for PGM (Fig. 6.15d and 6.15e).

605 Although PGE and TABS are undersaturated in natural silicate liquids, experimental
606 studies revealed that these elements, especially Pt and As, are able to self-organize into
607 nanoparticles (Helmy et al., 2013; Helmy and Bragagni, 2017). Helmy et al. (2013) found Pt-As
608 clusters in their high-temperature experiments, supporting the formation of PGE nanoclusters.
609 Recent studies have also revealed natural occurrences of nanometer-sized PGE particles, which
610 are mostly platinum arsenides (Kamenetsky et al., 2015; Maier et al., 2015; Arguin et al., 2016;
611 Barnes et al., 2016; González-Jiménez and Reich, 2017; González-Jiménez et al., 2018, 2019).
612 Moreover, Wirth et al. (2013) and Junge et al. (2015) found nanometer-sized PGM inclusions in
613 Pn crystals from the Bushveld Complex. Liang et al. (2019) have also recently found similar
614 particles included in various BMS from the Yangliuping deposit, China. These authors reported
615 that the inclusions are not oriented relative to the crystal lattice, and may possibly represent pre-
616 existing nanometer-sized clusters incorporated during sulfide growth.

617 However, the model of stabilization of nanocluster by TABS is not consistent with the
618 observation that the whole-rock ratio of TABS/PGE in the reefs is much lower (0.01 to 0.3) than
619 outside of the reefs (0.5 to 10)(Fig. 6.3). If PGE nanoclusters were critical to the formation of
620 reefs, and TABS lead to the formation of nanoclusters, then the TABS/PGE ratio should be
621 similar to that in TABS-PGM, because the nanocluster are pre-nucleation clusters. The low ratio
622 of TABS to PGE in the reefs confirms that TABS-PGM are not the major hosts for the PGE,
623 because most TABS-PGM have TABS to PGE ratios of 0.5 or higher (O'Driscoll and González-
624 Jiménez, 2016 and references therein).

625



626

627 Figure 6.15 - Schematic models illustrating the crystallization history of sulfide liquid in the reef samples, and the
 628 potential importance of TABS for stabilizing PGE nanoclusters, and consequently form PGM. See text for further
 629 explanation. Abbreviations: MSS: monosulfide solid solution; Po: pyrrhotite; Pn: pentlandite; Ccp: chalcopyrite; IPGE:
 630 Ru, Ir and Os; TABS: Te, As, Bi, Sb and Sn; PGE: platinum-group elements; PGM: platinum-group minerals.

631

632 Another major limitation to interpret our data using the nanoclusters hypothesis is the
 633 lack of experimental work investigating the possible roles of Te, Bi, Sb and Sn in forming PGE
 634 clusters, especially Pd clusters. We do acknowledge for the presence of nanometer-sized PGE
 635 particles in natural cases (Wirth et al., 2013; Junge et al., 2015; González-Jiménez et al., 2018,
 636 2019; Liang et al., 2019). However, most of the experimental and empirical studies have focused
 637 on the association of Pt and As to form nanoclusters (Helmy et al., 2013; Helmy and Bragagni,
 638 2017). In fact, these elements are rarely hosted by BMS (Barnes and Ripley, 2016 and references
 639 therein). On the contrary, Pd-Pt bismuth-tellurides are more common in the samples than Pt-
 640 arsenides. Therefore, experimental studies demonstrating the formation of TABS and PGE
 641 nanoclusters (other than Pt-arsenides), using realistic starting materials, would be required prior
 642 to a more convincing evaluation of the model.

643 **6.6.2 – The role of TABS during PGM exsolution**

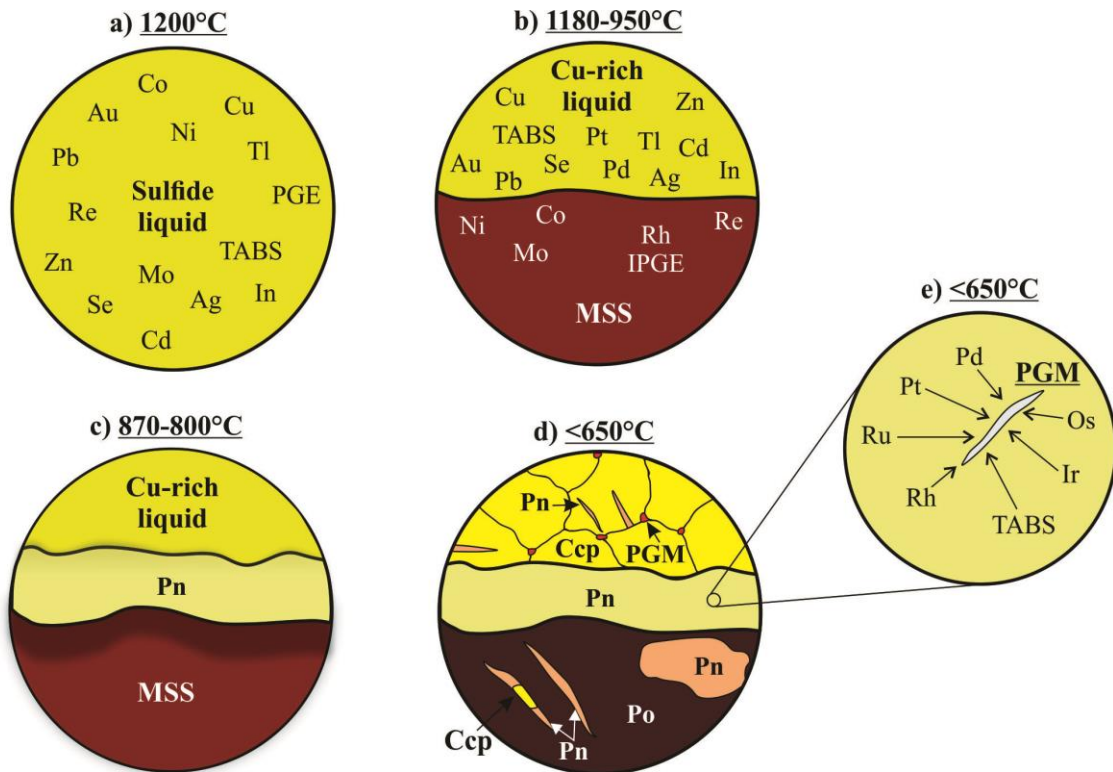
644

645 As outlined in the introduction, the disseminated sulfides could represent a sulfide liquid
646 which has undergone equilibrium crystallization (Fig. 6.16a). Elements compatible, or only
647 mildly incompatible with MSS (Ni, Co, Se, Mo, Rh, Ru, Re, Os and Ir; Mungall and Brenan,
648 2014; Liu and Brenan, 2015), would have partitioned into MSS, and subsequently been
649 distributed between Po and Pn when these minerals exsolved. Platinum-group minerals rich in
650 Rh, Ru, Os and Ir could also have exsolved during cooling. Elements compatible, or only mildly
651 incompatible with ISS (Cu, Zn, Ag, Cd, In, Sn; Liu and Brenan, 2015), partitioned into ISS and
652 subsequently into Ccp when it exsolved during cooling.

653 Palladium, Pt and TABS are incompatible with both MSS and ISS (Fig. 6.16b; Li et al.,
654 1996; Barnes et al., 1997; Mungall et al., 2005; Helmy et al., 2010; Liu and Brenan, 2015).
655 Therefore, very little Pt, Pd and TABS should be present in the BMS lattice, and thus Pt-Pd-
656 TABS PGM formed by exsolutions would be expected to be very rare. Most of the Pt-Pd PGM
657 would be expected to crystallize from the fractionated liquid, and be found among the BMS,
658 rather than included in them. Indeed, most the Pt-Pd PGM both in the Merensky and J-M reefs are
659 found at the margins of the BMS grains, and the majority are found in contact with Ccp as this
660 model would predict (Fig. 6.2; Prichard et al., 2004; Godel et al., 2007; Godel and Barnes,
661 2008b).

662 However, there are some Pt-Pd PGM included in BMS, and Pn contains the bulk of the
663 Pd in the reefs (Fig. 6.10 and 6.11). These two observations can be reconciled with the model as
664 follows. Although these elements are incompatible with both MSS and ISS, their partition
665 coefficients are not 0 (Liu and Brenan, 2015), and thus a small fraction of these elements are
666 included in the ISS and MSS. On cooling, and during S-loss, Pd, Pt and TABS could exsolve
667 from the ISS and MSS. Furthermore, Pn can form by peritectic reaction between the MSS and the
668 sulfide liquid, around 870°C (Fig. 6.16c; Mungall, 2007; Kosyakov and Sinyakova, 2012;
669 Kitakaze et al., 2016). Mansur et al. (2019a) investigated the distribution of chalcophile elements

670 in Pn found between Po and Ccp, and argued that this Pn formed by peritectic reaction.
 671 Palladium, Te and Bi were incorporated into the peritectic Pn from the fractionated sulfide liquid.
 672 This provides another mechanism for the incorporation of incompatible metals into Pn.
 673



674

675 Figure 6.16 - Schematic models illustrating the crystallization history of sulfide liquid in the reef samples, and the
 676 formation of PGM by exsolution from the BMS upon cooling. See text for further explanation. Abbreviations: MSS:
 677 monosulfide solid solution; Po: pyrrhotite; Pn: pentlandite; Ccp: chalcopyrite; IPGE: Ru, Ir and Os; TABS: Te, As, Bi,
 678 Sb and Sn; PGE: platinum-group elements; PGM: platinum-group minerals.

679

680 In order to explain the difference in the TABS concentrations in BMS in rocks from the
 681 reefs and those outside the reefs we propose the following model. Upon cooling, the BMS in the
 682 reefs were not able to accommodate all of the PGE in their structure, resulting in the exsolution of
 683 TABS-PGM, and sulfide PGM (Fig. 6.16d and 6.16e). Given the excess of PGE relative to TABS
 684 in the reef BMS, most of the TABS were accommodated in PGM. In contrast, for samples outside
 685 the reefs, the lower proportion of PGE to TABS allows more TABS to remain in the BMS lattice.

686 Junge et al. (2015) suggested that the initial concentration of TABS in BMS may control
687 the extent of PGM exsolution. In their transmission electron microscopy (TEM) studies of
688 samples from the UG-2 chromitite, Merensky Reef and Platreef, Wirth et al. (2013) and Junge et
689 al. (2015) investigated the mineralogical sitting of PGE. The authors found that PGE occur in
690 solid solution in BMS (especially Pn), and also as aligned PGM lamellae within BMS structure,
691 which they interpreted as exsolution lamellae. Junge et al. (2015) suggested that the absence of
692 possible reaction partners necessary to form PGM (TABS) forced some PGE to remain in the
693 BMS lattice. Our results support the observation that the PGM enclosed in sulfides combined
694 with TABS and exsolved as PGM upon cooling. However, the fraction of PGE retained in BMS
695 is similar in the BMS with low TABS concentrations, and those with high TABS concentrations
696 (Fig. 6.10 and 6.11). Therefore, we do not think that the TABS concentrations in the BMS limit
697 the PGM exsolution process. The PGE can exsolve not only as TABS PGM, but also as PGM
698 sulfides, and PGM alloys.

699

700 **6.6.3 - External addition of TABS and the implications for the PGM formation**

701

702 A summary of the PGM assemblage from mines along the entire Merensky Reef shows
703 that TABS-PGM make up 7 to 70% by volume of the PGM depending on the locality (Kinloch,
704 1982; McLaren and de Villiers, 1982), with the proportion of arsenides to tellurides varying from
705 0.4 to 22. The variability in PGM assemblage, combined with the observation that the
706 concentrations of PGE along the reef from mine to mine do not vary greatly, led Cawthorn et al.
707 (2002) to conclude that PGM assemblage is formed by secondary processes, and that they are not
708 implicated in the initial collection of the PGE. In our sample set, both from the Merensky and J-
709 M reefs, much of the PGE budget (except for Pt) is found in the BMS. The balance is found in
710 PGM, some of which we postulate to have formed by exsolutions, and some of which appear to
711 have crystallized among the PGM grains from fractionate sulfide liquid.

712 Although the TABS may not be essential to forming a reef, their concentrations in the
713 reef, and elsewhere, provide important petrogenetic information. In order to bring about sulfide
714 saturation, and collect the PGE, most primary magmas need to be contaminated with S-bearing
715 rocks (Li and Ripley, 2005; Ripley and Li, 2013). The primary magma would contain only a few
716 ppb of TABS, however, S-rich crustal rocks contain ppm levels of TABS (Barnes, 2016).
717 Therefore, along with the S the crustal rocks would also add TABS (Samalens et al., 2017), which
718 would then be collected by the sulfide liquid along with PGE, and eventually combine with PGE
719 to form PGM.

720 Duran et al. (2017) showed the concentrations of TABS in the sulfide liquid formed from
721 a primary magma would be much lower than the concentrations of TABS observed in the Ni-Cu-
722 PGE ores from the Noril'sk-Talnakh district. Their modeling suggests an enrichment factor of 2
723 to 200, relative to a sulfide formed from an uncontaminated magma. Duran et al. (2017) also
724 argued that the abundance of Sn-bearing PGM in massive sulfides of the Noril'sk-Talnakh mining
725 district reflects the assimilation of granitic rocks by the mafic magmas. Therefore, if crustal
726 contamination increases the concentration of TABS into the mafic magma, it could also affect the
727 PGM assemblage and sighting of PGE.

728 Different assemblages of PGM have been interpreted to reflect contamination of the
729 magma by different rock types. In the case of the Main Sulfide Zone of the Great Dyke, Oberthür
730 (2011) found different PGM assemblages in the North and South Chambers. In the North
731 chamber, PGM are predominantly bismuth-tellurides, whereas in the South Chamber these are
732 predominantly arsenides and sulfarsenides. At Sudbury, the PGM assemblage in the North and
733 South range deposits are different, with the North range containing more Sn-bearing PGE and the
734 South range more As-bearing PGM (Ames and Farrow, 2007). This difference is attributed to the
735 difference in the host rock with the North range being in contact with Archean gneiss and
736 granites, and the South range being in contact with Proterozoic volcano-sedimentary rocks (Ames
737 and Farrow, 2007).

738 The addition of TABS during crustal contamination may also influence the timing of
739 PGM formation. Dare et al. (2010a) argued that the higher activity of As in the Creighton Deposit
740 of the Sudbury South Range led to the early crystallization of As-bearing PGM at high
741 temperature (i.e., up to 1200°C). In the case of the Platreef of the Bushveld Complex, Hutchinson
742 et al. (2015) also suggest that the external addition of TABS led to the early crystallization of
743 PGM, and thus a lower proportion of PGE is hosted by the BMS. Thus, TABS concentrations can
744 be used both to deducing what type of crustal contamination has occurred, and the timing of PGM
745 formation.

746

747 **6.7 – Conclusions**

748

749 This contribution provides insights into the possible roles of Te, As, Bi, Sb and Sn
750 (TABS) during the formation of PGE deposits. Our main findings are:

751 1. - The ratio of TABS to PGE in reef rocks (0.01 to 0.3) is too low for the TABS to have acted as
752 stabilizers of pre-nucleation clusters (nanoclusters), and thus TABS nanoclusters are not essential
753 to form reefs.

754 2 – Whole-rock analyses reveal that the concentrations of TABS (except As) correlate positively
755 with S and PGE. This suggests that all the elements were initially collected by an immiscible
756 sulfide liquid. The distributions of As, and to a lesser extent Sb, are also controlled by the melt
757 fraction in the cumulate rocks, and this is also recorded by the presence and composition of K-
758 phlogopite in the case of the Merensky Reef.

759 3- During crystallization of the sulfide liquid a small portion of the TABS, Pd and Pt partitioned
760 into the MSS and ISS, but the bulk remained in the fractionated sulfide liquid. At below 870°C
761 there was a peritectic reaction between the fractionated liquid and MSS, which formed Pn, and

762 much of the Pd and some TABS partitioned into the Pn. The remainder of the TABS, Pd and Pt
763 crystallized as PGM between the BMS grains.

764 4 –The whole-rock concentrations of PGE and TABS are highest in the reefs, and the PGE
765 content of the BMS are highest in the reefs, but the TABS contents of the BMS from the reefs are
766 lower than TABS contents of BMS from outside the reefs. This is thought to be a consequence of
767 the PGE/TABS ratios of the whole rock. In the reefs, the PGE far exceed the TABS, thus during
768 exsolutions of PGM all of the TABS can be accommodated by the PGM, and very little remains
769 in the BMS. In contrast, in the rocks from outside of the reefs the TABS exceed the PGE. Thus,
770 not all of the TABS can be accommodated in PGM and some remain in the BMS.

771 5 – Understanding the processes that potentially upgrade the concentrations of TABS during the
772 formation of magmatic sulfide deposits is essential for understanding the distribution of PGE.
773 Among the potential processes, the crustal contamination has been shown to significantly increase
774 concentrations of TABS in mafic magmas. We suggest that the external addition of TABS needs
775 to be closely considered whenever investigating the mineralogical sitting of PGE.

776

777 **6.8 – Acknowledgements**

778

779 *This work was supported by a Canada Research Chair program grant to Sarah-Jane Barnes*
780 *(215503). We would like to thank Dany Savard and Audrey Lavoie (LabMaTer, UQAC) for their*
781 *assistance with LA-ICP-MS analyses. This manuscript benefited from insightful comments from*
782 *Steve Barnes, Rubén Piña, and one anonymous reviewer, and careful editorial handling by the*
783 *associate editor Edward Ripley.*

784

785

786 **6.9 - References**

- 787 Ames D.E. and Farrow C.E.G. (2007) Metallogeny of the Sudbury mining camp, Ontario. In
788 *Mineral deposits of Canada: a synthesis of major deposit-types, district metallogeny, the*
789 *evolution of geological provinces, and exploration methods* (ed. W.D. Goodfellow).
790 Geological Association of Canada, Special Publication no. 5. Mineral Deposits Division,
791 Geological Association of Canada, St. John's, pp. 329-350.
- 792 Arguin, J.P., Pagé P., Barnes S-J., Yu S.Y. and Song X.Y. (2016) The effect of chromite
793 crystallization on the distribution of osmium, iridium, ruthenium and rhodium in picritic
794 magmas: an example from the Emeishan Large Igneous Province, Southwestern China. *J.*
795 *Petrol.* **57(5)**, 1019-1048.
- 796 Ballhaus C., Ryan C.G., Mernagh T.P. and Green D.H. (1994) The partitioning of Fe, Ni, Cu, Pt,
797 and Au between sulfide, metal, and fluid phases: A pilot study. *Geochim. Cosmochim.*
798 *Acta* **58(2)**, 811-826.
- 799 Ballhaus C., Bockrath C., Wohlgemuth-Ueberwasser C., Laurenz V. and Berndt J. (2006)
800 Fractionation of the noble metals by physical processes. *Contrib. Mineral. Petrol.* **152(6)**,
801 667-684.
- 802 Barnes S-J. (2016) Chalcophile Elements. In *Encyclopedia of Geochemistry: A Comprehensive*
803 *Reference Source on the Chemistry of the Earth* (ed. W.M. White), pp. 1-5.
- 804 Barnes S.J. and Naldrett A.J. (1985) Geochemistry of the JM (Howland) Reef of the Stillwater
805 Complex, Minneapolis Adit area; I, Sulfide chemistry and sulfide-olivine
806 equilibrium. *Econ. Geol.* **80(3)**, 627-645.
- 807 Barnes S.J., Fisher L.A., Godel B., Pearce M.A., Maier W.D., Paterson D., Howard D.L., Ryan
808 C.G. and Laird J.S. (2016) Primary cumulus platinum minerals in the Monts de Cristal
809 Complex, Gabon: magmatic microenvironments inferred from high-definition X-ray
810 fluorescence microscopy. *Contrib. Mineral. Petrol.* **171(3)**, 23.

811 Barnes S-J. and Maier W.D. (2002) Platinum-group elements and microstructures of Normal
812 Merensky Reef from Impala Platinum Mines, Bushveld Complex. *J. Petrol.* **43(1)**, 103-
813 128.

814 Barnes S-J., Makovicky E., Makovicky M., Rose-Hansen J. and Karup-Moller S. (1997) Partition
815 coefficients for Ni, Cu, Pd, Pt, Rh, and Ir between monosulfide solid solution and sulfide
816 liquid and the formation of compositionally zoned Ni–Cu sulfide bodies by fractional
817 crystallization of sulfide liquid. *Can. J. Earth Sci.* **34**, 366-374.

818 Barnes S-J. and Ripley E.M. (2016) Highly siderophile and strongly chalcophile elements in
819 magmatic ore deposits. *Rev. Mineral. Geochem.* **81**, 725-774.

820 Barnes S-J., Pagé P. and Zientek M. (2020) The Lower Banded series of the Stillwater Complex,
821 Montana: whole-rock lithophile, chalcophile, and platinum-group element
822 distributions. *Miner. Deposita* **55**, 163-186.

823 Boudreau A. E. (2016) The Stillwater Complex, Montana—Overview and the significance of
824 volatiles. *Mineral. Mag.* **80(4)**, 585-637.

825 Brenan J.M. (2015) Se–Te fractionation by sulfide–silicate melt partitioning: Implications for the
826 composition of mantle-derived magmas and their melting residues. *Earth Planet. Sci.*
827 *Lett.* **422**, 45-57.

828 Cafagna F. and Jugo P.J. (2016) An experimental study on the geochemical behavior of highly
829 siderophile elements (HSE) and metalloids (As, Se, Sb, Te, Bi) in a mss-iss-pyrite system
830 at 650° C: a possible magmatic origin for Co-HSE-bearing pyrite and the role of
831 metalloid-rich phases in the fractionation of HSE. *Geochim. Cosmochim. Acta* **178**, 233-
832 258.

833 Campbell I.H., Naldrett A.J. and Barnes S.J. (1983) A model for the origin of the platinum-rich
834 sulfide horizons in the Bushveld and Stillwater Complexes. *J. Petrol.* **24**, 133-65.

835 Canali A.C., Brenan J.M. and Sullivan N.A. (2017) Solubility of platinum-arsenide melt and
836 sperrylite in synthetic basalt at 0.1 MPa and 1200° C with implications for arsenic

- 837 speciation and platinum sequestration in mafic igneous systems. *Geochim. Cosmochim.*
838 *Acta* **216**, 153-168.
- 839 Cawthorn R.G. (2002) Platinum-Group Element deposits of the Bushveld Complex in South
840 Africa. In *Geology, Geochemistry, Mineralogy and Mineral Beneficiation of Platinum*
841 *Group Element* (ed. L.J. Cabri). Canadian Institute of Mining, Metallurgy and Petroleum,
842 Special volume 54, pp. 389-429.
- 843 Cawthorn R.G. and Boerst K. (2006) Origin of the pegmatitic pyroxenite in the Merensky unit,
844 Bushveld Complex, South Africa. *J. Petrol.* **47(8)**, 1509-1530.
- 845 Chakraborty I. and Pradeep T. (2017) Atomically precise clusters of noble metals: emerging link
846 between atoms and nanoparticles. *Chem. Rev.* **117(12)**, 8208-8271.
- 847 Chen L.M., Song X.Y., Keays R.R., Tian Y.L., Wang Y.S., Deng Y.F. and Xiao J.F. (2013)
848 Segregation and fractionation of magmatic Ni-Cu-PGE sulfides in the western Jinchuan
849 intrusion, northwestern China: Insights from platinum group element geochemistry. *Econ.*
850 *Geol.* **108(8)**, 1793-1811.
- 851 Chen L.M., Song X.Y., Danyushevsky L.V., Wang Y.S., Tian Y.L. and Xiao J.F. (2015) A laser
852 ablation ICP-MS study of platinum-group and chalcophile elements in base metal sulfide
853 minerals of the Jinchuan Ni–Cu sulfide deposit, NW China. *Ore Geol. Rev.* **65**, 955-967.
- 854 Dare S.A.S., Barnes S-J., Prichard H.M. and Fisher P.C. (2010a) The timing and formation of
855 platinum-group minerals from the Creighton Ni-Cu-platinum-group element sulfide
856 deposit, Sudbury, Canada: Early crystallization of PGE-rich sulfarsenides. *Econ. Geol.*
857 **105**, 1071-1096.
- 858 Dare S.A.S., Barnes S-J. and Prichard H.M. (2010b) The distribution of platinum group elements
859 (PGE) and other chalcophile elements among sulfides from the Creighton Ni–Cu–PGE
860 sulfide deposit, Sudbury, Canada, and the origin of palladium in pentlandite. *Miner.*
861 *Deposita* **45**, 765-793.

- 862 Dare S.A.S., Barnes S-J., Prichard H.M. and Fisher P.C. (2014) Mineralogy and geochemistry of
863 Cu-rich ores from the McCreedy East Ni-Cu-PGE deposit (Sudbury, Canada):
864 Implications for the behavior of platinum group and chalcophile elements at the end of
865 crystallization of a sulfide liquid. *Econ. Geol.* **109**, 343-366.
- 866 Djon M.L.N. and Barnes S-J. (2012) Changes in sulfides and platinum-group minerals with the
867 degree of alteration in the Roby, Twilight, and High Grade Zones of the Lac des Iles
868 Complex, Ontario, Canada. *Miner. Deposita* **47**, 875-896.
- 869 D'Souza R.J. and Canil D. (2018) The partitioning of chalcophile elements between sediment
870 melts and fluids at 3 GPa, 950–1050° C with implications for slab fluids in subduction
871 zones. *Earth Planet. Sci. Lett.* **498**, 215-225.
- 872 Dunn T. and Sen C. (1994) Mineral/matrix partition coefficients for orthopyroxene, plagioclase,
873 and olivine in basaltic to andesitic systems: a combined analytical and experimental
874 study. *Geochim. Cosmochim. Acta* **58(2)**, 717-733.
- 875 Duran C.J., Barnes S-J. and Corkery J.T. (2016) Trace element distribution in primary sulfides
876 and Fe–Ti oxides from the sulfide-rich pods of the Lac des Iles Pd deposits, Western
877 Ontario, Canada: Constraints on processes controlling the composition of the ore and the
878 use of pentlandite compositions in exploration. *J. Geochem. Explor.* **166**, 45-63.
- 879 Duran C.J., Barnes S-J., Pleše P., Prašek M.K., Zientek M.L. and Pagé P. (2017) Fractional
880 crystallization-induced variations in sulfides from the Noril'sk-Talnakh mining district
881 (polar Siberia, Russia). *Ore Geol. Rev.* **90**, 326-351.
- 882 Eales H.V. and Cawthorn R.G. (1996) The Bushveld Complex. In *Layered Intrusions* (ed.
883 Cawthorn, R.G.). Elsevier, Amsterdam, pp. 181-230.
- 884 Fonseca R.O., Campbell I.H., O'Neill H.S.C. and Allen C.M. (2009) Solubility of Pt in sulphide
885 mattes: Implications for the genesis of PGE-rich horizons in layered intrusions. *Geochim.*
886 *Cosmochim. Acta* **73(19)**, 5764-5777.

- 887 Godel B. and Barnes S.-J. (2008a) Platinum-group elements in sulfide minerals and the whole
888 rocks of the JM Reef (Stillwater Complex): Implication for the formation of the reef.
889 *Chem. Geol.* **248**, 272-294.
- 890 Godel B. and Barnes S.-J. (2008b) Image analysis and composition of platinum-group minerals
891 in the JM Reef, Stillwater Complex. *Econ. Geol.* **103(3)**, 637-651.
- 892 Godel B., Barnes S.-J. and Maier, W.D. (2006) 3-D distribution of sulphide minerals in the
893 Merensky Reef (Bushveld Complex, South Africa) and the J-M Reef (Stillwater
894 Complex, USA) and their relationship to microstructures using X-ray computed
895 tomography. *J. Petrol.* **47**, 1853-1872.
- 896 Godel B., Barnes S.-J. and Maier W.D. (2007) Platinum-group elements in sulphide minerals,
897 platinum-group minerals, and whole-rocks of the Merensky Reef (Bushveld Complex,
898 South Africa): Implications for the formation of the reef. *J. Petrol.* **48**, 1569-1604.
- 899 Godel B., Barnes S.-J., Barnes S.-J. and Maier W.D. (2010) Platinum ore in three dimensions:
900 Insights from high-resolution X-ray computed tomography. *Geology* **38(12)**, 1127-1130.
- 901 Godel B., Barnes S.-J. and Maier W. D. (2011) Parental magma composition inferred from trace
902 element in cumulus and intercumulus silicate minerals: An example from the Lower and
903 Lower Critical Zones of the Bushveld Complex, South-Africa. *Lithos* **125(1-2)**, 537-552.
- 904 González-Jiménez J.M. and Reich M. (2017) An overview of the platinum-group element
905 nanoparticles in mantle-hosted chromite deposits. *Ore Geol. Rev.* **81**, 1236-1248.
- 906 González-Jiménez J.M., Deditius A., Gervilla F., Reich M., Suvorova A., Roberts M.P. and
907 Proenza, J.A. (2018) Nanoscale partitioning of Ru, Ir, and Pt in base-metal sulfides from
908 the Caridad chromite deposit, Cuba. *Am. Miner.* **103(8)**, 1208-1220.
- 909 González-Jiménez J.M., Roqué-Rosell J., Jiménez-Franco A., Tassara S., Nieto F., Gervilla F.
910 and Schilling M. (2019) Magmatic platinum nanoparticles in metasomatic silicate glasses
911 and sulfides from Patagonian mantle xenoliths. *Contrib. Mineral. Petrol.* **174(5)**, 47.
- 912 Harvey J. and Day J.M. (2016) Highly Siderophile and Strongly Chalcophile Elements in High-
913 Temperature Geochemistry and Cosmochemistry. *Rev. Mineral. Geochem.* **81**, 774p.

- 914 Hattori K.H., Arai S. and Clarke D.B. (2002) Selenium, tellurium, arsenic and antimony contents
915 of primary mantle sulfides. *Can. Mineral.* **40(2)**, 637-650.
- 916 Helmy H.M., Ballhaus C., Berndt J., Bockrath C. and Wohlgemuth-Ueberwasser C. (2007)
917 Formation of Pt, Pd and Ni tellurides: experiments in sulfide–telluride systems. *Contrib.*
918 *Mineral. Petrol.* **153(5)**, 577-591.
- 919 Helmy H.M., Ballhaus C., Wohlgemuth-Ueberwasser C., Fonseca R.O. and Laurenz V. (2010)
920 Partitioning of Se, As, Sb, Te and Bi between monosulfide solid solution and sulfide
921 melt–application to magmatic sulfide deposits. *Geochim. Cosmochim. Acta* **74**, 6174-
922 6179.
- 923 Helmy H.M., Ballhaus C. and Wirth R. (2013) Noble metal nanoclusters and nanoparticles
924 precede mineral formation in magmatic sulphide melts. *Nat. Commun.* **4**, 2045.
- 925 Helmy H.M. and Bragagni A. (2017) Platinum-group elements fractionation by selective
926 complexing, the Os, Ir, Ru, Rh-arsenide-sulfide systems above 1020° C. *Geochim.*
927 *Cosmochim. Acta* **216**, 169-183.
- 928 Holwell D.A. and McDonald I. (2007) Distribution of platinum-group elements in the Platreef at
929 Overysel, northern Bushveld Complex: A combined PGM and LA-ICP-MS study.
930 *Contrib. Mineral. Petrol.* **154**, 171-190.
- 931 Holwell B. D. and McDonald I. (2010) A review of the behaviour of platinum group elements
932 within natural magmatic sulfide ore systems. *Platinum Met. Rev.* **54(1)**, 26-36.
- 933 Hutchinson D., Foster J., Pritchard H. and Gilbert S. (2015) Concentration of particulate
934 platinum-group minerals during magma emplacement; a case study from the Merensky
935 Reef, Bushveld Complex. *J. Petrol.* **56**, 113-159.
- 936 Irvine T.N., Keith D.W. and Todd S.G. (1983) The J-M platinum-palladium reef of the Stillwater
937 Complex, Montana: II. Origin by double diffusive convective magma mixing and
938 implications for the Bushveld Complex. *Econ. Geol.* **78**, 1287-334.

- 939 Jochum K.P., Nohl U., Herwig K., Lammel E., Stoll B. and Hofmann A.W. (2005) GeoReM: a
940 new geochemical database for reference materials and isotopic standards. *Geostand.*
941 *Geoanal. Res.* **29**, 333-338.
- 942 Junge M., Wirth R., Oberthür T., Melcher F. and Schreiber A. (2015) Mineralogical siting of
943 platinum-group elements in pentlandite from the Bushveld Complex, South Africa.
944 *Miner. Deposita* **50**, 41-54.
- 945 Kamenetsky V.S., Park J.W., Mungall J.E., Pushkarev E.V., Ivanov A.V., Kamenetsky M.B. and
946 Yaxley G.M. (2015) Crystallization of platinum-group minerals from silicate melts:
947 Evidence from Cr-spinel-hosted inclusions in volcanic rocks. *Geology* **43(10)**, 903-906.
- 948 Keays R.R., Lightfoot P.C. and Hamlyn P.R. (2012) Sulfide saturation history of the Stillwater
949 Complex, Montana: chemostratigraphic variation in platinum group elements. *Miner.*
950 *Deposita* **47(1-2)**, 151-173.
- 951 Kinloch E.D. (1982) Regional trends in the platinum-group mineralogy of the critical zone of the
952 Bushveld Complex, South Africa. *Econ. Geol.* **77(6)**, 1328-1347.
- 953 Kitakaze A., Machida T. and Komatsu R. (2016) Phase relations in the Fe-Ni-S system from 875
954 to 650 °C. *Can. Mineral.* **54**, 1175-1186.
- 955 König S., Luguet A., Lorand J-P., Wombacher F. and Lissner M. (2012) Selenium and tellurium
956 systematics of the Earth's mantle from high precision analyses of ultra-depleted orogenic
957 peridotites. *Geochim. Cosmochim. Acta* **86**, 354-366.
- 958 König S., Lorand J-P., Luguet A. and Pearson D.G. (2014) A non-primitive origin of near-
959 chondritic S–Se–Te ratios in mantle peridotites: implications for the Earth's late
960 accretionary history. *Earth Planet. Sci. Lett.* **385**, 110-121.
- 961 Kosyakov V.I. and Sinyakova E.F. (2012) Physicochemical prerequisites for the formation of pri-
962 mary orebody zoning at copper-nickel sulfide deposits (by the example of the systems Fe-
963 Ni-S and Cu-Fe-S). *Russ. Geol. Geophys.* **53**, 861-882.

- 964 Li Y. and Audétat A. (2015) Effects of temperature, silicate melt composition, and oxygen
965 fugacity on the partitioning of V, Mn, Co, Ni, Cu, Zn, As, Mo, Ag, Sn, Sb, W, Au, Pb,
966 and Bi between sulfide phases and silicate melt. *Geochim. Cosmochim. Acta* **162**, 25-45.
- 967 Li C. and Ripley E.M. (2005) Empirical equations to predict the sulfur content of mafic magmas
968 at sulfide saturation and applications to magmatic sulfide deposits. *Miner.
969 Deposita* **40(2)**, 218-230.
- 970 Li C. and Ripley E.M. (2006) Formation of Pt–Fe alloy by desulfurization of Pt–Pd sulfide in the
971 J–M reef of the Stillwater complex, Montana. *Can. Mineral.* **44(4)**, 895-903.
- 972 Li C., Barnes S-J., Makovicky E., Rose-Hansen J. and Makovicky M. (1996) Partitioning of Ni,
973 Cu, Ir, Rh, Pt and Pd between monosulfide solid solution and sulfide liquid: Effects of
974 composition and temperature. *Geochim. Cosmochim. Acta* **60**, 1231-1238.
- 975 Li C., Ripley E.M., Sarkar A., Shin D. and Maier W.D. (2005) Origin of phlogopite-
976 orthopyroxene inclusions in chromites from the Merensky Reef of the Bushveld
977 Complex, South Africa. *Contrib. Mineral. Petrol.* **150(1)**, 119-130.
- 978 Liang Q.L., Song X.Y., Wirth R., Chen L.M. and Dai Z.H. (2019) Implications of nano-and
979 micrometer-size platinum-group element minerals in base metal sulfides of the
980 Yangliuping Ni-Cu-PGE sulfide deposit, SW China. *Chem. Geol.* **517**, 7-21.
- 981 Lissner M., König S., Luguét A., Le Roux P., Schuth S., Heuser A. and le Roex A.P. (2014)
982 Selenium and tellurium systematics in MORBs from the southern Mid-Atlantic Ridge
983 (47–50 S). *Geochim. Cosmochim. Acta* **144**, 379-402.
- 984 Liu Y. and Brenan J. (2015) Partitioning of platinum-group elements (PGE) and chalcogens (Se,
985 Te, As, Sb, Bi) between monosulfide-solid solution (MSS), intermediate solid solution
986 (ISS) and sulfide liquid at controlled fO₂–fS₂ conditions. *Geochim. Cosmochim. Acta*
987 **159**, 139-161.
- 988 Lodders K. (2003) Solar system abundances and condensation temperatures of the elements.
989 *Astrohphys. J.* **591**, 1220-1247.
- 990 Lorand J-P. and Alard O. (2010) Determination of selenium and tellurium concentrations in
991 Pyrenean peridotites (Ariege, France): new insight into S/Se/Te systematics of the upper
992 in mantle samples. *Chem. Geol.* **278(1-2)**, 120-130.

- 993 Maier W.D., Barnes S-J. and Groves D.I. (2013) The Bushveld Complex, South Africa: formation
994 of platinum–palladium, chrome-and vanadium-rich layers via hydrodynamic sorting of a
995 mobilized cumulate slurry in a large, relatively slowly cooling, subsiding magma
996 chamber. *Miner. Deposita* **48(1)**, 1-56.
- 997 Maier W.D., Rasmussen B., Fletcher I., Godel B., Barnes S.J., Fisher L., Yang S., Huhma H. and
998 Lahaye Y. (2015) Petrogenesis of the ~2.77 Ga Monts de Cristal Complex, Gabon:
999 evidence for direct precipitation of Pt- arsenides from basaltic magma. *J. Petrol.* **56**,
1000 1285-308.
- 1001 Makovicky M., Makovicky E. and Rose-Hansen J. (1986) Experimental studies on the solubility
1002 and distribution of platinum group elements in base metal sulfides in platinum deposits. In
1003 *Metallogeny of Basic and Ultrabasic Rocks* (ed. Gallagher M.J., Ixer R.A., Neary C.R.
1004 and Prichard H.M.). Institution of Mining and Metallurgy, pp. 415–425.
- 1005 Makovicky E. (2002) Ternary and quaternary phase systems in PGE. In *Geology, Geochemistry,*
1006 *Mineralogy and Mineral Beneficiation of Platinum Group Element* (ed. L.J. Cabri).
1007 Canadian Institute of Mining, Metallurgy and Petroleum, Special volume 54, pp. 131-
1008 175.
- 1009 Mansur E.T., Barnes S-J. and Duran C.J. (2019a) Textural and compositional evidence for the
1010 formation of pentlandite via peritectic reaction: Implications for the distribution of highly
1011 siderophile elements. *Geology* **47(4)**, 351-354.
- 1012 Mansur E.T., Barnes S-J., Savard D. and Webb P.C. (2019b) Determination of Te, As, Bi, Sb and
1013 Se (TABS) in Geological Reference Materials and GeoPT Proficiency Test Materials by
1014 Hydride Generation-Atomic Fluorescence Spectrometry (HG-AFS). *Geostand. Geoanal.*
1015 *Res.* doi.org/10.1111/ggr.12289
- 1016 Mansur E.T., Barnes S.J., Duran C.J. and Sluzhenikin S.F. (2019c) Distribution of chalcophile
1017 and platinum-group elements among pyrrhotite, pentlandite, chalcopyrite and cubanite

- 1018 from the Noril'sk-Talnakh ores: Implications for the formation of platinum-group
1019 minerals. *Miner. Deposita* 1-18.
- 1020 Mc Callum I.S., Raedeke L.D. and Mathez E.A. (1980) Investigations of the Stillwater Complex:
1021 part I. Stratigraphy and structure of the banded zone. *Am. J. Sci.* **280**, 59-87.
- 1022 McLaren C.H. and De Villiers J.P. (1982) The platinum-group chemistry and mineralogy of the
1023 UG-2 chromitite layer of the Bushveld Complex. *Econ. Geol.* **77(6)**, 1348-1366.
- 1024 Mungall J.E. (2007) Crystallization of magmatic sulfides: An empirical model and application to
1025 Sudbury ores. *Geochim. Cosmochim. Acta* **71(11)**, 2809-2819.
- 1026 Mungall J.E. and Brenan J.M. (2014) Partitioning of platinum-group elements and Au between
1027 sulfide liquid and basalt and the origins of mantle-crust fractionation of the chalcophile
1028 elements. *Geochim. Cosmochim. Acta* **125**, 265-89.
- 1029 Mungall J.E., Andrews D.R., Cabri L.J., Sylvester P.J. and Tubrett M. (2005) Partitioning of Cu,
1030 Ni, Au, and platinum-group elements between monosulfide solid solution and sulfide
1031 melt under controlled oxygen and sulfur fugacities. *Geochim. Cosmochim. Acta* **69**, 4349-
1032 4360.
- 1033 Naldrett A.J., Wilson A., Kinnaird J. and Chunnett G. (2009) PGE tenor and metal ratios within
1034 and below the Merensky Reef, Bushveld Complex: implications for its genesis. *J. Petrol.*
1035 **50(4)**, 625-659.
- 1036 O'Driscoll B. and González-Jiménez J.M. (2016) Petrogenesis of the platinum-group minerals.
1037 *Rev. Mineral. Geochem.* **81**, 489-578.
- 1038 Oberthür T. (2011) Platinum-group element mineralization of the Main Sulfide Zone, Great
1039 Dyke, Zimbabwe. *Rev. Econ. Geol.* **17**, 329-349.
- 1040 Osbahr I., Klemd R., Oberthür T., Brätz H. and Schouwstra R. (2013) Platinum-group element
1041 distribution in base-metal sulfides of the Merensky Reef from the eastern and western
1042 Bushveld Complex, South Africa. *Miner. Deposita* **48(2)**, 211-232.

- 1043 Osbahr I., Oberthür T., Klemd R. and Josties A. (2014) Platinum-group element distribution in
1044 base-metal sulfides of the UG2 chromitite, Bushveld Complex, South Africa - a
1045 reconnaissance study. *Miner. Deposita* **49(6)**, 655-665.
- 1046 Pagé P. and Barnes S-J. (2009) Using trace elements in chromites to constrain the origin of
1047 podiform chromitites in the Thetford Mines ophiolite, Québec, Canada. *Econ.*
1048 *Geol.* **104(7)**, 997-1018.
- 1049 Patten C., Barnes S-J., Mathez E.A. and Jenner F.E. (2013) Partition coefficients of chalcophile
1050 elements between sulfide and silicate melts and the early crystallization history of sulfide
1051 liquid: LA-ICP-MS analysis of MORB sulfide droplets. *Chem. Geol.* **358**, 170-188.
- 1052 Patten C.G., Pitcairn I.K., Teagle D.A. and Harris M. (2016) Mobility of Au and related elements
1053 during the hydrothermal alteration of the oceanic crust: implications for the sources of
1054 metals in VMS deposits. *Miner. Deposita* **51**, 179-200.
- 1055 Patten C.G., Pitcairn I.K. and Teagle D.A.H. (2017) Hydrothermal mobilisation of Au and other
1056 metals in supra-subduction oceanic crust: Insights from the Troodos ophiolite. *Ore Geol.*
1057 *Rev.* **86**, 487-508.
- 1058 Paton C., Hellstrom J., Paul B., Woodhead J. and Hergt J. (2011) Iolite: Freeware for the
1059 visualisation and processing of mass spectrometric data. *J. Anal. Atom. Spec.* **26**, 2508-
1060 2518.
- 1061 Peregoedova A., Barnes S.J. and Baker D.R. (2004) The formation of Pt–Ir alloys and Cu–Pd-rich
1062 sulfide melts by partial desulfurization of Fe–Ni–Cu sulfides: results of experiments and
1063 implications for natural systems. *Chem. Geol.* **208(1-4)**, 247-264.
- 1064 Piña R., Gervilla F., Barnes S-J., Ortega L. and Lunar R. (2012) Distribution of platinum-group
1065 and chalcophile elements in the aguablanca Ni-Cu sulfide deposit (SW Spain): Evidence
1066 from a LA-ICP-MS study. *Chem. Geol.* **302**, 61-75.
- 1067 Piña R., Gervilla F., Barnes S-J., Ortega L. and Lunar R. (2015) Liquid immiscibility between
1068 arsenide and sulfide melts: Evidence from a LA-ICP-MS study in magmatic deposits at
1069 Serranía de Ronda (Spain). *Miner. Deposita* **50**, 265-279.

- 1070 Prichard H., Hutchinson D. and Fisher P. (2004) Petrology and crystallization history of
1071 multiphase sulfide droplets in a mafic dike from Uruguay: Implications for the origin of
1072 Cu-Ni-PGE sulfide deposits. *Econ. Geol.* **99**, 365-376.
- 1073 Ripley E.M. and Li C. (2013) Sulfide saturation in mafic magmas: Is external sulfur required for
1074 magmatic Ni-Cu-(PGE) ore genesis?. *Econ. Geol.* **108(1)**, 45-58.
- 1075 Samalens N., Barnes S-J. and Sawyer E.W. (2017) The role of black shales as a source of sulfur
1076 and semimetals in magmatic nickel-copper deposits: Example from the Partridge River
1077 Intrusion, Duluth Complex, Minnesota, USA. *Ore Geol. Rev.* **81(1)**, 173-187.
- 1078 Scholten L., Watenphul A., Beermann O., Testemale D., Ames D. and Schmidt C. (2018) Nickel
1079 and platinum in high-temperature H₂O+ HCl fluids: Implications for hydrothermal
1080 mobilization. *Geochim. Cosmochim. Acta* **224**, 187-199.
- 1081 Sullivan N.A., Zajacz Z. and Brenan J.M. (2018) The solubility of Pd and Au in hydrous
1082 intermediate silicate melts: the effect of oxygen fugacity and the addition of Cl and S.
1083 *Geochim. Cosmochim. Acta* **231**, 15-29.
- 1084 Tredoux M., Lindsay N.M., Davies G. and McDonald I. (1995) The fractionation of platinum-
1085 group elements in magmatic systems, with the suggestion of a novel causal mechanism.
1086 *S. Afr. J. Geol.* **98**, 157-167.
- 1087 Von Gruenewaldt G. (1986) Platinum-group element chromitite associations in the Bushveld
1088 Complex. *Econ. Geol.* **81**, 1067-1079.
- 1089 Von Gruenewaldt G. (1989) Contrasting platinum-group element concentration patterns in
1090 cumulates of the Bushveld Complex. *Miner. Deposita.* **24(3)**, 219-229.
- 1091 Wang Z. and Becker H. (2013) Ratios of S, Se and Te in the silicate Earth require a volatile-rich
1092 late veneer. *Nature* **499**, 328-331.
- 1093 Wirth R., Reid D. and Schreiber A. (2013) Nanometer-sized platinum-group minerals (PGM) in
1094 base metal sulfides: new evidence for an orthomagmatic origin of the Merensky Reef
1095 PGE ore deposit, Bushveld Complex, South Africa. *Can. Mineral.* **51**, 143-155.

1096 Wood S.A. (2002) The aqueous geochemistry of the platinum group elements with applications to
1097 ore deposits. In *Geology, Geochemistry, Mineralogy and Mineral Benefication of*
1098 *Platinum Group Element* (ed. L.J. Cabri). Canadian Institute of Mining, Metallurgy and
1099 Petroleum, Special volume 54, pp. 211-249.

1100 Yudovskaya M.A., Kinnaird J.A., Grobler D.F., Costin G., Abramova V.D., Dunnett T. and
1101 Barnes S-J. (2017) Zonation of Merensky-style platinum-group element mineralization in
1102 Turfspruit thick reef facies (Northern Limb of the Bushveld Complex). *Econ.*
1103 *Geol.* **112(6)**, 1333-1365.

1104 Zientek M.L., Cooper R.W., Corson S.R. and Geraghty E.P. (2002) Platinum-group element
1105 mineralization in the Stillwater Complex, Montana. In *Geology, Geochemistry,*
1106 *Mineralogy and Mineral Benefication of Platinum Group Element* (ed. L.J. Cabri).
1107 Canadian Institute of Mining, Metallurgy and Petroleum, Special volume 54, pp. 459-
1108 481.

1109
1110
1111
1112
1113
1114
1115
1116
1117
1118
1119
1120
1121
1122
1123
1124
1125
1126
1127
1128
1129
1130
1131
1132

1
2
3
4
5
6
7
8
9
10
11
12
13
14
15
16
17
18
19
20
21
22
23
24

Chapitre 7 – Synthèse et remarques finales

25
26
27
28
29
30
31
32
33
34
35
36
37
38
39
40
41
42
43
44
45
46
47
48

49 **7.1 – Introduction**

50

51 Ce chapitre résume les principales conclusions de ce projet de doctorat et est divisé en
52 trois parties principales. La première partie fournit une synthèse globale des résultats, en se
53 concentrant sur les améliorations de la méthodologie et l'hypothèse qui devaient être testées. La
54 deuxième partie a indiqué le contexte général dans lequel la thèse a été insérée. Enfin, la
55 troisième partie fournit quelques questions soulevées par les résultats du projet et quelques
56 suggestions pour des études futures.

57

58 **7.2 – Synthèse des résultats**

59 **7.2.1 – Améliorations analytiques pour déterminer TABS dans les matériaux** 60 **géologiques**

61

62 La première partie de ce projet de doctorat s'est concentrée sur la mise en œuvre
63 d'une routine d'analyse au LabMaTer (UQAC) qui permet de mesurer de faibles concentrations de
64 TABS dans les matériaux géologiques. Comme présenté au chapitre 2, la méthode de la
65 spectroscopie de fluorescence atomique couplée à un générateur d'hydrure (HG-AFS) a été mise
66 en œuvre et a permis la plupart des analyses du projet. Plusieurs matériaux géologiques
67 internationaux ont été analysés afin de vérifier l'exactitude et la précision de la méthode. Les
68 résultats confirment son utilisation pour la quantification de TABS à de faibles niveaux (quelques
69 ppb).

70 La mise en œuvre de cette routine a non seulement permis le développement de ce projet,
71 mais peut également soutenir de futures enquêtes. Cela est principalement dû au fait que le
72 nombre d'études basées sur de TABS dans différents contextes a considérablement augmenté au
73 cours des dernières années (Pitcairn, 2004; Lorand et Alard, 2010; König, et al., 2012, 2014;
74 Jenner et O'Neill, 2012; Wang et Becker, 2013; Lissner et al., 2014; Yierpan et al., 2019; Maciag

75 et Brenan, 2020), et devrait continuer d'augmenter. Cependant, le nombre de laboratoires dans le
76 monde qui sont capables de mesurer les TABS à de faibles niveaux dans les matériaux
77 géologiques est toujours limité. Par conséquent, le projet contribue à de futures études et, de plus,
78 permet à LabMaTer (UQAC) de consolider une position dans l'analyse de ce groupe d'éléments.

79

80 **7.2.2 – L'histoire de cristallisation d'un liquide sulfuré immiscible**

81

82 La formation de gisements de sulfures magmatiques a fait l'objet de recherches au
83 cours des dernières décennies, à l'aide de divers outils (Naldrett, 2004; Barnes et Lightfoot, 2005).
84 Cependant, pour comprendre la formation de ces gisements, il faut d'abord considérer comment
85 cristallise un liquide sulfuré. Ce projet contribue à la compréhension globale de la formation de
86 dépôts magmatiques en fournissant des preuves textuelles et de composition pour la formation de
87 pentlandite à des températures élevées, via une réaction péritectique entre le MSS et le liquide
88 sulfuré, comme détaillé dans le chapitre 4. Les résultats soutiennent ce futur les investigations
89 devraient considérer cette étape supplémentaire lors de la formation des dépôts de sulfures
90 magmatiques.

91 Bien que l'amélioration de la compréhension de la cristallisation d'un liquide sulfuré n'ait
92 pas été l'objectif principal de ce projet, il s'agit d'un produit secondaire de nos recherches. De
93 plus, la compréhension du comportement des TABS lors du fractionnement du liquide sulfuré, et
94 par conséquent de leur rôle lors de la formation des gisements de sulfures magmatiques, repose
95 sur la compréhension du fractionnement du liquide sulfuré lui-même. En effet, l'une des
96 hypothèses étudiées est l'exsolution des MGP à partir des SMB, qui dépend finalement de la
97 façon dont les EGP et TABS peuvent être incorporés dans les SMB pendant la cristallisation. Par
98 conséquent, les résultats présentés au chapitre 4 soutiennent la formation de pentlandite via une
99 réaction péritectique, et l'incorporation de Pd et potentiellement de TABS dans son réseau
100 cristallin.

101 **7.2.3 – Rôle des TABS lors de la cristallisation fractionnée du liquide sulfuré**

102

103 Cette partie de la thèse répond au problème initial d'un liquide immiscible riche en TABS
104 pouvant se séparer du liquide sulfuré (Hanley 2007; Helmy et al.2007, 2013; Cafagna et Jugo,
105 2016; Sinyakova et al., 2017), ou les MGP pourraient cristalliser directement à partir du liquide
106 sulfuré (Dare et al., 2014; Duran et al., 2017). Les résultats des variations cryptiques des SMB du
107 district minier de Noril'sk-Talnakh confirment que les concentrations de TABS dans le liquide
108 sulfuré augmentent progressivement pendant la cristallisation fractionnée. Cette augmentation
109 progressive confirme également qu'aucune baisse majeure des concentrations de TABS dans le
110 liquide sulfuré ne s'est produite, comme cela serait attendu lors de la ségrégation de liquide
111 immiscible riche en TABS. De plus, les données expérimentales actuelles et les résultats de
112 modélisation (Li et Audétat, 2015; Liu et Brenan, 2015) soutiennent que même après 99,9% de
113 cristallisation fractionnée du liquide sulfuré, les concentrations en TABS ne sont pas
114 suffisamment élevées pour qu'un liquide immiscible se forme. Au contraire, après un
115 fractionnement étendu, les concentrations de Pt, Pd et TABS dans le liquide sulfuré atteignent des
116 niveaux qui permettent la cristallisation directe des MGP à partir du liquide sulfuré.

117 Dans l'ensemble, les résultats confirment le comportement incompatible des TABS
118 pendant la cristallisation fractionnée du liquide sulfuré et la cristallisation directe des MGP, au
119 lieu de la formation d'un liquide immiscible riche en TABS. Dans ce modèle, Pt, Pd et TABS
120 resteront dans les dernières portions fractionnées du liquide sulfuré et cristalliseront des MGP.
121 Cela peut avoir des implications importantes pour la distribution de Pt, Pd et TABS pendant
122 l'altération des gisements de sulfures magmatiques. En effet, la température de cristallisation de
123 ces MGP est faible (<600 ° C; Cabri et Laflamme, 1976; Hoffman et MacLean, 1976; Dare et al.,
124 2014; Duran et al., 2017), et ils peuvent être plus facilement remobilisés (Tomkins et al., 2007).
125 Par conséquent, il est possible que certaines des zones à faible S-haut-Pt-Pd trouvées autour des
126 intrusions soient le résultat de la remobilisation de ces portions les plus fractionnées du liquide
127 sulfuré (Péntek et al., 2008; Tuba et al. , 2014). Dans ces cas, les TABS ne joueraient pas

128 nécessairement un rôle actif lors du fractionnement du liquide sulfuré, mais pourrait être des
129 éléments importants lors de l'altération des gisements magmatiques de sulfure.

130

131 **7.2.4 – Rôle des TABS pendant l'exsolution des MGP**

132

133 Le contexte adéquat pour étudier le rôle de TABS pendant l'exsolution des MGP
134 est en considérant les gisements de sulfure magmatique qui ont subi une cristallisation à
135 l'équilibre. En effet, les variations des teneurs en TABS causées par la cristallisation fractionnée
136 peuvent être ignorées dans ces cas, et ainsi les effets des processus post-cumulus peuvent être
137 plus facilement évalués. Par conséquent, l'étude des *Reefs* à EGP des complexes du Bushveld et
138 Stillwater nous a permis d'évaluer l'hypothèse si les TABS jouent un rôle lors de l'exsolution des
139 MGP, ou même si la concentration des TABS dans les SMB pourraient être un facteur limitant
140 contrôlant l'extinction qui les exsolution des MGP peuvent avoir lieu (Makovicky et al., 1990;
141 Makovicky, 2002; Prichard et al., 2004; Godel et al., 2007; Holwell et McDonald, 2007; Godel et
142 Barnes, 2008; Wirth et al., 2013; Junge et al., 2015).

143 Les résultats présentés dans les chapitres 5 et 6 ont permis de comprendre comment
144 l'exsolution des MGP affecte le contenu des TABS dans les SMB. Les résultats confirment que
145 les EGP créent un potentiel chimique pour l'exsolution des MGP à partir des SMB. Par
146 conséquent, une fois que les EGP ont besoin d'un partenaire ligand pour exsolver à partir des
147 SMB, ils séquestrent les TABS du réseau des SMB. En conséquence, les SMB des échantillons
148 riches en EGP sont épuisés en TABS, et le budget de roche totale pour ces éléments est expliqué
149 par la présence des MGP. Cependant, il n'y a aucune preuve claire que la concentration initiale de
150 TABS dans les SMB est un facteur important limitant l'exsolution des MGP. Cela est
151 probablement dû au fait que, bien que les TABS soient les ligands les plus fréquents pour les
152 MGP, les EGP peuvent également s'exsolver sous la forme de sulfures ou des alloys.

153

154 **7.2.5 – La concentration des TABS dans les magmas initiaux qui forment des**
155 **gisements de EGP**

156

157 Cette partie du projet s'est concentrée sur l'évaluation de la concentration des TABS dans
158 les liquides initiaux qui cristallisent les gisements de EGP. Ainsi, l'étude du contenu des TABS
159 dans des échantillons de la *Marginal Zone* du complexe du Bushveld a permis de comprendre
160 quels processus affectent la distribution de TABS dans les magmas qui ont cristallisé certains des
161 plus grands gisements de PGE au monde. Les résultats confirment que la distribution des TABS
162 repose en grande partie sur leur comportement chalcophile (Li et Audétat, 2015; Liu et Brenan,
163 2015; Barnes, 2016). Le Te et le Se sont des éléments fortement chalcophiles, et leur distribution
164 est principalement contrôlée par les sulfures. Par contre, As et Sb ne sont que des éléments
165 légèrement chalcophiles, et leur distribution est principalement contrôlée par le degré
166 d'assimilation crustale des magmas. Le Bi est modérément chalcophile et sa distribution résulte
167 d'une combinaison des processus susmentionnés.

168

169 **7.3 – Contribution au débat actuel**

170

171 La thèse est insérée dans l'effort de recherche actuel pour mieux comprendre les
172 différents aspects de la formation des gisements de sulfures magmatiques. Bien que ces gisements
173 aient été largement étudiés au cours des dernières décennies, les récentes améliorations des
174 techniques analytiques ont permis d'étudier la distribution d'un groupe plus large de métaux,
175 comme le TABS, qui était l'objectif principal de ce projet. Nos modèles proposés pour le
176 comportement de TABS pendant la cristallisation fractionnée et à l'équilibre du liquide sulfuré
177 contribuent à cet effort continu pour comprendre la distribution des semi-métaux dans les
178 gisements de sulfure magmatique. De plus, les résultats de la concentration de TABS dans la
179 *Marginal Zone* du complexe du Bushveld contribuent à l'effort actuel de quantification de la
180 concentration de ces éléments dans les magmas ultramafiques et mafiques initiaux. Les résultats

181 pourraient soutenir de futures recherches visant non seulement à comprendre la distribution de
182 TABS dans les gisements de sulfures magmatiques, mais également des études fondamentales
183 visant à mieux contraindre le cycle géochimique des TABS.

184 Cette contribution est également alignée sur les efforts actuels pour comprendre la
185 distribution des métaux critiques dans divers réservoirs géologiques (Hattori et al., 2002; Lissner
186 et al., 2014; Patten et al., 2017, 2019; Samalens et al., 2017; Edmonds et al., 2018; Yierpan et al.,
187 2019; Wiesener et al., 2020). Comme indiqué au chapitre 1, il existe une demande croissante pour
188 ces métaux, en particulier pour le développement de technologies énergétiques sans émission de
189 carbone (Commission européenne, 2010 et 2014; Zweibel, 2010; Moss et al., 2013). Par
190 conséquent, les gisements de sulfures magmatiques pourraient éventuellement être considérés à
191 l'avenir comme une source potentielle de semi-métaux (USGS, 2020). Cependant, cette possibilité
192 est encore entravée par les informations limitées sur la concentration de semi-métaux dans les
193 gisements de sulfures magmatiques. Par conséquent, cette thèse fournit des informations sur ce
194 sujet et vise à contribuer à cet effort mondial actuel de recherche de métaux importants pour le
195 développement de sources d'énergie renouvelables.

196

197 **7.4 – Future investigations**

198

199 Suite aux études réalisées, plusieurs questions peuvent être posées et des investigations
200 futures proposées:

201 ➤ Il existe encore un manque de matériaux de référence géologiques bien caractérisés pour
202 les TABS à de faibles niveaux (inférieurs à 1 ppm). De futures investigations sont
203 nécessaires pour améliorer les connaissances sur les matériaux de référence, et ainsi
204 soutenir de meilleures routines analytiques pour TABS.

- 205 ➤ Il manque encore des études expérimentales sur les rôles potentiels des TABS (à
206 l'exception de As) dans la saturation des MGP à partir d'un magma silicaté.
- 207 ➤ Il y a un effort pour comprendre le cycle géochimique des TABS. Cependant, on sait
208 encore peu de choses sur les concentrations de ces éléments dans les magmas
209 ultramafiques et mafiques initiaux.
- 210 ➤ Le rôle de TABS lors de l'altération post-magmatique des gisements de sulfures
211 magmatiques n'est pas encore complètement compris et pourrait sûrement être amélioré
212 par de futures contributions.

213

214

215

216

217

218

219

220

221

222

223

224

225

226

227

228

229

230

231

232 **7.5 – Références**

- 233 Barnes, S-J. (2016) Chalcophile elements. In: White WM (Ed.) Encyclopedia of Geochemistry: A
234 Comprehensive Reference Source on the Chemistry of the Earth, Part of the series
235 Encyclopedia of Earth Sciences Series pp 1–5
- 236 Barnes, S-J., Lightfoot, P.C. (2005) Formation of magmatic nickel sulfide ore deposits and
237 processes affecting their copper and platinum group element contents. *Economic Geology*
238 100th Anniversary, 179–213
- 239 Cabri, L.J., Laflamme, J.H.G. (1976) The mineralogy of the platinum- group elements from some
240 copper-nickel deposits of the Sudbury area, Ontario. *Economic Geology*, 71: 1159-195.
- 241 Cafagna, F., Jugo, P.J. (2016) An experimental study on the geochemical behavior of highly
242 siderophile elements (HSE) and metalloids (As, Se, Sb, Te, Bi) in a mss-iss-pyrite system
243 at 650° c: A possible magmatic origin for Co-HSE-bearing pyrite and the role of
244 metalloid-rich phases in the fractionation of HSE. *Geochimica et Cosmochimica Acta*,
245 178: 233-258
- 246 Dare, S.A.S., Barnes, S-J., Prichard, H.M., Fisher, P.C. (2014) Mineralogy and geochemistry of
247 Cu-rich ores from the McCreedy East Ni-Cu-PGE deposit (Sudbury, Canada):
248 Implications for the behavior of platinum group and chalcophile elements at the end of
249 crystallization of a sulfide liquid. *Economic Geology*, 109: 343-366.
- 250 Duran, C.J., Barnes S-J., Plešem P., Prašekm M.K., Zientekm M.L., Pagé P. (2017) Fractional
251 crystallization-induced variations in sulfides from the Noril'sk-Talnakh mining district
252 (polar Siberia, Russia). *Ore Geology Reviews*, 90: 326-351.
- 253 Edmonds, M., Mather, T.A., Liu, E.J. (2018) A distinct metal fingerprint in arc volcanic
254 emissions. *Nature Geoscience*, 11(10): 790-794.
- 255 European Commission (2010) Critical Raw Materials for the EU. Report of the Ad-hoc Working
256 Group on Defining Critical Raw Materials. European Commission, Enterprise and
257 Industry.

258 European Commission (2014) Report on critical raw materials for the EU. Report of the Ad-hoc
259 Working Group on Defining Critical Raw Materials. European Commission, Enterprise
260 and Industry.

261 Godel, B., Barnes, S-J., Maier, W.D. (2007) Platinum-group elements in sulphide minerals,
262 platinum-group minerals, and whole-rocks of the Merensky Reef (Bushveld Complex,
263 South Africa): Implications for the formation of the reef. *Journal of Petrology*, 48: 1569-
264 1604.

265 Godel, B., Barnes, S-J. (2008) Platinum-group elements in sulfide minerals and the whole rocks
266 of the JM Reef (Stillwater Complex): Implication for the formation of the reef. *Chemical*
267 *Geology*, 248: 272-294.

268 Hanley, J.J. (2007) The role of arsenic-rich melts and mineral phases in the development of high-
269 grade Pt-Pd mineralization within komatiite-associated magmatic Ni-Cu sulfide horizons
270 at Dundonald Beach South, Abitibi subprovince, Ontario, Canada. *Economic Geology*,
271 102: 305-317.

272 Hattori, K.H., Arai, S., Clarke, D.B. (2002) Selenium, tellurium, arsenic and antimony contents of
273 primary mantle sulfides. *The Canadian Mineralogist*, 40(2): 637-650.

274 Helmy, H.M., Ballhaus, C., Berndt, J., Bockrath, C., Wohlgemuth-Ueberwasser, C. (2007)
275 Formation of Pt, Pd and Ni tellurides: Experiments in sulfide–telluride systems.
276 *Contributions to Mineralogy and Petrology*, 153: 577-591.

277 Helmy, H.M., Ballhaus, C., Fonseca, R., Nagel, T. (2013) Fractionation of platinum, palladium,
278 nickel, and copper in sulfide–arsenide systems at magmatic temperature. *Contributions to*
279 *Mineralogy and Petrology*, 166: 1725-1737.

280 Hoffman, E., MacLean, W.H. (1976) Phase relations of michenerite and merenskyite in the Pd-
281 Bi-Te system. *Economic Geology*, 71: 1461–1468.

282 Holwell, D., McDonald, I. (2007) Distribution of platinum-group elements in the Platreef at
283 Overysel, northern Bushveld Complex: A combined PGM and LA-ICP-MS study.
284 Contributions to Mineralogy and Petrology, 154: 171-190.

285 Jenner, F.E., O'Neill, H.S.C. (2012) Analysis of 60 elements in 616 ocean floor basaltic
286 glasses. *Geochemistry, Geophysics, Geosystems*, 13(2).

287 Junge, M., Wirth, R., Oberthür, T., Melcher, F., Schreiber, A. (2015) Mineralogical siting of
288 platinum-group elements in pentlandite from the Bushveld Complex, South Africa.
289 *Mineralium Deposita*, 50: 41-54.

290 König, S., Luguet, A., Lorand, J-P., Wombacher, F., Lissner, M. (2012) Selenium and tellurium
291 systematics of the Earth's mantle from high precision analyses of ultra-depleted orogenic
292 peridotites. *Geochimica et Cosmochimica Acta*, 86: 354-366.

293 König, S., Lorand, J-P., Luguet, A., Pearson, D.G. (2014) A non-primitive origin of near-
294 chondritic S–Se–Te ratios in mantle peridotites; implications for the Earth's late
295 accretionary history. *Earth and Planetary Science Letters*, 385: 110-121.

296 Li, Y., Audétat, A. (2015) Effects of temperature, silicate melt composition, and oxygen fugacity
297 on the partitioning of V, Mn, Co, Ni, Cu, Zn, As, Mo, Ag, Sn, Sb, W, Au, Pb, and Bi
298 between sulfide phases and silicate melt. *Geochimica et Cosmochimica Acta*, 162: 25-45.

299 Lissner, M., König, S., Luguet, A., Le Roux, P., Schuth, S., Heuser, A., le Roex, A.P. (2014)
300 Selenium and tellurium systematics in MORBs from the southern Mid-Atlantic Ridge
301 (47–50 S). *Geochimica et Cosmochimica Acta*, 144: 379-402.

302 Liu, Y., Brenan, J. (2015) Partitioning of platinum-group elements (PGE) and chalcogens (Se, Te,
303 As, Sb, Bi) between monosulfide-solid solution (MSS), intermediate solid solution (ISS)
304 and sulfide liquid at controlled fO_2 – fS_2 conditions. *Geochimica et Cosmochimica Acta*,
305 159: 139-161.

306 Lorand, J-P., Alard, O. (2010) Determination of selenium and tellurium concentrations in
307 Pyrenean peridotites (Ariege, France): new insight into S/Se/Te systematics of the upper
308 in mantle samples. *Chemical Geology*, 278(1-2): 120-130.

309 Maciag, B.J., Brenan, J.M. (2020) Speciation of Arsenic and Antimony in Basaltic
310 Magmas. *Geochimica et Cosmochimica Acta*, 276: 198-218.

311 Makovicky, E., Karup-Møller, S., Makovicky, M., Rose-Hansen, J. (1990) Experimental studies
312 on the phase systems Fe-Ni-Pd-S and Fe-Pt-Pd-As-S applied to PGE
313 deposits. *Mineralogy and Petrology*, 42(1-4): 307-319.

314 Makovicky, E. (2002) Ternary and quaternary phase systems in PGE: Canadian Institute of
315 Mining, Metallurgy and Petroleum, Special Volume 54: 131–175.

316 Moss, R.L., Tzimas, E., Kara, H., Willis, P., Kooroshy, J. (2013) The potential risks from metals
317 bottlenecks to the deployment of strategic energy technologies. *Energy Policy*, 55: 556-
318 564.

319 Naldrett, A.J. (2004) Magmatic sulphide deposits: Geology, geochemistry and exploration.
320 Springer-Verlag, Berlin: 728 p.

321 Patten, C.G., Pitcairn, I.K., Teagle, D.A.H. (2017) Hydrothermal mobilisation of Au and other
322 metals in supra-subduction oceanic crust: Insights from the Troodos ophiolite. *Ore
323 Geology Reviews*, 86: 487-508.

324 Patten, C.G.C., Pitcairn, I.K., Alt, J.C., Zack, T., Lahaye, Y., Teagle, D.A.H., Markdahl, K.
325 (2019) Metal fluxes during magmatic degassing in the oceanic crust: sulfide
326 mineralisation at ODP site 786B, Izu-Bonin forearc. *Mineralium Deposita*, 1-21.

327 Péntek, A., Molnár, F., Watkinson, D.H., Jones, P.C. (2008) Footwall-type Cu-Ni-PGE
328 Mineralization in the Broken Hammer Area, Wisner Township, North Range, Sudbury
329 Structure. *Economic Geology*, 103: 1005-1028.

330 Pitcairn, I.K. (2004) Sources of fluids and metals in orogenic gold deposits: the Otago Schists,
331 New Zealand. University of Southampton.

- 332 Prichard, H., Hutchinson, D., Fisher, P. (2004) Petrology and crystallization history of multiphase
333 sulfide droplets in a mafic dike from Uruguay: Implications for the origin of Cu-Ni-PGE
334 sulfide deposits. *Economic Geology*, 99: 365-376.
- 335 Samalens, N., Barnes, S.-J., Sawyer, E.W. (2017) The role of black shales as a source of sulfur
336 and semimetals in magmatic nickel-copper deposits: Example from the Partridge River
337 Intrusion, Duluth Complex, Minnesota, USA. *Ore Geology Reviews*, 81(1): 173-187.
- 338 Sinyakova, E.F., Kosyakov, V.I., Borisenko, A.S. (2017) Effect of the presence of As, Bi, and Te
339 on the behavior of Pt metals during fractionation crystallization of sulfide magma.
340 *Doklady Earth Sciences*, 477(2): 1422-1425.
- 341 Tuba, G., Molnár, F., Ames, D.E., Péntek, A., Watkinson, D.H., Jones, P.C. (2014) Multi-stage
342 hydrothermal processes involved in “low-sulfide” Cu (–Ni)–PGE mineralization in the
343 footwall of the Sudbury Igneous Complex (Canada): Amy Lake PGE zone, East Range.
344 *Mineralium Deposita*, 49: 7-47.
- 345 U.S. Geological Survey (2020) MineralCommodity Summaries. Accessed at
346 <<<https://www.usgs.gov/media/images/mineral-commodities-february-2020>>>
- 347 Wang, Z., Becker, H. (2013) Ratios of S, Se and Te in the silicate Earth require a volatile-rich late
348 veneer. *Nature*, 499: 328-331.
- 349 Wieser, P., Jenner, F., Edmonds, M., Maclennan, J., Kunz, B. (2020) Chalcophile elements track
350 the fate of sulfur at Kīlauea Volcano, Hawai’i. *Geochimica et Cosmochimica Acta*.
- 351 Wirth, R., Reid, D., Schreiber, A. (2013) Nanometer-sized platinum-group minerals (PGM) in
352 base metal sulfides: new evidence for an orthomagmatic origin of the Merensky Reef
353 PGE ore deposit, Bushveld Complex, South Africa. *The Canadian Mineralogist*, 51: 143-
354 155.
- 355 Yierpan, A., König, S., Labidi, J., Schoenberg, R. (2019) Selenium isotope and S-Se-Te
356 elemental systematics along the Pacific-Antarctic ridge: Role of mantle
357 processes. *Geochimica et Cosmochimica Acta*, 249: 199-224.

358 Zweibel, K. (2010) The Impact of Tellurium Supply on Cadmium Telluride Photovoltaics.
359 Science, 328: 699-701.

360

361

362

363

364

365

366

367

368

369

370

371

372

373

374

375

376

377

378

379

380

381

382

383

384

385

386
387
388
389
390
391
392
393
394
395
396
397
398
399
400
401
402
403
404
405
406
407
408
409
410
411
412
413

ANNEXE 1 - Complete dataset for Te, As, Bi, Sb and Se results for international reference materials, and GeoPt proficiency test samples, obtained by HG-AFS.

ID	GeoPT #	Rock type	Results (values in $\mu\text{g g}^{-1}$)				
			Te	As	Bi	Sb	Se
LoD (3σ)		Blank	0.010	0.019	0.016	0.026	0.002
LoQ (10σ)		Blank	0.032	0.064	0.055	0.088	0.008
CH-4		Gold ore (meta-anorthosite)	0.481	8.693	0.653	0.819	1.914
CH-4		Gold ore (meta-anorthosite)	0.508	7.975	0.831	0.769	2.001
CH-4		Gold ore (meta-anorthosite)	0.417	8.697	0.759	0.783	1.892
CH-4		Gold ore (meta-anorthosite)	0.386	8.057	0.658	0.912	1.952
CH-4		Gold ore (meta-anorthosite)	0.314	8.96	0.57	0.80	1.99
CH-4		Gold ore (meta-anorthosite)	0.316	8.86	0.55	0.91	1.96
CH-4		Gold ore (meta-anorthosite)	0.477	8.497	0.715	0.919	1.879
TDB-1		Diabase	0.045	1.972	0.043	0.853	0.373
TDB-1		Diabase	0.042	2.154	0.097	0.833	0.327
TDB-1		Diabase	0.055	2.503	0.045	0.884	0.330
TDB-1		Diabase	0.037	1.903	0.045	1.140	0.319
TDB-1		Diabase	0.038	2.28	0.09	1.24	0.376
TDB-1		Diabase	0.039	2.18	0.04	1.29	0.34
TDB-1		Diabase	0.034	1.891	0.089	0.998	0.303
KPT-1		Quartz diorite	0.605	1.975	0.919	11.372	2.975
KPT-1		Quartz diorite	0.528	1.931	0.841	10.900	3.182
KPT-1		Quartz diorite	0.465	1.729	0.782	11.067	2.931
KPT-1		Quartz diorite	0.471	2.424	0.840	11.466	2.982
KPT-1		Quartz diorite	0.426	2.32	0.93	11.02	2.86
KPT-1		Quartz diorite	0.442	2.58	1.01	10.69	2.79
KPT-1		Quartz diorite	0.546	2.091	1.028	11.026	2.992
OKUM		Komatiite	0.061	0.29	0.09	0.10	0.09
OKUM		Komatiite	0.051	0.23	0.07	0.13	0.10
OKUM		Komatiite	0.048	0.20	0.06	0.10	0.11
WPR-1		Peridotite	0.510	1.02	0.21	1.02	3.96
WPR-1		Peridotite	0.463	1.25	0.19	0.86	3.86
WPR-1		Peridotite	0.448	0.94	0.18	0.75	3.75
WMG-1		Gabbro	1.324	7.37	0.42	1.88	13.61
WMG-1		Gabbro	1.522	7.01	0.54	2.03	14.30
WMG-1		Gabbro	1.411	6.88	0.50	1.85	12.99
ANG		Anorthosite	0.010	0.020	0.050	0.118	0.029
ANG		Anorthosite	<0.01	0.025	0.083	0.108	0.021
ANG		Anorthosite	<0.01	0.027	0.075	0.126	0.033
BEN		Basalt	<0.01	1.852	<0.016	0.290	0.075
BEN		Basalt	<0.01	1.747	<0.016	0.301	0.061
BEN		Basalt	<0.01	1.824	<0.016	0.289	0.072
BIR-1		Basalt	<0.01	0.049	0.021	0.576	0.015
BIR-1		Basalt	<0.01	0.054	0.016	0.520	0.020
BIR-1		Basalt	<0.01	0.060	0.016	0.532	0.015
W-2		Diabase	0.012	0.789	0.095	0.778	0.085
W-2		Diabase	0.011	0.811	0.063	0.834	0.092
W-2		Diabase	0.011	0.700	0.060	0.746	0.082
WGB-1		Gabbro	0.017	1.542	0.055	1.755	0.098
WGB-1		Gabbro	0.011	1.656	0.040	1.829	0.081
WGB-1		Gabbro	0.012	1.588	0.063	1.846	0.097

ID	GeoPT #	Rock type	Results (values in $\mu\text{g g}^{-1}$)				
			Te	As	Bi	Sb	Se
OU-3	6	Nanhoron microgranite	<0.01	0.963	0.126	0.204	0.045
OU-3	6	Nanhoron microgranite	0.021	0.839	0.293	0.251	0.017
OU-3	6	Nanhoron microgranite	0.028	0.901	0.161	0.217	0.030
OU-3	6	Nanhoron microgranite	0.023	0.965	0.328	0.213	0.020
OU-4	8	Penmaenmawr microdiorite	0.036	1.365	0.107	0.346	0.022
OU-4	8	Penmaenmawr microdiorite	0.014	1.239	0.099	0.263	0.021
OU-4	8	Penmaenmawr microdiorite	0.016	1.255	0.091	0.302	0.020
OU-4	8	Penmaenmawr microdiorite	<0.01	1.407	0.062	0.246	0.012
CH-1	10	Marine sediment	0.094	3.796	0.256	0.961	0.554
CH-1	10	Marine sediment	0.080	3.822	0.346	0.941	0.560
CH-1	10	Marine sediment	0.078	3.613	0.319	0.942	0.549
CH-1	10	Marine sediment	0.069	3.361	0.317	0.995	0.510
OU-5	11	Leiton dolerite	0.042	2.448	0.085	0.511	0.019
OU-5	11	Leiton dolerite	0.038	2.391	0.061	0.462	0.020
OU-5	11	Leiton dolerite	0.033	2.348	0.102	0.481	0.022
OU-5	11	Leiton dolerite	<0.01	2.464	0.042	0.426	0.022
GAS	12	Serpentine	0.015	113.805	0.112	12.184	0.032
GAS	12	Serpentine	0.024	111.095	0.177	12.399	0.026
GAS	12	Serpentine	0.032	117.172	0.081	12.785	0.025
GAS	12	Serpentine	0.037	120.439	0.195	11.847	0.033
UoK							
Loess	13	Köln loess	0.023	6.314	0.134	0.385	0.030
UoK							
Loess	13	Köln loess	0.022	6.391	0.160	0.369	0.028
UoK							
Loess	13	Köln loess	0.018	6.864	0.153	0.391	0.027
UoK							
Loess	13	Köln loess	<0.01	6.311	0.190	0.254	0.029
MSAN	15	Ocean Floor sediment	0.082	7.022	0.046	0.372	0.507
MSAN	15	Ocean Floor sediment	0.068	6.839	0.119	0.467	0.527
MSAN	15	Ocean Floor sediment	0.082	7.133	0.124	0.433	0.485
MSAN	15	Ocean Floor sediment	0.080	7.649	0.158	0.555	0.613
BNV-1	16	Nevada basalt	0.015	2.383	0.060	0.192	0.031
BNV-1	16	Nevada basalt	0.046	2.185	0.065	0.154	0.021
BNV-1	16	Nevada basalt	0.013	2.496	0.062	0.168	0.025
BNV-1	16	Nevada basalt	0.017	2.368	0.064	0.141	0.022
OU-8	17	Calcareous sandstone	<0.01	0.888	0.036	0.137	0.008
OU-8	17	Calcareous sandstone	0.025	1.090	0.051	0.173	0.007
OU-8	17	Calcareous sandstone	<0.01	0.924	0.077	0.154	0.004
OU-8	17	Calcareous sandstone	<0.01	0.948	0.070	0.196	0.008
KPT-1	18	Quartz diorite	0.532	2.308	0.987	10.898	2.916
KPT-1	18	Quartz diorite	0.502	2.261	0.814	11.077	3.086
KPT-1	18	Quartz diorite	0.489	2.300	0.824	10.140	3.059
KPT-1	18	Quartz diorite	0.477	1.928	0.792	10.765	2.892
MGR-N	19	Gabbro	0.097	1.857	0.179	0.140	0.449
MGR-N	19	Gabbro	0.074	1.668	0.158	0.154	0.592
MGR-N	19	Gabbro	0.082	1.736	0.144	0.161	0.467
MGR-N	19	Gabbro	0.075	1.793	0.169	0.147	0.493

417

418

ID	GeoPT #	Rock type	Results (values in $\mu\text{g g}^{-1}$)				
			Te	As	Bi	Sb	Se
OPY-1	20	Ultramafic rock	0.043	0.345	0.033	0.183	0.117
OPY-1	20	Ultramafic rock	0.032	0.342	<0.016	0.221	0.093
OPY-1	20	Ultramafic rock	0.039	0.365	0.016	0.203	0.101
OPY-1	20	Ultramafic rock	0.033	0.245	<0.016	0.146	0.110
MGT-1	21	Granite	<0.01	1.901	1.038	0.297	<0.002
MGT-1	21	Granite	0.061	2.165	1.125	0.216	0.015
MGT-1	21	Granite	0.047	2.061	1.148	0.248	0.007
MGT-1	21	Granite	0.055	2.194	1.098	0.216	0.012
MBL-1	22	Basalt	0.202	1.595	0.081	0.219	0.026
MBL-1	22	Basalt	0.177	1.497	0.107	0.205	0.019
MBL-1	22	Basalt	0.185	1.734	0.091	0.261	0.042
MBL-1	22	Basalt	0.269	1.672	0.090	0.210	0.025
OU-9	23	Separation Lake pegmatite	0.235	2.588	0.023	6.024	<0.002
OU-9	23	Separation Lake pegmatite	0.210	2.756	0.061	7.171	0.006
OU-9	23	Separation Lake pegmatite	0.187	2.726	0.071	6.363	<0.002
OU-9	23	Separation Lake pegmatite	0.211	2.609	0.101	6.213	0.006
OU-10	24	Longmyndian greywacke	0.146	1.771	0.163	0.248	0.013
OU-10	24	Longmyndian greywacke	0.163	1.792	0.119	0.280	0.007
OU-10	24	Longmyndian greywacke	0.195	1.749	0.149	0.238	0.010
OU-10	24	Longmyndian greywacke	0.239	1.764	0.142	0.204	0.010
HTB-1	25	Basalt	0.272	0.218	0.022	0.208	0.159
HTB-1	25	Basalt	0.161	0.215	0.048	0.247	0.219
HTB-1	25	Basalt	0.229	0.192	0.051	0.217	0.134
HTB-1	25	Basalt	0.240	0.186	0.097	0.260	0.181
MGL-AND	27	Andesite	0.178	2.108	0.068	0.213	0.003
MGL-AND	27	Andesite	0.170	1.943	0.088	0.238	0.003
MGL-AND	27	Andesite	0.211	2.064	0.047	0.227	0.004
MGL-AND	27	Andesite	0.233	1.901	0.092	0.243	<0.002
NKT-1	29	Nephelinite	<0.01	1.858	0.053	0.389	0.036
NKT-1	29	Nephelinite	<0.01	1.744	0.026	0.351	0.036
NKT-1	29	Nephelinite	<0.01	1.822	0.061	0.337	0.032
NKT-1	29	Nephelinite	<0.01	1.920	0.070	0.352	0.035
CG-2	30	Syenite	<0.01	4.326	0.159	0.740	0.012
CG-2	30	Syenite	<0.01	4.399	0.179	0.856	0.011
CG-2	30	Syenite	0.024	4.219	0.196	0.843	0.012
CG-2	30	Syenite	<0.01	4.033	0.140	0.840	0.010
SdAR-1	31	Modified River Sediment	0.348	35.270	1.798	5.362	0.321
SdAR-1	31	Modified River Sediment	0.433	35.611	1.682	6.429	0.311
SdAR-1	31	Modified River Sediment	0.404	35.444	1.758	5.861	0.300
SdAR-1	31	Modified River Sediment	0.410	34.231	1.864	6.039	0.268
WG-1	32	Woodstock basalt	<0.01	0.676	0.077	0.074	0.020
WG-1	32	Woodstock basalt	<0.01	0.584	0.063	0.078	0.020
WG-1	32	Woodstock basalt	0.032	0.536	0.038	0.048	0.022
WG-1	32	Woodstock basalt	0.011	0.503	0.031	0.085	0.021

420

421

ID	GeoPT #	Rock type	Results (values in $\mu\text{g g}^{-1}$)				
			Te	As	Bi	Sb	Se
DBC-1	33	Ball Clay	0.307	3.250	1.599	1.586	2.471
DBC-1	33	Ball Clay	0.278	3.222	1.660	1.559	2.376
DBC-1	33	Ball Clay	0.241	3.223	1.540	1.530	2.346
DBC-1	33	Ball Clay	0.209	3.445	1.931	1.674	2.578
GRI-1	34	Granite	<0.01	0.941	0.073	0.225	0.048
GRI-1	34	Granite	<0.01	1.015	0.050	0.208	0.046
GRI-1	34	Granite	<0.01	1.036	0.056	0.197	0.049
GRI-1	34	Granite	<0.01	1.185	0.048	0.184	0.055
TLM-1	35	Tonalite	<0.01	2.319	0.104	1.471	0.010
TLM-1	35	Tonalite	<0.01	2.383	0.127	1.645	0.009
TLM-1	35	Tonalite	<0.01	2.353	0.060	1.546	0.010
TLM-1	35	Tonalite	<0.01	2.126	0.078	1.561	0.011
GSM-1	36	Gabbro	0.045	2.833	0.096	1.915	0.187
GSM-1	36	Gabbro	0.029	2.415	0.127	1.957	0.219
GSM-1	36	Gabbro	0.027	2.301	0.133	1.982	0.224
GSM-1	36	Gabbro	0.028	2.331	0.107	1.884	0.220
SdAR-M2	36A	Metal-rich sediment	1.136	76.240	1.151	111.257	3.775
SdAR-M2	36A	Metal-rich sediment	1.015	74.442	0.929	115.430	3.141
SdAR-M2	36A	Metal-rich sediment	1.215	70.763	0.957	112.124	3.110
SdAR-M2	36A	Metal-rich sediment	1.019	70.442	1.167	108.362	3.257
ORPT-1	37	Rhyolite	<0.01	0.384	0.031	0.307	0.003
ORPT-1	37	Rhyolite	<0.01	0.438	0.063	0.280	0.003
ORPT-1	37	Rhyolite	<0.01	0.450	0.071	0.203	0.010
ORPT-1	37	Rhyolite	<0.01	0.420	0.089	0.222	0.004
OU-7	38	Ardnamurchan gabbro	<0.01	0.143	0.024	0.080	0.077
OU-7	38	Ardnamurchan gabbro	<0.01	0.165	0.025	0.041	0.083
OU-7	38	Ardnamurchan gabbro	<0.01	0.153	0.042	0.061	0.084
OU-7	38	Ardnamurchan gabbro	<0.01	0.147	0.037	0.052	0.082
			Te	As	Bi	Sb	Se
HARZ01	38A	Modified harzburgite	0.017	0.302	0.048	1.092	0.025
HARZ01	38A	Modified harzburgite	<0.01	0.254	0.075	1.196	0.031
HARZ01	38A	Modified harzburgite	<0.01	0.252	0.094	1.186	0.032
HARZ01	38A	Modified harzburgite	0.017	0.319	0.090	1.227	0.038
SyMP-1	39	Syenite	0.132	3.722	0.809	0.238	0.179
SyMP-1	39	Syenite	0.155	3.793	0.805	0.245	0.177
SyMP-1	39	Syenite	0.137	3.672	0.831	0.228	0.183
SyMP-1	39	Syenite	0.127	3.476	0.755	0.213	0.187
MNS-1	39A	Nepheline syenite	0.015	23.082	1.163	2.887	0.037
MNS-1	39A	Nepheline syenite	0.023	21.687	0.949	3.153	0.030
MNS-1	39A	Nepheline syenite	0.023	23.036	1.107	3.225	0.040
MNS-1	39A	Nepheline syenite	0.018	20.771	1.030	3.436	0.034
ShWYO-1	40	Silty marine shale	0.086	10.520	0.343	0.985	0.555
ShWYO-1	40	Silty marine shale	0.074	11.196	0.338	0.836	0.603
ShWYO-1	40	Silty marine shale	0.068	10.191	0.323	0.877	0.548
ShWYO-1	40	Silty marine shale	0.058	9.195	0.329	0.930	0.554
ORA-1	41	Andesite	<0.01	0.263	0.058	0.901	0.005
ORA-1	41	Andesite	<0.01	0.244	0.038	0.976	<0.002
ORA-1	41	Andesite	<0.01	0.238	0.064	0.983	0.005
ORA-1	41	Andesite	<0.01	0.289	0.041	1.042	0.003

424
425
426
427
428
429
430
431
432
433
434
435
436
437
438
439
440
441
442
443
444
445
446
447
448
449
450
451

ANNEXE 2 - Whole-rock compositions of the samples from the Noril'sk-Talnakh mining district. Data from Duran et al. (2017). n.d. = not detected

ANNEXE 2

Sample ID	Ore type	Intrusion	Ag	As	Au	Bi	Cd	Co	Cu	Fe	In	Ir	Mo	Ni	Os
			ppm	ppm	ppm	ppm	ppm	ppm	%	%	ppm	ppm	ppm	%	ppm
90OMZS2-3	Cu-poor	Kharaelakh	3.93	3.40	0.05	0.25	1.22	1265	4.05	54.70	0.23	0.020	0.27	3.48	0.013
NR6	Cu-poor	Noril'sk I	2.65	3.20	0.13	0.55	0.67	2840	1.76	49.32	0.03	0.020	0.22	3.68	0.012
90KMZ5	Cu-poor	Talnakh	3.79	4.20	0.15	0.28	0.44	1382	3.94	46.40	0.08	0.370	0.94	4.97	0.180
90OMZS2-2	Cu-poor	Kharaelakh	13.43	5.00	0.40	0.86	5.52	1364	10.98	48.90	0.70	0.049	0.26	3.62	0.036
NR-13	Cu-poor	Kharaelakh	2.63	2.90	0.16	0.16	1.31	1900	6.13	43.54	0.23	0.049	0.38	3.92	0.022
NR-14	Cu-poor	Kharaelakh	2.82	3.50	0.11	0.19	1.52	1760	6.66	46.94	0.28	0.049	0.48	3.68	0.027
NR11	Cu-poor	Noril'sk I	10.86	6.00	2.29	2.83	1.25	1060	5.73	31.60	0.50	0.295	1.80	5.48	0.076
90OC13	Cu-rich	Kharaelakh	21.48	4.30	1.10	6.12	16.17	954	20.80	41.10	2.38	0.004	0.14	1.80	0.009
90OMZ67-5-1	Cu-rich	Kharaelakh	22.99	3.30	0.28	0.87	10.54	623	29.10	30.60	2.88	0.001	0.16	2.56	n.d.
90OMZS1-3	Cu-rich	Kharaelakh	21.41	4.50	1.40	2.50	10.91	908	22.75	39.80	1.84	0.044	0.12	2.13	0.043
NR15	Cu-rich	Kharaelakh	49.04	2.70	1.93	4.21	15.62	560	12.39	23.10	1.12	0.002	0.18	1.19	0.003
NR17	Cu-rich	Kharaelakh	73.08	7.50	3.13	11.30	29.45	1200	20.64	34.52	2.72	0.001	0.05	2.18	0.003
NR18	Cu-rich	Kharaelakh	31.05	2.50	2.35	2.12	17.61	430	13.25	21.71	2.00	0.000	0.16	1.11	0.001
90MC15	Cu-rich	Noril'sk I	47.96	11.60	8.00	6.85	11.46	923	24.45	33.30	1.94	0.013	0.32	7.14	0.004
90MC5	Cu-rich	Noril'sk I	17.63	13.70	0.78	9.83	16.53	651	25.15	31.10	2.21	0.002	0.25	5.94	0.001
NR8	Cu-rich	Noril'sk I	27.03	4.00	4.98	2.06	6.19	1130	19.30	30.08	1.60	0.095	0.37	4.08	0.052
NR10	Disseminated	Noril'sk I	0.39	1.70	0.15	0.02	0.10	111	0.41	11.15	0.04	0.022	0.19	0.24	0.006
NR9	Disseminated	Noril'sk I	0.64	2.40	0.16	0.23	0.10	71	0.43	9.03	0.05	0.017	0.46	0.17	0.003

ANNEXE 2 – Cont.

Sample ID	Pb	Pd	Pt	Re	Rh	Ru	S	Sb	Se	Sn	Te	Tl	Zn	(Pt+Pd)/(Rh+Ru+Ir+Os)
	ppm	ppm	ppm	ppm	ppm	ppm	%	ppm	ppm	ppm	ppm	ppm	ppm	
900MZS2-3	6.9	10.77	1.60	n.d.	0.240	0.057	30.50	< 0.06	50.2	2.32	0.87	0.337	130	37.5
NR6	25.0	8.29	1.52	n.d.	0.249	0.045	33.63	< 0.06	47.5	0.08	0.38	0.107	27	30.2
90KMZ5	2.5	26.00	5.20	0.00	3.500	1.000	32.00	0.06	57.0	0.57	1.56	1.597	42	6.2
900MZS2-2	33.1	18.00	3.10	n.d.	0.430	0.158	33.80	0.12	63.1	2.11	2.02	0.260	217	31.4
NR-13	7.8	7.49	1.46	n.d.	0.556	0.126	31.34	< 0.06	37.9	0.82	0.64	0.115	134	11.9
NR-14	7.6	8.45	1.54	n.d.	0.542	0.126	33.46	< 0.06	54.6	0.78	1.03	0.098	130	13.4
NR11	33.2	111.79	43.67	n.d.	3.412	0.577	23.24	0.19	92.1	6.43	14.28	1.094	91	35.7
90OC13	210.0	37.00	2.60	n.d.	0.033	0.015	32.88	0.52	87.4	15.74	16.05	0.800	581	647.1
900MZ67-5-1	185.0	28.00	1.90	n.d.	0.004	0.005	33.08	< 0.06	89.5	24.70	13.63	0.392	203	3250.0
900MZS1-3	88.4	29.15	7.50	n.d.	0.287	0.096	32.95	0.42	74.5	7.64	7.71	0.581	346	78.1
NR15	83.3	20.04	0.89	n.d.	0.005	0.005	19.58	0.12	47.4	8.05	7.26	0.462	303	1414.7
NR17	135.1	52.60	6.76	n.d.	0.400	0.009	32.60	0.54	128.6	12.62	22.31	1.226	389	143.6
NR18	5.8	15.28	1.33	n.d.	0.057	0.002	20.49	< 0.06	58.9	4.90	6.59	1.619	324	278.8
90MC15	3.1	270.00	74.00	0.014	0.450	0.037	33.25	0.85	166.0	17.67	50.81	1.088	328	683.2
90MC5	1.1	360.00	63.00	0.006	0.089	0.005	33.13	0.33	199.2	7.96	74.22	1.209	313	4368.0
NR8	17.8	148.79	76.56	n.d.	1.410	0.134	31.37	0.26	63.2	4.14	2.35	1.479	442	133.2
NR10	5.3	3.36	1.45	n.d.	0.219	0.052	1.62	< 0.06	3.7	0.62	0.54	0.140	93	16.1
NR9	2.0	5.15	1.63	n.d.	0.179	0.032	1.00	< 0.06	3.8	0.87	0.95	0.087	66	29.3

ANNEXE 3 – Analyses of reference materials used in the calibration of the LA-ICP-MS and in-house reference materials used to monitor the data quality for results from the Noril'sk-Talnakh mining district. Stdev= standard deviation; n= number of analyses; RSD= relative standard deviation; n.d.= not determined.

ANNEXE 3

	Isotope used	¹⁰⁹ Ag	⁷⁵ As	¹⁹⁷ Au	²⁰⁹ Bi	¹¹¹ Cd	⁵⁹ Co	⁶⁵ Cu	¹¹⁵ In	¹⁹³ Ir	⁹⁵ Mo	⁶¹ Ni	¹⁸⁹ Os
	Detection limit	0.007	0.065	0.008	0.004	0.037	0.007	0.187	0.005	0.004	0.020	0.643	0.017
	<i>RM used for calibration</i>	GSE-1g	GSE-1g	Po-727	GSE-1g	GSE-1g	GSE-1g	MASS-1	GSE-1g	Po-727	GSE-1g	GSE-1g	Po-727
	Concentrations used	200	260	45.8	320	160	380	13.4	370	48	390	440	46.7
	Stdev	20	90	2.4	30	50	20	0.05	60	1.2	30	30	2.6
		<i>Values obtained for reference materials used as monitors</i>											
JB-MSS-5 FeS in house monitor	Working value (UQAC)	60.9	79	35.9	76.1	<0.26	<1	0.021		40.21	<1	10675	42.58
	Stdev	3.7	11	4.8	2.9			0.007		0.53		1130	0.93
	This study (average)	58.8	57.78	37.57	84.19	0.2	0.14	0.023		39.75	0.52	10742	44.38
	Stdev (n= 22)	3.6	5.05	3.71	3.86	0.1	0.09	0.001		2.88	0.06	360	3.85
	RSD (%)	6.2	8.74	9.87	4.58	50.00	64.29	4.35		7.25	11.54	3.35	8.68
	Difference %	-3.43	26.86	4.65	10.63			12.20		-1.14		0.63	4.23
GSE-1g dopped basalt USGS	Working values (Georem, Te UQAC)			7				0.038					
	Stdev			n.d.				0.004					
	This study (average)			8.26				0.037					
	Stdev (n= 13)			0.67				0.001					
	RSD (%)			8.07				2.620					
	Difference %			18.00				-2.63					
MASS-1 ZnCuS pressed power pellet USGS	Working value (certificate)	50	65	47	60	60	60		50	46.2	59	97	<dl
	Stdev	5	3	n.d.	n.d.	7	10		n.d	n.d	9	15	
	This study (average)	67.06	56.84	54.6	68.96	52.84	74.5		62.01	58.49	63.95	108	<dl
	Stdev (n= 22)	2.24	2.67	5.18	1.57	3.62	2.47		1.67	8.06	1.56	23	
	RSD (%)	3.33	4.7	9.49	2.28	6.84	3.31		2.69	13.77	2.43	21	
	Difference %	34.12	12.55	16.17	14.93	11.93	24.17		24.02	26.60	8.39	11.63	

ANNEXE 3 – Cont.

	Isotope used	²⁰⁸ Pb	¹⁰⁸ Pd	¹⁹⁵ Pt	¹⁸⁵ Re	¹⁰³ Rh	¹⁰¹ Ru	¹²¹ Sb	⁸² Se	¹¹⁸ Sn	¹³⁰ Te	²⁰⁵ Tl	⁶⁶ Zn
	Detection limit	0.007	0.008	0.013	0.010	0.002	0.015	0.047	1.824	0.050	0.257	0.004	0.174
	<i>RM used for calibration</i>	GSE-1g	Po-727	Po-727	GSE-1g	Po-727	Po-727	GSE-1g	MASS-1	GSE-1g	MASS-1	MASS-1	MASS-1
	Concentrations used	378	43.4	35.5	78.9	41.6	36.5	450	51	280	15	50	210000
	Stdev	12	0.3	0.8	n.d.	0.3	0.3	110	4	50	n.d.	n.d.	500
		<i>Values obtained for reference materials used as monitors</i>											
JB-MSS-5 FeS in house monitor	Working value (UQAC)	71.5	54.04	40.3	20.7	61.4	21.72	59	59.7	<0.5	36.8	<dl	<10
	Stdev	4.5	4.4	4.8	n.d.	4.5	1.7	7.3	10.9		6.6		100.0
	This study (average)	77.9	63.65	38.99	21.7	59.97	19.96	75.32	58.41	0.87	39.36	<dl	<36
	Stdev (n= 22)	5.39	4.75	2.9	1.78	4.43	1.79	7.68	4.36	0.32	2.67		
	RSD (%)	6.92	7.46	7.44	8.20	7.39	8.97	10.20	7.46	36.78	6.78		
	Difference %	8.95	17.78	-3.25	4.83	-2.33	-8.10	27.66	-2.16		6.96		
GSE-1g dopped basalt USGS	Working values (Georem, Te UQAC)			30					20		n.d.	1.95	460
	Stdev			n.d.					16		n.d.	0.4	10
	This study (average)			21.21					45.71		180.92	1.39	398.7
	Stdev (n= 13)			3.45					6.7		14.83	0.06	29.1
	RSD (%)			16.25					14.66		8.20	4.54	7.3
	Difference %			-29.30					128.55		-28.72	-13.34	
MASS-1 ZnCuS pressed power pellet USGS	Working value (certificate)	68	<dl	51.9	<dl	<dl	<dl	60		59			
	Stdev	7		n.d.				9		6			
	This study (average)	79.02	<dl	58.96	<dl	<dl	<dl	72.91		58.81			
	Stdev (n= 22)	2.8		2.5				4.04		2.08			
	RSD (%)	3.54		4.26				5.55		3.54			
	Difference %	16.21		13.60				21.52		-0.32			

ANNEXE 4 - Complete data set of SEM-EDS and LA-ICP-MS analyses of pyrrhotite obtained for the Noril'sk-Talnakh mining district and median values for each sample. Abbreviations: N= number of individual analyses

ANNEXE 4

Sample	Ore type	Intrusion	S	Fe	⁵⁹ Co	⁶¹ Ni	⁶⁵ Cu	⁶⁶ Zn	⁷⁵ As	⁸² Se	⁹⁵ Mo	¹⁰¹ Ru	¹⁰³ Rh	¹⁰⁸ Pd
			%	%	ppm	ppm	ppm	ppm	ppm	ppm	ppm	ppm	ppm	ppm
Limit of detection			0.5	0.5	0.007	0.643	0.187	0.174	0.065	1.824	0.020	0.015	0.002	0.008
90OMZS2-3	Cu-poor	Kharaelakh	39.02	60.37	27.1	2986	2.3	143.4	0.065	57.6	0.28	0.015	0.174	0.008
90OMZS2-3	Cu-poor	Kharaelakh			52.4	3808	17.5	0.17	0.065	57.7	0.34	0.015	0.238	0.017
90OMZS2-3	Cu-poor	Kharaelakh			34.3	3659	3.2	0.17	0.065	54.2	0.34	0.015	0.201	0.008
90OMZS2-3	Cu-poor	Kharaelakh			36.3	3303	935.0	1.43	0.065	54.7	0.39	0.080	0.162	0.023
90OMZS2-3	Cu-poor	Kharaelakh			28.9	2936	317.9	0.17	0.065	55.3	0.52	0.054	0.272	0.008
90OMZS2-3	Cu-poor	Kharaelakh			24.0	2749	5.5	0.17	0.443	64.3	0.27	0.015	0.165	0.008
Median 90OMZS2-3 (N=6)			39.0	60.4	31.6	3145	11.5	0.17	0.065	56.4	0.34	0.015	0.188	0.008
90KMZ5	Cu-poor	Talnakh	38.6	59.8	158.9	9412	0.6	0.17	0.065	70.4	1.20	0.384	3.571	0.294
90KMZ5	Cu-poor	Talnakh			299.2	11531	1.6	0.17	0.065	71.1	1.38	0.520	3.733	0.543
90KMZ5	Cu-poor	Talnakh			149.6	8851	0.5	0.17	0.065	68.7	1.50	0.480	3.621	0.008
90KMZ5	Cu-poor	Talnakh			498.6	22813	1.7	0.17	0.065	67.3	1.17	0.531	3.827	3.116
90KMZ5	Cu-poor	Talnakh			662.6	24371	0.6	0.17	0.065	68.8	1.99	1.036	4.668	4.806
90KMZ5	Cu-poor	Talnakh			1340	47994	2.4	0.17	0.065	72.5	1.38	1.096	4.525	16.327
Median 90KMZ5 (N=6)			38.6	59.8	398.9	17172	1.1	0.17	0.065	69.6	1.38	0.525	3.780	1.829
NR-6	Cu-poor	Noril'sk I	39.5	58.4	208.8	8570	1.1	0.17	0.065	37.4	0.25	0.161	0.742	0.008
NR-6	Cu-poor	Noril'sk I			243.7	9125	9.3	0.17	0.065	34.0	0.42	0.199	0.529	0.124
NR-6	Cu-poor	Noril'sk I			542.3	16143	2.4	0.17	0.065	32.5	0.15	0.093	0.331	1.994
NR-6	Cu-poor	Noril'sk I			1109	22750	1.3	0.17	0.065	34.3	0.19	0.030	0.263	4.226
Median NR-6 (N=4)			39.5	58.4	393.0	12634	1.9	0.17	0.065	34.2	0.22	0.127	0.430	1.059

ANNEXE 4 – Cont.

Sample	Ore type	¹⁰⁹ Ag	¹¹¹ Cd	¹¹⁵ In	¹¹⁸ Sn	¹²¹ Sb	¹³⁰ Te	¹⁸⁵ Re	¹⁸⁹ Os	¹⁹³ Ir	¹⁹⁵ Pt	¹⁹⁷ Au	²⁰⁵ Tl	²⁰⁸ Pb	²⁰⁹ Bi
		ppm	ppm	ppm	ppm	ppm	ppm	ppm	ppm	ppm	ppm	ppm	ppm	ppm	ppm
Limit of detection		0.007	0.037	0.005	0.050	0.047	0.257	0.010	0.017	0.004	0.013	0.008	0.004	0.007	0.004
90OMZS2-3	Cu-poor	0.54	0.037	0.005	0.050	0.047	0.966	0.083	0.017	0.012	0.050	0.008	0.00	0.67	0.03
90OMZS2-3	Cu-poor	1.78	0.037	0.005	0.312	0.047	1.047	0.063	0.017	0.017	0.033	0.008	0.00	1.32	0.09
90OMZS2-3	Cu-poor	0.46	0.093	0.005	0.050	0.047	1.166	0.119	0.017	0.019	0.112	0.008	0.00	1.21	0.12
90OMZS2-3	Cu-poor	2.96	0.087	0.008	0.072	0.047	0.735	0.164	0.017	0.020	0.030	0.008	0.00	1.10	0.06
90OMZS2-3	Cu-poor	0.51	0.087	0.016	0.155	0.047	0.854	0.118	0.017	0.020	0.064	0.008	0.00	1.20	0.14
90OMZS2-3	Cu-poor	0.45	0.087	0.005	0.810	0.047	0.929	0.077	0.017	0.011	0.044	0.008	0.00	1.34	0.14
90OMZS2-3 (N=6)		0.52	0.087	0.005	0.113	0.047	0.947	0.100	0.017	0.018	0.047	0.008	0.00	1.20	0.11
90KMZ5	Cu-poor	0.86	0.037	0.005	0.050	0.073	1.627	0.287	0.166	0.385	0.268	0.008	0.00	0.15	0.16
90KMZ5	Cu-poor	0.58	0.037	0.005	0.050	0.047	1.646	0.381	0.209	0.418	0.069	0.008	0.00	0.12	0.15
90KMZ5	Cu-poor	0.21	0.037	0.005	0.050	0.047	1.546	0.302	0.182	0.362	0.088	0.008	0.00	0.09	0.16
90KMZ5	Cu-poor	2.64	0.037	0.005	0.050	0.047	1.571	0.344	0.201	0.433	0.264	0.008	0.02	0.80	0.41
90KMZ5	Cu-poor	1.83	0.037	0.005	0.050	0.047	1.496	0.385	0.332	0.611	0.286	0.008	0.00	0.19	0.16
90KMZ5	Cu-poor	5.09	0.089	0.005	0.050	0.047	1.907	0.344	0.252	0.544	0.679	0.008	0.00	0.20	0.20
90KMZ5 (N=6)		1.34	0.037	0.005	0.050	0.047	1.599	0.344	0.205	0.426	0.266	0.008	0.00	0.17	0.16
NR-6	Cu-poor	0.34	0.037	0.005	0.050	0.047	0.257	0.131	0.017	0.035	0.038	0.008	0.00	1.80	0.25
NR-6	Cu-poor	0.47	0.037	0.005	0.050	0.047	0.257	0.118	0.017	0.032	0.187	0.008	0.00	1.84	0.38
NR-6	Cu-poor	0.88	0.037	0.005	0.050	0.047	0.305	0.099	0.035	0.026	0.226	0.008	0.00	3.24	0.46
NR-6	Cu-poor	1.03	0.037	0.005	0.050	0.047	0.257	0.108	0.021	0.017	0.642	0.008	0.00	4.45	0.23
NR-6 (N=4)		0.67	0.037	0.005	0.050	0.047	0.257	0.113	0.019	0.029	0.206	0.008	0.00	2.54	0.31

ANNEXE 4 – Cont.

Sample	Ore type	Intrusion	S	Fe	⁵⁹ Co	⁶¹ Ni	⁶⁵ Cu	⁶⁶ Zn	⁷⁵ As	⁸² Se	⁹⁵ Mo	¹⁰¹ Ru	¹⁰³ Rh	¹⁰⁸ Pd
			%	%	ppm	ppm	ppm	ppm	ppm	ppm	ppm	ppm	ppm	ppm
Limit of detection			0.5	0.5	0.007	0.643	0.187	0.174	0.065	1.824	0.020	0.015	0.002	0.008
90OMZS2-2	Cu-poor	Kharaelakh			23.2	1969	5.5	0.45	0.065	50.2	0.34	0.176	0.834	0.008
90OMZS2-2	Cu-poor	Kharaelakh			21.0	1823	5.2	4.99	0.065	53.5	0.40	0.327	1.084	0.056
90OMZS2-2	Cu-poor	Kharaelakh			22.4	1775	4.9	0.35	0.065	51.9	0.37	0.211	0.836	0.008
90OMZS2-2	Cu-poor	Kharaelakh	38.6	60.0	20.2	1814	4.7	0.57	0.065	54.9	0.34	0.271	0.827	0.044
90OMZS2-2	Cu-poor	Kharaelakh			23.1	1876	3.3	0.57	0.065	54.6	0.29	0.246	1.134	0.008
90OMZS2-2	Cu-poor	Kharaelakh			22.3	1814	5.6	0.63	0.081	56.8	0.42	0.271	0.972	0.021
90OMZS2-2	Cu-poor	Kharaelakh			20.1	1703	3.4	0.80	0.070	59.8	0.44	0.297	1.091	0.033
Median 90OMZS2-2 (N=7)			38.6	60.0	22.3	1814	4.9	0.57	0.065	54.6	0.37	0.271	0.972	0.021
NR-13	Cu-poor	Kharaelakh			67.6	6289	0.7	0.22	0.065	32.4	0.44	0.186	0.818	0.008
NR-13	Cu-poor	Kharaelakh			83.6	5504	1.3	0.29	0.065	33.3	0.47	0.228	0.879	0.008
NR-13	Cu-poor	Kharaelakh	38.5	58.7	108.4	4743	0.5	0.36	0.065	35.7	0.44	0.165	0.832	0.008
NR-13	Cu-poor	Kharaelakh			73.9	4812	1.0	0.28	0.065	36.2	0.61	0.300	0.935	0.008
NR-13	Cu-poor	Kharaelakh			117.8	4145	0.2	0.22	0.065	33.3	0.56	0.202	1.159	0.008
NR-13	Cu-poor	Kharaelakh			62.0	6358	0.8	0.23	0.065	30.4	0.36	0.210	0.749	0.008
Median NR-13 (N=6)			38.5	58.7	78.8	5158	0.8	0.26	0.065	33.3	0.46	0.206	0.855	0.008
NR-14	Cu-poor	Kharaelakh			56.0	7000	1.6	0.34	0.065	43.3	0.66	0.395	2.244	0.008
NR-14	Cu-poor	Kharaelakh			70.2	6863	1.3	0.35	0.082	42.6	0.45	0.177	1.095	0.008
NR-14	Cu-poor	Kharaelakh			62.0	6445	1.5	0.24	0.065	41.5	0.39	0.224	1.035	0.008
NR-14	Cu-poor	Kharaelakh	38.3	58.3	85.3	6944	1.4	0.39	0.065	43.4	0.44	0.137	0.672	0.008
NR-14	Cu-poor	Kharaelakh			74.3	5398	0.9	0.31	0.065	43.6	0.37	0.193	0.625	0.023
NR-14	Cu-poor	Kharaelakh			87.7	5024	0.9	0.17	0.065	43.4	0.36	0.200	0.786	0.008
NR-14	Cu-poor	Kharaelakh			61.9	5940	20.6	0.21	0.065	43.4	0.37	0.186	1.129	0.008
Median NR-14 (N=7)			38.3	58.3	70.2	6445	1.4	0.31	0.065	43.4	0.39	0.193	1.035	0.008

ANNEXE 4 – Cont.

Sample	Ore type	¹⁰⁹ Ag	¹¹¹ Cd	¹¹⁵ In	¹¹⁸ Sn	¹²¹ Sb	¹³⁰ Te	¹⁸⁵ Re	¹⁸⁹ Os	¹⁹³ Ir	¹⁹⁵ Pt	¹⁹⁷ Au	²⁰⁵ Tl	²⁰⁸ Pb	²⁰⁹ Bi
		ppm	ppm	ppm	ppm	ppm	ppm	ppm	ppm	ppm	ppm	ppm	ppm	ppm	ppm
Limit of detection		0.007	0.037	0.005	0.050	0.047	0.257	0.010	0.017	0.004	0.013	0.008	0.004	0.007	0.004
90OMZS2-2	Cu-poor	0.30	0.049	0.005	0.050	0.047	1.022	0.165	0.066	0.095	0.013	0.008	0.00	1.88	0.05
90OMZS2-2	Cu-poor	0.35	0.037	0.005	0.050	0.047	1.247	0.177	0.079	0.110	0.141	0.008	0.01	2.57	0.06
90OMZS2-2	Cu-poor	0.62	0.061	0.005	0.050	0.047	1.060	0.168	0.082	0.061	0.030	0.008	0.00	3.24	0.07
90OMZS2-2	Cu-poor	0.40	0.037	0.005	0.055	0.047	1.284	0.126	0.069	0.089	0.096	0.008	0.00	3.20	0.15
90OMZS2-2	Cu-poor	0.90	0.037	0.005	0.050	0.047	1.028	0.184	0.080	0.106	0.106	0.010	0.01	2.83	0.14
90OMZS2-2	Cu-poor	0.38	0.037	0.005	0.050	0.047	0.997	0.156	0.058	0.084	0.066	0.008	0.00	2.08	0.03
90OMZS2-2	Cu-poor	0.36	0.037	0.007	0.064	0.047	0.879	0.193	0.057	0.099	0.107	0.008	0.01	2.32	0.17
90OMZS2-2 (N=7)		0.38	0.037	0.005	0.050	0.047	1.028	0.168	0.069	0.095	0.096	0.008	0.00	2.57	0.07
NR-13	Cu-poor	0.30	0.037	0.005	0.050	0.047	0.679	0.233	0.027	0.082	0.092	0.008	0.00	1.17	0.10
NR-13	Cu-poor	0.33	0.037	0.003	0.050	0.047	0.829	0.211	0.050	0.094	0.034	0.008	0.00	0.87	0.07
NR-13	Cu-poor	0.47	0.037	0.005	0.050	0.047	1.028	0.217	0.072	0.075	0.054	0.008	0.00	0.92	0.08
NR-13	Cu-poor	0.24	0.037	0.005	0.050	0.047	0.760	0.254	0.089	0.102	0.041	0.008	0.00	0.64	0.08
NR-13	Cu-poor	0.95	0.037	0.006	0.050	0.047	0.891	0.180	0.059	0.093	0.171	0.008	0.01	3.80	0.10
NR-13	Cu-poor	0.21	0.037	0.005	0.050	0.047	0.779	0.181	0.055	0.089	0.050	0.008	0.00	1.18	0.08
NR-13 (N=6)		0.31	0.037	0.005	0.050	0.047	0.804	0.214	0.057	0.091	0.052	0.008	0.00	1.04	0.08
NR-14	Cu-poor	0.38	0.037	0.005	0.050	0.047	0.717	0.189	0.059	0.099	0.134	0.008	0.00	0.90	0.17
NR-14	Cu-poor	0.17	0.037	0.005	0.137	0.047	0.810	0.166	0.046	0.089	0.074	0.008	0.00	0.44	0.09
NR-14	Cu-poor	0.23	0.037	0.005	0.050	0.047	1.010	0.158	0.066	0.070	0.072	0.008	0.00	0.53	0.12
NR-14	Cu-poor	0.62	0.037	0.005	0.050	0.047	0.773	0.151	0.064	0.072	0.099	0.008	0.00	0.64	0.08
NR-14	Cu-poor	0.83	0.037	0.005	0.050	0.047	1.097	0.147	0.057	0.079	0.156	0.008	0.00	1.16	0.12
NR-14	Cu-poor	0.17	0.037	0.005	0.050	0.047	0.966	0.163	0.052	0.069	0.110	0.008	0.00	0.47	0.14
NR-14	Cu-poor	0.31	0.037	0.005	0.050	0.047	0.841	0.145	0.054	0.059	0.067	0.008	0.00	0.73	0.12
NR-14 (N=7)		0.31	0.037	0.005	0.050	0.047	0.841	0.155	0.057	0.072	0.099	0.008	0.00	0.64	0.12

ANNEXE 4 – Cont.

Sample	Ore type	Intrusion	S	Fe	⁵⁹ Co	⁶¹ Ni	⁶⁵ Cu	⁶⁶ Zn	⁷⁵ As	⁸² Se	⁹⁵ Mo	¹⁰¹ Ru	¹⁰³ Rh	¹⁰⁸ Pd
			%	%	ppm	ppm	ppm	ppm	ppm	ppm	ppm	ppm	ppm	ppm
Limit of detection			0.5	0.5	0.007	0.643	0.187	0.174	0.065	1.824	0.020	0.015	0.002	0.008
NR-11	Cu-poor	Noril'sk I			509.9	50487	96.6	0.48	1.434	88.5	3.42	1.253	7.014	8.352
NR-11	Cu-poor	Noril'sk I			389.6	31601	0.5	0.17	0.785	94.7	3.98	1.279	7.268	2.392
NR-11	Cu-poor	Noril'sk I	38.4	59.0	297.3	34032	0.8	0.44	1.434	95.1	3.45	1.192	6.576	0.437
NR-11	Cu-poor	Noril'sk I			323.5	28547	0.7	0.20	0.898	102.2	3.37	1.386	6.775	2.405
NR-11	Cu-poor	Noril'sk I			363.4	32599	1.0	0.19	0.256	89.8	3.73	1.252	6.183	0.691
NR-11	Cu-poor	Noril'sk I			322.9	25431	1.0	0.17	0.108	95.7	3.85	1.237	6.289	0.960
	Median NR-11 (N=6)		38.4	59.0	343.4	32100	0.9	0.20	0.841	94.9	3.59	1.252	6.676	1.676
NR-8	Cu-rich	Noril'sk I			99.7	8913	10.1	1.43	1.060	33.5	0.06	0.015	0.002	0.373
NR-8	Cu-rich	Noril'sk I	39.0	58.3	124.7	9262	22.4	1.00	0.065	38.0	0.12	0.048	0.002	0.298
NR-8	Cu-rich	Noril'sk I			96.0	8701	330.3	21.82	0.605	54.8	5.30	0.015	0.002	0.819
	Median NR-8 (N=3)		39.0	58.3	99.7	8913	22.4	1.43	0.605	38.0	0.12	0.015	0.002	0.373
NR-18	Cu-rich	Kharaelakh	38.9	57.9	67.9	8228	548.5	274.3	0.065	92.2	0.02	0.015	0.002	6.313
NR-17	Cu-rich	Kharaelakh			104.1	2543	1.4	0.80	0.150	97.9	0.02	0.015	0.002	1.743
NR-17	Cu-rich	Kharaelakh			84.1	2711	84.1	1247	0.118	97.2	0.04	0.015	0.002	5.242
NR-17	Cu-rich	Kharaelakh			103.2	2749	1.1	81.65	0.156	95.4	0.31	0.015	0.002	2.440
NR-17	Cu-rich	Kharaelakh			73.7	2992	8.7	261.8	0.112	118.4	0.02	0.015	0.002	3.010
	Median NR-17 (N=4)		38.7	58.3	103.2	2749	5.7	84.77	0.150	97.9	0.02	0.015	0.002	2.440

ANNEXE 4 – Cont.

Sample	Ore type	¹⁰⁹ Ag	¹¹¹ Cd	¹¹⁵ In	¹¹⁸ Sn	¹²¹ Sb	¹³⁰ Te	¹⁸⁵ Re	¹⁸⁹ Os	¹⁹³ Ir	¹⁹⁵ Pt	¹⁹⁷ Au	²⁰⁵ Tl	²⁰⁸ Pb	²⁰⁹ Bi
		ppm	ppm	ppm	ppm	ppm	ppm	ppm	ppm	ppm	ppm	ppm	ppm	ppm	ppm
Limit of detection		0.007	0.037	0.005	0.050	0.047	0.257	0.010	0.017	0.004	0.013	0.008	0.004	0.007	0.004
NR-11	Cu-poor	4.97	0.037	0.005	0.050	0.047	3.303	0.233	0.430	0.698	0.075	0.048	0.01	17.51	1.79
NR-11	Cu-poor	2.68	0.037	0.005	0.087	0.047	4.176	0.188	0.324	0.654	1.589	0.032	0.02	19.20	3.43
NR-11	Cu-poor	2.48	0.037	0.005	0.050	0.047	4.463	0.213	0.299	0.630	2.743	0.008	0.05	10.85	1.32
NR-11	Cu-poor	1.74	0.037	0.005	0.100	0.047	4.887	0.164	0.368	0.642	0.043	0.028	0.02	16.21	0.89
NR-11	Cu-poor	2.95	0.037	0.005	0.050	0.047	3.758	0.147	0.305	0.679	0.673	0.017	0.03	28.67	1.34
NR-11	Cu-poor	1.86	0.037	0.005	0.050	0.047	3.341	0.184	0.337	0.673	0.077	0.007	0.02	8.23	0.82
	NR-11 (N=6)	2.58	0.037	0.005	0.050	0.047	3.967	0.186	0.330	0.664	0.375	0.022	0.02	16.86	1.33
NR-8	Cu-rich	0.72	0.037	0.005	0.050	0.047	0.393	0.010	0.017	0.004	0.013	0.041	0.17	1.12	0.21
NR-8	Cu-rich	1.18	0.087	0.005	0.050	0.047	0.257	0.010	0.017	0.004	0.013	0.008	0.00	3.74	0.34
NR-8	Cu-rich	0.90	0.305	0.091	0.067	0.047	0.729	0.010	0.017	0.004	0.187	0.008	0.00	2.72	0.69
	NR-8 (N=3)	0.90	0.087	0.005	0.050	0.047	0.393	0.010	0.017	0.004	0.013	0.008	0.00	2.72	0.34
NR-18	Cu-rich	16.21	12.466	0.230	0.050	0.047	8.726	0.010	0.017	0.004	0.312	0.021	0.60	3.80	6.11
NR-17	Cu-rich	4.49	0.081	0.005	0.262	0.047	3.179	0.010	0.017	0.004	0.040	0.008	0.05	68.56	2.56
NR-17	Cu-rich	14.59	55.474	0.286	0.193	0.047	10.970	0.010	0.017	0.004	0.026	0.031	0.05	199.5	2.80
NR-17	Cu-rich	5.17	3.615	0.044	0.050	0.047	4.363	0.010	0.017	0.004	0.013	0.008	0.03	51.73	1.02
NR-17	Cu-rich	21.75	10.596	0.125	0.636	0.069	12.092	0.010	0.017	0.004	0.118	0.023	0.02	29.36	0.79
	NR-17 (N=4)	5.17	3.802	0.050	0.262	0.047	4.363	0.010	0.017	0.004	0.026	0.010	0.03	68.56	1.37

ANNEXE 4 – Cont.

Sample	Ore type	Intrusion	S	Fe	⁵⁹ Co	⁶¹ Ni	⁶⁵ Cu	⁶⁶ Zn	⁷⁵ As	⁸² Se	⁹⁵ Mo	¹⁰¹ Ru	¹⁰³ Rh	¹⁰⁸ Pd
			%	%	ppm	ppm	ppm	ppm	ppm	ppm	ppm	ppm	ppm	ppm
Limit of detection			0.5	0.5	0.007	0.643	0.187	0.174	0.065	1.824	0.020	0.015	0.002	0.008
90OC13	Cu-rich	Kharaelakh			55.5	2431	529.8	137.1	0.065	50.4	0.02	0.015	0.002	0.633
90OC13	Cu-rich	Kharaelakh			21.1	1789	13401.0	617.1	0.065	48.2	0.03	0.015	0.002	2.075
90OC13	Cu-rich	Kharaelakh			28.2	1811	6295.3	286.7	0.065	65.9	0.02	0.015	0.002	2.639
90OC13	Cu-rich	Kharaelakh	37.9	62.0	32.2	2137	5.4	0.21	0.093	53.4	1.27	0.713	3.752	0.035
90OC13	Cu-rich	Kharaelakh			29.3	1988	3.3	0.32	0.065	55.2	2.18	1.112	3.839	0.230
90OC13	Cu-rich	Kharaelakh			27.4	1857	2.5	0.19	0.065	58.4	3.22	4.123	2.649	0.008
90OC13	Cu-rich	Kharaelakh			213.8	4201	2730.1	561.0	0.065	69.7	0.02	0.015	0.002	0.561
Median 90OC13 (N=7)			37.9	62.0	29.3	1988	529.8	137.1	0.065	55.2	0.03	0.015	0.002	0.561
90OMZS1-3	Cu-rich	Kharaelakh			25.1	691	230.6	0.51	0.065	46.0	0.02	0.016	0.002	0.146
90OMZS1-3	Cu-rich	Kharaelakh			12.6	649	2.6	0.22	0.065	60.5	1.66	1.993	3.815	0.019
90OMZS1-3	Cu-rich	Kharaelakh	38.4	61.0	139.0	2998	6482.3	3.43	0.065	49.4	0.02	0.015	0.002	1.309
90OMZS1-3	Cu-rich	Kharaelakh			10.8	431	9.6	0.34	0.065	49.2	0.72	1.196	2.630	0.010
90OMZS1-3	Cu-rich	Kharaelakh			9.2	287	1.8	0.24	0.065	53.5	0.87	1.034	3.241	0.013
90OMZS1-3	Cu-rich	Kharaelakh			15.0	514	6.2	0.34	0.065	110.7	0.02	0.015	0.002	0.008
Median 90OMZS1-3 (N=6)			38.4	61.0	13.8	581	7.9	0.34	0.065	51.5	0.37	0.525	1.316	0.016
NR-10	Disseminated	Noril'sk I			546.6	24433	1.0	0.21	0.141	105.7	0.66	4.771	17.321	0.610
NR-10	Disseminated	Noril'sk I	38.96	58.35	533.5	25181	1.1	0.24	0.181	104.7	0.48	4.726	16.692	0.785
NR-10	Disseminated	Noril'sk I			246.2	12279	0.5	0.19	0.181	107.8	0.55	2.164	10.584	0.474
Median NR-10 (N=6)			38.96	58.35	533.5	24433	1.0	0.21	0.181	105.7	0.55	4.726	16.692	0.610

ANNEXE 4 – Cont.

Sample	Ore type	¹⁰⁹ Ag	¹¹¹ Cd	¹¹⁵ In	¹¹⁸ Sn	¹²¹ Sb	¹³⁰ Te	¹⁸⁵ Re	¹⁸⁹ Os	¹⁹³ Ir	¹⁹⁵ Pt	¹⁹⁷ Au	²⁰⁵ Tl	²⁰⁸ Pb	²⁰⁹ Bi
		ppm	ppm	ppm	ppm	ppm	ppm	ppm	ppm	ppm	ppm	ppm	ppm	ppm	ppm
Limit of detection		0.007	0.037	0.005	0.050	0.047	0.257	0.010	0.017	0.004	0.013	0.008	0.004	0.007	0.004
90OC13	Cu-rich	1.15	2.119	0.044	0.436	0.047	1.184	0.010	0.017	0.004	0.079	0.008	0.04	211.9	0.06
90OC13	Cu-rich	3.55	10.596	0.617	1.621	0.047	9.973	0.010	0.017	0.004	0.050	0.015	0.39	405.1	0.19
90OC13	Cu-rich	2.99	4.924	0.147	1.583	0.047	3.117	0.010	0.017	0.004	0.081	0.008	1.08	120.9	0.14
90OC13	Cu-rich	0.37	0.037	0.005	0.050	0.047	2.767	0.311	0.072	0.175	0.070	0.008	0.03	2.18	0.68
90OC13	Cu-rich	0.48	0.037	0.005	0.050	0.047	2.954	0.457	0.082	0.266	0.039	0.008	0.02	2.99	0.73
90OC13	Cu-rich	0.64	0.049	0.005	0.050	0.047	0.536	1.642	1.328	1.446	0.013	0.008	0.02	4.48	0.15
90OC13	Cu-rich	1.90	9.287	0.157	0.330	0.047	5.111	0.010	0.017	0.004	0.068	0.075	0.15	208.2	0.12
90OC13 (N=7)		1.15	2.119	0.044	0.330	0.047	2.954	0.311	0.017	0.004	0.068	0.008	0.04	120.9	0.15
90OMZS1-3	Cu-rich	1.38	0.037	0.005	0.074	0.047	0.312	0.010	0.017	0.007	0.124	0.008	0.03	5.73	0.10
90OMZS1-3	Cu-rich	0.60	0.053	0.005	0.047	0.047	1.421	1.229	0.636	0.577	0.013	0.008	0.02	3.43	0.26
90OMZS1-3	Cu-rich	4.74	0.181	0.032	0.066	0.047	1.016	0.010	0.017	0.004	0.125	0.059	0.14	27.43	0.06
90OMZS1-3	Cu-rich	1.18	0.064	0.005	0.050	0.047	1.377	0.532	0.287	0.390	0.013	0.008	0.00	2.10	0.12
90OMZS1-3	Cu-rich	0.98	0.088	0.005	0.050	0.047	1.315	0.651	0.324	0.392	0.013	0.008	0.01	2.93	0.14
90OMZS1-3	Cu-rich	1.93	0.037	0.005	0.050	0.047	0.257	0.010	0.017	0.004	0.013	0.008	0.00	4.29	0.00
90OMZS1-3 (N=6)		1.28	0.059	0.005	0.050	0.047	1.166	0.271	0.152	0.198	0.013	0.008	0.01	3.86	0.11
NR-10	Disseminated	2.85	0.037	0.005	0.050	0.047	11.699	0.167	0.947	1.920	0.586	0.008	0.00	0.06	0.09
NR-10	Disseminated	3.62	0.037	0.005	0.050	0.047	11.082	0.160	0.885	1.889	0.891	0.008	0.00	0.04	0.09
NR-10	Disseminated	0.89	0.037	0.005	0.050	0.047	12.341	0.128	0.474	0.829	0.399	0.019	0.00	0.11	0.07
NR-10 (N=6)		2.85	0.037	0.005	0.050	0.047	11.699	0.160	0.885	1.889	0.586	0.008	0.00	0.06	0.09

ANNEXE 5 - Complete data set of SEM-EDS and LA-ICP-MS analyses of pentlandite obtained for the Noril'sk-Talnakh mining district and median values for each sample. Abbreviations: N= number of individual analyses

ANNEXE 5

Sample	Ore type	Intrusion	S	Fe	Ni	⁵⁹ Co	⁶⁵ Cu	⁶⁶ Zn	⁷⁵ As	⁸² Se	⁹⁵ Mo	¹⁰¹ Ru	¹⁰³ Rh	¹⁰⁸ Pd
			%	%	%	ppm	ppm	ppm	ppm	ppm	ppm	ppm	ppm	ppm
Limit of detection			0.5	0.5	0.5	0.007	0.187	0.174	0.065	1.824	0.020	0.015	0.002	0.008
90OMZS2-3	Cu-poor	Kharaelakh	33.5	34.2	31.1	14457	198.6	4.27	1.140	56.7	0.322	0.015	0.118	22.8
90OMZS2-3	Cu-poor	Kharaelakh				14554	32.6	2.83	0.065	52.7	0.212	0.015	0.166	6.2
90OMZS2-3	Cu-poor	Kharaelakh				14652	15.6	3.22	0.482	53.1	0.264	0.015	0.154	39.4
90OMZS2-3	Cu-poor	Kharaelakh				14619	9.5	4.53	1.302	51.8	1.042	0.015	0.002	38.3
90OMZS2-3	Cu-poor	Kharaelakh				13350	91.2	20.84	6.479	72.3	0.072	0.015	0.002	26.2
90OMZS2-3	Cu-poor	Kharaelakh				11917	114.0	2.44	0.065	51.8	0.260	0.015	0.002	30.7
Median 90OMZS2-3 (N=6)			33.5	34.2	31.1	14505	61.9	3.74	0.811	52.9	0.262	0.015	0.060	28.5
NR-6	Cu-poor	Noril'sk I	33.6	29.0	37.5	18364	35.8	0.17	0.065	29.2	0.208	0.296	0.209	33.8
NR-6	Cu-poor	Noril'sk I				12764	8.0	520.96	0.065	30.2	0.081	0.137	0.007	45.9
NR-6	Cu-poor	Noril'sk I				14978	25.1	126.98	0.684	29.6	0.101	0.173	0.049	48.4
Median NR-6 (N=3)			33.6	33.0	31.5	14978	25.1	126.98	0.065	29.6	0.101	0.173	0.049	45.9
90OMZS2-2	Cu-poor	Kharaelakh	34.0	27.0	38.5	11363	17.9	1.39	0.508	46.9	0.097	0.177	0.015	111.4
90OMZS2-2	Cu-poor	Kharaelakh				11266	8.1	0.29	0.267	41.4	2.051	0.205	0.034	105.2
90OMZS2-2	Cu-poor	Kharaelakh				11331	6.2	0.36	0.160	45.6	0.020	0.164	0.009	108.1
Median 90OMZS2-2 (N=3)			34.0	32.0	31.5	11331	8.1	0.36	0.267	45.6	0.097	0.177	0.015	108.1
NR-13	Cu-poor	Kharaelakh	33.4	30.3	35.9	11722	112006	1693.12	0.133	31.0	0.028	0.241	0.002	41.3
NR-13	Cu-poor	Kharaelakh				11461	8.8	0.68	0.137	26.9	0.345	0.296	0.579	41.7
NR-13	Cu-poor	Kharaelakh				13578	8987	371.18	0.146	27.2	0.244	0.257	0.321	51.0
NR-13	Cu-poor	Kharaelakh				5858	34188.0	201.87	0.065	25.1	0.319	0.245	0.002	30.9
NR-13	Cu-poor	Kharaelakh				13350	4.2	0.25	0.104	25.4	0.215	0.244	0.661	51.8
NR-13	Cu-poor	Kharaelakh				15661	110.7	1064.71	0.140	28.0	0.020	0.238	0.002	55.2
Median NR-13 (N=6)			33.4	33.3	29.9	12536	4549	286.53	0.135	27.1	0.230	0.244	0.162	46.4

ANNEXE 5 – Cont.

Sample	Ore type	¹⁰⁹ Ag	¹¹¹ Cd	¹¹⁵ In	¹¹⁸ Sn	¹²¹ Sb	¹³⁰ Te	¹⁸⁵ Re	¹⁸⁹ Os	¹⁹³ Ir	¹⁹⁵ Pt	¹⁹⁷ Au	²⁰⁵ Tl	²⁰⁸ Pb	²⁰⁹ Bi
		ppm	ppm	ppm	ppm	ppm	ppm	ppm	ppm	ppm	ppm	ppm	ppm	ppm	ppm
Limit of detection		0.007	0.037	0.005	0.050	0.047	0.257	0.010	0.017	0.004	0.013	0.008	0.004	0.007	0.004
90OMZS2-3	Cu-poor	17.45	0.037	0.005	1.69	0.072	1.30	0.049	0.017	0.020	0.716	0.008	0.485	10.29	0.50
90OMZS2-3	Cu-poor	6.84	0.037	0.008	0.42	0.047	0.91	0.068	0.017	0.013	0.111	0.008	0.446	10.13	0.33
90OMZS2-3	Cu-poor	19.80	0.143	0.158	0.40	0.078	1.17	0.079	0.017	0.007	0.319	0.008	1.019	40.37	0.47
90OMZS2-3	Cu-poor	5.86	0.037	0.034	0.72	0.072	0.52	0.079	0.037	0.014	0.368	0.008	0.238	10.74	0.85
90OMZS2-3	Cu-poor	6.09	0.247	0.099	0.52	0.107	3.97	0.010	0.017	0.004	0.225	0.008	1.661	175.82	0.28
90OMZS2-3	Cu-poor	3.13	8.466	0.005	0.42	0.047	1.96	0.010	0.017	0.004	0.212	0.008	0.612	34.51	0.28
90OMZS2-3 (N=6)		6.46	0.090	0.021	0.47	0.072	1.24	0.059	0.017	0.010	0.272	0.008	0.549	22.63	0.40
NR-6	Cu-poor	4.10	0.037	0.005	0.05	0.047	0.27	0.079	0.017	0.023	0.527	0.008	0.072	1.58	0.20
NR-6	Cu-poor	1.69	0.037	0.009	0.05	0.047	0.78	0.010	0.017	0.004	3.158	0.166	0.654	89.21	2.64
NR-6	Cu-poor	3.32	1.465	0.020	0.05	0.047	0.26	0.061	0.017	0.004	1.205	0.024	0.961	98.01	0.90
NR-6 (N=3)		3.32	0.037	0.009	0.05	0.047	0.27	0.061	0.017	0.004	1.205	0.024	0.654	89.21	0.90
90OMZS2-2	Cu-poor	5.18	0.078	0.005	0.22	0.047	1.70	0.010	0.017	0.014	0.109	0.008	0.175	42.33	0.63
90OMZS2-2	Cu-poor	2.64	0.032	0.005	0.05	0.047	0.35	0.599	0.104	0.004	0.032	0.008	0.163	7.13	0.01
90OMZS2-2	Cu-poor	2.18	0.037	0.006	0.05	0.059	1.47	0.010	0.017	0.004	0.062	0.008	0.036	2.75	0.04
90OMZS2-2 (N=3)		2.64	0.037	0.005	0.05	0.047	1.47	0.010	0.017	0.004	0.062	0.008	0.163	7.13	0.04
NR-13	Cu-poor	30.93	11.494	0.927	0.36	0.047	0.83	0.010	0.017	0.004	2.702	0.008	1.902	41.38	0.29
NR-13	Cu-poor	11.23	0.037	0.005	0.05	0.047	0.56	0.173	0.043	0.046	1.527	0.012	0.032	15.37	0.24
NR-13	Cu-poor	14.39	2.409	0.139	0.29	0.047	1.16	0.089	0.017	0.027	3.523	0.008	0.508	46.24	0.39
NR-13	Cu-poor	13.12	2.149	0.152	0.23	0.047	0.71	0.492	0.173	0.107	1.459	0.008	0.136	27.29	0.43
NR-13	Cu-poor	9.87	0.037	0.005	0.05	0.047	0.50	0.156	0.017	0.054	3.093	0.024	0.140	16.61	0.18
NR-13	Cu-poor	4.27	4.884	0.169	0.16	0.047	0.93	0.010	0.017	0.004	2.579	0.019	0.104	22.69	0.27
NR-13 (N=6)		12.18	2.279	0.146	0.20	0.047	0.77	0.122	0.017	0.037	2.641	0.010	0.138	24.99	0.28

ANNEXE 5 – Cont.

Sample	Ore type	Intrusion	S	Fe	Ni	⁵⁹ Co	⁶⁵ Cu	⁶⁶ Zn	⁷⁵ As	⁸² Se	⁹⁵ Mo	¹⁰¹ Ru	¹⁰³ Rh	¹⁰⁸ Pd
			%	%	%	ppm	ppm	ppm	ppm	ppm	ppm	ppm	ppm	ppm
Limit of detection			0.5	0.5	0.5	0.007	0.187	0.174	0.065	1.824	0.020	0.015	0.002	0.008
NR-14	Cu-poor	Kharaelakh				16378	537.2	478.63	0.212	39.4	0.781	0.054	0.002	63.4
NR-14	Cu-poor	Kharaelakh				21652	3.6	0.12	0.156	41.6	0.316	0.289	0.508	69.2
NR-14	Cu-poor	Kharaelakh	33.2	30.3	35.3	19829	328.9	30.93	0.326	38.9	0.345	0.369	0.288	108.1
NR-14	Cu-poor	Kharaelakh				15987	4363.0	117.22	0.156	41.8	0.277	0.376	0.789	53.5
NR-14	Cu-poor	Kharaelakh				17029	41.7	0.62	0.179	39.4	0.306	0.309	0.620	59.1
Median NR-14 (N=5)			33.2	32.3	32.3	17029	328.9	30.93	0.179	39.4	0.316	0.309	0.508	63.4
NR-11	Cu-poor	Noril'sk I				6037	0.7	0.22	0.316	82.1	2.800	1.219	8.563	993.1
NR-11	Cu-poor	Noril'sk I				6642	5.4	130.24	0.550	80.7	1.888	1.158	4.734	475.4
NR-11	Cu-poor	Noril'sk I	33.4	30.6	37.4	5802	1.9	0.33	0.081	79.8	7.163	0.804	11.982	1439
NR-11	Cu-poor	Noril'sk I				6453	1.6	0.57	0.456	86.0	2.507	1.218	6.925	470.5
NR-11	Cu-poor	Noril'sk I				6125	5.9	0.39	0.612	74.9	15.303	1.116	12.080	1696
NR-11	Cu-poor	Noril'sk I				6707	1.2	0.39	0.160	83.4	2.090	1.487	6.219	471.8
Median NR-11 (N=6)			33.4	30.6	37.4	6289	1.7	0.39	0.386	81.4	2.654	1.188	7.744	734.2
NR-8	Cu-rich	Noril'sk I				5688	6.0	0.17	0.498	56.7	0.020	3.211	17.322	2478
NR-8	Cu-rich	Noril'sk I				5802	1.7	0.17	0.648	52.7	0.020	2.819	20.252	1967
NR-8	Cu-rich	Noril'sk I	32.4	30.2	37.6	7717	104.2	19.21	0.065	65.4	0.912	2.869	15.463	833.5
NR-8	Cu-rich	Noril'sk I				5926	6.8	0.17	0.671	56.3	0.020	1.587	16.605	1801
Median NR-8 (N=4)			32.4	30.2	39.6	5864	6.4	0.17	0.573	56.5	0.020	2.844	16.963	1884
90MC15	Cu-rich	Noril'sk I				4203	11103	3.22	1.156	120.8	0.550	0.149	0.777	760.9
90MC15	Cu-rich	Noril'sk I				4370	16085	4.85	0.257	122.8	0.316	0.126	0.011	769.7
90MC15	Cu-rich	Noril'sk I	31.2	31.2	35.4	4412	15.6	0.44	2.400	125.4	1.455	1.086	5.333	641.4
90MC15	Cu-rich	Noril'sk I				3943	14229	78.14	2.116	123.4	1.605	0.401	4.830	683.0
90MC15	Cu-rich	Noril'sk I				4894	21.2	0.34	0.485	132.2	1.400	0.215	1.797	732.6
Median 90MC15 (N=5)			31.2	31.2	35.4	4370	11103	3.22	1.156	123.4	1.400	0.215	1.797	732.6

ANNEXE 5 – Cont.

Sample	Ore type	¹⁰⁹ Ag	¹¹¹ Cd	¹¹⁵ In	¹¹⁸ Sn	¹²¹ Sb	¹³⁰ Te	¹⁸⁵ Re	¹⁸⁹ Os	¹⁹³ Ir	¹⁹⁵ Pt	¹⁹⁷ Au	²⁰⁵ Tl	²⁰⁸ Pb	²⁰⁹ Bi
		ppm	ppm	ppm	ppm	ppm	ppm	ppm	ppm	ppm	ppm	ppm	ppm	ppm	ppm
Limit of detection		0.007	0.037	0.005	0.050	0.047	0.257	0.010	0.017	0.004	0.013	0.008	0.004	0.007	0.004
NR-14	Cu-poor	2.18	2.963	0.198	0.07	0.085	0.44	0.642	0.072	0.004	1.735	0.008	0.257	15.99	0.21
NR-14	Cu-poor	1.14	0.037	0.005	0.11	0.047	0.68	0.175	0.065	0.075	3.523	0.011	0.009	0.73	0.03
NR-14	Cu-poor	3.26	0.189	0.025	0.40	0.179	0.97	0.113	0.036	0.045	6.772	0.014	0.119	8.76	0.62
NR-14	Cu-poor	4.59	0.814	0.101	0.05	0.047	0.26	0.141	0.055	0.052	0.902	0.042	0.241	16.21	0.21
NR-14	Cu-poor	1.64	0.037	0.005	0.05	0.047	0.62	0.118	0.050	0.054	0.710	0.033	0.049	5.76	0.10
NR-14 (N=5)		2.18	0.189	0.025	0.07	0.047	0.62	0.141	0.055	0.052	1.735	0.014	0.119	8.76	0.21
NR-11	Cu-poor	2.28	0.055	0.005	0.05	0.047	3.97	0.156	0.225	0.547	0.433	0.008	0.189	1.97	0.28
NR-11	Cu-poor	4.82	0.037	0.005	0.07	0.047	3.91	0.133	0.221	0.453	0.977	0.041	3.451	16.28	0.58
NR-11	Cu-poor	1.66	0.037	0.029	0.88	0.059	1.37	0.160	0.088	0.456	0.843	0.035	1.449	1.21	0.03
NR-11	Cu-poor	3.00	0.037	0.005	0.06	0.047	2.51	0.154	0.316	0.537	0.013	0.015	0.606	3.26	0.15
NR-11	Cu-poor	3.22	0.037	0.005	0.07	0.047	4.82	0.208	0.221	0.554	0.446	0.046	1.335	2.04	0.29
NR-11	Cu-poor	2.12	0.078	0.005	0.08	0.047	3.09	0.175	0.274	0.583	2.116	0.019	1.368	25.07	0.91
NR-11 (N=6)		2.64	0.037	0.005	0.07	0.047	3.50	0.158	0.223	0.542	0.645	0.027	1.351	2.65	0.29
NR-8	Cu-rich	0.64	0.037	0.005	0.05	0.047	2.18	0.543	0.697	1.602	37.021	0.030	0.099	57.31	1.43
NR-8	Cu-rich	0.54	0.037	0.005	0.13	0.047	2.16	0.419	0.537	1.742	31.713	0.008	0.091	51.12	0.35
NR-8	Cu-rich	6.22	0.469	0.005	0.22	0.047	2.57	0.582	0.755	1.934	11.754	0.518	2.702	13.51	1.99
NR-8	Cu-rich	0.92	0.087	0.005	0.05	0.047	0.81	0.282	0.280	0.889	22.955	0.056	0.899	1.50	0.05
NR-8 (N=4)		0.78	0.062	0.005	0.09	0.047	2.17	0.481	0.617	1.672	27.334	0.043	0.499	32.32	0.89
90MC15	Cu-rich	17.61	0.446	0.005	0.09	0.047	35.88	0.093	0.017	0.004	4.558	0.008	0.335	7.75	1.60
90MC15	Cu-rich	33.54	0.599	0.009	0.07	0.047	34.42	0.010	0.017	0.004	1.986	0.008	1.726	11.56	0.23
90MC15	Cu-rich	8.14	0.075	0.037	0.05	0.047	33.41	0.560	0.017	0.016	0.837	0.008	0.270	2.51	0.79
90MC15	Cu-rich	53.72	2.605	0.426	0.08	0.047	36.50	0.541	0.017	0.009	2.930	0.019	0.648	14.62	1.07
90MC15	Cu-rich	59.58	0.055	0.005	0.05	0.047	39.56	0.165	0.017	0.004	0.133	0.008	0.130	0.48	1.58
90MC15 (N=5)		33.54	0.446	0.009	0.07	0.047	35.88	0.165	0.017	0.004	1.986	0.008	0.335	7.75	1.07

ANNEXE 5 – Cont.

Sample	Ore type	Intrusion	S	Fe	Ni	⁵⁹ Co	⁶⁵ Cu	⁶⁶ Zn	⁷⁵ As	⁸² Se	⁹⁵ Mo	¹⁰¹ Ru	¹⁰³ Rh	¹⁰⁸ Pd
			%	%	%	ppm	ppm	ppm	ppm	ppm	ppm	ppm	ppm	ppm
Limit of detection			0.5	0.5	0.5	0.007	0.187	0.174	0.065	1.824	0.020	0.015	0.002	0.008
90MC5	Cu-rich	Noril'sk I				3487	11363	1.08	0.524	170.6	0.365	0.247	0.725	996.3
90MC5	Cu-rich	Noril'sk I				4106	24094	1.89	0.101	168.7	0.031	0.051	0.002	1016
90MC5	Cu-rich	Noril'sk I	31.2	30.6	35.6	3787	17257	9.12	0.176	170.0	0.208	0.196	0.026	961.1
90MC5	Cu-rich	Noril'sk I				3256	19471	3.87	0.081	166.4	0.020	0.119	0.002	1035
90MC5	Cu-rich	Noril'sk I				3399	9931	1.05	0.514	171.9	0.238	0.153	0.345	1369
90MC5	Cu-rich	Noril'sk I				3725	12308	1.73	0.071	168.3	0.020	0.067	0.002	998.9
Median 90MC5 (N=6)			31.2	30.6	35.6	3606	14782	1.81	0.138	169.3	0.120	0.136	0.014	1007
NR-18	Cu-rich	Kharaelakh				5333	2377	23.77	0.065	71.3	0.020	0.423	0.002	270.2
NR-18	Cu-rich	Kharaelakh	33.1	29.8	37.0	5525	60.9	3.74	0.065	72.9	0.020	0.360	0.002	296.0
NR-18	Cu-rich	Kharaelakh				7098	81.4	0.98	0.065	65.8	0.020	0.344	0.002	386.8
NR-18	Cu-rich	Kharaelakh				6512	13.3	390.72	0.065	72.9	0.042	0.167	0.055	2683
Median NR-18 (N=4)			33.1	29.8	37.0	6019	71.1	13.76	0.065	72.1	0.020	0.352	0.002	341.4
NR-17	Cu-rich	Kharaelakh				9996	2.9	0.52	0.397	77.5	0.020	0.198	0.007	521.9
NR-17	Cu-rich	Kharaelakh				10208	5.2	0.48	0.254	82.4	0.025	0.138	0.002	394.0
NR-17	Cu-rich	Kharaelakh				9778	250.7	0.93	0.234	81.7	0.020	0.095	0.002	391.0
NR-17	Cu-rich	Kharaelakh	33.2	31.4	35.1	10719	18.9	0.36	0.459	89.5	0.020	0.133	0.002	369.6
NR-17	Cu-rich	Kharaelakh				10777	2.9	0.61	0.160	82.7	0.020	0.142	0.093	627.4
NR-17	Cu-rich	Kharaelakh				10341	1.4	0.30	0.241	89.5	0.020	0.096	0.002	502.1
NR-17	Cu-rich	Kharaelakh				9843	31.6	1.27	0.202	91.8	0.021	0.115	0.013	502.7
NR-17	Cu-rich	Kharaelakh				9690	1.2	0.43	0.195	88.6	0.020	0.197	0.084	710.5
Median NR-17 (N=8)			33.2	31.4	35.1	10102	4.1	0.50	0.238	85.6	0.020	0.135	0.005	502.4

ANNEXE 5 – Cont.

Sample	Ore type	¹⁰⁹ Ag	¹¹¹ Cd	¹¹⁵ In	¹¹⁸ Sn	¹²¹ Sb	¹³⁰ Te	¹⁸⁵ Re	¹⁸⁹ Os	¹⁹³ Ir	¹⁹⁵ Pt	¹⁹⁷ Au	²⁰⁵ Tl	²⁰⁸ Pb	²⁰⁹ Bi
		ppm	ppm	ppm	ppm	ppm	ppm	ppm	ppm	ppm	ppm	ppm	ppm	ppm	ppm
Limit of detection		0.007	0.037	0.005	0.050	0.047	0.257	0.010	0.017	0.004	0.013	0.008	0.004	0.007	0.004
90MC5	Cu-rich	35.30	0.847	0.005	0.05	0.047	66.29	0.089	0.059	0.024	3.842	0.008	0.290	8.53	1.33
90MC5	Cu-rich	26.34	1.169	0.005	0.06	0.047	63.69	0.010	0.017	0.004	4.135	0.008	0.384	8.17	0.08
90MC5	Cu-rich	21.07	1.302	0.005	0.06	0.047	67.86	0.016	0.017	0.004	6.838	0.008	0.378	16.70	0.37
90MC5	Cu-rich	57.31	1.325	0.031	0.07	0.047	65.71	0.010	0.017	0.004	2.670	0.008	0.886	13.25	0.02
90MC5	Cu-rich	33.21	0.606	0.005	0.05	0.047	60.33	0.041	0.017	0.004	6.219	0.008	0.205	4.95	1.62
90MC5	Cu-rich	40.70	0.931	0.012	0.06	0.047	52.10	0.010	0.017	0.004	2.475	0.008	0.355	6.45	0.03
90MC5 (N=6)		34.25	1.050	0.005	0.06	0.047	64.70	0.013	0.017	0.004	3.989	0.008	0.366	8.35	0.22
NR-18	Cu-rich	2.74	0.707	0.640	0.32	0.047	8.37	0.010	0.017	0.004	0.150	0.008	2.637	21.49	1.76
NR-18	Cu-rich	1.19	0.173	0.113	0.16	0.047	8.50	0.010	0.017	0.004	0.189	0.017	1.250	7.85	1.19
NR-18	Cu-rich	0.62	0.140	0.015	0.07	0.047	8.82	0.010	0.017	0.004	0.013	0.008	0.521	3.74	0.04
NR-18	Cu-rich	0.81	0.037	0.005	0.05	0.047	5.89	0.010	0.017	0.004	0.251	0.008	0.606	0.46	0.10
NR-18 (N=4)		1.00	0.156	0.064	0.11	0.047	8.43	0.010	0.017	0.004	0.169	0.008	0.928	5.80	0.65
NR-17	Cu-rich	1.99	0.037	0.008	0.08	0.047	8.24	0.010	0.017	0.004	0.221	0.104	0.485	12.47	0.10
NR-17	Cu-rich	2.51	0.062	0.009	0.52	0.047	2.68	0.010	0.017	0.004	0.013	0.410	1.403	70.00	0.12
NR-17	Cu-rich	6.55	0.049	0.034	0.13	0.047	8.76	0.010	0.017	0.004	0.137	0.703	0.291	7.49	0.06
NR-17	Cu-rich	4.20	0.037	0.021	0.32	0.047	4.40	0.556	0.017	0.004	0.462	0.892	1.657	99.96	0.20
NR-17	Cu-rich	4.72	0.037	0.005	0.05	0.047	5.96	0.010	0.017	0.004	0.044	1.823	0.726	32.89	0.05
NR-17	Cu-rich	3.85	0.037	0.005	0.05	0.047	2.56	0.010	0.017	0.004	0.106	0.619	0.775	31.26	0.05
NR-17	Cu-rich	4.46	0.130	0.021	0.08	0.047	6.06	0.010	0.017	0.004	0.124	0.847	1.374	19.89	0.05
NR-17	Cu-rich	2.93	0.037	0.005	2.28	0.072	3.16	0.010	0.017	0.004	0.035	0.501	0.110	1.63	0.03
NR-17 (N=8)		4.02	0.037	0.008	0.10	0.047	5.18	0.010	0.017	0.004	0.115	0.661	0.751	25.58	0.06

ANNEXE 5 – Cont.

Sample	Ore type	Intrusion	S	Fe	Ni	⁵⁹ Co	⁶⁵ Cu	⁶⁶ Zn	⁷⁵ As	⁸² Se	⁹⁵ Mo	¹⁰¹ Ru	¹⁰³ Rh	¹⁰⁸ Pd
			%	%	%	ppm	ppm	ppm	ppm	ppm	ppm	ppm	ppm	ppm
Limit of detection			0.5	0.5	0.5	0.007	0.187	0.174	0.065	1.824	0.020	0.015	0.002	0.008
900MZ67-5-1	Cu-rich	Kharaelakh				9442	657.7	4.07	0.586	114.0	0.423	0.077	0.038	227.9
900MZ67-5-1	Cu-rich	Kharaelakh	34.0	33.4	32.0	11103	299.6	7.03	5.731	112.7	0.091	0.127	0.002	180.2
900MZ67-5-1	Cu-rich	Kharaelakh				10256	46.6	1.32	1.237	116.9	0.127	0.033	0.002	40.4
Median 900MZ67-5-1 (N=3)			33.0	28.4	39.0	10256	299.6	4.07	1.237	114.0	0.127	0.077	0.002	180.2
900C13	Cu-rich	Kharaelakh				17192	5.3	6.84	0.150	57.3	0.020	0.134	0.005	50.3
900C13	Cu-rich	Kharaelakh				17810	3.0	1.27	0.085	62.5	0.020	0.088	0.002	96.4
900C13	Cu-rich	Kharaelakh				16899	60.6	3.42	0.143	100.9	0.020	0.171	0.007	67.1
900C13	Cu-rich	Kharaelakh	32.9	33.5	32.6	17941	3.6	0.19	0.130	46.6	0.020	0.042	0.004	51.2
900C13	Cu-rich	Kharaelakh				17615	14.0	0.28	0.065	52.7	0.020	0.015	0.002	55.5
900C13	Cu-rich	Kharaelakh				17778	8.7	0.36	0.137	48.5	0.022	0.137	0.002	54.8
900C13	Cu-rich	Kharaelakh				19145	42.3	3.09	0.199	59.3	0.020	0.382	0.003	52.5
Median 900C13 (N=7)			32.9	33.5	32.6	17778	8.7	1.27	0.137	57.3	0.020	0.134	0.003	54.8
900MZS1-3	Cu-rich	Kharaelakh				11500	102.2	0.90	0.133	52.8	0.020	0.033	0.003	140.3
900MZS1-3	Cu-rich	Kharaelakh	33.6	35.4	30.1	11461	188.8	0.98	0.212	46.2	0.029	0.057	0.006	123.1
Median 900MZS1-3 (N=2)			33.6	35.4	30.1	11481	145.5	0.94	0.173	49.5	0.024	0.045	0.005	131.7
NR-10	Disseminated	Noril'sk I				9257	0.8	0.19	0.065	94.1	1.986	5.730	17.029	680.8
NR-10	Disseminated	Noril'sk I	33.2	29.9	36.9	8931	1.4	1.04	0.140	91.8	0.902	6.476	14.815	260.5
NR-10	Disseminated	Noril'sk I				9801	3.1	0.39	0.215	98.3	2.833	3.420	10.614	625.2
Median NR-10 (N=3)			33.2	29.9	36.9	9257	1.4	0.39	0.140	94.1	1.986	5.730	14.815	625.2

ANNEXE 5 – Cont.

Sample	Ore type	¹⁰⁹ Ag	¹¹¹ Cd	¹¹⁵ In	¹¹⁸ Sn	¹²¹ Sb	¹³⁰ Te	¹⁸⁵ Re	¹⁸⁹ Os	¹⁹³ Ir	¹⁹⁵ Pt	¹⁹⁷ Au	²⁰⁵ Tl	²⁰⁸ Pb	²⁰⁹ Bi
		ppm	ppm	ppm	ppm	ppm	ppm	ppm	ppm	ppm	ppm	ppm	ppm	ppm	ppm
Limit of detection		0.007	0.037	0.005	0.050	0.047	0.257	0.010	0.017	0.004	0.013	0.008	0.004	0.007	0.004
900MZ67-5-1	Cu-rich	22.79	0.150	0.005	4.75	0.068	16.35	0.010	0.017	0.004	0.013	0.035	8.205	32.56	0.06
900MZ67-5-1	Cu-rich	14.65	0.104	0.018	0.60	0.267	17.22	0.010	0.017	0.004	0.166	0.008	0.892	74.24	1.34
900MZ67-5-1	Cu-rich	3.29	0.037	0.005	1.92	0.047	16.83	0.010	0.017	0.004	0.013	0.008	0.247	25.72	1.43
900MZ67-5-1 (N=3)		14.65	0.104	0.005	1.92	0.068	16.83	0.010	0.017	0.004	0.013	0.008	0.892	32.56	1.34
900C13	Cu-rich	4.20	0.104	0.019	0.18	0.047	8.82	0.010	0.017	0.004	0.111	0.008	0.580	58.28	0.68
900C13	Cu-rich	13.32	0.046	0.036	0.29	0.047	11.53	0.010	0.017	0.004	0.104	0.008	0.078	27.68	0.63
900C13	Cu-rich	7.36	0.137	0.145	15.66	1.107	4.23	0.010	0.017	0.004	0.023	0.065	11.917	145.87	0.79
900C13	Cu-rich	1.93	0.037	0.005	0.64	0.047	4.69	0.010	0.017	0.004	0.014	0.008	0.628	21.95	0.11
900C13	Cu-rich	4.00	0.037	0.007	0.05	0.047	3.74	0.010	0.017	0.004	0.013	0.008	0.518	7.20	0.08
900C13	Cu-rich	3.83	0.037	0.016	0.05	0.047	5.18	0.010	0.017	0.004	0.013	0.008	0.171	17.84	0.17
900C13	Cu-rich	7.07	0.104	0.035	0.25	0.047	7.42	0.010	0.017	0.004	0.013	0.010	2.022	13.28	0.16
900C13 (N=7)		4.20	0.046	0.019	0.25	0.047	5.18	0.010	0.017	0.004	0.014	0.008	0.580	21.95	0.17
900MZS1-3	Cu-rich	21.78	0.085	0.005	0.15	0.047	6.09	0.010	0.017	0.004	0.287	0.008	4.558	167.03	0.31
900MZS1-3	Cu-rich	9.61	0.059	0.005	0.31	0.055	3.97	0.010	0.017	0.004	0.075	0.010	4.428	332.11	1.02
900MZS1-3 (N=2)		15.69	0.072	0.005	0.23	0.051	5.03	0.010	0.017	0.004	0.181	0.009	4.493	249.57	0.67
NR-10	Disseminated	0.76	0.037	0.005	0.05	0.047	7.13	0.156	1.381	2.247	15.596	0.008	0.078	2.12	0.10
NR-10	Disseminated	1.06	0.037	0.005	0.22	0.047	9.93	0.225	1.149	2.227	2.442	0.075	1.068	21.03	0.06
NR-10	Disseminated	0.34	0.037	0.005	0.05	0.047	10.00	0.197	0.609	1.241	28.392	0.008	0.342	6.87	0.01
NR-10 (N=3)		0.76	0.037	0.005	0.05	0.047	9.93	0.197	1.149	2.227	15.596	0.008	0.342	6.87	0.06

ANNEXE 6 - Complete data set of SEM-EDS and LA-ICP-MS analyses of chalcopyrite obtained for the Noril'sk-Talnakh mining district and median values for each sample. Abbreviations: N= number of individual analyses; n.r.= not reported.

ANNEXE 6

Sample	Ore type	Intrusion	S	Fe	Cu	⁵⁹ Co	⁶¹ Ni	⁶⁶ Zn	⁷⁵ As	⁸² Se	⁹⁵ Mo	¹⁰¹ Ru	¹⁰³ Rh	¹⁰⁸ Pd
			%	%	%	ppm	ppm	ppm	ppm	ppm	ppm	ppm	ppm	ppm
Limit of detection			0.5	0.5	0.5	0.007	0.643	0.174	0.065	1.824	0.020	0.015	n.r.	0.008
90OMZS2-3	Cu-poor	Kharaelakh				0.822	26.2	569	5.42	52.3	0.040	0.198	n.r.	0.074
90OMZS2-3	Cu-poor	Kharaelakh				0.843	38.6	351	4.56	53.3	0.029	0.231	n.r.	0.028
90OMZS2-3	Cu-poor	Kharaelakh				0.426	76.1	223	0.07	57.2	0.020	0.061	n.r.	0.008
90OMZS2-3	Cu-poor	Kharaelakh	35.0	32.3	32.5	6.695	37.4	733	0.07	54.5	0.020	0.039	n.r.	0.008
90OMZS2-3	Cu-poor	Kharaelakh				1.187	79.1	438	0.47	51.6	0.020	0.095	n.r.	0.008
90OMZS2-3	Cu-poor	Kharaelakh				4.565	133.9	642	0.07	50.8	0.029	0.058	n.r.	0.008
90OMZS2-3	Cu-poor	Kharaelakh				0.453	32.3	288	3.62	57.5	0.020	0.042	n.r.	0.008
Median 90OMZS2-3 (N=7)			35.0	32.3	32.5	0.843	38.6	438	0.47	53.3	0.020	0.061	n.r.	0.008
90KMZ5	Cu-poor	Talnakh				0.216	10.7	400	0.07	61.8	0.020	0.048	n.r.	0.008
90KMZ5	Cu-poor	Talnakh				0.545	51.7	306	0.07	63.0	1.801	0.103	n.r.	0.008
90KMZ5	Cu-poor	Talnakh	33.3	31.2	34.1	10.955	270.8	295	0.67	59.9	2.069	0.133	n.r.	0.014
90KMZ5	Cu-poor	Talnakh				0.234	12.2	405	0.07	60.9	0.020	0.092	n.r.	0.008
90KMZ5	Cu-poor	Talnakh				18.562	654.2	466	0.07	60.5	0.061	0.118	n.r.	1.021
Median 90KMZ5 (N=5)			33.3	31.2	34.1	0.545	51.7	400	0.07	60.9	0.061	0.103	n.r.	0.008
NR-6	Cu-poor	Noril'sk I				10.651	639.0	587	0.07	28.9	0.020	0.156	n.r.	0.304
NR-6	Cu-poor	Noril'sk I				7.303	699.9	411	0.07	28.5	0.020	0.204	n.r.	0.171
NR-6	Cu-poor	Noril'sk I	35.1	30.3	34.0	0.432	52.9	563	0.07	27.4	0.020	0.204	n.r.	0.008
NR-6	Cu-poor	Noril'sk I				0.913	47.2	432	0.07	26.0	0.020	0.143	n.r.	0.045
Median NR-6 (N=4)			35.1	30.3	34.0	4.108	346.0	498	0.07	27.9	0.020	0.180	n.r.	0.108

ANNEXE 6 – Cont.

Sample	Ore type	¹⁰⁹ Ag	¹¹¹ Cd	¹¹⁵ In	¹¹⁸ Sn	¹²¹ Sb	¹³⁰ Te	¹⁸⁵ Re	¹⁸⁹ Os	¹⁹³ Ir	¹⁹⁵ Pt	¹⁹⁷ Au	²⁰⁵ Tl	²⁰⁸ Pb	²⁰⁹ Bi
		ppm	ppm	ppm	ppm	ppm	ppm	ppm	ppm	ppm	ppm	ppm	ppm	ppm	ppm
Limit of detection		0.007	0.037	0.005	0.050	0.047	0.257	0.010	0.017	0.004	0.013	0.008	0.004	0.007	0.004
90OMZS2-3	Cu-poor	2.62	7.21	1.62	2.62	0.143	1.64	0.010	0.017	0.004	0.639	0.008	0.011	44.73	0.064
90OMZS2-3	Cu-poor	5.90	6.97	1.58	2.43	0.107	1.13	0.010	0.017	0.004	0.013	0.008	0.019	10.59	0.062
90OMZS2-3	Cu-poor	2.76	4.90	1.71	1.53	0.047	2.29	0.010	0.017	0.004	0.013	0.008	0.028	15.28	0.064
90OMZS2-3	Cu-poor	1.79	8.79	2.31	2.88	0.047	2.77	0.010	0.017	0.004	0.073	0.008	0.045	52.64	0.155
90OMZS2-3	Cu-poor	4.56	6.36	1.38	1.94	0.047	1.70	0.010	0.017	0.004	0.013	0.008	0.004	42.72	0.118
90OMZS2-3	Cu-poor	4.02	6.66	1.50	2.80	0.047	1.16	0.010	0.017	0.004	0.013	0.008	0.040	8.98	0.052
90OMZS2-3	Cu-poor	3.37	5.33	1.88	1.97	0.075	3.22	0.010	0.017	0.004	0.295	0.008	0.044	19.87	0.079
90OMZS2-3 (N=7)		3.37	6.66	1.62	2.43	0.047	1.70	0.010	0.017	0.004	0.013	0.008	0.028	19.87	0.064
90KMZ5	Cu-poor	12.81	3.62	0.80	3.85	0.047	2.25	0.010	0.017	0.004	0.210	0.008	0.004	1.99	0.219
90KMZ5	Cu-poor	13.94	3.65	0.38	1.17	0.113	1.36	0.334	0.228	0.268	0.487	0.008	0.087	2.23	0.175
90KMZ5	Cu-poor	12.51	3.47	0.15	0.26	0.076	1.13	0.410	0.180	0.149	0.882	0.008	1.022	6.97	0.609
90KMZ5	Cu-poor	11.62	3.77	0.49	2.16	0.047	2.46	0.010	0.017	0.004	0.456	0.008	0.008	1.72	0.170
90KMZ5	Cu-poor	13.48	4.93	0.52	1.54	0.047	2.01	0.164	0.017	0.004	0.277	0.008	2.130	3.69	0.110
90OKMZ5 (N=5)		12.81	3.65	0.49	1.54	0.047	2.01	0.164	0.017	0.004	0.456	0.008	0.087	2.23	0.175
NR-6	Cu-poor	2.74	11.69	0.75	0.16	0.047	0.39	0.010	0.017	0.004	0.051	0.008	0.019	18.26	0.197
NR-6	Cu-poor	2.01	9.04	0.53	0.09	0.047	0.33	0.010	0.017	0.004	0.085	0.008	0.004	11.78	0.096
NR-6	Cu-poor	4.08	13.54	0.50	0.05	0.047	0.51	0.010	0.017	0.004	0.030	0.008	0.009	14.15	0.086
NR-6	Cu-poor	2.14	9.62	0.73	0.10	0.047	0.50	0.010	0.017	0.004	0.119	0.008	0.009	11.02	0.108
NR-6 (N=4)		2.44	10.65	0.63	0.10	0.047	0.44	0.010	0.017	0.004	0.068	0.008	0.009	12.96	0.102

ANNEXE 6 – Cont.

Sample	Ore type	Intrusion	S	Fe	Cu	⁵⁹ Co	⁶¹ Ni	⁶⁶ Zn	⁷⁵ As	⁸² Se	⁹⁵ Mo	¹⁰¹ Ru	¹⁰³ Rh	¹⁰⁸ Pd
			%	%	%	ppm	ppm	ppm	ppm	ppm	ppm	ppm	ppm	ppm
Limit of detection			0.5	0.5	0.5	0.007	0.643	0.174	0.065	1.824	0.020	0.015	n.r.	0.008
90OMZS2-2	Cu-poor	Kharaelakh				0.034	7.4	301	0.07	49.9	0.020	0.085	n.r.	0.008
90OMZS2-2	Cu-poor	Kharaelakh				0.186	9.4	453	0.07	55.4	0.020	0.063	n.r.	0.008
90OMZS2-2	Cu-poor	Kharaelakh				0.061	5.8	260	0.07	48.4	0.020	0.085	n.r.	0.008
90OMZS2-2	Cu-poor	Kharaelakh	35.7	30.3	34.3	0.107	7.2	353	0.07	51.6	0.020	0.070	n.r.	0.008
90OMZS2-2	Cu-poor	Kharaelakh				0.070	9.0	453	0.07	54.7	0.020	0.097	n.r.	0.008
90OMZS2-2	Cu-poor	Kharaelakh				2.008	14.0	374	0.05	56.1	0.020	0.100	n.r.	0.008
90OMZS2-2	Cu-poor	Kharaelakh				0.100	7.5	459	0.07	58.1	0.020	0.119	n.r.	0.008
Median 90OMZS2-2 (N=7)			35.7	30.3	34.3	0.100	7.5	374	0.07	54.7	0.020	0.085	n.r.	0.008
NR-13	Cu-poor	Kharaelakh				0.721	57.8	782	0.07	29.0	0.020	0.134	n.r.	0.008
NR-13	Cu-poor	Kharaelakh				0.569	52.3	694	0.07	29.4	0.020	0.122	n.r.	0.008
NR-13	Cu-poor	Kharaelakh	34.9	30.2	33.7	1.126	130.8	779	0.07	30.8	0.020	0.132	n.r.	0.008
NR-13	Cu-poor	Kharaelakh				0.557	54.2	642	0.07	29.5	0.020	0.109	n.r.	0.008
NR-13	Cu-poor	Kharaelakh				0.943	65.7	1095	0.07	29.5	0.020	0.091	n.r.	0.008
NR-13	Cu-poor	Kharaelakh				0.383	51.4	520	0.07	29.1	0.020	0.137	n.r.	0.008
Median NR-13 (N=7)			34.9	30.2	33.7	0.645	56.0	736	0.07	29.4	0.020	0.127	n.r.	0.008
NR-14	Cu-poor	Kharaelakh				0.353	53.3	566	0.07	38.7	0.020	0.119	n.r.	0.008
NR-14	Cu-poor	Kharaelakh				0.218	59.0	444	0.07	38.3	0.020	0.122	n.r.	0.017
NR-14	Cu-poor	Kharaelakh	34.8	30.2	33.9	0.529	58.7	764	0.07	37.3	0.020	0.112	n.r.	0.008
NR-14	Cu-poor	Kharaelakh				0.919	79.4	405	0.07	37.6	0.020	0.116	n.r.	0.008
NR-14	Cu-poor	Kharaelakh				0.505	69.1	666	0.07	37.1	0.020	0.131	n.r.	0.008
NR-14	Cu-poor	Kharaelakh				0.240	58.4	466	0.07	39.7	0.020	0.115	n.r.	0.008
Median NR-14 (N=6)			34.8	30.2	33.9	0.429	58.9	516	0.07	38.0	0.020	0.117	n.r.	0.008

ANNEXE 6 – Cont.

Sample	Ore type	¹⁰⁹ Ag	¹¹¹ Cd	¹¹⁵ In	¹¹⁸ Sn	¹²¹ Sb	¹³⁰ Te	¹⁸⁵ Re	¹⁸⁹ Os	¹⁹³ Ir	¹⁹⁵ Pt	¹⁹⁷ Au	²⁰⁵ Tl	²⁰⁸ Pb	²⁰⁹ Bi
		ppm	ppm	ppm	ppm	ppm	ppm	ppm	ppm	ppm	ppm	ppm	ppm	ppm	ppm
Limit of detection		0.007	0.037	0.005	0.050	0.047	0.257	0.010	0.017	0.004	0.013	0.008	0.004	0.007	0.004
90OMZS2-2	Cu-poor	2.67	10.25	2.25	0.67	0.047	2.16	0.010	0.017	0.004	0.044	0.008	0.059	44.43	0.015
90OMZS2-2	Cu-poor	2.64	13.05	2.60	1.05	0.047	2.28	0.010	0.017	0.004	0.020	0.008	0.011	94.33	0.019
90OMZS2-2	Cu-poor	2.31	9.77	2.46	0.91	0.047	2.31	0.010	0.017	0.004	0.038	0.008	0.004	71.21	0.020
90OMZS2-2	Cu-poor	2.28	12.93	2.31	0.91	0.047	2.58	0.010	0.017	0.004	0.023	0.008	0.008	79.09	0.014
90OMZS2-2	Cu-poor	2.40	13.30	2.02	1.30	0.047	2.65	0.010	0.017	0.004	0.047	0.008	0.008	56.48	0.017
90OMZS2-2	Cu-poor	2.30	11.50	2.50	0.79	0.047	2.89	0.010	0.017	0.004	0.019	0.008	0.019	45.04	0.030
90OMZS2-2	Cu-poor	1.91	12.39	2.14	1.38	0.047	2.80	0.010	0.017	0.004	0.033	0.008	0.004	74.71	0.017
90OMZS2-2 (N=7)		2.31	12.39	2.31	0.91	0.047	2.58	0.010	0.017	0.004	0.033	0.008	0.008	71.21	0.017
NR-13	Cu-poor	0.53	6.54	1.27	2.43	0.047	0.87	0.010	0.017	0.004	0.097	0.008	0.004	25.84	0.073
NR-13	Cu-poor	0.77	5.93	1.48	2.38	0.047	0.77	0.010	0.017	0.004	0.176	0.008	0.096	19.69	0.116
NR-13	Cu-poor	1.34	7.18	1.43	1.70	0.047	1.24	0.010	0.017	0.004	0.175	0.008	0.011	30.55	0.081
NR-13	Cu-poor	0.70	6.03	1.23	2.35	0.047	1.29	0.010	0.017	0.004	0.138	0.008	0.004	24.59	0.060
NR-13	Cu-poor	1.83	11.29	1.35	1.67	0.047	0.82	0.010	0.017	0.004	0.114	0.008	0.049	31.04	0.074
NR-13	Cu-poor	0.63	4.84	1.15	2.35	0.047	1.00	0.010	0.017	0.004	0.086	0.008	0.004	44.00	0.059
NR-13 (N=7)		0.73	6.28	1.31	2.35	0.047	0.94	0.010	0.017	0.004	0.126	0.008	0.008	28.19	0.073
NR-14	Cu-poor	0.65	6.88	1.42	1.47	0.047	0.97	0.010	0.017	0.004	0.074	0.008	0.095	23.43	0.093
NR-14	Cu-poor	0.63	5.48	1.49	1.83	0.047	0.86	0.010	0.017	0.004	0.062	0.008	0.058	45.16	0.090
NR-14	Cu-poor	1.07	8.46	1.46	2.18	0.047	1.55	0.010	0.017	0.004	0.240	0.008	0.012	21.73	0.079
NR-14	Cu-poor	1.20	5.90	1.73	2.68	0.047	1.79	0.010	0.017	0.004	0.396	0.008	0.009	12.35	0.098
NR-14	Cu-poor	1.30	8.37	1.33	1.73	0.047	1.18	0.010	0.017	0.004	0.140	0.008	0.426	33.20	0.199
NR-14	Cu-poor	1.54	7.88	1.72	1.63	0.047	0.81	0.010	0.017	0.004	0.097	0.008	0.158	42.39	0.127
NR-14 (N=6)		1.14	7.38	1.48	1.78	0.047	1.08	0.010	0.017	0.004	0.119	0.008	0.076	28.32	0.096

ANNEXE 6 – Cont.

Sample	Ore type	Intrusion	S	Fe	Cu	⁵⁹ Co	⁶¹ Ni	⁶⁶ Zn	⁷⁵ As	⁸² Se	⁹⁵ Mo	¹⁰¹ Ru	¹⁰³ Rh	¹⁰⁸ Pd
			%	%	%	ppm	ppm	ppm	ppm	ppm	ppm	ppm	ppm	ppm
Limit of detection			0.5	0.5	0.5	0.007	0.643	0.174	0.065	1.824	0.020	0.015	n.r.	0.008
NR-11	Cu-poor	Noril'sk I	33.3	30.7	34.8	0.146	24.6	505	0.07	87.9	0.158	0.103	n.r.	0.089
NR-11	Cu-poor	Noril'sk I				30.734	2221	414	0.07	81.8	0.020	0.122	n.r.	11.893
NR-11	Cu-poor	Noril'sk I				0.131	15.8	272	0.07	72.7	0.020	0.103	n.r.	0.027
NR-11	Cu-poor	Noril'sk I				0.035	10.8	341	0.07	85.0	0.020	0.106	n.r.	0.021
Median NR-11 (N=4)						33.3	30.7	34.8	0.138	20.2	377	0.07	83.4	0.020
NR-8	Cu-rich	Noril'sk I	34.7	30.2	33.6	0.639	37.7	627	0.07	42.6	0.020	0.164	n.r.	0.008
NR-8	Cu-rich	Noril'sk I				0.292	25.9	730	0.61	41.5	0.020	0.201	n.r.	0.038
NR-8	Cu-rich	Noril'sk I				6.086	210.0	673	0.07	39.2	0.020	0.179	n.r.	1.010
NR-8	Cu-rich	Noril'sk I				0.338	22.8	563	0.07	45.0	0.020	0.182	n.r.	0.071
NR-8	Cu-rich	Noril'sk I				2.130	203.9	569	0.07	39.7	0.020	0.130	n.r.	1.071
Median NR-8 (N=5)			34.7	30.2	33.6	0.639	37.7	627	0.07	41.5	0.020	0.179	n.r.	0.071
90MC15	Cu-rich	Noril'sk I	33.5	30.5	34.6	0.009	49.3	83	0.22	135.7	0.058	0.080	n.r.	0.911
90MC15	Cu-rich	Noril'sk I				0.007	48.4	83	0.16	138.5	0.085	0.045	n.r.	0.384
90MC15	Cu-rich	Noril'sk I				0.015	44.4	76	0.14	133.6	0.079	0.090	n.r.	0.626
90MC15	Cu-rich	Noril'sk I				0.761	410.8	72	0.16	130.5	0.055	0.066	n.r.	0.730
90MC15	Cu-rich	Noril'sk I				0.074	56.6	213	0.13	133.6	0.097	0.092	n.r.	0.756
90MC15	Cu-rich	Noril'sk I				0.008	42.6	73	0.20	132.7	0.082	0.094	n.r.	1.017
Median 90MC15 (N=6)			33.5	30.5	34.6	0.012	48.8	79	0.16	133.6	0.081	0.085	n.r.	0.743

ANNEXE 6 – Cont.

Sample	Ore type	¹⁰⁹ Ag	¹¹¹ Cd	¹¹⁵ In	¹¹⁸ Sn	¹²¹ Sb	¹³⁰ Te	¹⁸⁵ Re	¹⁸⁹ Os	¹⁹³ Ir	¹⁹⁵ Pt	¹⁹⁷ Au	²⁰⁵ Tl	²⁰⁸ Pb	²⁰⁹ Bi
		ppm	ppm	ppm	ppm	ppm	ppm	ppm	ppm	ppm	ppm	ppm	ppm	ppm	ppm
Limit of detection		0.007	0.037	0.005	0.050	0.047	0.257	0.010	0.017	0.004	0.013	0.008	0.004	0.007	0.004
NR-11	Cu-poor	28.30	4.50	1.58	0.40	0.047	11.53	0.010	0.017	0.007	0.195	0.008	0.100	6.66	1.102
NR-11	Cu-poor	35.60	4.69	1.72	0.09	0.047	12.66	0.010	0.017	0.004	0.350	0.012	0.274	33.59	0.057
NR-11	Cu-poor	27.48	2.83	1.19	0.48	0.047	4.90	0.010	0.017	0.004	0.347	0.008	0.061	17.53	0.161
NR-11	Cu-poor	29.06	3.41	1.40	0.28	0.047	7.18	0.010	0.017	0.004	0.323	0.008	0.137	18.23	0.124
NR-11 (N=4)		28.68	3.96	1.49	0.34	0.047	9.36	0.010	0.017	0.004	0.335	0.008	0.119	17.88	0.143
NR-8	Cu-rich	14.76	8.37	1.61	2.37	0.047	1.80	0.010	0.017	0.004	0.044	0.008	0.167	2.96	0.108
NR-8	Cu-rich	18.71	8.64	1.68	1.95	0.047	1.95	0.010	0.017	0.004	0.107	0.008	0.082	8.70	0.138
NR-8	Cu-rich	14.64	7.97	1.94	7.42	0.047	1.90	0.010	0.017	0.004	0.155	0.008	0.155	10.68	0.188
NR-8	Cu-rich	17.56	7.30	2.14	2.62	0.047	2.00	0.010	0.017	0.004	0.043	0.008	0.444	13.27	0.487
NR-8	Cu-rich	46.56	7.06	1.33	1.80	0.047	1.75	0.010	0.017	0.004	0.063	0.008	0.144	4.75	0.142
NR-8 (N=5)		17.56	7.97	1.68	2.37	0.047	1.90	0.010	0.017	0.004	0.063	0.008	0.155	8.70	0.142
90MC15	Cu-rich	11.75	3.86	1.31	0.05	0.047	39.47	0.010	0.017	0.004	0.037	0.008	0.828	1.44	0.017
90MC15	Cu-rich	12.14	3.77	1.77	0.05	0.047	39.19	0.010	0.017	0.004	0.029	0.008	1.019	1.16	0.004
90MC15	Cu-rich	7.77	3.56	1.41	0.05	0.047	39.29	0.010	0.017	0.004	0.033	0.008	1.056	1.19	0.004
90MC15	Cu-rich	10.16	4.17	0.76	0.05	0.047	39.44	0.010	0.017	0.004	0.025	0.008	1.083	0.87	0.008
90MC15	Cu-rich	14.73	5.84	1.71	0.05	0.047	40.14	0.010	0.017	0.004	0.042	0.008	1.086	1.47	0.004
90MC15	Cu-rich	9.13	3.16	1.12	0.05	0.047	39.99	0.010	0.017	0.004	0.023	0.008	0.989	1.13	0.005
90MC15 (N=6)		10.95	3.82	1.36	0.05	0.047	39.45	0.010	0.017	0.004	0.031	0.008	1.038	1.17	0.004

ANNEXE 6 – Cont.

Sample	Ore type	Intrusion	S	Fe	Cu	⁵⁹ Co	⁶¹ Ni	⁶⁶ Zn	⁷⁵ As	⁸² Se	⁹⁵ Mo	¹⁰¹ Ru	¹⁰³ Rh	¹⁰⁸ Pd
			%	%	%	ppm	ppm	ppm	ppm	ppm	ppm	ppm	ppm	ppm
Limit of detection			0.5	0.5	0.5	0.007	0.643	0.174	0.065	1.824	0.020	0.015	n.r.	0.008
90MC5	Cu-rich	Noril'sk I				0.116	41.4	121	0.07	172.5	0.041	0.078	n.r.	5.701
90MC5	Cu-rich	Noril'sk I				0.077	41.1	66	0.07	179.2	0.076	0.116	n.r.	2.720
90MC5	Cu-rich	Noril'sk I	32.4	30.7	33.3	0.057	29.6	152	0.07	172.2	0.020	0.099	n.r.	4.402
90MC5	Cu-rich	Noril'sk I				0.102	35.9	107	0.07	174.7	0.022	0.073	n.r.	5.266
90MC5	Cu-rich	Noril'sk I				0.049	41.1	68	0.07	172.2	0.067	0.116	n.r.	4.198
90MC5	Cu-rich	Noril'sk I				0.042	36.7	75	0.07	168.3	0.113	0.106	n.r.	2.602
Median 90MC5 (N=6)			32.4	30.7	33.3	0.067	38.9	91	0.07	172.4	0.054	0.103	n.r.	4.300
NR-18	Cu-rich	Kharaelakh				0.170	36.2	364	0.07	74.2	0.020	0.134	n.r.	3.122
NR-18	Cu-rich	Kharaelakh	34.7	30.1	33.9	60.860	486.9	405	0.07	72.7	0.020	0.166	n.r.	1.306
NR-18	Cu-rich	Kharaelakh				0.149	32.9	584	0.07	76.7	0.020	0.143	n.r.	3.442
NR-18	Cu-rich	Kharaelakh				0.085	36.5	311	0.07	69.1	0.020	0.131	n.r.	0.287
Median NR-18 (N=4)			34.7	30.1	33.9	0.160	36.4	384	0.07	73.5	0.020	0.138	n.r.	2.214
NR-17	Cu-rich	Kharaelakh				0.563	75.2	426	0.07	88.9	0.020	0.097	n.r.	0.538
NR-17	Cu-rich	Kharaelakh				0.730	61.2	417	0.07	88.9	0.020	0.125	n.r.	0.700
NR-17	Cu-rich	Kharaelakh				1.035	67.6	1126	0.11	88.9	0.020	0.097	n.r.	0.008
NR-17	Cu-rich	Kharaelakh	34.5	30.1	33.7	0.234	50.8	459	0.07	90.7	0.020	0.112	n.r.	0.008
NR-17	Cu-rich	Kharaelakh				6.725	270.8	581	0.09	87.9	0.020	0.097	n.r.	1.392
NR-17	Cu-rich	Kharaelakh				0.186	38.3	393	0.07	92.2	0.020	0.100	n.r.	0.473
NR-17	Cu-rich	Kharaelakh				0.329	43.2	584	0.08	111.1	0.020	0.116	n.r.	0.731
Median NR-17 (N=7)			34.5	30.1	33.7	0.563	61.2	459	0.07	88.9	0.020	0.100	n.r.	0.538

ANNEXE 6 – Cont.

Sample	Ore type	¹⁰⁹ Ag	¹¹¹ Cd	¹¹⁵ In	¹¹⁸ Sn	¹²¹ Sb	¹³⁰ Te	¹⁸⁵ Re	¹⁸⁹ Os	¹⁹³ Ir	¹⁹⁵ Pt	¹⁹⁷ Au	²⁰⁵ Tl	²⁰⁸ Pb	²⁰⁹ Bi
		ppm	ppm	ppm	ppm	ppm	ppm	ppm	ppm	ppm	ppm	ppm	ppm	ppm	ppm
Limit of detection		0.007	0.037	0.005	0.050	0.047	0.257	0.010	0.017	0.004	0.013	0.008	0.004	0.007	0.004
90MC5	Cu-rich	9.94	6.03	1.10	0.07	0.047	64.42	0.010	0.017	0.004	0.033	0.008	0.319	0.46	0.006
90MC5	Cu-rich	12.57	5.08	0.14	0.05	0.047	69.44	0.010	0.017	0.004	0.016	0.008	0.374	0.23	0.004
90MC5	Cu-rich	11.49	6.03	0.53	0.05	0.047	61.04	0.010	0.017	0.004	0.085	0.008	0.708	0.58	0.004
90MC5	Cu-rich	10.38	6.30	1.22	0.05	0.047	69.99	0.010	0.017	0.004	0.032	0.008	0.858	0.32	0.004
90MC5	Cu-rich	11.29	5.57	0.41	0.09	0.047	63.36	0.010	0.017	0.004	0.079	0.008	1.041	0.14	0.004
90MC5	Cu-rich	10.27	5.69	0.51	0.05	0.047	52.34	0.010	0.017	0.004	0.046	0.008	0.968	0.13	0.004
90MC5 (N=6)		10.83	5.86	0.52	0.05	0.047	63.89	0.010	0.017	0.004	0.040	0.008	0.783	0.28	0.004
NR-18	Cu-rich	8.31	21.21	2.06	1.97	0.047	9.62	0.010	0.017	0.004	0.420	0.012	0.539	0.32	0.895
NR-18	Cu-rich	8.19	21.82	3.90	2.30	0.047	7.21	0.010	0.017	0.004	0.076	0.010	0.050	0.48	0.609
NR-18	Cu-rich	5.10	26.17	2.49	1.64	0.047	9.25	0.010	0.017	0.004	0.246	0.016	0.155	0.22	1.643
NR-18	Cu-rich	2.86	14.27	3.86	1.56	0.047	5.66	0.010	0.017	0.004	0.030	0.010	0.134	0.42	0.578
NR-18 (N=4)		6.64	21.51	3.17	1.80	0.047	8.23	0.010	0.017	0.004	0.161	0.011	0.145	0.37	0.752
NR-17	Cu-rich	21.61	34.69	3.78	6.57	0.047	12.45	0.010	0.017	0.004	0.265	1.278	0.128	23.92	0.913
NR-17	Cu-rich	10.47	37.12	3.44	4.92	0.047	13.57	0.010	0.017	0.004	0.456	0.056	0.110	12.72	0.353
NR-17	Cu-rich	8.79	69.68	4.70	3.20	0.047	14.36	0.010	0.017	0.004	0.822	0.055	0.085	16.25	0.609
NR-17	Cu-rich	2.68	36.91	3.32	6.85	0.047	6.33	0.010	0.017	0.004	0.113	0.027	0.071	24.10	0.148
NR-17	Cu-rich	8.92	44.43	2.80	4.19	0.047	11.93	0.010	0.017	0.004	0.484	0.053	0.105	27.23	0.639
NR-17	Cu-rich	6.94	37.73	3.66	4.63	0.047	11.84	0.010	0.017	0.004	0.170	0.075	0.154	16.89	0.197
NR-17	Cu-rich	8.67	46.25	5.09	3.97	0.047	17.07	0.010	0.017	0.004	0.316	0.075	0.133	22.40	0.262
NR-17 (N=7)		8.79	37.73	3.66	4.63	0.047	12.45	0.010	0.017	0.004	0.316	0.056	0.110	22.40	0.353

ANNEXE 6 – Cont.

Sample	Ore type	Intrusion	S	Fe	Cu	⁵⁹ Co	⁶¹ Ni	⁶⁶ Zn	⁷⁵ As	⁸² Se	⁹⁵ Mo	¹⁰¹ Ru	¹⁰³ Rh	¹⁰⁸ Pd
			%	%	%	ppm	ppm	ppm	ppm	ppm	ppm	ppm	ppm	ppm
Limit of detection			0.5	0.5	0.5	0.007	0.643	0.174	0.065	1.824	0.020	0.015	n.r.	0.008
900MZ67-5-1	Cu-rich	Kharaelakh	35.5	30.7	34.5	0.186	73.0	371	0.17	93.4	0.051	0.087	n.r.	0.008
900MZ67-5-1	Cu-rich	Kharaelakh				0.186	82.8	596	0.08	85.8	0.058	0.091	n.r.	0.008
900MZ67-5-1	Cu-rich	Kharaelakh				0.195	67.3	320	0.19	91.6	0.055	0.082	n.r.	0.008
900MZ67-5-1	Cu-rich	Kharaelakh				0.219	73.3	116	0.11	86.9	0.086	0.111	n.r.	0.008
Median 900MZ67-5-1 (N=4)			35.5	30.7	34.5	0.190	73.2	345	0.14	89.3	0.056	0.089	n.r.	0.008
900C13	Cu-rich	Kharaelakh	33.9	30.6	34.4	0.761	25.3	633	0.07	58.4	0.020	0.122	n.r.	0.113
900C13	Cu-rich	Kharaelakh				0.170	14.9	298	0.07	65.7	0.020	0.079	n.r.	0.069
900C13	Cu-rich	Kharaelakh				0.216	15.5	490	0.07	65.7	0.020	0.100	n.r.	0.008
900C13	Cu-rich	Kharaelakh				0.176	14.0	533	0.07	57.8	0.020	0.060	n.r.	0.008
900C13	Cu-rich	Kharaelakh				1.339	42.9	2130	0.07	61.5	0.020	0.088	n.r.	0.008
900C13	Cu-rich	Kharaelakh				0.204	15.5	332	0.07	59.2	0.020	0.091	n.r.	0.007
900C13	Cu-rich	Kharaelakh				0.316	15.9	432	0.07	60.7	0.020	0.089	n.r.	0.008
Median 900C13 (N=7)			33.9	30.6	34.4	0.216	15.5	490	0.07	60.7	0.020	0.089	n.r.	0.008
900MZS1-3	Cu-rich	Kharaelakh	35.0	31.0	33.6	0.082	3.4	161	0.07	66.0	0.020	0.091	n.r.	0.008
900MZS1-3	Cu-rich	Kharaelakh				0.092	5.4	253	0.07	64.8	0.020	0.046	n.r.	0.008
900MZS1-3	Cu-rich	Kharaelakh				18.258	9.1	202	0.07	72.1	0.020	0.075	n.r.	1.402
900MZS1-3	Cu-rich	Kharaelakh				0.093	5.3	181	0.07	62.0	0.020	0.069	n.r.	0.070
900MZS1-3	Cu-rich	Kharaelakh				0.882	4.0	178	0.07	67.0	0.020	0.089	n.r.	0.028
900MZS1-3	Cu-rich	Kharaelakh				0.096	5.5	180	0.07	70.6	0.020	0.082	n.r.	0.008
900MZS1-3	Cu-rich	Kharaelakh				0.228	8.8	201	0.07	72.4	0.183	0.065	n.r.	0.008
Median 900MZS1-3 (N=7)			35.0	31.0	33.6	0.096	5.4	181	0.07	67.0	0.020	0.075	n.r.	0.008

ANNEXE 6 – Cont.

Sample	Ore type	¹⁰⁹ Ag	¹¹¹ Cd	¹¹⁵ In	¹¹⁸ Sn	¹²¹ Sb	¹³⁰ Te	¹⁸⁵ Re	¹⁸⁹ Os	¹⁹³ Ir	¹⁹⁵ Pt	¹⁹⁷ Au	²⁰⁵ Tl	²⁰⁸ Pb	²⁰⁹ Bi
		ppm	ppm	ppm	ppm	ppm	ppm	ppm	ppm	ppm	ppm	ppm	ppm	ppm	ppm
Limit of detection		0.007	0.037	0.005	0.050	0.047	0.257	0.010	0.017	0.004	0.013	0.008	0.004	0.007	0.004
900MZ67-5-1	Cu-rich	15.18	24.47	4.43	19.14	0.047	14.24	0.010	0.017	0.004	0.013	0.012	0.113	163.1	0.012
900MZ67-5-1	Cu-rich	13.09	29.52	3.88	25.35	0.047	12.87	0.010	0.017	0.004	0.013	0.008	0.121	57.76	0.041
900MZ67-5-1	Cu-rich	21.33	23.13	4.15	12.29	0.047	14.27	0.010	0.017	0.004	0.013	0.015	0.119	220.0	0.025
900MZ67-5-1	Cu-rich	31.83	14.85	3.70	22.55	0.047	13.82	0.010	0.017	0.004	0.013	0.008	0.109	185.0	0.019
900MZ67-5-1 (N=4)		18.26	23.80	4.01	20.84	0.047	14.03	0.010	0.017	0.004	0.013	0.010	0.116	174.1	0.022
900C13	Cu-rich	7.30	16.46	4.26	2.29	0.047	11.93	0.010	0.017	0.004	0.417	0.008	0.069	90.38	0.417
900C13	Cu-rich	8.92	10.25	4.62	2.01	0.047	13.69	0.010	0.017	0.004	0.110	0.008	0.085	175.6	0.087
900C13	Cu-rich	5.75	15.70	4.58	1.38	0.047	11.69	0.010	0.017	0.004	0.320	0.008	0.088	60.10	0.347
900C13	Cu-rich	6.79	16.13	4.18	3.18	0.047	11.78	0.010	0.017	0.004	0.073	0.008	0.064	75.10	0.143
900C13	Cu-rich	7.55	43.21	4.49	1.28	0.047	11.96	0.010	0.017	0.004	0.080	0.008	0.195	79.42	0.091
900C13	Cu-rich	5.42	11.69	4.27	1.54	0.047	10.16	0.010	0.017	0.004	0.079	0.008	0.191	115.0	0.081
900C13	Cu-rich	5.07	13.94	4.77	2.56	0.047	9.65	0.010	0.017	0.004	0.077	0.008	0.138	145.2	0.237
900C13 (N=7)		6.79	15.70	4.49	2.01	0.047	11.78	0.010	0.017	0.004	0.080	0.008	0.088	90.38	0.143
900MZS1-3	Cu-rich	4.25	8.12	3.21	0.05	0.047	7.91	0.010	0.017	0.004	0.032	0.035	0.027	246.5	0.013
900MZS1-3	Cu-rich	3.76	10.13	3.07	0.06	0.047	7.79	0.010	0.017	0.004	0.018	0.050	0.033	195.1	0.006
900MZS1-3	Cu-rich	5.82	9.89	2.98	0.85	0.047	8.65	0.010	0.017	0.004	0.560	0.067	0.051	83.07	0.496
900MZS1-3	Cu-rich	4.09	7.15	2.95	0.05	0.047	6.93	0.010	0.017	0.004	0.103	0.063	0.017	107.1	0.176
900MZS1-3	Cu-rich	4.31	8.95	2.99	0.05	0.047	8.03	0.010	0.017	0.004	0.158	0.077	0.029	139.7	0.092
900MZS1-3	Cu-rich	3.68	8.46	2.86	0.05	0.047	8.58	0.010	0.017	0.004	0.122	0.051	0.046	195.7	0.049
900MZS1-3	Cu-rich	4.56	9.71	2.89	0.05	0.047	9.04	0.010	0.017	0.004	0.152	0.058	0.320	203.6	0.054
900MZS1-3 (N=7)		4.25	8.95	2.98	0.05	0.047	8.03	0.010	0.017	0.004	0.122	0.058	0.033	195.1	0.054

ANNEXE 6 – Cont.

Sample	Ore type	Intrusion	S	Fe	Cu	⁵⁹ Co	⁶¹ Ni	⁶⁶ Zn	⁷⁵ As	⁸² Se	⁹⁵ Mo	¹⁰¹ Ru	¹⁰³ Rh	¹⁰⁸ Pd
			%	%	%	ppm	ppm	ppm	ppm	ppm	ppm	ppm	ppm	ppm
Limit of detection			0.5	0.5	0.5	0.007	0.643	0.174	0.065	1.824	0.020	0.015	n.r.	0.008
NR-15	Cu-rich	Kharaelakh				0.201	50.8	399	0.07	62.7	0.020	0.073	n.r.	0.182
NR-15	Cu-rich	Kharaelakh	33.7	31.5	33.9	13.998	477.8	307	0.10	56.9	0.020	0.093	n.r.	3.985
NR-15	Cu-rich	Kharaelakh				3.043	127.8	545	0.07	58.1	0.020	0.058	n.r.	0.662
NR-15	Cu-rich	Kharaelakh				4.565	255.6	612	0.07	60.4	0.020	0.100	n.r.	0.570
Median NR-15 (N=4)			33.7	31.5	33.9	3.804	191.7	472	0.07	59.3	0.020	0.083	n.r.	0.616
NR-10	Disseminated	Noril'sk I				0.825	53.3	3317	0.07	78.4	0.020	0.091	n.r.	0.008
NR-10	Disseminated	Noril'sk I	34.5	30.3	33.9	1.430	72.7	3895	0.07	84.3	0.020	0.131	n.r.	0.075
NR-10	Disseminated	Noril'sk I				0.694	66.0	1935	0.07	82.5	0.020	0.109	n.r.	0.008
Median NR-10 (N=3)			34.5	30.3	33.9	0.825	66.0	3317	0.07	82.5	0.020	0.109	n.r.	0.008
NR-9	Disseminated	Noril'sk I				882.470	2221	444	0.07	136.3	0.020	0.096	n.r.	14.056
NR-9	Disseminated	Noril'sk I				760.750	1735	882	0.07	147.6	0.020	0.109	n.r.	12.975
NR-9	Disseminated	Noril'sk I	33.6	31.6	34.0	3256.010	6968	1613	0.12	128.7	0.029	0.099	n.r.	16.622
NR-9	Disseminated	Noril'sk I				432.106	1339	493	0.13	120.5	0.033	0.049	n.r.	17.310
NR-9	Disseminated	Noril'sk I				1825.800	3469	505	0.07	145.5	0.020	0.066	n.r.	8.462
Median NR-9 (N=5)			33.6	31.6	34.0	882.470	2221	505	0.07	136.3	0.020	0.096	n.r.	14.056

ANNEXE 6 – Cont.

Sample	Ore type	¹⁰⁹ Ag	¹¹¹ Cd	¹¹⁵ In	¹¹⁸ Sn	¹²¹ Sb	¹³⁰ Te	¹⁸⁵ Re	¹⁸⁹ Os	¹⁹³ Ir	¹⁹⁵ Pt	¹⁹⁷ Au	²⁰⁵ Tl	²⁰⁸ Pb	²⁰⁹ Bi
		ppm	ppm	ppm	ppm	ppm	ppm	ppm	ppm	ppm	ppm	ppm	ppm	ppm	ppm
Limit of detection		0.007	0.037	0.005	0.050	0.047	0.257	0.010	0.017	0.004	0.013	0.008	0.004	0.007	0.004
NR-15	Cu-rich	1.70	20.39	2.02	0.05	0.047	5.26	0.010	0.017	0.004	0.013	0.008	0.043	11.23	0.286
NR-15	Cu-rich	3.44	17.25	2.11	0.15	0.047	8.31	0.010	0.017	0.004	0.030	0.008	0.047	63.90	2.769
NR-15	Cu-rich	3.13	27.39	2.28	0.20	0.047	8.76	0.010	0.017	0.004	0.013	0.027	0.029	16.71	0.320
NR-15	Cu-rich	3.13	26.05	1.99	0.12	0.047	6.91	0.010	0.017	0.004	0.024	0.012	0.031	19.35	0.499
NR-15 (N=4)		3.13	23.22	2.07	0.14	0.047	7.61	0.010	0.017	0.004	0.018	0.010	0.037	18.03	0.409
NR-10	Disseminated	2.83	3.01	1.46	0.14	0.047	16.43	0.010	0.017	0.007	0.682	0.015	0.004	1.61	0.034
NR-10	Disseminated	1.96	5.20	1.38	0.10	0.047	14.39	0.010	0.017	0.008	1.263	0.026	0.004	40.75	0.063
NR-10	Disseminated	2.50	2.77	1.53	0.05	0.047	17.62	0.010	0.017	0.004	0.192	0.026	0.037	7.82	0.022
NR-10 (N=3)		2.50	3.01	1.46	0.10	0.047	16.43	0.010	0.017	0.007	0.682	0.026	0.004	7.82	0.034
NR-9	Disseminated	11.53	0.97	2.11	1.37	0.047	40.38	0.010	0.018	0.004	0.013	0.008	0.110	24.22	1.357
NR-9	Disseminated	9.68	1.46	2.06	1.28	0.047	47.74	0.010	0.017	0.004	0.013	0.008	0.064	24.65	1.226
NR-9	Disseminated	10.86	2.50	1.89	2.59	0.047	45.16	0.010	0.017	0.004	0.013	0.008	0.066	20.72	1.418
NR-9	Disseminated	14.91	1.03	1.77	0.96	0.085	36.82	0.010	0.017	0.004	0.014	0.019	0.374	20.75	1.552
NR-9	Disseminated	10.86	0.83	2.34	1.86	0.047	45.13	0.010	0.017	0.004	0.013	0.008	0.262	16.68	0.657
NR-9 (N=5)		10.86	1.03	2.06	1.37	0.047	45.13	0.010	0.017	0.004	0.013	0.008	0.110	20.75	1.357

ANNEXE 7 - Complete data set of SEM-EDS and LA-ICP-MS analyses of cubanite obtained for the Noril'sk-Talnakh mining district and median values for each sample. Abbreviations: N= number of individual analyses; n.r.= not reported.

ANNEXE 7

Sample	Ore type	Intrusion	S	Fe	Cu	⁵⁹ Co	⁶¹ Ni	⁶⁶ Zn	⁷⁵ As	⁸² Se	⁹⁵ Mo	¹⁰¹ Ru	¹⁰³ Rh	¹⁰⁸ Pd
			%	%	%	ppm	ppm	ppm	ppm	ppm	ppm	ppm	ppm	ppm
Limit of detection			0.5	0.5	0.5	0.007	0.643	0.174	0.065	1.824	0.020	0.015	n.r.	0.008
90MC15	Cu-rich	Noril'sk I	34.0	41.0	23.2	0.05	18.9	103.3	0.20	143.2	0.09	0.041	n.r.	0.981
90MC15	Cu-rich	Noril'sk I				0.16	33.3	156.4	0.17	142.0	0.04	0.078	n.r.	0.910
90MC15	Cu-rich	Noril'sk I				0.07	29.2	189.3	0.26	144.8	0.13	0.090	n.r.	0.670
90MC15	Cu-rich	Noril'sk I				0.23	444	502.0	0.32	141.6	0.11	0.070	n.r.	0.958
90MC15	Cu-rich	Noril'sk I				0.14	85.2	452.7	0.23	139.1	0.10	0.059	n.r.	0.843
90MC15	Cu-rich	Noril'sk I				0.18	30.0	307.8	0.16	146.1	0.07	0.049	n.r.	1.063
Median 90MC15 (N=6)						34.0	41.0	23.2	0.15	31.7	248.5	0.21	142.6	0.10
90MZS1-3	Cu-rich	Kharaelakh	34.8	41.4	22.3	13.99	235	13.6	0.07	69.3	0.02	0.054	n.r.	0.038
90MZS1-3	Cu-rich	Kharaelakh				76.95	1646	91.8	0.07	64.2	0.02	0.044	n.r.	0.671
90MZS1-3	Cu-rich	Kharaelakh				10.29	230	21.4	0.07	78.6	0.02	0.045	n.r.	0.054
90MZS1-3	Cu-rich	Kharaelakh				1.36	32.9	4.2	0.07	73.6	0.02	0.054	n.r.	0.080
90MZS1-3	Cu-rich	Kharaelakh				0.38	16.5	18.1	0.07	67.1	0.02	0.082	n.r.	0.008
90MZS1-3	Cu-rich	Kharaelakh				5.56	104	197.5	0.07	21.3	0.02	0.078	n.r.	0.017
90MZS1-3	Cu-rich	Kharaelakh				1.31	43.2	56.4	0.07	74.2	0.02	0.053	n.r.	0.008
90MZS1-3	Cu-rich	Kharaelakh				156.37	2922	42.4	0.07	71.6	0.02	0.068	n.r.	0.844
Median 90MZS1-3 (N=8)			34.8	41.4	22.3	7.92	167	31.9	0.07	70.5	0.02	0.054	n.r.	0.046
90MZS2-2	Cu-poor	Kharaelakh	34.5	41.7	22.8	5.35	198	366.2	0.07	52.6	0.02	0.098	n.r.	0.008

ANNEXE 7 – Cont.

Sample	Ore type	¹⁰⁹ Ag	¹¹¹ Cd	¹¹⁵ In	¹¹⁸ Sn	¹²¹ Sb	¹³⁰ Te	¹⁸⁵ Re	¹⁸⁹ Os	¹⁹³ Ir	¹⁹⁵ Pt	¹⁹⁷ Au	²⁰⁵ Tl	²⁰⁸ Pb	²⁰⁹ Bi
		ppm	ppm	ppm	ppm	ppm	ppm	ppm	ppm	ppm	ppm	ppm	ppm	ppm	ppm
Limit of detection		0.007	0.037	0.005	0.050	0.047	0.257	0.010	0.017	0.004	0.013	0.008	0.004	0.007	0.004
90MC15	Cu-rich	29.18	5.97	1.55	0.050	0.047	41.68	0.010	0.017	0.004	0.055	0.008	1.066	1.19	0.004
90MC15	Cu-rich	34.98	8.56	1.50	0.070	0.047	39.67	0.010	0.017	0.004	0.041	0.008	1.053	0.90	0.004
90MC15	Cu-rich	35.97	8.72	1.02	0.050	0.047	40.16	0.010	0.017	0.004	0.026	0.008	1.037	1.29	0.009
90MC15	Cu-rich	40.90	24.65	1.76	0.050	0.047	40.90	0.010	0.017	0.004	0.030	0.014	1.181	1.50	0.004
90MC15	Cu-rich	37.41	22.80	1.13	0.050	0.047	41.31	0.010	0.017	0.004	0.041	0.008	1.074	1.82	0.005
90MC15	Cu-rich	55.06	15.39	2.37	0.050	0.047	39.71	0.010	0.017	0.004	0.016	0.008	1.090	1.41	0.004
90MC15 (N=6)		36.69	12.06	1.52	0.050	0.047	40.53	0.010	0.017	0.004	0.036	0.008	1.070	1.35	0.004
90OMZS1-3	Cu-rich	14.90	0.67	0.84	0.050	0.047	8.52	0.010	0.017	0.004	0.251	0.026	0.058	34.98	0.140
90OMZS1-3	Cu-rich	11.32	2.55	0.33	0.050	0.047	5.09	0.010	0.017	0.004	0.030	0.026	0.071	9.59	0.019
90OMZS1-3	Cu-rich	7.70	1.08	0.08	0.050	0.047	4.61	0.010	0.017	0.004	0.144	0.015	0.032	7.90	0.095
90OMZS1-3	Cu-rich	9.75	0.45	0.04	0.060	0.047	5.60	0.010	0.017	0.004	0.477	0.136	0.015	4.49	0.391
90OMZS1-3	Cu-rich	5.64	1.07	0.84	0.050	0.047	7.16	0.010	0.017	0.004	0.024	0.058	0.027	14.16	0.023
90OMZS1-3	Cu-rich	4.50	7.08	0.70	0.119	0.049	0.38	0.010	0.017	0.004	0.013	0.015	0.807	44.85	0.009
90OMZS1-3	Cu-rich	10.66	1.93	0.12	0.050	0.047	7.78	0.010	0.017	0.004	0.128	0.020	0.118	26.62	0.067
90OMZS1-3	Cu-rich	10.90	1.69	0.39	0.050	0.047	3.95	0.010	0.017	0.004	0.039	0.072	0.154	18.06	0.029
90OMZS1-3 (N=8)		10.21	1.38	0.36	0.050	0.047	5.34	0.010	0.017	0.004	0.083	0.026	0.065	16.11	0.048
90OMZS2-2	Cu-poor	21.11	25.68	2.23	0.737	0.047	2.34	0.010	0.017	0.004	0.013	0.008	0.028	87.20	0.021

ANNEXE 8 - Partition coefficients of elements between pentlandite (Pn) and pyrrhotite (Po), Pn and chalcopyrite (Ccp), Ccp and Po, and Ccp and cubanite (Cbn) calculated for each sample from the Noril'sk-Talnakh mining district. The median partition coefficients are the median values of individual partition coefficients calculated for all samples. Results in red are below detection limits and were not used for calculation. Abbreviations: N= number of individual analyses; n.r.= not reported.

ANNEXE 8

<i>Pentlandite and Pyrrhotite (DPn/Po)</i>	Co	Cu	Zn	As	Se	Mo	Ru	Rh	Pd	Ag	Cd	In
	ppm	ppm	ppm	ppm	ppm	ppm	ppm	ppm	ppm	ppm	ppm	ppm
Pentlandite median values - 900MZS2-3 (N=6)	14505	61.9	3.7	0.81	52.9	0.26	0.01	0.06	28.5	6.46	0.09	0.02
Pyrrhotite median values - 900MZS2-3 (N=6)	32	11.5	0.2	0.07	56.4	0.34	0.01	0.19	0.01	0.52	0.09	0.01
DPn/Po - 900MZS2-3	459	5.4			0.9	0.76		0.32		12.33	1.03	
Pentlandite median values - NR-6 (N=3)	14978	25.1	127.0	0.07	29.6	0.10	0.17	0.05	45.9	3.32	0.04	0.01
Pyrrhotite median values - NR-6 (N=4)	393	1.9	0.2	0.07	34.2	0.22	0.13	0.43	1.1	0.67	0.04	0.01
DPn/Po - NR-6	38	13.4	730.3		0.9	0.46	1.37	0.11	43.3	4.94		
Pentlandite median values - NR-8 (N=4)	5864	6.4	0.2	0.57	56.5	0.02	2.84	16.96	1883.6	0.78	0.06	0.01
Pyrrhotite median values - NR-8 (N=3)	100	22.4	1.4	0.60	38.0	0.12	0.01	0.00	0.4	0.90	0.09	0.01
DPn/Po - NR-8	59	0.3	0.1	0.95	1.5				5056.4	0.86	0.71	
Pentlandite median values - NR-18 (N=4)	6019	71.1	13.8	0.07	72.1	0.02	0.35	0.00	341.4	1.00	0.16	0.06
Pyrrhotite median values -NR-18 (N=1)	68	548.5	274.3	0.07	92.2	0.02	0.01	0.00	6.3	16.21	12.47	0.23
DPn/Po - NR-18	89	0.1	0.1		0.8				54.1	0.06	0.01	0.28
Pentlandite median values - NR-17 (N=8)	10102	4.1	0.5	0.24	85.6	0.02	0.14	0.00	502.4	4.02	0.04	0.01
Pyrrhotite median values - NR-17 (N=5)	103	5.7	84.8	0.15	97.9	0.02	0.01	0.00	2.4	5.17	3.80	0.05
DPn/Po - NR-17	98	0.7	0.0	1.59	0.9				205.9	0.78		0.16
Pentlandite median values - 90OC13 (N=7)	17778	8.7	1.3	0.14	57.3	0.02	0.13	0.00	54.8	4.20	0.05	0.02
Pyrrhotite median values - 90OC13 (N=7)	29	529.8	137.1	0.07	55.2	0.03	0.01	0.00	0.6	1.15	2.12	0.04
DPn/Po - 90OC13	607	0.0	0.0		1.0				97.8	3.64	0.02	0.44
Pentlandite median values - 900MZS1-3 (N=2)	11481	145.5	0.9	0.17	49.5	0.02	0.04	0.00	131.7	15.69	0.07	0.01
Pyrrhotite median values - 900MZS1-3 (N=6)	14	7.9	0.3	0.07	51.5	0.37	0.53	1.32	0.02	1.28	0.06	0.01
DPn/Po - 900MZS1-3	830	18.5	2.8		1.0	0.07	0.08	0.00	8383.8	12.28	1.22	

ANNEXE 8 – Cont.

<i>Pentlandite and Pyrrhotite (DPn/Po)</i>	Sn	Sb	Te	Re	Os	Ir	Pt	Au	Tl	Pb	Bi
	ppm	ppm	ppm	ppm	ppm	ppm	ppm	ppm	ppm	ppm	ppm
Pentlandite median values - 90OMZS2-3 (N=6)	0.47	0.07	1.24	0.06	0.02	0.01	0.27	0.01	0.55	22.63	0.40
Pyrrhotite median values - 90OMZS2-3 (N=6)	0.11	0.05	0.95	0.10	0.02	0.02	0.05	0.01	0.00	1.20	0.11
DPn/Po - 90OMZS2-3	4.18		1.31	0.58		0.54	5.78			18.81	3.77
Pentlandite median values - NR-6 (N=3)	0.05	0.05	0.27	0.06	0.02	0.00	1.20	0.02	0.65	89.21	0.90
Pyrrhotite median values - NR-6 (N=4)	0.05	0.05	0.26	0.11	0.02	0.03	0.21	0.01	0.00	2.54	0.31
DPn/Po - NR-6				0.54			5.84			35.08	2.85
Pentlandite median values - NR-8 (N=4)	0.09	0.05	2.17	0.48	0.62	1.67	27.33	0.04	0.50	32.32	0.89
Pyrrhotite median values - NR-8 (N=3)	0.05	0.05	0.39	0.01	0.02	0.00	0.01	0.01	0.00	2.72	0.34
DPn/Po - NR-8			5.53							11.89	2.65
Pentlandite median values - NR-18 (N=4)	0.11	0.05	8.43	0.01	0.02	0.00	0.17	0.01	0.93	5.80	0.65
Pyrrhotite median values -NR-18 (N=1)	0.05	0.05	8.73	0.01	0.02	0.00	0.31	0.02	0.60	3.80	6.11
DPn/Po - NR-18			0.97				0.54		1.53	1.52	0.11
Pentlandite median values - NR-17 (N=8)	0.10	0.05	5.18	0.01	0.02	0.00	0.11	0.66	0.75	25.58	0.06
Pyrrhotite median values - NR-17 (N=5)	0.26	0.05	4.36	0.01	0.02	0.00	0.03	0.01	0.03	68.56	1.37
DPn/Po - NR-17	0.40		1.19				4.39	66.28	21.50	0.37	0.04
Pentlandite median values - 90OC13 (N=7)	0.25	0.05	5.18	0.01	0.02	0.00	0.01	0.01	0.58	21.95	0.17
Pyrrhotite median values - 90OC13 (N=7)	0.33	0.05	2.95	0.01	0.02	0.00	0.07	0.01	0.04	120.92	0.15
DPn/Po - 90OC13	0.76		1.75				0.21		12.91	0.18	1.18
Pentlandite median values - 90OMZS1-3 (N=2)	0.23	0.05	5.03	0.01	0.02	0.00	0.18	0.01	4.49	249.57	0.67
Pyrrhotite median values - 90OMZS1-3 (N=6)	0.05	0.05	1.17	0.27	0.15	0.20	0.01	0.01	0.01	3.86	0.11
DPn/Po - 90OMZS1-3			4.32		0.11				300.37	64.69	6.27

ANNEXE 8 – Cont.

<i>Pentlandite and Pyrrhotite (DPn/Po)</i>	Co	Cu	Zn	As	Se	Mo	Ru	Rh	Pd	Ag	Cd	In
	ppm	ppm	ppm	ppm	ppm	ppm	ppm	ppm	ppm	ppm	ppm	ppm
Pentlandite median values - NR-10 (N=3)	9257	1.4	0.4	0.14	94.1	1.99	5.73	14.81	625.2	0.76	0.04	0.01
Pyrrhotite median values - NR-10 (N=6)	534	1.0	0.2	0.18	105.7	0.55	4.73	16.69	0.6	2.85	0.04	0.01
DPn/Po - NR-10	17	1.4	1.9	0.77	0.9	3.62	1.21	0.89	1024.4	0.26		
Pentlandite median values - 900MZS2-2 (N=3)	11331	8.1	0.4	0.27	45.6	0.10	0.18	0.02	108.1	2.64	0.04	0.01
Pyrrhotite median values - 900MZS2-2 (N=7)	22	4.9	0.6	0.07	54.6	0.37	0.27	0.97	0.02	0.38	0.04	0.01
DPn/Po - 900MZS2-2	508	1.7	0.6		0.8	0.26	0.65	0.02	5069.0	6.95		
Pentlandite median values - NR-13 (N=6)	12536	4548.6	286.5	0.14	27.1	0.23	0.24	0.16	46.4	12.18	2.28	0.15
Pyrrhotite median values - NR-13 (N=6)	79	0.8	0.3	0.07	33.3	0.46	0.21	0.86	0.01	0.31	0.04	0.01
DPn/Po - NR-13	159	6031.1	1121		0.8	0.50	1.19	0.19		39.07		
Pentlandite median values - NR-14 (N=5)	17029	328.9	30.9	0.18	39.4	0.32	0.31	0.51	63.4	2.18	0.19	0.03
Pyrrhotite median values - NR-14 (N=7)	70	1.4	0.3	0.07	43.4	0.39	0.19	1.04	0.01	0.31	0.04	0.01
DPn/Po - NR-14	242	236.6	99.3		0.9	0.80	1.60	0.49		7.01		
Pentlandite median values - NR-11 (N=6)	6289	1.7	0.4	0.39	81.4	2.65	1.19	7.74	734.2	2.64	0.04	0.01
Pyrrhotite median values - NR-11 (N=6)	343	0.9	0.2	0.84	94.9	3.59	1.25	6.68	1.7	2.58	0.04	0.01
DPn/Po - NR-11	18	1.9	2.0	0.46	0.9	0.74	0.95	1.16	438.1	1.02		
DPn/Po median values	129	1.8	1.9	0.86	0.9	0.62	1.19	0.26	438.1	4.29	0.71	0.28
DPn/Po min	17	0.0	0.0	0.46	0.8	0.07	0.08	0.00	43.3	0.06	0.01	0.16
DPn/Po max	830	6031.1	1121	1.59	1.5	3.62	1.60	1.16	8383.8	39.07	1.22	0.44

ANNEXE 8 – Cont.

<i>Pentlandite and Pyrrhotite (DPn/Po)</i>	Sn	Sb	Te	Re	Os	Ir	Pt	Au	Tl	Pb	Bi
	ppm	ppm	ppm	ppm	ppm	ppm	ppm	ppm	ppm	ppm	ppm
Pentlandite median values - NR-10 (N=3)	0.05	0.05	9.93	0.20	1.15	2.23	15.60	0.01	0.34	6.87	0.06
Pyrrhotite median values - NR-10 (N=6)	0.05	0.05	11.70	0.16	0.89	1.89	0.59	0.01	0.00	0.06	0.09
DPn/Po - NR-10			0.85	1.23	1.30	1.18	26.62			119.81	0.61
Pentlandite median values - 900MZS2-2 (N=3)	0.05	0.05	1.47	0.01	0.02	0.00	0.06	0.01	0.16	7.13	0.04
Pyrrhotite median values - 900MZS2-2 (N=7)	0.05	0.05	1.03	0.17	0.07	0.10	0.10	0.01	0.00	2.57	0.07
DPn/Po - 900MZS2-2			1.43				0.65		32.65	2.77	0.56
Pentlandite median values - NR-13 (N=6)	0.20	0.05	0.77	0.12	0.02	0.04	2.64	0.01	0.14	24.99	0.28
Pyrrhotite median values - NR-13 (N=6)	0.05	0.05	0.80	0.21	0.06	0.09	0.05	0.01	0.00	1.04	0.08
DPn/Po - NR-13			0.96	0.57		0.40	50.74			24.01	3.60
Pentlandite median values - NR-14 (N=5)	0.07	0.05	0.62	0.14	0.06	0.05	1.74	0.01	0.12	8.76	0.21
Pyrrhotite median values - NR-14 (N=7)	0.05	0.05	0.84	0.16	0.06	0.07	0.10	0.01	0.00	0.64	0.12
DPn/Po - NR-14			0.74	0.89	0.98	0.73	17.51			13.78	1.81
Pentlandite median values - NR-11 (N=6)	0.07	0.05	3.50	0.16	0.22	0.54	0.64	0.03	1.35	2.65	0.29
Pyrrhotite median values - NR-11 (N=6)	0.05	0.05	3.97	0.19	0.33	0.66	0.37	0.02	0.02	16.86	1.33
DPn/Po - NR-11	1.41		0.88	0.85	0.68	0.82	1.72	1.20	69.93	0.16	0.22
DPn/Po median values	1.08		1.19	0.47	0.83	0.73	5.08	33.74	27.08	12.83	1.50
DPn/Po min	0.40		0.74	0.35	0.11	0.40	0.21	1.20	1.53	0.16	0.04
DPn/Po max	4.18		5.53	1.23	1.30	1.18	50.74	66.28	300.37	119.81	6.27

ANNEXE 8 – Cont.

<i>Pentlandite and Chalcopyrite (DPn/Ccp)</i>	Co	Cu	Zn	As	Se	Mo	Ru	Rh	Pd	Ag	Cd	In
	ppm	ppm	ppm	ppm	ppm	ppm	ppm	ppm	ppm	ppm	ppm	ppm
Pentlandite median values - 90OMZS2-3 (N=6)	14505	3.7	0.81	52.9	0.26	0.01	0.06	28.5	6.46	0.09	0.02	0.47
Chalcopyrite median values - 90OMZS2-3 (N=7)	0.8	438.2	0.47	53.3	0.02	0.06	n.r.	0.01	3.37	6.66	1.62	2.43
DPn/Ccp - 90OMZS2-3	17209	0.01	1.73	0.99					1.92	0.01	0.01	0.19
Pentlandite median values - NR-6 (N=3)	14978	127.0	0.07	29.6	0.10	0.17	0.05	45.9	3.32	0.04	0.01	0.05
Chalcopyrite median values - NR-6 (N=4)	4.1	497.5	0.07	27.9	0.02	0.18	n.r.	0.11	2.44	10.65	0.63	0.10
DPn/Ccp - NR-6	3646	0.26		1.06		0.96		424.8	1.36		0.01	
Pentlandite median values - NR-8 (N=4)	5864	0.2	0.57	56.5	0.02	2.84	16.96	1883.6	0.78	0.06	0.01	0.09
Chalcopyrite median values - NR-8 (N=5)	0.6	626.9	0.07	41.5	0.02	0.18	n.r.	0.07	17.56	7.97	1.68	2.37
DPn/Ccp - NR-8	9176		8.78	1.36		15.91		26498.0	0.04	0.01		0.04
Pentlandite median values - 90MC15 (N=5)	4370	3.2	1.16	123.4	1.40	0.21	1.80	732.6	33.54	0.45	0.01	0.07
Chalcopyrite median values - 90MC15 (N=6)	0.0	79.1	0.16	133.6	0.08	0.08	n.r.	0.74	10.95	3.82	1.36	0.05
DPn/Ccp - 90MC15	358984	0.04	7.30	0.92	17.36	2.54		985.8	3.06	0.12	0.01	
Pentlandite median values - 90MC5 (N=6)	3606	1.8	0.14	169.3	0.12	0.14	0.01	1007.4	34.25	1.05	0.01	0.06
Chalcopyrite median values - 90MC5 (N=6)	0.1	91.0	0.07	172.4	0.05	0.10	n.r.	4.30	10.83	5.86	0.52	0.05
DPn/Ccp - 90MC5	53865	0.02		0.98	2.21	1.32		234.3	3.16	0.18		
Pentlandite median values - NR-18 (N=4)	6019	13.8	0.07	72.1	0.02	0.35	0.00	341.4	1.00	0.16	0.06	0.11
Chalcopyrite median values - NR-18 (N=4)	0.2	384.5	0.07	73.5	0.02	0.14	n.r.	2.21	6.64	21.51	3.17	1.80
DPn/Ccp - NR-18	37674	0.04	1.00	0.98		2.54		154.2	0.15	0.01	0.02	0.06
Pentlandite median values - NR-17 (N=8)	10102	0.5	0.24	85.6	0.02	0.14	0.00	502.4	4.02	0.04	0.01	0.10
Chalcopyrite median values - NR-17 (N=7)	0.6	459.2	0.07	88.9	0.02	0.10	n.r.	0.54	8.79	37.73	3.66	4.63
DPn/Ccp - NR-17	17944	0.00		0.96		1.35		933.0	0.46		0.00	0.02
Pentlandite median values - 90OMZ67-5-1 (N=3)	10256	4.1	1.24	114.0	0.13	0.08	0.00	3.2	14.65	0.10	0.01	1.92
Chalcopyrite median values - 90OMZ67-5-1 (N=4)	0.2	345.4	0.14	89.3	0.06	0.09	n.r.	0.01	18.26	23.80	4.01	20.84
DPn/Ccp - 90OMZ67-5-1	53842	0.01	8.74	1.28	2.26	0.86			0.80	0.00		0.09

ANNEXE 8 – Cont.

<i>Pentlandite and Chalcopyrite (DPn/Ccp)</i>	Sn	Sb	Te	Re	Os	Ir	Pt	Au	Tl	Pb	Bi
	ppm	ppm	ppm	ppm	ppm	ppm	ppm	ppm	ppm	ppm	ppm
Pentlandite median values - 90OMZS2-3 (N=6)	0.07	1.24	0.09	0.02	0.01	0.27	0.01	0.55	22.63	0.40	
Chalcopyrite median values - 90OMZS2-3 (N=7)	0.05	1.70	0.01	0.02	0.00	0.01	0.01	0.03	19.87	0.06	
DPn/Ccp - 90OMZS2-3		0.73				20.31		19.39	1.14	6.22	
Pentlandite median values - NR-6 (N=3)	0.05	0.27	0.09	0.02	0.00	1.20	0.02	0.65	89.21	0.90	
Chalcopyrite median values - NR-6 (N=4)	0.05	0.44	0.01	0.02	0.00	0.07	0.01	0.01	12.96	0.10	
DPn/Ccp - NR-6		0.60				17.75		72.90	6.88	8.79	
Pentlandite median values - NR-8 (N=4)	0.05	2.17	0.73	0.41	1.7	27.33	0.04	0.50	32.32	0.89	
Chalcopyrite median values - NR-8 (N=5)	0.05	1.90	0.01	0.02	0.00	0.06	0.01	0.16	8.70	0.14	
DPn/Ccp - NR-8		1.15				433.94		3.21	3.71	6.27	
Pentlandite median values - 90MC15 (N=5)	0.05	35.88	0.25	0.02	0.00	1.99	0.01	0.34	7.75	1.07	
Chalcopyrite median values - 90MC15 (N=6)	0.05	39.45	0.01	0.02	0.00	0.03	0.01	1.04	1.17	0.00	
DPn/Ccp - 90MC15		0.91				63.99		0.32	6.61	242.31	
Pentlandite median values - 90MC5 (N=6)	0.05	64.70	0.02	0.02	0.00	3.99	0.01	0.37	8.35	0.22	
Chalcopyrite median values - 90MC5 (N=6)	0.05	63.89	0.01	0.02	0.00	0.04	0.01	0.78	0.28	0.00	
DPn/Ccp - 90MC5		1.01				100.44		0.47	29.99		
Pentlandite median values - NR-18 (N=4)	0.05	8.43	0.01	0.02	0.00	0.17	0.01	0.93	5.80	0.65	
Chalcopyrite median values - NR-18 (N=4)	0.05	8.23	0.01	0.02	0.00	0.16	0.01	0.14	0.37	0.75	
DPn/Ccp - NR-18		1.02				1.05		6.42	15.68	0.86	
Pentlandite median values - NR-17 (N=8)	0.05	5.18	0.01	0.02	0.00	0.11	0.66	0.75	25.58	0.06	
Chalcopyrite median values - NR-17 (N=7)	0.05	12.45	0.01	0.02	0.00	0.32	0.06	0.11	22.40	0.35	
DPn/Ccp - NR-17		0.42				0.36	11.74	6.83	1.14	0.16	
Pentlandite median values - 90OMZ67-5-1 (N=3)	0.07	16.83	0.01	0.02	0.00	0.01	0.01	0.89	32.56	1.34	
Chalcopyrite median values - 90OMZ67-5-1 (N=4)	0.05	14.03	0.01	0.02	0.00	0.01	0.01	0.12	174.06	0.02	
DPn/Ccp - 90OMZ67-5-1		1.20						7.72	0.19	61.66	

ANNEXE 8 – Cont.

<i>Pentlandite and Chalcopyrite (DPn/Ccp)</i>	Co	Cu	Zn	As	Se	Mo	Ru	Rh	Pd	Ag	Cd	In
	ppm	ppm	ppm	ppm	ppm	ppm	ppm	ppm	ppm	ppm	ppm	ppm
Pentlandite median values - 90OC13 (N=7)	17778	1.3	0.14	57.3	0.02	0.13	0.00	54.8	4.20	0.05	0.02	0.25
Chalcopyrite median values - 90OC13 (N=7)	0.2	489.9	0.07	60.7	0.02	0.09	n.r.	0.01	6.79	15.70	4.49	2.01
DPn/Ccp - 90OC13	82284	0.00		0.94		1.50			0.62	0.00	0.00	0.12
Pentlandite median values - 90OMZS1-3 (N=2)	11481	0.9	0.17	49.5	0.02	0.04	0.00	131.7	15.69	0.07	0.01	0.23
Chalcopyrite median values - 90OMZS1-3 (N=7)	0.1	181.4	0.07	67.0	0.02	0.07	n.r.	0.01	4.25	8.95	2.98	0.05
DPn/Ccp - 90OMZS1-3	119016	0.01		0.74		0.60			3.69	0.01		
Pentlandite median values - NR-10 (N=3)	9257	0.4	0.14	94.1	1.99	5.73	14.81	625.2	0.76	0.04	0.01	0.05
Chalcopyrite median values - NR-10 (N=3)	0.8	3316.9	0.07	82.5	0.02	0.11	n.r.	0.01	2.50	3.01	1.46	0.10
DPn/Ccp - NR-10	11225	0.00		1.14		52.37			0.30			
Pentlandite median values - 90OMZS2-2 (N=3)	11331	0.4	0.27	45.6	0.10	0.18	0.02	108.1	2.64	0.04	0.01	0.05
Chalcopyrite median values - 90OMZS2-2 (N=7)	0.1	374.3	0.07	54.7	0.02	0.09	n.r.	0.01	2.31	12.39	2.31	0.91
DPn/Ccp - 90OMZS2-2	112836	0.00		0.83		2.08			1.14			
Pentlandite median values - NR-13 (N=6)	12536	286.5	0.14	27.1	0.23	0.24	0.16	46.4	12.18	2.28	0.15	0.20
Chalcopyrite median values - NR-13 (N=7)	0.6	736.4	0.07	29.4	0.02	0.13	n.r.	0.01	0.73	6.28	1.31	2.35
DPn/Ccp - NR-13	19432	0.39		0.92		1.93			16.57	0.36	0.11	0.08
Pentlandite median values - NR-14 (N=5)	17029	30.9	0.18	39.4	0.32	0.31	0.51	63.4	2.18	0.19	0.03	0.07
Chalcopyrite median values - NR-14 (N=6)	0.4	515.8	0.07	38.0	0.02	0.12	n.r.	0.01	1.14	7.38	1.48	1.78
DPn/Ccp - NR-14	39689	0.06		1.04		2.63			1.92	0.03	0.02	0.04
Pentlandite median values - NR-11 (N=6)	6289	0.4	0.39	81.4	2.65	1.19	7.74	734.2	2.64	0.04	0.01	0.07
Chalcopyrite median values - NR-11 (N=4)	0.1	377.3	0.07	83.4	0.02	0.10	n.r.	0.06	28.68	3.96	1.49	0.34
DPn/Ccp - NR-11	45422	0.00		0.98		11.37		12691	0.09			0.21
DPn/Ccp median values	39689	0.01	7.30	0.98	2.26	2.00		933	1.14	0.01	0.01	0.08
DPn/Ccp min	3646	0.00	1.00	0.74	2.21	0.60		154.2	0.04	0.00	0.00	0.02
DPn/Ccp max	358984	0.39	8.78	1.36	17.36	52.37		26498	16.57	0.36	0.11	0.21

ANNEXE 8 – Cont.

<i>Pentlandite and Chalcopyrite (DPn/Ccp)</i>	Sn	Sb	Te	Re	Os	Ir	Pt	Au	Tl	Pb	Bi
	ppm	ppm	ppm	ppm	ppm	ppm	ppm	ppm	ppm	ppm	ppm
Pentlandite median values - 90OC13 (N=7)	0.05	5.18	0.01	0.02	0.00	0.01	0.01	0.58	21.95	0.17	
Chalcopyrite median values - 90OC13 (N=7)	0.05	11.78	0.01	0.02	0.00	0.08	0.01	0.09	90.38	0.14	
DPn/Ccp - 90OC13		0.44				0.17		6.57	0.24	1.21	
Pentlandite median values - 90OMZS1-3 (N=2)	0.05	5.03	0.01	0.02	0.00	0.18	0.01	4.49	249.57	0.67	
Chalcopyrite median values - 90OMZS1-3 (N=7)	0.05	8.03	0.01	0.02	0.00	0.12	0.06	0.03	195.06	0.05	
DPn/Ccp - 90OMZS1-3		0.63				1.48		135.47	1.28	12.43	
Pentlandite median values - NR-10 (N=3)	0.05	9.93	0.30	0.76	2.2	15.60	0.01	0.34	6.87	0.06	
Chalcopyrite median values - NR-10 (N=3)	0.05	16.43	0.01	0.02	0.01	0.68	0.03	0.00	7.82	0.03	
DPn/Ccp - NR-10		0.60			332.7	22.88			0.88	1.72	
Pentlandite median values - 90OMZS2-2 (N=3)	0.05	1.47	0.01	0.02	0.00	0.06	0.01	0.16	7.13	0.04	
Chalcopyrite median values - 90OMZS2-2 (N=7)	0.05	2.58	0.01	0.02	0.00	0.03	0.01	0.01	71.21	0.02	
DPn/Ccp - 90OMZS2-2		0.57				1.91		21.40	0.10	2.39	
Pentlandite median values - NR-13 (N=6)	0.05	0.77	0.19	0.02	0.04	2.64	0.01	0.14	24.99	0.28	
Chalcopyrite median values - NR-13 (N=7)	0.05	0.94	0.01	0.02	0.00	0.13	0.01	0.01	28.19	0.07	
DPn/Ccp - NR-13		0.82				20.91		18.05	0.89	3.82	
Pentlandite median values - NR-14 (N=5)	0.05	0.62	0.21	0.04	0.05	1.74	0.01	0.12	8.76	0.21	
Chalcopyrite median values - NR-14 (N=6)	0.05	1.08	0.01	0.02	0.00	0.12	0.01	0.08	28.32	0.10	
DPn/Ccp - NR-14		0.58				14.62		1.56	0.31	2.22	
Pentlandite median values - NR-11 (N=6)	0.05	3.50	0.24	0.15	0.54	0.64	0.03	1.35	2.65	0.29	
Chalcopyrite median values - NR-11 (N=4)	0.05	9.36	0.01	0.02	0.00	0.33	0.01	0.12	17.88	0.14	
DPn/Ccp - NR-11		0.37				1.93		11.39	0.15	2.01	
DPn/Ccp median values		0.63			332.67	16.19	11.74	7.27	1.14	3.11	
DPn/Ccp min		0.37			332.67	0.17	11.74	0.32	0.10	0.16	
DPn/Ccp max		1.20			332.67	433.94	11.74	135.47	29.99	242.31	

ANNEXE 8 – Cont.

<i>Chalcopyrite and Pyrrhotite (DCcp/Po)</i>	Co	Cu	Zn	As	Se	Mo	Ru	Rh	Pd	Ag	Cd	In
	ppm	ppm	ppm	ppm	ppm	ppm	ppm	ppm	ppm	ppm	ppm	ppm
Chalcopyrite median values - 90OMZS2-3 (N=7)	0.8	39	438.2	0.47	53.3	0.02	0.06	n.r.	0.01	3.37	6.66	1.62
Pyrrhotite median values - 90OMZS2-3 (N=6)	31.6	3145	0.2	0.07	56.4	0.34	0.01	0.19	0.01	0.52	0.09	0.01
DCcp/Po - 90OMZS2-3	0.03	0.01			0.94					6.44	76.60	
Chalcopyrite median values - 90OKMZ5 (N=5)	0.5	52	399.9	0.07	60.9	0.06	0.10	n.r.	0.01	12.81	3.65	0.49
Pyrrhotite median values - 90KMZ5 (N=6)	398.9	17172	0.2	0.07	69.6	1.38	0.53	3.78	1.83	1.34	0.04	0.01
DCcp/Po - 90OKMZ5	0.00	0.00			0.87	0.04	0.20			9.54		
Chalcopyrite median values - NR-6 (N=4)	4.1	346	497.5	0.07	27.9	0.02	0.18	n.r.	0.11	2.44	10.65	0.63
Pyrrhotite median values - NR-6 (N=4)	393.0	12634	0.2	0.07	34.2	0.22	0.13	0.43	1.06	0.67	0.04	0.01
DCcp/Po - NR-6	0.01	0.03			0.82		1.42		0.10	3.63		
Chalcopyrite median values - NR-8 (N=5)	0.6	38	626.9	0.07	41.5	0.02	0.18	n.r.	0.07	17.56	7.97	1.68
Pyrrhotite median values - NR-8 (N=3)	99.7	8913	1.4	0.60	38.0	0.12	0.01	0.00	0.37	0.90	0.09	0.01
DCcp/Po - NR-8	0.01	0.00	437.26		1.09				0.19	19.43	91.64	
Chalcopyrite median values - NR-18 (N=4)	0.2	36	384.5	0.07	73.5	0.02	0.14	n.r.	2.21	6.64	21.51	3.17
Pyrrhotite median values - NR-18 (N=1)	67.9	8228	274.3	0.07	92.2	0.02	0.01	0.00	6.31	16.21	12.47	0.23
DCcp/Po - NR-18	0.00	0.00	1.40		0.80				0.35	0.41	1.73	13.77
Chalcopyrite median values - NR-17 (N=7)	0.6	61	459.2	0.07	88.9	0.02	0.10	n.r.	0.54	8.79	37.73	3.66
Pyrrhotite median values - NR-17 (N=5)	103.2	2749	84.8	0.15	97.9	0.02	0.01	0.00	2.44	5.17	3.80	0.05
DCcp/Po - NR-17	0.01	0.02	5.42		0.91				0.22	1.70	9.92	73.00
Chalcopyrite median values - 90OC13 (N=7)	0.2	16	489.9	0.07	60.7	0.02	0.09	n.r.	0.01	6.79	15.70	4.49
Pyrrhotite median values - 90OC13 (N=7)	29.3	1988	137.1	0.07	55.2	0.03	0.01	0.00	0.56	1.15	2.12	0.04
DCcp/Po - 90OC13	0.01	0.01	3.57		1.10					5.88	7.41	102.27
Chalcopyrite median values - 90OMZS1-3 (N=7)	0.1	5	181.4	0.07	67.0	0.02	0.07	n.r.	0.01	4.25	8.95	2.98
Pyrrhotite median values - 90OMZS1-3 (N=6)	13.8	581	0.3	0.07	51.5	0.37	0.53	1.32	0.02	1.28	0.06	0.01
DCcp/Po - 90OMZS1-3	0.01	0.01	533.89		1.30		0.14			3.33	152.69	

ANNEXE 8 – Cont.

<i>Chalcopyrite and Pyrrhotite (DCcp/Po)</i>	Sn	Sb	Te	Re	Os	Ir	Pt	Au	Tl	Pb	Bi
	ppm	ppm	ppm	ppm	ppm	ppm	ppm	ppm	ppm	ppm	ppm
Chalcopyrite median values - 90OMZS2-3 (N=7)	2.43	0.05	1.70	0.01	0.02	0.00	0.01	0.01	0.03	19.87	0.06
Pyrrhotite median values - 90OMZS2-3 (N=6)	0.11	0.05	0.95	0.10	0.02	0.02	0.05	0.01	0.00	1.20	0.11
DCcp/Po - 90OMZS2-3	21.43		1.80				0.28			16.52	0.61
Chalcopyrite median values - 90OKMZ5 (N=5)	1.54	0.05	2.01	0.16	0.02	0.00	0.46	0.01	0.09	2.23	0.18
Pyrrhotite median values - 90OKMZ5 (N=6)	0.05	0.05	1.60	0.34	0.21	0.43	0.27	0.01	0.00	0.17	0.16
DCcp/Po - 90OKMZ5			1.25	0.48			1.72			13.24	1.07
Chalcopyrite median values - NR-6 (N=4)	0.10	0.05	0.44	0.01	0.02	0.00	0.07	0.01	0.01	12.96	0.10
Pyrrhotite median values - NR-6 (N=4)	0.05	0.05	0.26	0.11	0.02	0.03	0.21	0.01	0.00	2.54	0.31
DCcp/Po - NR-6							0.33			5.10	0.32
Chalcopyrite median values - NR-8 (N=5)	2.37	0.05	1.90	0.01	0.02	0.00	0.06	0.01	0.16	8.70	0.14
Pyrrhotite median values - NR-8 (N=3)	0.05	0.05	0.39	0.01	0.02	0.00	0.01	0.01	0.00	2.72	0.34
DCcp/Po - NR-8			4.83							3.20	0.42
Chalcopyrite median values - NR-18 (N=4)	1.80	0.05	8.23	0.01	0.02	0.00	0.16	0.01	0.14	0.37	0.75
Pyrrhotite median values - NR-18 (N=1)	0.05	0.05	8.73	0.01	0.02	0.00	0.31	0.02	0.60	3.80	6.11
DCcp/Po - NR-18			0.94				0.52	0.54	0.24	0.10	0.12
Chalcopyrite median values - NR-17 (N=7)	4.63	0.05	12.45	0.01	0.02	0.00	0.32	0.06	0.11	22.40	0.35
Pyrrhotite median values - NR-17 (N=5)	0.26	0.05	4.36	0.01	0.02	0.00	0.03	0.01	0.03	68.56	1.37
DCcp/Po - NR-17	17.68		2.85				12.09	5.64	3.15	0.33	0.26
Chalcopyrite median values - 90OC13 (N=7)	2.01	0.05	11.78	0.01	0.02	0.00	0.08	0.01	0.09	90.38	0.14
Pyrrhotite median values - 90OC13 (N=7)	0.33	0.05	2.95	0.01	0.02	0.00	0.07	0.01	0.04	120.92	0.15
DCcp/Po - 90OC13	6.09		3.99				1.18		1.97	0.75	0.98
Chalcopyrite median values - 90OMZS1-3 (N=7)	0.05	0.05	8.03	0.01	0.02	0.00	0.12	0.06	0.03	195.06	0.05
Pyrrhotite median values - 90OMZS1-3 (N=6)	0.05	0.05	1.17	0.27	0.15	0.20	0.01	0.01	0.01	3.86	0.11
DCcp/Po - 90OMZS1-3			6.89						2.22	50.56	0.50

ANNEXE 8 – Cont.

<i>Chalcopyrite and Pyrrhotite (DCcp/Po)</i>	Co	Cu	Zn	As	Se	Mo	Ru	Rh	Pd	Ag	Cd	In
	ppm	ppm	ppm	ppm	ppm	ppm	ppm	ppm	ppm	ppm	ppm	ppm
Chalcopyrite median values - NR-10 (N=3)	0.8	66	3316.9	0.07	82.5	0.02	0.11	n.r.	0.01	2.50	3.01	1.46
Pyrrhotite median values - NR-10 (N=6)	533.5	24433	0.2	0.18	105.7	0.55	4.73	16.69	0.61	2.85	0.04	0.01
DCcp/Po - NR-10	0.00	0.00	16125.66		0.78		0.02			0.88		
Chalcopyrite median values - 900MZS2-2 (N=7)	0.1	8	374.3	0.07	54.7	0.02	0.09	n.r.	0.01	2.31	12.39	2.31
Pyrrhotite median values - 900MZS2-2 (N=7)	22.3	1814	0.6	0.07	54.6	0.37	0.27	0.97	0.02	0.38	0.04	0.01
DCcp/Po - 900MZS2-2	0.00	0.00	652.71		1.00		0.31			6.07		
Chalcopyrite median values - NR-13 (N=7)	0.6	56	736.4	0.07	29.4	0.02	0.13	n.r.	0.01	0.73	6.28	1.31
Pyrrhotite median values - NR-13 (N=6)	78.8	5158	0.3	0.07	33.3	0.46	0.21	0.86	0.01	0.31	0.04	0.01
DCcp/Po - NR-13	0.01	0.01	2881.62		0.88		0.62			2.36		
Chalcopyrite median values - NR-14 (N=6)	0.4	59	515.8	0.07	38.0	0.02	0.12	n.r.	0.01	1.14	7.38	1.48
Pyrrhotite median values - NR-14 (N=7)	70.2	6445	0.3	0.07	43.4	0.39	0.19	1.04	0.01	0.31	0.04	0.01
DCcp/Po - NR-14	0.01	0.01	1655.02		0.88		0.61			3.65		
Chalcopyrite median values - NR-11 (N=4)	0.1	20	377.3	0.07	83.4	0.02	0.10	n.r.	0.06	28.68	3.96	1.49
Pyrrhotite median values - NR-11 (N=6)	343.4	32100	0.2	0.84	94.9	3.59	1.25	6.68	1.68	2.58	0.04	0.01
DCcp/Po - NR-11	0.00	0.00	1921.83		0.88		0.08		0.03	11.11		
DCcp/Po median values	0.01	0.01	593.3		0.88	0.04	0.26		0.19	3.65	43.26	73.00
DCcp/Po min	0.00	0.00	1.4		0.78	0.04	0.02		0.03	0.41	1.73	13.77
DCcp/Po max	0.03	0.03	16125.7		1.30	0.04	1.42		0.35	19.43	152.69	102.27

ANNEXE 8 – Cont.

<i>Chalcopyrite and Pyrrhotite (DCcp/Po)</i>	Sn	Sb	Te	Re	Os	Ir	Pt	Au	Tl	Pb	Bi
	ppm	ppm	ppm	ppm	ppm	ppm	ppm	ppm	ppm	ppm	ppm
Chalcopyrite median values - NR-10 (N=3)	0.10	0.05	16.43	0.01	0.02	0.01	0.68	0.03	0.00	7.82	0.03
Pyrrhotite median values - NR-10 (N=6)	0.05	0.05	11.70	0.16	0.89	1.89	0.59	0.01	0.00	0.06	0.09
DCcp/Po - NR-10			1.40			0.00	1.16	3.18		136.38	0.36
Chalcopyrite median values - 90OMZS2-2 (N=7)	0.91	0.05	2.58	0.01	0.02	0.00	0.03	0.01	0.01	71.21	0.02
Pyrrhotite median values - 90OMZS2-2 (N=7)	0.05	0.05	1.03	0.17	0.07	0.10	0.10	0.01	0.00	2.57	0.07
DCcp/Po - 90OMZS2-2			2.51				0.34		1.53	27.66	0.24
Chalcopyrite median values - NR-13 (N=7)	2.35	0.05	0.94	0.01	0.02	0.00	0.13	0.01	0.01	28.19	0.07
Pyrrhotite median values - NR-13 (N=6)	0.05	0.05	0.80	0.21	0.06	0.09	0.05	0.01	0.00	1.04	0.08
DCcp/Po - NR-13			1.16				2.43			27.09	0.94
Chalcopyrite median values - NR-14 (N=6)	1.78	0.05	1.08	0.01	0.02	0.00	0.12	0.01	0.08	28.32	0.10
Pyrrhotite median values - NR-14 (N=7)	0.05	0.05	0.84	0.16	0.06	0.07	0.10	0.01	0.00	0.64	0.12
DCcp/Po - NR-14			1.28				1.20			44.54	0.81
Chalcopyrite median values - NR-11 (N=4)	0.34	0.05	9.36	0.01	0.02	0.00	0.33	0.01	0.12	17.88	0.14
Pyrrhotite median values - NR-11 (N=6)	0.05	0.05	3.97	0.19	0.33	0.66	0.37	0.02	0.02	16.86	1.33
DCcp/Po - NR-11	6.82		2.36				0.89		6.14	1.06	0.11
DCcp/Po median values	12.25		2.08	0.31		0.00	1.16	3.18	2.09	13.24	0.42
DCcp/Po min	6.09		0.94	0.31		0.00	0.28	0.54	0.24	0.10	0.11
DCcp/Po max	21.43		6.89	0.48		0.00	12.09	5.64	6.14	136.38	1.07

ANNEXE 8 – Cont.

<i>Chalcopyrite and Cubanite (DCcp/Cbn)</i>	Co	Cu	Zn	As	Se	Mo	Ru	Rh	Pd	Ag	Cd	In
	ppm	ppm	ppm	ppm	ppm	ppm	ppm	ppm	ppm	ppm	ppm	ppm
Chalcopyrite median values - 90MC15 (N=6)	0.01	49	79.1	0.16	133.6	0.08	0.08	n.r.	0.74	10.95	3.82	1.36
Cubanite median values - 90MC15 (N=6)	0.15	32	248.5	0.21	142.6	0.10	0.06	n.r.	0.93	36.69	12.06	1.52
DCcp/Cbn - 90MC15	0.08	1.5	0.32	0.74	0.94	0.83	1.32		0.80	0.30	0.32	0.89
Chalcopyrite median values - 90OMZS1-3 (N=7)	0.10	5	181.4	0.07	67.0	0.02	0.07	n.r.	0.01	4.25	8.95	2.98
Cubanite median values - 90OMZS1-3 (N=8)	7.92	167	31.9	0.07	70.5	0.02	0.05	n.r.	0.05	10.21	1.38	0.36
DCcp/Cbn - 90OMZS1-3	0.01	0.03	5.69		0.95		1.38			0.42	6.46	8.27
Chalcopyrite median values - 90OMZS2-2 (N=7)	0.10	8	374.3	0.07	54.7	0.02	0.09	n.r.	0.01	2.31	12.39	2.31
Cubanite median values - 90OMZS2-2 (N=1)	5.35	198	366.2	0.07	52.6	0.02	0.10	n.r.	0.01	21.11	25.68	2.23
DCcp/Cbn - 90OMZS2-2	0.02	0.04	1.02		1.04		0.87			0.11	0.48	1.04
DCcp/Cbn median values	0.02	0.04	1.02	0.74	0.95	0.83	1.32		0.80	0.30	0.48	1.04
DCcp/Cbn min	0.01	0.03	0.32	0.74	0.94	0.83	0.87		0.80	0.11	0.32	0.89
DCcp/Cbn max	0.08	1.54	5.69	0.74	1.04	0.83	1.38		0.80	0.42	6.46	8.27

ANNEXE 8 – Cont.

<i>Chalcopyrite and Cubanite (DCcp/Cbn)</i>	Sn	Sb	Te	Re	Os	Ir	Pt	Au	Tl	Pb	Bi
	ppm	ppm	ppm	ppm	ppm	ppm	ppm	ppm	ppm	ppm	ppm
Chalcopyrite median values - 90MC15 (N=6)	0.05	0.05	39.45	0.01	0.02	0.00	0.03	0.01	1.04	1.17	0.00
Cubanite median values - 90MC15 (N=6)	0.05	0.05	40.53	0.01	0.02	0.00	0.04	0.01	1.07	1.35	0.00
DCcp/Cbn - 90MC15			0.97				0.87		0.97	0.87	
Chalcopyrite median values - 90OMZS1-3 (N=7)	0.05	0.05	8.03	0.01	0.02	0.00	0.12	0.06	0.03	195.06	0.05
Cubanite median values - 90OMZS1-3 (N=8)	0.05	0.05	5.34	0.01	0.02	0.00	0.08	0.03	0.06	16.11	0.05
DCcp/Cbn - 90OMZS1-3			1.50				1.46	2.25	0.51	12.11	1.12
Chalcopyrite median values - 90OMZS2-2 (N=7)	0.91	0.05	2.58	0.01	0.02	0.00	0.03	0.01	0.01	71.21	0.02
Cubanite median values - 90OMZS2-2 (N=1)	0.74	0.05	2.34	0.01	0.02	0.00	0.01	0.01	0.03	87.20	0.02
DCcp/Cbn - 90OMZS2-2	1.24		1.10						0.27	0.82	0.78
DCcp/Cbn median values	1.24		1.10				1.17	2.25	0.51	0.87	0.95
DCcp/Cbn min	1.24		0.97				0.87	2.25	0.27	0.82	0.78
DCcp/Cbn max	1.24		1.50				1.46	2.25	0.97	12.11	1.12

ANNEXE 9 - Average proportion (%) of each element hosted in pyrrhotite (Po), pentlandite (Pn), chalcopyrite (Ccp), cubanite (Cbn) and sum, from the Cu-poor and Transitional, Cu-rich and Cu-rich (with cubanite) ores of the Noril'sk-Talnakh mining district. The whole-rock data used for the mass balance calculations is reported by Duran et al. (2017) (ANNEXE 2). Abbreviations: BMS= base-metal sulfides; n.r.= not reported; N= number of samples

ANNEXE 9

Ore Type/BMS	Ag	As	Au	Bi	Cd	Co	In	Ir	Mo	Os	Pb	Pd	Pt	Rh	Ru	Sb	Se	Sn	Te	Tl	Zn
Cu-poor and transitional massive sulfides (N= 7)																					
Po	7%	0%	0%	26%	0%	2%	0%	85%	70%	108%	8%	0%	2%	79%	80%	0%	50%	0%	51%	0%	0%
Pn	9%	1%	0%	12%	0%	86%	1%	7%	7%	0%	19%	68%	4%	3%	23%	0%	8%	1%	7%	15%	1%
Ccp	8%	0%	0%	3%	82%	0%	104%	0%	0%	0%	36%	0%	0%	n.r.	17%	0%	14%	14%	21%	1%	78%
Sum	24%	1%	0%	41%	83%	89%	105%	92%	76%	108%	63%	68%	6%	82%	120%	0%	71%	14%	78%	16%	80%
Cu-rich massive sulfide (N= 7)																					
Po	2%	0%	0%	3%	3%	2%	0%	n.r.	2%	n.r.	11%	1%	0%	n.r.	n.r.	0%	18%	0%	5%	1%	6%
Pn	1%	0%	0%	1%	0%	69%	0%	n.r.	1%	n.r.	2%	49%	0%	n.r.	n.r.	0%	5%	0%	5%	3%	0%
Ccp	19%	0%	0%	2%	59%	0%	68%	n.r.	0%	n.r.	19%	1%	1%	n.r.	n.r.	0%	46%	14%	46%	5%	57%
Sum	21%	0%	0%	6%	62%	71%	68%	n.r.	3%	n.r.	33%	51%	1%	n.r.	n.r.	0%	70%	15%	57%	10%	63%
Cu-rich massive sulfide with cubanite (N= 2)																					
Po	1%	0%	0%	1%	0%	0%	0%	n.r.	48%	n.r.	1%	0%	0%	n.r.	n.r.	0%	11%	0%	2%	0%	0%
Pn	10%	1%	0%	3%	0%	91%	0%	n.r.	45%	n.r.	35%	43%	0%	n.r.	n.r.	0%	10%	0%	9%	30%	0%
Ccp	13%	0%	1%	1%	33%	0%	67%	n.r.	3%	n.r.	74%	0%	0%	n.r.	n.r.	0%	50%	0%	53%	30%	22%
Cbn	9%	0%	0%	0%	9%	0%	7%	n.r.	3%	n.r.	5%	0%	0%	n.r.	n.r.	1%	13%	0%	11%	8%	6%
Sum	32%	1%	1%	4%	43%	92%	74%	n.r.	99%	n.r.	114%	43%	1%	n.r.	n.r.	1%	83%	1%	75%	69%	29%

ANNEXE 10 - Analyses of reference materials used to monitor the data quality for whole-rock TABS and Se results from the Marginal Zone of the Bushveld Complex. Normal font certificate or assigned value, italics average of literature values and Mansur et al. (2019) (Chapter 2) for CH-4 and TDB-1, median of GeoPt18 round for KPT-1. Detection limit = $3 \times \sigma$ of the blank; Stdev = standard deviation; RSD= relative standard deviation; n= number of individual analyses

ANNEXE 10

		As	Bi	Sb	Se	Te
		ppm	ppm	ppm	ppm	ppm
Reference material	Detection limit	<i>0.003</i>	<i>0.005</i>	<i>0.005</i>	<i>0.002</i>	<i>0.006</i>
CH-4 Anorthosite CANMET	Certificate value	8.80	0.6	0.77	2.1	<i>0.36</i>
	Stdev	0.60	0.2	0.4	0.2	<i>0.072</i>
	This study	8.34	0.73	0.861	1.942	0.438
	Stdev (n= 4)	0.21	0.14	0.076	0.042	0.032
	Relative stdev	2.55	18.67	8.86	2.15	7.31
TDB-1 Diabase CANMET	Certificate value	2.50	<i>0.063</i>	1	<i>0.38</i>	<i>0.036</i>
	Stdev	0.50	<i>0.0189</i>	0.4	<i>0.032</i>	<i>0.007</i>
	This study	2.01	0.088	0.938	0.372	0.032
	Stdev (n= 4)	0.19	0.008	0.057	0.073	0.005
	Relative stdev	9.44	9.04	6.03	19.55	16.07
GeoPT-18/ KPT-1 Sulfide-bearing dolerite IAG	Assigned value	2.20	0.94	10.10	2.90	<i>0.35</i>
	Stdev	0.26	0.19	1.27	0.46	<i>0.08</i>
	This study	2.28	0.902	11.08	2.93	0.47
	Stdev (n= 4)	0.11	0.095	0.156	0.047	0.046
	Relative stdev	4.85	10.58	1.40	1.62	9.81

ANNEXE 11 - Complete dataset of whole-rock TABS and Se analyses of samples from the Marginal Zone of the Bushveld Complex obtained in this study, and results previously reported by Barnes and Maier (2002) and Barnes et al. (2009; 2010) used for comparison. The TABS and Se values for upper (Hu and Gao 2008) and lower (Rudnick and Gao 2003) continental crust, komatiite and MORB (Arevalo and McDonough 2010) used for comparison are also reported. The geological reference material OKUM is used as a proxy for a komatiite composition (IAGEO). Values in bold are below the detection limit and were replaced by half of the detection limit values. All values in ppm. DL - Detection limit; n.r. - not reported

ANNEXE 11

Sample	Unit	Texture	This study				
			As	Bi	Sb	Se	Te
<i>DL</i>			<i>0.003</i>	<i>0.005</i>	<i>0.005</i>	<i>0.002</i>	<i>0.006</i>
DI-225	B-1	Quenched	1.702	0.043	0.148	0.104	0.020
CD-001		Quenched	2.765	0.058	0.164	0.128	0.013
CD-017		Quenched	3.079	0.097	0.383	0.157	0.033
DI-204		Quenched	0.824	0.026	0.064	0.116	0.016
ECBV-018		Granular	1.720	0.068	0.174	0.111	0.016
ECBV-019		Quenched	1.716	0.051	0.200	0.157	0.024
ECBV-021		Quenched	1.663	0.044	0.157	0.104	0.018
ECBV-049A		Granular	0.127	0.014	0.019	0.122	0.016
ECBV-105		Granular	2.927	0.082	0.222	0.121	0.022
ECBV-106		Quenched	2.490	0.035	0.157	0.103	0.008
ECBV-111		Granular	1.395	0.022	0.322	0.020	0.004
Average B-1			1.855	0.049	0.183	0.113	0.017
Bc-6	B-2	Fine-grained	0.124	0.006	0.003	0.060	0.003
Bc-25		Fine-grained	0.176	0.010	0.008	0.051	0.003
CO-066		Granular	0.070	0.017	0.018	0.051	0.006
CO-253		Granular	0.069	0.017	0.015	0.267	0.018
ECBV-025		Granular	0.032	0.015	0.012	0.102	0.007
ECBV-026		Granular	0.060	0.003	0.032	0.158	0.012
ECBV-058		Granular	0.178	0.017	0.014	0.033	0.010
ECBV-064		Granular	0.354	0.006	0.056	0.035	0.003
Average B-2			0.133	0.011	0.020	0.095	0.008

ANNEXE 11 – Cont.

Sample	Unit	Texture	This study				
			As	Bi	Sb	Se	Te
<i>DL</i>			<i>0.003</i>	<i>0.005</i>	<i>0.005</i>	<i>0.002</i>	<i>0.006</i>
CO-048	B-3	Fine-grained	0.077	0.006	0.032	0.019	0.003
CO-252		Fine-grained	0.030	0.013	0.008	0.011	0.003
ECBV-013		Fine-grained	0.093	0.003	0.028	0.022	0.003
ECBV-063		Fine-grained	0.152	0.013	0.006	0.121	0.008
Average B-3			0.088	0.009	0.019	0.043	0.004
60:40 mixture of B1:B2			1.166	0.034	0.117	0.106	0.013
Upper Continental Crust (UC)			5.700	0.230	0.750	0.083	0.027
Lower Continental Crust (LC)			0.200	0.200	0.100	0.170	0.005
Komatiite (OKUM)			0.450	0.010	0.020	0.210	0.020
MORB			0.18	0.07	0.07	0.11	0.02
Bulk 60% komatiite + 40% Upper Crust			2.388	0.134	0.342	0.099	0.023
AFC 30% UC with komatiite + 27% fractation crystallization			2.483	0.161	0.371	0.140	0.030
AFC 30% LC with komatiite + 27% fractation crystallization			0.255	0.149	0.108	0.175	0.021

ANNEXE 11 – Cont.

		Data from Barnes and Maier (2002) and Barnes et al (2009; 2010)												
Sample	Unit	S	Ni	Cu	Os	Ir	Ru	Rh	Pt	Pd	Hf	La	Sm	Th
DI-225	B-1	619	n.r.	58	n.r.	n.r.	n.r.	n.r.	n.r.	n.r.	n.r.	n.r.	n.r.	n.r.
CD-001		466	241	46	0.00033	0.00049	0.00329	0.0017	0.02165	0.01516	1.91	19.36	2.79	3.38
CD-017		491	408	67	0.00043	0.00074	0.00257	0.00191	0.02502	0.01682	1.29	15.17	2.5	2.5
DI-204		465	300	47	<0.1	0.0002	0.00096	0.00186	0.01458	0.01129	1.34	12.88	2.02	2.59
ECBV-018		360	336	44	0.0011	0.00052	<2	0.002	0.025	0.015	1.76	16.74	2.35	3.68
ECBV-019		439	288	45	0.00123	0.00106	0.00227	0.00195	0.0193	0.01249	1.84	17.44	2.4	4.02
ECBV-021		619	190	58	0.00034	0.00053	0.00313	0.00182	0.01935	0.02193	2.36	20.7	3.14	3.93
ECBV-049A		400	324	54	n.r.	n.r.	n.r.	n.r.	n.r.	n.r.	1.96	17.24	3.08	1.76
ECBV-105		426	165	53	0.00016	0.00044	<2	0.0013	0.015	0.0117	2.78	22.82	3.65	4.96
ECBV-106		280	220	55	0.00035	0.00031	<2	0.0017	0.015	0.0075	1.93	20.85	3.22	4.25
ECBV-111		n.r.	368	39	n.r.	n.r.	n.r.	n.r.	n.r.	n.r.	1.92	16.78	2.84	3.58
Average B-1		457	284	51.5	0.001	0.001	0.002	0.002	0.019	0.014	1.91	18.00	2.80	3.47
Bc-6	B-2	168	121	77.8	<0.15	0.00023	0.00125	0.00108	0.01099	0.00957	1.5	15.3	3.85	0.65
Bc-25		56	125	77.8	<0.15	0.0002	0.0006	0.00071	0.01238	0.0072	1.5	15.26	3.89	0.59
CO-066		165	86	51	<0.15	0.00016	0.0004	0.00037	0.00453	0.00155	n.r.	n.r.	n.r.	
CO-253		299	104	110	<0.15	0.0001	0.00016	0.00021	0.00217	0.00135	1.1	15.56	4.26	0.52
ECBV-025		n.r.	122	84.4	<0.1	0.00002	<2	<0.3	0.002	<2	1.38	14	3.75	0.417
ECBV-026		160	148	111.1	0.00012	0.00024	<2	<0.3	0.008	0.0046	1.11	12.89	3.34	0.632
ECBV-058		79	173	42.5	<0.1	0.00038	<2	0.0005	0.021	0.0117	0.87	11.71	2.84	0.381
ECBV-064		111	125	66.9	<0.1	0.00023	<2	0.0012	0.014	0.0108	1.47	16.17	4.09	1.146
Average B-2		148	126	77.7	0.000	0.000	0.001	0.001	0.009	0.007	1.28	14.41	3.72	0.62
CO-048	B-3	44	163	75	0.00023	0.00036	0.0018	0.00112	0.0184	0.00765	0.4	3.42	1.17	0.27
CO-252		53	123	3	0.00019	0.00047	0.00182	0.00122	0.01998	0.00589	0.2	1.78	0.72	0.03
ECBV-013		81	151	9.9	<0.1	0.00027	<2	0.0008	0.015	0.0054	0.74	5.14	1.36	0.564
ECBV-063		520	151	278.8	n.r.	n.r.	n.r.	n.r.	n.r.	n.r.	0.78	6.98	2.39	0.457
Average B-3		175	147	91.7	0.0002	0.0004	0.002	0.001	0.018	0.006	0.53	4.33	1.41	0.33025
60:40 mixture of B1:B2		333.214	220.600	61.948	0.000	0.000	0.002	0.001	0.015	0.011	1.80	14.10	2.97	2.56

ANNEXE 12 - Modelling of the distribution of TABS, Se and Pd in the Merensky Reef at the Impala and Rustenburg sections. Observed values for TABS and Se are from Chapter 6 (ANNEXE 15). All values in ppm.

ANNEXE 12

Intrusion	Locality	Sample	Rock	Height (cm)	Melt	S	wt frac cum sul	Cumulate sil and oxide	As melt	As sul	As sum	As observed	As model/obs
Bushveld Complex	Impala mine	IM-1	Norite	108	0.166	1560	0.004	0.830	0.192	0.009	0.201	0.065	3.080
		IM-3	Norite	98	0.194	1880	0.005	0.802	0.224	0.011	0.236	0.086	2.743
		IM-5	Norite	88	0.206	2560	0.007	0.788	0.238	0.016	0.254	0.117	2.179
		IM-7	Melanorite	78	0.274	4480	0.012	0.714	0.318	0.028	0.346	0.184	1.884
		IM-9	Melanorite	68	0.343	7320	0.020	0.637	0.398	0.046	0.444	0.228	1.945
		IM-11	Melanorite	58	0.276	4560	0.012	0.712	0.320	0.028	0.348	0.198	1.760
		IM-13	Melanorite	48	0.509	680	0.000	0.491	0.590	0.001	0.591	0.444	1.330
		IM-15	Melanorite	38	0.526	880	0.001	0.473	0.611	0.002	0.613	0.413	1.486
		IM-17	Melanorite	28	0.522	680	0.000	0.477	0.606	0.001	0.607	0.225	2.695
		IM-18	Melanorite	23	0.345	1360	0.003	0.652	0.400	0.007	0.407	0.216	1.886
		IM-19	Melanorite	18	0.341	4680	0.012	0.647	0.395	0.029	0.424	0.227	1.869
		IM-20	Melanorite	13	0.198	12120	0.034	0.768	0.230	0.079	0.309	0.178	1.741
		IM-21	Melanorite	8	0.236	20480	0.058	0.706	0.273	0.134	0.408	0.115	3.530
		IM-22	Upper Chromitite	6	0.055	3400	0.010	0.936	0.064	0.022	0.086	0.109	0.788
		IM-23	Mela-norite	3	0.086	5960	0.017	0.897	0.100	0.039	0.139	0.081	1.720
		IM-24	Lower Chromitite	0	0.103	4080	0.011	0.885	0.120	0.026	0.146	0.069	2.111
		IM-25	Anorthosite	-3	0.101	4080	0.011	0.888	0.117	0.026	0.143	0.082	1.755
		IM-26	Leuconorite	-8	0.068	18320	0.052	0.880	0.079	0.121	0.200	0.096	2.088
		IM-27	Leuconorite	-17	0.068	4480	0.013	0.920	0.078	0.029	0.108	0.052	2.085
		IM-28	Leuconorite	-23	0.085	9720	0.028	0.887	0.099	0.064	0.163	0.060	2.708
IM-30	Leuconorite	-33	0.086	440	0.001	0.913	0.100	0.002	0.102	0.035	2.915		
IM-32	Leuconorite	-48	0.104	196	0.000	0.896	0.120	0.001	0.121	0.003			
IM-34	Leuconorite	-58	0.091	173	0.000	0.909	0.106	0.001	0.106	0.003			
IM-36	Leuconorite	-68	0.077	178	0.000	0.922	0.090	0.001	0.090	0.036	2.503		

ANNEXE 12 – Cont.

Intrusion	Locality	Sample	Bi melt	Bi sul	Bi sum	Bi observed	Bi model/obs	Sb melt	Sb sul	Sb sum	Sb obs	Sb model/obs	Te melt	Te sul	Te sum	Te obs	Te model/obs
Bushveld Complex	Impala mine	IM-1	0.006	0.035	0.040	0.008	4.808	0.020	0.002	0.022	0.040	0.549	0.002	0.019	0.022	0.065	0.331
		IM-3	0.007	0.042	0.049	0.022	2.184	0.023	0.003	0.026	0.022	1.190	0.003	0.023	0.026	0.124	0.210
		IM-5	0.007	0.059	0.066	0.029	2.269	0.024	0.004	0.028	0.006	4.968	0.003	0.032	0.035	0.098	0.360
		IM-7	0.009	0.105	0.114	0.157	0.727	0.032	0.007	0.040	0.011	3.464	0.004	0.058	0.062	0.316	0.195
		IM-9	0.012	0.174	0.185	0.166	1.114	0.041	0.012	0.052	0.033	1.582	0.005	0.096	0.101	0.303	0.333
		IM-11	0.010	0.107	0.116	0.060	1.940	0.033	0.007	0.040	0.021	1.880	0.004	0.059	0.063	0.186	0.337
		IM-13	0.018	0.004	0.022	0.014	1.510	0.060	0.000	0.061	0.031	1.939	0.007	0.002	0.010	0.022	0.433
		IM-15	0.018	0.009	0.027	0.005	5.344	0.062	0.001	0.063	0.026	2.427	0.008	0.005	0.012	0.049	0.256
		IM-17	0.018	0.004	0.022	0.008	2.838	0.062	0.000	0.062	0.015	4.042	0.008	0.002	0.010	0.020	0.481
		IM-18	0.012	0.025	0.037	0.110	0.338	0.041	0.002	0.043	0.024	1.743	0.005	0.014	0.019	0.129	0.147
		IM-19	0.012	0.214	0.226	0.543	0.416	0.040	0.007	0.048	0.048	0.997	0.005	0.539	0.544	0.679	0.801
		IM-20	0.007	0.588	0.595	0.846	0.703	0.023	0.020	0.044	0.036	1.198	0.003	1.481	1.483	1.555	0.954
		IM-21	0.008	0.998	1.006	0.938	1.073	0.028	0.034	0.062	0.039	1.610	0.003	2.514	2.518	2.390	1.053
		IM-22	0.002	0.165	0.167	0.285	0.585	0.006	0.006	0.012	0.025	0.482	0.001	0.415	0.416	0.322	1.291
		IM-23	0.003	0.290	0.293	0.210	1.391	0.010	0.010	0.020	0.043	0.470	0.001	0.729	0.731	0.408	1.791
		IM-24	0.004	0.196	0.200	0.172	1.161	0.012	0.007	0.019	0.017	1.114	0.002	0.494	0.495	0.399	1.242
		IM-25	0.003	0.196	0.200	0.160	1.252	0.012	0.007	0.019	0.060	0.312	0.001	0.494	0.496	0.511	0.969
		IM-26	0.002	0.900	0.902	0.733	1.231	0.008	0.031	0.039	0.054	0.717	0.001	2.267	2.268	2.599	0.873
		IM-27	0.002	0.218	0.220	0.313	0.703	0.008	0.007	0.015	0.022	0.700	0.001	0.548	0.549	0.855	0.642
		IM-28	0.003	0.475	0.478	0.399	1.199	0.010	0.016	0.026	0.029	0.917	0.001	1.197	1.198	1.198	1.000
IM-30	0.003	0.009	0.012	0.005	2.180	0.010	0.001	0.011	0.005	2.079	0.001	0.005	0.006	0.009	0.650		
IM-32	0.004	0.002	0.006	0.013	0.467	0.012	0.000	0.012	0.009	1.386	0.002	0.001	0.003	0.011	0.253		
IM-34	0.003	0.002	0.005	0.005	0.959	0.011	0.000	0.011	0.009	1.150	0.001	0.001	0.002	0.006	0.387		
IM-36	0.003	0.003	0.005	0.005	0.958	0.009	0.000	0.009	0.010	0.903	0.001	0.001	0.003	0.006	0.396		

ANNEXE 12 – Cont.

Intrusion	Locality	Sample	Rock	Height (cm)	Melt	S	wt frac cum sul	Cumulate sil and oxide	As melt	As sul	As sum	As observed	As model/obs
Bushveld Complex	Rustenburg mine	M4	Melanorite	27	0.124	9800	0.028	0.848	0.144	0.064	0.208	0.123	1.686
		M3	Melanorite	23	0.077	8900	0.025	0.898	0.089	0.058	0.147	0.143	1.029
		M2	Melanorite	18	0.116	7400	0.021	0.863	0.135	0.048	0.183	0.076	2.405
		M1	Melanorite	13.5	0.133	32100	0.091	0.775	0.155	0.212	0.366	0.143	2.559
		UC	Upper Chromitite	10	0.134	5300	0.015	0.852	0.155	0.034	0.189	0.070	2.688
		CGM-2	Coarse-grained melanorite	6	0.113	13900	0.039	0.847	0.132	0.091	0.223	0.203	1.101
		CGM-1	Coarse-grained melanorite	2	0.135	30700	0.087	0.778	0.156	0.203	0.359	0.126	2.842
		LC	Lower Chromitite	0	0.168	4700	0.013	0.819	0.195	0.030	0.225	0.046	4.903
AN	Anorthosite	-2	0.114	3700	0.010	0.875	0.133	0.024	0.156	0.071	2.214		

Intrusion	Locality	Sample	Bi melt	Bi sul	Bi sum	Bi observed	Bi model/obs	Sb melt	Sb sul	Sb sum	Sb obs	Sb model/obs	Te melt	Te sul	Te sum	Te obs	Te model/obs
Bushveld Complex	Rustenburg mine	M4	0.004	0.477	0.481	0.378	1.272	0.015	0.016	0.031	0.034	0.923	0.002	1.202	1.203	0.857	1.404
		M3	0.003	0.435	0.438	0.369	1.186	0.009	0.015	0.024	0.060	0.402	0.001	1.096	1.097	0.832	1.318
		M2	0.004	0.359	0.363	0.400	0.909	0.014	0.012	0.026	0.033	0.782	0.002	0.905	0.906	0.760	1.192
		M1	0.005	1.576	1.581	1.404	1.126	0.016	0.054	0.070	0.062	1.124	0.002	3.970	3.972	4.453	0.892
		UC	0.005	0.255	0.259	0.329	0.788	0.016	0.009	0.025	0.037	0.656	0.002	0.642	0.644	0.748	0.861
		CGM-2	0.004	0.680	0.684	0.605	1.130	0.013	0.023	0.037	0.028	1.302	0.002	1.712	1.714	1.763	0.972
		CGM-1	0.005	1.507	1.512	1.561	0.968	0.016	0.052	0.068	0.040	1.706	0.002	3.796	3.798	4.389	0.865
		LC	0.006	0.223	0.229	0.353	0.650	0.020	0.008	0.028	0.048	0.573	0.002	0.563	0.565	0.573	0.986
AN	0.004	0.177	0.181	0.220	0.820	0.014	0.006	0.020	0.011	1.773	0.002	0.445	0.447	0.666	0.672		

ANNEXE 12 – Cont.

Intrusion	Locality	Se melt	Se sul	Se sum	Se obs	Se model/obs	Pd melt	Pd sul	Pd sum	Pd observed	Pd model/obs
Bushveld Complex	Rustenburg mine	0.013	3.505	3.518	4.143	0.849	0.001	4.559	4.560	2.16	2.111
		0.008	3.196	3.204	3.860	0.830	0.001	4.158	4.158	2.36	1.762
		0.012	2.639	2.651	2.843	0.932	0.001	3.432	3.433	2.22	1.547
		0.014	11.580	11.594	14.646	0.792	0.001	15.062	15.064	11.9	1.266
		0.014	1.872	1.886	1.994	0.945	0.001	2.434	2.436	4.27	0.570
		0.012	4.994	5.006	5.656	0.885	0.001	6.496	6.497	5.94	1.094
		0.014	11.072	11.087	14.323	0.774	0.001	14.402	14.403	16.29	0.884
		0.018	1.642	1.659	1.630	1.018	0.002	2.135	2.137	4.4	0.486
		0.012	1.299	1.311	1.567	0.836	0.001	1.690	1.691	4.03	0.420

Composition of the cumulate sulfides using zone refining equation		$C_s = c_i * (D - (D - 1)) * \text{EXP}(-1/D * N)$					
	N	As	Bi	Sb	Te	Se	Pd
Composition of the cumulate sulfide inside reef C _{sul}	20000	2.32	17.26	0.59	43.47	126.79	164.92
Composition of the cumulate sulfide outside reef	350	2.32	8.71	0.59	4.81	32.15	3.66
C _i = 60:40 mixture B ₁ +B ₂		1.160	0.035	0.118	0.015	0.106	0.0105
D sul/sil		2	500	5	3000	1200	40000

ANNEXE 13 - Analyses of reference materials used to monitor the data quality for whole-rock TABS and Se results from the Merensky Reef and J-M Reef of the Bushveld and Stillwater Complexes. Normal font certificate or assigned value, italics average of literature values and Mansur et al. (2019) (Chapter 2) for CH-4 and TDB-1, median of GeoPt18 round for KPT-1. Detection limit = 3*sigma of the blank; Stdev = standard deviation; RSD= relative standard deviation; n= number of individual analyses

ANNEXE 13

		As	Bi	Sb	Se	Te
		ppm	ppm	ppm	ppm	ppm
Reference material	Detection limit ppm	<i>0.003</i>	<i>0.005</i>	<i>0.005</i>	<i>0.002</i>	<i>0.006</i>
CH-4 Anorthosite CANMET	Certificate value	8.80	0.6	0.77	2.1	0.36
	Stdev	0.60	0.2	0.4	0.2	0.072
	RDS%	6.82	33.33	51.95	9.52	20.00
	This study	8.34	0.73	0.861	1.942	0.438
	Stdev (n= 4)	0.21	0.14	0.076	0.042	0.032
	Relative difference %	5.18	21.69	11.83	7.52	21.70
TDB-1 Diabase CANMET	Certificate value	2.50	<i>0.063</i>	1	<i>0.38</i>	<i>0.036</i>
	Stdev	0.50	<i>0.0189</i>	0.4	<i>0.032</i>	<i>0.007</i>
	RDS%	20.00	30.00	40.00	8.42	20.00
	This study	2.01	0.088	0.938	0.372	0.032
	Stdev (n= 4)	0.19	0.008	0.057	0.073	0.005
	Relative difference %	19.42	39.08	6.20	2.21	10.99
GeoPT-18/ KPT-1 Sulfide-bearing dolerite IAG	Certificate value	2.20	0.94	10.10	2.71	0.35
	Stdev	0.53	0.19	1.27	0.46	0.09
	RDS%	24.09	20.21	12.57	16.97	25.71
	This study	2.28	0.902	11.08	2.93	0.47
	Stdev (n= 4)	0.11	0.095	0.156	0.047	0.046
	Relative difference %	3.56	4.04	9.69	8.12	34.95

ANNEXE 14 - Analyses of reference materials used in the calibration of the LA-ICP-MS and in-house reference materials used to monitor the data quality for analyses of sulfide minerals and phlogopite from the Bushveld and Stillwater Complexes. Stdev= standard deviation; n= number of analyses; RSD= relative standard deviation; n.d.= not determined.

ANNEXE 14

Reference materials and results for base sulfide minerals													
Element	³⁴ S	⁵⁷ Fe	⁵⁹ Co	⁶¹ Ni	⁶⁵ Cu	⁶⁶ Zn	⁷⁵ As	⁸² Se	⁹⁵ Mo	¹⁰¹ Ru	¹⁰³ Rh	¹⁰⁸ Pd	¹⁰⁹ Ag
Detection limits	58.364		0.008	0.306	0.182	0.079	0.044	0.617	0.008	0.008	0.001	0.027	0.003
<i>Reference materials</i>	Po-727	Po-727	MASS-1	GSE-1g	MASS-1	MASS-1	MASS-1	MASS-1	MASS-1	Po-727	Po-727	Po-727	MASS-1
Concentrations used	390900	610700	60	440	134000	210000	65	51	59	36.5	41.6	43.4	50
Stdev	1600	2100	10	30	500	5000	3	4	9	0.3	0.3	0.3	5
JB-MSS-5 Working value	404700	570000	0.28	10487	208	n.d.	79.0	47.3	0.23	21.7	61.4	65.2	53
Stdev	n.d.	9000	0.02	n.d.	24	n.d.	11.0	13.4	0.02	2.3	7.2	5.1	4.9
AVE JB-MSS-5	388912		0.623	10799	216	8	63.3	61.5	0.45	19.8	57.8	50.3	46.3
Stdev (n= 25)	26000.17		0.36	390	25	3	5.2	5.1	0.10	1.5	4.1	3.2	2.2
RSD (%)	7%		57%	4%	11%	34%	8%	8%	23%	7%	7%	6%	5%
GSE-1 g Working value	n.d.	98717	380		380	460	260	20	390	n.d.	n.d.	n.d.	200
Stdev	n.d.	2332	20		40	10	90	16	30	n.d.	n.d.	n.d.	20
AVE GSE-1g	2502.16		335.76		382	407	342	51	384	0.05	34.9	105	152
Stdev (n= 25)	1344.73		14.20		33	29	12	10	16	0.02	9.4	27	11
RSD (%)	54%		4%		9%	7%	4%	20%	4%	31%	27%	26%	7%
MASS-1 Working value	276000	156000		97						n.d.	n.d.	n.d.	
Stdev	1000	1000		15						n.d.	n.d.	n.d.	
AVE MASS-1	265472	IS		105						0.01	0.7	0.98	
Stdev (n= 25)	14339.86			10						0.00	0.2	0.14	
RSD (%)	5%			9%						31%	23%	14%	
UQAC FeS-1 Working value	400000	450000	637	25000	23000	275	1050	310	66	65	64	60	155
Stdev	12000	n.d.	47	1500	1300	28	105	42	4	6.5	5.6	6	16
AVE UQAC-FeS-1	376848		614.5188	24687	21614	254	1141	304	69	71.1	59.8	43.7	134
Stdev (n= 25)	24153.25		26.33	871	690	22	53	13	1	2.3	2.0	5.7	10
RSD (%)	6%		4%	4%	3%	9%	5%	4%	2%	3%	3%	13%	7%

ANNEXE 14 – Cont.

Reference materials and results for base sulfide minerals													
Element	¹¹¹ Cd	¹¹⁵ In	¹¹⁸ Sn	¹²¹ Sb	¹²⁸ Te	¹⁸⁵ Re	¹⁸⁹ Os	¹⁹³ Ir	¹⁹⁵ Pt	¹⁹⁷ Au	²⁰⁵ Tl	²⁰⁸ Pb	²⁰⁹ Bi
Detection limits	0.025	0.014	0.018	0.012	0.079	0.004	0.008	0.002	0.004	0.007	0.002	0.005	0.002
<i>Reference materials</i>	MASS-1	GSE-1g	MASS-1	MASS-1	MASS-1	GSE-1g	Po-727	Po-727	Po-727	Po-727	MASS-1	MASS-1	MASS-1
Concentrations used	60	370	59	60	15	78.9	46.7	48	35.5	45.8	50	68	60
Stdev	7	60	6	9	n.d.	n.d.	2.6	1.2	0.8	2.4	n.d.	7	n.d.
JB-MSS-5 Working value	0.13	n.d.	n.d.	61	44	21	42.6	40.2	39.9	35.9	n.d.	72	76
Stdev	0.04	n.d.	n.d.	7	3	n.d.	0.9	0.5	1	4.8	n.d.	5	3
AVE JB-MSS-5	0.08	0.05	1.0	54	32	24	53.8	38.6	35.3	33.0	0.02	65	73
Stdev (n= 25)	0.06	0.09	0.5	4	4	3	2.6	2.3	1.8	4.9	0.04	3	6
RSD (%)	71%	173%	52%	7%	13%	8%	5%	6%	5%	15%	221%	5%	9%
GSE-1 g Working value	160		280	450	n.d.		n.d.	n.d.	30	7	2	378	320
Stdev	50		50	110	n.d.		n.d.	n.d.	n.d.	n.d.	n.d.	12	30
AVE GSE-1g	227		319	337	208		0.02	23.6	18.5	6.8	1.4	328	297
Stdev (n= 25)	24		12	13	12		0.01	9.5	6.2	1.2	0.1	24	15
RSD (%)	11%		4%	4%	6%		51%	40%	33%	18%	5%	7%	5%
MASS-1 Working value		50				n.d.	n.d.	46.3	51.9	47			
Stdev		n.d.				n.d.	n.d.	n.d.	n.d.	n.d.			
AVE MASS-1		61.6				0.01	0.01	59.9	49.9	47.3			
Stdev (n= 25)		2.2				0.02	0.00	1.5	2.3	3.2			
RSD (%)		4%				126%	83%	3%	5%	7%			
UQAC FeS-1 Working value	n.d.	9.4	180	88	170	70	75	60	50	65	n.d.	90	120
Stdev	n.d.	1.1	18	9	17	7	15	6	10	6.5	n.d.	9	20
AVE UQAC-FeS-1	2.2	10.1	182	81	141	85	90	55.8	41.5	64.1	0.3	83	108
Stdev (n= 25)	0.3	0.5	12	9	7	4	5	3.4	5.4	6.0	0.1	5	4
RSD (%)	13%	5%	7%	11%	5%	4%	5%	6%	13%	9%	22%	6%	4%

ANNEXE 14 – Cont.

Correction for interferences	
Ru ¹⁰¹ corrected for Ni ⁶¹	1% Ni produced approximately 0.007 ppm Ru
Pd ¹⁰⁸ corrected for Cd ¹⁰⁸	1ppm Cd produced approximately 0.034 ppm Pd
Rh ¹⁰³ corrected for Cu ⁶³	1% Cu produced approximately 0.1 ppm Rh
In ¹¹⁵ corrected for Sn ¹¹⁵	1ppm Sn produced approximately 0.004 ppm In

ANNEXE 14 – Cont.

Reference materials and results for K-phlogopite													
Element	²⁹ Si	²⁴ Mg	²⁷ Al	⁵⁷ Fe	³⁹ K	⁴⁷ Ti	⁵² Cr	⁶¹ Ni	⁵¹ V	⁵⁵ Mn	⁴⁴ Ca	²³ Na	⁷ Li
Detection limits	167.94	0.32893	0.68745	2.14068	1.35378	0.33845	0.75978	0.15372	508.446	0.68034	16.41300	0.59071	0.196
<i>Reference materials</i>	GSE-1g	GSE-1g	GSE-1g	GSE-1g	GSE-1g	GSE-1g	GSE-1g	GSE-1g	GSE-1g	GSE-1g	GSE-1g	GSE-1g	GSE-1g
Concentrations	250994	21106	68804	98717	21800	450	400	440	440	590	52858	28934	430
Stdev	7011	181	2117	2332	200	42	80	30	20	20	2143	1484	60
Working value	224259	51318	92145	72598	1577	7012	300.2	145.7	238	1255	86787	15506	6
Stdev	9418	6935	12438	13310	166	1319	21.5	18.9	27	93	4643	1335	1.4
AVE G-Prob6	226067	51230	76670	74333	1475	7200	340	152	264	1307	88467	14413	5.8
Stdev (n=4)	4629	637	5929	3591	169	199	12	10	17	75	2023	743	0.2
RSD (%)	2%	1%	8%	5%	11%	3%	3%	7%	6%	6%	2%	5%	4%
Working value	248657	21709	70922	103381	25300	7432	42	58	44	220	51429	26709	43
Stdev	3739	241	1588	777	300	360	3	4	2	20	714	1484	6
AVE GSD-1g	244700	21300	67000	100933	24083	7817	44.2	60.4	43.8	221	51940	25120	42.6
Stdev (n=4)	2030	349	4371	4050	600	59	2.2	2.0	1.9	9	367	687	1.9
RSD (%)	1%	2%	7%	4%	2%	1%	5%	3%	4%	4%	1%	3%	4%
Working value	327180	465	10797	458	486	434	405	458.7	442	485	82144	99415	485
Stdev	-	54	-	9	92	30	64	4	86	10	-	-	44
AVE NIST SRM 610	339267	604	13043	517	702	609	474	562	492	496	94167	103433	466
Stdev (n=4)	5498	44	1951	55	116	16	17	28	20	15	1002	3402	15
RSD (%)	2%	7%	15%	11%	17%	3%	4%	5%	4%	3%	1%	3%	3%
Working value	336061	77	11167	51	66.3	44	36	38.8	39	38	85002	103858	42
Stdev	-	60	-	2	0.8	10	6	0.2	8	2	-	-	6
AVE NIST SRM 612	359167	107	14373	58	68	62	45	54	42.9	42	94067	106333	49
Stdev (n=4)	4252	5	1350	5	5.6	11	2	8.9	2	4	231	2914	2
RSD (%)	1%	5%	9%	9%	8%	17%	4%	16%	4%	10%	0%	3%	5%

ANNEXE 14 – Cont.

Reference materials and results for K-phlogopite													
Element	⁹ Be	¹¹ B	⁴⁵ Sc	⁵⁹ Co	⁶⁵ Cu	⁶⁶ Zn	⁶⁹ Ga	⁷² Ge	⁷⁵ As	⁸⁵ Rb	⁸⁸ Sr	⁹⁰ Zr	⁹³ Nb
Detection limits	0.092	0.243	0.047	0.015	0.085	0.183	0.050	0.252	0.112	0.055	0.011	0.014	0.009
<i>Reference materials</i>	GSE-1g	GSE-1g	GSE-1g	GSE-1g	GSE-1g	GSE-1g	GSE-1g	GSE-1g	GSE-1g	GSE-1g	GSE-1g	GSE-1g	GSE-1g
Concentrations	490	330	530	380	380	460	490	320	260	356	447	410	420
Stdev	80	120	20	20	40	10	70	80	90	4	5	30	40
Working value	0.4	-	36.8	46.9	89.5	70.8	16.0	1.26	-	-	166.6	55.1	4.16
Stdev	0.14	-	2.6	3.5	20.3	16.6	2.0	0.41	-	-	26.1	2.4	0.41
AVE G-Prob6	0.42	2.8	39.4	48.5	76.7	75.3	24.7	1.21	1.88	1.76	166.4	54.5	3.96
Stdev (n=4)	0.02	0.5	0.3	2.8	6.6	6.3	0.9	0.08	0.16	0.07	3.5	0.9	0.06
RSD (%)	4%	16%	1%	6%	9%	8%	3%	7%	8%	4%	2%	2%	2%
Working value	46	50	52	40	42	54	54	32	27	37.3	69.4	42	42
Stdev	5	20	2	2	2	2	7	8	8	0.4	0.7	2	3
AVE GSD-1g	49.7	49.1	54	39.3	44.5	52.5	51.7	30.6	24.8	34.8	68.9	43.4	41.7
Stdev (n=4)	0.5	1.0	0.7	1.6	6.6	2.5	1.0	0.7	1.7	0.8	1.1	1.7	1.0
RSD (%)	1%	2%	1%	4%	15%	5%	2%	2%	7%	2%	2%	4%	2%
Working value	466	356	441	405	430	456	438	426	317	425.7	515.5	440	419
Stdev	38	14	20	46	48	38	22	20	24	0.8	0.5	16	116
AVE NIST SRM 610	553	310	511	430	502	490	432	357	288	434.4	522.3	486	482
Stdev (n=4)	10	14	23	17	20	21	14	18	6	19.5	5.1	16	6
RSD (%)	2%	4%	5%	4%	4%	4%	3%	5%	2%	4%	1%	3%	1%
Working value	38	35	41	35	37	38	36	35	37	31.4	78.4	38	40
Stdev	6	6	8	4	6	8	4	6	14	0.4	0.2	4	6
AVE NIST SRM 612	47	44	46	39	43	124	38	32	33	34.6	81.4	44	42
Stdev (n=4)	1	1	1	1	7	61	1	1	2	0.6	0.7	2.5	1.6
RSD (%)	1%	3%	3%	2%	16%	49%	1%	3%	6%	2%	1%	6%	4%

ANNEXE 14 – Cont.

Reference materials and results for K-phlogopite												
Element	⁹⁵ Mo	¹⁰⁷ Ag	¹¹⁵ In	¹¹⁸ Sn	¹²¹ Sb	¹³³ Cs	¹³⁷ Ba	¹⁷⁸ Hf	¹⁸¹ Ta	²⁰⁵ Tl	²⁰⁸ Pb	²⁰⁹ Bi
Detection limits	0.047	0.032	0.007	0.073	0.024	0.040	0.053	0.014	0.003	0.006	0.006	0.005
<i>Reference materials</i>	GSE-1g	GSE-1g	GSE-1g	GSE-1g	GSE-1g	GSE-1g	GSE-1g	GSE-1g	GSE-1g	GSE-1g	GSE-1g	GSE-1g
Concentrations	390	200	370	280	450	310	427	395	390	2	378	320
Stdev	30	20	60	50	110	20	5	7	40		12	30
Working value	-	-	-	1.33	0.13	0.04	173	1.52	0.28	-	3.28	-
Stdev	-	-	-	0.71	0.01	0.01	26	0.15	0.03	-	0.78	-
AVE G-Prob6	0.426	0.96	0.06	1.60	0.17	0.13	165	1.44	0.24	0.02	3.48	0.02
Stdev (n=4)	0.037	0.03	0.01	0.16	0.06	0.09	7	0.02	0.00	0.00	0.19	0.01
RSD (%)	9%	3%	15%	10%	36%	65%	4%	1%	2%	20%	5%	41%
Working value	39	23	38	29	43	32	67	39	40	0.9	50	35
Stdev	3	3	5	6	7	2	1	2	4	0.1	2	4
AVE GSD-1g	37.4	21.0	36.4	27.2	42.1	31.3	67.1	40.0	40.0	0.82	45.9	30.7
Stdev (n=4)	0.7	0.4	0.5	0.4	0.9	0.1	0.7	1.6	0.9	0.05	1.0	1.2
RSD (%)	2%	2%	1%	2%	2%	0%	1%	4%	2%	6%	2%	4%
Working value	410	239	441	396	369	361	435	432	452	61	426	358
Stdev	58	38	64	36	56	136	46	30	78	4	1	98
AVE NIST SRM 610	447	256	420	395	427	401	475	455	456	67	442	373
Stdev (n=4)	11	10	12	16	13	6	9	12	2	2	13	14
RSD (%)	3%	4%	3%	4%	3%	1%	2%	3%	1%	3%	3%	4%
Working value	38	22	43	38	38	42	39.7	35	40	15.1	38.57	30
Stdev	4	0.3	8	4	4	6	0.8	8	4	1.4	0.2	12
AVE NIST SRM 612	41	22	39	48	42	49	42.4	37	40	15	39.0	35
Stdev (n=4)	0.3	0.2	0.7	2.8	0.2	2.8	2.1	0.9	1.6	1.0	1.3	0.3
RSD (%)	1%	1%	2%	6%	0%	6%	5%	2%	4%	7%	3%	1%

ANNEXE 15 - Complete dataset of whole-rock TABS and Se analyses of samples from the Bushveld and Stillwater Complexes obtained in this study, and results previously reported by Barnes and Maier (2002), Godel et al. (2007), Godel and Barnes (2008) and Barnes et al. (2020) used for comparison. Values in bold are below the detection limit and were replaced by half of the detection limit values. All values in ppm. DL - Detection limit; bdl – below detection limit.

ANNEXE 15

Intrusion	Locality	Sample	Rock	Sulfide texture	Height (cm)	This study				
						As (ppm)	Bi (ppm)	Sb (ppm)	Se (ppm)	Te (ppm)
			Detection limit			<i>0.003</i>	<i>0.005</i>	<i>0.005</i>	<i>0.002</i>	<i>0.006</i>
Bushveld Complex	Impala mine	IM-1	Norite	Minor disseminated	108	0.065	0.008	0.040	0.446	0.065
		IM-3	Norite	Minor disseminated	98	0.086	0.022	0.022	0.557	0.124
		IM-5	Norite	Minor disseminated	88	0.117	0.029	0.006	0.737	0.098
		IM-7	Melanorite	Disseminated interstitial	78	0.184	0.157	0.011	1.396	0.316
		IM-9	Melanorite	Disseminated interstitial	68	0.228	0.166	0.033	1.438	0.303
		IM-11	Melanorite	Minor disseminated	58	0.198	0.060	0.021	1.255	0.186
		IM-13	Melanorite	Minor disseminated	48	0.444	0.014	0.031	0.229	0.022
		IM-15	Melanorite	Disseminated interstitial	38	0.413	0.005	0.026	0.314	0.049
		IM-17	Melanorite	Disseminated interstitial	28	0.225	0.008	0.015	0.178	0.020
		IM-18	Melanorite	Disseminated interstitial	23	0.216	0.110	0.024	0.540	0.129
		IM-19	Melanorite	Disseminated interstitial	18	0.227	0.543	0.048	2.804	0.679
		IM-20	Melanorite	Disseminated interstitial	13	0.178	0.846	0.036	5.103	1.555
		IM-21	Melanorite	Disseminated interstitial	8	0.115	0.938	0.039	7.098	2.390
		IM-22	Upper Chromitite	Disseminated interstitial	6	0.109	0.285	0.025	1.067	0.322
		IM-23	Mela-norite	Disseminated interstitial	3	0.081	0.210	0.043	2.033	0.408
		IM-24	Lower Chromitite	Disseminated interstitial	0	0.069	0.172	0.017	1.356	0.399
		IM-25	Anorthosite	Disseminated interstitial	-3	0.082	0.160	0.060	1.629	0.511
		IM-26	Leuconorite	Disseminated interstitial	-8	0.096	0.733	0.054	5.921	2.599
		IM-27	Leuconorite	Disseminated interstitial	-17	0.052	0.313	0.022	1.477	0.855
		IM-28	Leuconorite	Disseminated interstitial	-23	0.060	0.399	0.029	2.930	1.198
IM-30	Leuconorite	Minor disseminated	-33	0.035	<i>0.005</i>	<i>0.005</i>	0.096	0.009		
IM-32	Leuconorite	Minor disseminated	-48	<i>0.003</i>	0.013	0.009	0.026	0.011		
IM-34	Leuconorite	Minor disseminated	-58	<i>0.003</i>	<i>0.005</i>	0.009	0.022	<i>0.006</i>		
IM-36	Leuconorite	Minor disseminated	-68	0.036	<i>0.005</i>	0.010	0.025	<i>0.006</i>		

ANNEXE 15 – Cont.

Sample	Barnes and Maier (2002)												(TABS)/(Pd+Pt)
	S (ppm)	Cu (ppm)	Ni (ppm)	Os (ppb)	Ir (ppb)	Ru (ppb)	Rh (ppb)	Pt (ppb)	Pd (ppb)	Au (ppb)	Se/Te	Hf (ppm)	
IM-1	1560	303	905	<1	1.08	5	2.7	35	21	51	6.85	0.350	11.16
IM-3	1880	359	1105	<1	1.07	8	1.8	50	20	75	4.50	0.340	11.58
IM-5	2560	437	1354	1.6	1.50	5	2	53	17	93	7.52	0.320	14.09
IM-7	4480	793	2300	2.5	3.9	27	4.6	169	42	235	4.42	0.600	9.78
IM-9	7320	941	2736	4	5.5	18	7	213	44	266	4.75	0.720	8.44
IM-11	4560	649	1858	4.5	5.3	35	11	144	30	165	6.73	0.710	9.88
IM-13	680	164	789	2.9	2.1	9	3.8	39	8	23	10.19	1.330	15.78
IM-15	880	208	875	<1	2.0	11	2.9	41	27	35	6.42	1.030	11.85
IM-17	680	169	765	1.4	2.8	17	6.1	68	53	36	8.77	0.820	3.69
IM-18	1360	315	834	4.7	4.7	27	15	136	147	44	4.18	0.490	3.60
IM-19	4680	1412	2468	23	27	144	68	1062	1381	366	4.13	0.640	1.76
IM-20	12120	2231	5424	82	31	116	89	6418	3064	1250	3.28	0.090	0.81
IM-21	20480	2452	8143	267	322	1628	682	18987	6330	1268	2.97	0.380	0.42
IM-22	3400	1215	2130	413	552	2708	1141	22827	2056	315	3.31	0.05	0.07
IM-23	5960	936	3060	254	308	1692	830	13369	2807	1076	4.98	0.160	0.17
IM-24	4080	887	3400	715	1264	6140	2665	37320	4173	339	3.40	0.310	0.05
IM-25	4080	691	1411	97	105	600	286	5126	3025	389	3.18	0.070	0.30
IM-26	18320	2442	6448	262	307	1752	770	18276	9871	2000	2.28	0.05	0.33
IM-27	4480	836	2117	105	94	704	263	5660	3699	754	1.73	0.050	0.29
IM-28	9720	1318	3680	166	79	1051	394	4302	3032	1153	2.45	0.110	0.63
IM-30	440	105	298	<1	2.4	<5	6.4	91	52	21	10.19	0.100	1.05
IM-32	196	69	223	0.9	0.42	<5	1.9	8	<4	2	2.39	0.200	
IM-34	173	46	205	<0.6	0.37	<5	1.2	<4	<2	2	3.47	0.130	
IM-36	178	46	203	<1	0.57	7	1.1	6	<3	1	3.98	0.05	

ANNEXE 15 – Cont.

Intrusion	Locality	Sample	Rock	Sulfide texture	Height (cm)	This study				
						As (ppm)	Bi (ppm)	Sb (ppm)	Se (ppm)	Te (ppm)
Bushveld Complex	Rustenburg mine	M4	Melanorite	Disseminated interstitial	27	0.123	0.378	0.034	4.143	0.857
		M3	Melanorite	Disseminated interstitial	23	0.143	0.369	0.060	3.860	0.832
		M2	Melanorite	Disseminated interstitial	18	0.076	0.400	0.033	2.843	0.760
		M1	Melanorite	Disseminated interstitial	13.5	0.143	1.404	0.062	14.646	4.453
		UC	Upper Chromitite	Disseminated interstitial	10	0.070	0.329	0.037	1.994	0.748
		CGM-2	Coarse-grained melanorite	Disseminated interstitial	6	0.203	0.605	0.028	5.656	1.763
		CGM-1	Coarse-grained melanorite	Disseminated interstitial	2	0.126	1.561	0.040	14.323	4.389
		LC	Lower Chromitite	Disseminated interstitial	0	0.046	0.353	0.048	1.630	0.573
		AN	Anorthosite	Minor disseminated	-2	0.071	0.220	0.011	1.567	0.666
Stillwater Complex	East Boulder mine	ST-12	Melatroctolite	Disseminated interstitial		0.385	0.437	0.022	5.609	3.075
		ST-14	Anorthosite	Disseminated interstitial		0.064	0.164	0.005	1.883	0.771
		ST-16	Leuconorite	Disseminated interstitial		0.080	0.266	0.005	6.922	1.848
		ST-17	Olivine melagabbronorite	Disseminated interstitial		0.017	0.155	0.018	1.654	0.739
	Stillwater mine	P-3	Leucogabbronorite	Disseminated interstitial		0.045	0.338	0.005	7.043	4.477
		P-4	Anorthosite	Disseminated interstitial		0.017	0.399	0.005	6.668	3.381
	Lower Banded Series (GNII)	BS-18	Leucogabbronorite	Disseminated interstitial		0.026	0.050	0.016	2.060	0.303

ANNEXE 15 – Cont.

Godel et al. (2007)													
Sample	S (ppm)	Cu (ppm)	Ni (ppm)	Os (ppb)	Ir (ppb)	Ru (ppb)	Rh (ppb)	Pt (ppb)	Pd (ppb)	Au (ppb)	Se/Te	Hf (ppm)	(TABS)/(Pd+Pt)
M4	9800	1400	4200	70	70	320	170	5210	2160	220	4.83	0.180	0.75
M3	8900	1100	4100	90	100	640	200	2480	2360	420	4.64	0.140	1.09
M2	7400	1000	2900	90	100	360	210	3140	2220	340	3.74	0.210	0.77
M1	32100	2800	13700	490	630	2780	1690	16550	11900	1270	3.29	0.140	0.73
UC	5300	1400	2300	260	350	1700	1000	13450	4270	310	2.67	0.360	0.18
CGM-2	13900	4300	4400	140	140	600	400	8840	5940	4640	3.21	0.210	0.56
CGM-1	30700	3500	13100	580	580	2530	1340	42080	16290	2560	3.26	0.370	0.35
LC	4700	1300	2200	730	1110	5410	3800	33100	4400	340	2.84	0.420	0.07
AN	3700	900	1300	100	120	500	420	5340	4030	330	2.35	0.080	0.27
Godel and Barnes (2008)													
	S (ppm)	Cu (ppm)	Ni (ppm)	Os (ppb)	Ir (ppb)	Ru (ppb)	Rh (ppb)	Pt (ppb)	Pd (ppb)	Au (ppb)	Se/Te	Hf (ppm)	
ST-12	7520	1768.15	3787.1	1155	383	785	2400	166355	248678	3489	1.82	0.220	0.02
ST-14	3320	689.03	919.44	68	36	113	313	7811	40757	669	2.44	0.110	0.06
ST-16	10090	1835.13	3120.93	156	30	132	201	23007	45007	727	3.75	0.110	0.13
ST-17	2690	443.77	1917.85	91	32	68	281	11391	37134	498	2.24	0.170	0.05
Barnes et al. (2020)													
P-3	8024	1703	2543	227.7	97.99	297.4	890.6	28260	118400	2481	1.57	0.140	0.08
P-4	9804	2865	4212	68.52	30.86	95.12	222	9479	39330	826.5	1.97	0.090	0.21
BS-18	3043	1192	941	bdl	bdl	bdl	bdl	0.695	1.926	54.85	6.80	0.045	936.77

ANNEXE 16 - Complete data set of LA-ICP-MS analyses of K-Phlogopite obtained in this study for the Merensky Reef at the Impala mine. Values in wt% for major and minor elements, and in ppm for trace elements. The SiO₂ values are from Li et al. (2005). LOD – limit of detection.

ANNEXE 16

Sample	SiO ₂	Na ₂ O	MgO	Al ₂ O ₃	K ₂ O	CaO	TiO ₂	V ₂ O ₅	Cr ₂ O ₃	MnO ₂	FeO	NiO
LOD		0.00006	0.00003	0.00007	0.00014	0.00164	0.00003	0.05084	0.00008	0.00007	0.00021	0.00002
IM-13	40.23	0.18	19.99	14.04	8.92	0.01	2.72	0.238	0.45	0.04	8.99	0.18
IM-13	40.23	0.18	19.52	13.74	8.99	0.02	3.53	0.311	0.57	0.04	9.09	0.19
IM-13	40.23	0.18	18.50	14.15	8.88	0.00	5.41	0.218	0.95	0.04	8.49	0.21
IM-13	40.23	0.15	19.40	14.10	9.06	0.02	4.09	0.192	0.72	0.04	8.50	0.21
IM-13	40.23	0.15	18.60	14.13	8.99	0.00	4.84	0.227	0.84	0.04	8.67	0.22
IM-13	40.23	0.16	18.28	14.16	9.04	0.01	5.08	0.228	0.94	0.04	8.81	0.22
IM-13	40.23	0.19	18.18	13.64	8.74	0.15	4.92	0.556	1.20	0.03	9.02	0.20
IM-13	40.23	0.20	18.02	13.74	8.82	0.00	5.13	0.445	0.97	0.04	9.20	0.20
IM-13	40.23	0.19	17.92	13.63	8.87	0.10	5.32	0.532	1.16	0.04	9.16	0.20
IM-13	40.23	0.16	17.95	13.61	8.89	0.05	5.17	0.534	1.41	0.03	9.10	0.20
IM-13	40.23	0.20	17.64	13.61	8.92	0.15	5.34	0.531	1.34	0.03	9.26	0.21
IM-13	40.23	0.16	17.95	13.59	8.69	0.27	5.27	0.520	1.08	0.03	9.07	0.20
IM-13	40.23	0.17	18.39	14.12	8.65	0.15	4.76	0.511	0.87	0.04	9.02	0.19
IM-13	40.23	0.15	20.15	14.10	9.10	0.00	2.52	0.129	0.68	0.04	8.68	0.17
IM-13	40.23	0.10	21.26	14.49	9.41	0.49	0.73	0.083	0.24	0.04	8.41	0.17
IM-15	40.23	0.14	19.04	14.12	9.13	0.67	4.05	0.193	0.80	0.04	8.53	0.22
IM-15	40.23	0.15	18.40	13.70	9.14	0.05	5.06	0.201	1.04	0.04	8.64	0.22
IM-15	40.23	0.19	19.43	13.98	9.10	0.00	3.98	0.206	0.70	0.04	8.45	0.22
IM-15	40.23	0.21	18.32	13.74	9.02	0.05	5.54	0.217	0.96	0.04	8.70	0.22
IM-15	40.23	0.17	20.55	13.93	9.26	0.02	2.10	0.122	0.47	0.04	8.33	0.18
IM-15	40.23	0.20	19.16	13.79	8.97	0.00	4.54	0.221	0.82	0.04	8.39	0.21
IM-15	40.23	0.17	20.08	13.91	9.02	0.09	3.33	0.167	0.61	0.03	8.15	0.19
IM-15	40.23	0.16	20.70	14.04	8.95	0.43	2.17	0.140	0.49	0.03	8.13	0.18
IM-15	40.23	0.16	21.19	14.19	9.12	0.00	1.32	0.077	0.39	0.03	8.31	0.16
IM-15	40.23	0.17	20.64	14.14	8.90	0.00	2.21	0.138	0.47	0.04	8.13	0.21

ANNEXE 16 – Cont.

Sample	⁷ Li	⁹ Be	¹¹ B	⁴⁵ Sc	⁵⁹ Co	⁶⁵ Cu	⁶⁶ Zn	⁶⁹ Ga	⁷² Ge	⁷⁵ As	⁸⁵ Rb	⁸⁸ Sr	⁹⁰ Zr
LOD	0.196	0.092	0.243	0.047	0.015	0.085	0.183	0.050	0.252	0.112	0.055	0.011	0.014
IM-13	10.08	0.25	25.96	35.39	114.8	1.76	59.84	49.1	0.99	4.11	559	1.69	9.30
IM-13	9.20	0.19	18.57	44.71	114.9	1.90	64.80	92.9	0.86	1.88	508	1.99	8.26
IM-13	7.19	0.32	4.13	24.38	112.8	2.56	56.02	331.9	0.59	0.28	462	2.86	9.44
IM-13	7.45	0.16	6.16	22.79	110.6	1.77	60.59	179.4	0.83	0.38	532	1.83	6.92
IM-13	6.65	0.11	2.65	22.75	113.4	4.36	58.98	310.8	0.62	0.25	508	2.92	15.95
IM-13	6.75	0.24	2.88	23.29	112.4	5.41	59.12	445.1	0.82	0.20	461	3.97	15.89
IM-13	7.45	0.25	5.82	53.65	108.7	2.01	47.99	219.5	0.63	0.15	456	4.30	5.02
IM-13	8.22	0.26	5.60	75.83	116.3	2.30	51.30	274.2	0.66	0.18	455	3.41	6.38
IM-13	7.84	0.28	5.82	64.09	115.7	2.37	48.68	254.1	0.68	0.11	452	3.92	4.87
IM-13	6.75	0.27	5.95	57.28	113.8	3.93	44.48	222.3	0.74	0.11	461	3.47	4.93
IM-13	8.17	0.27	5.59	55.97	117.4	3.77	47.81	252.3	0.71	0.14	449	4.04	5.09
IM-13	6.54	0.21	6.12	49.03	116.1	1.65	44.06	176.9	0.67	0.11	510	4.06	4.74
IM-13	7.41	0.21	5.48	30.76	113.1	1.52	49.94	155.2	0.54	0.15	491	4.50	7.39
IM-13	12.07	0.24	16.82	18.65	110.0	1.59	62.12	39.1	0.90	0.93	606	1.18	4.54
IM-13	10.25	0.11	18.93	18.63	104.2	2.08	64.17	23.0	1.09	1.05	632	2.33	18.86
IM-15	7.29	0.12	2.29	21.86	111.7	2.11	58.19	215.2	0.60	0.15	552	2.84	9.79
IM-15	6.20	0.25	2.38	22.66	114.7	2.45	57.57	268.6	0.79	0.13	475	3.52	12.12
IM-15	9.35	0.26	6.27	21.76	112.6	3.74	59.64	202.0	0.67	0.51	499	2.38	11.20
IM-15	7.18	0.39	6.97	22.37	114.0	2.97	56.41	313.3	0.63	0.32	501	3.71	7.97
IM-15	11.58	0.24	31.16	23.37	106.4	1.04	60.54	32.6	0.85	1.78	600	1.62	9.25
IM-15	7.68	0.47	7.20	24.03	115.0	6.66	58.59	219.2	0.77	0.34	482	2.32	11.53
IM-15	9.60	0.35	12.51	18.95	110.1	1.41	55.36	58.1	0.73	0.72	552	1.63	8.78
IM-15	10.77	0.25	15.95	18.00	110.3	1.69	60.13	35.5	0.80	1.31	609	2.84	9.73
IM-15	10.86	0.14	26.60	20.81	106.7	0.95	59.52	27.3	0.93	2.95	618	1.18	12.42
IM-15	12.14	0.24	15.47	20.10	110.3	17.71	53.94	39.4	0.77	0.97	579	0.97	11.85

ANNEXE 16 – Cont.

Sample	⁹³ Nb	⁹⁵ Mo	¹⁰⁷ Ag	¹¹⁵ In	¹¹⁸ Sn	¹²¹ Sb	¹³³ Cs	¹³⁷ Ba	¹⁷⁸ Hf	¹⁸¹ Ta	²⁰⁵ Tl	²⁰⁸ Pb	²⁰⁹ Bi
LOD	0.009	0.047	0.032	0.007	0.073	0.024	0.040	0.053	0.014	0.003	0.006	0.006	0.005
IM-13	37.71	0.19	0.03	0.04	2.97	0.25	7.78	506	0.52	2.15	3.89	1.87	0.589
IM-13	33.68	0.10	0.03	0.04	3.30	0.17	5.48	1196	0.47	1.63	3.62	1.78	0.009
IM-13	45.16	0.16	0.03	0.05	4.40	0.06	3.84	4900	0.42	1.39	3.30	1.44	0.005
IM-13	52.89	0.18	0.03	0.04	4.58	0.04	4.85	2588	0.37	1.55	3.93	1.04	0.005
IM-13	33.06	0.26	0.06	0.05	5.10	0.08	4.88	4566	0.65	1.18	3.51	1.66	0.010
IM-13	35.84	0.15	0.07	0.05	4.73	0.06	3.61	6497	0.58	1.30	3.39	1.90	0.013
IM-13	5.43	0.05	0.03	0.03	2.53	0.02	4.63	3239	0.21	0.20	3.28	1.29	0.005
IM-13	10.93	0.07	0.03	0.04	2.25	0.03	3.93	4075	0.28	0.47	3.11	1.49	0.005
IM-13	4.62	0.05	0.03	0.03	2.15	0.03	3.99	3808	0.18	0.23	3.12	1.18	0.005
IM-13	2.59	0.05	0.06	0.03	2.32	0.02	4.03	3268	0.18	0.12	3.45	1.45	0.005
IM-13	4.88	0.05	0.05	0.03	2.51	0.03	3.74	3842	0.21	0.21	3.24	1.38	0.005
IM-13	3.77	0.05	0.03	0.03	2.21	0.04	4.32	2622	0.19	0.25	3.54	1.06	0.005
IM-13	2.67	0.05	0.03	0.03	3.42	0.02	4.68	2251	0.33	0.23	3.54	1.38	0.005
IM-13	51.99	0.18	0.03	0.04	4.05	0.11	7.02	380	0.36	2.28	4.35	0.98	0.005
IM-13	51.60	0.35	0.04	0.06	4.95	0.17	20.99	115	1.48	5.82	4.55	0.83	0.005
IM-15	44.66	0.21	0.20	0.06	5.57	0.04	4.37	3368	0.45	1.28	4.20	1.25	0.005
IM-15	46.15	0.16	0.17	0.05	4.88	0.04	3.87	4335	0.51	1.34	3.49	1.70	0.005
IM-15	57.03	0.19	0.12	0.05	6.03	0.10	4.17	3106	0.54	1.71	3.60	2.61	0.011
IM-15	45.43	0.14	0.12	0.04	4.29	0.07	4.41	4937	0.39	1.46	3.48	3.13	0.007
IM-15	83.46	0.41	0.12	0.06	6.18	0.23	10.92	268	0.58	3.57	4.37	1.43	0.007
IM-15	55.62	0.23	0.23	0.06	5.50	0.08	4.05	3370	0.54	1.47	3.63	2.65	0.009
IM-15	71.88	0.30	0.29	0.06	5.39	0.12	5.52	688	0.44	2.29	4.16	1.97	0.005
IM-15	81.40	0.47	0.26	0.06	6.04	0.19	8.94	310	0.55	3.42	4.28	1.85	0.008
IM-15	76.99	0.64	0.17	0.06	5.28	0.29	9.98	214	0.89	3.80	4.38	4.30	0.009
IM-15	80.34	0.26	0.05	0.07	6.21	0.11	7.94	381	0.65	3.36	4.24	0.86	0.005

ANNEXE 17 - Complete data set of LA-ICP-MS analyses of pyrrhotite obtained in this study and median values for each sample from the Bushveld and Stillwater Complexes. The Fe values used for internal standardization are from Godel et al. (2008a) for samples from the Stillwater Complex, Godel et al. (2007) for samples from the Rustenburg mine, and stoichiometric values (i.e., 62.3%) for samples from the Impala mine. LOD - limit of detection.

ANNEXE 17

Intrusion	Locality	Sample	Rock	Height (cm)	³⁴ S	⁵⁹ Co	⁶¹ Ni	⁶⁵ Cu	⁶⁶ Zn	⁷⁵ As	⁸² Se	⁹⁵ Mo	¹⁰¹ Ru	¹⁰³ Rh	¹⁰⁸ Pd	¹⁰⁹ Ag
LOD					58	0.008	0.306	0.276	0.079	0.044	0.6	0.008	0.008	0.001	0.027	0.003
Bushveld Complex	Impala mine	IM-1	Norite	108	364631	111.57	4363	0.75	0.079	2.244	195.8	0.090	0.751	0.066	0.090	0.058
					426961	143.98	5373	0.65	0.187	2.680	175.0	0.008	1.025	0.099	0.122	0.077
					370240	157.29	3335	5.33	0.079	1.496	163.3	0.056	1.266	0.121	0.122	0.164
					378343	169.54	5074	1.25	0.436	2.493	159.4	0.212	0.915	0.061	0.085	0.224
Median IM-1					374292	150.64	4718	1.00	0.133	2.369	169.2	0.073	0.970	0.082	0.106	0.121
Bushveld Complex	Impala mine	IM-3	Norite	98	330349	84.77	4114	1.99	0.079	2.243	98.5	0.008	0.641	0.063	0.090	0.139
					354658	86.64	4525	0.85	0.625	1.434	183.9	0.044	0.109	0.001	0.102	0.089
					330972	90.38	4488	1.75	0.079	22.439	94.2	0.008	1.618	2.867	0.079	0.165
					362137	87.89	4893	0.85	1.434	5.496	184.4	0.046	0.265	0.090	0.027	0.128
					365254	87.26	4581	0.64	0.079	1.371	165.0	0.053	1.265	0.123	0.134	0.125
Median IM-3					354658	87.26	4525	0.85	0.079	2.243	165.0	0.044	0.641	0.090	0.090	0.128
Bushveld Complex	Impala mine	IM-5	Norite	88	319184	128.86	7854	1.05	0.079	0.997	150.8	0.014	0.157	0.003	0.051	0.127
					329726	42.38	4930	2.43	0.243	0.990	159.4	0.142	0.365	0.004	0.356	0.232
					349671	67.32	7168	1.41	0.079	1.336	160.0	0.022	0.433	0.001	0.155	0.355
					330972	64.82	6669	0.95	0.748	1.932	181.9	0.062	0.241	0.053	0.027	0.218
					361514	41.14	4675	1.50	0.313	1.309	177.6	0.049	0.265	0.074	0.099	0.212
					359644	41.76	4170	1.23	0.079	2.119	155.8	0.021	0.465	0.014	0.656	0.318
Median IM-5					340322	53.60	5800	1.32	0.161	1.322	159.7	0.035	0.315	0.009	0.127	0.225
Bushveld Complex	Impala mine	IM-7	Melanorite	78	361514	7.48	4743	3.24	0.935	0.810	166.9	1.496	2.272	0.211	2.355	0.175
					355281	13.84	5797	2.51	0.561	1.448	188.8	0.636	2.359	0.077	1.200	0.319
					342815	18.14	5298	2.87	0.123	0.935	196.3	0.193	1.972	0.055	4.556	0.169
					390077	8.04	5080	1.19	19.946	2.306	199.2	0.106	0.259	0.069	3.666	0.343
Median IM-7					358398	10.94	5189	2.69	0.748	1.191	192.6	0.414	2.122	0.073	3.010	0.247

ANNEXE 17 – Cont.

Intrusion	Locality	Sample	¹¹¹ Cd	¹¹⁵ In	¹¹⁸ Sn	¹²¹ Sb	¹²⁸ Te	¹⁸⁵ Re	¹⁸⁹ Os	¹⁹³ Ir	¹⁹⁵ Pt	¹⁹⁷ Au	²⁰⁵ Tl	²⁰⁸ Pb	²⁰⁹ Bi
LOD			0.025	0.014	0.018	0.012	0.079	0.004	0.008	0.002	0.004	0.007	0.002	0.005	0.002
Bushveld Complex	Impala mine	IM-1	0.224	0.014	0.099	0.012	0.505	0.367	0.287	0.175	0.016	0.007	0.002	0.168	0.699
			0.143	0.014	0.059	0.012	1.079	0.150	0.201	0.137	0.032	0.014	0.002	0.467	0.455
			0.060	0.014	0.107	0.012	0.455	0.130	0.131	0.092	0.004	0.017	0.002	0.493	0.517
			0.081	0.014	0.124	0.012	1.184	0.561	0.642	0.118	0.256	0.007	0.017	0.302	0.580
Median IM-1			0.112	0.014	0.103	0.012	0.792	0.258	0.244	0.128	0.024	0.010	0.002	0.385	0.549
Bushveld Complex	Impala mine	IM-3	0.075	0.014	0.110	0.012	0.686	0.004	0.422	0.122	0.019	0.007	0.002	0.380	0.461
			0.156	0.014	0.133	0.012	1.256	0.082	0.369	0.075	0.004	0.007	0.002	0.530	1.436
			0.076	0.014	0.122	0.012	0.935	0.102	0.310	0.648	0.380	0.007	0.002	0.150	1.247
			0.050	0.014	0.086	0.012	2.320	0.055	0.206	0.086	0.004	0.007	0.002	0.365	0.942
			0.181	0.014	0.059	0.012	0.943	0.099	0.193	0.207	0.004	0.007	0.002	0.268	1.842
Median IM-3			0.076	0.014	0.110	0.012	0.943	0.082	0.310	0.122	0.004	0.007	0.002	0.365	1.247
Bushveld Complex	Impala mine	IM-5	0.025	0.014	0.123	0.012	0.180	0.057	0.146	0.039	0.004	0.007	0.002	0.275	1.524
			0.131	0.014	0.102	0.012	0.386	0.137	0.156	0.056	0.016	0.009	0.002	0.178	1.530
			0.125	0.014	0.150	0.012	1.274	0.139	0.355	0.084	0.004	0.007	0.002	0.704	0.948
			0.206	0.014	0.087	0.012	0.563	0.199	0.217	0.097	0.004	0.007	0.002	0.318	0.701
			0.086	0.014	0.200	0.012	0.517	0.181	0.150	0.076	0.004	0.007	0.002	0.330	0.654
			0.293	0.014	0.033	0.012	0.879	0.200	0.233	0.037	0.009	0.007	0.002	0.133	1.787
Median IM-5			0.128	0.014	0.113	0.012	0.540	0.160	0.187	0.066	0.004	0.007	0.002	0.297	1.236
Bushveld Complex	Impala mine	IM-7	0.243	0.014	0.203	0.012	0.230	0.530	3.114	1.063	2.680	0.007	0.002	1.683	0.002
			0.135	0.014	0.097	0.012	0.307	0.543	2.672	0.606	1.371	0.012	0.002	1.240	0.017
			0.136	0.014	0.076	0.012	0.449	0.139	3.176	0.588	0.760	0.112	0.009	1.434	0.031
			0.249	0.014	0.102	0.012	0.102	0.211	2.026	0.773	0.480	0.007	0.029	4.924	0.018
Median IM-7			0.190	0.014	0.099	0.012	0.268	0.371	2.893	0.690	1.066	0.009	0.006	1.558	0.018

ANNEXE 17 – Cont.

Intrusion	Locality	Sample	Rock	Height (cm)	³⁴ S	⁵⁹ Co	⁶¹ Ni	⁶⁵ Cu	⁶⁶ Zn	⁷⁵ As	⁸² Se	⁹⁵ Mo	¹⁰¹ Ru	¹⁰³ Rh	¹⁰⁸ Pd	¹⁰⁹ Ag
LOD					58	0.008	0.306	0.276	0.079	0.044	0.6	0.008	0.008	0.001	0.027	0.003
Bushveld Complex	Impala mine	IM-9	Melanorite	68	332328	9.72	1456	1.09	0.079	0.686	160.1	0.268	0.480	0.090	0.632	0.263
					312897	10.85	193	5.80	1.435	0.249	178.2	0.030	0.947	0.038	0.212	0.605
					354034	44.88	7230	2.68	0.123	1.808	183.0	0.187	0.743	0.145	0.100	0.087
					377720	22.38	6856	3.55	0.566	1.310	180.5	0.149	1.242	0.074	2.665	0.168
					361514	55.47	4164	43.01	2.255	1.122	168.3	0.313	0.484	0.096	1.003	0.187
					324116	31.17	4619	153.90	13.089	1.377	174.4	0.150	0.091	0.157	0.233	0.287
Median IM-9					343181	26.77	4391	4.67	1.001	1.216	176.3	0.168	0.613	0.093	0.433	0.225
Bushveld Complex	Impala mine	IM-11	Melanorite	58	335959	44.50	6096	4.05	0.659	1.123	256.8	0.093	0.968	0.052	0.090	0.268
					343438	40.23	5971	4.11	0.323	1.873	198.2	0.015	0.020	0.142	0.102	0.642
					344685	42.37	6420	3.18	0.312	1.683	243.7	0.008	0.195	0.001	0.256	0.397
					330972	27.24	5859	5.22	0.079	1.748	218.2	0.058	0.108	0.063	0.099	0.384
					348425	76.67	4612	4.86	0.250	0.873	237.0	0.087	0.016	0.110	0.122	0.243
					359184	53.60	4301	1.40	0.499	1.934	199.5	0.075	0.008	0.088	0.099	0.240
					364007	44.00	7716	5.67	0.448	0.856	250.6	0.100	0.793	0.098	0.066	0.176
Median IM-11					344685	44.00	5971	4.11	0.323	1.683	237.0	0.075	0.108	0.088	0.099	0.268
Bushveld Complex	Impala mine	IM-13	Melanorite	48	403844	43.01	9038	2.10	1.122	0.686	180.6	0.008	0.281	0.001	0.076	0.431
					330349	43.56	4488	3.62	0.376	7.978	187.0	0.008	0.539	0.355	0.053	0.114
					314143	37.90	4425	4.80	0.811	0.561	129.6	0.008	0.359	0.155	0.027	0.997
					396310	39.27	4189	152.91	3.366	0.044	187.6	0.031	0.060	0.012	0.090	0.265
					374603	36.15	5984	1.37	1.456	0.044	158.2	0.037	0.027	0.096	0.122	0.132
					362137	124.04	6981	2.31	0.256	0.937	160.8	0.022	0.009	0.002	0.102	0.289
					347178	40.51	6669	2.56	0.495	1.488	186.9	0.102	0.008	0.122	0.023	0.158
Median IM-13					362137	40.51	5984	2.56	0.811	0.686	180.6	0.022	0.060	0.096	0.076	0.265

ANNEXE 17 – Cont.

Intrusion	Locality	Sample	¹¹¹ Cd	¹¹⁵ In	¹¹⁸ Sn	¹²¹ Sb	¹²⁸ Te	¹⁸⁵ Re	¹⁸⁹ Os	¹⁹³ Ir	¹⁹⁵ Pt	¹⁹⁷ Au	²⁰⁵ Tl	²⁰⁸ Pb	²⁰⁹ Bi
LOD			0.025	0.014	0.018	0.012	0.079	0.004	0.008	0.002	0.004	0.007	0.002	0.005	0.002
Bushveld Complex	Impala mine	IM-9	0.156	0.014	0.206	0.012	0.873	1.247	0.199	0.256	0.004	0.007	0.002	0.598	1.364
			0.225	0.014	0.145	0.012	1.060	0.081	0.311	0.150	0.004	0.013	0.002	0.480	0.866
			0.605	0.014	0.143	0.012	0.810	0.212	0.249	0.224	0.032	0.007	0.002	0.517	0.923
			0.139	0.014	0.211	0.012	0.586	0.182	0.223	0.449	0.031	0.035	0.002	0.393	1.348
			1.234	0.014	0.106	0.012	0.413	0.154	0.175	0.323	0.004	0.050	0.002	0.320	0.773
			0.025	0.014	0.100	0.012	0.967	0.393	0.322	0.345	0.004	0.007	0.010	0.368	1.910
Median IM-9			0.191	0.014	0.144	0.012	0.841	0.197	0.236	0.290	0.004	0.010	0.002	0.436	1.136
Bushveld Complex	Impala mine	IM-11	0.132	0.014	0.118	0.012	0.393	0.122	0.299	0.104	0.037	0.007	0.002	0.379	1.486
			0.856	0.014	0.367	0.069	0.652	0.004	0.221	0.002	0.004	0.026	0.002	1.159	1.035
			0.182	0.014	0.134	0.012	0.324	0.303	0.143	0.090	0.004	0.021	0.002	0.474	0.605
			1.033	0.014	1.033	0.012	0.287	0.249	0.190	0.124	0.004	0.010	0.002	0.654	0.798
			0.193	0.014	0.402	0.012	0.767	0.053	0.193	0.002	0.004	0.020	0.002	0.376	1.947
			0.362	0.014	0.303	0.012	0.436	0.087	0.211	0.066	0.034	0.007	0.002	0.735	1.128
Median IM-11			0.193	0.014	0.303	0.012	0.393	0.122	0.211	0.090	0.004	0.010	0.002	0.474	1.128
Bushveld Complex	Impala mine	IM-13	0.212	0.014	0.018	0.065	0.623	0.004	0.093	0.002	0.004	0.022	0.051	1.808	1.977
			0.287	0.014	0.251	0.168	1.197	0.255	0.148	0.032	0.162	0.007	0.002	1.122	0.986
			0.089	0.014	1.032	0.075	1.130	0.299	0.027	0.002	0.004	0.007	0.002	3.931	5.111
			0.897	0.014	0.187	0.012	1.234	0.200	0.121	0.051	0.004	0.011	0.008	0.274	1.467
			0.231	0.014	0.299	0.012	0.760	0.069	0.234	0.002	0.004	0.028	0.015	0.792	2.362
			0.455	0.014	0.478	0.012	0.900	0.105	0.013	0.042	0.004	0.032	0.024	0.605	0.841
Median IM-13			0.287	0.014	0.251	0.012	0.900	0.105	0.093	0.032	0.004	0.022	0.015	0.792	1.977

ANNEXE 17 – Cont.

Intrusion	Locality	Sample	Rock	Height (cm)	³⁴ S	⁵⁹ Co	⁶¹ Ni	⁶⁵ Cu	⁶⁶ Zn	⁷⁵ As	⁸² Se	⁹⁵ Mo	¹⁰¹ Ru	¹⁰³ Rh	¹⁰⁸ Pd	¹⁰⁹ Ag
LOD					58	0.008	0.306	0.276	0.079	0.044	0.6	0.008	0.008	0.001	0.027	0.003
Bushveld Complex	Impala mine	IM-15	Melanorite	38	335335	19.70	4033	5.18	0.190	0.632	170.8	0.008	0.008	0.001	0.099	0.405
					335335	34.28	4351	9.66	0.326	0.561	154.4	0.008	0.060	0.124	0.069	1.683
Median IM-15					335335	26.99	4192	7.42	0.258	0.597	162.6	0.008	0.034	0.063	0.084	1.044
Bushveld Complex	Impala mine	IM-17	Melanorite	28	355281	19.01	3422	3.43	0.256	1.247	255.7	0.054	0.008	0.001	0.027	0.272
					339699	20.82	4550	4.43	1.522	0.125	211.9	0.105	0.209	0.063	0.070	0.135
					350918	41.20	5236	8.12	1.122	0.189	293.0	0.099	0.146	0.024	0.079	0.116
					373980	26.55	4139	2.37	0.079	0.571	245.7	0.022	0.032	0.079	0.123	0.115
Median IM-17					353099	23.69	4344	3.93	0.689	0.380	250.7	0.076	0.089	0.044	0.074	0.125
Bushveld Complex	Impala mine	IM-18	Melanorite	23	379590	27.92	3709	14.34	0.079	2.496	248.7	0.069	0.008	0.088	0.212	0.087
					348425	24.56	3453	6.23	0.364	1.676	286.7	0.101	0.072	0.076	0.086	0.049
					361514	47.99	6432	2.18	0.254	3.054	238.7	0.029	3.783	0.241	0.322	0.118
Median IM-18					361514	27.92	3709	6.23	0.254	2.496	248.7	0.069	0.072	0.088	0.212	0.087
Bushveld Complex	Impala mine	IM-19	Melanorite	18	398858	66.69	5859	2.12	0.079	1.621	183.3	0.043	0.589	0.088	6.333	0.050
					355281	21.94	5205	1.76	0.079	4.488	212.5	0.461	7.738	0.099	2.666	0.095
					377720	21.88	5535	1.98	0.251	3.241	268.0	0.337	5.736	0.055	0.989	0.090
					368994	23.12	4986	2.30	0.567	4.477	203.2	0.271	4.191	0.145	1.022	0.065
					327233	61.71	6358	154.25	0.689	4.986	199.0	0.280	5.655	0.179	0.369	0.143
					362761	28.86	5946	112.19	0.350	5.236	205.7	0.318	8.220	0.091	2.337	0.067
					398912	19.63	4799	71.26	1.367	6.108	224.1	0.467	0.480	0.233	0.478	0.188
					398912	8.35	3241	5.80	0.079	2.182	172.0	0.255	4.122	0.184	3.670	0.148
362543	17.33	4862	1.56	11.843	1.745	218.6	0.149	1.120	0.216	4.002	0.062					
Median IM-19					368994	21.94	5205	2.30	0.350	4.477	205.7	0.280	4.191	0.145	2.337	0.090

ANNEXE 17 – Cont.

Intrusion	Locality	Sample	¹¹¹ Cd	¹¹⁵ In	¹¹⁸ Sn	¹²¹ Sb	¹²⁸ Te	¹⁸⁵ Re	¹⁸⁹ Os	¹⁹³ Ir	¹⁹⁵ Pt	¹⁹⁷ Au	²⁰⁵ Tl	²⁰⁸ Pb	²⁰⁹ Bi
LOD			0.025	0.014	0.018	0.012	0.079	0.004	0.008	0.002	0.004	0.007	0.002	0.005	0.002
Bushveld Complex	Impala mine	IM-15	0.585	0.014	0.106	0.012	2.309	0.099	0.020	0.002	0.004	0.007	0.012	0.555	0.767
			0.162	0.014	0.087	0.012	1.230	0.143	0.047	0.002	0.004	0.007	0.002	0.002	4.365
Median IM-15			0.374	0.014	0.096	0.012	1.770	0.121	0.033	0.002	0.004	0.007	0.007	2.460	1.723
Bushveld Complex	Impala mine	IM-17	0.436	0.014	0.070	0.012	0.478	0.099	0.231	0.043	0.004	0.007	0.013	2.082	1.393
			0.160	0.014	0.099	0.012	0.580	0.355	0.687	0.063	0.007	0.019	0.002	0.929	1.194
			0.129	0.014	0.077	0.012	0.118	0.106	0.386	0.079	0.004	0.029	0.002	1.066	0.330
			2.032	0.014	0.102	0.012	0.966	0.064	0.512	0.009	0.004	0.016	0.002	0.879	2.654
Median IM-17			0.298	0.014	0.088	0.012	0.529	0.102	0.449	0.053	0.004	0.017	0.002	0.997	1.293
Bushveld Complex	Impala mine	IM-18	0.118	0.014	0.224	0.012	1.109	0.206	0.592	0.055	0.029	0.022	0.199	3.054	0.126
			0.195	0.014	0.102	0.012	0.537	0.099	0.689	0.244	0.004	0.007	0.043	1.776	0.522
			0.587	0.014	0.302	0.012	0.399	0.120	0.841	0.879	0.021	0.007	0.039	0.337	0.418
Median IM-18			0.195	0.014	0.224	0.012	0.537	0.120	0.689	0.244	0.021	0.007	0.043	1.776	0.418
Bushveld Complex	Impala mine	IM-19	0.025	0.016	0.199	0.012	0.524	0.386	0.755	1.200	0.004	0.030	0.156	51.111	0.199
			0.255	0.014	0.302	0.012	0.330	0.424	1.483	2.637	0.081	0.007	0.002	0.330	0.206
			0.025	0.014	0.193	0.012	0.090	0.648	1.764	2.051	0.131	0.007	0.002	0.802	0.212
			0.025	0.014	0.092	0.012	0.081	0.549	1.215	2.238	0.033	0.007	0.002	0.302	0.143
			0.164	0.014	0.203	0.082	0.212	0.324	1.284	1.321	0.007	0.007	0.002	0.661	0.125
			0.367	0.014	0.040	0.034	0.231	0.368	1.627	2.593	0.004	0.007	0.028	0.237	0.445
			0.380	0.014	0.233	0.012	0.156	0.455	1.870	0.067	0.004	0.007	0.062	1.816	0.115
			0.442	0.018	0.181	0.065	0.989	0.854	2.202	0.002	0.004	0.007	0.069	0.767	0.580
			0.025	0.014	0.111	0.012	0.367	0.154	1.546	0.368	0.059	0.007	0.019	0.717	0.181
Median IM-19			0.164	0.014	0.193	0.012	0.231	0.424	1.546	1.321	0.007	0.007	0.019	0.717	0.199

ANNEXE 17 – Cont.

Intrusion	Locality	Sample	Rock	Height (cm)	³⁴ S	⁵⁹ Co	⁶¹ Ni	⁶⁵ Cu	⁶⁶ Zn	⁷⁵ As	⁸² Se	⁹⁵ Mo	¹⁰¹ Ru	¹⁰³ Rh	¹⁰⁸ Pd	¹⁰⁹ Ag
LOD					58	0.008	0.306	0.276	0.079	0.044	0.6	0.008	0.008	0.001	0.027	0.003
Bushveld Complex	Impala mine	IM-20	Melanorite	13	386446	15.46	5535	3.80	0.079	4.799	192.4	0.374	3.480	0.073	0.900	0.045
					384576	13.77	5448	3.94	0.365	4.486	238.0	0.363	6.234	0.121	1.200	0.132
					358398	16.21	5797	2.70	0.079	6.233	211.8	0.430	5.669	0.059	0.745	0.120
					367747	15.58	4986	5.36	2.930	2.122	248.1	0.120	1.461	0.135	0.967	0.003
					351541	13.34	1976	3.38	1.234	1.763	156.9	0.024	2.566	0.246	2.337	0.070
					386174	23.87	6856	4.30	0.241	0.879	256.2	0.266	4.026	0.106	5.023	0.138
					390009	18.45	5360	3.86	1.240	0.044	277.7	0.105	3.684	0.079	0.234	0.164
Median IM-20					384576	15.58	5448	3.86	0.365	2.122	238.0	0.266	3.684	0.106	0.967	0.120
Bushveld Complex	Impala mine	IM-21	Melanorite	8	330349	186.99	3889	7.42	0.079	2.867	167.0	0.281	15.146	0.293	0.255	1.203
					377097	9.16	3684	8.41	0.079	3.740	177.3	0.126	2.201	0.345	0.323	0.436
					373980	14.40	5173	5.55	1.830	3.927	212.0	0.117	10.893	0.125	1.233	0.102
					365796	14.83	3416	201.25	0.878	2.930	201.3	0.175	2.226	0.134	0.423	0.100
					373357	14.96	4139	3.30	0.257	3.677	210.2	0.099	6.234	0.099	5.332	0.088
					357693	10.22	4482	2.48	0.785	2.057	214.7	0.144	4.234	0.345	4.200	0.055
Median IM-21					369576	14.62	4014	6.48	0.521	3.303	205.8	0.135	5.234	0.214	0.828	0.101
Bushveld Complex	Impala mine	IM-22	Upper Chromitite	6	398912	11.22	4488	2.01	0.079	4.987	189.4	0.075	5.211	0.131	0.212	1.371
					342815	10.10	3802	1.68	0.897	2.431	162.7	0.210	2.106	0.545	0.900	0.474
					386446	18.14	5672	3.20	2.022	3.303	189.5	0.125	6.283	0.386	2.022	1.060
					415118	17.58	6108	2.80	11.345	3.615	239.3	0.218	6.964	0.474	0.897	0.661
					375227	16.39	5298	2.08	0.079	4.494	215.4	0.168	4.587	1.244	4.033	1.434
					395172	15.15	4637	3.26	1.255	0.533	233.1	0.355	3.801	0.233	0.246	0.386
					416988	16.14	4893	1.28	0.567	0.165	243.1	0.268	4.054	0.210	0.746	1.069
Median IM-22					395172	16.14	4893	2.08	0.897	3.303	215.4	0.210	4.587	0.386	0.897	1.060

ANNEXE 17 – Cont.

Intrusion	Locality	Sample	¹¹¹ Cd	¹¹⁵ In	¹¹⁸ Sn	¹²¹ Sb	¹²⁸ Te	¹⁸⁵ Re	¹⁸⁹ Os	¹⁹³ Ir	¹⁹⁵ Pt	¹⁹⁷ Au	²⁰⁵ Tl	²⁰⁸ Pb	²⁰⁹ Bi
LOD			0.025	0.014	0.018	0.012	0.079	0.004	0.008	0.002	0.004	0.007	0.002	0.005	0.002
Bushveld Complex	Impala mine	IM-20	0.633	0.014	0.037	0.012	0.357	0.866	0.857	1.184	0.150	0.026	0.002	0.899	0.129
			0.254	0.014	0.110	0.012	0.224	0.337	0.879	2.553	0.355	0.014	0.002	0.943	0.118
			0.025	0.014	0.204	0.012	2.032	0.168	1.228	1.278	0.305	0.035	0.002	0.854	1.224
			0.106	0.014	0.200	0.143	0.387	0.142	0.499	0.569	0.004	0.007	0.002	0.237	0.205
			0.122	0.014	0.201	0.100	1.256	0.479	0.008	2.056	0.014	0.007	0.002	0.537	0.168
			0.117	0.014	0.072	0.044	0.397	0.511	0.823	1.047	0.187	0.007	0.002	0.262	0.268
			0.175	0.030	0.230	0.012	0.617	0.573	1.022	0.792	0.039	0.031	0.002	0.642	0.374
Median IM-20			0.122	0.014	0.200	0.012	0.397	0.479	0.857	1.184	0.150	0.014	0.002	0.642	0.205
Bushveld Complex	Impala mine	IM-21	0.025	0.014	0.072	0.012	0.367	0.405	2.680	2.930	1.621	0.007	0.002	34.905	3.615
			0.037	0.014	0.095	0.069	0.422	0.233	0.051	0.867	0.060	0.007	0.125	14.398	0.138
			0.025	0.014	0.087	0.012	0.145	0.318	3.696	3.241	0.115	0.007	0.002	0.518	0.556
			0.237	0.014	0.230	0.012	0.356	0.327	1.951	0.972	0.499	0.007	0.002	0.581	2.233
			0.025	0.014	0.122	0.012	0.268	0.456	1.066	0.349	0.004	0.007	0.002	0.511	0.056
			0.025	0.014	0.087	0.012	0.079	0.319	1.172	0.480	0.156	0.007	0.002	0.885	0.2233.
Median IM-21			0.025	0.014	0.091	0.012	0.312	0.323	1.561	0.920	0.135	0.007	0.002	0.733	0.556
Bushveld Complex	Impala mine	IM-22	0.099	0.014	0.096	0.012	0.655	0.236	1.265	0.787	0.308	0.007	0.040	2.256	2.221
			0.088	0.014	0.109	0.012	0.262	0.423	2.038	1.639	0.004	0.007	0.002	1.072	0.075
			1.234	0.014	0.402	0.012	0.079	0.295	6.700	5.572	0.586	0.007	0.002	0.549	0.062
			1.022	0.014	0.140	0.032	0.542	0.399	6.233	8.652	0.792	0.007	0.002	0.740	0.123
			0.255	0.014	0.256	0.012	1.233	0.374	6.358	5.261	0.598	0.007	0.002	0.754	0.031
			0.182	0.014	0.018	0.060	0.688	0.357	6.108	4.048	0.262	0.018	0.002	0.779	0.133
			0.049	0.014	0.330	0.012	0.079	0.338	5.610	3.572	0.143	0.007	0.002	1.060	0.061
Median IM-22			0.182	0.014	0.140	0.012	0.542	0.357	6.108	4.048	0.308	0.007	0.002	0.779	0.075

ANNEXE 17 – Cont.

Intrusion	Locality	Sample	Rock	Height (cm)	³⁴ S	⁵⁹ Co	⁶¹ Ni	⁶⁵ Cu	⁶⁶ Zn	⁷⁵ As	⁸² Se	⁹⁵ Mo	¹⁰¹ Ru	¹⁰³ Rh	¹⁰⁸ Pd	¹⁰⁹ Ag
LOD					58	0.008	0.306	0.276	0.079	0.044	0.6	0.008	0.008	0.001	0.027	0.003
Bushveld Complex	Impala mine	IM-24	Lower Chromitite	0	387693	13.15	4238	137.63	0.589	0.044	200.7	0.102	1.233	0.560	0.805	0.106
					393302	13.59	4176	1.43	0.566	1.184	230.0	0.077	1.624	1.233	0.215	1.653
					394549	15.40	4301	0.54	1.230	1.022	223.8	0.059	2.055	3.566	1.233	0.125
					360891	27.43	3303	13.09	0.079	0.945	249.2	0.122	5.201	0.474	2.022	1.745
					372733	13.70	9350	3.68	0.079	0.748	179.5	0.154	3.829	0.393	0.892	0.193
					415118	21.19	5423	5.58	0.079	1.811	211.3	0.075	2.886	2.122	0.498	0.437
					414495	13.28	4494	94.23	0.259	2.475	214.3	0.163	3.014	0.978	0.588	0.183
Median IM-24					393302	13.70	4301	5.58	0.259	1.022	214.3	0.102	2.886	0.978	0.805	0.193
Bushveld Complex	Impala mine	IM-26	Leuconorite	-8	429454	17.33	8228	1.87	0.079	1.060	167.1	0.474	1.781	1.452	2.122	0.119
					370240	13.20	5859	2.93	2.805	1.253	158.9	0.362	1.439	0.119	0.989	0.107
					379590	17.14	7667	2.39	1.099	2.677	188.3	0.126	1.648	1.346	0.755	0.150
					363384	17.02	6283	0.96	0.422	2.063	197.5	0.162	5.622	0.162	3.205	0.640
					395172	19.14	6108	1.12	0.522	2.992	200.1	0.460	2.566	3.234	5.022	0.086
					387069	25.06	4519	2.81	0.358	1.738	188.9	0.561	1.870	0.405	2.012	0.231
Median IM-26					383330	17.23	6196	2.13	0.472	1.901	188.6	0.411	1.826	0.876	2.067	0.134
Bushveld Complex	Impala mine	IM-28	Leuconorite	-23	365145	18.01	4986	8.11	8.539	1.529	145.2	0.046	1.203	0.423	2.666	0.220
					339699	19.88	3254	7.29	0.498	0.633	183.9	0.059	4.567	0.090	0.789	0.352
					358398	18.26	5485	5.81	1.234	2.478	168.3	0.149	0.838	0.125	0.588	0.152
					371487	24.68	4612	5.71	0.258	2.970	242.8	0.062	6.225	0.119	2.188	0.241
Median IM-28					361771	19.07	4799	6.55	0.866	2.003	176.1	0.061	2.885	0.122	1.488	0.231

ANNEXE 17 – Cont.

Intrusion	Locality	Sample	¹¹¹ Cd	¹¹⁵ In	¹¹⁸ Sn	¹²¹ Sb	¹²⁸ Te	¹⁸⁵ Re	¹⁸⁹ Os	¹⁹³ Ir	¹⁹⁵ Pt	¹⁹⁷ Au	²⁰⁵ Tl	²⁰⁸ Pb	²⁰⁹ Bi
LOD			0.025	0.014	0.018	0.012	0.079	0.004	0.008	0.002	0.004	0.007	0.002	0.005	0.002
Bushveld Complex	Impala mine	IM-24	0.149	0.014	0.136	0.090	0.566	0.243	0.666	5.428	0.308	0.007	0.002	0.854	0.144
			0.489	0.014	0.097	0.075	1.202	0.131	2.032	3.060	0.039	0.007	0.002	0.887	0.002
			0.655	0.014	0.206	0.055	0.804	0.079	0.299	1.646	0.087	0.007	0.002	0.777	0.024
			0.423	0.014	0.137	0.012	0.157	0.311	0.106	0.530	0.004	0.007	0.002	1.812	0.552
			0.545	0.014	0.018	0.097	0.202	0.170	5.423	4.079	0.310	0.007	0.016	1.689	0.037
			0.234	0.014	0.123	0.052	0.106	0.214	4.027	3.556	0.343	0.007	0.075	2.326	0.002
			0.305	0.014	0.087	0.026	0.967	0.145	4.675	2.989	0.362	0.007	0.002	0.960	0.112
Median IM-24			0.423	0.014	0.123	0.055	0.566	0.170	2.032	3.060	0.308	0.007	0.002	0.960	0.037
Bushveld Complex	Impala mine	IM-26	0.179	0.014	0.162	0.012	0.661	0.090	5.049	2.549	0.010	0.007	0.002	1.116	0.042
			0.168	0.014	0.130	0.031	3.111	0.810	3.864	1.745	0.249	0.007	0.055	2.619	0.124
			0.099	0.014	0.121	0.012	0.904	0.154	2.468	1.527	0.004	0.007	0.002	1.022	0.090
			0.145	0.014	0.150	0.012	0.579	0.218	3.117	3.664	0.044	0.007	0.002	1.180	0.068
			0.274	0.014	0.189	0.056	2.115	0.138	3.677	1.945	0.092	0.007	0.002	1.309	0.123
			0.212	0.014	0.323	0.081	0.985	0.312	2.842	3.702	0.069	0.007	0.026	2.182	0.062
Median IM-26			0.174	0.014	0.156	0.021	0.944	0.186	3.397	2.247	0.056	0.007	0.002	1.244	0.079
Bushveld Complex	Impala mine	IM-28	0.123	0.014	0.210	0.042	0.414	0.120	0.530	0.874	0.011	0.007	0.023	2.057	0.170
			0.097	0.014	0.124	0.012	0.989	0.090	0.922	0.357	0.037	0.007	0.181	1.684	0.255
			0.256	0.014	0.256	0.012	0.698	0.200	2.244	0.835	0.405	0.007	0.087	2.119	0.047
			0.123	0.014	0.115	0.012	2.322	0.004	2.836	0.474	0.004	0.007	0.002	0.891	0.170
Median IM-28			0.123	0.014	0.167	0.012	0.843	0.105	1.583	0.654	0.024	0.007	0.055	1.870	0.170

ANNEXE 17 – Cont.

Intrusion	Locality	Sample	Rock	Height (cm)	³⁴ S	⁵⁹ Co	⁶¹ Ni	⁶⁵ Cu	⁶⁶ Zn	⁷⁵ As	⁸² Se	⁹⁵ Mo	¹⁰¹ Ru	¹⁰³ Rh
LOD					58	0.008	0.306	0.276	0.079	0.044	0.6	0.008	0.008	0.001
Bushveld Complex	Rustenburg mine	AN	Anorthosite	-2	393194	20.32	3110	1.31	0.234	0.044	246.9	0.123	2.057	0.922
					399427	15.08	4949	7.60	0.562	0.044	224.4	0.673	6.669	0.323
					415118	12.34	4868	6.61	1.234	0.820	237.5	0.670	3.490	0.199
					407638	26.80	4157	5.24	0.436	0.436	213.8	0.480	10.122	1.522
Median AN					403532	17.70	4513	5.92	0.499	0.240	230.9	0.575	5.080	0.623
Bushveld Complex	Rustenburg mine	LC	Lower chromitite	0	416364	10.80	3815	2.99	3.022	0.172	172.0	0.455	3.553	1.069
					381460	8.41	3441	6.98	0.997	0.487	153.3	0.224	1.566	0.256
					407015	10.66	4232	6.11	1.127	0.250	168.9	0.256	6.255	0.522
					406174	11.28	4843	2.12	0.251	0.476	213.7	0.221	2.512	0.123
Median LC					406594	10.73	4023	4.55	1.062	0.363	170.5	0.240	3.032	0.389
Bushveld Complex	Rustenburg mine	CGM-1	Coarse-grained melanorite	2	376310	16.14	3297	2.71	3.054	0.224	210.4	0.054	4.232	0.261
					394549	19.63	3428	11.84	6.856	0.156	200.1	0.143	8.720	0.456
					373871	15.21	3279	2.26	0.268	0.280	198.3	0.187	4.718	0.312
					402652	7.15	1215	4.55	0.586	0.405	195.1	0.240	6.239	0.367
					404522	11.53	3272	4.74	0.087	0.172	193.8	0.312	8.352	0.654
					393302	12.65	3734	5.49	0.293	0.511	203.8	0.524	33.658	1.452
387015	10.54	3709	4.36	0.236	0.479	197.4	0.333	12.092	0.524					
Median CGM-1					393302	12.65	3297	4.55	0.293	0.280	198.3	0.240	8.352	0.456

ANNEXE 17 – Cont.

Locality	Sample	¹⁰⁸ Pd	¹⁰⁹ Ag	¹¹¹ Cd	¹¹⁵ In	¹¹⁸ Sn	¹²¹ Sb	¹²⁸ Te	¹⁸⁵ Re	¹⁸⁹ Os	¹⁹³ Ir	¹⁹⁵ Pt	¹⁹⁷ Au	²⁰⁵ Tl	²⁰⁸ Pb	²⁰⁹ Bi
LOD		0.027	0.003	0.025	0.014	0.018	0.012	0.079	0.004	0.008	0.002	0.004	0.007	0.002	0.005	0.002
Rustenburg mine	AN	0.211	0.757	0.322	0.024	0.150	0.012	1.200	0.123	0.522	2.113	5.367	0.033	0.007	5.634	0.323
		2.034	0.122	0.989	0.090	0.249	0.012	2.123	0.435	4.924	5.553	1.384	0.007	0.002	0.960	1.123
		1.032	0.399	1.367	0.014	0.125	0.012	0.567	0.368	3.690	2.518	0.997	0.007	0.002	3.615	0.175
		0.455	0.108	0.262	0.019	0.456	0.026	0.337	0.318	1.272	1.922	0.549	0.010	0.006	1.932	0.134
Median AN		0.744	0.261	0.655	0.021	0.199	0.012	0.883	0.343	2.481	2.316	1.191	0.008	0.004	2.774	0.249
Rustenburg mine	LC	0.203	0.082	0.211	0.014	0.093	0.027	0.293	0.119	1.596	6.869	0.623	0.007	0.002	0.760	0.255
		0.234	0.153	0.323	0.030	0.117	0.012	0.412	0.187	0.754	2.424	0.218	0.007	0.007	1.521	0.046
		0.123	0.145	1.234	0.023	0.018	0.087	0.100	0.349	1.991	0.636	0.193	0.007	0.002	1.496	0.302
		0.099	0.523	0.025	0.099	0.322	0.069	0.155	0.158	5.291	1.795	0.871	0.009	0.002	2.194	0.167
Median LC		0.163	0.149	0.267	0.026	0.105	0.048	0.224	0.172	1.793	2.110	0.421	0.007	0.002	1.508	0.211
Rustenburg mine	CGM-1	0.456	0.150	0.025	0.014	0.268	0.012	0.079	0.236	5.934	3.914	0.115	0.007	0.002	0.866	0.039
		0.233	0.451	0.025	0.014	0.060	0.012	0.399	0.160	8.564	7.168	0.617	0.007	0.002	0.657	0.153
		0.644	0.113	0.224	0.097	0.041	0.020	0.280	0.141	6.644	4.506	0.486	0.007	0.002	0.524	0.566
		1.120	0.374	0.155	0.014	0.038	0.012	0.755	0.018	5.460	2.618	0.287	0.007	0.002	0.729	0.065
		0.311	1.233	0.025	0.079	0.566	0.012	0.249	0.611	6.171	5.590	0.358	0.007	0.002	0.718	0.060
		0.122	0.194	0.655	0.014	0.449	0.012	0.280	0.580	8.228	8.913	0.742	0.007	0.002	1.377	0.243
		0.234	0.978	1.234	0.014	0.156	2.805	0.234	0.461	5.485	5.292	0.293	0.007	0.002	0.526	0.745
Median CGM-1		0.311	0.374	0.155	0.014	0.156	0.012	0.280	0.236	6.171	5.292	0.358	0.007	0.002	0.718	0.153

ANNEXE 17 – Cont.

Intrusion	Locality	Sample	Rock	Height (cm)	³⁴ S	⁵⁹ Co	⁶¹ Ni	⁶⁵ Cu	⁶⁶ Zn	⁷⁵ As	⁸² Se	⁹⁵ Mo	¹⁰¹ Ru	¹⁰³ Rh
LOD					58	0.008	0.306	0.276	0.079	0.044	0.6	0.008	0.008	0.001
Bushveld Complex	Rustenburg mine	CGM-2	Coarse-grained melanorite	6	375850	7.35	1109	3.43	0.303	0.044	173.9	0.290	10.347	0.140
					390809	7.79	1346	5.25	0.866	0.337	165.8	0.405	25.244	0.291
					410131	9.47	1415	5.73	1.047	0.443	178.3	0.263	19.946	0.209
					367124	14.86	1795	3.65	7.255	0.181	190.1	0.187	38.520	5.111
					372110	4.92	1729	2.57	1.233	0.044	177.4	0.008	0.181	0.405
					391432	11.30	1664	5.50	0.356	0.619	185.7	0.271	20.320	0.188
					419481	10.25	1377	5.38	0.518	0.287	204.1	0.160	10.970	1.103
395796	9.60	1222	6.30	0.517	0.418	196.4	0.162	14.772	0.323					
Median CGM-2					391121	9.54	1396	5.31	0.692	0.312	182.0	0.225	17.359	0.307
Bushveld Complex	Rustenburg mine	UC	Upper chromitite	10	408885	11.66	3060	6.73	1.450	0.253	215.2	0.190	2.618	0.123
					423844	11.14	2680	2.93	0.193	0.570	244.3	0.124	8.352	0.090
					406310	125.22	2817	3.67	0.079	0.774	215.0	0.157	1.870	0.567
					388316	86.96	2188	8.14	0.564	0.869	166.4	0.370	1.278	1.200
					413248	14.74	4450	2.66	0.989	0.234	198.8	0.523	4.438	0.099
422597	11.91	3858	2.62	3.254	0.169	202.6	0.499	1.172	0.422					
Median UC					408885	14.74	3060	2.93	0.880	0.467	215.0	0.237	2.618	0.322
Bushveld Complex	Rustenburg mine	M-1	Melanorite	13.5	406392	7.23	1421	6.54	0.320	0.461	154.0	0.343	4.550	0.126
					391432	9.66	1527	3.62	0.522	0.424	158.6	0.479	17.203	0.323
					403275	7.30	1652	4.11	0.132	0.256	169.5	0.206	5.610	0.211
					403275	8.52	1602	2.74	0.079	0.522	194.3	0.181	2.830	0.367
					381920	9.04	1502	7.73	0.751	0.123	204.4	0.181	1.085	1.256
					411378	4.80	711	7.98	0.079	0.426	185.1	0.009	2.531	0.989
					390194	6.36	798	6.98	0.266	0.312	233.3	0.240	4.924	0.122
Median M-1					397042	8.60	1527	4.36	0.320	0.256	185.1	0.206	4.550	0.267

ANNEXE 17 – Cont.

Locality	Sample	¹⁰⁸ Pd	¹⁰⁹ Ag	¹¹¹ Cd	¹¹⁵ In	¹¹⁸ Sn	¹²¹ Sb	¹²⁸ Te	¹⁸⁵ Re	¹⁸⁹ Os	¹⁹³ Ir	¹⁹⁵ Pt	¹⁹⁷ Au	²⁰⁵ Tl	²⁰⁸ Pb	²⁰⁹ Bi
LOD		0.027	0.003	0.025	0.014	0.018	0.012	0.079	0.004	0.008	0.002	0.004	0.007	0.002	0.005	0.002
Rustenburg mine	CGM-2	0.233	0.234	0.025	0.014	0.789	0.012	0.386	0.478	4.737	4.675	0.199	0.007	0.002	0.611	0.323
		0.456	0.349	0.255	0.090	0.224	0.012	0.545	0.474	6.856	6.563	0.208	0.007	0.002	1.103	0.040
		1.098	0.293	0.076	0.014	0.018	0.012	0.789	0.430	5.248	5.684	0.231	0.007	0.006	1.172	0.074
		1.124	0.667	0.233	0.037	0.327	0.012	0.243	0.054	9.474	6.545	0.411	0.436	0.002	2.168	0.505
		0.212	0.786	0.025	0.014	1.322	0.012	0.176	0.004	0.008	0.567	1.245	0.118	0.002	1.172	0.026
		0.345	0.206	0.145	0.014	0.168	0.012	0.256	0.062	6.607	5.984	0.212	0.007	0.002	1.028	0.072
		0.445	0.425	0.589	0.016	0.018	0.012	0.171	0.052	3.802	5.049	0.107	0.007	0.002	1.134	1.233
		0.523	0.779	0.025	0.014	0.355	0.012	1.234	0.124	6.117	5.859	0.112	0.007	0.003	2.019	0.900
Median CGM-2		0.450	0.387	0.110	0.014	0.276	0.012	0.321	0.093	5.682	5.772	0.210	0.007	0.002	1.153	0.198
Rustenburg mine	UC	0.989	0.659	0.227	0.014	1.109	0.012	0.401	0.231	0.258	17.826	5.547	0.007	0.002	2.001	0.062
		2.356	0.078	0.856	0.014	1.033	0.012	0.303	0.362	2.294	4.749	0.758	0.017	0.002	0.767	0.323
		0.122	0.162	0.099	0.014	0.130	0.013	0.079	0.355	1.608	1.864	0.390	0.007	0.007	1.508	1.300
		0.367	0.341	1.323	0.014	0.566	0.012	0.423	0.573	0.868	2.132	0.573	0.007	0.002	2.759	0.048
		0.136	0.455	0.031	0.014	0.107	0.012	1.022	0.443	4.974	3.677	0.137	0.012	0.002	0.804	0.522
		0.367	0.562	0.122	0.016	0.789	0.020	0.174	0.580	4.351	2.493	1.197	0.007	0.003	0.785	0.100
Median UC		0.367	0.341	0.122	0.014	0.566	0.012	0.317	0.443	2.294	3.677	0.573	0.007	0.002	0.804	0.123
Rustenburg mine	M-1	2.255	0.169	0.025	0.014	0.018	0.012	0.079	0.598	3.615	3.727	0.062	0.007	0.002	0.698	0.123
		0.989	0.249	0.255	0.014	0.237	0.016	0.079	0.723	7.978	5.797	0.350	0.007	0.002	1.091	0.032
		0.789	0.128	0.029	0.070	0.257	0.012	1.200	0.280	3.989	3.671	0.240	0.007	0.002	1.234	0.323
		0.367	0.237	0.855	0.014	0.136	0.012	0.104	0.330	2.562	0.735	0.055	0.016	0.002	2.199	0.256
		0.756	1.200	0.755	0.233	0.150	0.012	0.566	0.246	1.540	0.467	0.081	0.007	0.002	2.231	0.044
		2.365	0.362	0.090	0.014	0.633	0.012	0.878	0.358	2.811	1.116	0.066	0.007	0.002	1.147	0.020
		1.563	0.503	0.025	0.014	0.855	0.012	0.237	0.704	4.301	2.774	0.337	0.007	0.004	1.828	0.045
Median M-1		0.989	0.237	0.178	0.014	0.150	0.012	0.237	0.358	3.397	2.774	0.118	0.007	0.002	1.234	0.045

ANNEXE 17 – Cont.

Intrusion	Locality	Sample	Rock	Height (cm)	³⁴ S	⁵⁹ Co	⁶¹ Ni	⁶⁵ Cu	⁶⁶ Zn	⁷⁵ As	⁸² Se	⁹⁵ Mo	¹⁰¹ Ru	¹⁰³ Rh
LOD					58	0.008	0.306	0.276	0.079	0.044	0.6	0.008	0.008	0.001
Bushveld Complex	Rustenburg mine	M-2	Melanorite	18	406364	8.04	1577	2.24	0.180	0.320	214.6	0.136	5.092	0.234
					413248	9.47	1708	3.43	0.079	0.044	226.9	0.125	4.369	0.136
					407584	11.84	2182	2.97	1.337	0.131	202.0	0.095	5.379	0.786
					387693	12.03	1957	4.36	0.079	0.269	203.7	0.322	5.815	0.122
					380836	12.72	2231	4.60	0.399	0.580	184.4	0.197	10.845	2.367
					371947	23.56	1302	15.15	4.200	0.430	201.9	7.417	25.056	0.717
Median M-2					397029	11.94	1833	3.90	0.290	0.295	202.9	0.166	5.597	0.475
Bushveld Complex	Rustenburg mine	M-3	Melanorite	23	402652	25.18	5485	4.32	0.218	0.233	179.3	0.423	3.771	0.233
					392029	21.57	6065	3.68	12.256	0.566	207.6	3.802	5.223	0.099
					387069	29.17	6090	3.66	2.200	0.274	179.0	0.312	5.173	0.322
					401871	22.31	6221	4.36	0.343	0.305	213.6	0.178	5.547	0.989
					390186	22.94	6152	4.74	0.590	0.143	194.5	0.436	4.263	0.123
					387693	19.88	5610	3.20	0.381	0.044	225.0	0.490	5.260	0.087
Median M-3					391107	22.63	6077	4.00	0.486	0.254	201.0	0.430	5.198	0.178
Bushveld Complex	Rustenburg mine	M-4	Melanorite	27	372733	18.14	4656	1.93	0.411	0.146	181.5	0.169	11.593	5.622
					380836	10.85	3572	3.82	3.567	0.633	216.5	0.255	0.605	0.877
					375850	12.22	3815	4.11	0.516	0.310	191.7	0.167	4.575	0.256
					431947	8.15	3272	1.02	0.328	0.900	162.1	0.122	0.343	0.367
					413248	20.26	4438	2.99	0.545	0.044	203.7	0.119	8.539	0.790
					389563	14.90	3858	2.63	0.430	0.206	191.4	0.147	4.799	0.256
Median M-4					385199	13.56	3836	2.81	0.473	0.258	191.5	0.157	4.687	0.578

ANNEXE 17 – Cont.

Locality	Sample	¹⁰⁸ Pd	¹⁰⁹ Ag	¹¹¹ Cd	¹¹⁵ In	¹¹⁸ Sn	¹²¹ Sb	¹²⁸ Te	¹⁸⁵ Re	¹⁸⁹ Os	¹⁹³ Ir	¹⁹⁵ Pt	¹⁹⁷ Au	²⁰⁵ Tl	²⁰⁸ Pb	²⁰⁹ Bi
LOD		0.027	0.003	0.025	0.014	0.018	0.012	0.079	0.004	0.008	0.002	0.004	0.007	0.002	0.005	0.002
Rustenburg mine	M-2	0.890	0.900	0.025	0.022	0.088	0.012	0.305	0.240	4.020	2.026	0.136	0.007	0.002	0.667	0.099
		0.545	0.255	0.211	0.014	0.049	0.012	2.002	0.268	5.069	1.758	0.188	0.007	0.002	1.024	0.212
		2.333	0.112	0.122	0.086	0.256	0.012	1.522	0.242	4.949	2.562	0.171	0.007	0.002	1.180	0.036
		4.226	0.236	0.025	0.014	0.034	0.035	0.079	0.274	3.017	1.938	0.064	0.007	0.002	1.183	0.655
		3.225	0.074	0.138	0.045	0.421	0.018	1.367	0.278	3.902	2.848	0.103	0.007	0.002	1.258	0.032
		0.989	0.103	0.025	0.014	0.123	1.122	0.900	4.176	8.602	10.035	17.889	0.007	0.004	0.948	0.522
Median M-2		1.661	0.174	0.074	0.018	0.106	0.015	1.133	0.271	4.485	2.294	0.154	0.007	0.002	1.102	0.155
Rustenburg mine	M-3	7.559	0.196	0.126	0.014	0.099	0.012	0.367	0.232	0.898	0.717	0.073	0.007	0.002	1.098	0.203
		0.900	1.323	0.025	0.123	0.084	0.012	0.215	0.891	1.159	0.935	0.073	0.007	0.004	1.109	0.119
		0.248	0.102	0.323	0.014	0.122	0.016	0.079	0.425	1.147	0.960	0.035	0.007	0.002	0.644	0.522
		0.789	0.133	0.025	0.023	0.018	0.012	0.558	0.287	0.979	0.935	0.151	0.007	0.002	0.947	0.118
		0.566	0.855	0.099	0.014	0.367	0.012	0.699	0.154	0.891	0.748	0.004	0.007	0.002	0.904	0.095
		0.478	0.789	0.076	0.014	0.755	0.012	2.226	0.224	1.377	0.979	0.010	0.007	0.436	0.668	0.123
Median M-3		0.677	0.492	0.087	0.014	0.111	0.012	0.462	0.260	1.063	0.935	0.054	0.007	0.002	0.926	0.121
Rustenburg mine	M-4	0.989	1.022	0.063	0.014	0.234	0.012	1.323	0.014	2.101	1.658	0.055	0.007	0.002	0.810	0.022
		0.633	0.199	2.221	0.033	0.422	0.012	0.255	0.157	0.479	0.142	0.004	0.007	0.002	1.558	0.123
		5.633	0.149	0.025	0.099	0.127	0.012	0.190	0.006	1.614	0.742	0.083	0.007	0.002	0.689	0.096
		1.200	0.146	0.029	0.014	0.018	0.012	0.223	0.004	0.505	0.068	0.004	0.007	0.002	0.972	0.102
		0.300	0.175	0.090	0.122	0.086	0.012	0.986	0.526	2.612	2.412	0.271	0.007	0.002	1.343	0.211
		0.256	0.396	0.153	0.014	0.234	0.012	0.310	0.413	2.480	1.247	0.190	0.007	0.011	2.674	0.027
Median M-4		0.811	0.187	0.077	0.024	0.180	0.012	0.283	0.086	1.857	0.994	0.069	0.007	0.002	1.158	0.099

ANNEXE 17 – Cont.

Intrusion	Locality	Sample	Rock	³⁴ S	⁵⁹ Co	⁶¹ Ni	⁶⁵ Cu	⁶⁶ Zn	⁷⁵ As	⁸² Se	⁹⁵ Mo	¹⁰¹ Ru	¹⁰³ Rh	¹⁰⁸ Pd
LOD				58	0.008	0.306	0.276	0.079	0.044	0.6	0.008	0.008	0.001	0.027
Stillwater Complex	East Boulder mine	ST-12	Mela troctolite	378343	42.57	947	5.61	0.079	0.174	255.6	0.056	0.249	1.023	27.200
				442543	17.70	89	19.32	1.371	0.236	157.7	0.008	0.106	1.322	2.022
				375850	23.75	430	517.34	0.349	0.044	176.4	0.062	1.003	0.263	21.023
				406392	50.49	464	218.16	0.623	0.206	196.3	0.044	0.845	0.122	1.185
				386446	25.37	315	11.22	0.168	0.135	236.2	0.008	1.321	0.345	32.022
				418858	14.52	221	8.35	0.524	0.166	134.6	0.014	0.599	0.099	4.337
Median ST-12				396419	24.56	373	15.27	0.436	0.170	186.4	0.029	0.722	0.304	12.680
Stillwater Complex	East Boulder mine	ST-14	Anorthosite	413871	47.93	3790	0.37	0.079	0.044	245.6	0.008	1.988	0.504	5.022
				417611	101.60	5373	1.06	0.249	0.145	221.3	0.098	2.132	1.102	2.102
				437557	94.87	4226	0.28	0.125	0.044	229.4	0.276	0.318	0.202	9.225
				394549	73.55	5678	8.73	0.393	0.162	253.7	0.008	0.143	0.262	14.021
				405063	61.71	4525	0.93	0.598	0.044	274.3	0.145	3.235	0.458	15.234
				420104	51.98	4257	2.06	0.461	0.168	246.8	0.008	2.973	0.425	10.322
404440	76.04	4774	2.49	0.243	0.354	245.6	0.008	3.771	1.097	6.545				
Median ST-14				413871	73.55	4525	1.06	0.249	0.145	245.6	0.008	2.132	0.458	9.225
Stillwater Complex	East Boulder mine	ST-16	Leuconorite	394549	50.67	7018	3.37	0.810	0.044	240.6	0.087	1.489	0.878	3.022
				417584	76.15	8041	2.62	0.380	0.199	273.6	0.293	2.100	0.083	37.394
				399535	71.06	7293	1.62	0.767	0.044	259.9	0.349	2.611	0.201	2.018
				422597	74.48	8602	1.18	0.175	0.099	263.7	0.039	0.879	0.123	0.989
				412625	89.76	8041	1.87	0.079	0.314	254.3	0.137	0.885	0.001	4.211
				388939	44.07	7897	2.49	0.079	0.056	263.2	0.452	1.994	0.922	4.040
Median ST-16				406080	72.77	7969	2.18	0.277	0.077	261.6	0.215	1.741	0.162	3.531

ANNEXE 17 – Cont.

Locality	Sample	¹⁰⁹ Ag	¹¹¹ Cd	¹¹⁵ In	¹¹⁸ Sn	¹²¹ Sb	¹²⁸ Te	¹⁸⁵ Re	¹⁸⁹ Os	¹⁹³ Ir	¹⁹⁵ Pt	¹⁹⁷ Au	²⁰⁵ Tl	²⁰⁸ Pb	²⁰⁹ Bi
LOD		0.003	0.025	0.014	0.018	0.012	0.079	0.004	0.008	0.002	0.004	0.007	0.002	0.005	0.002
East Boulder mine	ST-12	3.255	0.211	0.014	0.125	0.014	0.079	0.004	0.168	0.823	0.004	0.007	0.002	0.343	0.024
		0.879	0.655	0.014	0.018	0.012	0.187	0.032	0.231	0.411	0.004	0.007	0.002	0.935	0.489
		0.262	0.088	0.014	0.018	0.012	0.079	0.004	0.118	0.386	0.008	0.009	0.002	0.580	0.011
		2.979	0.025	0.014	0.214	0.012	0.322	0.025	0.042	0.318	0.004	0.012	0.002	1.878	4.363
		0.137	0.126	0.014	0.025	0.012	0.199	0.048	0.037	0.330	0.088	0.007	0.002	0.430	0.002
		0.891	0.037	0.014	0.086	0.012	0.079	0.004	0.026	0.189	0.022	0.007	0.034	1.646	0.032
Median ST-12		0.885	0.107	0.014	0.055	0.012	0.133	0.015	0.080	0.358	0.006	0.007	0.002	0.757	0.028
East Boulder mine	ST-14	0.455	0.025	0.014	0.037	0.014	0.120	0.007	0.052	4.450	0.024	0.007	0.002	1.621	0.002
		1.355	0.069	0.018	0.337	0.012	0.274	0.022	0.318	2.780	0.015	0.007	0.090	3.927	0.097
		0.898	0.025	0.014	0.237	0.012	0.352	0.096	0.436	1.134	0.004	0.007	0.002	2.743	0.005
		0.399	1.023	0.014	0.018	0.012	0.115	0.010	0.031	0.328	0.230	0.007	0.006	5.797	0.989
		0.799	1.632	0.014	0.112	0.026	0.218	0.008	0.355	2.898	0.013	0.007	0.099	1.533	0.003
		0.259	0.025	0.120	0.452	0.012	0.099	0.088	0.256	2.711	0.004	0.007	0.002	1.215	2.022
		0.312	0.976	0.014	0.044	0.012	0.079	0.004	0.260	3.758	0.004	0.007	0.002	1.315	0.542
Median ST-14		0.455	0.069	0.014	0.112	0.012	0.120	0.010	0.260	2.780	0.013	0.007	0.002	1.621	0.097
East Boulder mine	ST-16	0.443	0.099	0.014	0.234	0.048	0.499	0.623	0.305	0.170	0.027	0.007	0.006	2.306	0.002
		0.735	0.112	0.014	0.323	0.012	0.197	0.632	0.972	1.178	0.123	0.007	0.003	0.443	1.234
		0.150	0.025	0.014	0.056	0.012	0.337	0.561	1.184	1.234	0.019	0.007	0.002	5.700	0.976
		0.212	0.212	0.014	0.099	0.012	0.137	0.118	0.916	0.779	0.198	0.008	0.002	0.573	0.097
		0.648	1.323	0.014	0.018	0.012	0.756	0.499	1.004	0.611	0.099	0.007	0.004	1.751	0.004
		1.255	0.025	0.014	0.037	0.012	0.112	0.062	1.191	1.010	0.034	0.007	0.002	0.424	0.005
Median ST-16		0.545	0.106	0.014	0.077	0.012	0.267	0.530	0.988	0.894	0.067	0.007	0.002	1.162	0.051

ANNEXE 17 – Cont.

Intrusion	Locality	Sample	Rock	³⁴ S	⁵⁹ Co	⁶¹ Ni	⁶⁵ Cu	⁶⁶ Zn	⁷⁵ As	⁸² Se	⁹⁵ Mo	¹⁰¹ Ru	¹⁰³ Rh	¹⁰⁸ Pd
LOD				58	0.008	0.306	0.276	0.079	0.044	0.6	0.008	0.008	0.001	0.027
Stillwater Complex	East Boulder mine	ST-17	Olivine gabbronorite	344685	1.84	152	8.10	0.187	0.187	144.0	0.008	1.367	0.001	1.234
				359021	2.62	24	20.57	0.079	0.499	119.1	0.008	2.589	0.098	5.366
				339699	1.70	268	2.93	0.374	0.044	249.3	0.008	0.106	0.123	0.978
				393926	2.71	354	13.71	0.630	0.605	251.2	0.008	0.979	0.086	2.656
				357151	2.56	256	23.69	0.249	0.125	177.6	0.050	0.156	0.001	5.689
Median ST-17				357151	2.56	256	13.71	0.249	0.187	177.6	0.008	0.979	0.086	2.656
Stillwater Complex	Stillwater mine	P-4	Anorthosite	454386	16.83	6270	0.93	1.234	0.623	383.1	0.076	1.190	0.013	0.063
				397665	15.43	6831	0.42	0.256	0.586	428.1	0.099	1.782	0.605	0.855
				404522	21.32	5747	0.28	0.456	0.823	409.9	0.123	1.795	0.524	1.022
				404522	21.44	7480	0.28	0.224	0.530	413.7	0.008	1.895	1.646	0.122
Median P-4				404522	19.07	6551	0.35	0.356	0.605	411.8	0.087	1.789	0.564	0.489
Stillwater Complex	Stillwater mine	P-3	Leuco gabbronorite	421974	24.06	3054	0.69	0.567	0.044	344.7	0.059	3.054	0.021	0.098
				420728	24.37	2568	1.43	0.190	0.044	327.2	0.098	2.973	0.544	1.022
				424467	24.31	4182	0.28	2.655	0.106	336.0	0.126	4.145	0.307	2.033
				445036	22.50	4351	1.12	0.633	0.159	304.2	0.019	4.700	0.068	0.027
				402652	23.93	2774	0.28	0.368	0.243	294.2	0.041	2.823	0.100	0.522
				410755	25.49	3802	0.28	0.255	0.126	310.4	0.031	3.939	0.174	0.052
Median P-3				421351	24.18	3428	0.48	0.467	0.116	318.8	0.050	3.497	0.137	0.310

ANNEXE 17 – Cont.

Locality	Sample	¹⁰⁹ Ag	¹¹¹ Cd	¹¹⁵ In	¹¹⁸ Sn	¹²¹ Sb	¹²⁸ Te	¹⁸⁵ Re	¹⁸⁹ Os	¹⁹³ Ir	¹⁹⁵ Pt	¹⁹⁷ Au	²⁰⁵ Tl	²⁰⁸ Pb	²⁰⁹ Bi
LOD		0.003	0.025	0.014	0.018	0.012	0.079	0.004	0.008	0.002	0.004	0.007	0.002	0.005	0.002
East Boulder mine	ST-17	0.024	0.044	0.014	0.156	0.017	0.125	0.004	0.032	0.131	0.004	0.007	0.088	0.324	0.002
		1.234	3.256	0.014	0.120	0.012	0.097	0.004	0.099	0.100	0.004	0.007	0.002	0.299	0.009
		0.175	0.755	0.014	0.255	0.012	0.123	0.017	0.008	1.720	0.004	0.007	0.014	0.486	0.234
		0.046	1.656	0.014	0.057	0.012	0.233	0.020	0.053	1.359	0.014	0.007	0.057	0.355	0.125
		0.978	0.978	0.014	0.018	0.025	0.079	0.016	0.059	0.698	0.004	0.007	0.004	0.330	0.002
Median ST-17		0.175	0.978	0.014	0.120	0.012	0.123	0.016	0.053	0.698	0.004	0.007	0.014	0.330	0.009
Stillwater mine	P-4	0.131	0.025	0.014	0.018	0.019	0.423	0.017	0.480	0.760	0.075	0.007	0.002	2.618	0.589
		0.157	1.233	0.014	0.120	0.012	0.146	0.059	0.461	1.022	0.545	0.007	0.003	0.436	0.098
		0.146	0.589	0.014	0.093	0.012	0.150	0.013	0.069	0.424	0.014	0.007	0.090	0.386	0.007
		0.131	0.025	0.014	0.123	0.012	0.234	0.123	0.237	0.505	0.006	0.007	0.100	0.499	0.102
Median P-4		0.139	0.307	0.014	0.107	0.012	0.192	0.038	0.349	0.633	0.044	0.007	0.046	0.467	0.100
Stillwater mine	P-3	0.841	0.025	0.014	0.036	0.012	0.123	0.007	0.231	3.889	0.022	0.007	0.002	4.862	0.200
		0.657	0.031	0.014	0.018	0.029	0.323	0.057	0.342	3.447	0.004	0.007	0.037	4.363	0.123
		0.430	1.033	0.014	0.211	0.032	0.561	0.037	0.337	4.737	0.004	0.007	0.002	2.556	0.355
		0.611	0.026	0.014	0.099	0.019	0.274	0.123	0.232	4.363	0.323	0.011	0.002	3.802	0.005
		0.792	0.123	0.014	0.075	0.062	0.175	0.005	0.224	3.709	0.256	0.007	0.002	12.466	0.099
		0.380	0.025	0.014	0.048	0.012	0.326	0.004	0.181	5.130	0.004	0.007	0.002	1.166	0.099
Median P-3		0.634	0.029	0.014	0.061	0.024	0.298	0.022	0.232	4.126	0.013	0.007	0.002	4.083	0.111

ANNEXE 17 – Cont.

Intrusion	Locality	Sample	Rock	³⁴ S	⁵⁹ Co	⁶¹ Ni	⁶⁵ Cu	⁶⁶ Zn	⁷⁵ As	⁸² Se	⁹⁵ Mo	¹⁰¹ Ru	¹⁰³ Rh	¹⁰⁸ Pd
LOD				58	0.008	0.306	0.276	0.079	0.044	0.6	0.008	0.008	0.001	0.027
Stillwater Complex	Banded Series	BS-18	Leuco gabbronorite	456256	116.06	15645	0.28	0.131	0.212	233.7	0.305	0.008	0.001	0.027
				444413	111.26	12703	0.28	1.033	0.700	216.3	0.118	0.008	0.001	0.079
				441296	126.28	12852	0.28	3.256	0.143	215.7	0.203	0.097	0.001	0.027
				458126	155.70	13021	0.28	0.299	0.137	197.0	0.237	0.008	0.001	0.088
				446283	119.67	13052	0.28	0.266	0.566	215.0	0.356	0.090	0.001	0.027
				446906	112.51	13326	0.28	0.642	0.348	181.4	0.368	0.122	0.001	0.027
				471215	133.64	12491	0.28	0.461	0.150	198.2	0.199	0.008	0.001	0.027
				459995	136.25	11537	0.28	0.873	0.259	239.3	0.143	0.008	0.001	0.027
				439427	118.61	11357	0.28	2.356	0.355	167.7	0.199	0.008	0.001	0.099
				436933	142.92	11874	0.28	0.242	1.322	210.7	0.567	0.008	0.001	0.027
				421351	137.75	15526	0.62	0.118	0.789	229.4	0.008	0.008	0.001	0.027
Median BS-18				446906	133.64	12703	0.28	0.370	0.231	210.7	0.203	0.008	0.001	0.027
Stillwater Complex	Picket Pin	PP-AN	Anorthosite	445036	88.57	6825	0.28	0.212	0.044	195.1	0.131	2.435	0.979	0.989
				414495	124.04	8726	0.28	2.369	1.566	195.7	0.162	1.269	0.866	0.200
				420104	93.00	7673	1.37	0.405	0.088	188.2	0.411	1.631	4.625	0.689
				422597	137.13	9412	0.60	0.966	0.219	128.4	0.008	0.989	0.989	0.545
				413871	84.15	7068	0.28	0.231	0.044	192.6	0.107	1.519	1.907	1.023
				392679	85.21	6289	0.28	2.522	0.367	184.5	1.002	1.207	2.007	0.456
				422597	99.48	8489	0.28	0.588	0.099	189.5	0.137	1.306	0.954	0.878
				400782	86.83	7230	0.28	1.367	0.162	184.4	0.935	1.369	3.235	2.655
				415118	84.39	6619	0.28	0.112	0.175	171.4	0.873	1.637	2.954	4.367
				390186	92.87	6700	0.28	0.079	0.189	171.3	0.323	0.802	1.215	0.589
Median PP-AN				415118	92.87	7068	0.28	0.405	0.162	184.5	0.243	1.369	1.907	0.689

ANNEXE 17 – Cont.

Locality	Sample	¹⁰⁹ Ag	¹¹¹ Cd	¹¹⁵ In	¹¹⁸ Sn	¹²¹ Sb	¹²⁸ Te	¹⁸⁵ Re	¹⁸⁹ Os	¹⁹³ Ir	¹⁹⁵ Pt	¹⁹⁷ Au	²⁰⁵ Tl	²⁰⁸ Pb	²⁰⁹ Bi
LOD		0.003	0.025	0.014	0.018	0.012	0.079	0.004	0.008	0.002	0.004	0.007	0.002	0.005	0.002
Banded Series	BS-18	0.673	0.025	0.014	0.094	0.012	0.079	2.119	0.008	0.002	0.004	0.007	0.022	2.605	0.592
		0.176	0.025	0.014	0.071	0.012	0.380	0.679	0.008	0.002	0.004	0.007	0.002	1.901	0.367
		0.517	0.025	0.014	0.099	0.012	0.079	0.004	0.008	0.002	0.004	0.007	0.002	2.263	0.492
		0.147	0.025	0.014	0.123	0.012	0.079	1.496	0.008	0.002	0.004	0.007	0.002	1.702	0.133
		0.105	0.099	0.014	0.099	0.012	0.079	0.004	0.008	0.002	0.004	0.007	0.002	2.119	0.892
		0.536	0.523	0.014	0.323	0.012	0.598	1.621	0.008	0.002	0.004	0.007	0.002	5.547	1.362
		0.241	0.025	0.014	0.018	0.012	0.362	0.004	0.008	0.002	0.004	0.007	0.002	2.269	0.123
		0.219	0.025	0.014	0.255	0.012	0.312	1.122	0.008	0.002	0.004	0.007	0.002	1.589	0.115
		0.319	0.025	0.014	0.089	0.012	0.511	1.309	0.008	0.002	0.004	0.007	0.002	2.625	1.536
		0.371	0.025	0.014	0.067	0.012	0.779	4.051	0.008	0.002	0.004	0.007	0.002	1.982	0.229
		0.280	0.025	0.014	0.122	0.012	0.079	0.004	0.008	0.014	0.004	0.007	0.002	1.178	0.137
Median BS-18		0.241	0.025	0.014	0.098	0.012	0.079	0.679	0.008	0.002	0.004	0.007	0.002	1.982	0.367
Picket Pin	PP-AN	0.656	0.122	0.014	0.108	0.012	0.079	0.617	1.103	0.511	0.057	0.007	0.002	0.206	0.002
		0.423	1.932	0.014	0.018	0.012	0.079	0.467	0.555	0.642	0.059	0.007	0.016	0.399	0.002
		0.567	0.087	0.014	0.233	0.012	0.900	1.303	0.673	0.398	0.079	0.007	0.002	0.280	0.012
		0.330	2.369	0.014	0.103	0.012	0.079	0.455	0.008	0.002	0.004	0.007	0.002	0.492	0.090
		0.120	0.025	0.014	0.078	0.012	0.455	0.152	0.954	0.542	0.025	0.007	0.002	0.242	0.012
		0.156	2.333	0.014	0.065	0.012	0.656	0.122	0.467	0.045	0.004	0.007	0.002	0.505	0.023
		0.164	0.099	0.014	0.099	0.012	0.079	0.514	0.561	0.475	0.042	0.007	0.002	0.499	0.014
		0.176	0.234	0.014	0.367	0.012	0.456	0.542	0.623	0.510	0.050	0.007	0.002	0.249	0.013
		0.123	0.523	0.014	0.200	0.012	0.079	0.841	0.735	0.623	0.106	0.007	0.002	0.124	0.099
		0.168	0.025	0.014	0.018	0.012	0.099	0.099	0.085	0.158	0.004	0.007	0.002	0.748	0.089
Median PP-AN		0.168	0.122	0.014	0.103	0.012	0.099	0.514	0.623	0.510	0.050	0.007	0.002	0.399	0.014

ANNEXE 18 - Complete data set of LA-ICP-MS analyses of pentlandite obtained in this study and median values for each sample from the Bushveld and Stillwater Complexes. The Fe values used for internal standardization are from Godel et al. (2008a) for samples from the Stillwater Complex, Godel et al. (2007) for samples from the Rustenburg mine, and stoichiometric values (i.e., 32.6%) for samples from the Impala mine. LOD - limit of detection.

ANNEXE 18

Intrusion	Locality	Sample	Rock	Height (cm)	³⁴ S	⁵⁹ Co	⁶¹ Ni	⁶⁵ Cu	⁶⁶ Zn	⁷⁵ As	⁸² Se	⁹⁵ Mo	¹⁰¹ Ru	¹⁰³ Rh	¹⁰⁸ Pd	¹⁰⁹ Ag
LOD					58	0.004	0.3	0.28	0.079	0.044	0.6	0.008	0.01	0.00	0.03	0.003
Bushveld Complex	Impala mine	IM-1	Norite	108	347928	12438	342816	58.32	5.633	15.373	149.3	0.008	0.24	0.22	2.86	2.833
					336715	12256	390720	1.63	0.079	15.210	134.4	0.119	0.35	0.38	2.31	1.205
Median IM-1					342322	12347	366768	29.97	2.856	15.291	141.9	0.063	0.29	0.30	2.58	2.019
Bushveld Complex	Impala mine	IM-3	Norite	98	355968	8882	340912	0.66	0.311	25.920	166.5	0.031	0.70	0.35	2.04	0.318
					391160	10917	407388	0.32	0.079	10.823	187.8	0.098	0.18	0.11	2.42	1.529
					372912	10566	385064	0.69	0.585	12.430	182.3	0.008	1.22	0.38	3.72	1.206
					322575	8563	376768	0.28	0.814	10.419	128.6	0.234	1.27	0.78	2.14	0.324
					341880	8759	363048	10.09	0.079	25.397	159.5	0.020	0.81	0.18	3.35	0.814
					332112	10712	379560	2.47	0.537	9.712	123.5	0.008	0.01	1.12	1.79	0.147
Median IM-3					348924	9724	378164	0.68	0.424	11.627	163.0	0.025	0.75	0.36	2.28	0.569
Bushveld Complex	Impala mine	IM-5	Norite	88	314249	10173	364672	0.52	0.456	1.791	154.5	0.035	0.38	0.18	2.89	0.378
					281970	9052	390256	0.68	0.554	2.116	163.1	0.122	0.18	0.21	2.90	0.414
					344806	10368	364753	3.26	0.179	2.898	157.8	0.270	0.01	0.79	2.96	0.687
					299574	10452	353512	1.92	1.074	0.358	159.1	0.008	1.16	0.86	3.87	0.505
Median IM-5					306911	10270	364713	1.30	0.505	1.954	158.4	0.078	0.28	0.50	2.93	0.459
Bushveld Complex	Impala mine	IM-7	Melanorite	78	319088	7131	380952	45.58	2.735	2.344	167.9	0.053	4.52	19.15	86.24	8.140
					315464	6645	366144	18.12	4.531	2.483	157.9	0.027	3.74	11.24	78.75	6.376
Median IM-7					317276	6888	373548	31.85	3.633	2.414	162.9	0.040	4.13	15.20	82.49	7.258
Bushveld Complex	Impala mine	IM-9	Melanorite	68	346528	8763	349615	216.59	2.266	0.249	165.4	0.088	1.93	0.09	1.79	0.690
					321225	8489	367928	3.06	0.079	16.931	146.8	0.130	0.41	0.34	4.02	0.356
					282946	7896	374482	4.23	1.888	1.088	166.7	0.111	0.23	0.23	14.32	1.104
					292063	8393	320730	47.86	1.237	7.489	98.7	0.039	0.52	0.19	1.40	6.838
					329714	8177	380954	7.81	4.070	6.610	155.8	0.098	0.41	0.04	3.22	1.498
Median IM-9					321225	8393	367928	7.81	1.888	6.610	155.8	0.098	0.41	0.19	3.22	1.104

ANNEXE 18 – Cont.

Intrusion	Locality	Sample	¹¹¹ Cd	¹¹⁵ In	¹¹⁸ Sn	¹²¹ Sb	¹²⁸ Te	¹⁸⁵ Re	¹⁸⁹ Os	¹⁹³ Ir	¹⁹⁵ Pt	¹⁹⁷ Au	²⁰⁵ Tl	²⁰⁸ Pb	²⁰⁹ Bi
LOD			0.025	0.014	0.018	0.012	0.079	0.004	0.008	0.002	0.004	0.007	0.002	0.005	0.002
Bushveld Complex	Impala mine	IM-1	0.267	0.014	0.147	0.137	43.211	0.123	0.13	0.09	0.00	0.007	5.079	15.759	2.758
			0.085	0.088	0.072	0.012	45.258	0.225	0.56	0.17	0.00	0.107	0.142	1.726	2.568
Median IM-1			0.176	0.051	0.109	0.074	44.235	0.174	0.35	0.13	0.00	0.057	2.611	8.742	2.663
Bushveld Complex	Impala mine	IM-3	0.025	0.014	0.018	0.012	33.214	0.339	0.24	0.04	0.01	0.009	1.071	5.530	1.577
			0.075	0.211	0.100	0.012	34.836	0.071	0.01	0.03	0.00	0.030	0.033	0.068	0.655
			0.252	0.566	0.084	0.012	50.453	0.395	0.11	0.05	0.03	0.007	0.019	2.925	2.011
			0.136	0.014	0.067	0.012	11.168	0.113	0.03	0.04	0.00	0.009	0.039	0.324	2.215
			0.140	0.014	0.018	0.117	24.094	0.236	0.11	0.03	0.00	0.037	0.189	1.074	1.187
			0.137	0.032	0.018	0.012	39.377	0.083	0.04	0.02	0.00	0.036	0.479	2.572	2.826
Median IM-3			0.136	0.023	0.043	0.012	34.025	0.174	0.07	0.04	0.00	0.019	0.114	1.823	1.794
Bushveld Complex	Impala mine	IM-5	0.117	0.014	0.018	0.012	8.005	0.189	0.08	0.04	0.00	0.007	0.114	0.365	0.122
			0.026	0.014	0.018	0.012	10.777	0.169	0.10	0.07	0.01	0.018	0.038	0.150	0.817
			0.025	0.014	0.018	0.012	6.940	0.004	0.02	0.29	0.02	0.016	2.572	4.396	1.335
			0.218	0.014	0.018	0.098	10.628	0.004	0.20	0.00	0.00	0.037	1.205	7.163	2.684
Median IM-5			0.072	0.014	0.018	0.012	9.316	0.086	0.09	0.06	0.01	0.017	0.659	2.380	1.076
Bushveld Complex	Impala mine	IM-7	0.130	0.014	0.018	0.161	0.241	0.153	4.30	2.55	2.67	0.007	3.321	7.814	0.018
			0.154	0.123	0.050	0.137	0.134	0.319	3.81	1.07	4.43	0.011	0.638	2.987	0.025
Median IM-7			0.142	0.068	0.034	0.149	0.188	0.236	4.06	1.81	3.55	0.009	1.979	5.401	0.021
Bushveld Complex	Impala mine	IM-9	0.114	0.014	0.124	0.068	28.107	0.149	0.58	0.39	0.00	0.007	0.117	0.957	4.661
			2.024	0.756	0.018	0.065	27.192	0.303	0.58	0.35	0.01	0.014	0.104	0.863	2.247
			1.022	0.014	0.146	0.110	19.182	0.505	0.11	0.26	0.00	0.007	11.070	35.490	1.791
			0.208	0.067	0.088	0.114	30.932	0.199	0.11	0.10	0.00	0.027	0.160	2.120	3.028
			0.025	0.014	0.018	0.091	19.862	0.081	0.09	0.12	0.00	0.012	2.019	11.950	5.275
Median IM-9			0.208	0.014	0.088	0.091	27.192	0.199	0.11	0.26	0.00	0.012	0.160	2.120	3.028

ANNEXE 18 – Cont.

Intrusion	Locality	Sample	Rock	Height (cm)	³⁴ S	⁵⁹ Co	⁶¹ Ni	⁶⁵ Cu	⁶⁶ Zn	⁷⁵ As	⁸² Se	⁹⁵ Mo	¹⁰¹ Ru	¹⁰³ Rh	¹⁰⁸ Pd	¹⁰⁹ Ag
LOD					58	0.004	0.3	0.28	0.079	0.044	0.6	0.008	0.01	0.00	0.03	0.003
Bushveld Complex	Impala mine	IM-11	Melanorite	58	309320	9921	365144	52.10	2.051	4.233	154.9	0.069	5.55	0.18	2.11	1.628
					330621	8896	393962	1.24	0.079	1.502	158.8	0.008	0.28	0.57	2.89	0.228
					324432	10047	323504	4.92	0.079	3.614	151.0	0.008	2.36	0.14	2.14	0.879
					349784	10094	371203	2.83	1.097	8.400	168.6	0.097	0.77	0.28	2.05	1.220
					296296	9238	350263	6.25	0.079	3.321	133.5	0.008	0.46	0.18	1.57	0.280
					335368	10489	364685	19.54	0.789	4.624	147.8	0.008	0.58	0.68	2.28	2.179
Median IM-11					327526	9984	364915	5.58	0.434	3.923	152.9	0.008	0.67	0.23	2.13	1.050
Bushveld Complex	Impala mine	IM-13	Melanorite	48	306447	12472	371022	0.81	1.335	20.187	260.5	0.070	0.95	1.76	5.20	0.283
					367678	16606	363513	0.85	1.172	17.257	237.7	0.008	1.59	0.31	6.48	0.508
					328856	10363	358160	0.86	0.391	24.094	150.8	0.122	0.39	0.32	3.29	0.427
					302808	1366	387464	2.60	0.586	38.746	198.6	0.008	1.10	1.59	3.19	0.424
Median IM-13					317652	11418	367268	0.85	0.879	22.141	218.2	0.039	1.03	0.95	4.24	0.426
Bushveld Complex	Impala mine	IM-15	Melanorite	38	330248	12405	328856	15.30	3.972	30.932	152.7	0.008	3.18	5.77	1.81	12.698
Median IM-15					330248	12405	328856	15.30	3.972	30.932	152.7	0.008	3.18	5.77	1.81	12.698
Bushveld Complex	Impala mine	IM-17	Melanorite	28	326992	10387	328902	26.55	2.116	9.768	127.8	0.008	0.99	2.36	13.20	0.716
					296257	12275	346103	7.49	0.716	9.931	155.1	0.026	0.72	0.28	35.11	0.912
					309378	12177	361416	6.84	0.896	2.182	145.4	0.157	0.10	0.47	8.22	0.501
Median IM-17					309378	12177	346103	7.49	0.896	9.768	145.4	0.026	0.72	0.47	13.20	0.716
Bushveld Complex	Impala mine	IM-18	Melanorite	23	328758	9866	380261	387	6.186	5.958	151.9	0.008	0.14	18.62	49.48	1.081
					297598	18559	354904	866	0.079	9.866	137.4	0.021	1.21	8.23	14.34	0.803
Median IM-18					313178	14212	367583	627	3.133	7.912	144.6	0.015	0.68	13.42	31.91	0.942

ANNEXE 18 – Cont.

Intrusion	Locality	Sample	¹¹¹ Cd	¹¹⁵ In	¹¹⁸ Sn	¹²¹ Sb	¹²⁸ Te	¹⁸⁵ Re	¹⁸⁹ Os	¹⁹³ Ir	¹⁹⁵ Pt	¹⁹⁷ Au	²⁰⁵ Tl	²⁰⁸ Pb	²⁰⁹ Bi
LOD			0.025	0.014	0.018	0.012	0.079	0.004	0.008	0.002	0.004	0.007	0.002	0.005	0.002
Bushveld Complex	Impala mine	IM-11	0.025	0.014	0.303	0.012	17.521	0.316	1.17	0.22	0.00	0.017	0.143	2.019	1.332
			0.179	0.014	0.018	0.012	12.465	0.174	0.02	0.00	0.00	0.007	0.021	0.215	0.163
			0.293	0.088	0.153	0.012	9.442	0.094	0.01	0.10	0.00	0.022	0.716	2.051	2.609
			0.173	1.002	0.052	0.101	14.001	0.137	0.19	0.16	0.00	0.007	0.407	5.893	0.879
			2.878	0.014	0.018	0.012	9.679	0.352	0.03	0.06	0.00	0.020	0.010	0.163	2.255
			0.025	0.645	0.211	0.012	21.164	0.095	0.16	0.11	0.00	0.023	0.293	1.302	1.531
Median IM-11			0.176	0.051	0.103	0.012	13.233	0.155	0.10	0.10	0.00	0.018	0.218	1.661	1.431
Bushveld Complex	Impala mine	IM-13	0.423	0.014	0.148	0.111	22.466	0.081	0.21	0.08	0.03	0.024	0.127	0.381	1.205
			0.878	0.014	0.119	0.012	14.558	0.228	0.22	0.01	0.00	0.007	0.137	0.912	1.742
			0.025	1.033	0.116	0.091	16.280	0.163	0.23	0.06	0.00	0.022	0.002	0.169	0.120
			0.025	0.014	0.358	0.012	23.350	0.004	0.01	0.12	0.00	0.007	0.089	0.757	1.407
Median IM-13			0.224	0.014	0.133	0.051	19.373	0.122	0.22	0.07	0.00	0.014	0.108	0.569	1.306
Bushveld Complex	Impala mine	IM-15	0.326	0.069	0.328	0.012	33.769	0.267	0.33	0.03	0.00	0.033	24.094	76.842	2.768
Median IM-15			0.326	0.069	0.328	0.012	33.769	0.267	0.33	0.03	0.00	0.033	24.094	76.842	2.768
Bushveld Complex	Impala mine	IM-17	0.391	0.014	0.124	0.012	21.815	0.065	0.60	0.01	0.00	0.007	0.456	38.095	0.891
			0.989	1.224	0.125	0.279	12.940	0.004	0.36	0.11	0.04	0.009	0.672	18.234	0.671
			0.025	0.014	0.166	0.012	18.466	0.133	0.21	0.02	0.00	0.007	0.254	3.191	2.391
Median IM-17			0.391	0.014	0.125	0.012	18.466	0.065	0.36	0.02	0.00	0.007	0.456	18.234	0.891
Bushveld Complex	Impala mine	IM-18	0.475	0.014	0.257	0.146	15.075	0.186	0.57	0.19	0.03	0.013	0.391	6.024	0.176
			2.554	0.088	0.018	0.012	5.112	0.004	0.01	0.10	0.00	0.007	4.233	13.024	0.353
Median IM-18			1.515	0.051	0.138	0.079	10.094	0.095	0.29	0.14	0.02	0.010	2.312	9.524	0.265

ANNEXE 18 – Cont.

Intrusion	Locality	Sample	Rock	Height (cm)	³⁴ S	⁵⁹ Co	⁶¹ Ni	⁶⁵ Cu	⁶⁶ Zn	⁷⁵ As	⁸² Se	⁹⁵ Mo	¹⁰¹ Ru	¹⁰³ Rh	¹⁰⁸ Pd	¹⁰⁹ Ag
LOD					58	0.004	0.3	0.28	0.079	0.044	0.6	0.008	0.01	0.00	0.03	0.003
Bushveld Complex	Impala mine	IM-19	Melanorite	18	351648	9638	403753	0.63	2.963	2.930	169.3	0.008	1.02	5.26	133.20	0.840
					313553	7000	375023	765.20	2.475	1.465	72.9	0.008	0.37	15.99	216.85	0.648
					324298	9657	401203	1.50	0.079	1.302	215.9	0.008	9.47	21.07	242.57	0.658
					309247	7163	420154	1.36	0.079	0.716	185.6	0.094	15.11	15.03	230.20	0.479
					328714	6772	358176	87.91	0.079	1.140	201.9	0.008	5.53	22.00	302.21	0.332
					309281	8010	364096	2.34	0.521	2.051	273.5	0.110	3.15	16.15	247.34	0.274
					348134	11103	357183	4.25	0.079	1.009	129.9	0.026	17.23	39.02	135.78	0.570
					354873	6317	322344	129.44	0.079	1.100	195.4	0.008	4.03	16.97	201.34	0.628
Median IM-19					326506	7586	369560	3.30	0.079	1.221	190.5	0.008	4.78	16.56	223.52	0.599
Bushveld Complex	Impala mine	IM-20	Melanorite	13	319075	4200	364724	30.61	4.786	0.195	162.8	0.052	0.01	16.54	81.18	0.583
					337411	6838	338624	126.27	0.079	0.535	115.9	0.008	6.12	0.18	26.04	0.401
					320016	10233	315226	11.40	0.079	1.335	93.1	0.123	0.23	52.24	128.90	0.736
					351626	5177	423280	24.42	0.079	0.474	179.3	0.302	1.26	11.01	142.94	0.456
					348475	9754	335368	19.02	0.079	2.214	180.1	0.008	3.11	4.23	117.91	0.736
					319124	5698	324949	1.49	0.124	1.146	197.6	0.008	0.66	4.92	102.89	0.664
					315832	9654	345136	18.56	0.079	0.684	156.3	1.004	0.01	8.22	102.66	0.563
					312685	6479	377696	17.58	0.079	1.530	117.9	0.008	0.88	21.98	144.25	1.335
					283314	7033	328902	5.08	0.079	0.357	218.2	0.008	0.79	15.60	51.12	0.459
					319127	7684	328844	13.35	0.079	0.548	203.6	0.078	0.01	4.59	56.32	1.400
Median IM-20					319126	6935	336996	18.07	0.079	0.616	171.0	0.030	0.72	9.61	102.78	0.624

ANNEXE 18 – Cont.

Intrusion	Locality	Sample	¹¹¹ Cd	¹¹⁵ In	¹¹⁸ Sn	¹²¹ Sb	¹²⁸ Te	¹⁸⁵ Re	¹⁸⁹ Os	¹⁹³ Ir	¹⁹⁵ Pt	¹⁹⁷ Au	²⁰⁵ Tl	²⁰⁸ Pb	²⁰⁹ Bi
LOD			0.025	0.014	0.018	0.012	0.079	0.004	0.008	0.002	0.004	0.007	0.002	0.005	0.002
Bushveld Complex	Impala mine	IM-19	0.260	0.014	0.018	0.012	3.502	0.114	0.05	0.21	0.00	0.007	1.856	5.861	0.703
			0.025	0.014	0.131	0.012	0.625	0.251	1.05	2.47	0.00	0.011	5.210	28.653	0.177
			0.182	0.027	0.018	0.012	1.823	0.166	2.64	3.45	0.00	0.010	1.888	3.614	0.040
			0.025	0.014	0.098	0.012	0.781	0.599	5.80	2.07	0.04	0.007	0.021	0.651	0.072
			2.013	0.022	0.102	0.042	0.790	0.293	2.21	1.57	0.00	0.007	0.348	1.042	0.121
			0.039	0.069	0.060	0.012	2.833	0.144	0.72	0.80	0.00	0.007	2.149	4.982	0.234
			0.025	0.014	0.018	0.012	0.699	0.004	0.04	3.23	0.00	0.007	2.312	9.768	0.789
			2.441	0.014	0.091	0.012	0.753	0.257	2.02	0.82	0.00	0.007	0.444	7.825	0.055
Median IM-19			0.111	0.014	0.076	0.012	0.786	0.208	1.54	1.82	0.00	0.007	1.872	5.421	0.149
Bushveld Complex	Impala mine	IM-20	0.025	0.122	0.086	0.012	0.237	0.254	1.47	1.36	0.00	0.007	0.041	2.344	0.117
			0.091	0.056	0.018	0.012	0.757	0.004	0.01	2.02	0.00	0.024	0.046	1.433	0.352
			0.025	0.014	0.057	0.012	3.647	1.006	1.12	0.04	0.00	0.007	0.127	3.223	0.124
			1.079	0.014	0.018	0.012	0.315	0.720	1.27	1.27	0.01	0.007	0.002	0.565	0.045
			0.231	2.001	0.127	0.012	1.140	0.287	0.76	0.41	0.00	0.007	2.150	6.512	0.202
			0.025	0.014	0.062	0.012	0.959	0.475	0.49	0.05	0.00	0.026	1.477	2.590	0.358
			0.989	0.062	0.208	0.081	0.079	0.238	0.42	4.66	0.00	0.007	0.059	1.368	1.848
			0.878	0.014	0.018	0.012	0.098	0.004	1.24	0.02	0.00	0.007	0.062	0.394	0.878
			0.025	0.014	0.099	0.069	0.079	0.326	1.37	1.58	0.02	0.007	0.107	0.804	0.757
			0.184	0.014	0.097	0.012	0.228	0.110	0.31	0.39	0.02	0.007	8.791	21.815	0.869
Median IM-20			0.138	0.014	0.074	0.012	0.276	0.270	0.94	0.84	0.00	0.007	0.085	1.888	0.355

ANNEXE 18 – Cont.

Intrusion	Locality	Sample	Rock	Height (cm)	³⁴ S	⁵⁹ Co	⁶¹ Ni	⁶⁵ Cu	⁶⁶ Zn	⁷⁵ As	⁸² Se	⁹⁵ Mo	¹⁰¹ Ru	¹⁰³ Rh	¹⁰⁸ Pd	¹⁰⁹ Ag
LOD					58	0.004	0.3	0.28	0.079	0.044	0.6	0.008	0.01	0.00	0.03	0.003
Bushveld Complex	Impala mine	IM-21	Melanorite	8	338624	4396	328953	5.14	0.362	0.637	120.3	0.008	2.99	14.65	160.85	0.723
					338577	4527	340578	72.15	0.079	0.393	144.2	0.075	5.00	1.54	162.80	1.090
					343301	8956	361566	541.20	1.921	0.781	123.3	0.008	0.01	6.26	301.21	1.397
					338601	5340	384208	20.51	0.079	1.089	166.1	0.510	6.70	3.55	256.48	1.357
					328768	4949	257224	15.63	0.079	0.205	159.9	0.098	22.54	20.19	72.61	1.029
					315468	6284	338656	3.45	0.079	0.488	160.9	0.045	20.26	15.24	36.15	0.892
					351702	6349	371254	4.69	2.898	0.456	154.0	0.065	14.62	35.88	56.97	0.700
Median IM-21					338601	5340	340578	15.63	0.079	0.488	154.0	0.065	6.70	14.65	160.85	1.029
Bushveld Complex	Impala mine	IM-22	Upper Chromitite	6	317786	4754	372698	14.65	0.079	1.823	132.8	0.008	2.17	47.54	143.58	1.563
					270135	2368	361423	8.14	0.985	2.442	109.7	0.310	0.20	58.23	89.22	4.558
					393976	5503	348392	2.41	2.423	0.297	136.5	0.008	1.21	3.55	149.77	4.884
					325600	2670	398616	16.28	4.884	0.670	143.3	0.159	0.01	9.22	105.50	32.560
					323972	4591	366987	4.56	2.344	0.391	124.8	0.008	4.36	11.85	284.26	3.907
Median IM-22					323972	4591	366987	8.14	2.344	0.670	132.8	0.008	1.21	11.85	143.58	4.558
Bushveld Complex	Impala mine	IM-24	Lower Chromitite	0	335368	4689	375236	1.02	0.079	0.044	188.8	0.357	9.70	244.20	285.22	1.368
					312576	4624	337955	140.82	0.658	0.725	170.6	0.008	7.00	137.08	325.20	4.742
					302808	5000	339243	87.31	0.387	1.661	186.9	0.008	5.27	94.42	175.18	1.357
					397232	4917	385398	1.89	0.079	2.670	274.3	0.008	16.23	62.52	199.59	0.612
					374440	5861	428973	1.94	0.127	1.563	262.6	0.872	28.02	615.38	92.15	1.370
					354785	5144	376755	1.73	1.254	0.700	164.9	0.008	2.86	729.34	387.23	7.814
					329711	5613	336132	8.47	0.079	0.044	224.7	1.023	31.96	413.51	172.57	1.237
					312523	4587	374658	0.43	1.875	1.628	151.7	0.008	14.38	145.22	200.25	1.446
Median IM-24					332540	4958	374947	1.91	0.257	1.144	187.9	0.008	12.04	194.71	199.92	1.369

ANNEXE 18 – Cont.

Intrusion	Locality	Sample	¹¹¹ Cd	¹¹⁵ In	¹¹⁸ Sn	¹²¹ Sb	¹²⁸ Te	¹⁸⁵ Re	¹⁸⁹ Os	¹⁹³ Ir	¹⁹⁵ Pt	¹⁹⁷ Au	²⁰⁵ Tl	²⁰⁸ Pb	²⁰⁹ Bi
LOD			0.025	0.014	0.018	0.012	0.079	0.004	0.008	0.002	0.004	0.007	0.002	0.005	0.002
Bushveld Complex	Impala mine	IM-21	0.025	0.014	0.020	0.012	0.300	0.221	0.81	2.79	0.85	0.007	0.002	100.936	1.023
			1.033	2.666	0.075	0.046	0.326	0.068	0.25	3.23	0.60	0.007	1.758	9.776	0.062
			0.112	0.014	0.076	0.078	0.079	0.056	0.01	0.86	1.17	0.015	1.498	13.147	1.552
			0.412	3.001	0.104	0.012	0.358	0.274	2.57	1.01	0.92	0.007	2.279	9.123	0.068
			0.025	0.989	0.018	0.012	0.130	0.273	5.89	12.37	8.56	0.021	10.680	53.073	6.089
			0.025	0.014	0.122	0.012	0.197	0.241	5.57	4.36	0.13	0.015	2.051	21.164	0.107
			0.228	0.014	0.879	0.086	0.652	0.116	5.24	3.32	0.16	0.007	1.890	39.144	0.030
Median IM-21			0.112	0.014	0.076	0.012	0.300	0.221	2.57	3.23	0.85	0.007	1.890	21.164	0.107
Bushveld Complex	Impala mine	IM-22	0.143	0.014	0.037	0.012	0.723	0.345	7.00	4.66	5.70	0.007	0.879	9.125	0.039
			2.112	0.689	0.076	0.012	0.783	0.004	1.04	11.23	0.85	0.007	0.958	24.746	0.381
			0.877	0.014	0.018	0.012	0.230	0.245	0.11	0.22	1.82	0.007	0.697	7.897	0.422
			0.025	0.723	2.605	0.123	0.079	0.004	2.03	0.98	0.94	0.007	4.558	59.585	0.125
			0.202	0.014	0.124	0.079	0.356	0.300	5.08	3.19	2.34	0.007	2.702	19.862	0.101
Median IM-22			0.202	0.014	0.076	0.012	0.356	0.245	2.03	3.19	1.82	0.007	0.958	19.862	0.125
Bushveld Complex	Impala mine	IM-24	0.025	0.015	0.070	0.012	0.130	0.088	3.97	22.23	3.65	0.007	1.009	3.940	0.021
			0.025	0.088	0.018	0.012	0.488	0.240	2.18	7.10	3.26	0.007	0.065	2.182	0.026
			0.756	0.014	0.018	0.012	1.042	0.189	2.18	4.72	4.07	0.007	0.890	4.367	0.046
			0.088	0.122	0.211	0.040	0.210	0.092	1.40	11.75	4.40	0.007	0.042	0.628	0.002
			0.211	0.014	0.098	0.012	0.240	0.057	1.09	26.05	5.54	0.007	0.018	1.563	1.689
			0.025	0.233	0.018	0.012	0.244	0.004	4.03	23.12	4.20	0.007	0.221	1.878	0.002
			0.025	0.033	0.018	0.099	1.237	0.319	18.88	10.09	2.18	0.007	0.002	0.540	0.002
			0.025	0.014	0.087	0.012	0.386	0.423	15.01	7.20	4.04	0.021	0.052	2.214	2.211
Median IM-24			0.025	0.024	0.044	0.012	0.315	0.141	3.08	10.92	4.05	0.007	0.059	2.030	0.024

ANNEXE 18 – Cont.

Intrusion	Locality	Sample	Rock	Height (cm)	³⁴ S	⁵⁹ Co	⁶¹ Ni	⁶⁵ Cu	⁶⁶ Zn	⁷⁵ As	⁸² Se	⁹⁵ Mo	¹⁰¹ Ru	¹⁰³ Rh	¹⁰⁸ Pd	¹⁰⁹ Ag
LOD					58	0.004	0.3	0.28	0.079	0.044	0.6	0.008	0.01	0.00	0.03	0.003
Bushveld Complex	Impala mine	IM-26	Leuconorite	-8	329102	4103	315923	192.74	25.071	1.237	170.0	0.033	0.10	5.26	208.38	3.821
					309411	4037	387542	6.02	2.996	1.777	185.4	0.008	0.54	2.22	354.91	2.817
					351724	3223	325600	8.47	8.767	1.831	175.4	2.605	0.01	8.92	236.38	0.635
					304110	4435	347456	5.44	11.233	1.368	155.6	0.008	0.72	43.63	175.82	0.899
					319073	3028	399792	29.96	10.419	0.707	169.6	0.008	0.01	52.10	257.23	0.433
Median IM-26					319073	4037	347456	8.47	10.419	1.368	170.0	0.008	0.10	8.92	236.38	0.899
Bushveld Complex	Impala mine	IM-28	Leuconorite	-23	302825	6642	351648	4.04	6.838	0.433	142.9	0.038	1.50	25.07	402.82	1.270
					319133	3972	383498	13.97	0.079	0.301	137.5	0.008	0.01	16.25	319.09	3.557
					Median IM-28					310979	5307	367573	9.00	3.458	0.367	140.2

ANNEXE 18 – Cont.

Intrusion	Locality	Sample	¹¹¹ Cd	¹¹⁵ In	¹¹⁸ Sn	¹²¹ Sb	¹²⁸ Te	¹⁸⁵ Re	¹⁸⁹ Os	¹⁹³ Ir	¹⁹⁵ Pt	¹⁹⁷ Au	²⁰⁵ Tl	²⁰⁸ Pb	²⁰⁹ Bi
LOD			0.025	0.014	0.018	0.012	0.079	0.004	0.008	0.002	0.004	0.007	0.002	0.005	0.002
Bushveld Complex	Impala mine	IM-26	0.237	0.039	0.511	0.078	0.456	0.086	2.42	1.80	1.11	0.016	17.582	34.839	3.061
			0.025	0.023	0.179	0.012	1.864	0.010	1.18	8.99	0.06	0.007	3.451	12.698	0.781
			0.088	0.014	0.109	0.036	0.410	0.035	1.75	0.42	1.40	0.007	1.865	9.125	1.107
			0.634	0.054	0.173	0.012	0.267	0.028	2.77	18.88	4.64	0.023	4.265	33.537	6.121
			0.025	0.014	0.231	0.012	0.491	0.195	4.33	0.72	0.92	0.062	1.954	10.094	0.199
Median IM-26			0.088	0.023	0.179	0.012	0.456	0.035	2.42	1.80	1.11	0.016	3.451	12.698	1.107
Bushveld Complex	Impala mine	IM-28	0.025	0.014	0.195	0.036	0.164	0.280	3.19	1.53	3.39	0.012	0.218	7.684	0.205
			0.566	0.014	0.070	0.012	0.489	0.004	1.28	1.97	3.35	0.007	4.037	13.675	0.515
Median IM-28			0.296	0.014	0.133	0.024	0.327	0.142	2.24	1.75	3.37	0.009	2.128	10.680	0.360

ANNEXE 18 – Cont.

Intrusion	Locality	Sample	Rock	Height (cm)	³⁴ S	⁵⁹ Co	⁶¹ Ni	⁶⁵ Cu	⁶⁶ Zn	⁷⁵ As	⁸² Se	⁹⁵ Mo	¹⁰¹ Ru	¹⁰³ Rh
LOD					58	0.004	0.3	0.28	0.079	0.044	0.6	0.008	0.01	0.00
Bushveld Complex	Rustenburg mine	AN	Anorthosite	-2	360439	4461	328205	0.91	0.079	0.044	198.0	0.037	8.42	321.02
					357464	8965	356858	58.61	0.079	1.069	260.3	0.008	4.16	53.56
Median AN					358952	6713	342531	29.76	0.079	0.557	229.1	0.022	6.29	187.29
Bushveld Complex	Rustenburg mine	LC	Lower chromitite	0	359462	5503	339926	2.08	2.605	0.044	183.5	0.008	7.20	5.76
					344402	4819	319088	12.05	1.693	0.698	240.0	0.058	4.68	31.58
					354733	5756	358224	2.67	0.539	1.270	231.4	0.368	1.59	44.84
Median LC					354733	5503	339926	2.67	1.693	0.698	231.4	0.058	4.68	31.58
Bushveld Complex	Rustenburg mine	CGM-1	Coarse-grained melanorite	2	347223	4734	336019	7.78	0.684	0.079	258.5	0.062	18.16	51.84
					365974	4702	332324	14.00	0.912	0.720	262.1	0.091	4.09	29.34
					330158	6414	291738	10.81	0.300	0.749	259.2	0.008	12.01	19.01
					354742	4298	324298	1.15	0.402	0.586	117.2	0.042	5.72	62.74
					331135	4302	308994	1.37	0.303	0.514	169.3	0.012	17.83	15.21
Median CGM-1					347223	4702	324298	7.78	0.402	0.586	258.5	0.042	12.01	29.34
Bushveld Complex	Rustenburg mine	CGM-2	Coarse-grained melanorite	6	335374	5379	302808	5.40	0.139	0.044	156.9	0.218	19.79	7.81
					301506	5275	269271	6.81	0.079	0.044	184.6	0.814	9.53	14.72
					322995	4838	285265	6.56	0.402	0.044	111.4	0.124	3.77	29.63
					332438	5405	319739	4.75	0.156	0.046	128.9	0.008	6.44	8.79
					334066	5210	309320	9.44	0.199	0.078	121.4	0.008	2.26	23.08
					328766	4689	283272	7.72	0.358	0.091	161.8	0.293	18.94	17.68
					322670	5665	287830	3.65	0.079	0.044	250.7	0.008	25.06	54.38
Median CGM-2					328766	5275	287830	6.56	0.156	0.044	156.9	0.124	9.53	17.68

ANNEXE 18 – Cont.

Locality	Sample	¹⁰⁸ Pd	¹⁰⁹ Ag	¹¹¹ Cd	¹¹⁵ In	¹¹⁸ Sn	¹²¹ Sb	¹²⁸ Te	¹⁸⁵ Re	¹⁸⁹ Os	¹⁹³ Ir	¹⁹⁵ Pt	¹⁹⁷ Au	²⁰⁵ Tl	²⁰⁸ Pb	²⁰⁹ Bi
LOD		0.03	0.003	0.025	0.014	0.018	0.012	0.079	0.004	0.008	0.002	0.004	0.007	0.002	0.005	0.002
Rustenburg mine	AN	114.61	0.762	1.022	0.014	0.142	0.012	0.122	0.201	0.90	13.00	3.81	0.020	0.028	2.377	0.002
		369.23	0.446	0.877	0.014	0.088	0.012	0.211	0.029	1.02	17.39	8.56	0.007	0.781	3.878	0.009
Median AN		241.92	0.604	0.950	0.014	0.115	0.012	0.167	0.115	0.96	15.19	6.18	0.013	0.405	3.127	0.005
Rustenburg mine	LC	133.17	6.488	0.072	0.014	0.135	0.069	0.211	0.004	0.13	1.66	9.86	0.007	0.033	0.847	0.090
		309.08	0.651	0.025	0.014	0.023	0.199	0.586	0.136	4.20	5.54	7.20	0.007	1.302	10.014	0.020
		199.27	1.595	0.025	0.014	0.018	0.012	0.147	0.667	5.73	4.40	6.84	0.007	0.163	6.610	0.056
Median LC		199.27	1.595	0.025	0.014	0.023	0.069	0.211	0.136	4.20	4.40	7.20	0.007	0.163	6.610	0.056
Rustenburg mine	CGM-1	162.80	1.648	0.140	0.014	0.018	0.080	0.274	0.179	7.20	8.89	0.73	0.019	2.312	15.954	0.038
		169.31	5.112	0.025	0.014	0.057	0.102	0.879	0.293	4.92	4.49	0.86	0.007	2.158	19.536	0.117
		228.25	5.689	2.004	0.014	0.018	0.068	0.079	1.032	6.71	3.97	3.00	0.007	1.172	19.679	0.075
		137.07	2.409	0.078	0.014	0.018	0.012	0.079	0.381	3.39	10.32	1.17	0.008	0.231	42.328	0.005
		170.61	2.699	0.025	0.014	0.018	0.012	0.111	0.127	4.56	5.19	2.80	0.007	0.306	0.374	0.143
Median CGM-1		169.31	2.699	0.078	0.014	0.018	0.068	0.111	0.293	4.92	5.19	1.17	0.007	1.172	19.536	0.075
Rustenburg mine	CGM-2	186.24	1.511	0.025	0.014	0.018	0.012	2.051	0.374	3.84	4.98	0.44	0.007	0.002	0.302	0.038
		177.45	2.507	0.025	0.014	0.047	0.012	1.628	0.580	2.64	5.89	0.54	0.012	0.723	9.801	0.042
		132.19	5.210	1.333	0.014	0.091	0.012	0.251	0.099	3.88	5.44	0.88	0.007	0.050	2.605	0.326
		283.27	3.354	0.025	0.014	0.077	0.030	0.697	0.140	7.42	6.28	0.36	0.007	0.008	0.124	0.002
		297.60	3.126	0.025	0.014	0.039	0.012	0.274	0.195	2.30	6.12	0.48	0.007	0.035	0.951	0.002
		257.22	2.865	0.900	0.014	0.018	0.071	0.212	0.111	5.94	6.84	0.40	0.007	0.417	5.698	0.013
Median CGM-2		257.22	2.963	0.025	0.014	0.039	0.012	0.457	0.140	3.88	6.12	0.44	0.007	0.035	1.613	0.013

ANNEXE 18 – Cont.

Intrusion	Locality	Sample	Rock	Height (cm)	³⁴ S	⁵⁹ Co	⁶¹ Ni	⁶⁵ Cu	⁶⁶ Zn	⁷⁵ As	⁸² Se	⁹⁵ Mo	¹⁰¹ Ru	¹⁰³ Rh
LOD					58	0.004	0.3	0.28	0.079	0.044	0.6	0.008	0.01	0.00
Bushveld Complex	Rustenburg mine	UC	Upper chromitite	10	343198	5789	328530	0.42	0.197	0.847	94.4	0.008	0.32	25.66
					343212	6377	320521	1.79	0.079	0.044	186.2	0.008	7.51	41.03
					359882	5763	356844	3.00	1.042	0.044	184.3	0.211	1.55	135.33
					356206	5747	352625	3.26	0.726	0.814	226.9	0.087	1.88	13.74
Median UC					349709	5776	340578	2.39	0.462	0.429	185.3	0.047	1.72	33.34
Bushveld Complex	Rustenburg mine	M-1	Melanorite	13.5	334256	5011	310297	3.81	0.555	0.267	147.2	0.008	7.19	22.34
					387474	4959	293691	7.59	1.056	0.466	233.5	0.076	19.53	57.11
					328836	5646	301506	8.27	0.587	0.238	206.1	0.008	6.21	23.93
					334717	4793	280342	2.38	0.079	0.569	241.6	0.574	5.14	30.83
					310297	4896	276760	3.35	2.986	1.205	106.8	0.078	23.11	119.82
					331461	6412	299878	3.29	0.781	0.163	82.4	0.069	0.10	13.02
					313623	6219	276434	2.68	0.079	0.088	118.8	0.008	2.34	12.70
					332125	13350	315931	4.37	0.079	0.044	138.7	0.008	7.28	13.02
					330484	5697	283598	7.20	5.303	1.107	173.5	0.027	7.29	16.64
					310948	5893	253317	8.82	0.079	0.346	184.0	0.064	4.00	0.54
312585	6675	322561	2.57	0.079	0.098	175.8	0.036	24.02	23.22					
Median M-1					330484	5697	293691	3.81	0.555	0.267	173.5	0.036	7.19	22.34
Bushveld Complex	Rustenburg mine	M-2	Melanorite	18	333089	5734	344810	2.80	0.977	0.247	177.5	1.302	24.08	25.92
					333740	6286	366626	10.74	0.752	0.169	186.5	0.072	0.68	4.59
					329507	7066	338950	1.43	0.260	0.044	199.9	0.030	2.37	2.49
					319077	4363	310622	172.57	1.184	0.075	155.3	0.038	24.22	21.98
					323321	5207	338146	0.41	0.079	0.044	145.5	0.008	36.13	44.28
Median M-2					329507	5734	338950	2.80	0.752	0.075	177.5	0.038	24.08	21.98

ANNEXE 18 – Cont.

Locality	Sample	¹⁰⁸ Pd	¹⁰⁹ Ag	¹¹¹ Cd	¹¹⁵ In	¹¹⁸ Sn	¹²¹ Sb	¹²⁸ Te	¹⁸⁵ Re	¹⁸⁹ Os	¹⁹³ Ir	¹⁹⁵ Pt	¹⁹⁷ Au	²⁰⁵ Tl	²⁰⁸ Pb	²⁰⁹ Bi
LOD		0.03	0.003	0.025	0.014	0.018	0.012	0.079	0.004	0.008	0.002	0.004	0.007	0.002	0.005	0.002
Rustenburg mine	UC	472.12	0.878	0.069	0.014	0.156	0.020	0.236	0.137	0.49	1.31	7.39	0.007	0.005	2.507	0.003
		446.07	1.354	0.025	0.014	0.171	0.012	0.246	0.554	7.16	6.97	8.69	0.007	0.145	4.037	0.019
		90.52	0.469	1.355	0.014	0.300	0.061	0.436	0.143	3.45	1.86	9.08	0.007	0.010	0.720	0.123
		91.16	1.097	0.288	0.014	0.018	0.012	0.079	0.259	3.52	3.56	9.02	0.007	1.693	11.476	0.038
Median UC		268.62	0.987	0.178	0.014	0.164	0.016	0.241	0.201	3.48	2.71	8.86	0.007	0.077	3.272	0.028
Rustenburg mine	M-1	180.06	3.484	0.025	0.014	0.052	0.012	0.609	0.449	3.87	3.29	1.27	0.007	0.094	2.833	0.002
		163.45	3.601	0.060	0.014	0.018	0.012	1.270	0.430	9.57	13.76	0.59	0.007	0.319	8.075	0.002
		169.31	2.618	0.025	0.014	0.018	0.049	2.019	0.400	6.28	10.39	1.71	0.007	1.114	8.270	0.051
		155.96	5.633	0.025	0.356	0.077	0.012	0.287	0.479	2.77	4.00	1.65	0.007	0.025	1.237	0.088
		161.82	3.940	0.145	0.014	0.090	0.012	0.176	0.716	5.50	8.60	2.98	0.007	0.169	5.177	0.348
		174.20	1.693	0.025	0.014	0.018	0.012	0.599	0.105	0.01	1.38	4.00	0.007	0.013	1.335	0.002
		184.29	2.051	0.025	0.021	0.018	0.012	0.468	0.215	1.89	1.77	2.70	0.007	0.002	0.436	0.002
		153.35	2.247	0.189	0.014	0.018	0.012	0.869	0.348	5.05	2.47	3.03	0.018	0.002	3.302	0.002
		130.57	2.605	0.025	0.822	0.179	0.012	0.521	0.212	5.34	3.54	1.70	0.007	0.055	2.125	0.016
		89.22	2.214	0.025	0.014	0.069	0.012	0.079	0.089	1.17	0.26	1.28	0.007	0.277	13.102	0.065
234.43	1.804	0.025	0.222	0.018	0.012	0.079	0.313	4.95	4.23	3.87	0.007	0.009	1.954	0.002		
Median M-1		163.45	2.605	0.025	0.014	0.018	0.012	0.521	0.348	4.95	3.54	1.71	0.007	0.055	2.833	0.002
Rustenburg mine	M-2	156.94	1.456	0.025	0.014	0.018	0.182	0.322	14.978	5.70	5.25	6.67	0.007	1.188	11.298	0.488
		905.17	1.032	0.742	0.588	0.111	0.018	0.169	0.335	0.97	0.91	11.14	0.007	0.267	10.322	0.014
		167.68	0.749	1.022	0.014	0.018	0.012	0.079	0.410	5.76	3.71	4.17	0.007	1.595	5.275	0.002
		94.74	1.211	0.176	0.122	0.018	0.024	0.313	0.332	4.66	4.06	0.01	0.007	0.088	2.784	0.103
		179.73	0.208	0.025	0.014	0.066	0.012	0.079	0.017	7.23	7.49	6.90	0.007	0.023	0.724	0.137
Median M-2		167.68	1.032	0.176	0.014	0.018	0.018	0.169	0.335	5.70	4.06	6.67	0.007	0.267	5.275	0.103

ANNEXE 18 – Cont.

Intrusion	Locality	Sample	Rock	Height (cm)	³⁴ S	⁵⁹ Co	⁶¹ Ni	⁶⁵ Cu	⁶⁶ Zn	⁷⁵ As	⁸² Se	⁹⁵ Mo	¹⁰¹ Ru	¹⁰³ Rh
LOD					58	0.004	0.3	0.28	0.079	0.044	0.6	0.008	0.01	0.00
Bushveld Complex	Rustenburg mine	M-3	Melanorite	23	329182	5057	353927	0.99	0.218	0.469	181.7	0.034	4.52	4.59
					335368	6154	368234	0.47	0.079	0.717	189.8	0.578	6.73	4.66
					331786	5307	371066	2.18	0.079	0.333	133.8	0.133	4.61	4.86
					322344	11201	352315	1.76	0.079	0.374	195.0	0.008	5.82	4.10
					348392	5372	375623	0.95	0.340	0.287	172.2	0.026	4.52	35.12
					333803	8544	349369	1.68	0.270	0.371	178.8	0.008	6.80	4.53
Median M-3					332795	5763	361081	1.33	0.149	0.373	180.2	0.030	5.21	4.62
Bushveld Complex	Rustenburg mine	M-4	Melanorite	27	323726	5330	366348	59.21	1.241	0.216	167.6	0.008	28.51	7.62
					357834	5988	325417	5.96	293.040	0.466	191.5	0.316	17.18	8.76
					348383	7522	354551	8.57	2.121	0.264	170.9	0.008	10.08	38.02
					319414	6512	333414	0.79	0.079	0.044	148.2	0.008	5.85	26.21
					308018	8974	319266	814.26	0.259	0.159	85.3	0.008	0.13	0.00
Median M-4					323726	6512	333414	8.57	1.241	0.216	167.6	0.008	10.08	8.76

ANNEXE 18 – Cont.

Locality	Sample	¹⁰⁸ Pd	¹⁰⁹ Ag	¹¹¹ Cd	¹¹⁵ In	¹¹⁸ Sn	¹²¹ Sb	¹²⁸ Te	¹⁸⁵ Re	¹⁸⁹ Os	¹⁹³ Ir	¹⁹⁵ Pt	¹⁹⁷ Au	²⁰⁵ Tl	²⁰⁸ Pb	²⁰⁹ Bi
LOD		0.03	0.003	0.025	0.014	0.018	0.012	0.079	0.004	0.008	0.002	0.004	0.007	0.002	0.005	0.002
Rustenburg mine	M-3	41.61	1.074	0.878	0.123	0.018	0.012	2.475	0.041	0.31	1.03	0.00	0.007	0.182	3.061	0.125
		39.39	0.846	0.080	0.014	0.098	0.012	6.512	1.595	1.34	1.58	0.04	0.027	0.081	1.465	0.065
		40.05	0.768	0.656	0.700	0.018	0.012	2.865	0.092	0.78	9.67	0.00	0.007	0.124	2.786	0.098
		128.21	0.473	0.025	1.556	0.093	0.012	4.558	0.321	1.38	1.29	0.00	0.007	0.074	2.247	0.094
		39.27	0.876	0.050	0.014	0.018	0.127	1.473	0.391	0.74	0.84	0.01	0.007	0.384	1.959	0.046
		75.22	8.791	0.097	0.014	0.067	0.012	2.898	0.135	1.13	0.82	0.00	0.007	1.610	9.302	0.135
Median M-3		40.83	0.861	0.088	0.068	0.043	0.012	2.882	0.228	0.95	1.16	0.00	0.007	0.153	2.516	0.096
Rustenburg mine	M-4	67.40	1.426	0.025	0.014	0.068	0.052	0.079	0.093	3.55	2.45	3.19	0.007	0.147	3.647	0.014
		39.66	6.512	0.966	0.120	0.070	0.296	2.930	1.726	2.25	2.15	2.74	7.814	0.977	29.304	0.195
		49.32	1.003	0.147	0.212	0.029	0.100	2.990	0.141	1.95	1.75	0.02	0.007	0.661	8.694	0.189
		179.41	1.553	0.145	0.014	0.067	0.026	0.079	0.384	3.35	3.19	5.18	0.007	0.011	2.339	0.002
		148.15	2.352	0.025	0.014	0.094	0.012	0.079	0.004	0.01	0.00	3.74	0.007	0.016	0.462	0.011
Median M-4		67.40	1.553	0.145	0.014	0.068	0.052	0.079	0.141	2.25	2.15	3.19	0.007	0.147	3.647	0.014

ANNEXE 18 – Cont.

Intrusion	Locality	Sample	Rock	³⁴ S	⁵⁹ Co	⁶¹ Ni	⁶⁵ Cu	⁶⁶ Zn	⁷⁵ As	⁸² Se	⁹⁵ Mo	¹⁰¹ Ru	¹⁰³ Rh	¹⁰⁸ Pd
LOD				58	0.004	0.3	0.28	0.079	0.044	0.6	0.008	0.01	0.00	0.03
Stillwater Complex	East Boulder mine	ST-12	Mela troctolite	283272	10908	251038	7945	7.489	0.065	240.9	0.008	122.30	273.04	19847.36
				324949	11526	265690	83	0.228	0.254	527.5	0.008	147.16	287.18	20521.76
				308994	10647	280016	6838	2.442	0.423	511.2	0.008	179.72	239.93	19894.14
				299552	11917	270248	218	0.749	0.521	547.0	0.008	218.47	288.15	14945.03
				303785	10354	250061	1698	8.791	0.044	320.4	0.008	107.86	258.83	18982.48
				303785	10191	280993	90	0.256	0.249	505.7	0.010	90.03	239.64	15270.63
				294994	9052	262759	3024	6.219	0.121	472.1	0.008	88.67	314.18	16214.87
				315506	12308	259503	9214	1.433	0.044	386.9	0.012	70.49	312.28	18819.68
306064	9768	243549	4759	3.907	0.044	221.4	0.008	81.81	197.91	17094.00				
Median ST-12				303785	10647	262759	3024	2.442	0.121	472.1	0.008	107.86	273.04	18819.68
Stillwater Complex	East Boulder mine	ST-14	Anorthosite	379324	7521	374440	2.96	2.548	0.044	436.3	0.008	2.17	61.84	2428.98
				377696	6694	351184	7.16	0.488	1.074	423.3	0.008	5.00	43.54	11363.44
				356858	6707	347415	1.04	0.623	1.172	410.3	0.008	3.63	53.75	5158.72
				373789	7424	373463	15.95	0.458	0.228	407.0	0.008	4.24	41.92	4544.15
				330256	6382	315832	0.46	0.326	0.260	351.6	0.008	3.53	31.91	3256.00
Median ST-14				373789	6707	351184	2.96	0.488	0.260	410.3	0.008	3.63	43.54	4544.15
Stillwater Complex	East Boulder mine	ST-16	Leuconorite	382580	5600	393976	1.47	1.442	0.651	239.6	0.323	1.08	17.49	3187.22
				349369	4689	344680	1.14	3.254	0.044	267.0	0.488	3.54	9.51	4460.72
				364672	4982	361416	0.72	4.255	0.044	309.3	0.008	1.91	16.51	3913.71
				343182	4786	363370	1.69	5.670	0.054	286.9	0.332	4.68	16.67	3943.01
				384208	4884	394912	17.91	8.113	0.341	293.0	0.042	0.87	12.28	3428.16
				330720	3810	462352	1.66	3.332	0.554	384.2	0.107	7.02	14.71	2428.98
Median ST-16				357020	4835	378673	1.56	3.794	0.198	289.9	0.215	2.72	15.61	3670.93

ANNEXE 18 – Cont.

Locality	Sample	¹⁰⁹ Ag	¹¹¹ Cd	¹¹⁵ In	¹¹⁸ Sn	¹²¹ Sb	¹²⁸ Te	¹⁸⁵ Re	¹⁸⁹ Os	¹⁹³ Ir	¹⁹⁵ Pt	¹⁹⁷ Au	²⁰⁵ Tl	²⁰⁸ Pb	²⁰⁹ Bi
LOD		0.003	0.025	0.014	0.018	0.012	0.079	0.004	0.008	0.002	0.004	0.007	0.002	0.005	0.002
East Boulder mine	ST-12	6.740	0.858	0.014	0.018	0.012	0.079	0.107	19.18	17.91	0.45	0.007	0.013	0.554	0.002
		10.256	0.622	0.014	0.029	0.039	0.684	0.315	42.98	40.93	0.52	0.007	0.006	0.322	0.009
		22.011	0.456	0.014	0.033	0.055	0.912	0.150	60.83	36.04	0.09	0.007	0.002	0.264	0.002
		11.787	0.270	0.014	0.124	0.012	0.195	0.347	61.21	43.63	0.31	0.013	0.031	0.387	0.002
		8.075	0.120	0.014	0.036	0.012	0.716	0.415	9.34	17.00	0.15	0.007	0.060	0.065	0.002
		6.024	0.186	0.014	0.065	0.012	0.163	0.120	20.64	25.95	0.27	0.011	0.002	0.034	0.002
		7.945	0.274	0.014	0.042	0.012	0.423	0.124	12.93	23.57	0.46	0.007	0.030	0.781	0.002
		2.813	1.250	0.014	0.137	0.035	0.698	0.386	15.91	33.22	0.20	0.007	0.007	0.251	0.008
5.503	1.165	0.014	0.081	0.059	0.554	0.425	16.22	21.68	0.28	0.007	0.022	3.810	0.003		
Median ST-12		7.945	0.456	0.014	0.042	0.012	0.554	0.315	19.18	25.95	0.28	0.007	0.013	0.322	0.002
East Boulder mine	ST-14	0.540	0.025	0.014	0.046	0.033	0.201	0.004	0.65	13.74	5.27	0.007	0.944	6.772	0.002
		2.898	0.994	0.019	0.018	0.085	0.260	0.098	0.41	2.20	0.67	0.008	1.465	9.442	0.004
		1.328	0.072	0.014	0.100	0.072	0.944	0.130	0.20	2.48	0.08	0.007	1.107	4.200	0.008
		3.875	1.346	0.019	0.130	0.052	2.084	0.004	0.36	3.42	7.36	0.029	0.423	1.791	0.012
		2.116	0.163	0.014	0.018	0.013	1.220	0.201	0.49	6.02	4.23	0.007	0.619	6.838	0.021
Median ST-14		2.116	0.163	0.014	0.046	0.052	0.944	0.098	0.41	3.42	4.23	0.007	0.944	6.772	0.008
East Boulder mine	ST-16	0.713	0.100	0.014	0.085	0.012	0.651	0.004	0.48	0.61	1.22	0.008	0.003	0.254	0.002
		0.987	0.101	0.014	0.059	0.012	1.465	0.582	1.79	0.55	4.22	0.007	0.002	0.208	0.098
		1.433	1.554	0.014	0.049	0.012	0.977	0.098	1.30	1.13	3.53	0.007	0.014	0.749	0.076
		0.537	0.335	0.014	0.018	0.012	1.856	0.218	1.76	1.21	7.29	0.007	0.002	0.091	0.004
		1.172	1.332	0.014	0.018	0.012	1.433	0.123	1.07	0.20	3.47	0.011	0.012	1.107	0.012
		1.042	0.211	0.014	0.018	0.012	0.293	0.358	1.91	1.98	5.76	0.007	0.002	0.323	0.002
Median ST-16		1.014	0.273	0.014	0.034	0.012	1.205	0.170	1.53	0.87	3.88	0.007	0.002	0.289	0.008

ANNEXE 18 – Cont.

Intrusion	Locality	Sample	Rock	³⁴ S	⁵⁹ Co	⁶¹ Ni	⁶⁵ Cu	⁶⁶ Zn	⁷⁵ As	⁸² Se	⁹⁵ Mo	¹⁰¹ Ru	¹⁰³ Rh	¹⁰⁸ Pd
LOD				58	0.004	0.3	0.28	0.079	0.044	0.6	0.008	0.01	0.00	0.03
Stillwater Complex	East Boulder mine	ST-17	Olivine melagabbonorite	294713	4978	211034	2702	358.160	0.232	367.9	0.008	21.78	83.01	3679.26
				313736	4777	269638	12536	302.400	0.912	302.8	0.008	18.20	75.15	14000.67
				278201	2716	249918	19536	10.745	0.619	433.0	0.008	25.72	173.11	2682.94
				289133	6317	221127	12796	344.240	0.293	312.6	0.036	20.41	329.11	4265.33
				312576	5438	203638	1628	52.221	0.044	302.8	0.072	34.28	342.85	6207.53
Median ST-17				294713	4978	221127	12536	302.400	0.293	312.6	0.008	21.78	173.11	4265.33
Stillwater Complex	Stillwater mine	P-4	Anorthosite	361416	1527	363695	2.05	2.247	0.488	284.5	0.008	2.51	5.87	1826.61
				403744	1475	416768	1.04	0.079	0.185	253.3	0.023	2.19	6.04	1800.57
				364346	1635	397232	1.95	0.163	0.044	279.3	0.014	3.01	6.35	1667.48
				352625	1651	370858	0.28	0.079	0.044	354.9	0.010	6.47	6.72	1976.39
				349369	1817	373789	0.34	0.293	0.044	306.1	0.013	7.51	4.01	1934.06
357183	1719	379324	0.28	0.079	0.406	308.5	0.008	2.92	3.38	2031.74				
Median P-4				359300	1643	376556	0.69	0.121	0.115	295.3	0.012	2.97	5.96	1880.34
Stillwater Complex	Stillwater mine	P-3	Leuco gabbonorite	348392	3643	338298	6.19	2.312	0.508	390.7	0.036	7.87	32.01	4142.45
				322018	3744	332112	7.07	1.001	0.150	174.5	0.008	6.86	11.31	7684.16
				340252	4233	315181	3.09	3.225	0.044	219.1	0.008	8.00	31.68	7651.60
				354904	4581	344485	5.54	0.182	0.288	332.1	0.008	6.41	14.47	8302.80
				323646	4428	324623	28.98	2.037	0.456	259.2	0.029	4.16	30.74	6153.84
Median P-3				340252	4233	332112	6.19	2.037	0.288	259.2	0.008	6.86	30.74	7651.60

ANNEXE 18 – Cont.

Locality	Sample	¹⁰⁹ Ag	¹¹¹ Cd	¹¹⁵ In	¹¹⁸ Sn	¹²¹ Sb	¹²⁸ Te	¹⁸⁵ Re	¹⁸⁹ Os	¹⁹³ Ir	¹⁹⁵ Pt	¹⁹⁷ Au	²⁰⁵ Tl	²⁰⁸ Pb	²⁰⁹ Bi
LOD		0.003	0.025	0.014	0.018	0.012	0.079	0.004	0.008	0.002	0.004	0.007	0.002	0.005	0.002
East Boulder mine	ST-17	2.670	0.554	0.014	0.274	0.012	1.009	0.059	9.25	8.79	3.87	0.007	0.228	0.326	0.010
		6.772	3.972	0.014	0.140	0.075	1.107	0.060	8.07	8.53	3.42	0.007	0.085	2.116	0.002
		9.377	0.130	0.014	0.055	0.023	0.170	0.014	5.30	2.26	1.81	0.007	0.004	0.563	0.007
		7.758	1.009	0.014	0.056	0.018	0.847	0.027	3.74	4.18	5.31	0.007	0.040	2.084	0.012
		6.675	0.025	0.014	0.114	0.012	0.699	0.004	4.17	11.20	5.11	0.007	0.002	0.791	0.002
Median ST-17		6.772	0.554	0.014	0.114	0.018	0.847	0.027	5.30	8.53	3.87	0.007	0.040	0.791	0.007
Stillwater mine	P-4	0.365	0.046	0.014	0.192	0.012	0.749	0.004	0.26	2.58	5.99	0.007	1.003	4.428	0.006
		1.133	0.025	0.014	0.348	0.016	0.079	0.023	0.50	0.18	6.74	0.009	1.042	4.103	0.085
		1.569	0.025	0.014	0.169	0.012	0.122	0.004	1.55	0.33	0.03	0.007	1.791	2.670	0.002
		1.071	0.025	0.228	0.068	0.012	4.037	0.031	0.73	0.46	0.02	0.007	0.466	1.400	0.002
		1.534	0.025	0.014	0.018	0.029	3.419	0.030	0.78	0.02	0.01	0.007	0.153	2.671	0.009
		0.423	0.036	0.014	0.13556425.	0.027	3.842	0.062	0.46	1.54	0.04	0.007	0.042	0.182	0.005
Median P-4		1.102	0.025	0.014	0.169	0.014	2.084	0.027	0.62	0.39	0.04	0.007	0.734	2.670	0.006
Stillwater mine	P-3	10.973	0.025	0.014	0.107	0.057	6.675	0.019	0.23	4.21	0.04	0.007	1.661	52.096	0.029
		7.293	0.025	0.014	0.018	0.012	2.409	0.005	0.19	5.37	5.73	0.007	0.342	1.595	0.002
		3.777	0.025	0.014	0.182	0.104	0.619	0.008	0.45	4.53	6.64	0.007	1.058	8.140	0.002
		7.228	0.033	0.014	0.201	0.107	0.908	0.028	0.45	5.47	6.81	0.007	0.684	9.117	0.008
		12.373	0.025	0.014	0.018	0.062	0.624	0.055	0.33	5.18	4.59	0.007	0.008	1.661	0.002
Median P-3		7.293	0.025	0.014	0.107	0.062	0.908	0.019	0.33	5.18	5.73	0.007	0.684	8.140	0.002

ANNEXE 18 – Cont.

Intrusion	Locality	Sample	Rock	³⁴ S	⁵⁹ Co	⁶¹ Ni	⁶⁵ Cu	⁶⁶ Zn	⁷⁵ As	⁸² Se	⁹⁵ Mo	¹⁰¹ Ru	¹⁰³ Rh	¹⁰⁸ Pd
LOD				58	0.004	0.3	0.28	0.079	0.044	0.6	0.008	0.01	0.00	0.03
Stillwater Complex	Banded Series	BS-18	Leuco gabbro	354912	9377	363744	1.11	0.521	1.042	214.9	0.358	0.01	0.01	0.04
				394627	9465	374766	0.84	0.117	5.372	303.1	0.008	0.01	0.00	0.15
				357977	9605	404395	0.28	0.384	4.982	226.6	0.008	0.07	0.00	0.09
				403744	5926	386536	0.75	0.079	0.347	192.1	0.008	0.14	0.00	0.13
				416768	6740	373789	31.86	0.336	4.265	325.3	0.068	0.01	0.03	0.13
				433048	8303	392022	1.27	0.427	0.628	163.1	0.008	0.07	0.00	0.20
				410582	8107	400488	1.33	35.816	0.326	175.5	0.008	0.08	0.00	0.16
				351233	8283	349279	2.70	0.619	0.430	182.3	0.067	0.04	0.00	0.16
				406349	8694	354676	2.28	0.079	5.796	254.0	0.008	0.01	0.03	0.11
				415140	8436	356072	520.96	5.210	3.744	285.2	0.049	0.01	0.02	0.10
				361416	7717	407000	0.28	0.188	1.595	341.9	0.008	0.18	0.00	0.04
376072	7316	361326	1.40	2.084	1.758	282.9	0.081	0.24	0.00	0.17				
396581	7433	420024	0.73	3.223	5.470	297.3	0.169	0.04	0.01	0.19				
Median BS-18				396581	8283	374766	1.27	0.427	1.758	254.0	0.008	0.04	0.00	0.13
Stillwater Complex	Picket Pin	PP-AN	Anorthosite	410256	8726	291412	6.71	49.784	0.257	218.2	0.008	0.14	15.63	81.35
				399377	12015	372161	34.19	29.304	0.218	227.3	0.099	1.06	0.66	67.02
				403146	12698	356442	1.70	45.258	0.306	342.9	0.008	0.08	1.05	28.76
				407749	12210	376068	1.30	11.526	0.249	231.2	0.391	1.35	6.25	19.72
				395612	12470	356817	976.80	20.187	0.215	377.4	0.008	0.05	1.04	205.99
				437281	11168	329226	0.72	58.282	0.044	284.6	0.147	0.15	5.11	11.29
				414489	9823	297924	1.20	3.191	0.475	232.5	0.313	0.23	11.33	2.70
				388351	9967	354249	2.33	34.286	0.231	302.5	1.498	1.09	2.60	13.47
Median PP-AN				405447	11591	355346	2.01	31.795	0.240	258.5	0.123	0.19	3.86	24.24

ANNEXE 18 – Cont.

Locality	Sample	¹⁰⁹ Ag	¹¹¹ Cd	¹¹⁵ In	¹¹⁸ Sn	¹²¹ Sb	¹²⁸ Te	¹⁸⁵ Re	¹⁸⁹ Os	¹⁹³ Ir	¹⁹⁵ Pt	¹⁹⁷ Au	²⁰⁵ Tl	²⁰⁸ Pb	²⁰⁹ Bi
LOD		0.003	0.025	0.014	0.018	0.012	0.079	0.004	0.008	0.002	0.004	0.007	0.002	0.005	0.002
Banded Series	BS-18	1.986	0.025	0.039	0.018	0.012	89.536	0.033	0.01	0.00	0.00	0.007	1.368	9.135	1.198
		0.996	0.025	0.014	0.018	0.012	66.422	0.004	0.01	0.00	0.00	0.007	0.002	1.986	1.728
		0.306	0.025	0.014	0.018	0.012	91.168	0.004	0.01	0.02	0.00	0.007	0.002	0.531	0.416
		1.954	0.025	0.014	0.018	0.012	29.019	0.004	0.01	0.00	0.00	0.007	0.140	11.396	0.749
		2.572	0.025	0.014	0.108	0.012	41.677	0.004	0.01	0.01	0.00	0.007	0.046	0.716	1.254
		2.396	0.025	0.014	0.078	0.012	46.345	0.004	0.01	0.00	0.00	0.007	0.101	7.847	0.619
		0.599	0.199	0.014	0.117	0.012	35.568	0.004	0.01	0.00	0.00	0.007	0.057	1.188	0.493
		1.009	0.025	0.014	0.293	0.814	16.671	0.004	0.01	0.00	0.00	0.007	0.434	140.008	2.311
		0.342	0.025	0.014	0.101	0.012	166.707	1.377	0.01	0.04	0.00	0.007	0.002	0.619	0.908
		1.107	0.505	0.014	0.102	0.423	55.873	0.075	0.01	0.00	0.00	0.007	2.898	39.072	1.511
		0.785	0.025	0.014	0.018	0.287	119.821	0.104	0.01	0.00	0.00	0.007	0.036	18.885	0.440
		0.801	0.025	0.014	0.150	1.140	89.214	0.078	0.01	0.00	0.00	0.007	0.739	64.794	0.695
6.121	0.025	0.014	0.018	0.106	151.078	0.027	0.01	0.00	0.00	0.088	3.093	22.141	1.563		
Median BS-18		1.009	0.025	0.014	0.078	0.012	66.422	0.004	0.01	0.00	0.00	0.007	0.101	9.135	0.908
Picket Pin	PP-AN	1.164	1.465	0.037	0.018	0.012	0.079	0.004	0.10	0.38	0.20	0.007	0.140	7.261	0.029
		0.518	1.563	0.014	0.018	0.012	0.456	0.004	0.52	0.29	0.10	0.007	0.576	13.057	0.041
		2.201	2.735	0.014	0.018	0.012	0.079	0.004	0.05	0.05	5.05	0.007	0.876	15.368	0.007
		0.863	2.344	0.014	0.018	0.012	0.088	0.651	0.88	0.29	3.32	0.007	0.540	10.452	0.002
		4.265	3.484	0.014	0.018	0.012	0.079	0.039	0.01	0.03	0.78	0.007	0.654	24.453	0.008
		0.150	1.335	0.014	0.018	0.012	0.079	0.749	0.38	0.98	0.52	0.007	0.098	1.801	0.020
		0.684	0.492	0.014	0.018	0.012	0.079	1.237	0.51	1.55	5.14	0.007	0.060	0.944	0.002
		1.439	1.381	0.014	0.018	0.012	0.079	1.693	0.35	0.41	0.79	0.007	0.215	12.210	0.004
Median PP-AN		1.014	1.514	0.014	0.018	0.012	0.079	0.345	0.36	0.34	0.79	0.007	0.378	11.331	0.008

ANNEXE 19 - Complete data set of LA-ICP-MS analyses of chalcopyrite obtained in this study and median values for each sample from the Bushveld and Stillwater Complexes. The Fe values used for internal standardization are from Godel et al. (2008a) for samples from the Stillwater Complex, Godel et al. (2007) for samples from the Rustenburg mine, and stoichiometric values (i.e., 30.4%) for samples from the Impala mine. LOD - limit of detection; n.r. – not reported.

ANNEXE 19

Intrusion	Locality	Sample	Rock	Height (cm)	³⁴ S	⁵⁹ Co	⁶¹ Ni	⁶⁵ Cu	⁶⁶ Zn	⁷⁵ As	⁸² Se	⁹⁵ Mo	¹⁰¹ Ru	¹⁰³ Rh	¹⁰⁸ Pd	¹⁰⁹ Ag
LOD					58	0.008	0.31	0.2	0.1	0.044	0.6	0.008	0.008	0.001	0.027	0.003
Bushveld Complex	Impala mine	IM-1	Norite	108	324909	1.035	82.77	326514	240.4	1.704	94.6	0.008	0.008	n.r.	0.064	13.085
					328340	7.912	94.33	404719	356.0	0.852	95.6	0.023	0.030	n.r.	0.123	1.369
Median IM-1					326624	4.473	88.55	365616	298.2	1.278	95.1	0.016	0.019	n.r.	0.093	7.227
Bushveld Complex	Impala mine	IM-3	Norite	98	329431	10.133	60.86	325297	243.4	0.641	95.9	0.054	0.008	n.r.	0.027	0.855
					290911	17.649	1004.51	317689	225.2	1.430	68.5	0.008	0.008	n.r.	0.234	1.278
					310260	0.149	41.69	362117	187.1	0.700	67.6	0.008	0.027	n.r.	0.084	1.735
Median IM-3					310260	10.133	60.86	325297	225.2	0.700	68.5	0.008	0.008	n.r.	0.084	1.278
Bushveld Complex	Impala mine	IM-5	Norite	88	330042	0.307	46.25	334730	224.0	1.461	66.9	0.063	0.015	n.r.	0.122	0.968
					297217	3.236	39.86	346984	245.3	0.192	71.8	0.008	0.061	n.r.	0.257	1.461
					313828	0.256	35.30	321103	241.3	0.312	74.2	0.030	0.055	n.r.	0.027	1.339
					298214	9.129	89.77	334562	244.8	1.674	81.6	0.008	0.030	n.r.	0.066	0.992
Median IM-5					306021	1.771	43.06	334646	243.0	0.886	73.0	0.019	0.043	n.r.	0.094	1.165
Bushveld Complex	Impala mine	IM-7	Melanorite	78	296388	0.228	63.29	318298	268.1	1.369	85.5	0.064	0.058	n.r.	0.255	10.529
					322558	0.067	58.73	335339	252.0	1.065	95.7	0.008	0.156	n.r.	2.527	1.674
					334783	1.023	35.60	318906	288.2	1.126	112.9	0.026	0.024	n.r.	1.067	1.704
					300648	0.008	68.47	329861	294.6	0.943	108.0	0.008	0.012	n.r.	0.099	1.876
					312737	2.130	109.55	356031	331.7	1.075	82.5	0.008	0.043	n.r.	0.566	1.765
Median IM-7					312737	0.228	63.29	329861	288.2	1.075	95.7	0.008	0.043	n.r.	0.566	1.765
Bushveld Complex	Impala mine	IM-9	Melanorite	68	285129	0.052	51.77	318865	244.7	0.712	90.4	0.021	0.040	n.r.	0.443	0.952
					336346	0.097	57.82	328340	161.0	0.669	80.6	0.015	0.014	n.r.	0.129	0.551
					317554	0.113	50.21	352075	234.3	0.044	92.5	0.098	0.015	n.r.	0.027	1.083
					280869	3.465	64.21	380375	274.5	0.761	105.9	0.008	0.063	n.r.	0.357	0.782
					280565	0.061	47.17	341729	235.2	0.556	62.1	0.085	0.024	n.r.	0.099	1.400
					322390	0.128	52.34	341685	359.1	0.243	59.9	0.008	0.008	n.r.	0.145	1.019
Median IM-9					301342	0.105	52.05	341707	240.0	0.613	85.5	0.018	0.020	n.r.	0.137	0.986

ANNEXE 19 – Cont.

Intrusion	Locality	Sample	¹¹¹ Cd	¹¹⁵ In	¹¹⁸ Sn	¹²¹ Sb	¹²⁸ Te	¹⁸⁵ Re	¹⁸⁹ Os	¹⁹³ Ir	¹⁹⁵ Pt	¹⁹⁷ Au	²⁰⁵ Tl	²⁰⁸ Pb	²⁰⁹ Bi
LOD			0.025	0.014	0.018	0.012	0.079	0.004	0.008	0.002	0.004	0.007	0.002	0.005	0.002
Bushveld Complex	Impala mine	IM-1	1.187	0.346	0.134	0.131	0.822	0.004	0.008	0.036	0.004	0.103	0.131	28.300	1.987
			2.130	0.397	0.335	0.052	1.704	0.051	0.024	0.002	0.004	0.007	0.024	20.084	2.518
Median IM-1			1.658	0.372	0.234	0.091	1.263	0.027	0.016	0.019	0.004	0.055	0.077	24.192	2.253
Bushveld Complex	Impala mine	IM-3	1.248	0.733	0.234	0.012	1.826	0.023	0.008	0.002	0.067	0.007	0.002	5.417	2.050
			1.156	0.918	0.219	0.012	1.461	0.004	0.008	0.113	0.004	0.041	0.026	9.433	2.080
			1.238	1.542	0.423	0.012	2.822	0.004	0.008	0.002	0.004	0.007	0.002	11.868	1.829
Median IM-3			1.238	0.918	0.234	0.012	1.826	0.004	0.008	0.002	0.004	0.007	0.002	9.433	2.050
Bushveld Complex	Impala mine	IM-5	0.943	1.147	0.018	0.012	2.069	0.055	0.008	0.002	0.004	0.007	0.002	4.686	2.651
			1.095	1.679	0.102	0.012	2.248	0.004	0.045	0.002	0.004	0.007	0.009	5.690	0.685
			1.035	1.518	0.094	0.012	1.095	0.004	0.008	0.002	0.004	0.015	0.002	7.577	1.812
			0.913	0.608	0.323	0.012	3.217	0.128	0.064	0.082	0.004	0.011	0.002	9.129	1.613
Median IM-5			0.989	1.333	0.098	0.012	2.158	0.029	0.026	0.002	0.004	0.009	0.002	6.634	1.713
Bushveld Complex	Impala mine	IM-7	2.259	1.497	2.465	0.499	0.079	0.098	0.008	0.004	0.007	0.007	0.030	13.815	0.084
			3.195	1.574	1.448	0.012	0.426	0.004	0.201	0.103	0.004	0.027	0.002	11.046	0.061
			2.434	3.155	2.678	0.012	0.368	0.102	0.008	0.002	0.064	0.007	0.030	152.150	0.231
			3.165	1.451	1.795	0.012	0.107	0.004	0.082	0.002	0.017	0.015	0.029	51.427	0.039
			2.982	0.862	0.511	0.012	0.225	0.004	0.008	0.023	0.004	0.007	0.070	31.343	0.030
Median IM-7			2.982	1.497	1.795	0.012	0.225	0.004	0.008	0.004	0.007	0.007	0.030	31.343	0.061
Bushveld Complex	Impala mine	IM-9	5.688	0.218	0.228	0.012	3.104	0.004	0.008	0.002	0.023	0.009	0.002	6.056	3.956
			3.682	2.122	0.073	0.012	2.282	0.004	0.012	0.128	0.019	0.026	0.002	3.925	1.804
			1.430	0.851	0.155	0.012	2.826	0.054	0.122	0.002	0.004	0.007	0.009	8.186	2.479
			1.720	1.076	0.365	0.012	1.643	0.004	0.008	0.002	0.006	0.007	0.033	8.764	3.402
			1.735	0.860	0.192	0.012	3.913	0.004	0.013	0.003	0.005	0.010	0.002	7.851	1.369
			2.465	0.872	0.408	0.012	1.339	0.023	0.008	0.002	0.004	0.007	0.002	8.794	4.895
Median IM-9			2.100	0.866	0.210	0.012	2.554	0.004	0.010	0.002	0.006	0.008	0.002	8.018	2.940

ANNEXE 19 – Cont.

Intrusion	Locality	Sample	Rock	Height (cm)	³⁴ S	⁵⁹ Co	⁶¹ Ni	⁶⁵ Cu	⁶⁶ Zn	⁷⁵ As	⁸² Se	⁹⁵ Mo	¹⁰¹ Ru	¹⁰³ Rh	¹⁰⁸ Pd	¹⁰⁹ Ag
LOD					58	0.008	0.31	0.2	0.1	0.044	0.6	0.008	0.008	0.001	0.027	0.003
Bushveld Complex	Impala mine	IM-11	Melanorite	58	331478	0.008	55.69	344772	383.4	1.400	89.5	0.008	0.015	n.r.	0.069	1.406
					298346	0.057	52.04	360805	273.6	1.371	79.7	0.008	0.122	n.r.	0.027	0.971
					327868	0.175	52.35	338074	323.5	0.335	87.3	0.066	0.025	n.r.	0.234	0.934
					316472	5.476	62.38	331781	287.0	0.340	84.3	0.008	0.099	n.r.	0.145	1.433
					286358	0.134	51.80	328955	261.7	0.044	93.4	0.102	0.008	n.r.	0.099	1.318
Median IM-11					316472	0.134	52.35	338074	287.0	0.340	87.3	0.008	0.025	n.r.	0.099	1.318
Bushveld Complex	Impala mine	IM-13	Melanorite	48	297605	0.180	41.71	365160	199.0	0.456	94.3	0.008	0.008	n.r.	2.066	1.948
					322128	0.721	59.34	323471	238.0	0.431	97.0	0.107	0.102	n.r.	0.066	0.977
					295171	0.198	53.25	315863	197.5	0.730	72.1	0.008	0.021	n.r.	0.048	1.522
					272957	4.613	70.90	365452	205.7	0.044	67.9	0.056	0.036	n.r.	0.027	1.217
Median IM-13					296388	0.459	56.30	344315	202.4	0.443	83.2	0.032	0.029	n.r.	0.057	1.369
Bushveld Complex	Impala mine	IM-15	Melanorite	38	320320	3.422	54.77	332601	293.6	0.822	84.0	0.012	0.020	n.r.	0.343	1.059
Median IM-15					320320	3.422	54.77	332601	293.6	0.822	84.0	0.012	0.020	n.r.	0.343	1.059
Bushveld Complex	Impala mine	IM-17	Melanorite	28	313733	0.099	46.86	349945	328.6	2.617	109.5	0.008	0.052	n.r.	0.124	1.165
					321037	0.131	41.99	351467	309.5	0.044	98.6	0.018	0.076	n.r.	0.244	1.293
Median IM-17					317385	0.115	44.43	350706	319.1	1.331	104.1	0.013	0.064	n.r.	0.184	1.229
Bushveld Complex	Impala mine	IM-18	Melanorite	23	313429	0.843	124.76	318910	289.7	0.609	100.7	0.008	0.008	n.r.	0.027	0.998
					324688	0.219	40.47	336860	357.6	1.709	106.1	0.100	0.036	n.r.	0.987	1.159
					319819	18.867	401.88	352923	307.6	1.278	102.2	0.066	0.011	n.r.	0.050	1.071
Median IM-18					319819	0.843	124.76	336860	307.6	1.278	102.2	0.066	0.011	n.r.	0.050	1.071

ANNEXE 19 – Cont.

Intrusion	Locality	Sample	¹¹¹ Cd	¹¹⁵ In	¹¹⁸ Sn	¹²¹ Sb	¹²⁸ Te	¹⁸⁵ Re	¹⁸⁹ Os	¹⁹³ Ir	¹⁹⁵ Pt	¹⁹⁷ Au	²⁰⁵ Tl	²⁰⁸ Pb	²⁰⁹ Bi
LOD			0.025	0.014	0.018	0.012	0.079	0.004	0.008	0.002	0.004	0.007	0.002	0.005	0.002
Bushveld Complex	Impala mine	IM-11	1.674	0.908	0.648	0.061	2.769	0.004	0.008	0.003	0.040	0.043	0.002	11.633	2.161
			1.400	0.914	0.435	0.012	1.917	0.004	0.008	0.002	0.004	0.019	0.002	11.959	3.886
			1.928	0.930	0.230	0.012	1.430	0.104	0.009	0.075	0.004	0.029	0.014	10.498	2.129
			2.158	2.986	0.210	0.012	1.217	0.004	0.008	0.002	0.004	0.030	0.002	12.355	1.348
			1.704	0.915	0.180	0.012	3.522	0.054	0.055	0.009	0.004	0.007	0.009	11.229	2.491
Median IM-11			1.704	0.915	0.230	0.012	1.917	0.004	0.008	0.003	0.004	0.029	0.002	11.633	2.161
Bushveld Complex	Impala mine	IM-13	0.822	1.204	0.170	0.012	1.187	0.013	0.012	0.002	0.004	0.013	0.002	7.925	2.475
			1.004	1.789	0.104	0.012	2.552	0.004	0.008	0.002	0.004	0.007	0.002	8.003	1.083
			0.774	0.766	0.113	0.012	2.339	0.066	0.023	0.002	0.004	0.026	0.002	6.664	2.313
			0.609	2.321	0.207	0.012	1.244	0.004	0.008	0.002	0.004	0.031	0.032	7.912	0.149
Median IM-13			0.798	1.497	0.141	0.012	1.791	0.008	0.010	0.002	0.004	0.019	0.002	7.919	1.698
Bushveld Complex	Impala mine	IM-15	1.675	1.506	0.167	0.012	2.765	0.021	0.008	0.002	0.004	0.007	0.011	16.858	1.659
Median IM-15			1.675	1.506	0.167	0.012	2.765	0.021	0.008	0.002	0.004	0.007	0.011	16.858	1.659
Bushveld Complex	Impala mine	IM-17	1.856	1.237	0.368	0.012	1.669	0.004	0.054	0.002	0.004	0.007	0.002	8.338	1.663
			2.587	4.563	0.140	0.012	2.308	0.103	0.008	0.002	0.004	0.014	0.002	13.102	0.537
Median IM-17			2.221	2.900	0.254	0.012	1.989	0.053	0.031	0.002	0.004	0.010	0.002	10.720	1.100
Bushveld Complex	Impala mine	IM-18	1.522	0.836	0.105	0.037	0.852	0.047	0.008	0.002	0.004	0.007	0.024	14.302	0.060
			2.802	1.691	0.237	0.012	0.447	0.004	0.021	0.002	0.004	0.007	0.034	14.211	0.505
			2.039	1.807	0.055	0.012	0.344	0.004	0.123	0.099	0.004	0.007	0.046	8.277	0.286
Median IM-18			2.039	1.691	0.105	0.012	0.447	0.004	0.021	0.002	0.004	0.007	0.034	14.211	0.286

ANNEXE 19 – Cont.

Intrusion	Locality	Sample	Rock	Height (cm)	³⁴ S	⁵⁹ Co	⁶¹ Ni	⁶⁵ Cu	⁶⁶ Zn	⁷⁵ As	⁸² Se	⁹⁵ Mo	¹⁰¹ Ru	¹⁰³ Rh	¹⁰⁸ Pd	¹⁰⁹ Ag
LOD					58	0.008	0.31	0.2	0.1	0.044	0.6	0.008	0.008	0.001	0.027	0.003
Bushveld Complex	Impala mine	IM-19	Melanorite	18	340607	0.654	94.03	345953	347.2	2.800	79.1	0.010	0.053	n.r.	0.031	0.676
					309473	0.258	64.82	338386	284.8	2.161	72.4	0.008	0.031	n.r.	0.027	0.627
					323345	0.103	28.60	330720	244.4	1.217	84.1	0.008	0.027	n.r.	0.233	1.506
					322410	0.161	33.17	328964	252.6	1.680	83.4	0.100	0.021	n.r.	0.562	1.321
					315863	0.129	32.56	335643	289.1	2.008	73.0	0.008	0.018	n.r.	0.755	1.269
					329253	0.286	35.32	344468	288.7	1.735	75.1	0.008	0.024	n.r.	1.213	1.382
					301257	0.338	39.93	331886	262.0	1.102	75.8	0.048	0.232	n.r.	0.233	0.879
					343859	0.079	31.95	338686	301.3	2.708	83.7	0.008	0.060	n.r.	0.027	2.130
					309579	0.131	14.61	318567	241.0	1.248	76.4	0.036	0.008	n.r.	0.027	2.800
Median IM-19					322410	0.161	33.17	335643	284.8	1.735	76.4	0.008	0.027	n.r.	0.233	1.321
Bushveld Complex	Impala mine	IM-20	Melanorite	13	300344	0.085	32.86	377332	245.6	1.682	65.1	0.046	0.051	n.r.	0.027	0.897
					339998	0.082	35.91	336556	253.8	2.313	70.0	0.012	0.024	n.r.	0.257	0.849
					305213	0.137	28.62	353522	324.6	1.582	78.2	0.008	0.048	n.r.	0.244	2.556
					328476	4.747	123.74	337403	233.7	0.250	57.5	0.020	0.313	n.r.	0.531	0.888
					296378	0.114	33.78	343859	264.7	0.044	55.4	0.017	0.027	n.r.	0.034	0.946
					314646	0.008	28.91	352707	257.4	0.365	65.6	0.008	0.072	n.r.	0.312	0.864
					322254	0.008	39.56	343555	236.0	2.800	81.2	0.008	0.051	n.r.	1.012	0.822
					334867	1.652	34.60	339295	218.5	1.071	80.3	0.062	0.017	n.r.	0.090	0.803
					307647	0.008	24.69	377382	221.2	1.643	75.2	0.008	0.045	n.r.	0.066	2.617
					315847	2.336	31.34	336520	273.9	2.465	87.9	0.155	0.099	n.r.	0.122	1.099
					303996	0.008	32.69	341425	358.2	2.282	92.5	0.008	0.039	n.r.	0.422	2.465
Median IM-20					314646	0.085	32.86	343555	253.8	1.643	75.2	0.012	0.048	n.r.	0.244	0.897

ANNEXE 19 – Cont.

Intrusion	Locality	Sample	¹¹¹ Cd	¹¹⁵ In	¹¹⁸ Sn	¹²¹ Sb	¹²⁸ Te	¹⁸⁵ Re	¹⁸⁹ Os	¹⁹³ Ir	¹⁹⁵ Pt	¹⁹⁷ Au	²⁰⁵ Tl	²⁰⁸ Pb	²⁰⁹ Bi
LOD			0.025	0.014	0.018	0.012	0.079	0.004	0.008	0.002	0.004	0.007	0.002	0.005	0.002
Bushveld Complex	Impala mine	IM-19	1.984	0.993	1.400	0.012	0.094	0.004	0.020	0.004	0.004	0.007	0.002	14.728	0.119
			2.179	1.108	1.494	0.012	0.079	0.022	0.008	0.002	0.004	0.007	0.002	8.425	0.119
			1.702	1.105	1.482	0.012	0.244	0.004	0.008	0.002	0.004	0.018	0.002	10.011	0.059
			1.765	1.227	1.491	0.012	0.079	0.004	0.008	0.026	0.004	0.007	0.002	11.022	0.054
			2.234	0.989	0.867	0.012	0.158	0.004	0.024	0.034	0.004	0.007	0.002	96.159	0.101
			2.708	1.180	1.083	0.012	0.099	0.004	0.008	0.002	0.004	0.016	0.002	39.863	0.137
			2.526	1.079	0.475	0.046	0.359	0.056	0.055	0.045	0.004	0.007	0.002	8.399	0.487
			2.739	1.076	1.978	0.012	0.079	0.042	0.008	0.002	0.004	0.007	0.002	7.422	0.131
			3.986	5.263	1.193	0.012	0.423	0.004	0.008	0.002	0.018	0.007	0.002	5.295	0.103
Median IM-19			2.234	1.105	1.400	0.012	0.099	0.004	0.008	0.002	0.004	0.007	0.002	10.011	0.119
Bushveld Complex	Impala mine	IM-20	3.226	1.242	1.531	0.012	0.455	0.004	0.008	0.002	0.004	0.029	0.002	11.898	0.341
			3.176	0.894	1.976	0.012	0.079	0.004	0.233	0.122	0.004	0.025	0.002	13.998	0.192
			3.591	1.158	1.339	0.030	0.216	0.062	0.008	0.006	0.004	0.007	0.002	18.867	0.752
			3.224	0.884	1.190	0.012	0.128	0.102	0.008	0.002	0.012	0.007	0.019	8.366	0.313
			3.773	0.911	1.330	0.012	0.277	0.004	0.008	0.002	0.008	0.007	0.002	11.320	0.277
			2.579	1.220	0.995	0.012	0.365	0.004	0.034	0.033	0.010	0.016	0.002	7.821	0.216
			2.800	1.142	2.200	0.012	0.189	0.004	0.008	0.002	0.004	0.007	0.002	72.423	0.180
			2.642	1.093	1.518	0.012	0.079	0.062	0.008	0.022	0.004	0.007	0.002	9.555	0.219
			2.574	3.561	1.378	0.012	0.210	0.004	0.027	0.002	0.004	0.007	0.002	8.520	0.228
			2.837	1.079	2.069	0.012	0.122	0.004	0.008	0.002	0.004	0.007	0.002	7.790	0.201
			3.185	1.111	1.585	0.012	0.079	0.004	0.008	0.002	0.004	0.007	0.002	37.429	0.338
Median IM-20			3.176	1.111	1.518	0.012	0.189	0.004	0.008	0.002	0.004	0.007	0.002	11.320	0.228

ANNEXE 19 – Cont.

Intrusion	Locality	Sample	Rock	Height (cm)	³⁴ S	⁵⁹ Co	⁶¹ Ni	⁶⁵ Cu	⁶⁶ Zn	⁷⁵ As	⁸² Se	⁹⁵ Mo	¹⁰¹ Ru	¹⁰³ Rh	¹⁰⁸ Pd	¹⁰⁹ Ag
LOD					58	0.008	0.31	0.2	0.1	0.044	0.6	0.008	0.008	0.001	0.027	0.003
Bushveld Complex	Impala mine	IM-21	Melanorite	8	318602	0.101	34.39	345076	249.8	1.286	74.9	0.008	0.039	n.r.	2.033	0.910
					351467	2.127	41.74	339639	258.7	1.978	85.9	0.032	0.013	n.r.	0.211	0.855
					318602	6.655	40.78	333503	228.2	0.553	66.0	0.008	0.124	n.r.	0.086	1.126
					304979	0.562	41.08	336252	276.9	1.765	65.7	0.008	0.072	n.r.	0.095	0.901
					316436	0.099	41.38	332602	413.8	1.004	68.0	0.065	0.036	n.r.	1.236	0.910
					348518	0.231	51.97	332771	242.5	1.887	73.6	0.008	0.060	n.r.	0.562	1.528
Median IM-21					318602	0.397	41.23	334877	254.2	1.525	70.8	0.008	0.050	n.r.	0.387	0.910
Bushveld Complex	Impala mine	IM-22	Upper Chromitite	6	333209	2.300	37.73	347511	328.6	1.795	74.8	0.011	0.091	n.r.	1.365	1.266
					328948	0.088	46.27	347206	303.1	2.739	75.1	0.048	0.036	n.r.	0.755	1.254
					326514	0.566	51.43	356979	410.8	1.688	77.2	0.057	0.054	n.r.	1.455	1.287
					345685	0.090	47.78	345381	319.5	2.039	87.2	0.016	0.011	n.r.	0.158	1.310
					359758	0.263	62.08	355422	250.7	1.136	85.2	0.008	1.024	n.r.	0.234	1.539
					353333	0.008	45.07	347815	398.6	2.678	92.2	0.008	0.008	n.r.	0.085	0.986
Median IM-22					339447	0.177	47.02	347663	324.1	1.917	81.2	0.013	0.045	n.r.	0.494	1.277
Bushveld Complex	Impala mine	IM-24	Lower Chromitite	0	324758	1.233	26.17	342642	268.7	0.740	76.7	0.008	0.012	n.r.	1.022	5.903
					325297	0.233	24.34	327731	256.5	0.253	66.6	0.008	0.015	n.r.	0.788	10.864
					332904	4.266	30.73	358161	281.2	0.822	67.0	0.018	0.014	n.r.	2.215	1.564
					326425	0.008	28.86	357016	244.0	0.655	77.9	0.008	0.039	n.r.	0.845	1.701
					339599	2.769	65.14	386461	189.0	0.367	85.8	0.023	0.008	n.r.	0.027	7.364
					340512	0.087	66.95	350554	157.6	0.310	76.1	0.090	0.039	n.r.	0.522	1.439
					334730	0.008	43.21	341537	237.4	1.124	73.0	0.008	0.082	n.r.	0.267	1.199
Median IM-24					332904	0.233	30.73	350554	244.0	0.655	76.1	0.008	0.015	n.r.	0.788	1.701

ANNEXE 19 – Cont.

Intrusion	Locality	Sample	¹¹¹ Cd	¹¹⁵ In	¹¹⁸ Sn	¹²¹ Sb	¹²⁸ Te	¹⁸⁵ Re	¹⁸⁹ Os	¹⁹³ Ir	¹⁹⁵ Pt	¹⁹⁷ Au	²⁰⁵ Tl	²⁰⁸ Pb	²⁰⁹ Bi
LOD			0.025	0.014	0.018	0.012	0.079	0.004	0.008	0.002	0.004	0.007	0.002	0.005	0.002
Bushveld Complex	Impala mine	IM-21	2.820	1.660	1.272	0.012	0.079	0.004	0.065	0.002	0.004	0.007	0.002	2.860	0.016
			3.720	2.066	0.764	0.012	0.423	0.004	0.008	0.054	0.043	0.007	0.002	5.508	0.079
			3.239	1.533	1.147	0.012	0.079	0.124	0.008	0.002	0.012	0.007	0.018	5.934	0.033
			3.804	0.698	0.660	0.012	0.327	0.004	0.008	0.122	0.004	0.013	0.002	14.363	0.095
			4.747	0.627	0.673	0.012	0.079	0.053	0.244	0.002	0.017	0.007	0.002	8.642	0.118
			4.260	4.562	0.426	0.012	0.222	0.004	0.008	0.002	0.033	0.014	0.020	12.872	0.463
Median IM-21			3.762	1.596	0.718	0.012	0.151	0.004	0.008	0.002	0.014	0.007	0.002	7.288	0.087
Bushveld Complex	Impala mine	IM-22	4.382	1.105	0.769	0.012	0.079	0.004	0.010	0.002	0.034	0.007	0.002	16.037	0.058
			4.595	1.510	1.522	0.012	0.567	0.004	0.008	0.002	0.005	0.007	0.002	12.202	0.002
			6.025	1.820	1.728	0.012	0.207	0.004	0.008	0.123	0.004	0.007	0.002	15.763	0.018
			4.712	1.664	1.719	0.033	0.099	0.004	0.008	0.002	0.004	0.007	0.002	13.922	0.023
			2.678	1.185	0.444	0.012	0.149	0.004	0.008	0.002	0.004	0.007	0.037	7.181	0.002
			7.242	1.002	1.561	0.012	0.143	0.004	0.008	0.002	0.018	0.007	0.002	5.721	0.021
Median IM-22			4.654	1.348	1.541	0.012	0.146	0.004	0.008	0.002	0.004	0.007	0.002	13.062	0.019
Bushveld Complex	Impala mine	IM-24	2.612	2.309	0.289	0.012	0.079	0.004	0.008	0.002	0.025	0.014	0.002	3.073	0.014
			7.455	2.160	0.157	0.012	0.079	0.004	0.008	0.002	0.024	0.007	0.016	12.598	0.014
			3.624	1.566	0.296	0.012	0.139	0.004	0.008	0.002	0.015	0.007	0.002	10.820	0.041
			2.860	3.266	0.173	0.012	0.103	0.004	0.101	0.002	0.046	0.007	0.040	9.370	0.060
			4.656	2.072	0.156	0.012	0.211	0.004	0.008	0.201	0.004	0.007	0.002	3.834	0.002
			3.784	1.384	0.462	0.012	0.451	0.004	0.008	0.002	0.070	0.013	0.107	10.924	0.133
			3.712	1.266	0.076	0.040	0.525	0.004	0.008	0.002	0.006	0.007	0.002	4.991	0.017
Median IM-24			3.712	2.072	0.173	0.012	0.139	0.004	0.008	0.002	0.024	0.007	0.002	9.370	0.017

ANNEXE 19 – Cont.

Intrusion	Locality	Sample	Rock	Height (cm)	³⁴ S	⁵⁹ Co	⁶¹ Ni	⁶⁵ Cu	⁶⁶ Zn	⁷⁵ As	⁸² Se	⁹⁵ Mo	¹⁰¹ Ru	¹⁰³ Rh	¹⁰⁸ Pd	¹⁰⁹ Ag
LOD					58	0.008	0.31	0.2	0.1	0.044	0.6	0.008	0.008	0.001	0.027	0.003
Bushveld Complex	Impala mine	IM-26	Leuconorite	-8	314038	0.119	56.60	334539	324.7	0.913	88.2	0.015	0.039	n.r.	0.323	1.413
					327427	0.092	59.03	365160	328.3	1.339	88.6	0.123	0.033	n.r.	2.311	1.190
					334870	0.526	53.56	345569	339.3	0.548	78.5	0.008	0.012	n.r.	0.655	1.431
					316168	15.023	45.69	339026	297.9	2.168	86.7	0.099	0.027	n.r.	0.566	1.479
					316558	2.433	36.50	343513	313.4	0.860	70.6	0.008	0.020	n.r.	1.036	1.473
Median IM-26					316558	0.526	53.56	343513	324.7	0.913	86.7	0.015	0.027	n.r.	0.655	1.431
Bushveld Complex	Impala mine	IM-28	Leuconorite	-23	316476	0.350	55.08	322862	253.7	1.445	60.3	0.231	0.032	n.r.	0.551	0.931
					317689	1.327	51.12	349758	234.6	1.095	83.1	0.082	0.008	n.r.	0.123	0.886
					335947	0.274	65.12	326686	264.0	1.343	86.1	0.426	0.032	n.r.	2.033	1.007
					343992	0.132	77.90	332579	353.0	0.325	72.3	0.082	0.014	n.r.	0.098	1.187
Median IM-28					326818	0.312	60.10	329632	258.8	1.219	77.7	0.157	0.023	n.r.	0.337	0.969

ANNEXE 19 – Cont.

Intrusion	Locality	Sample	¹¹¹ Cd	¹¹⁵ In	¹¹⁸ Sn	¹²¹ Sb	¹²⁸ Te	¹⁸⁵ Re	¹⁸⁹ Os	¹⁹³ Ir	¹⁹⁵ Pt	¹⁹⁷ Au	²⁰⁵ Tl	²⁰⁸ Pb	²⁰⁹ Bi
LOD			0.025	0.014	0.018	0.012	0.079	0.004	0.008	0.002	0.004	0.007	0.002	0.005	0.002
Bushveld Complex	Impala mine	IM-26	5.538	3.616	6.451	0.012	0.235	0.004	0.008	0.002	0.012	0.008	0.025	410.805	0.064
			4.321	1.387	6.908	0.012	0.228	0.004	0.008	0.002	0.013	0.007	0.022	164.322	0.074
			3.073	1.461	5.903	0.012	0.201	0.004	0.058	0.120	0.004	0.007	0.016	213.010	0.048
			2.891	2.624	5.112	0.012	0.079	0.004	0.008	0.002	0.010	0.007	0.002	7.394	0.076
			8.923	1.698	4.138	0.012	0.362	0.004	0.008	0.002	0.007	0.007	0.002	368.203	0.045
Median IM-26			4.321	1.698	5.903	0.012	0.228	0.004	0.008	0.002	0.010	0.007	0.016	213.010	0.064
Bushveld Complex	Impala mine	IM-28	1.887	1.147	0.977	0.012	0.079	0.004	0.008	0.002	0.004	0.007	0.040	17.345	0.111
			5.636	3.457	2.404	0.012	0.412	0.004	0.126	0.002	0.004	0.007	0.002	5.234	0.030
			2.350	1.247	3.439	0.012	0.232	0.004	0.008	0.107	0.004	0.007	0.066	5.632	0.076
			1.552	1.659	3.986	0.012	0.356	0.004	0.100	0.002	0.110	0.007	0.058	4.412	0.167
Median IM-28			2.118	1.453	2.921	0.012	0.294	0.004	0.054	0.002	0.004	0.007	0.049	5.433	0.094

ANNEXE 19 – Cont.

Intrusion	Locality	Sample	Rock	Height (cm)	³⁴ S	⁵⁹ Co	⁶¹ Ni	⁶⁵ Cu	⁶⁶ Zn	⁷⁵ As	⁸² Se	⁹⁵ Mo	¹⁰¹ Ru	¹⁰³ Rh
LOD					58	0.008	0.31	0.2	0.1	0.044	0.6	0.008	0.008	0.001
Bushveld Complex	Rustenburg mine	AN	Anorthosite	-2	376723	0.110	55.99	329994	329.9	0.044	82.2	0.014	0.008	n.r.
					362243	0.121	59.95	323167	374.3	0.524	86.4	0.008	0.008	n.r.
					381592	0.091	65.73	328786	363.9	1.308	85.9	0.066	0.024	n.r.
Median AN					376723	0.110	59.95	328786	363.9	0.524	85.9	0.014	0.008	n.r.
Bushveld Complex	Rustenburg mine	LC	Lower chromitite	0	360679	0.099	27.39	323775	249.7	0.344	79.0	0.008	0.040	n.r.
					386765	0.071	22.84	343853	244.7	0.044	91.9	0.037	0.008	n.r.
					379766	0.050	26.47	341334	260.5	0.044	88.0	0.008	0.008	n.r.
					356157	2.034	27.97	312212	268.4	0.044	79.4	0.052	0.008	n.r.
					358770	0.114	31.04	335822	266.9	0.044	99.5	0.008	0.008	n.r.
					381288	0.120	26.20	328786	280.6	0.044	79.0	0.024	0.018	n.r.
Median LC					370223	0.107	26.93	332304	263.7	0.044	83.7	0.016	0.008	n.r.
Bushveld Complex	Rustenburg mine	CGM-1	Coarse-grained melanorite	2	346598	0.107	20.40	308560	347.5	0.292	77.0	0.008	0.009	n.r.
					344373	4.200	21.91	329125	246.5	0.641	92.2	0.179	0.021	n.r.
					392456	0.487	55.94	324688	298.2	0.044	81.6	0.066	0.143	n.r.
Median CGM-1					346598	0.487	21.91	324688	298.2	0.292	81.6	0.066	0.021	n.r.
Bushveld Complex	Rustenburg mine	CGM-2	Coarse-grained melanorite	6	346902	0.017	15.52	313733	411.2	0.210	101.9	0.009	0.016	n.r.
					362669	2.022	21.62	325601	316.5	0.432	164.9	0.097	0.023	n.r.
					349945	0.143	13.08	308865	176.2	0.137	185.0	0.142	4.017	n.r.
					351457	0.055	19.48	309169	243.1	0.371	82.6	0.008	0.019	n.r.
					346689	5.622	80.03	318257	189.6	0.412	79.2	0.268	4.595	n.r.
Median CGM-2					349945	0.143	19.48	313733	243.1	0.371	101.9	0.097	0.023	n.r.

ANNEXE 19 – Cont.

Locality	Sample	¹⁰⁸ Pd	¹⁰⁹ Ag	¹¹¹ Cd	¹¹⁵ In	¹¹⁸ Sn	¹²¹ Sb	¹²⁸ Te	¹⁸⁵ Re	¹⁸⁹ Os	¹⁹³ Ir	¹⁹⁵ Pt	¹⁹⁷ Au	²⁰⁵ Tl	²⁰⁸ Pb	²⁰⁹ Bi
LOD		0.027	0.003	0.025	0.014	0.018	0.012	0.079	0.004	0.008	0.002	0.004	0.007	0.002	0.005	0.002
Rustenburg mine	AN	1.057	1.546	19.232	1.885	3.013	0.012	0.079	0.004	0.008	0.002	0.021	0.007	0.011	1.448	0.002
		0.988	8.757	19.901	3.094	3.165	0.012	0.314	0.004	0.027	0.002	0.049	0.007	0.028	1.826	0.004
		2.122	3.347	20.266	2.010	3.712	0.012	0.120	0.004	0.008	0.002	0.004	0.013	0.090	2.130	0.057
Median AN		1.057	3.347	19.901	2.010	3.165	0.012	0.120	0.004	0.008	0.002	0.021	0.007	0.028	1.826	0.004
Rustenburg mine	LC	0.755	1.129	10.864	2.147	0.286	0.012	0.365	0.004	0.008	0.087	0.004	0.007	0.002	6.147	0.002
		0.212	6.844	10.224	2.248	0.240	0.012	0.167	0.004	0.008	0.002	0.004	0.007	0.002	3.043	0.020
		0.027	1.369	10.498	1.781	0.587	0.015	0.289	0.013	0.008	0.002	0.011	0.007	0.003	1.619	0.002
		1.210	1.302	13.663	2.433	0.332	0.012	0.079	0.004	0.008	0.002	0.004	0.007	0.006	2.294	0.002
		0.567	7.881	18.045	4.697	0.499	0.058	0.356	0.004	0.008	0.002	0.004	0.011	0.002	1.692	0.011
Median LC		0.400	1.336	11.274	2.341	0.309	0.012	0.228	0.004	0.008	0.002	0.004	0.007	0.002	2.669	0.007
Rustenburg mine	CGM-1	3.125	1.044	4.138	1.120	0.018	0.012	0.204	0.004	0.008	0.002	0.004	0.007	0.013	4.668	0.015
		1.240	1.707	4.346	3.326	0.077	0.082	0.079	0.004	0.008	0.005	0.004	0.023	0.016	4.838	0.008
		0.786	3.499	12.111	2.473	0.179	0.207	0.079	0.004	0.008	0.002	0.004	0.021	0.017	3.712	0.012
Median CGM-1		1.240	1.707	4.346	2.473	0.077	0.082	0.079	0.004	0.008	0.002	0.004	0.021	0.016	4.668	0.012
Rustenburg mine	CGM-2	0.589	1.954	3.987	0.681	0.061	0.012	0.125	0.004	0.008	0.002	0.004	0.007	0.002	2.404	0.002
		0.475	2.042	3.350	0.691	0.018	0.012	0.098	0.004	0.008	0.006	0.004	0.007	0.006	2.221	0.006
		4.589	2.039	3.013	0.651	0.103	0.012	0.146	0.016	1.095	1.619	0.037	0.007	0.002	2.291	0.152
		3.256	1.327	2.647	1.089	0.018	0.012	0.190	0.004	0.008	0.002	0.011	0.007	0.008	5.266	0.002
		0.878	1.823	2.574	1.360	0.107	0.012	0.262	0.493	5.569	2.891	0.170	0.007	0.026	11.630	0.131
Median CGM-2		0.878	1.954	3.013	0.691	0.061	0.012	0.146	0.004	0.008	0.006	0.011	0.007	0.006	2.404	0.006

ANNEXE 19 – Cont.

Intrusion	Locality	Sample	Rock	Height (cm)	³⁴ S	⁵⁹ Co	⁶¹ Ni	⁶⁵ Cu	⁶⁶ Zn	⁷⁵ As	⁸² Se	⁹⁵ Mo	¹⁰¹ Ru	¹⁰³ Rh
LOD					58	0.008	0.31	0.2	0.1	0.044	0.6	0.008	0.008	0.001
Bushveld Complex	Rustenburg mine	UC	Upper chromitite	10	393156	0.124	23.74	319515	362.1	0.044	80.9	0.008	0.011	n.r.
					377941	0.856	87.37	324271	343.9	0.513	68.8	0.086	0.018	n.r.
					389504	0.083	25.26	322558	357.2	0.487	75.2	0.008	0.024	n.r.
					371889	0.229	17.69	332418	185.0	0.321	105.0	0.155	0.008	n.r.
					380376	7.567	124.57	319985	377.6	0.254	65.4	0.008	0.008	n.r.
					366682	0.199	43.51	322148	371.2	0.323	71.5	0.008	0.013	n.r.
Median UC					379158	0.214	34.39	322353	359.7	0.322	73.4	0.008	0.012	n.r.
Bushveld Complex	Rustenburg mine	M-1	Melanorite	13.5	349336	0.040	16.13	320428	295.2	0.044	128.7	0.061	0.046	n.r.
					370158	1.308	279.96	313429	392.5	0.552	137.5	0.213	2.008	n.r.
					369725	0.008	16.79	324080	224.3	0.307	80.6	0.008	0.008	n.r.
					345381	0.018	7.00	319926	188.7	0.494	75.3	0.126	0.008	n.r.
					352579	0.057	9.87	321949	544.7	0.274	75.7	0.008	0.008	n.r.
					347112	0.104	29.52	333374	323.7	0.791	107.7	0.025	0.064	n.r.
Median M-1					350957	0.049	16.46	321189	309.4	0.400	94.2	0.043	0.027	n.r.
Bushveld Complex	Rustenburg mine	M-2	Melanorite	18	331383	0.234	35.91	316525	447.3	0.044	63.0	0.008	0.049	n.r.
					345685	0.058	51.73	318298	426.0	0.044	67.0	0.145	0.008	n.r.
					327587	0.060	39.81	312516	333.7	0.246	77.2	0.008	0.009	n.r.
					331991	0.097	22.52	310690	325.3	0.067	95.2	0.099	0.033	n.r.
					336860	0.094	37.75	318602	365.2	0.562	84.7	0.008	0.013	n.r.
					342033	3.067	38.34	314342	285.1	0.044	129.3	0.008	0.021	n.r.
Median M-2					334426	0.096	38.04	315433	349.4	0.056	81.0	0.008	0.017	n.r.

ANNEXE 19 – Cont.

Locality	Sample	¹⁰⁸ Pd	¹⁰⁹ Ag	¹¹¹ Cd	¹¹⁵ In	¹¹⁸ Sn	¹²¹ Sb	¹²⁸ Te	¹⁸⁵ Re	¹⁸⁹ Os	¹⁹³ Ir	¹⁹⁵ Pt	¹⁹⁷ Au	²⁰⁵ Tl	²⁰⁸ Pb	²⁰⁹ Bi
LOD		0.027	0.003	0.025	0.014	0.018	0.012	0.079	0.004	0.008	0.002	0.004	0.007	0.002	0.005	0.002
Rustenburg mine	UC	0.266	16.219	43.515	1.683	0.018	0.012	0.079	0.004	0.008	0.003	0.219	0.007	0.019	10.772	0.002
		0.456	1.768	14.546	1.582	0.141	0.012	0.535	0.004	0.008	0.097	0.055	0.007	0.002	5.356	0.016
		1.036	1.887	20.327	1.865	0.064	0.012	0.168	0.007	0.008	0.002	0.004	0.007	0.002	7.340	0.018
		0.099	1.310	19.475	1.671	0.123	0.012	0.217	0.004	0.008	0.002	0.004	0.007	0.002	3.865	0.002
		2.011	1.935	16.463	1.351	0.018	0.012	0.079	0.024	0.008	0.084	0.004	0.007	0.002	6.158	0.029
		0.102	1.485	17.071	1.108	0.097	0.012	0.312	0.004	0.008	0.002	0.058	0.007	0.008	6.482	0.023
Median UC		0.361	1.827	18.273	1.626	0.080	0.012	0.192	0.004	0.008	0.002	0.029	0.007	0.002	6.320	0.017
Rustenburg mine	M-1	0.027	2.982	6.755	3.544	0.110	0.012	0.187	0.061	0.008	0.055	0.125	0.007	0.023	16.432	0.016
		0.027	2.297	10.285	0.337	0.161	0.024	0.259	0.356	2.313	0.721	0.228	0.007	0.020	8.689	0.100
		0.027	0.636	3.925	1.500	0.522	0.012	0.079	0.004	0.008	0.002	0.011	0.007	0.013	8.969	0.002
		0.027	0.666	3.269	1.089	0.231	0.012	0.321	0.066	0.008	0.002	0.004	0.037	0.002	4.899	0.012
		0.027	1.032	4.869	1.129	0.018	0.012	0.123	0.021	0.008	0.002	0.013	0.009	0.002	6.451	0.005
		0.027	1.990	9.403	1.281	0.146	0.012	0.456	0.021	0.008	0.233	0.088	0.007	0.016	16.889	0.058
Median M-1		0.027	1.511	5.812	1.205	0.154	0.012	0.223	0.041	0.008	0.028	0.051	0.007	0.015	8.829	0.014
Rustenburg mine	M-2	0.027	2.097	13.328	1.475	0.180	0.012	0.079	0.120	0.008	0.002	0.081	0.007	0.004	6.573	0.002
		0.027	1.346	13.237	3.655	0.176	0.012	0.174	0.004	0.008	0.522	0.039	0.029	0.009	5.538	0.008
		0.027	1.062	8.825	1.491	0.455	0.016	0.079	0.004	0.008	0.002	0.004	0.007	0.005	7.060	0.015
		0.027	4.729	15.580	2.458	0.295	0.012	0.116	0.004	0.008	0.090	0.079	0.007	0.002	1.701	0.025
		0.027	1.297	10.620	1.066	0.146	0.012	0.566	0.046	0.008	0.002	0.004	0.007	0.002	4.595	0.022
		0.027	0.904	10.681	1.104	0.157	0.012	0.735	0.004	0.008	0.002	0.599	0.007	0.012	11.411	0.320
Median M-2		0.027	1.321	11.959	1.483	0.178	0.012	0.145	0.004	0.008	0.002	0.059	0.007	0.005	6.056	0.019

ANNEXE 19 – Cont.

Intrusion	Locality	Sample	Rock	Height (cm)	³⁴ S	⁵⁹ Co	⁶¹ Ni	⁶⁵ Cu	⁶⁶ Zn	⁷⁵ As	⁸² Se	⁹⁵ Mo	¹⁰¹ Ru	¹⁰³ Rh
LOD					58	0.008	0.31	0.2	0.1	0.044	0.6	0.008	0.008	0.001
Bushveld Complex	Rustenburg mine	M-3	Melanorite	23	329861	0.201	61.77	314951	763.8	0.121	80.0	0.256	0.012	n.r.
					324992	12.449	48.69	313125	310.7	0.240	78.0	0.008	0.042	n.r.
					338990	0.132	43.82	315559	343.3	0.402	74.6	0.107	0.008	n.r.
					359076	4.523	52.95	336688	364.0	0.044	79.2	0.008	0.014	n.r.
					334121	0.055	40.17	321341	397.2	0.099	72.7	0.076	0.014	n.r.
Median M-3					334121	0.201	48.69	315559	364.0	0.121	78.0	0.076	0.014	n.r.
Bushveld Complex	Rustenburg mine	M-4	Melanorite	27	341778	0.086	46.56	326215	419.9	0.044	79.0	0.008	0.008	n.r.
					337530	2.034	58.12	323428	372.4	0.170	77.4	0.010	0.024	n.r.
					347511	0.110	50.26	327839	287.6	0.112	81.9	0.008	0.008	n.r.
					330470	13.466	69.99	319979	302.8	0.044	98.6	0.008	0.008	n.r.
					349976	0.943	45.34	338976	232.2	0.044	88.9	0.057	0.012	n.r.
					359089	1.023	23.44	316776	329.3	0.236	82.6	0.066	0.024	n.r.
Median M-4					344644	0.983	48.41	324821	316.0	0.078	82.2	0.009	0.010	n.r.

ANNEXE 19 – Cont.

Locality	Sample	¹⁰⁸ Pd	¹⁰⁹ Ag	¹¹¹ Cd	¹¹⁵ In	¹¹⁸ Sn	¹²¹ Sb	¹²⁸ Te	¹⁸⁵ Re	¹⁸⁹ Os	¹⁹³ Ir	¹⁹⁵ Pt	¹⁹⁷ Au	²⁰⁵ Tl	²⁰⁸ Pb	²⁰⁹ Bi
LOD		0.027	0.003	0.025	0.014	0.018	0.012	0.079	0.004	0.008	0.002	0.004	0.007	0.002	0.005	0.002
Rustenburg mine	M-3	0.027	0.937	22.214	4.203	3.585	0.012	0.271	0.004	0.008	0.745	0.004	0.007	0.007	2.161	0.042
		0.027	1.157	14.120	1.469	3.533	0.012	0.134	0.088	0.008	0.002	0.004	0.007	0.002	1.409	0.040
		0.027	1.004	12.142	1.395	2.145	0.012	0.117	0.004	0.008	0.002	0.004	0.007	0.009	6.299	0.225
		0.027	0.973	14.424	3.227	3.076	0.012	0.250	0.004	0.008	0.002	0.004	0.007	0.002	1.680	0.056
		0.027	1.083	13.176	1.526	2.927	0.012	1.022	0.066	0.008	0.066	0.004	0.007	0.002	3.256	0.098
Median M-3		0.027	1.004	14.120	1.526	3.076	0.012	0.250	0.004	0.008	0.002	0.004	0.007	0.002	2.161	0.056
Rustenburg mine	M-4	0.027	1.175	12.872	2.211	0.977	0.012	1.211	0.122	0.008	0.002	0.012	0.007	0.002	3.867	0.026
		0.027	0.870	12.263	1.411	0.368	0.012	0.079	0.004	0.008	0.002	0.029	0.007	0.010	8.673	0.051
		0.027	0.837	9.616	2.082	1.233	0.012	0.562	0.004	0.008	0.002	0.091	0.007	0.002	9.586	0.050
		0.027	3.280	12.385	1.282	0.651	0.012	0.436	0.004	0.008	1.023	0.004	0.007	0.004	2.663	0.098
		0.027	0.870	8.946	1.430	0.116	0.012	0.429	0.099	0.008	0.002	0.004	0.007	0.002	6.177	0.770
0.027	3.712	10.803	0.943	0.158	0.012	0.079	0.004	0.018	0.232	0.018	0.052	0.019	4.230	0.027		
Median M-4		0.027	1.022	11.533	1.420	0.510	0.012	0.432	0.004	0.008	0.002	0.015	0.007	0.003	5.204	0.050

ANNEXE 19 – Cont.

Intrusion	Locality	Sample	Rock	³⁴ S	⁵⁹ Co	⁶¹ Ni	⁶⁵ Cu	⁶⁶ Zn	⁷⁵ As	⁸² Se	⁹⁵ Mo	¹⁰¹ Ru	¹⁰³ Rh	¹⁰⁸ Pd
LOD				58	0.008	0.31	0.2	0.1	0.044	0.6	0.008	0.008	0.001	0.027
Stillwater Complex	East Boulder mine	ST-12	Mela troctolite	330774	2.830	33.47	340816	184.8	0.248	227.6	0.008	0.216	n.r.	1.146
				385548	4.601	34.62	317290	144.7	0.156	189.9	0.037	0.110	n.r.	1.858
Median ST-12				358161	3.715	34.05	329053	164.7	0.202	208.7	0.022	0.163	n.r.	1.502
Stillwater Complex	East Boulder mine	ST-14	Anorthosite	361204	0.210	44.73	348119	234.9	0.044	174.7	0.008	0.015	n.r.	0.027
				349641	0.301	72.42	339295	284.5	0.122	157.9	0.015	0.033	n.r.	0.212
				363943	0.207	36.52	337773	260.8	0.365	146.1	0.008	0.046	n.r.	0.521
				362726	0.298	40.17	322988	263.8	0.183	161.6	0.024	0.120	n.r.	0.027
				353292	0.316	28.91	348424	256.8	0.426	153.4	0.008	0.008	n.r.	3.245
				356031	0.417	45.04	339903	332.8	0.213	143.3	0.008	0.088	n.r.	0.321
Median ST-14				358618	0.300	42.45	339599	262.3	0.198	155.6	0.008	0.040	n.r.	0.266
Stillwater Complex	East Boulder mine	ST-16	Leuconorite	362421	4.869	21.61	362726	598.8	0.044	183.2	0.335	0.099	n.r.	0.027
				363639	0.450	5.17	340207	489.9	0.091	188.4	0.009	0.123	n.r.	0.027
				357553	0.435	5.78	330596	569.0	0.396	211.8	0.008	0.013	n.r.	0.126
				357575	0.320	7.91	359378	368.2	0.548	174.4	0.256	0.030	n.r.	0.027
				356335	1.826	133.89	346902	337.8	0.639	186.8	0.186	0.096	n.r.	3.365
				330375	0.073	24.65	350554	529.5	0.044	197.8	0.199	0.008	n.r.	0.324
Median ST-16				357564	0.443	14.76	348728	509.7	0.243	187.6	0.192	0.063	n.r.	0.076
Stillwater Complex	East Boulder mine	ST-17	Olivine mela gabbronorite	341425	267.784	286.04	274783	1551.3	0.390	234.3	0.076	0.008	n.r.	0.027
				361698	197.795	221.39	322139	161.3	0.255	162.8	0.008	0.098	n.r.	0.268
				348424	37.733	139.45	309473	549.1	0.517	185.6	0.124	0.008	n.r.	0.161
				352379	52.100	51.73	317994	489.3	0.304	198.4	0.008	0.061	n.r.	0.544
Median ST-17				350401	124.947	180.42	313733	519.2	0.347	192.0	0.042	0.034	n.r.	0.214

ANNEXE 19 – Cont.

Locality	Sample	¹⁰⁹ Ag	¹¹¹ Cd	¹¹⁵ In	¹¹⁸ Sn	¹²¹ Sb	¹²⁸ Te	¹⁸⁵ Re	¹⁸⁹ Os	¹⁹³ Ir	¹⁹⁵ Pt	¹⁹⁷ Au	²⁰⁵ Tl	²⁰⁸ Pb	²⁰⁹ Bi	
LOD		0.003	0.025	0.014	0.018	0.012	0.079	0.004	0.008	0.002	0.004	0.007	0.002	0.005	0.002	
East Boulder mine	ST-12	0.943	0.904	0.036	0.143	0.024	0.079	0.004	0.090	0.002	0.004	0.024	0.352	1.156	0.090	
		1.917	0.339	0.136	0.204	0.012	0.169	0.004	0.120	0.076	0.030	0.007	0.256	2.383	0.105	
Median ST-12		1.430	0.622	0.086	0.174	0.018	0.124	0.004	0.105	0.039	0.017	0.016	0.304	1.769	0.097	
East Boulder mine	ST-14	3.286	1.156	0.218	0.201	0.012	0.304	0.004	0.008	0.002	0.004	0.007	0.002	20.297	0.002	
		2.821	1.278	0.456	0.018	0.012	0.091	0.004	0.015	0.042	0.004	0.007	0.076	11.716	0.015	
		13.267	1.856	0.267	0.103	0.012	0.517	0.004	0.008	0.002	0.016	0.007	0.010	13.602	0.002	
		8.094	0.761	0.231	0.521	0.012	0.396	0.004	0.085	0.066	0.008	0.007	0.002	8.064	0.003	
		14.211	1.795	0.270	0.119	0.012	0.211	0.004	0.012	0.002	0.007	0.007	0.007	0.012	11.594	0.006
		10.194	1.126	0.246	0.354	0.012	1.233	0.004	0.008	0.063	0.004	0.007	0.007	0.036	7.364	0.057
Median ST-14		9.144	1.217	0.257	0.160	0.012	0.350	0.004	0.010	0.022	0.005	0.007	0.011	11.655	0.005	
East Boulder mine	ST-16	41.324	5.690	0.751	0.183	0.012	0.099	1.522	0.207	0.005	0.140	0.007	0.007	11.837	0.014	
		33.656	8.886	0.772	0.243	0.012	0.232	0.004	0.008	0.002	0.243	0.007	0.002	3.895	0.010	
		32.895	8.916	1.523	0.216	0.012	0.079	0.004	0.008	0.002	0.026	0.007	0.002	1.001	0.003	
		33.138	8.338	0.732	0.563	0.016	0.082	0.004	0.008	0.002	0.076	0.007	0.003	5.264	0.015	
		33.321	8.520	0.766	0.262	0.012	0.079	0.004	0.010	0.002	0.097	0.007	0.002	4.504	0.010	
		34.508	8.307	0.863	0.386	0.012	0.152	0.004	0.008	0.002	0.004	0.037	0.027	6.116	0.013	
Median ST-16		33.488	8.429	0.769	0.253	0.012	0.090	0.004	0.008	0.002	0.087	0.007	0.003	4.884	0.012	
East Boulder mine	ST-17	0.660	13.998	0.317	0.018	0.079	0.310	0.004	0.030	0.049	0.004	0.007	0.271	3.704	0.024	
		0.934	0.669	0.123	0.018	0.012	0.079	0.004	0.008	0.002	0.015	0.007	0.210	4.291	0.002	
		0.954	1.613	0.655	0.052	0.057	0.609	0.004	0.057	0.057	0.004	0.033	0.222	10.285	0.103	
		3.588	0.974	0.374	0.037	0.064	0.422	0.004	0.008	0.023	0.004	0.007	0.455	10.985	0.086	
Median ST-17		0.944	1.293	0.346	0.027	0.061	0.366	0.004	0.019	0.036	0.004	0.007	0.246	7.288	0.055	

ANNEXE 19 – Cont.

Intrusion	Locality	Sample	Rock	³⁴ S	⁵⁹ Co	⁶¹ Ni	⁶⁵ Cu	⁶⁶ Zn	⁷⁵ As	⁸² Se	⁹⁵ Mo	¹⁰¹ Ru	¹⁰³ Rh	¹⁰⁸ Pd
LOD				58	0.008	0.31	0.2	0.1	0.044	0.6	0.008	0.008	0.001	0.027
Stillwater Complex	Stillwater mine	P-4	Anorthosite	353901	0.043	13.69	331991	206.9	0.044	127.5	0.008	0.008	n.r.	0.027
				365464	0.055	18.87	341120	282.7	0.061	142.1	0.062	0.027	n.r.	0.467
				378245	0.100	31.65	353597	317.7	0.546	144.9	0.040	0.008	n.r.	0.122
				363983	0.008	22.82	348125	256.2	0.044	141.2	0.008	0.030	n.r.	1.323
				359683	0.094	23.43	345989	260.2	0.267	161.4	0.086	0.066	n.r.	0.255
				383722	4.022	34.69	349641	280.0	0.044	156.8	0.008	0.052	n.r.	0.027
Median P-4				364724	0.075	23.13	347057	270.1	0.053	143.5	0.024	0.029	n.r.	0.189
Stillwater Complex	Stillwater mine	P-3	Leuco gabbro-norite	360596	6.086	1308.49	342946	499.1	0.347	197.9	0.008	0.014	n.r.	24.154
				351771	0.271	7.76	337469	483.8	0.044	188.6	0.063	0.102	n.r.	0.423
				355727	0.578	14.30	338382	727.3	0.044	209.7	0.077	0.037	n.r.	2.662
				351467	0.371	6.48	331383	184.1	0.044	197.2	0.010	0.030	n.r.	6.478
				358465	0.152	14.31	344163	213.0	0.044	218.5	0.052	0.017	n.r.	0.544
				352988	1.478	23.48	332600	538.6	0.253	218.8	0.008	0.043	n.r.	0.636
Median P-3				354357	0.475	14.31	337925	491.4	0.044	203.8	0.031	0.033	n.r.	1.649

ANNEXE 19 – Cont.

Locality	Sample	¹⁰⁹ Ag	¹¹¹ Cd	¹¹⁵ In	¹¹⁸ Sn	¹²¹ Sb	¹²⁸ Te	¹⁸⁵ Re	¹⁸⁹ Os	¹⁹³ Ir	¹⁹⁵ Pt	¹⁹⁷ Au	²⁰⁵ Tl	²⁰⁸ Pb	²⁰⁹ Bi
LOD		0.003	0.025	0.014	0.018	0.012	0.079	0.004	0.008	0.002	0.004	0.007	0.002	0.005	0.002
Stillwater mine	P-4	2.587	5.508	0.222	0.070	0.027	0.761	0.004	0.008	0.002	0.274	0.007	0.002	2.952	0.017
		2.666	4.625	0.177	0.057	0.021	0.122	0.004	0.059	0.048	0.004	0.008	0.002	0.949	0.002
		0.545	4.291	0.152	0.018	0.012	0.274	0.004	0.008	0.002	0.004	0.008	0.002	0.761	0.023
		1.537	2.708	0.204	0.122	0.012	0.168	0.004	0.063	0.036	0.009	0.007	0.003	1.716	0.024
		0.742	4.199	0.164	0.018	0.012	0.131	0.004	0.008	0.002	0.017	0.009	0.002	1.865	0.002
		0.761	3.925	0.137	0.018	0.012	0.079	0.004	0.076	0.103	0.004	0.010	0.005	2.069	0.002
Median P-4		1.149	4.245	0.171	0.038	0.012	0.149	0.004	0.033	0.019	0.007	0.008	0.002	1.791	0.009
Stillwater mine	P-3	8.338	5.660	1.519	0.645	0.023	0.173	0.004	0.008	0.007	0.051	0.010	0.016	7.394	0.002
		8.155	5.812	1.547	0.581	0.012	0.079	0.004	0.008	0.002	0.004	0.007	0.005	11.563	0.109
		7.090	7.912	0.974	0.326	0.021	0.079	0.004	0.096	0.057	0.032	0.012	0.019	24.587	0.002
		12.476	3.256	0.949	0.322	0.019	0.099	0.004	0.008	0.002	0.137	0.007	0.023	11.320	0.002
		9.646	4.351	0.459	0.088	0.012	0.118	0.004	0.086	0.103	0.004	0.007	0.002	6.269	0.057
		8.124	7.760	0.523	0.131	0.012	0.210	0.004	0.008	0.002	0.004	0.007	0.002	5.599	0.002
Median P-3		8.247	5.736	0.962	0.324	0.015	0.108	0.004	0.008	0.004	0.018	0.007	0.010	9.357	0.002

ANNEXE 19 – Cont.

Intrusion	Locality	Sample	Rock	³⁴ S	⁵⁹ Co	⁶¹ Ni	⁶⁵ Cu	⁶⁶ Zn	⁷⁵ As	⁸² Se	⁹⁵ Mo	¹⁰¹ Ru	¹⁰³ Rh	¹⁰⁸ Pd
LOD				58	0.008	0.31	0.2	0.1	0.044	0.6	0.008	0.008	0.001	0.027
Stillwater Complex	Banded Series	BS-18	Leuco gabbronorite	371550	0.173	20.39	332904	401.7	0.044	186.2	0.008	0.008	n.r.	0.027
				375506	0.383	7.30	329253	480.8	0.044	171.3	0.008	0.008	n.r.	0.027
				371855	0.472	17.35	321037	245.9	0.116	159.1	0.008	0.008	n.r.	0.027
				366986	0.402	14.52	332296	380.4	0.044	145.5	0.008	0.008	n.r.	0.027
				370333	0.453	19.17	334730	443.1	0.302	140.9	0.008	0.008	n.r.	0.027
				361508	11.563	213.01	330774	442.5	0.044	149.1	0.008	0.008	n.r.	0.027
				359987	1.461	79.12	327427	463.4	0.044	150.0	0.008	0.008	n.r.	0.027
				365769	0.241	7.55	335034	459.5	0.044	144.5	0.008	0.008	n.r.	0.027
				359789	0.140	0.31	333209	380.7	0.326	130.5	0.008	0.008	n.r.	0.027
				359074	2.434	6.42	331078	505.1	0.044	143.6	0.008	0.008	n.r.	0.027
				353287	0.138	2.89	335454	493.0	0.290	131.5	0.008	0.008	n.r.	0.027
				353215	0.161	3.59	338077	417.3	0.044	151.8	0.008	0.008	n.r.	0.027
				348119	0.167	12.48	337796	317.1	0.113	151.5	0.008	0.008	n.r.	0.027
Median BS-18				363639	0.353	13.50	332600	429.9	0.074	150.8	0.008	0.008	n.r.	0.027
Stillwater Complex	Picket Pin	PP-AN	Anorthosite	351459	0.341	15.52	317254	191.4	0.044	124.2	0.008	0.090	n.r.	0.216
				368785	0.186	0.31	331368	271.7	0.192	96.2	0.008	0.008	n.r.	0.090
				346293	0.210	0.31	333909	270.8	0.119	124.5	0.008	0.008	n.r.	0.027
				339903	0.283	2.98	319819	248.6	0.124	126.6	0.008	0.047	n.r.	1.022
				354814	0.514	44.51	328948	223.7	0.044	135.1	0.008	0.015	n.r.	0.027
				341479	0.313	8.54	320732	327.4	0.044	121.4	0.008	0.057	n.r.	0.027
				341729	0.396	17.95	331254	318.9	0.044	125.7	0.008	0.021	n.r.	0.063
				342338	0.289	8.03	324992	307.3	0.143	125.4	0.008	0.008	n.r.	0.076
				350249	0.718	176.49	324384	346.9	0.044	123.9	0.008	0.008	n.r.	0.855
				353276	0.359	48.69	324384	322.6	0.044	131.8	0.008	0.008	n.r.	0.345
Median PP-AN				350249	0.341	9.74	324992	271.7	0.044	124.5	0.008	0.015	n.r.	0.076

ANNEXE 19 – Cont.

Locality	Sample	¹⁰⁹ Ag	¹¹¹ Cd	¹¹⁵ In	¹¹⁸ Sn	¹²¹ Sb	¹²⁸ Te	¹⁸⁵ Re	¹⁸⁹ Os	¹⁹³ Ir	¹⁹⁵ Pt	¹⁹⁷ Au	²⁰⁵ Tl	²⁰⁸ Pb	²⁰⁹ Bi
LOD		0.003	0.025	0.014	0.018	0.012	0.079	0.004	0.008	0.002	0.004	0.007	0.002	0.005	0.002
Banded Series	BS-18	15.915	2.830	0.744	0.533	0.012	10.955	0.004	0.008	0.002	0.004	0.007	0.012	10.437	1.126
		3.128	3.499	0.337	0.231	0.012	0.487	0.004	0.008	0.002	0.004	0.007	0.155	12.750	1.993
		5.264	1.826	0.191	0.097	0.055	0.487	0.004	0.008	0.002	0.004	0.007	0.010	8.916	1.268
		10.468	2.769	0.327	0.341	0.012	2.252	0.004	0.008	0.002	0.004	0.007	0.002	6.786	1.505
		10.766	2.760	0.306	0.338	0.012	5.082	0.004	0.008	0.002	0.004	0.007	0.002	6.857	0.529
		14.546	3.317	0.537	0.347	0.012	7.699	0.004	0.008	0.002	0.004	0.007	0.002	11.168	0.612
		15.458	3.560	0.519	0.344	0.012	11.229	0.004	0.008	0.002	0.004	0.007	0.002	5.964	1.822
		9.424	2.952	1.136	0.566	0.012	3.104	0.004	0.008	0.002	0.004	0.007	0.011	9.007	0.569
		11.259	1.978	0.385	1.187	0.012	1.445	0.004	0.008	0.002	0.004	0.007	0.012	8.155	1.657
		7.577	4.169	1.145	0.752	0.012	13.054	0.004	0.008	0.002	0.004	0.007	0.011	10.072	1.257
		6.594	3.895	1.096	0.679	0.012	0.715	0.004	0.008	0.002	0.004	0.007	0.014	10.529	1.310
		7.358	2.374	0.618	1.695	0.012	4.960	0.004	0.008	0.002	0.004	0.007	0.002	4.625	0.975
3.064	2.221	0.661	0.597	0.012	11.411	0.004	0.008	0.002	0.004	0.007	0.002	7.121	1.771		
Median BS-18		9.946	2.891	0.528	0.379	0.012	2.678	0.004	0.008	0.002	0.004	0.007	0.006	8.962	1.191
Picket Pin	PP-AN	1.184	6.634	0.620	0.085	0.012	0.079	0.004	0.008	0.002	0.103	0.007	0.017	8.460	0.088
		0.514	9.007	0.554	0.067	0.012	0.142	0.004	0.054	0.042	0.004	0.007	0.002	0.499	0.007
		0.697	7.925	0.699	0.158	0.012	0.099	0.004	0.087	0.034	0.004	0.007	0.002	2.100	0.036
		1.147	8.794	0.623	0.091	0.012	0.079	0.004	0.100	0.002	0.004	0.007	0.002	3.086	0.027
		37.733	8.216	0.709	0.100	0.012	0.102	0.004	0.037	0.068	0.058	0.007	0.008	2.343	0.095
		0.326	8.673	0.623	0.168	0.012	0.079	0.004	0.008	0.002	0.004	0.007	0.002	1.205	0.002
		0.274	8.399	0.669	0.128	0.012	0.098	0.004	0.062	0.095	0.004	0.007	0.002	1.102	0.046
		0.329	8.884	0.633	0.018	0.012	0.455	0.004	0.022	0.002	0.004	0.007	0.002	1.439	0.014
		1.022	9.920	0.678	0.149	0.012	0.212	0.004	0.008	0.002	0.004	0.007	0.002	2.252	0.091
		2.921	9.798	0.703	0.776	0.012	0.079	0.004	0.008	0.002	0.004	0.007	0.002	2.282	0.023
Median PP-NA		1.022	8.673	0.669	0.103	0.012	0.098	0.004	0.022	0.002	0.004	0.007	0.002	2.252	0.036

ANNEXE 20 - Average proportion (%) of each element hosted in pyrrhotite (Po), pentlandite (Pn), chalcopyrite (Ccp), phlogopite (phlog) and sum, from different localities of the Bushveld and Stillwater Complexes. Abbreviations: BMS= base-metal sulfides; n.r.= not reported; n.d.= not determined; N= number of samples.

ANNEXE 20

Intrusion	Locality	BMS	Co	Pd	Ir	Pt	Rh	Os	Ru	Au	Sb
Bushveld Complex	Impala Mine - samples above the Merensky Reef interval (N= 8)	Po	0.2%	1.1%	15.3%	0.0%	4.0%	41.3%	11.2%	0.0%	0.1%
		Pn	21.7%	27.3%	7.1%	0.0%	21.8%	16.4%	13.3%	0.0%	0.2%
		Ccp phlog	0.0%	0.5%	0.1%	0.0%	n.r.	0.7%	0.2%	0.0%	0.1%
		Sum	22.0%	29.0%	22.4%	0.0%	25.8%	58.4%	24.7%	0.1%	6.9%
Bushveld Complex	Impala Mine, Merensky Reef - Silicate rocks only (N= 6)	Po	0.2%	0.5%	16.1%	0.0%	1.0%	21.9%	6.6%	0.0%	0.5%
		Pn	58.3%	53.9%	21.8%	0.1%	77.7%	16.9%	6.1%	0.0%	0.4%
		Ccp	0.0%	0.0%	0.0%	0.0%	n.r.	0.1%	0.0%	0.0%	0.2%
		Sum	58.5%	54.4%	38.0%	0.1%	78.7%	38.9%	12.8%	0.0%	1.1%
Bushveld Complex	Impala Mine, Merensky Reef - Chromitites only (N= 2)	Po	0.0%	0.0%	0.6%	0.0%	0.0%	1.1%	0.1%	0.0%	0.2%
		Pn	17.0%	38.8%	5.2%	0.1%	33.9%	3.1%	1.0%	0.0%	0.4%
		Ccp	0.0%	0.1%	0.0%	0.0%	n.r.	0.0%	0.0%	0.0%	0.2%
		Sum	17.0%	38.9%	5.8%	0.1%	33.9%	4.2%	1.1%	0.0%	0.8%
Bushveld Complex	Rustenburg Mine, Merensky Reef - Silicate rocks only (N= 7)	Po	0.1%	0.3%	26.1%	0.0%	1.0%	33.4%	13.2%	0.0%	0.4%
		Pn	54.2%	50.7%	40.0%	0.4%	61.4%	16.0%	15.5%	0.0%	0.6%
		Ccp	0.0%	0.0%	0.0%	0.0%	n.r.	0.0%	0.0%	0.0%	0.2%
		Sum	54.3%	51.0%	66.0%	0.5%	62.4%	49.5%	28.7%	0.0%	1.2%
Bushveld Complex	Rustenburg Mine, Merensky Reef - Chromitites only (N= 2)	Po	0.0%	0.0%	1.9%	0.0%	0.1%	3.7%	0.8%	0.0%	0.2%
		Pn	20.1%	35.9%	3.9%	0.3%	13.9%	19.6%	2.7%	0.0%	0.6%
		Ccp	0.0%	0.0%	0.0%	0.0%	n.r.	0.0%	0.0%	0.0%	0.1%
		Sum	20.1%	36.0%	5.8%	0.3%	14.0%	23.4%	3.5%	0.0%	0.9%

ANNEXE 20 – Cont.

Intrusion	Locality	BMS	Bi	As	Te	Se	Cd	Pb	Sn	Zn
Bushveld Complex	Impala Mine - samples above the Merensky Reef interval (N= 8)	Po	14.14%	5.53%	2.19%	61.54%	n.d.	n.d.	n.d.	n.d.
		Pn	11.85%	9.38%	74.14%	52.53%	n.d.	n.d.	n.d.	n.d.
		Ccp	7.33%	0.53%	2.60%	16.56%	n.d.	n.d.	n.d.	n.d.
		phlog	<1.5	3.00%						
		Sum	33.32%	18.44%	78.93%	130.64%	n.d.	n.d.	n.d.	n.d.
Bushveld Complex	Impala Mine, Merensky Reef - Silicate rocks only (N= 6)	Po	0.49%	33.47%	0.58%	73.90%	n.d.	n.d.	n.d.	n.d.
		Pn	0.45%	5.47%	0.30%	39.30%	n.d.	n.d.	n.d.	n.d.
		Ccp	0.09%	6.39%	0.07%	10.51%	n.d.	n.d.	n.d.	n.d.
		Sum	1.04%	45.33%	0.95%	123.71%	n.d.	n.d.	n.d.	n.d.
Bushveld Complex	Impala Mine, Merensky Reef - Chromitites only (N= 2)	Po	0.03%	2.71%	0.18%	21.05%	n.d.	n.d.	n.d.	n.d.
		Pn	0.17%	8.66%	0.63%	79.84%	n.d.	n.d.	n.d.	n.d.
		Ccp	0.02%	4.27%	0.12%	20.39%	n.d.	n.d.	n.d.	n.d.
		Sum	0.23%	15.64%	0.93%	121.28%	n.d.	n.d.	n.d.	n.d.
Bushveld Complex	Rustenburg Mine, Merensky Reef - Silicate rocks only (N= 7)	Po	0.36%	2.51%	0.40%	47.70%	n.d.	n.d.	n.d.	n.d.
		Pn	0.04%	2.67%	0.16%	47.84%	n.d.	n.d.	n.d.	n.d.
		Ccp	0.01%	2.03%	0.06%	8.55%	n.d.	n.d.	n.d.	n.d.
		Sum	0.42%	7.21%	0.62%	104.10%	n.d.	n.d.	n.d.	n.d.
Bushveld Complex	Rustenburg Mine, Merensky Reef - Chromitites only (N= 2)	Po	0.13%	1.98%	0.11%	29.32%	n.d.	n.d.	n.d.	n.d.
		Pn	0.08%	6.98%	0.23%	73.30%	n.d.	n.d.	n.d.	n.d.
		Ccp	0.02%	1.18%	0.13%	18.03%	n.d.	n.d.	n.d.	n.d.
		Sum	0.23%	10.14%	0.47%	120.66%	n.d.	n.d.	n.d.	n.d.

ANNEXE 20 – Cont.

Intrusion	Locality	BMS	Co	Pd	Ir	Pt	Rh	Os	Ru	Au	Sb
Stillwater Complex	East Boulder Mine - J-M Reef (N= 4)	Po	0.5%	0.1%	17.2%	0.0%	0.9%	0.8%	2.7%	0.0%	0.7%
		Pn	49.1%	62.6%	45.8%	0.1%	88.0%	12.2%	76.1%	0.0%	1.3%
		Ccp	0.0%	0.0%	0.1%	0.0%	n.r.	0.0%	0.1%	0.0%	0.5%
		Sum	49.7%	62.7%	63.1%	0.1%	88.9%	13.1%	78.9%	0.0%	2.5%
Stillwater Complex	Stillwater Mine - J-M Reef (N= 2)	Po	0.3%	0.0%	25.2%	0.0%	2.2%	2.2%	4.5%	0.0%	7.5%
		Pn	42.1%	51.5%	27.3%	0.1%	28.2%	5.6%	26.3%	0.0%	17.1%
		Ccp	0.0%	0.0%	0.3%	0.0%	n.r.	0.2%	0.1%	0.0%	3.6%
		Sum	42.3%	51.5%	52.8%	0.1%	30.5%	8.0%	30.8%	0.0%	28.2%
Stillwater Complex	Banded Series - Gabbro-norite II (N= 1)	Po	0.5%	2.3%	n.d.	1.0%	n.d.	n.d.	n.d.	0.0%	0.1%
		Pn	45.6%	17.1%	n.d.	1.5%	n.d.	n.d.	n.d.	0.0%	0.2%
		Ccp	0.0%	5.0%	n.d.	2.1%	n.d.	n.d.	n.d.	0.0%	0.3%
		Sum	46.1%	24.4%	n.d.	4.6%	n.d.	n.d.	n.d.	0.1%	0.6%

ANNEXE 20 – Cont.

Intrusion	Locality	BMS	Bi	As	Te	Se	Cd	Pb	Sn	Zn
Stillwater Complex	East Boulder Mine - J-M Reef (N= 4)	Po	0.14%	1.07%	0.05%	35.41%	0.36%	0.12%	0.22%	0.00%
		Pn	0.02%	1.55%	0.43%	69.95%	0.82%	0.29%	0.15%	0.05%
		Ccp	0.04%	1.11%	0.05%	16.59%	1.97%	0.83%	0.32%	1.65%
		Sum	0.19%	3.72%	0.52%	121.96%	3.15%	1.25%	0.69%	1.70%
Stillwater Complex	Stillwater Mine - J-M Reef (N= 2)	Po	0.23%	13.21%	0.05%	40.69%	3.75%	0.83%	0.40%	0.03%
		Pn	0.01%	6.19%	0.42%	38.86%	0.66%	2.23%	0.94%	0.05%
		Ccp	0.01%	1.52%	0.02%	16.17%	87.31%	1.44%	0.43%	21.22%
		Sum	0.25%	20.92%	0.49%	95.73%	91.72%	4.51%	1.78%	21.30%
Stillwater Complex	Banded Series - Gabbro-norite II (N= 1)	Po	1.22%	1.48%	0.04%	17.02%	0.10%	0.30%	0.15%	0.00%
		Pn	4.55%	16.99%	55.07%	30.95%	0.16%	2.09%	0.18%	0.00%
		Ccp	8.52%	1.02%	3.17%	26.23%	25.90%	2.92%	1.23%	5.31%
		Sum	14.29%	19.49%	58.28%	74.21%	26.16%	5.30%	1.56%	5.32%